Time-Dependent Strength Gain in Recently Disturbed Granular Materials

by

David A. Saftner

A dissertation submitted in partial fulfillment
of the requirements for the degree of
Doctor of Philosophy
(Civil Engineering)
in The University of Michigan
2011

Doctoral Committee:

Professor Roman D. Hryciw, Co-Chair
Associate Professor Russell A. Green, Co-Chair, Virginia Tech
Associate Professor Jerome P. Lynch
Associate Professor Nilton O. Renno
Assistant Professor Adda Athanasopolos-Zekkos

To Missy, Sam, and Pete, the best family a person could hope to have.

Acknowledgements

I am very thankful to have been able study under my co-advisors, Professors Russell Green and Roman Hryciw. Their mentorship throughout graduate school has been instrumental to the success of this project and will continue to improve my life long after graduation. Their encouragement, dedication, and guidance have greatly increased my professional abilities and provided an example that I will strive to follow.

I would like to thank my dissertation committee, Professors Jerome Lynch, Adda Athanasopoulos-Zekkos, and Nilton Renno. Each has improved the quality of this work and has better prepared me for future endeavors.

Throughout my time at the University of Michigan, I received outstanding support and I would like to specifically thank the following people. Professor Richard Woods provided excellent advice on instrumentation, data acquisition, laboratory testing, and engineering practice. Jan Pantolin kept field and laboratory equipment running, improved the testing plan, and made the eight hour drive between Ann Arbor and Griffin pass quickly. Bob Fischer built a large amount of equipment that was vital to the field instrumentation and laboratory experimentation programs. Dr. Yongsub Jung deserves special thanks for his efforts during field testing, sacrificing his personal time for the good of my research, and for being an excellent officemate. I would like to thank Dr. Andy Zimmerman and Dr. Andrew Schwartz for their help and dedication teaching me data acquisition and ensuring field data acquisition went smoothly. Mulzer Crushed Stone, Inc. and Pioneer Seed provided their land for the field experimentation. Chris Stone and Bob Lingerfelt of Mulzer Crushed Stone, Inc. donated a great deal of their personal time. The outstanding people I served with in the 4th Engineer Battalion shaped the way I approach my professional life and I would like to thank them.

This work was partially funded by NSF NEESR-II grant CMMI 0530378. The University of Michigan's Rackham Graduate Fellowship, the American Society of Engineering Education and Department of Defense's National Defense Science and Engineering Graduate Fellowship, and the Federal Emergency Management Agency and Earthquake Engineering Research Institute's

National Earthquake Hazard Reduction Program Graduate Fellowship also supported my graduate studies.

I owe a special thanks to my family. My siblings, Lori, Matt, and Steve, helped make my childhood enjoyable and have been treasured friends in adulthood. My parents, Donald and Joyce, instilled in me morals, confidence, and a love of learning that lead directly to any success I have enjoyed both in this project and in life in general. I cannot express my appreciation for their sacrifices and efforts throughout the years.

My sons, Sam and Pete, make my life fun and keep me focused on what it truly important. Finally, and most importantly, I would like to thank my wife, Missy. She is the best person I have ever met and this work could not have been attempted without her support.

Table of Contents

List of Tables

List of Figures

Chapter 1

Introduction

1.1 Objective of Research

Following remedial densification to increase strength or reduce liquefaction potential of loose sand layers, minimum metrics from *in situ* geotechnical tests are generally established to confirm the improvement. However, experience has shown that *in situ* test results change with time after a disturbance, demonstrating that both the *in situ* test results and time play an important role in quantifying the improvement. The goal of this research is to develop predictive methods to account for time-dependent changes to *in situ* geotechnical test results in recently disturbed sand.

1.2 Background and Approach to the Problem

Because of existing infrastructure, new construction projects are increasingly planned on sites that would previously not have been chosen for development, i.e. loose sand deposits such as alluvium and hydraulic fills. These sites are at higher risk of liquefaction during earthquakes. Liquefaction is a phenomenon that occurs in loose, saturated sand under rapid loading, such as earthquake shaking. Loose sands tend to contract during shearing; however, when the loading occurs quickly, the pore fluid does not have an opportunity to drain and allow contraction of the soil skeleton. As a result, the pore fluid pressure increases, decreasing the soil's effective stress. This is particularly damaging because both deformation and soil strength are controlled by effective stress. As the soil loses strength during liquefaction, surface structures tend to sink, while buried structures can even rise. Although liquefaction is temporary, lasting seconds to hours depending on the site conditions, it contributes greatly to damage caused during earthquakes.

Techniques for mitigating liquefaction risk have been developed over the years. Because dense sands do not demonstrate the contractive behavior that leads to liquefaction, one approach to mitigate liquefaction is to increase the soil density. Examples of remedial densification methods include explosive densification, vibro-compaction, impact piers, and deep dynamic compaction. In order to assure successful treatment, *in situ* geotechnical tests, such as the standard penetration

test (SPT), cone penetration test (CPT), dilatometer test (DMT), and shear wave velocity (V_s) measurements, are conducted and used in quality assurance (QA) metrics. Previous research has provided several methods of using *in situ* test results to estimate both density and liquefaction resistance.

However, experience has shown that, following a disturbance such as produced by an earthquake, or following deposition of fill, or after remedial densification, *in situ* test results change with time. The monitoring of *in situ* test results following remedial densification provided the first evidence of a phenomenon now commonly called "sand aging." Sand aging is the time-dependent strength and/or stiffness gain in recently disturbed granular deposits. A manifestation of sand aging is shown graphically in Figure 1-1. In this case, vibro-compaction was used to densify hydraulic fill in order to expand the Chek Lap Kok Hong Kong airport (Debats and Sims, 1997). While vibro-compaction did cause an increase in penetration resistance, CPT results taken two weeks following vibro-compaction were generally below the minimum acceptable target CPT tip resistance (q_c). However, tests performed six weeks after densification yielded results, for the most part, above the QA metric despite no additional soil improvement efforts or additional settlement. The difference between the two week CPT results and six week CPT results demonstrates the crux of sand aging.

Sand aging has historically been recorded following man-made disturbances. Soil improvement projects, using disturbance methods such as explosive densification, vibro-compaction, and deep dynamic compaction, make up the majority of documented *in situ* sand aging case histories. However, aging has also been recorded following fresh deposition of cohesionless soils (Mitchell and Solymar, 1984). Examples include increasing q_c and V_s following hydraulic deposition of fill and of mine tailings. Additionally, a variety of laboratory tests, including cyclic triaxial tests, direct shear tests, and resonant column tests, on reconstituted specimens have also provided evidence of sand aging (Seed, 1979; Daramola, 1980; Thomann, 1990). The wide range of conditions under which sand aging has occurred and the magnitude of the changes to soil properties demonstrate that the phenomenon is not simply an academic curiosity, but has the potential to impact a wide array of geotechnical applications. A better understanding of sand aging could lead to better designed densification programs, which would both decrease cost of construction and improve public safety.

A majority of the research on sand aging has focused on determining the mechanisms that drive the phenomenon. A chemical mechanism was the first to be proposed (Denisov and Reltov, 1961;

Mitchell & Solymar, 1984). As silica and carbonate precipitates from the pore fluid, cementation forms between sand grains, increasing a soil's strength and stiffness. A mechanical mechanism was also proposed (Mesri et al., 1990; Schmertmann, 1991) where individual particle reorientation and asperity shearing or crushing leads to a stronger soil skeleton without causing measureable density changes. Additionally, dissolution of bubbles introduced in the pore fluid through either blast gases generated during explosive densification or compressed air/water used to insert a vibro-flot in vibro-compaction would cause local voids to collapse and led to a transition into a stronger soil packing with time (Dowding and Hryciw, 1986). Furthermore, biological activity could change the pH level of the pore fluid, making precipitation and other chemical processes more likely (Mitchell and Santamarina, 2005). While it is likely that a combination of these mechanisms influence the aging behavior, the mechanical mechanism is widely accepted as the dominate mechanism.

Though still not completely defined, the mechanisms controlling sand aging are better understood as a result of research performed in the past three decades. However, comparatively little research has been performed on predicting sand aging. As shown in Figure 1-1, the most common way of dealing with sand aging is to allow time for aging to occur, then performing *in situ* testing to quantify improvement. An aging correction factor would prevent delays in construction that can result from this waiting time. Four such methods of predicting increases in penetration resistance have been proposed (Schmertmann et al., 1986; Mesri et al., 1990; Charlie et al., 1992; Joshi et al., 1995). While more aging predictive methods have been developed for changes in stiffness and liquefaction resistance, this dissertation will focus on penetration resistance because QA metrics for soil improvement projects are most often based on penetration resistance.

Schmertmann et al. (1986) based their prediction method on data collected from a pilot improvement project at a specific job site. While this method predicted aging at this site very accurately, it is not as accurate when applied to other sites. Joshi et al. (1995) developed their method under the assumption that pore fluid chemistry controls sand aging. While this method may accurately describe the effects of pore fluid on aging, it does not account for the other factors that influence overall behavior of the soil system. Both Mesri et al. (1990) and Charlie et al. (1992) propose relationships that include empirical constants that account for differences in soil properties at varying sites and differences in disturbance methods. The difficulty that arises when applying these prediction methods comes in values for these constants. Even when considering a single disturbance method, such as explosive densification, the values of these empirical

constants vary a great deal due to differing site conditions. Therefore, the validity of the calibration constants for other sites is uncertain.

Multiple improvement methods are rarely performed on a given deposit because a single method is usually more economical. This is unfortunate because it is difficult to separate differences in aging due to soil mineralogy, grain size distribution, shape, etc. and differences in aging due to disturbance method. Therefore, the project described in this dissertation performed two different disturbance methods at the same field site, a third disturbance method at a separate field site, and also included a laboratory test program on soil taken from the both field sites. Accordingly, it would be possible to isolate the effects of disturbance method on aging. Similarly, by using the same soil from a site in laboratory experiments, it was possible to compare the field aging results to laboratory aging. By applying the lessons learned in this research to the information available from previous sand aging studies, a prediction method could be developed that would account for disturbance method, soil mineralogy, grain size distribution, and other factors. By using factors that would be determined in a typical geotechnical investigation, this method would represent an improvement to previously developed approaches because it would be based on a wider database and would be applicable to wider range of conditions.

1.3 Organization of the Dissertation

The main focus of this dissertation is the development of a method of predicting sand aging effects for a wide variety of conditions. Chapter 2 reviews previous work on time-dependent behavior in sands. Summaries of previous research projects and case histories are presented, providing evidence of the varying magnitudes of aging effects and the varying conditions under which aging was observed. While Chapter 2 includes a brief discussion of the mechanisms causing sand aging, the focus of this dissertation is on the development of a widely applicable aging prediction method. Therefore, the primary goal of the literature review is to determine what work has already been accomplished in the development of a predictive method and what improvements still need to be made.

Chapter 3 discusses the geostatistical methods that will be used to analyze the *in situ* data collected for this project. Geostatistics is a method of accounting for statistical data collected at different points in space or time. For general geotechnical use, this represents a method of describing spatial variability across a site. Specific to this project, geostatistics provides a means of demonstrating that the time-dependent changes to *in situ* test results are the result of the aging process rather than a function of spatial variability.

Chapter 4 concentrates on the explosive densification field test. It describes initial site investigation, blast design, instrumentation and data collection, implementation of the blast design, and post-blast testing. Results from *in situ* testing are presented and geostatistical analysis provides evidence that changes to *in situ* test results are due to aging and not spatial variability. A comparison of liquefaction risk calculated using different *in situ* tests is also provided.

Chapter 5 centers on field experiments using the Network for Earthquake Engineering Simulation (NEES) vibroseis. This chapter expands on the pre-disturbance site investigation described in the previous chapter. It also describes the NEES equipment, instrumentation and data collection, experimental design, experiment implementation, and post-shake testing. Experimental results and geostatistical analysis are presented.

Chapter 6 describes the field experiment using impact piers . This field experiment was conducted at a different field site than the other two experiments, so the results of the site investigation are presented. A description of the installation process, testing plan, experiment implementation and post-installation testing is provided. Experimental results and a comparison of liquefaction risk calculated using different *in situ* tests are presented.

Chapter 7 focuses on the laboratory testing. A significant portion of the laboratory testing program consisted of characterizing soil taken from the field sites. This allowed for comparison between aging effects recorded at this project's field site to those recorded in previous studies as a function of different soil properties. Cyclic triaxial tests were performed on soil samples from one field site and allowed to age for varying time periods prior to testing. Details and results of laboratory testing are presented in this chapter.

In Chapter 8, the results of this project's experiments are summarized and compared to aging effects from projects reported from previous studies. The methodology of creating a predictive aging predictive method is discussed. Finally, the method developed through this research is presented.

Chapter 9 discusses an interesting topic that is not central to the development of an aging prediction method, aged liquefaction resistance. Several methods of accounting for additional liquefaction resistance based on the geologic age of a deposit have been previously proposed. Based on the assumption that explosive densification disrupts a soil skeleton, one could use *in situ* test results recorded immediately following the blast to represent *in situ* results immediately following deposition. Using results recorded immediately following the blast to determine "fresh"

liquefaction resistance, results recorded one year after the blast to find liquefaction resistance one year after deposition, and results recorded before the blast to find the liquefaction resistance at the field site's geologic age, this chapter compares and discusses the various aged liquefaction resistance methods previously proposed.

Finally, Chapter 10 summarizes the dissertation. Conclusions and recommendations for future work are also included.

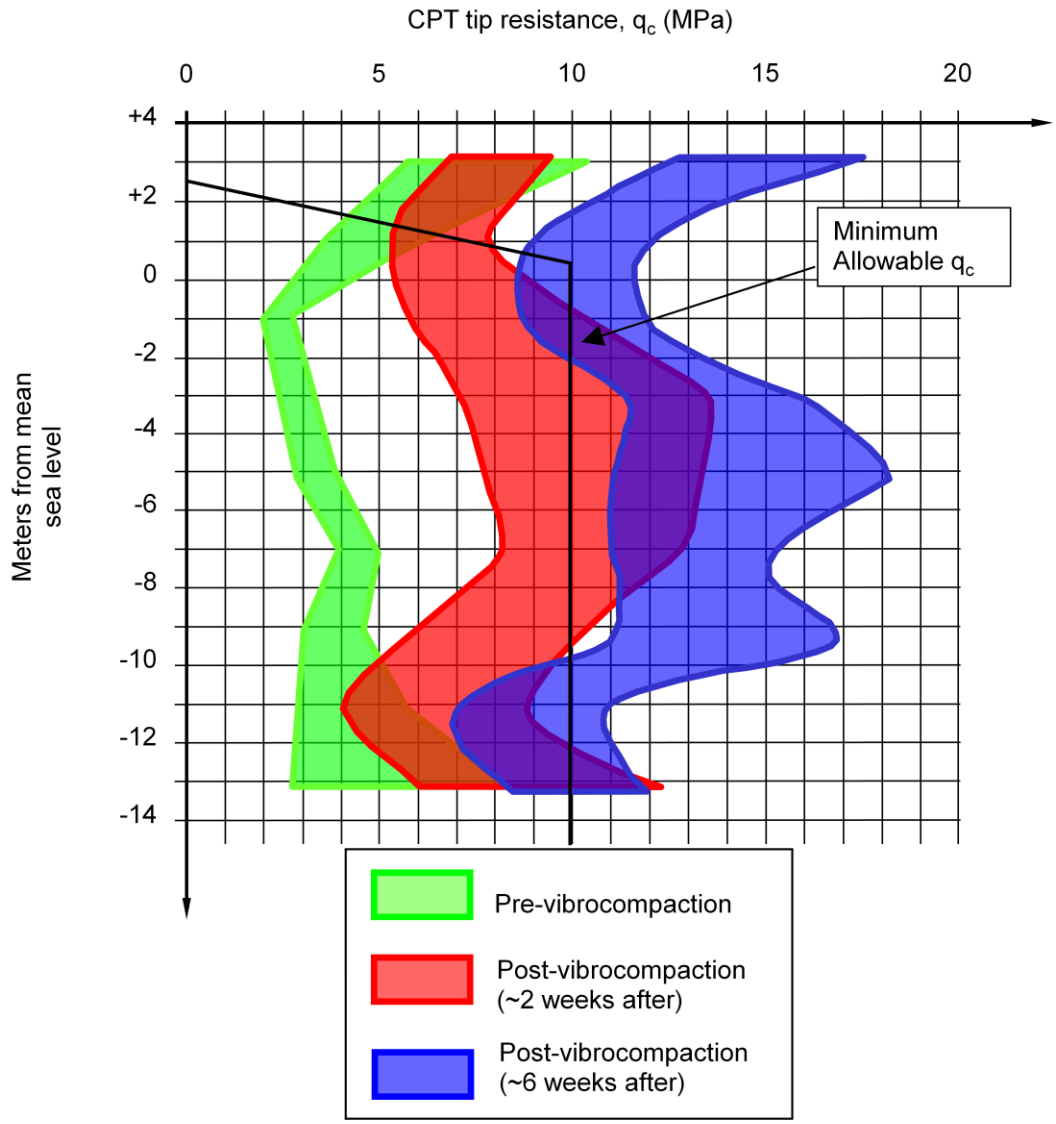

Figure 1-1. CPT tip resistance results from a vibrocompaction project on the Hong Kong airport expansion (adapted from Debats and Sims, 1997).

Chapter 2

Review of Sand Aging Literature

2.1 Introduction

Numerous case histories on sand aging and research studies focused on sand aging have been published. The object of this chapter is to summarize the available field and laboratory data documenting sand aging effects and to review previous work on sand aging prediction methods, with an emphasis on penetration resistance prediction methods. The intent of this review is to identify the areas where previously introduced prediction methods could be improved and develop a large database from which this dissertation's sand aging prediction method will be built.

The first section of this chapter will summarize previous observations of sand aging occurring for periods of weeks, months, and several years. These projects illustrate both the body of knowledge that motivated this study and populate a database that will be used to develop a predictive method later in the dissertation. Understanding the soil/site conditions and disturbance methods used in these projects is essential when comparing the aging effects of one project to another. This section summarizes 41 sand aging projects in preparation for development of a predictive sand aging method.

The majority of sand aging research has focused on the mechanisms behind sand aging, the second section of this chapter will summarize the different theories underlying the phenomenon. Four primary mechanisms have previously been proposed: a mechanical mechanism, a chemical mechanism, a dissolving bubble mechanism, and a biological mechanism. The mechanical mechanism is the most widely accepted mechanism; however, under the right circumstances, each of these mechanisms could affect sand aging behavior. It is important to understand the underlying causes of the phenomenon in order to determine which factors should be considered when developing a predictive method.

Previous research has not completely defined the mechanisms that drive sand aging; however, the phenomenon's underlying mechanisms are better defined than the phenomenon's effects. Several predictive methods have been proposed; however, allowing time for sand aging to manifest itself is the most common method of accounting for sand aging. Of the existing predictive methods, the first was proposed by Seed (1979) and deals directly with liquefaction resistance determined in laboratory tests. The relationships focuses on changes in shear modulus with time have also been proposed (Afifi and Woods, 1971; Anderson and Stokoe, 1978). However, because the most common geotechnical site investigation methods are performed using penetration resistance, this dissertation will focus on methods used to predict time-dependent increases in penetration resistance. The four previously proposed methods of predicting changes in penetration resistance with time are summarized in this chapter.

2.2 Overview of Previous Sand Aging Studies

Literature on the subject of sand aging has generally fallen into four categories: field projects, laboratory studies, modeling, and pile set-up studies. This section will summarize the lessons learned from projects in each of these areas.

2.2.1 Sand Aging Observed in Field Projects

A literature review conducted as part of this dissertation found 19 field projects that investigate sand aging. They will be reviewed in chronological order by publication date. A summary of the soil conditions in these projects is provided in Table 2-1, while the chemical composition, general description, and depositional details are provided in Table 2-2.

2.2.1.1 Hydroelectric Plant, Soviet Union (Denisov et al., 1963)

During construction of a factory and hydroelectric power plant along the Volga River in today's Russia, observations of increasing standard penetration test (SPT) blow count (N) with time were recorded in fill material. The fine to medium grained, clean, quartz sand was mined from the river and placed on site. As shown in Table 2-3, tests conducted 140 days following deposition showed that SPT-N had doubled from values observed immediately after deposition. This project also demonstrated the sensitivity of sand deposits following explosive densification. Blasts set off in these fill deposits resulted in a decrease in penetration resistance, showing that some aging effects had been destroyed in the disturbance.

2.2.1.2 Jebba Dam, Nigeria (Solymar, 1984; Solymar et al., 1984, Mitchell and Solymar, 1984, Mitchell, 1986a & 1986b)

In this project, the 42m high rock fill Jebba Dam dammed the Niger River two miles upstream from Jebba, Nigeria. The initial site investigation showed that the ~70m of sand on which the dam was to be built was highly variable and generally loose. Soil improvement was required to increase the relative density and, therefore, the liquefaction resistance of the deposit. Vibro-compaction was used to densify the upper 30m of the site. Because the equipment used to emplace the vibro-flot could not extend deeper than 30m, explosive densification was used between 30 and 45m.

Results of cone penetration tests (CPT) taken after explosive densification are shown in Figure 2-1. There was an immediate decrease in CPT tip resistance (q_c) followed by a time-dependent strength gain until tip resistance exceeded the desired values. No additional settlement was observed during the time between CPT soundings. As an experiment, a blast casing was vibrated into the ground, causing no measureable densification. CPT results after the casings insertion were lower than results prior to the insertion. CPT tip resistance eventually recovered to pre-disturbance levels. CPT results following vibro-compaction are shown in Figure 2-2. There was no initial loss of strength, but time-dependent strength gain was still observed. As shown in Figure 2-3, aging effects were also seen after deposition of fill at the site.

The greatest time-dependent changes occurred following explosive densification. Mitchell (1986b) hypothesizes that this is due to lower initial relative density in soils improved using explosive densification. Mitchell and Solymar (1984) proposed a chemical mechanism for the aging phenomenon, explaining that precipitation of silica or other materials from the pore fluid could cement particle contacts.

2.2.1.3 St. John's River Power Park Site, Florida (Schmertmann et al., 1986; Schmertmann, 1987; Schmertmann, 1991)

A coal-fired power plant was built between Jacksonville, Florida and the Florida coast. In order to avoid the cost of deep foundations, engineers planned to improve the loose sand, allowing it to support the heavy foundation loads from the power plant. The contractor on the project used deep dynamic compaction (DDC), a process where a large weight is repeatedly dropped on the soil surface in a regular pattern to densify it.

CPT and dilatometer testing (DMT) was performed to quantify the improvement. Figure 2-4 shows the aging effects following DDC. The upper layer show time-dependent changes for the first 50-60 days following disturbance. The lower layer, however, was not greatly affected by DDC and did not show aging effects. Figure 2-4 also shows that increasing the number of drops during DDC lead to greater aging.

Due to the knowledge acquired at this test site, Schmertmann et al. (1986) were able to determine the sand aging effects at the site. During the main improvement, if CPT results did not initially meet quality assurance (QA) standards, a time-improvement factor was applied to account for sand aging. Lessons from this project led Schmertmann (1991) to propose a mechanical mechanism for sand aging. He hypothesized that small slippage between particles would result in greater interlocking and a stronger soil skeleton.

2.2.1.4 Harriet's Bluff, Georgia (Hryciw, 1986; Hryciw and Dowding, 1988)

Harriet's Bluff is near the Atlantic coast in southeast Georgia. CPT and DMT results were used to study explosive densification as part of a field study designed to augment a larger laboratory study on this soil improvement method. As depicted in Figure 2-5, CPT results immediately following the blast show a drop in q_c. While this is typical in explosive densification projects, tests conducted 30 days following the blast did not show an improvement. Hryciw (1986) suggests that disruption of cementation could have caused the behavior.

2.2.1.5 Beaufort Sea, Canada (Jefferies et al., 1988; Stewart and Hodge, 1988; Rogers et al., 1990; Jefferies and Rogers, 1993)

Several islands were built using hydraulic fill in the Beaufort Sea north of western Canada. Following liquefaction of hydraulic fill during dynamic ice loading on several islands, explosive densification was used to densify the sand fill. As shown in Figure 2-6, there was little recorded change to CPT results with time following placement of hydraulic fill. However, Figure 2-7 shows that subsequent explosive densification caused an initial decrease, followed by time-dependent increase to q_c. Rogers et al. (1990) report that, in some cases, q_c more than doubled in the two weeks following explosive densification. Stewart and Hodge (1988) attribute the aging behavior to dissolution of blast gas and development of cementation.

2.2.1.6 Port Noire Harbor, Canada (Dumas and Beaton, 1988)

Hydraulic fill of medium to coarse sand was densified using DDC as part of construction of the Port Noire Harbor at Sept-Iles, Quebec. As pictured in Figure 2-8, Dumas and Beaton (1988) report that q_c did not decrease immediately following DDC and doubled within as little as 18 days. They also make the important observation that the magnitude of sand aging effects decrease with depth. Because the energy imparted to the soil from DDC also decreases with depth, they hypothesize that aging increases with increasing disturbance.

2.2.1.7 Fort McMurray, Canada (Handford, 1988)

This project focuses on the use of explosive densification to improve an oil-sand mine tailings dam's liquefaction resistance. As shown in Figure 2-9, SPT-N increased from pre-blast values within days of explosive densification. Tests conducted 45 days after explosive densification showed continued improvement.

2.2.1.8 Douglas Lake, Michigan (Thomann, 1990; Thomann and Hryciw, 1992a & 1992b)

Thomann and Hryciw (1992a) conducted a field aging study at the University of Michigan Biological Station at Douglas Lake in northern Michigan. Explosive densification was employed in a medium to fine sand layer; however, a down-hole nuclear device showed no change in the soil's density. This was confirmed by the lack of surface settlements. CPT q_c, shown in Figure 2-10, did not change with time following the blast and there was no trend to V_s data obtained using the seismic cone penetration test (SCPT), as pictured in Figure 2-11. Demonstrated in Figure 2-12, an interesting result is that DMT results showed no increase in horizontal stress. While these results could be interpreted as evidence opposed to Schmertmann's (1991) mechanical mechanism for aging, Thomann and Hryciw (1992a) point out that the disturbance caused by inserting the DMT blade may decrease its ability to detect changes. Thomann and Hryciw (1992a) hypothesize that because the sand at Douglas Lake did not increase in density, aging beyond the initial values of q_c, V_s, and DMT indices was not possible.

2.2.1.9 Fort McMurray, Canada (Fordham et al., 1991)

Fordham et al. (1991) describe a second project designed to decrease the risk of liquefaction in oil sand tailings near Ft. McMurray, Canada through the use of explosive densification. They recommend developing a site specific blast design and tested several designs on a portion of the tailings dam. As shown in Figure 2-13, CPT results initially failed to meet the minimum tip

resistance requirements. However, sand aging effects increased the tip resistance at each test site to acceptable levels within four months. This project was conducted in the same area, but by a different company and on a different tailings dam than the other Fort McMurray project described in Section 2.2.1.7.

2.2.1.10 South Platte River, Colorado (Charlie et al., 1992a & 1992b)

In this project, Charlie et al. (1992b) used explosive densification to disturb a site along the South Platte River near Greely, Colorado that contains poorly graded, dense sand. Because the sand layers were initially dense, CPT q_c following the blast was significantly less than prior to the blast. As shown in Figure 2-14, CPT results from 18 weeks after the blast show an increase when compared to tests immediately following the blast, but the site never aged to a point where q_c returned to pre-blast values. Charlie et al. (1992b) propose that temperature plays a role in the aging process, supporting a chemical mechanism that drives the aging process. They show a trend where soils located in warmer climates demonstrate greater aging effects. While the discussion to the original paper makes some adjustments to the proposed relationship (Jefferies and Rogers, 1993), the trend of increased aging effects with increased temperature remained the same after the adjustment.

2.2.1.11 Sainte Marguerite Dam, Canada (Wheeler, 1995)

Wheeler (1995) describes an explosive densification project designed to increase liquefaction resistance of a dam northwest of Sept Iles, Quebec. As pictured in Figure 2-15, q_c fell immediately after the blast, but after 35 days of aging, q_c had increased 60% from its initial values.

2.2.1.12 Chek Lap Kok Airport, Hong Kong (Ng et al., 1996; Debats and Sims, 1997; Covil et al., 1997)

Hydraulically filled marine sand was placed in order to expand the Chek Lap Kok Airport in Hong Kong. All three of the afore mentioned papers report aging following vibro-compaction designed to densify the very loose fill material and allow for construction of the airport. Covil et al. (1997) also document the fill material demonstrating sand aging behavior following deposition. As shown in Figure 1-1, after initially failing to meet QA metrics, penetration resistance increased to acceptable levels.

One interesting note on this project is that, due to the deposition process, fine grained lenses formed in the fill material. Debats and Sims (1997) believe that these layers may have prevented quick dissipation of excess pore pressures that typically occur in clean sands. They therefore propose that excess pore pressure dissipation may play a greater role at this site than in other sand aging case histories.

2.2.1.13 Treasure Island, California (Rollins et al., 2000; Ashford et al., 2004)

Field tests were performed at the National Geotechnical Experimentation Site on Treasure Island, located in the San Francisco Bay, California. They were designed to test pile performance during liquefaction. Rollins et al. (2000) and Ashford et al. (2004) conducted CPT before and after inducing liquefaction using explosive densification. As pictured in Figure 2-16, tests run 42 days following the blast showed that CPT q_c had doubled compared to pre-blast values and was 2.5 times greater than observed immediately after the blast.

2.2.1.14 Cooper River Bridge, South Carolina (Brown and Camp, 2002; Camp, 2004; Camp et al., 2008)

Camp et al. (2008) discuss the results of a blast induced liquefaction test near the Cooper River Bridge in Charleston, South Carolina. CPT results from before and after the blast show a decrease in q_c. As shown in Figure 2-17, post-blast testing occurred immediately after the blast, one month following the blast, and seven years following the blast. Because CPT results immediately after the blast were conducted prior to dissipation of excess pore pressure, comparing these results to tests at one month and seven years is problematic; however, the lack of aging between one month and seven year testing is an important observation.

2.2.1.15 Fraser River, Canada (Howie and Amini, 2004)

Howie and Amini (2004) compare SCPT results using the pseudo-interval and interval methods, using the penetration of the cone as a disturbance. The interval SCPT test uses two accelerometers and is able to measure arrival time of the same shear wave at two different depths. The pseudo-interval test uses one accelerometer in the cone and depends upon the generation of a new shear wave at each depth to find V_s in a layer. Howie and Amini (2004) pushed the seismic cone to a given depth and monitored V_s with time after penetration stopped. While the interval test did not show time effects, results from the pseudo-interval test, pictured in Figure 2-18, showed increasing V_s with time. The interval test results did not change with time because each accelerometer was equally affected by the time-dependent changes in the surrounding soil. The

pseudo-interval test was more affected by disturbed soil. Howie and Amini (2004) recorded time-dependent changes to V_s up to an hour after pushing the cone.

2.2.1.16 Mississippi Embayment, Arkansas and Tennessee (Liao and Mayne, 2005)

Liao and Mayne (2005) set off large blasts deep in a thick layer of clean, quartz sand as part of the Mississippi Embayment Seismic Excitation Experiment (ESEE). Two sites were used; both near the boot heal of Missouri in the New Madrid seismic zone: Marked Tree, Arkansas and Tiptonville, Tennessee. Using one borehole in Marked Tree and two boreholes in Tiptonville, Liao and Mayne (2005) loaded 1180 kg of ammonium nitrate in the upper 24.4 m of each borehole. At both sites, SCPT tests performed before, 2 days after, and 229 days after the blast showed a drop in q_c and V_s following the blast with no time-dependent recovery. Results from the Marked Tree, Arkansas site are shown in Figure 2-19.

2.2.1.17 Charleston, South Carolina (Narsilio, 2006; Bachus et al., 2008; Narsilio et al., 2009)

This explosive densification project was performed approximately 35 miles west of Charleston, South Carolina. Settlements were recorded both at the surface using topographic measurements and with depth using settlement tubes. These measurements showed that a great majority of the settlement occurred within the first 24 hours after blasting (Bachus et al., 2008). However, spectral analysis of surface waves (SASW) analysis showed that the V_s increased with time beyond the time where settlement was occurring (Narsilio, 2006), as shown in Figure 2-20. As pictured in Figure 2-21, q_c was initially lowered, but eventually showed an increase approximately one year following the final blast.

2.2.1.18 Wildlife Site, California (Holzer and Youd, 2007)

While Holzer and Youd (2007) did not publish these specific results until 2007, the work for this study was performed four and a half months after the 1987 Superstition Hills earthquake. In preparation for placing the array at the site, CPT results were recorded as part of a site investigation prior to instrumenting this geotechnical test site. Following the earthquake, three CPTs were performed within 1 m of each of the pre-earthquake CPTs. The results of these tests are presented in Figure 2-22. There is no obvious sign of change in q_c readings.

2.2.1.19 Massey Tunnel, Canada (Rollins and Anderson, 2008)

Rollins and Anderson (2008) used drains in an attempt to dissipate the excess pore pressure that leads to liquefaction in their experiment south of the Massey Tunnel near Vancouver, British

Columbia. Explosives were used to generate excess pore pressures and the drains did not prevent liquefaction. However, explosive densification generates excess pore pressures very quickly. Drains may be more effective in dissipating pressures that build more slowly, following an earthquake, for example. In terms of aging, this project is interesting because sand aging was observed following insertion of the drains and following explosive densification. The CPT results from this project also demonstrate variability. As shown in Figure 2-23, there is not a consistent trend with time in tests performed 7, 14, 28, and 56 days following the blast; however, a clear difference between pre- and post-blast CPT results can be made.

2.2.2 Sand Aging Observed in Laboratory Studies

A literature review conducted as part of this dissertation found 16 laboratory studies that investigate the sand aging phenomenon. They will be reviewed in chronological order by publication date. A summary of soil conditions in these projects is provided in Table 2-1 while the chemical composition, general description, and depositional details are provided in Table 2-2.

2.2.2.1 Vibrating Plate Experiment (Denisov and Reltov, 1961)

As illustrated in Figure 2-24, Denisov and Reltov (1961) placed sand grains on a glass plate and, after allowing the grains to sit for a given time period, recorded the shear force required to displace the grains. As shown in Figure 2-25, the force required to move the grains increased with time, up to 14 days. Denisov and Reltov (1961) hypothesize that silica acid gel films cement the particle to the glass plate and cause the aging phenomenon.

2.2.2.2 Resonant Column Tests Using Ottawa and Agsco Sand (Afifi, 1970; Afifi and Woods, 1971; Afifi and Richart, 1973)

In these experiments, medium-grained sand, fine-grained sand, silt, and clay were tested in a resonant column device. Afifi and Woods (1971) showed that changes to void ratio could not account for increases in V_s, an indication that aging, a previously unaccounted for factor, played an important role in sand behavior. As demonstrated in Figure 2-26, they also showed that the relationship between V_s and the logarithm of time could be accounted for with two lines, intersecting at 1,000 minutes. Even considering these results, they suggest that relationships predicting shear modulus using confining pressure and void ratio proposed by Hardin and Richart (1963) are still valid for most engineering applications.

2.2.2.3 Resonant Column Tests Using Ottawa, Agsco, and Quartz Sand (Anderson and Stokoe, 1978)

Anderson and Stokoe (1978) conducted resonant column tests on many types of soil, including the coarse grained soils mentioned in the title of this subsection. They found that, in terms of V_s increase with time, fine and coarse grained soils behave similarly during secondary consolidation. An example of their findings using Ottawa sand is presented in Figure 2-27. Their work shows that time effects in uniform coarse grained soils are independent of grain size for sands with mean grain size (D_{50}) greater than 0.05mm. They also propose a method of accounting for the change in soil stiffness with time which is discussed in more detail in Section 2.4.2.2.

2.2.2.4 Triaxial Tests Using Ham River Sand (Daramola, 1980)

Daramola (1980) ran triaxial tests on four samples of Ham River sand prepared at the same density. One was tested immediately and the others were aged for 10, 30, and 152 days, respectively. As shown in Figure 2-28, the 10 day sample behaved similar to the fresh sample, while the other samples showed increased stiffness and decreased strain to failure. Daramola (1980) proposed a relationship for increases to Young's modulus, *E*, with time, which predicts roughly a 50% increase in *E* during every log cycle of time.

2.2.2.5 Penetration Resistance Tests Using Evanston Beach Sand (Hryciw, 1986; Dowding and Hryciw, 1986)

Dowding and Hryciw (1986) used blasting caps embedded in a liquefaction tank to simulate explosive densification in the field, recording penetration resistance before the blast and with time following the blast. Results from these tests are presented in Figure 2-29. A drop in penetration resistance was recorded after the blast followed by time-dependent increase in penetration resistance. Hryciw (1986) also monitored penetration resistance with time following deposition with no blast disturbance. This test also showed aging, but a lesser magnitude. One important aspect of this study is recognition of the importance of spatial variability. Dowding and Hryciw (1986) ran enough penetration resistance tests to quantify the spatial variability of penetration resistance tests prior to the blast. This allowed them to demonstrate that the differences in penetration resistance with time were due to aging, and not simply variations due to spatial variability.

Dowding and Hryciw (1986) also proposed that dissolution of bubbles contributed to aging. They observed that, while liquefying the sand in the tank in order to begin another test, bubbles escaped

from the blast area 15 days after the previous blast. The presence of these bubbles showed that blast gas remained in the sand voids long after the blast. Bubbles create large local voids over which the surrounding sand would arch, creating an overall weaker soil skeleton that would strengthen with time as the bubbles dissolved into solution.

2.2.2.6 Oedometer and Triaxial Tests Using Ottawa and Brenda Mine Tailings Sand (Mejia et al., 1988)

Mejia et al. (1988) ran 1-D oedometer and triaxial tests to determine deformation behavior of sands with time. After monitoring creep of Ottawa and Brenda Mine tailings sand for 20 minutes, as pictured in Figure 2-30, they determined that creep increases as stress ratio increases and decreases as relative density increases.

2.2.2.7 Resonant Column Tests Using Agsco and Ottawa Sands (Thomann, 1990; Thomann and Hryciw, 1992a; Hryciw and Thomann, 1993)

Thomann and Hryciw (1992a) discuss their tests on two sand types using a quasi-static torsional shear resonant column device. After preparing the samples isotropically and allowing them to consolidate for at least 24 hours, recording shear modulus with time, they subjected the samples to varying levels of strain, from 10^{-4}% to 10%. As typical results shown in Figure 2-31 demonstrate, they found the shear strain amplitude governed both the initial decrease in shear modulus, *G*, and the time-dependent increase in *G* following the disturbance. Confining stress played a minor role and the number of cycles at a given shear strain amplitude was nearly meaningless. This study was important because it demonstrated that one can expect greater aging effects following greater disturbances.

2.2.2.8 Direct Simple Shear Tests Using Holliston Sand (Miller, 1994)

Miller (1994) created a direct simple shear device in order to study aging effects on the small strain behavior of sands. These experiments showed a small increase in *G* in samples aged for 7 to 8 weeks compared to fresh samples. Additionally, threshold strain, the strain required to begin producing excess pore pressure in undrained conditions, was found in increase with age.

2.2.2.9 Penetration Resistance Tests Using River and Beaufort Sea Sands (Kaniraj et al., 1991; Joshi et al., 1995)

Joshi et al. (1995) prepared five different samples in PVC pipes and pushed four probes into each at various times following sample preparation. Three samples contained river sand, one each in

dry conditions, saturated with distilled water, and saturated with sea water, while two samples contained Beaufort Sea sand, one each saturated with distilled water and saturated with sea water. Results from river sand saturated in distilled water are shown in Figure 2-32. Saturated samples showed more aging effects than the dry sample and river sand showed more aging effects than Beaufort Sea sand. At each test period, Joshi et al. (1995) would push the probes ~2 mm, than leave the probes in place until the following test. In pilot studies, they found that previous probe advancements did affect subsequent probe advances compared to tests where the probe was advanced without stops. In addition, the differences in penetration resistance following aging exceeded the differences that were due only to stopping the probe during advancement.

The authors proposed that because Beaufort Sea sand is more rounded, it offered less frictional resistance following reorientation and did not age as much as the more angular river sand. They additionally hypothesize that water aids in generation of precipitates. Scanning electron microscope (SEM) photographs show precipitates on sands aged in both distilled and sea water, with more precipitates on sands aged in sea water. However, inspection of the samples after aging showed that the bonds were weak. Given this evidence, the authors propose that particle reorientation was the dominate mechanism with cementation playing a minor role. They also propose a predictive method for penetration resistance based on the type of pore fluid and time under which the soil is aged.

2.2.2.10 Penetration Resistance Tests Using Evanston, Density, and Lighthouse Sands (Mitchell et al., 1997; Baxter, 1999; Baxter and Mitchell, 2004)

Baxter and Mitchell (2004) set up soil samples in rigid walled containers using the three above mentioned sands prepared using several different pore fluids, relative densities, and temperatures in an experiment designed to study the chemical mechanism behind sand aging. They monitored V_s, mini-cone penetration resistance, SEM pictures, and electronic conductivity of the pore fluid. The experiment found a small increase in V_s with time in the majority of samples, as shown in Figure 2-33. Baxter (1999) offers the fact that the arrival time of the shear wave in fresh and aged samples differed by only ~0.02 msec as an explanation for the few samples that did not show a time-dependent increase in V_s. However, Figure 2-34 shows that mini-cone penetration did not increase with time in these samples. Baxter and Mitchell (2004) mention that the rigid walled containers may have been too small in diameter and could have affected the penetration resistance. However, because the same system was used in fresh and aged samples, it is presumed that any changes in penetration resistance due to aging would still have been observed despite the

possibility of the rigid wall's influence on penetration resistance. A major conclusion of this study focuses on the chemical mechanism of aging and will be discussed in more detail in a later section of this literature review.

2.2.2.11 Creep Tests Using Antelope Valley and Crushed Coral Sand and Glass Beads (Lade and Liu, 1998; Lade et al., 2009; Lade and Karimpour, 2010)

In separate studies, Lade and Liu (1998) and Lade et al. (2009) studied creep effects on Antelope Valley sand and crushed coral sand, respectively. Figure 2-35 shows typical creep results for crushed coral sand. In both cases, strain rate did not affect creep results, a significant difference from the behavior of clays. Lade and Karimpour (2010) attribute this behavior to static fatigue. They propose that particle breakage could explain the results from these tests. To support this hypothesis, the static fatigue of glass beads was studied. While there was great variability in the results of the glass bead tests, the authors propose that, when averaged over a large assembly of particles, the static fatigue behavior would become more predictable, as was the case in earlier experiments on Antelope Valley and crushed coral sand.

2.2.2.12 Sliding Plate Tests Using Glass Beads (Losert et al., 2000)

Losert et al. (2000) describe an experiment where an acrylic plate was pushed over a layer of glass beads. After initially shearing the glass beads by displacing the plate, they monitored the force required to shear the beads again after a period of aging. They found that, when load was not maintained following the initial shearing, there was no time-dependent strengthening in the material. However, as shown in Figure 2-36, when load was maintained following initial shearing, the material showed strengthening that was linear with the logarithm of time. Additionally, they found that the strengthening of material saturated in water was nearly three orders of magnitude greater than the strengthening of dry material. Losert et al. (2000) suggest that the mechanism that best explains this behavior is spatial arrangement of the beads and arrangement of the micro-contacts resulting in greater contact area.

2.2.2.13 Triaxial Tests Using Fraser River Sand (Howie et al., 2001a & 2001b; Howie et al., 2002)

Howie et al. (2002) ran triaxial tests on loose Fraser River sand and monitored V_s with time. While recording time-dependent stiffness increases, they found that stress ratio played a significant role in aging effects. When higher stress ratios were used, stiffness increased more

with age. As shown in Figure 2-37, this work showed V_s increasing linearly with the logarithm of time.

2.2.2.14 Triaxial Tests Using Leighton Buzzard and Montpellier Sands and Glass Beads (Bowman, 2002; Bowman and Soga, 2003; Bowman and Soga, 2005)

Bowman and Soga (2003) measured creep through axial and radial strain in several triaxial tests at various stress paths during the aging period. Typical results from these tests are presented in Figure 2-38. They found that dense sands show greater aging effects because they are more capable of maintaining strong force networks that develop during aging. Weaker particles age less because breakages decrease the number of particle contacts and interlock. Similar to Howie et al. (2002), Bowman and Soga (2003) also found that greater stress ratios lead to greater aging effects. These results inspired a microscopic investigation of aging. The details and results of this study will be discussed in more detail in Section 2.3.2.

2.2.2.15 Triaxial Tests Using Ottawa Sand (LeClerc, 2008)

LeClerc (2008) studied gas dissipation and its effect on aging through triaxial tests on samples of Ottawa sand prepared to 50% and 80% relative density using air and CO_2 to make these samples partially saturated. Air was used to simulate conditions following vibro-compaction and CO_2 to simulate post-blast conditions. The 80% relative density samples did not age very much, while the 50% relative density samples showed a marked increase in strength and stiffness. Results from the 50% relative density using CO_2 are presented in Figure 2-39. The 50% samples aged two weeks behaved similar to the 80% samples. While this study found that the type of gas did not influence aging effects, the work shows that gas dissipation does contribute to aging.

2.2.2.16 Photo-Elastic Tests Using Glass Rods (Jirathanathaworn, 2009; Jirathanathaworn et al., 2010)

Jirathanathaworn et al. (2010) designed a system to measure changes in horizontal stress in an assembly of glass rods representing a 2-dimensional (2-D) soil assembly using photo-elasticity. As pictured in Figure 2-40, Jirathanathaworn (2009) found increases in horizontal stress with time in the majority of his tests. To overcome some of the variability in his results, Jirathanathaworn (2009) recommends using a larger specimen, allowing further study on the development and changes in force chains through the assembly.

2.2.3 Sand Aging Observed in Models

A literature review conducted as part of this dissertation found two modeling studies that investigate the sand aging phenomenon. They will be reviewed in chronological order by publication date. A summary of soil conditions in these projects is provided in Table 2-1, while the chemical composition, general description, and depositional details are provided in Table 2-2.

2.2.3.1 Discrete Element Modeling with Resonant Column Tests (Wang et al., 2008; Wang and Tsui, 2008; Wang and Tsui, 2009)

Wang et al. (2008) report the results of a discrete element model (DEM) of sand aging. They ran three experiments each on dense and loose samples: a sample with no aging, a sample aged until there was a 1.7% decrease in porosity due to creep, and a fresh sample with the aged sample's porosity. They found higher strength and *E* in aged samples than either fresh sample. Most interesting however, was their finding that the contact stress had a smaller standard deviation in aged samples, suggesting that aging distributes contact stresses.

Wang and Tsui (2008 and 2009) used the results of resonant column tests on Ottawa and Toyoura sand to validate their DEM results. In their model, medium dense sands aged the most, while less aging occurred in dense and loose sands. An example of the results for dense Toyoura sand is presented in Figure 2-41. They suggested that dense sands already have a fairly uniform distribution of contact stress and are not greatly affected by aging, while loose sands are likely prone to local collapse. Their experiments also show that large strain shearing destroys any aging effects. While unloading also destroys the majority of time-dependent strength and stiffness gain, there is some locked-in aging that withstands loading-unloading cycles. Finally, they find that the addition of fines to clean sands increase the amount of creep and, therefore, the magnitude of aging effects.

2.2.3.2 Finite Element Modeling with Compression Tests (Ghiabi and Selvadurai, 2009)

Ghiabi and Selvadurai (2009) ran oedometric compression tests on glass beads. As shown in Figure 2-42, they found that the void ratio of the glass bead samples decreased during a 24 hour aging period following the application of load. Because the hydraulic conductivity of the beads is high, this behavior is attributed to mechanical rearrangement rather than pore pressure dissipation. The authors developed an ABAQUS finite element model (FEM) based on the theory of viscoplasticity and found that the model produced results in good agreement with the experimental results.

2.2.4 Pile Set-Up

Pile set-up is defined as a time-dependent increase in pile load capacity with time. A literature review conducted as part of this dissertation found four projects that document the pile set-up phenomenon. They will be reviewed in chronological order by publication date. A summary of soil conditions in these projects is provided in Table 2-1, while chemical composition, general description, and depositional details are provided in Table 2-2.

2.2.4.1 Several Sites, Denmark and Germany (Skov and Denver, 1988)

Skov and Denver (1988) report stress-wave analysis results taken during pile driving and after an aging period at sites in Alborg, Denmark, Hamburg harbor, Germany, Nykobing, Denmark, and Hamburg, Germany. The authors report an increase in bearing capacity predicted by the stress-wave methods in both sand and clay soils and attribute the pile set-up to pore pressure dissipation. Typical results are pictured in Figure 2-43. While the high hydraulic conductivity in sands makes this a more likely explanation in fine grained soils rather than course grained, these project case histories still provide excellent examples of the phenomenon.

2.2.4.2 Orsa, Sweden (Astedt et al., 1992)

Astedt et al. (1992) discuss increases in bearing capacity with time in piles driven into sand in Orsa, Sweden. Typical results are presented in Figure 2-44. Instrumentation near the piles demonstrates that these changes cannot be attributed to pore pressure dissipation because the excess pore pressure build-up was relatively small and short in duration. Additionally, they drove steel rods into the ground near the piles and witnessed similar set-up behavior. They recommend this as an inexpensive method of studying pile set-up in the future.

2.2.4.3 JFK Airport, New York (York et al., 1994)

York et al. (1994) present the results of test loading and dynamic measurements analyzed using the wave equation on piles driven during the expansion and modernization of JFK Airport in New York City. A summary of their results is provided in Figure 2-45. They monitored excess pore pressure generation and dissipation and determined that neither set-up nor relaxation can be attributed to changes in pore pressure. They attribute both set-up and relaxation to redistribution of stresses. In the case of set-up, more contacts, especially in dense, well-graded sands, lead to higher bearing capacity for piles, while locally high horizontal stresses that built up during pile driving in very dense sands relax with time. It is important to note that the strength gain reported

by York et al. (1994) is compared relative to the end of pile driving, so it includes both pile set-up and strength gain due to higher effective stresses after the dissipation of excess pore pressure.

2.2.4.4 Dunkirk, France (Chow et al., 1998; Jardine and Standing, 1999)

Chow et al. (1998) tested piles five years after they were initially installed in Dunkirk, France. A summary of their results and results from multiple studies reported in the literature is included in Figure 2-46. After comparing the results of these tests to test results from previous studies, the authors draw conclusions about the mechanisms behind pile set-up. They considered corrosion of the piles increasing the interface friction and, therefore, increasing bearing capacity. However, dynamic tests showed that the side friction gains were in portions of the piles that did not show corrosion. Additionally, non-corrosive materials also displayed pile set-up. They also considered an increase in shear modulus and friction angle with time as the cause of set-up. However, models show that this would affect smaller diameter piles more, a fact which is not born out in the literature. They propose that changes in the highly disturbed zone surrounding the pile are the major cause of pile set-up. Supported by observations that show no set-up in bored piles in sand, they hypothesize that creep in the disturbed area around the pile weakens the arching around that zone and increases radial stresses on the pile.

Jardine and Standing (1999) tested cyclic loading effects on pile capacity and developed an FEM capable of reliably demonstrating this behavior. However, of particular interest is the set-up they witnessed in their test piles placed in Dunkirk, France. Set-up was recorded for the first 100 days and slowed significantly after that. Additionally, the soil demonstrated a ductile response shortly after installation with a brittle response developing with time. These results are similar to other researchers' findings on stiffness increases with time in laboratory tests.

2.2.5 Variability in Geotechnical Engineering

Because soil is not a homogeneous material, spatial variability is an important consideration in most geotechnical applications. This is especially true in sand aging because test results from one time period are compared to results from another time period, with the difference being attributed to aging. When several tests are performed, as shown in Figure 1-1, one can qualitatively assess the spatial variability and determine with a reasonable degree of confidence that the changes in test results are time-dependent and not a function of spatial variability. However, when few tests are performed, it can be difficult to interpret if differences between tests are due to time or variability. For example, Figure 2-47 shows the results of laboratory penetration resistance tests

performed by Baxter (1999). Without considering the dashed lines that represent baseline tests on similarly prepared fresh samples, it appears that the penetration resistance increases with time in this sample. However, comparison of the aged results to the full range of fresh results show that all of the aged test results fall within the range of fresh results. Therefore, it is difficult to conclude that this sample experienced aging.

Several studies have attempted to quantify variability and lessen its impact on a project's uncertainty. One method of accomplishing this is through the use of geostatistics. Geostatistics was first developed for work in the mining industry in the 1950s. The basic premise of this statistical method is that measurements from locations closer to a point of interest better inform a prediction than measurements further away (Chiles and Delfiner, 1999). Using a method called kriging, which will be discussed in more detail in Chapter 3, one can estimate a property's value and error bound that accounts for the spatial distribution of the known data set. Several examples of the use of geostatistics in geotechnical engineering are provided in the following paragraphs.

2.2.5.1 SPT, Treasure Island, California (Parsons and Frost, 2002)

Parsons and Frost (2002) analyzed the quality of site investigation using geostatistics. They used an existing database of SPT results on Treasure Island, California and determined the risk of liquefaction in areas where no tests existed. Because extensive geotechnical testing has been performed on Treasure Island, they also examined the impact of fewer *in situ* tests on their analysis.

2.2.5.2 CPT, National Geotechnical Experimental Sites Database (Phoon et al., 2003; Phoon et al., 2004)

Phoon et al. (2003 and 2004) discuss the use of geostatistics in order to determine the boundaries between soil layers using CPT results. They provide evidence that this method is an improvement on the common practice of visually interpreting CPT logs in order to determine soil layering. Additionally, this method was demonstrated to be accurate even when visual clues to layering were not clear.

2.2.5.3 Soil Layering, Channel Tunnel (Hammah and Curran, 2006)

Hammah and Curran (2006) encourage greater use of geostatistics in geotechnical engineering, especially in site investigations. They summarize the use of geostatistics in the construction of the Channel Tunnel. A governing criteria in selecting tunnel alignment was locating the tunnel in

chalk marl and avoiding the neighboring layer of gault clay. A geostatistical analysis, based on a database that was updated throughout the project with new data from ongoing construction, accurately predicted the boundary between these layers and greatly eased construction.

2.2.5.4 Shear Wave Velocity, San Francisco Bay (Thompson et al., 2006)

Thompson et al. (2006) discuss the application of geostatistics at regional, rather than local, scales. Using SCPT results from across the San Francisco Bay area, they predicted V_s in the upper 10 m of soil across a greater than 100 km^2 area. Using their predicted V_s values and the September 5, 2003 Berkeley earthquake record, they were able to fairly accurately predict recorded ground motions. Thompson et al. (2006) acknowledge weakness the data feeding their predictions because SCPT results are not deep enough to characterize the shear wave velocity in the upper 30 m of soil and note that they plan to conduct another study once enough SASW data is available.

2.2.5.5 Liquefaction Resistance, Adapazari, Turkey (Baker et al., 2006; Baker and Faber, 2008)

Baker and Faber (2008) present the results of their geostatistical model predicting liquefaction under a portion of a neighborhood block in Adapazari, Turkey. They chose this location for demonstration purposes only and their method can be applied to any location. The geostatistical model they used is able to be applied to a variety of inputs and most of the paper focuses on the model inputs. Baker and Faber (2008) use an SPT-based empirical liquefaction relationship, several assumptions on the consistency of the *in situ* measurements, and a probabilistic seismic hazard analysis. However, the model they propose is adaptable to other methods of dealing with the inherent uncertainty of both the soil conditions between sampling points and the input motions. Baker and Faber (2008) demonstrate that geostatistics is a reasonable tool to help account for spatial variability in liquefaction analyses.

2.3 Overview of Proposed Sand Aging Mechanisms

The majority of the sand aging literature focuses on the mechanisms that control the phenomenon. While this dissertation focuses on sand aging effects, an understanding of mechanisms is required in order to determine the soil and environmental factors that influence aging and, therefore, should be included in a predictive method. There are four primary mechanisms that have been proposed to explain why sand aging occurs: chemical, mechanical, dissolution of bubbles, and biological mechanisms. This section will summarize the research on sand aging mechanisms.

2.3.1 Chemical Mechanism

The chemical mechanism explains sand aging through the precipitation of dissolved minerals, forming cementation between sand grains. This was first proposed by Denisov and Reltov (1961) following their vibrating plate experiments. This was also the mechanism proposed by Mitchell and Solymar (1984) in the first major field examination of the sand aging phenomenon to appear in American literature.

Charlie et al. (1992) studied aging following explosive densification at a field site in Colorado. In developing a method for predicting increase in penetration resistance, Charlie et al. (1992) noted that temperature seemed to affect the aging process, with warmer climates showing greater time-dependent increase in *in situ* test results. Temperature has a greater effect on chemical processes than mechanical processes, so this observation supports the theory that a chemical mechanism controls aging behavior.

Joshi et al. (1995) performed a laboratory study that proposed a chemical mechanism, in combination with other mechanisms, contributing to sand aging behavior. As evidence of cementation, they present SEM photographs of sand grains with precipitates at the contacts. They also found that there were more precipitates in samples aged in sea water compared to samples aged in distilled water.

More recently, Yun and Santamarina (2005) studied the effects of cementation on Nevada sand. The authors studied the effects of artificial cementation added to the sand, density, and vertical effective stress. Of these, cementation was by far the most influential factor in the soil's shear wave velocity. Similar findings were also reported by Acar (1987). As Yun and Santamarina (2005) point out, natural cementation affects soil deposits that undergo wetting-drying cycles, contact yield, and solution precipitation. While natural deposits may not become as cemented as the samples in these laboratory studies, for example, Yun and Santamarina (2005) studied samples that contained 2% and 4% Portland cement by weight, increasing cementation shows the same trends as natural deposits undergoing sand aging. This evidence supports the chemical mechanism by demonstrating that cementation can produce similar aging effects as those seen in the field.

Baxter (1999) designed a laboratory study designed specifically to study the chemical mechanism. Evanston Beach, Density, and Lighthouse sands were aged using four types of pore fluid: air, distilled water, distilled water saturated with CO_2, and ethylene glycol. Distilled water

was used as a control. Cementation is less likely in air rather than saturated materials, so the dry sample was included for comparison with a sample where chemical aging was not likely. Because CO_2 is a product of explosions, water saturated with CO_2 replicated pore fluid following blasting. The amount of CO_2 in solution in this study was unrealistically high compared to field cases following explosive densification, but a trend could be determined from this work. Water saturated with CO_2 has a lower pH, encouraging the dissolution of carbonates and therefore, chemical aging. Finally, the solubility of both silicates and carbonates are low in ethylene glycol, lowering the chance of chemical aging. The differences in these samples were designed to test impact that the chemical mechanisms impact the aging process.

However, the samples in this study did not show evidence of aging. Electrical conductivity tests on the pore fluid of the various samples showed interesting results. Evanston sand samples had the greatest changes in electrical conductivity because they have the greatest percentage of soluble fractions of the three sand types. As a result of the amount of dissolved ions, samples aged in CO_2 saturated water had the highest electrical conductivity, while ethylene glycol samples showed little change because silica and carbon were not dissolving into solution. Mineralogical tests showed that all of the samples aged in water were super-saturated with silica and the tests using Evanston beach sand aged in CO_2 saturated water at high temperatures were super-saturated with carbonates. Despite the conditions being right for the chemical mechanism, sand aging did not occur in these samples and SEM photographs showed no precipitation on the grains. In order to explain the different results between these photographs and those from Joshi et al. (1995), Baxter (1999) shows that samples that were not completely drained prior to SEM analysis did have precipitates on the sand grains.

In summary, it has been shown that precipitation of minerals and cementation at sand grain contact points does cause strength and stiffness increases. Also, the amount of cementation does increase with time under the right circumstances. However, the chemical aging mechanism does not explain all cases where sand aging has occurred. Additionally, Baxter's (1999) dissertation work showed that, even when conditions are right for mineral precipitation, chemical aging does not always occur.

2.3.2 Mechanical Mechanism

Schmertmann (1987 and 1991) and Mesri et al. (1990) were the first to propose a mechanical mechanism to explain the sand aging phenomenon. They propose that particle rotation and reorientation, as well as grain crushing and asperity shearing occur over time, leading to a more

efficient packing and stronger soil skeleton. Mesri et al. (1990) propose that increased micro- and macro-interlocking during secondary compression would lead to the strength and stiffness gains. They also point out that the sand aging phenomenon has been seen to occur faster than one can expect cementation to develop and that sand aging is seen in large strain tests where a brittle mechanism like cementation is unlikely to account for the magnitude of time-dependent changes. Evidence of sand aging in dry states has also led researchers to search for a non-chemical explanation.

Schmertmann (1991) used the IDS test, a special form of triaxial test, as evidence of mechanical aging. The "I" stands for the components of strength that are independent of effective stress, while the "D" stands for the components of strength that are dependent on effective stress. This test is explained in Figure 2-48. In Figure 2-48(a), one can see a method of creating two soil samples under different effective stresses but with similar soil structures due to the negligible change in void ratio. These two samples would then be subjected to triaxial testing, while maintaining constant major principal effective stress by changing pore pressure as deviator load is added. As shown in Figure 2-48(b), the sample with high effective stress would have higher strength at all strains. From this information, one could construct the Mohr-Coulomb envelope seen in Figure 2-48(c). Considering several strain levels allows one to create the graph found in Figure 2-48(d). One can also run IDS tests on a single specimen and vary the pore pressure to produce different effective stresses while guaranteeing the same soil structure. IDS tests on clay have shown that this is true in cohesive soils, but no IDS tests on sands are reported in the literature. Schmertmann (1991) hypothesized that aged samples of sand will behave similarly to aged cohesive soils.

Recent laboratory work has provided evidence in support of a mechanical mechanism. Bowman (2002) injected resin into samples after subjecting them to different loading to allow study of particle orientation. She found that particles became oriented with the long axis perpendicular to the major principle stress, suggesting particle rotation. Her results also show that these preferential orientations cannot withstand changes in major principle stress direction. As shown in Figure 2-49, spatial analysis of voids shows greater interlocking with time through higher variance in the results (showing patches of densely packed particles as well as loose areas). Additionally laboratory work by Jirathanathaworn (2009) showed that horizontal stress increases with time. Lade and Karimpour's (2010) work also supports a mechanical mechanism of aging, proposing static fatigue leading to particle breakage. Finally, Wang et al. (2010) performed creep tests on Yangtze River sand, recording the grain size distribution after varying periods of time

under a given confining pressure. As shown in Figure 2-50, the soil gets progressively finer with more time under sustained load, providing evidence of particle breakage and a mechanical aging mechanism.

2.3.3 Bubble Dissolution Mechanism

Hryciw (1986) proposed that the dissolution of bubbles introduced during explosive densification could contribute to sand aging behavior. Blast gas bubbles, or air bubbles introduced during the insertion of a vibro-flot, would create local voids that would collapse with time as the bubbles dissolve into solution. The soil skeleton would then transition from one where sand arches over local voids into a stronger packing. Hryciw (1986) found greater aging effects when more gas was introduced through the use of larger explosives. Additionally, aging was greater closer to the blast, where gas bubbles were more abundant.

While this behavior could be explained through Thomann and Hryciw's (1992a) observation that a larger level of disturbance leads to greater aging effects, other laboratory work has shown that bubble dissolution affects aging. LeClerc (2008) focused on the bubble dissolution mechanism. She found that samples of Ottawa sand prepared to 50% relative density and partially saturated with air and CO_2 aged significantly over a two week period. Because aging occurs in situations without air bubbles, such as deep dynamic compaction and deposition of fill, bubble dissolution is not the sole mechanism of sand aging. However, research has shown that it does contribute.

2.3.4 Biological Mechanism

A biological aging mechanism may more accurately be described as a subset of the chemical aging mechanism because biological changes make precipitation more likely. As described by Mitchell and Santamarina (2005), biological activity can locally change the pH of pore fluid and make the conditions more favorable for the precipitation of minerals that lead to cementation. However, bacteria and energy for their reproduction would need to be present in larger quantities with time in order for a biological mechanism to control sand aging behavior. Biological activity can account for time-dependent strength gain, but only under a set of circumstances that are not representative of a large number of the sand aging case histories.

2.3.5 Summary

The earliest explanation for sand aging was a chemical mechanism. As more case histories became available and sand aging was witnessed in situations where chemical processes were

unlikely to occur, a mechanical mechanism was proposed. Dissolution of bubbles and biological activity has been shown to influence aging behavior under the right set of circumstances. In the past decade, studies have shown that aging has failed to occur under seemingly ideal conditions for precipitation and cementation (Baxter and Mitchell, 2004) and that particle rotation occurs with time (Bowman and Soga, 2003), suggesting that mechanical processes are more likely to affect aging behavior than chemical processes. Recent summaries of the sand aging research by Mitchell (2004 and 2008), Mitchell and Soga (2005), and Soga (2005) have pointed to a combination of mechanisms, with the mechanical mechanism dominating in most cases. Considering all the evidence presented in this section, it is clear that a combination of mechanisms may contribute to sand aging. Because the goal of this dissertation is to develop a method that can predict sand aging effects, it is important to consider factors that contribute to each these mechanisms.

2.4 Overview of Proposed Predictive Sand Aging Predictive Methods

While the majority of sand aging research has not focused on predicting the phenomenon's effects, several predictive relationships have been proposed. These can be generally grouped into three categories: liquefaction resistance, shear wave, and penetration resistance predictive methods. This section will summarize the previously proposed sand aging predictive methods.

2.4.1 Liquefaction Resistance Aging Prediction Methods

Sand aging is of engineering interest primarily because soil improvement projects designed to increase a deposit's liquefaction resistance could be better designed with a greater understanding of sand aging. While many researchers have developed relationships that account for sand aging effects through *in situ* or laboratory test results, some researchers have directly studied changes to liquefaction resistance with time. These aging methods are summarized here.

2.4.1.1 Seed (1979)

In his seminal work on liquefaction resistance, Seed (1979) discusses time under a sustained load as one of the major factors influencing the liquefaction resistance of a soil. As seen in Figure 2-51, he cites *in situ* test data on soil deposits that have aged for hundreds to over one thousand years. Seed (1979) augments this work with triaxial tests aged for a period of one to one hundred days. The chart presented in Figure 2-51 provided one of the first methods of accounting for sand aging by directly relating the age of a deposit to increased liquefaction resistance.

2.4.1.2 Geologically Aged Deposit Liquefaction Resistance

Expanding on the ideas proposed by Seed (1979), many researchers have studied the liquefaction resistance of geologically aged deposits (Kramer and Arango, 1998; Lewis et al., 1999; Arango et al., 2000; Monahan et al., 2000; Lewis et al., 2004; Leon et al., 2006; Monaco and Schmertmann, 2007; Moss et al., 2008; Hayati et al., 2008; Andrus et al., 2009). These relationships focus on liquefaction resistance of deposits aged over hundreds to thousands of years. Because these deposits show greater aging effects from deposits aged for weeks to months, results reported in literature suggest a difference between short term sand aging and long term sand aging. The work performed by the researchers cited above can be extrapolated to short time frames, but is better applied to the longer time frames for which it was developed. Chapter 9 of this dissertation addresses geologically aged deposit liquefaction resistance in greater detail.

2.4.2 Shear Wave Velocity Aging Prediction Methods

The following sections describe predictive relationships between time and V_s, which is often related to *E* or *G* versus time. The relationship first proposed by Anderson and Stokoe (1978) and modified by others several times has become the widely accepted standard. Equations 2-1 and 2-2 demonstrate how V_s is related to *G* and how *G* is related to *E*, respectively.

$$V_s = \sqrt{\frac{G}{\rho}} \qquad \ldots(2\text{-}1)$$

$$G = \frac{E}{2(1+\nu)} \qquad \ldots(2\text{-}2)$$

Where ρ is mass density and ν is Poisson's ratio.

2.4.2.1 Afifi and Woods (1971)

After running resonant column tests on sands, silts, and clays, Afifi and Woods (1971) found a bilinear *G* versus the logarithm of time relationship, as shown in Figure 2-26. The two lines intersected at approximately 1,000 minutes. Most of the soils exhibited the end of primary consolidation at about 1,000 minutes, which led to the selection of $G_{1,000}$ as the basis for comparison in the ratio. Because of the linear relationship between shear modulus and the logarithm of time following 1,000 minutes, as expressed in Equation 2-3, Afifi and Woods (1971) propose that consolidation test data on a given soil can be used to predict shear modulus increase in the field.

$$\frac{\Delta G_{per\ log\ cycle}}{G_{1{,}000\ min}} = constant \quad \ldots(2\text{-}3)$$

2.4.2.2 Anderson and Stokoe (1978)

Anderson and Stokoe (1978) initially proposed changes to Equation 2-3 for predicting *G* of aged soil. Since this predictive method's proposition, others (Mesri et al., 1990; Schmertmann, 1991; Jamiolokowski and Manassero, 1995) have also proposed modifications to Equation 2-3, including changing the reference *G* from *G* measured at 1,000 minutes to *G* at the end of primary consolidation, recognizing that the end of primary consolidation varies by soil. The resulting relationship, Equation 2-4, is the most widely accepted today for predicting changes to shear modulus with time.

$$\frac{G_{t>t_p}}{G_{t_p}} = 1 + N_G \log\left(\frac{t}{t_p}\right) \quad \ldots(2\text{-}4)$$

$$N_G = \left(\frac{\Delta G}{\log {}^{t}/_{t_p}}\right)\left(\frac{1}{G_{t_p}}\right)100\% \quad \ldots(2\text{-}5)$$

Where t_p is the time at the end of primary consolidation.

2.4.3 Penetration Resistance Aging Prediction Methods

This section presents four predictive relationships for penetration resistance versus time. These prediction methods include a site specific relationship and methods of predicting aging effects using empirical adjustment factors.

2.4.3.1 Schmertmann et al. (1986)

During construction of the St. John's River Power Park near Jacksonville, Florida, a section of the site was set aside to test the proposed ground improvement methods for the loose sand by DDC. By monitoring CPT results with time following DDC, Schmertmann et al. (1986) were able to develop a site specific predictive relationship between q_c and time following DDC and q_c after sand aging had fully manifested itself. This relationship is presented in Table 2-4. Schmertmann et al. (1986) very accurately predicted sand aging effects on the rest of the St. John's River Power Park site. However, applying their method to other sites was not as effective because of differences in the soil and disturbance methods.

2.4.3.2 Mesri et al. (1990)

Based on studies of secondary compression of sands, Mesri et al. (1990) proposed Equation 2-5, for penetration resistance increase with time after soil modification:

$$\frac{q_c}{(q_c)_R} = \left(\frac{t}{t_R}\right)^{C_D C_\alpha / C_c} \quad \ldots(2\text{-}5)$$

Where $(q_c)_R$ is a reference tip resistance at a reference time, t_R, after the end of primary consolidation, q_c is tip resistance measured at time $t > t_R$, C_c is the compression index, C_α is the secondary compression index, and C_D is a parameter reflecting the impact of disturbance method. While compression tests on sand are not part of a typical site investigation, Mesri et al. (1990) used data from previous studies to show that the ratio C_α/C_c does not vary considerably in sands, allowing the use of typical values in this relationship without adverse effects. Using data from Solymar (1984), Dowding and Hryciw (1986), and Schmertmann et al. (1986), Mesri et al. (1990) back calculated values of C_D and found their relationship to accurately predict sand aging effects in each of these varied situations. However, C_D is difficult to predict for a new site. The back-calculated values of C_D varied over an order of magnitude from 2.9 to 23. Mesri et al.'s (1990) study showed the importance of mechanical processes, such as secondary compression, in explaining the sand aging process, but improvements capturing other factors' effects would allow this approach to be applicable to new situations where sand aging is expected to occur.

2.4.3.3 Charlie et al. (1992b)

Charlie et al. (1992b) used data from their research project involving explosive densification along the South Platte River near Greely, Colorado, as well as data from Mitchell and Solymar (1984), Schmertmann (1987), Jefferies et al. (1988), and Fordham et al. (1991), to develop the following model for penetration resistance increase with time:

$$\frac{(q_c)_{N\ weeks}}{(q_c)_{1\ week}} = 1 + K \log N \quad \ldots(2\text{-}6)$$

Where N is the number of weeks since disturbance and K is an empirical constant. The value of K varies over nearly two orders of magnitude from 0.02 to 1. Charlie et al. (1992b) propose that K varies as a function of mean annual air temperature. In a discussion to Charlie et al.'s (1992b) work, Jefferies and Rogers (1993) provide clarification of some of the data used in the model's original formation and show less of a temperature correlation than was originally proposed, as shown in Figure 2-52. Temperature's impact on aging effects supports a chemical mechanism, where the development of cementation would be slowed at colder temperatures. In any case, the

difficulty in predicting *K* using only information typically found in a geotechnical site investigation limits the predictive ability of this otherwise useful relationship.

2.4.3.4 Joshi et al. (1995)

Joshi et al. (1995) proposed another aging model, Equation 2-7, based on their experiments involving aging laboratory samples with different pore fluids:

$$\frac{q_c}{q_1} = at^b \quad \ldots(2\text{-}7)$$

Where q_1 is the penetration resistance one day after deposition/disturbance, *t* is time in days, and *a* and *b* are empirical constants that depend on the type of pore fluid. Proposed values of *a* and *b* are presented in Table 2-5. Joshi et al. (1995) concede that mechanical processes play a major role in sand aging, yet this equation seemingly accounts only for chemical processes by considering only the type of pore fluid through the empirical constants. Because the research summarized in this chapter shows that several factors contribute to sand aging, the utility of this model to future projects is limited by its consideration of only pore fluid.

2.5 Conclusion

The body of knowledge on sand aging has increased significantly in recent decades. The studies summarized here have shed light on both sand aging mechanisms and sand aging effects. The increased database of sand aging effects in the field and laboratory create a better opportunity to develop a model that predicts sand aging effects based on the type of information that would typically be collected in a geotechnical site investigation. Both the enlarged database and an improved understanding of the underlying mechanisms provide an excellent opportunity to develop predictive models that account for penetration resistance increases with time following disturbance in sand.

Table 2-1. Summary of soil properties for the projects described in this chapter.

Sand, Section #	C_u	C_c	D_{10} (mm)	D_{50} (mm)	USCS Classification	$\gamma_{d,max}$ (kN/m^3)	$\gamma_{d,min}$ (kN/m^3)	e_{min}	e_{max}	Reference
Jebba Dam, 2.2.1.2	2.94	0.94	0.31	1	SP	18.8	15.8	0.39	0.65	Mitchell, 1986b
Harriet's Bluff, 2.2.1.4	1.60	1.11	0.075	0.12	SP					Hryciw, 1986
Beaufort Sea, 2.2.1.5 and 2.2.2.9	2.67	1.04	0.14	0.33	SP	14.3	16.3			Joshi et al., 1995
Pointe Noire Harbor, 2.2.1.6	3.06			0.79						Dumas and Beaton, 1988
Fort McMurray, 2.2.1.7 and 2.2.1.9	2.30	1.17	0.09	1.17	SP			0.52	0.84	Handford, 1988
Douglas Lake, 2.2.1.8	2.42	1.04	0.11	0.20	SP			0.54	0.82	Thomann, 1990
South Platte River, 2.2.1.10	4.17 to 5.75		0.51 to 0.62	2.1 to 2.3	SP	16.6	19.1	0.37	0.56	Charlie et al., 1992a
Chek Lap Kok Airport, 2.2.1.12	4.5			0.8				0.40	0.77	Covil et al., 1997
Treasure Island, 2.2.1.13				0.2 to 0.3	SP					Rollins et al., 2000

Table 2-1 (Continued). Summary of soil properties for the projects described in this chapter.

Sand, Section #	C_u	C_c	D_{10} (mm)	D_{50} (mm)	USCS Classification	$\gamma_{d,max}$ (kN/m^3)	$\gamma_{d,min}$ (kN/m^3)	e_{min}	e_{max}	Reference
Fraser River, 2.2.1.15 and 2.2.2.13	1.88		0.16	0.271				0.63	0.96	Howie and Amini, 2004
Charleston, 2.2.1.17	1.47	0.88	0.15	0.21	SP		12.5	0.52	1.10	Narsilio, 2006
Wildlife Site, 2.2.1.18				0.091	SM					Holzer and Youd, 2007
Massey Tunnel, 2.2.1.19	2.35	1.51	0.085	0.19	SP					Rollins and Anderson, 2008
Ottawa, 2.2.2.2 and 2.2.2.3	1.60	1.20	0.27	0.41	SP	17.8	15.4	0.47	0.69	Afifi and Woods, 1971
Agsco #1, 2.2.2.2 and 2.2.2.3	1.20	1.01	0.20	0.24	SP	15.2		0.71		Afifi and Woods, 1971
Evanston Beach, 2.2.2.5 and 2.2.2.10	1.50	1.03	0.15	0.20	SP	16.8	14.7			Hryciw, 1986
Ottawa C-109, 2.2.2.6	1.50			0.40				0.50	0.82	Mejia et al., 1988
Brenda Mine Tailings, 2.2.2.6	1.60			0.40				0.69	1.06	Mejia et al., 1988

Table 2-1 (Continued). Summary of soil properties for the projects described in this chapter.

Sand, Section #	C_u	C_c	D_{10} (mm)	D_{50} (mm)	USCS Classification	$\gamma_{d,max}$ (kN/m^3)	$\gamma_{d,min}$ (kN/m^3)	e_{min}	e_{max}	Reference
Ottawa 100-200, 2.2.2.7	1.89		0.07					0.60	0.90	Thomann, 1990
Agsco 100-200, 2.2.2.7	1.86		0.07					0.60	0.90	Thomann, 1990
Holliston OO, 2.2.2.8	2			0.30						Miller, 1994
River, 2.2.2.9	2.39	1.12	0.12	0.45	SP	16.6	14.6			Joshi et al., 1995
Density, 2.2.2.10	1.93	1.04		0.50	SP	17.5	15.1	0.49	0.72	Baxter, 2001
Crushed Coral, 2.2.2.11	~1	~1	0.15		SP			0.70	1.22	Lade et al., 2009
Antelope Valley, 2.2.2.11	~1	~1			SP			0.98	1.24	Lade and Liu, 1998
Glass Beads, 2.2.2.12				0.10						Losert et al., 2000
Leighton Buzzard, 2.2.2.14			0.12	0.15				0.60	1.01	Bowman, 2002

Table 2-1 (Continued). Summary of soil properties for the projects described in this chapter.

Sand, Section #	C_u	C_c	**D_{10} (mm)**	D_{50} (mm)	USCS Classification	$\gamma_{d,max}$ (kN/m^3)	$\gamma_{d,min}$ (kN/m^3)	e_{min}	e_{max}	Reference
Montpellier, 2.2.2.14			**0.18**	0.24				0.72	0.93	Bowman, 2002
Glass Beads, 2.2.2.14			**0.21**	0.26				0.61	0.77	Bowman, 2002
Ottawa, 2.2.2.15	1.28	1.08	**0.40**	0.50	SP	17.0	15.3			LeClerc, 2008
Ottawa 20-30, 2.2.3.1			**0.65**	0.85				0.48	0.75	Wang and Tsui, 2009
Toyoura, 2.2.3.1			**0.16**	0.22				0.59	0.99	Wang and Tsui, 2009
JFK Airport, 2.2.4.3	2.90	1.25	**0.11**							York et al., 1994
Dunkirk, 2.2.4.4				0.25						Chow and Liu, 1998

Table 2-2. Summary of chemical properties and depositional details for the soil in the projects described in this chapter.

Sand, Section #	% Quartz	% Feldspar	Other minerals	Description	Age	Depositional Process	Reference
Volga River, 2.2.1.1	Mostly			Fine to medium grained, rounded, clean			Denisov et al., 1963
Jebba Dam, 2.2.1.2	92	2	Granite, volcanic, gneiss, chert				Solymar, 1984
Jacksonville, 2.2.1.3	Mostly			Clean	Recent Pleistocene	Naturally filled in marine estuary	Schmertmann et al., 1986
Harriet's Bluff, 2.2.1.4				Fine sand with silty lenses		Coastal	Hryciw, 1986
Beaufort Sea, 2.2.1.5					Fresh	Hydraulic fill	Jefferies et al., 1988
Port Noire Harbor, 2.2.1.6				Clean, medium to coarse grained	Fresh	Hydraulic fill	Dumas and Beaton, 1988
Fort McMurray, 2.2.1.7 and 2.2.1.9	95	2	Iron Oxide		Fresh	Mine tailings	Handford, 1988
Douglas Lake, 2.2.1.8				Medium to fine grained, subangular	Pleistocene	Shallow water lake sand	Thomann, 1990

Table 2-2 (Continued). Summary of chemical properties and depositional details for the soil in the projects described in this chapter.

Sand, Section #	% Quartz	% Feldspar	Other minerals	Description	Age	Depositional Process	Reference
South Platte River, 2.2.1.10	80	5	Volcanic	Poorly graded, gravely sand	Pleistocene and Holocene		Charlie et al., 1992a
Sainte Marguerite Dam, 2.2.1.11				Loose river sand		River deposit	Wheeler, 1995
Chek Lop Kok Airport, 2.2.1.12	85-90	5-10	Calcium carbonate	Very heterogeneous due to fill method	Fresh	Hydraulic fill	Covil et al., 1997
Treasure Island, 2.2.1.13				Fine sand or silty sand with thin layers of lean clay	~70 years	Hydraulic fill	Ashford et al., 2004
Cooper River Bridge, 2.2.1.14	Mostly		Phosphate and clay		Pleistocene	Marine sediments	Camp, 2004
Fraser River, 2.2.1.15				Grey, uniform, semi-angular, medium grained	Holocene	River delta	Howie and Amini, 2004
Mississippi Embayment, 2.2.1.16				Clean, quartz sand			Liao and Mayne, 2005

Table 2-2 (Continued). Summary of chemical properties and depositional details for the soil in the projects described in this chapter.

Sand, Section #	% Quartz	% Feldspar	Other minerals	Description	Age	Depositional Process	Reference
Charleston, 2.2.1.17				Fine, black sand	Pleistocene	Coastal	Narsilio, 2006
Wildlife Site, 2.2.1.18				High fines content, 36%	~100 years	River flood plane	Holzer and Youd, 2007
Massey Tunnel, 2.2.1.19	40	10	Misc. rock fragments	Clean alluvial sand	<200 years	Alluvial	Rollins and Anderson, 2008
Evanston Beach, 2.2.2.5 and 2.2.2.10	Mostly			Fine, poorly graded, brown sand	Fresh (lab work)	Pluviation	Hryciw, 1986
Brenda Mine Tailings, 2.2.2.6	35	50		Angular	Fresh (lab work)		Mejia et al., 1988
Density, 2.2.2.10	99		Iron Oxide	White, rounded, poorly graded sand	Fresh (lab work)	Pluviation	Baxter, 1999
JFK Airport, 2.2.4.3				Fine to medium sand, <10% fines	Late Wisconsin	Glacial	York et al., 1994
Dunkirk, 2.2.4.4	84	8	Calcium carbonate	Rounded to sub-rounded	900-2100 years	Coastal	Chow et al., 1998

Table 2-3. Blow count in fill material placed at a hydroelectric plant along the Volga River (Denisov et al., 1963).

Number of days after deposition	10-20	20-40	40-50	60	100-140
SPT-N (blows)	2.1	2.2	3.1	3.3	4.4

Table 2-4. Aging factors determined by observation of sand aging at St. John's River Power Park, Florida (Schmertmann et al., 1986).

Time between improvement and CPT (days)	Factor by which to multiply q_c
5	1.35
10	1.2
15	1.15
20	1.12
30	1.06
40	1.03
50	1.01
60	1.00

Table 2-5. Average values of environmental condition constants in penetration resistance aging predictive method (Joshi et al., 1995).

	a	b
Dry state	0.90	0.06
Distilled water	0.75	0.15
Sea water	0.70	0.17

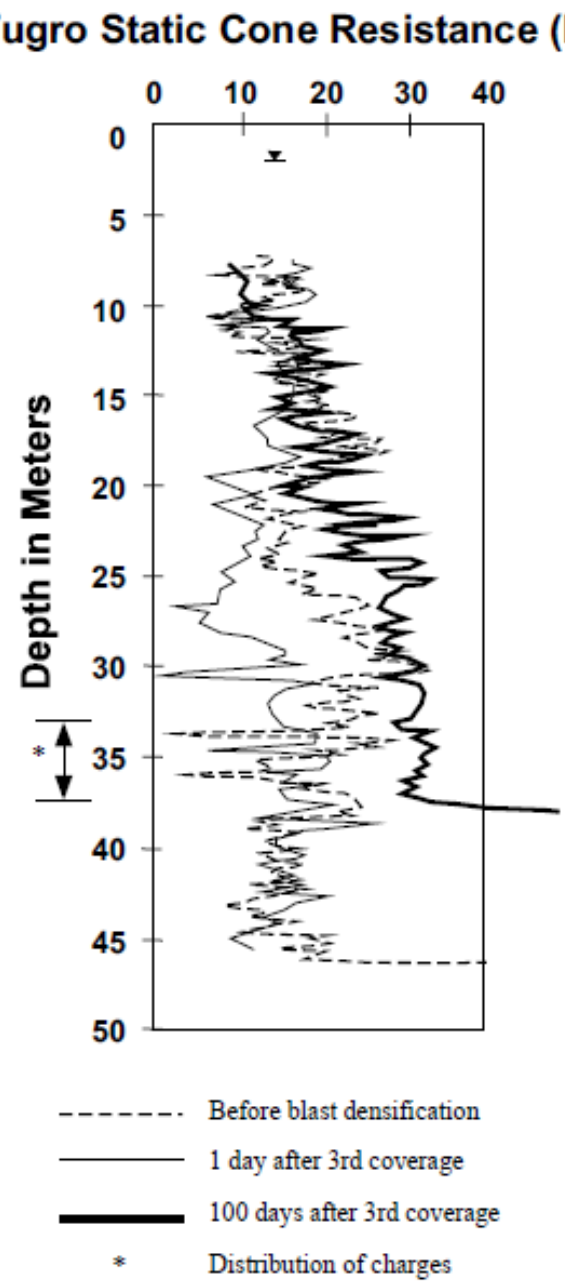

Figure 2-1. Time-dependent increase in penetration resistance following explosive densification at the Jebba Dam site, Nigeria (Baxter, 1999 after Solymar, 1984).

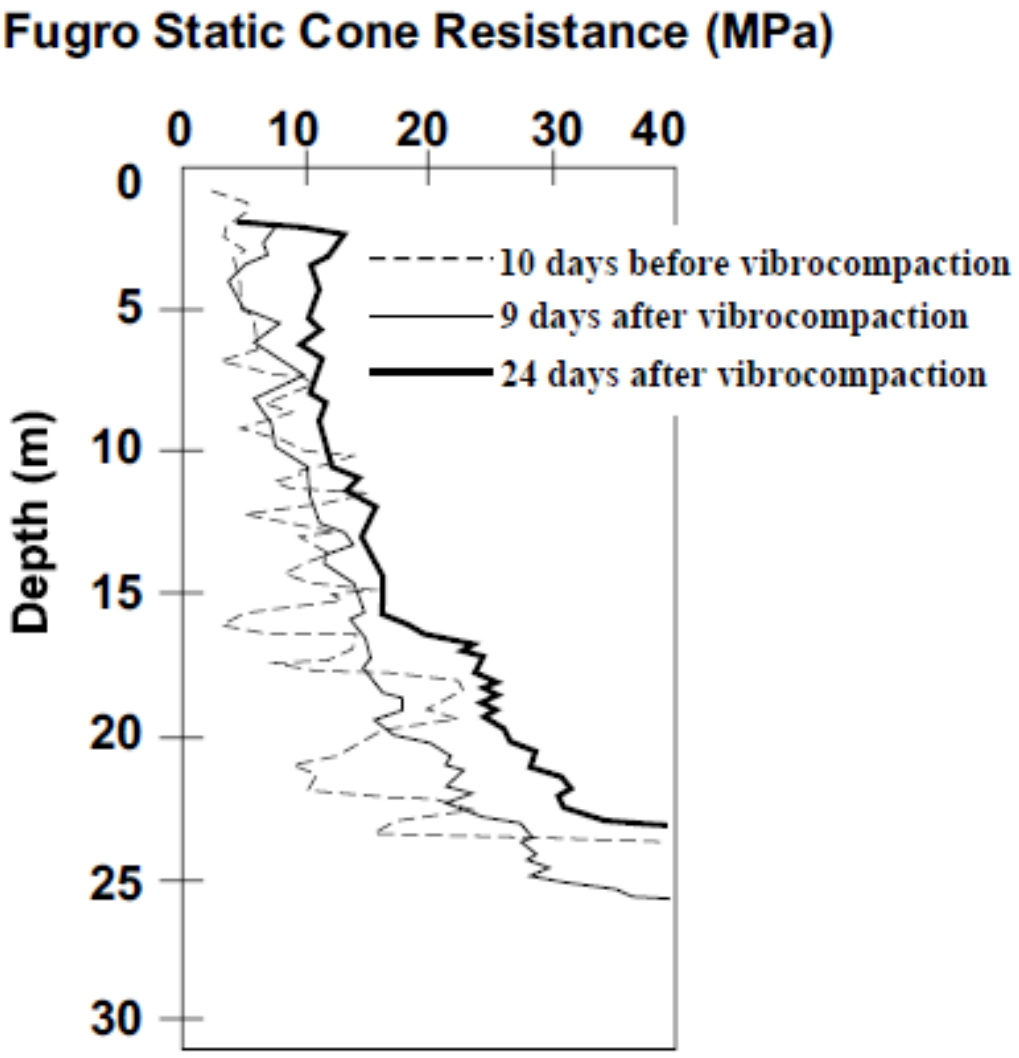

Figure 2-2. Time-dependent increase in penetration resistance following vibro-compaction at the Jebba Dam site, Nigeria (Baxter, 1999 after Mitchell and Solymar, 1984).

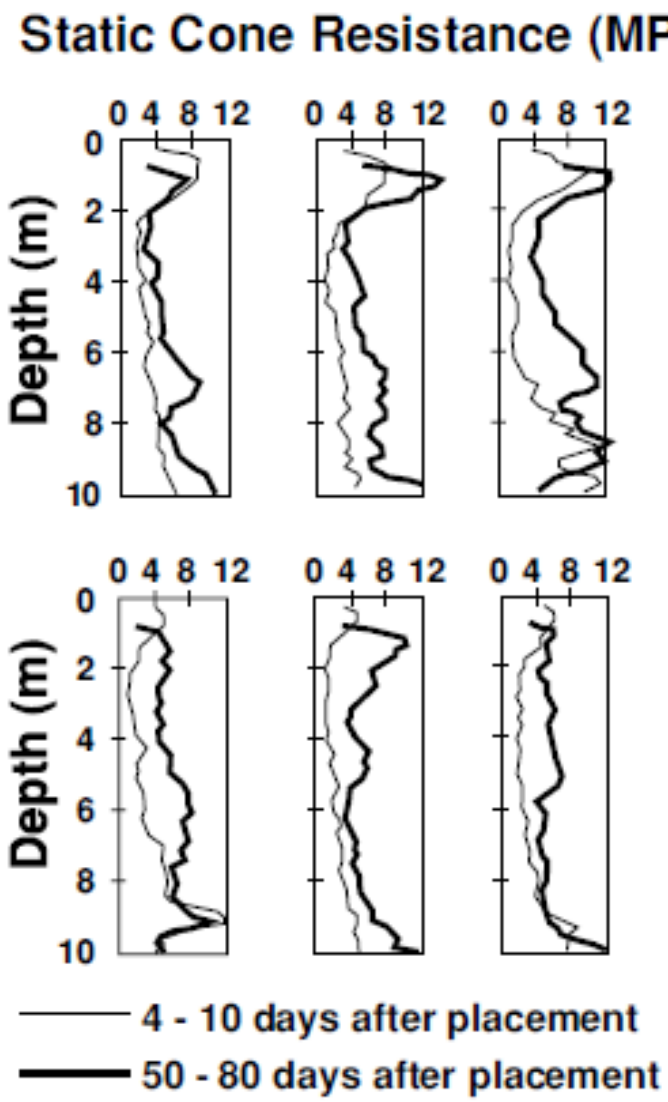

Figure 2-3. Time-dependent increase in penetration resistance following deposition of fill at the Jebba Dam site, Nigeria (Baxter, 1999 after Mitchell and Solymar, 1984).

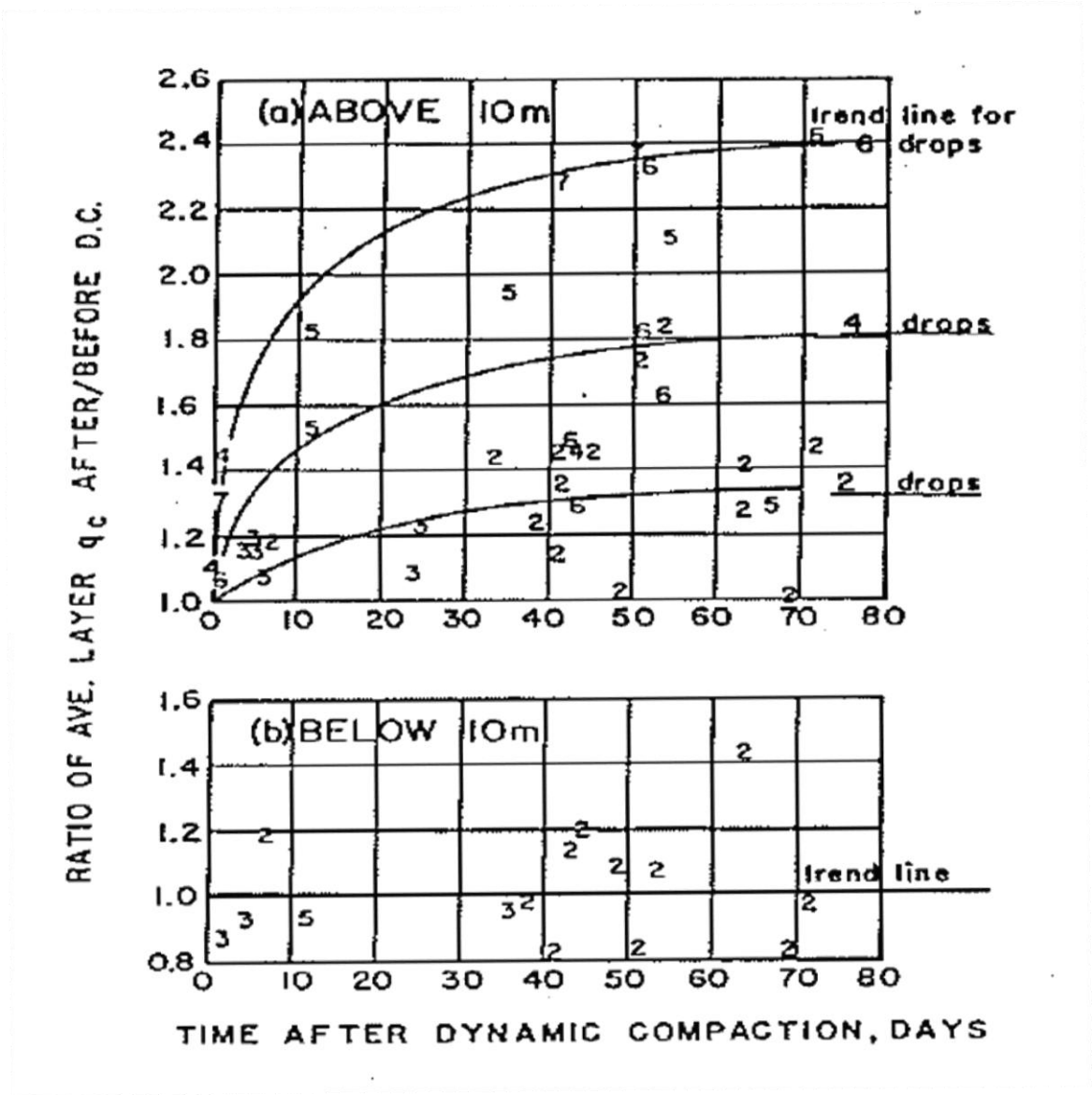

Figure 2-4. Time-dependent increase in penetration resistance following deep dynamic compaction at the St. John's River Power Park site, Florida (a) in the sand layers at 10m of depth and shallower, (b) in sand layers deeper than 10m (Schmertmann et al., 1986).

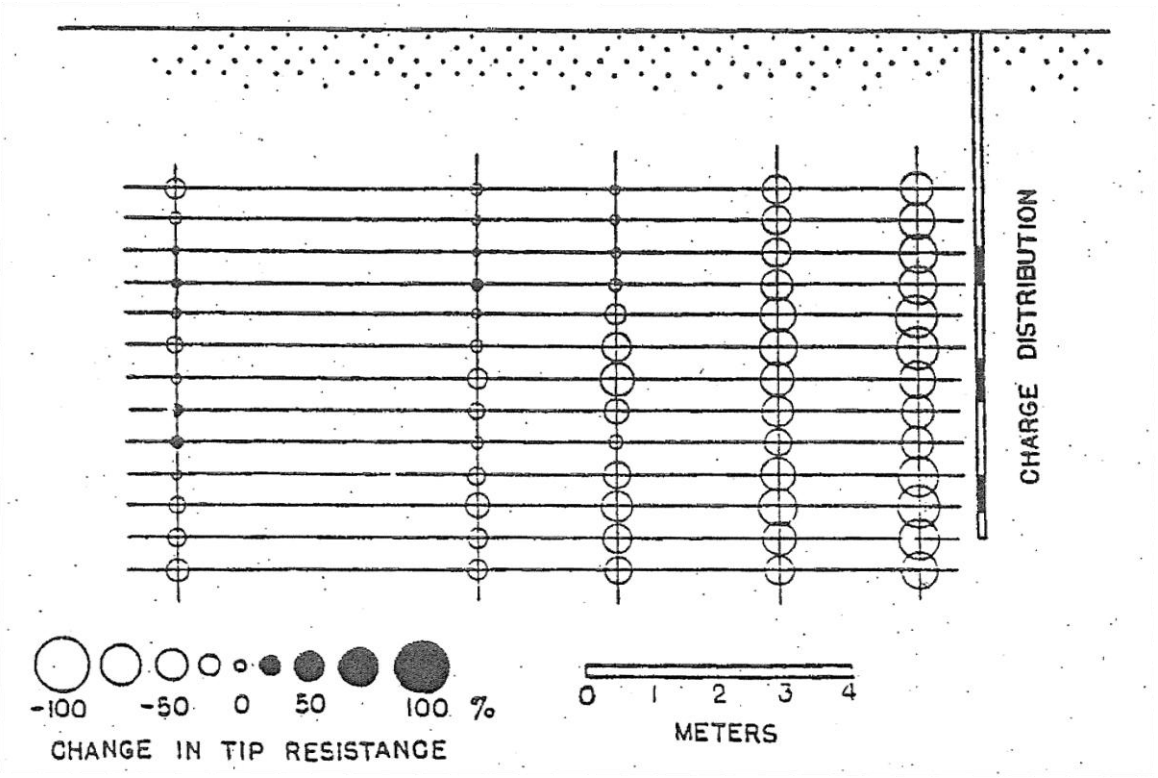

Figure 2-5. Decrease in penetration resistance following explosive densification at Harriet's Bluff, Georgia (Hryciw, 1986).

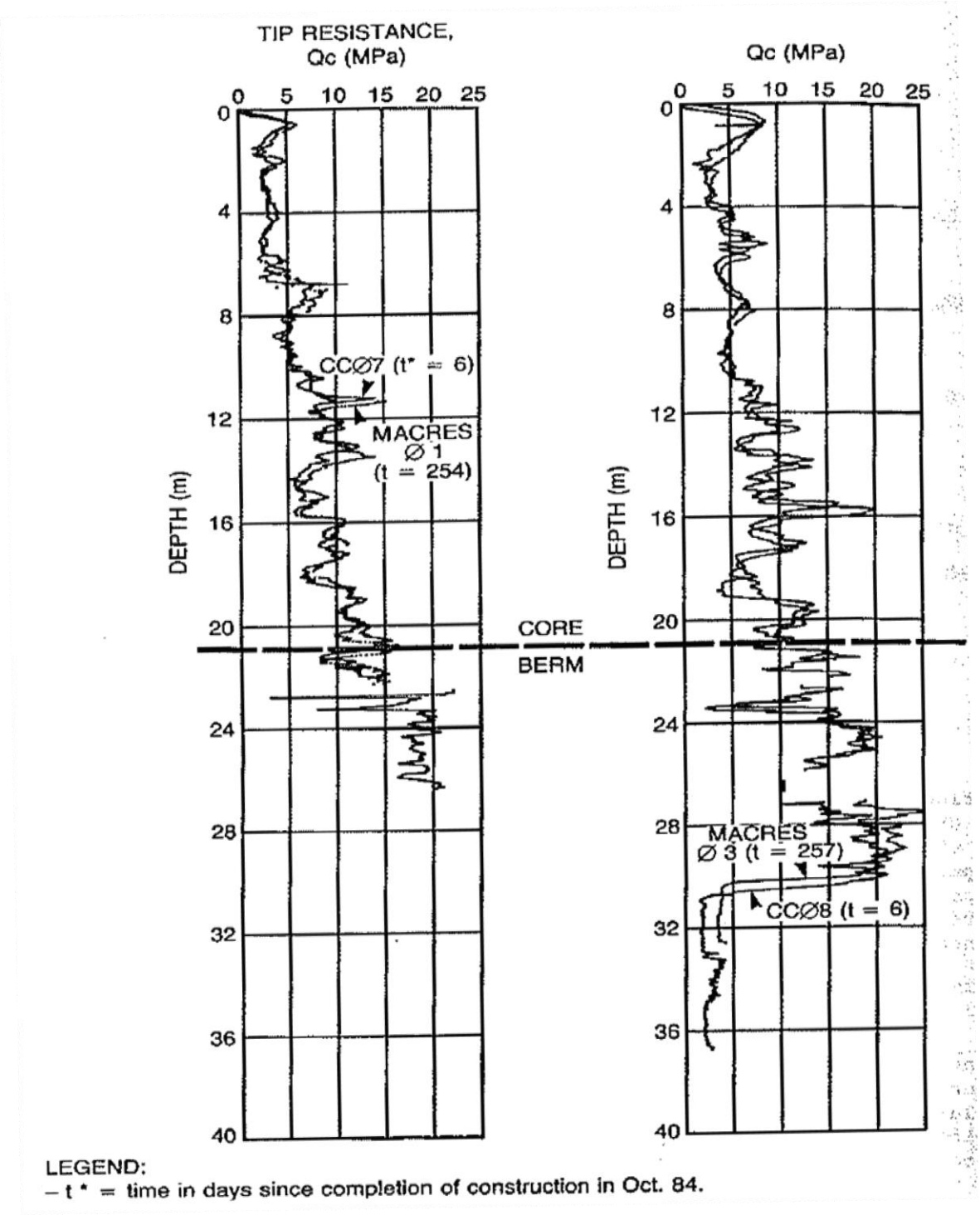

Figure 2-6. Penetration resistance measurements following deposition of fill in the Beaufort Sea, Canada show little change with time (Jefferies et al., 1988). A berm was built to protect the core from waves. The maximum height of the berm is depicted with the dashed line.

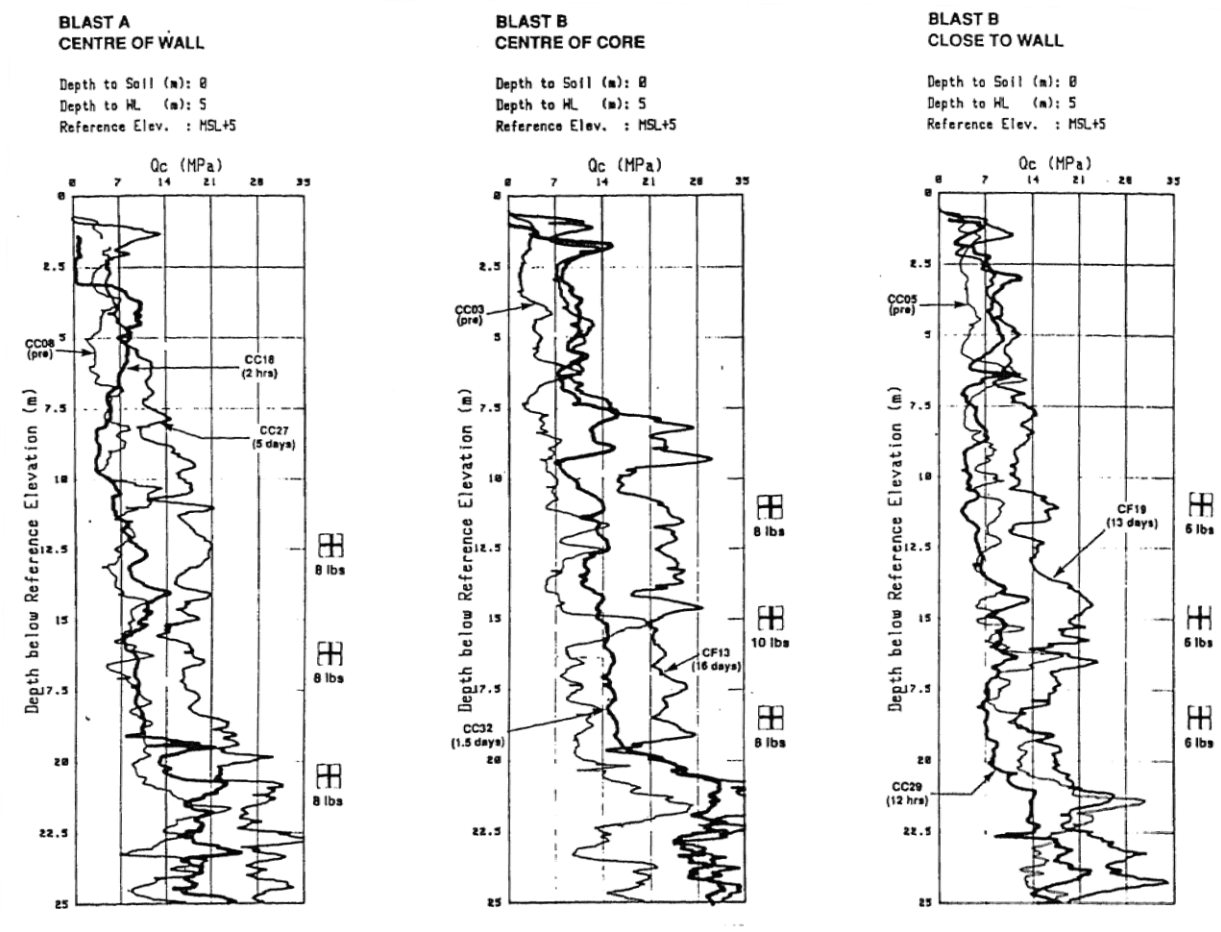

Figure 2-7. Time-dependent increase in penetration resistance following explosive densification in the Beaufort Sea, Canada (Rogers et al., 1990).

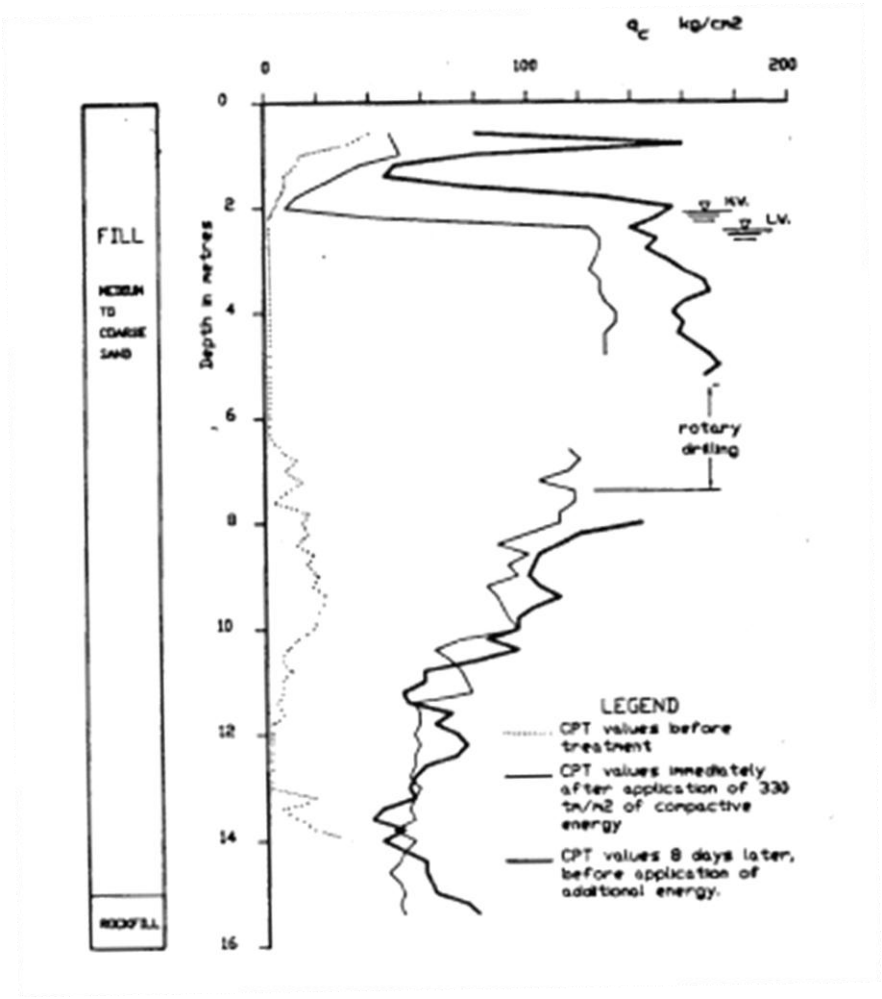

Figure 2-8. Time-dependent increase in penetration resistance following deep dynamic compaction at Port Noire Harbor, Canada (Dumas and Beaton, 1988).

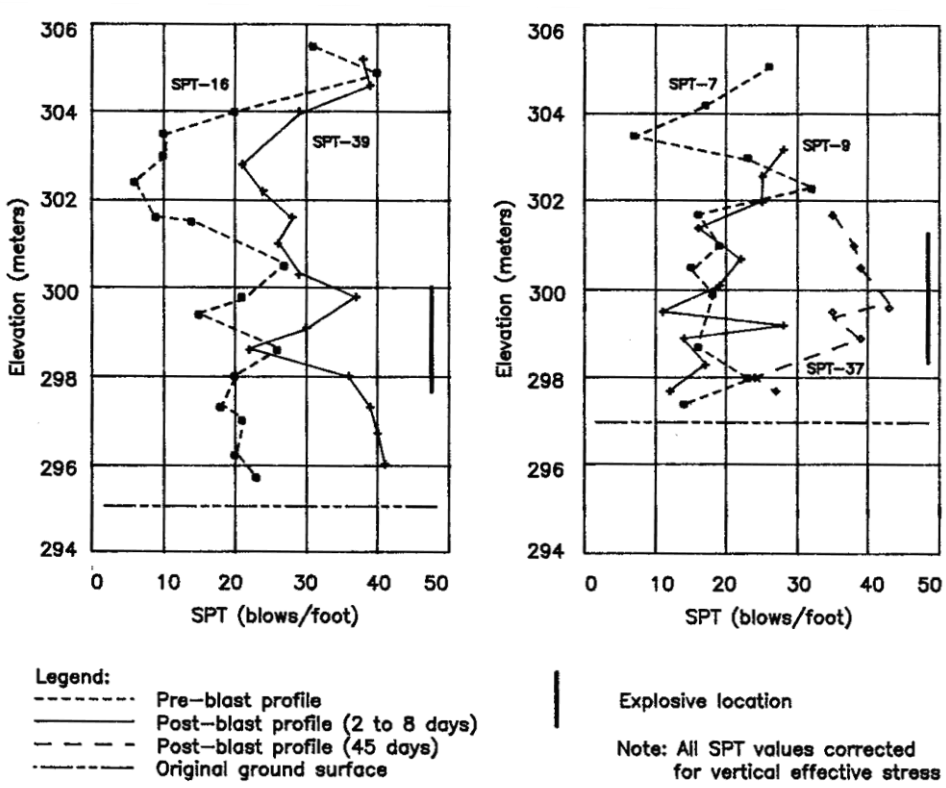

Figure 2-9. Time-dependent increase in blow count following explosive densification at Fort McMurray, Canada (Handford, 1988).

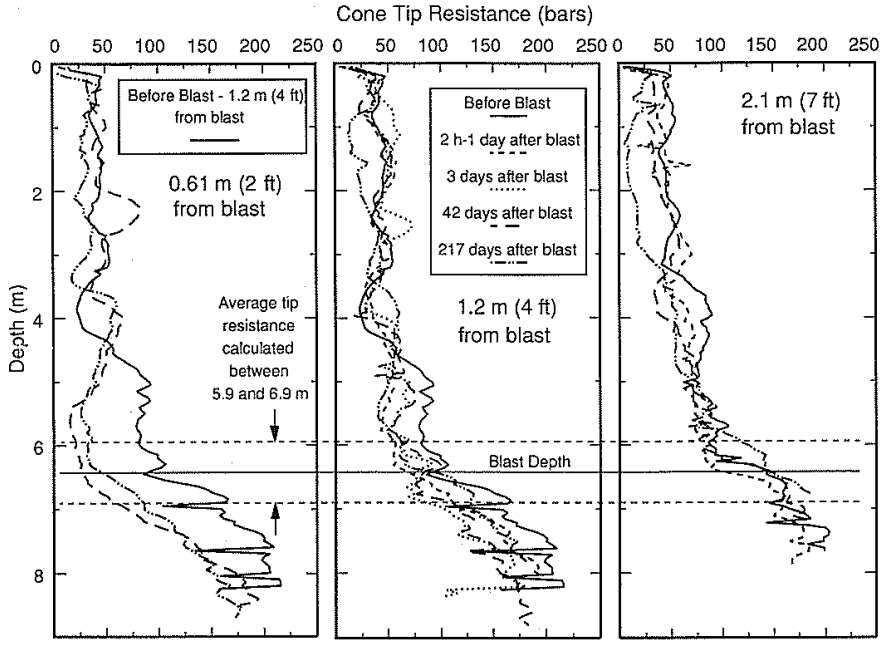

Figure 2-10. Penetration resistance measurements following explosive densification at Douglas Lake, Michigan show little change with time (Thomann and Hrcyiw, 1992a).

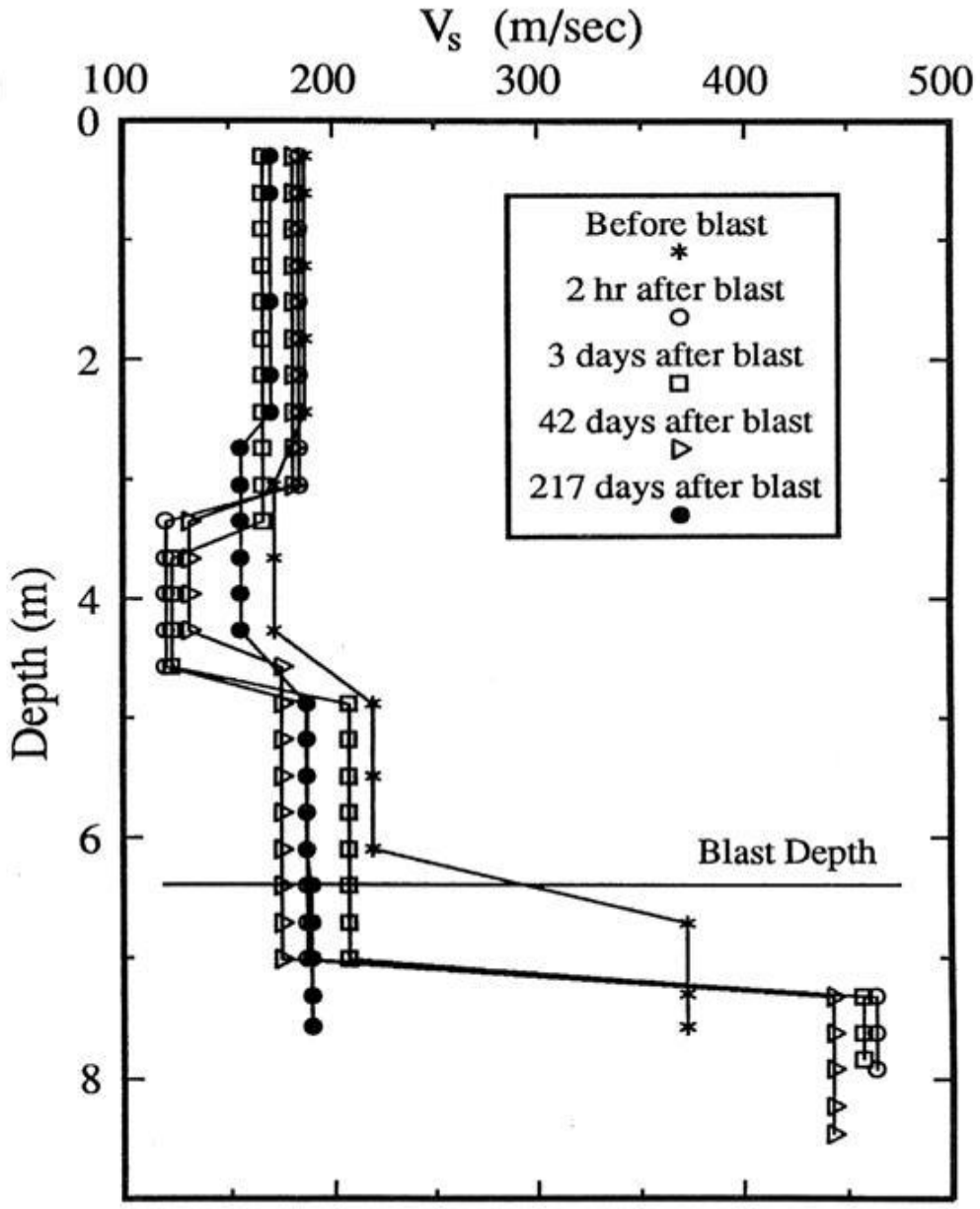

Figure 2-11. Down-hole shear wave velocity following explosive densification at Douglas Lake, Michigan fails to show a trend with time (Thomann, 1990).

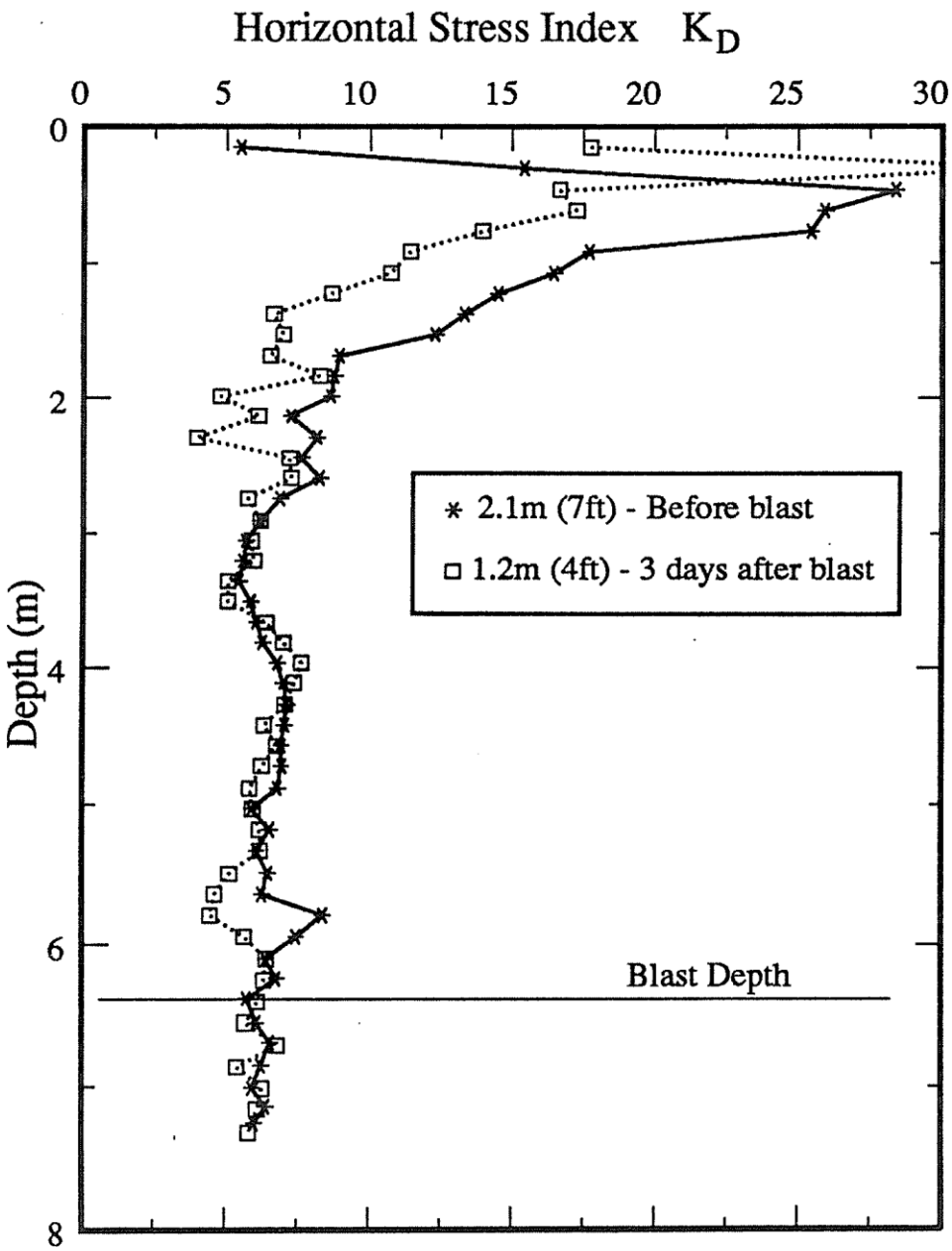

Figure 2-12. DMT Horizontal Stress Index following explosive densification at Douglas Lake, Michigan shows little change with time (Thomann, 1990).

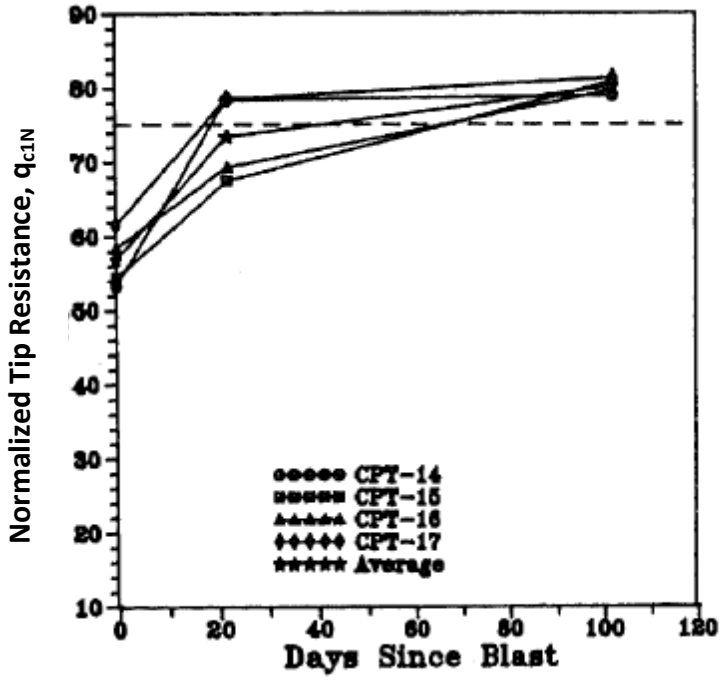

Figure 2-13. Penetration resistance increase following explosive densification near Ft. McMurray, Canada (adapted from Fordham et al., 1991).

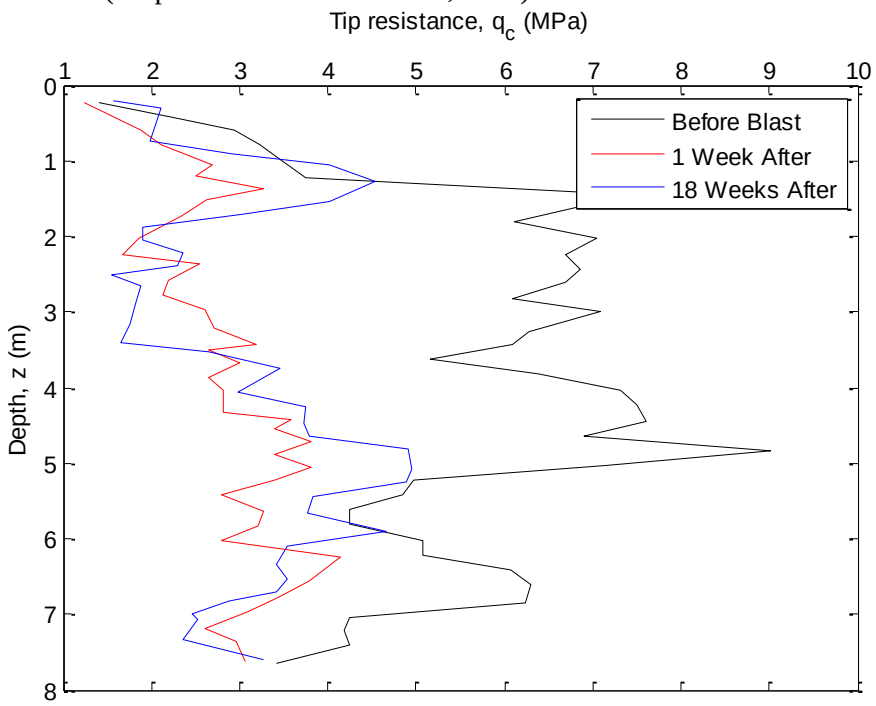

Figure 2-14. Penetration resistance increase following explosive densification along the South Platte River, Colorado (adapted from Charlie et al., 1992b).

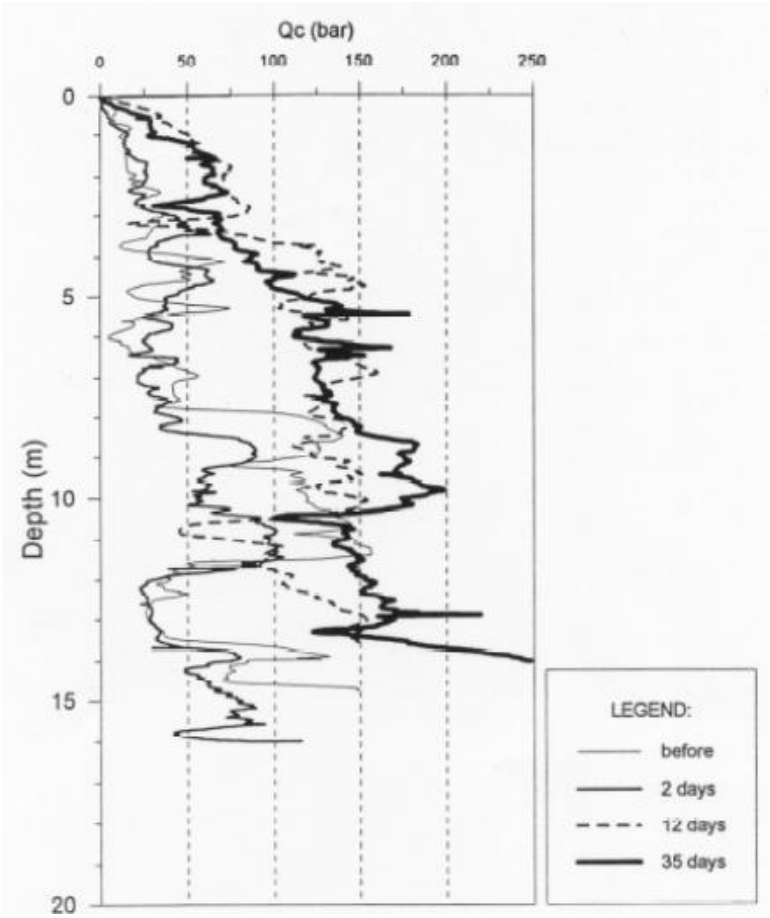

Figure 2-15. Penetration resistance increase following explosive densification at Sainte Marguerite Dam, Canada (Baxter, 1999 after Wheeler, 1995).

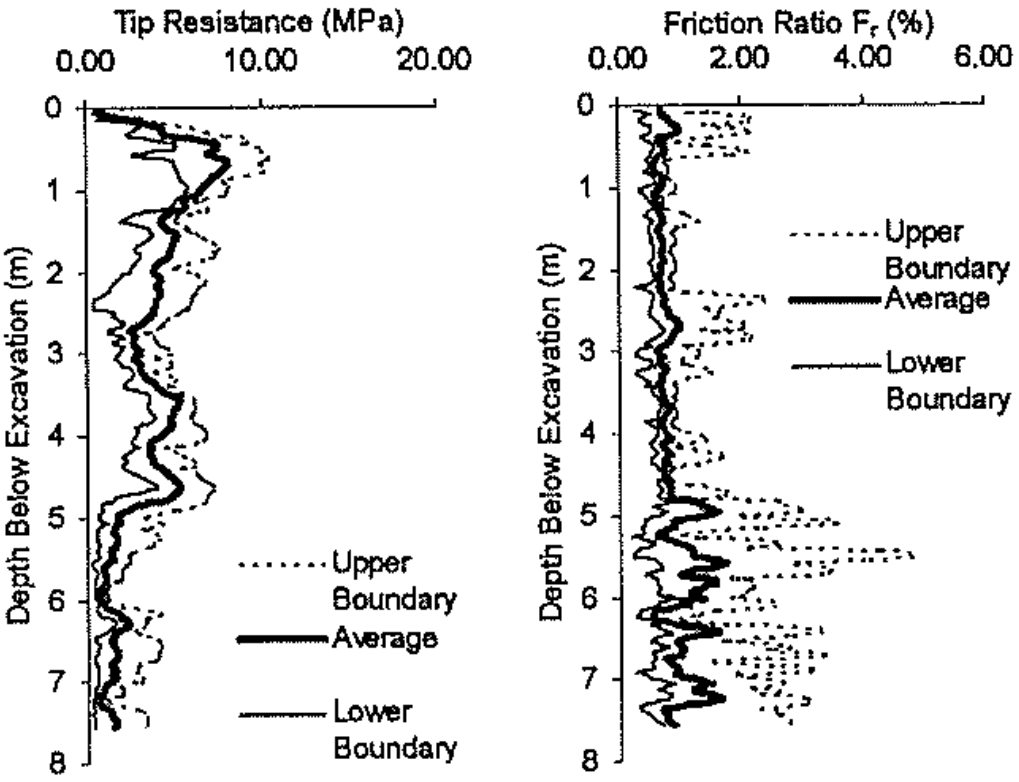

Figure 2-16. Penetration resistance increase before and following vibro-compaction at the Hong Kong airport (Ashford et al., 2004).

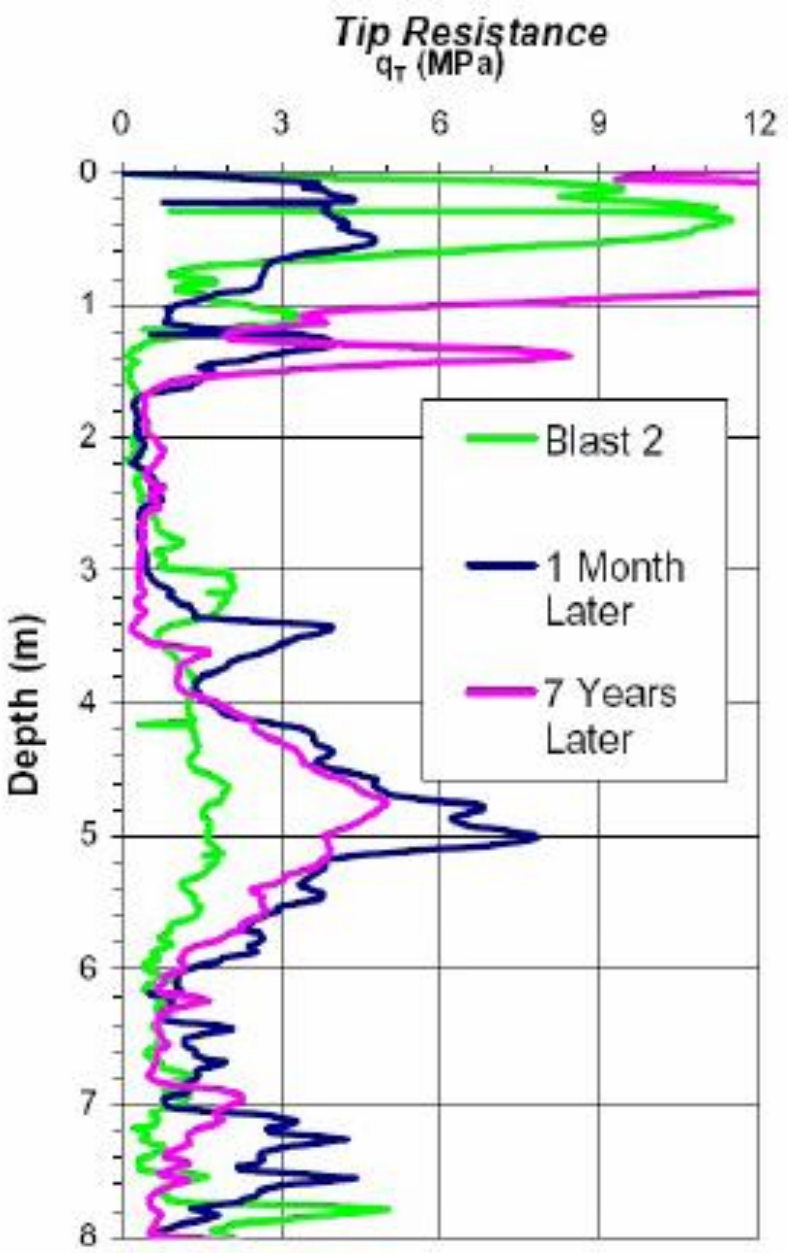

Figure 2-17. Penetration resistance remains fairly constant between one month and seven years after explosive densification near the Cooper River Bridge, South Carolina (Camp et al., 2008).

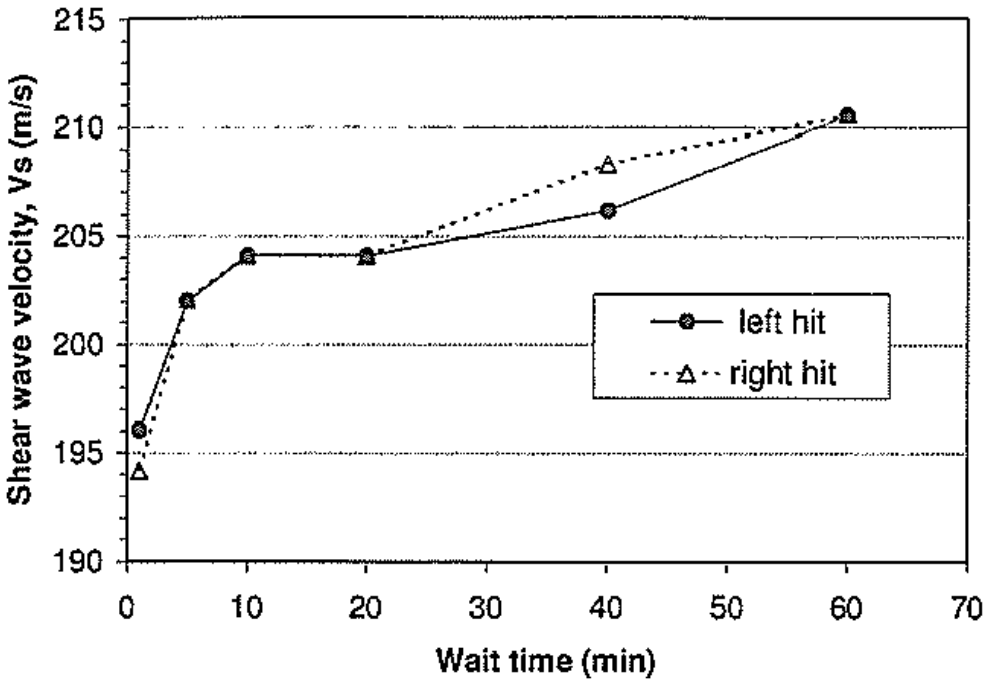

Figure 2-18. Shear wave velocity increases with time during a pause in advancement of an SCPT test near the Fraser River, Canada (Howie and Amini, 2004).

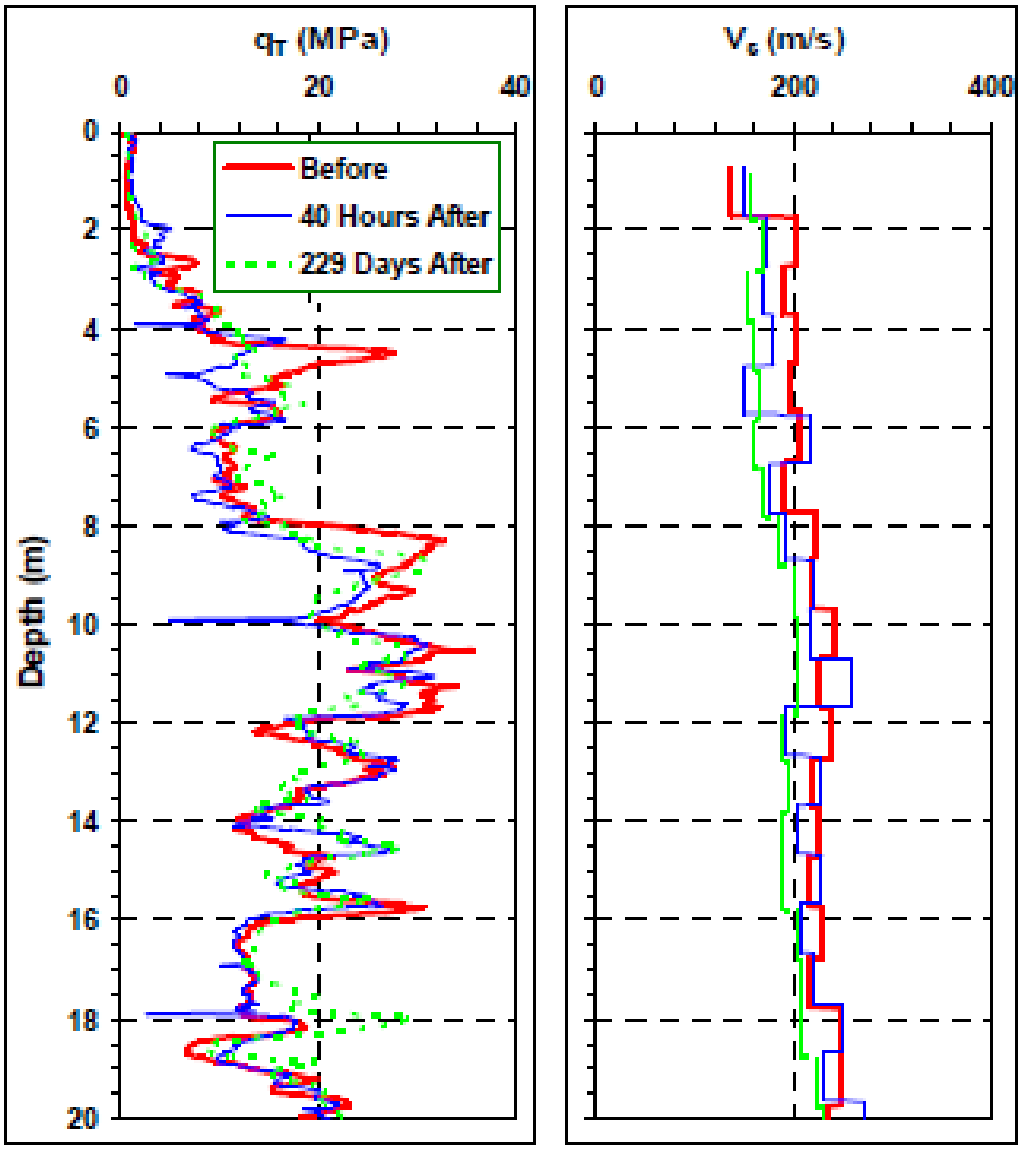

Figure 2-19. Penetration resistance and shear wave velocity do not change significantly with time following explosive densification in the Mississippi Embayment (after Liao and Mayne, 2005).

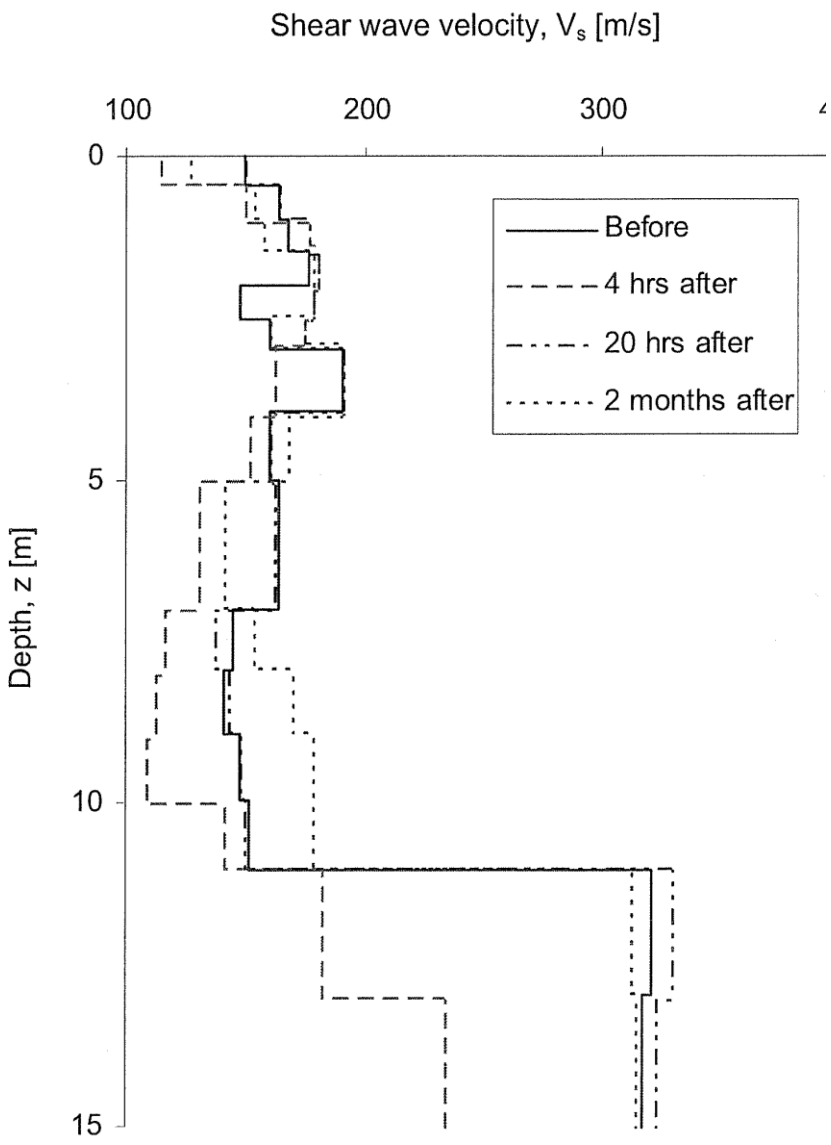

Figure 2-20. Shear wave velocity increases with time following explosive densification near Charleston, South Carolina (Narsilio, 2006).

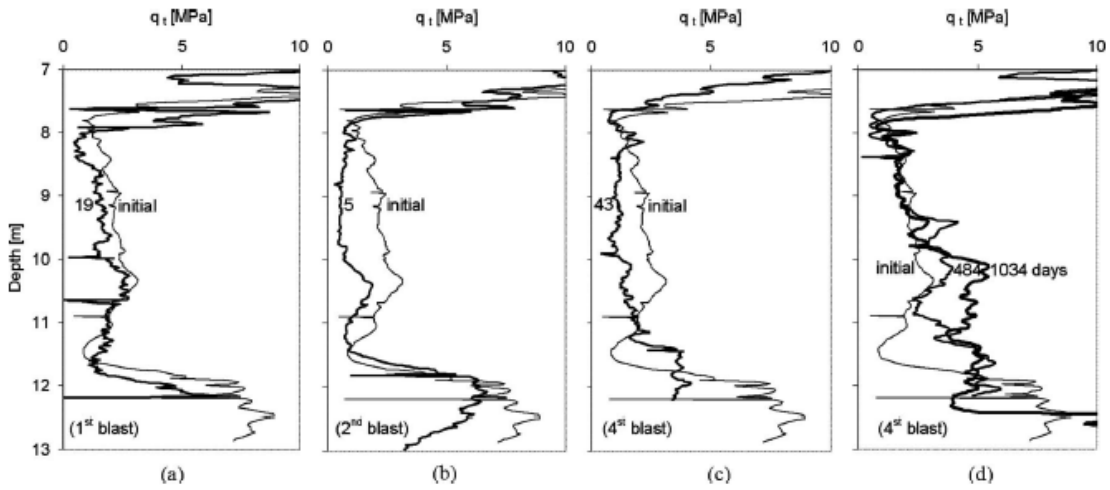

Figure 2-21. Penetration resistance changes with time following explosive densification near Charleston, South Carolina: (a) 19 days after first blast, (b) 5 days after second blast, (c) 43 days after final blast, and (d) 484 and 1,034 days after the final blast (Narsilio et al., 2009).

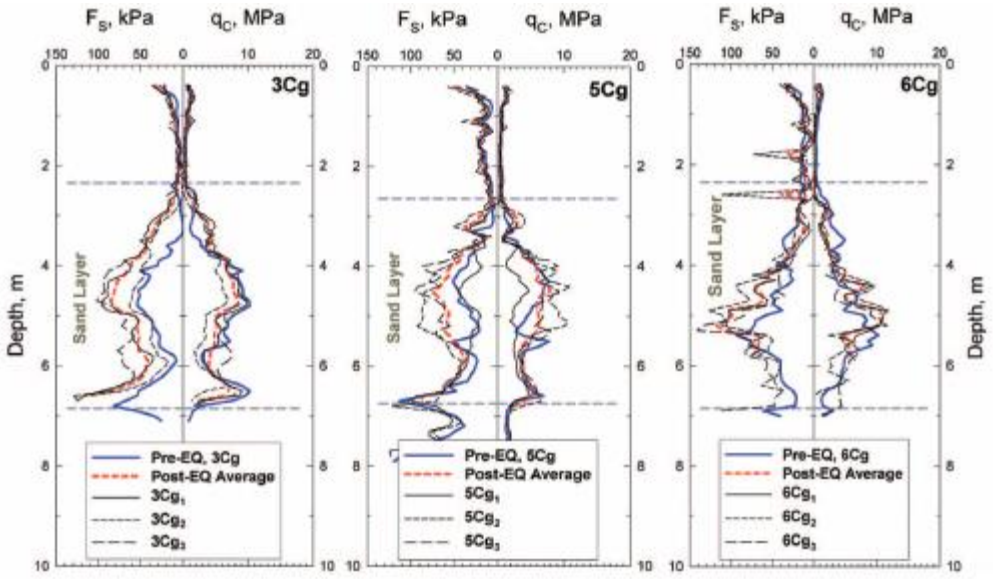

Figure 2-22. Penetration resistance before and 4.5 months after the 1987 Superstition Hills earthquake at three sites in the Wildlife Liquefaction Array (Holzer and Youd, 2007).

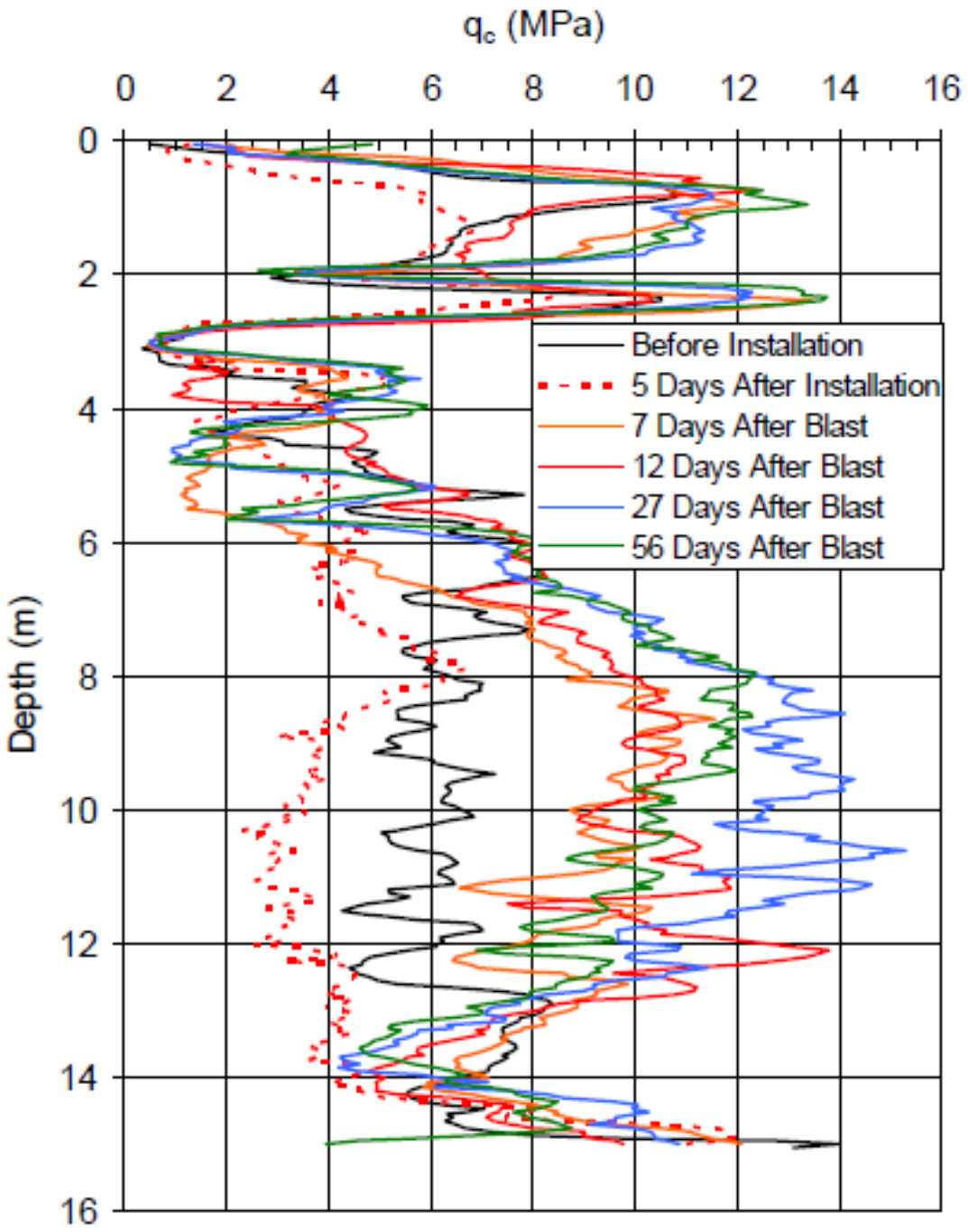

Figure 2-23. Penetration resistance increase following explosive densification near the Massey Tunnel, Canada (Rollins and Anderson, 2008).

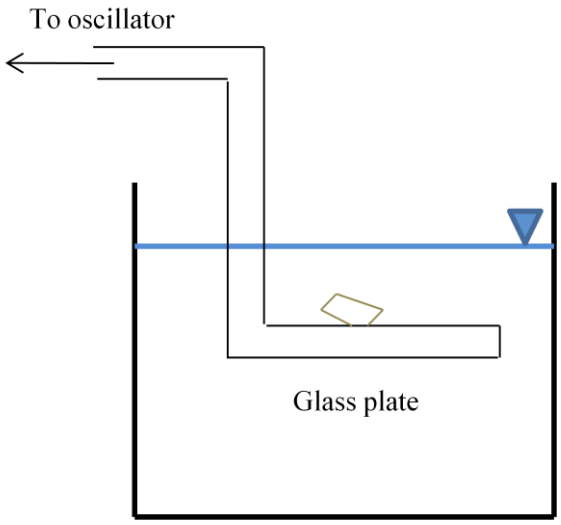

Figure 2-24. Vibrating plate experimental set-up (adapted from Denisov and Reltov, 1961).

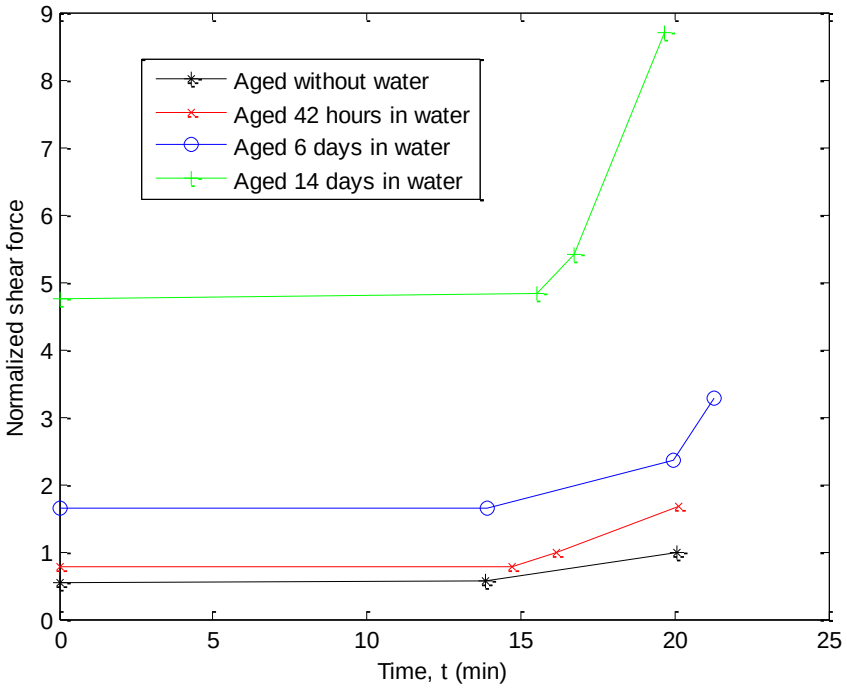

Figure 2-25. Normalized shear force increase with time in the vibrating plate experiment (adapted from Denisov and Reltov, 1961).

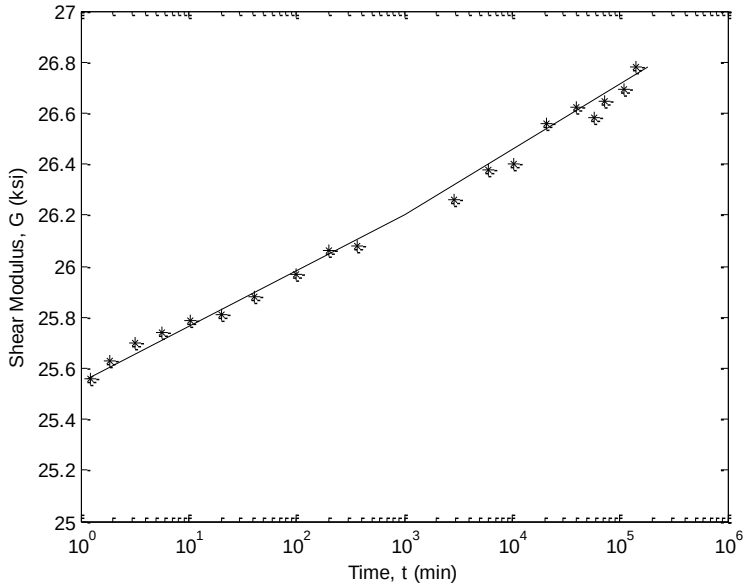

Figure 2-26. Shear modulus increase with time as determined by resonant column tests (adapted from Afifi and Woods, 1971).

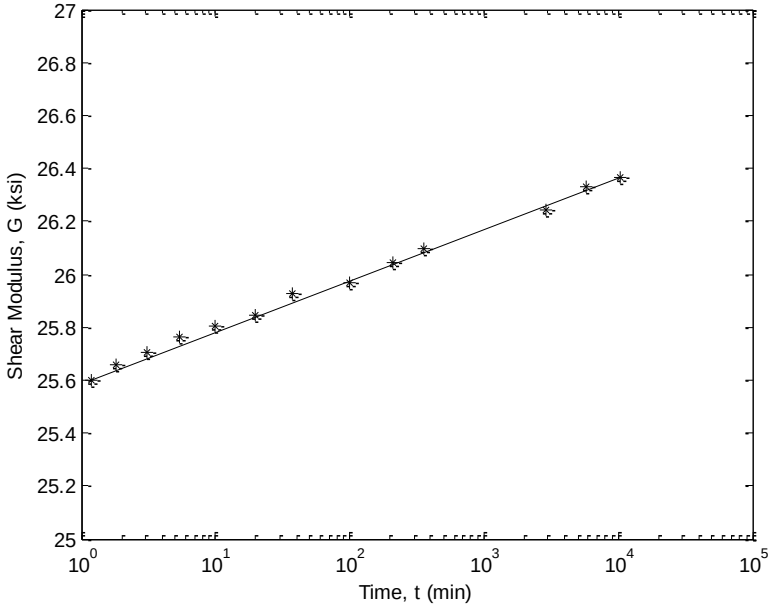

Figure 2-27. Shear modulus increase with time as determined by resonant column tests (adapted from Anderson and Stokoe, 1978).

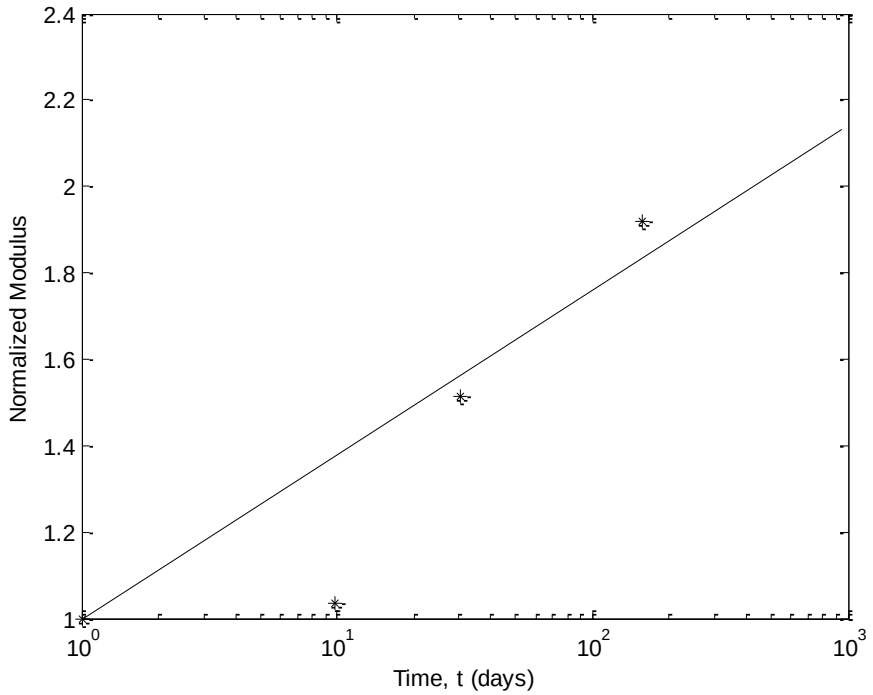

Figure 2-28. Normalized shear force increase with time in the vibrating plate experiment (Daramola, 1980).

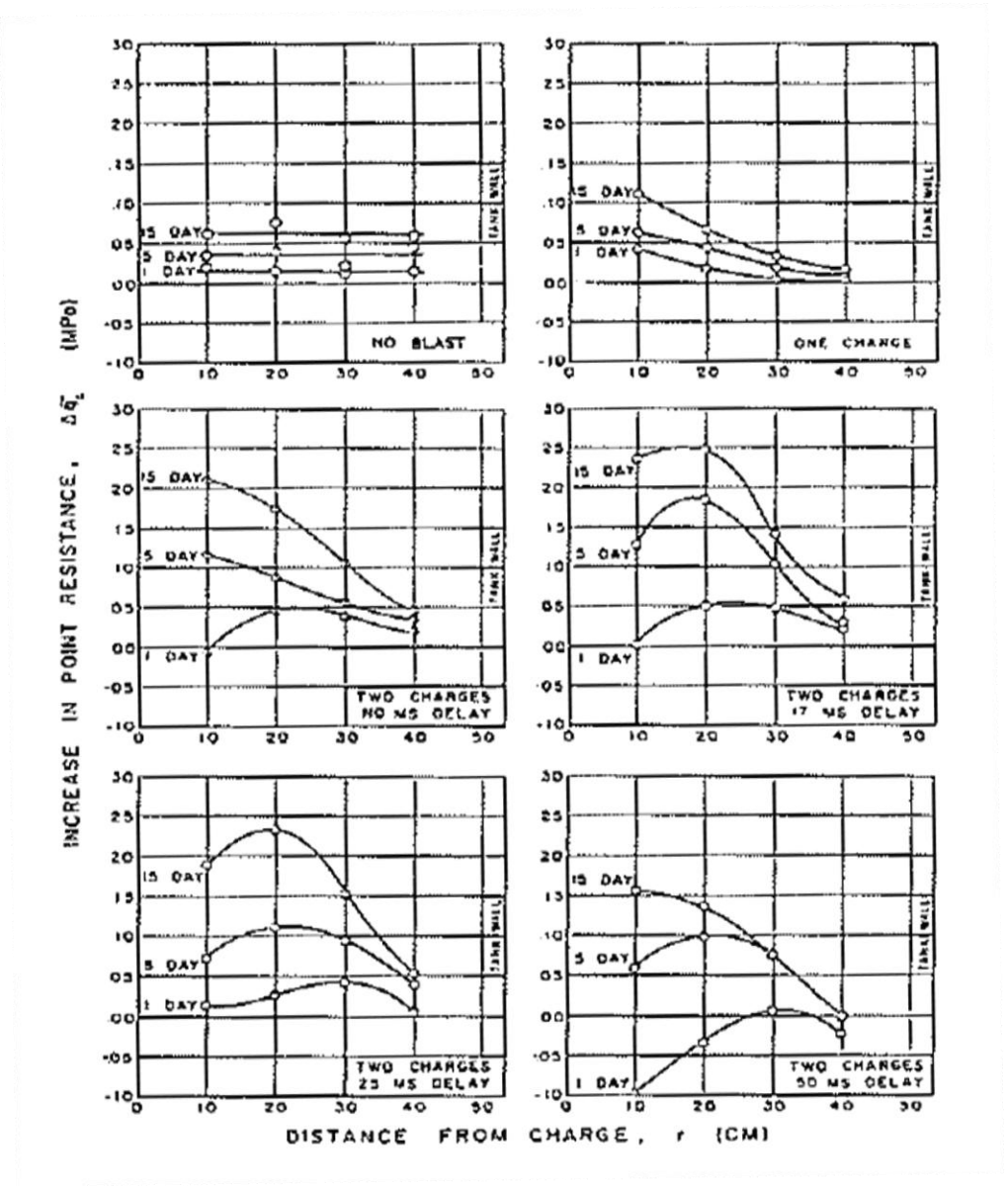

Figure 2-29. Penetration resistance increase with time after laboratory explosive densification tests (Dowding and Hryciw, 1986).

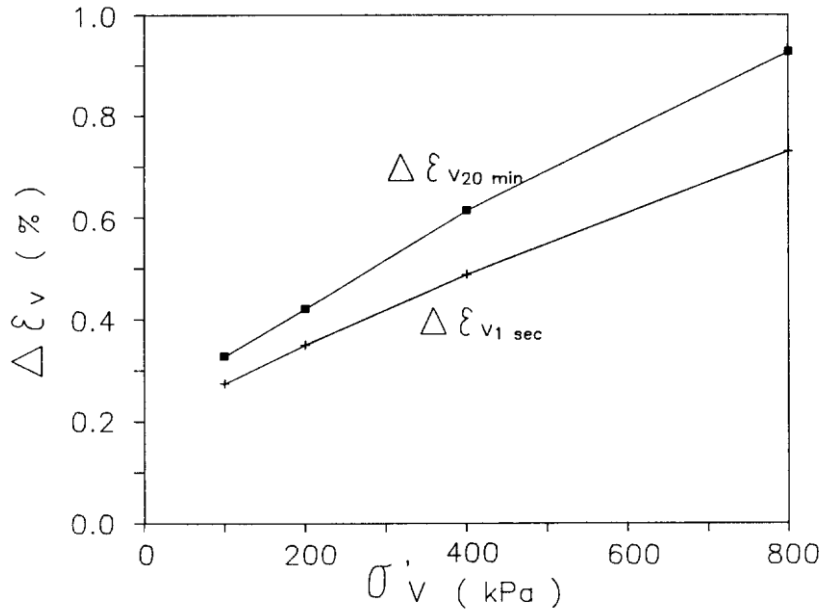

Figure 2-30. Instant and creep strains in 1-D oedometer tests (Mejia et al., 1988).

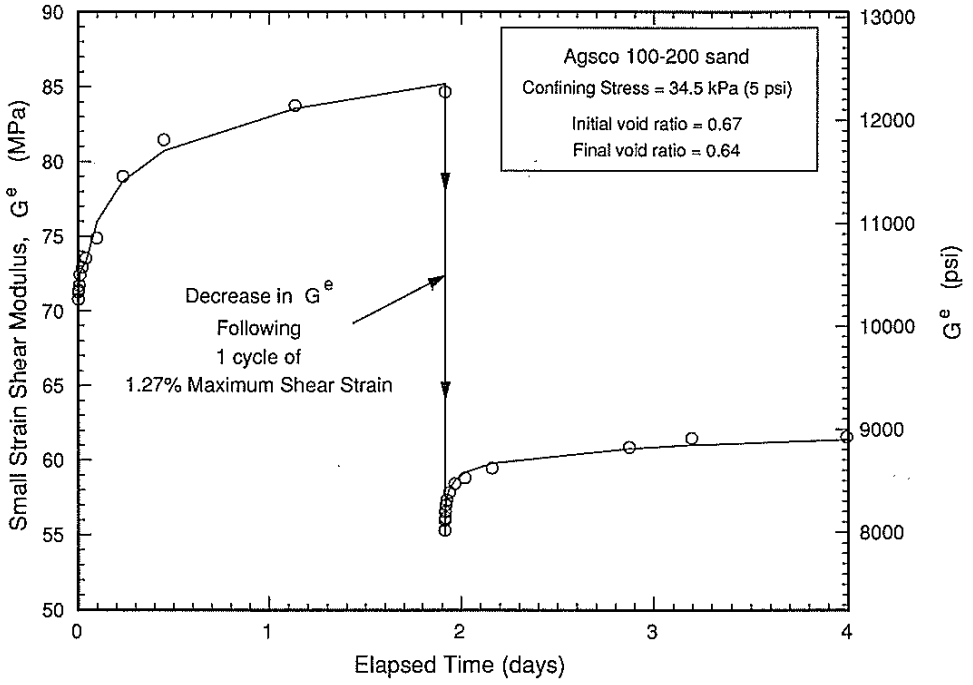

Figure 2-31. Typical change in shear modulus with time following high amplitude shearing in resonant column tests (Thomann and Hryciw, 1992a).

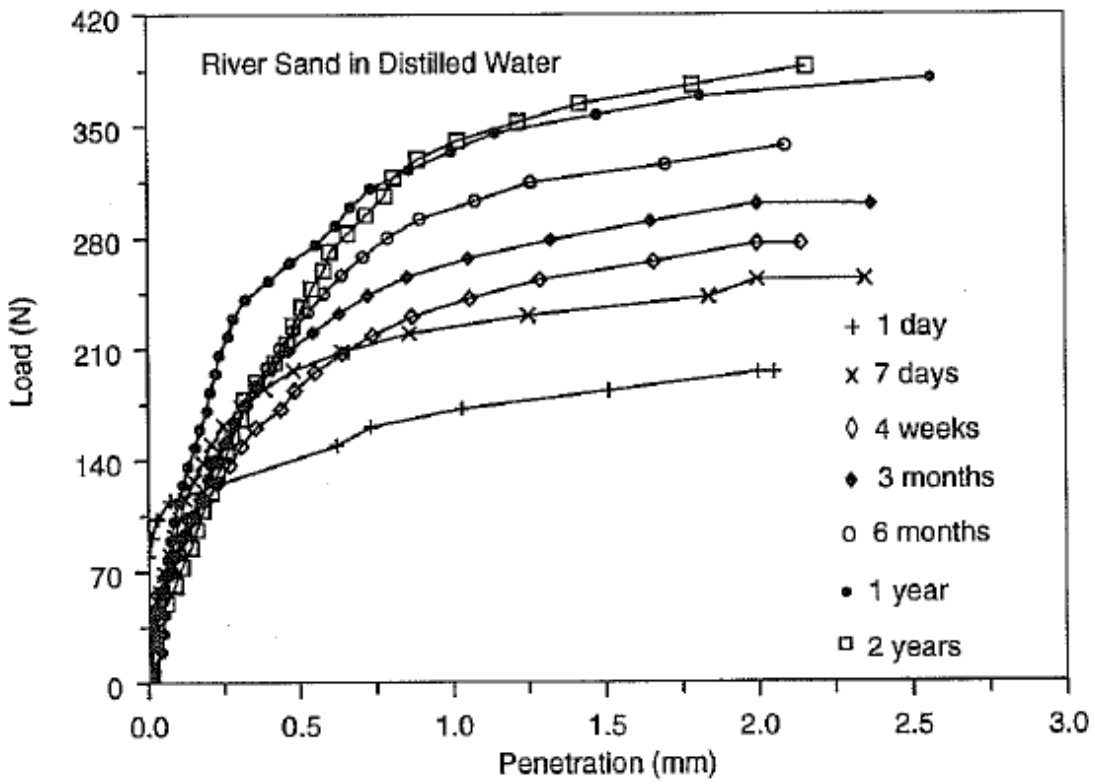

Figure 2-32. Increasing penetration resistance following laboratory sample preparation of river sand submerged in distilled water (Joshi et al., 1995).

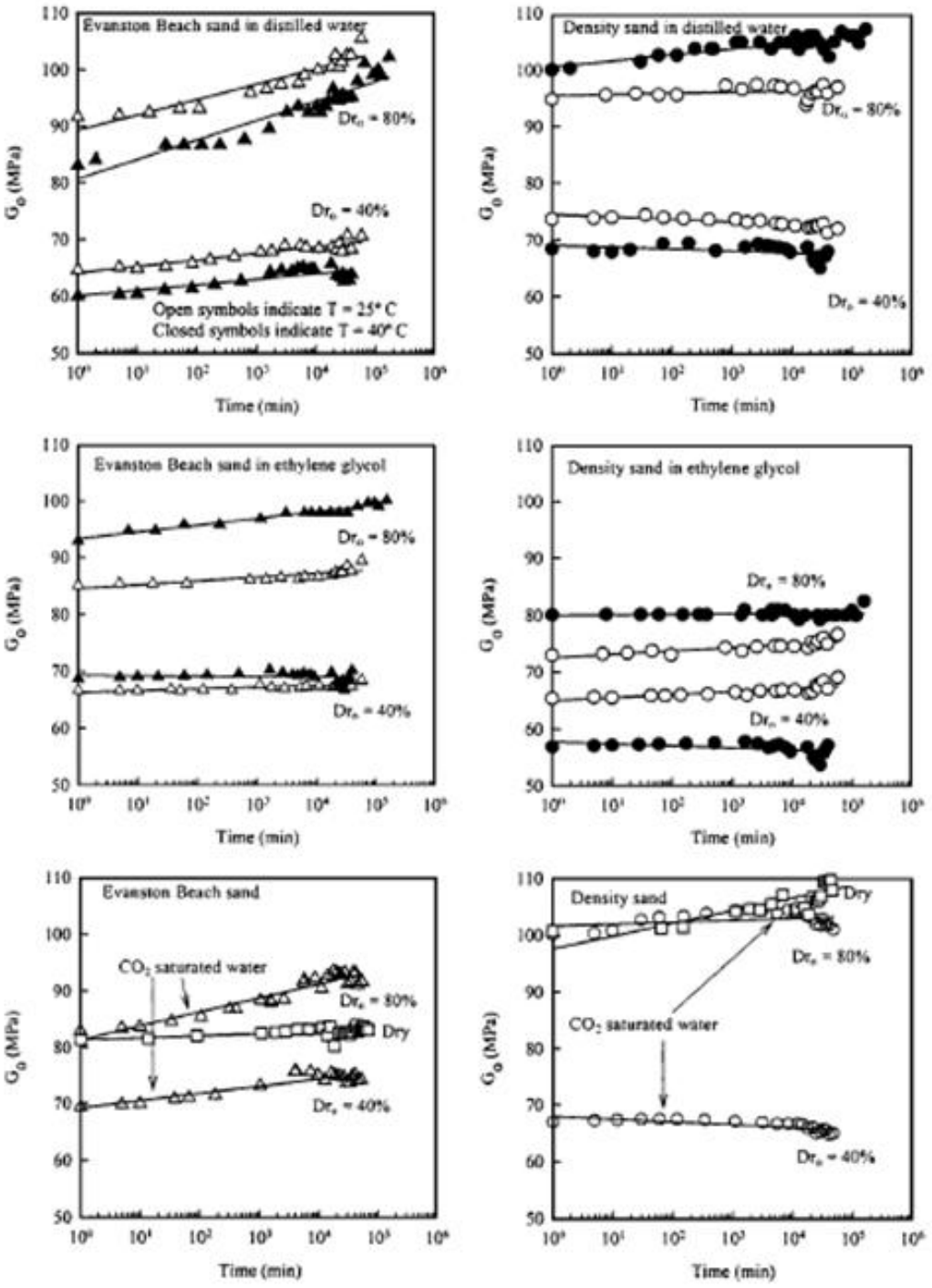

Figure 2-33. Shear wave velocity measurements from laboratory specimens using different sands and different pore fluids (Baxter and Mitchell, 2004).

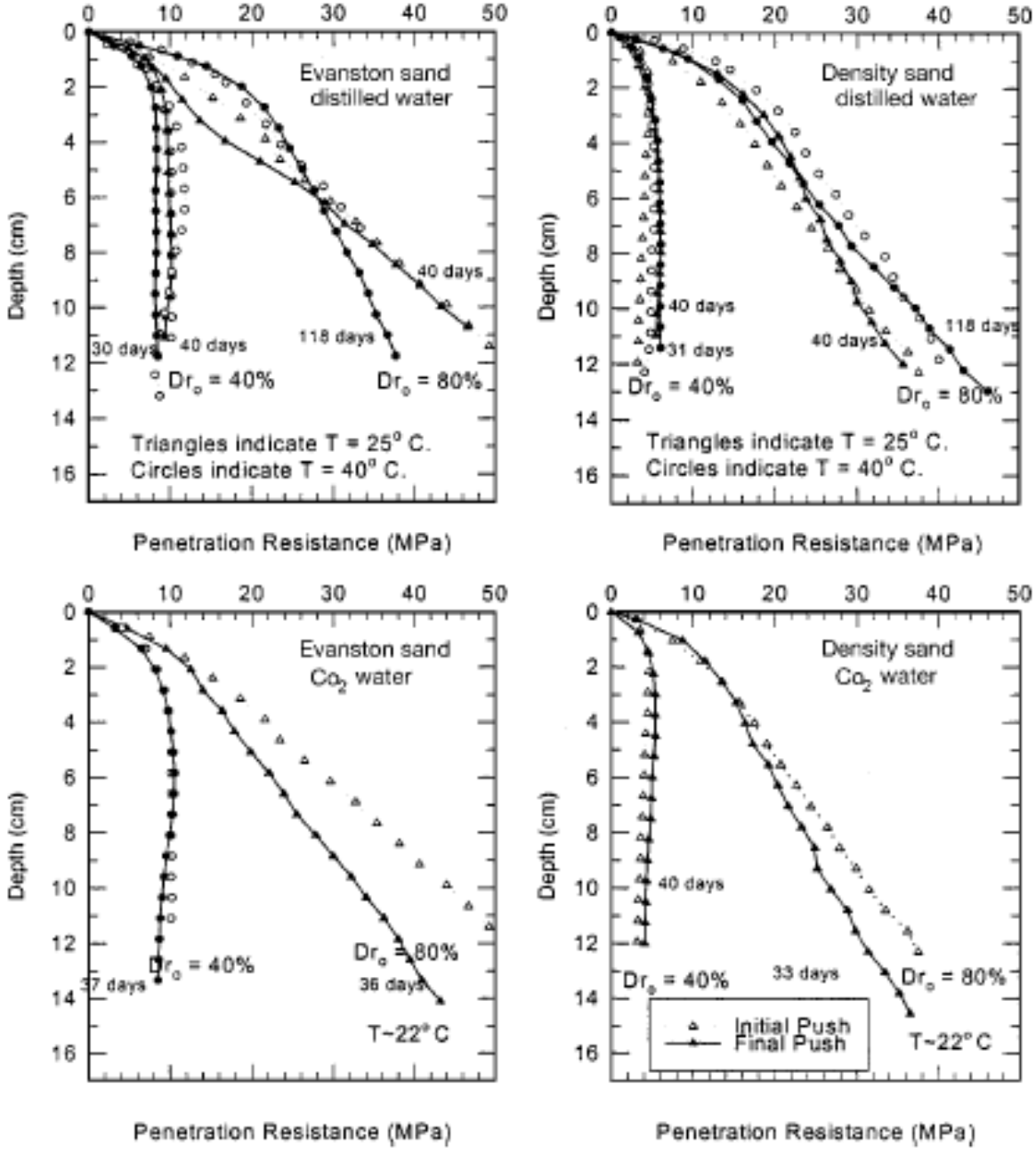

Figure 2-34. Penetration resistance measurements from laboratory specimens using different sand and different pore fluids (Baxter and Mitchell, 2004).

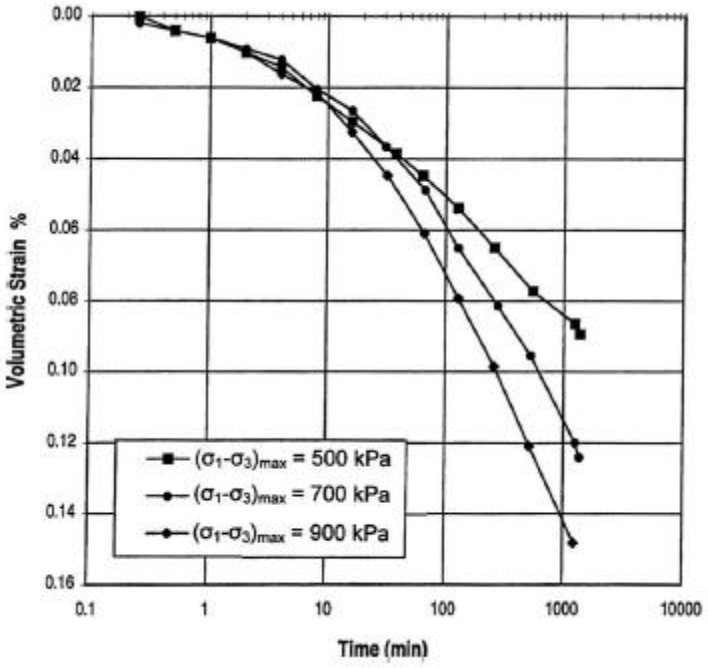

Figure 2-35. Volumetric strain versus the logarithm of time in creep tests on crushed coral sand (Lade et al., 2009).

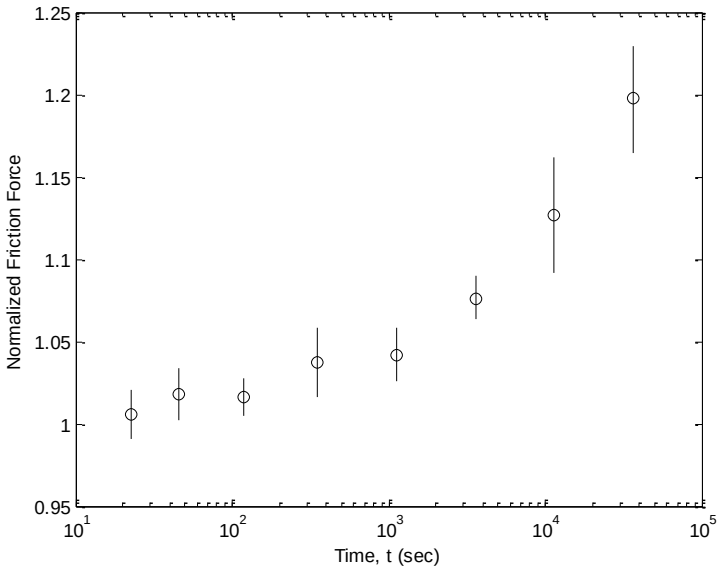

Figure 2-36. Ratio of the force required to move a plate across aged glass beads to the force required to move the plate across freshly deposited glass beads (adapted from Losert et al., 2000).

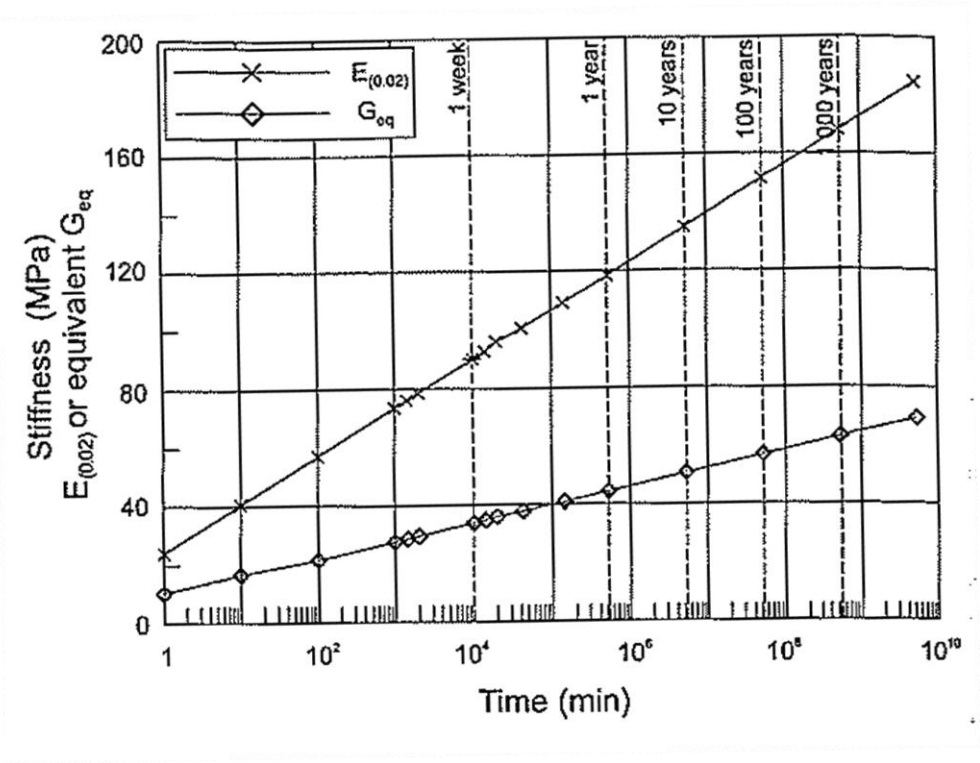

Figure 2-37. Increasing modulus with time following laboratory sample preparation (Howie et al., 2002).

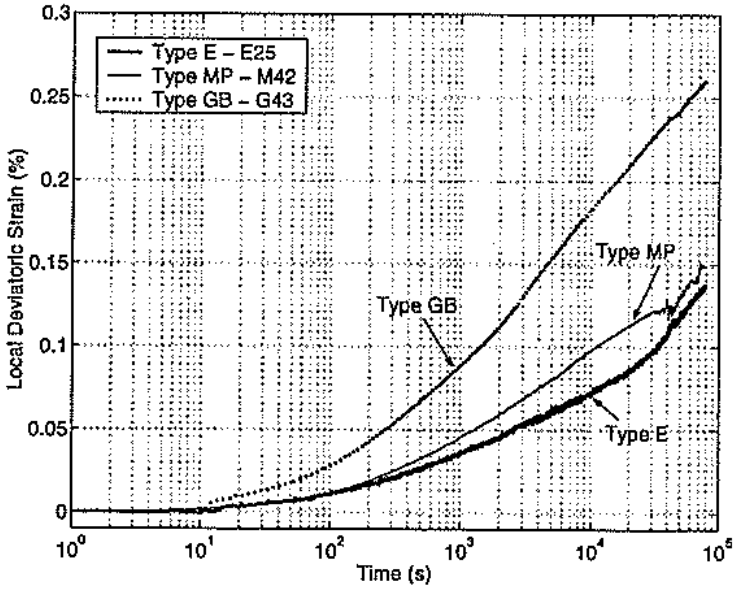

Figure 2-38. Creep behavior for glass beads (Type GB), Montpellier beach sand (Type MP), and Leighton Buzzard sand (Type E) (Bowman and Soga, 2003).

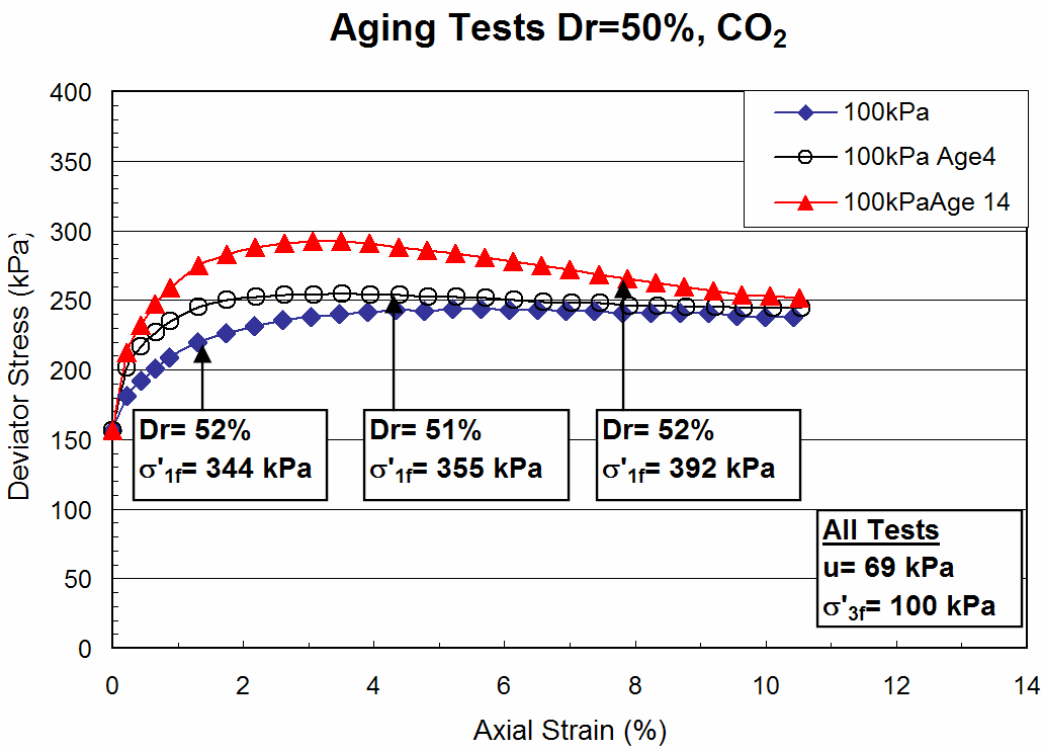

Figure 2-39. Triaxial results from tests on partially saturated sand containing CO_2 (LeClerc, 2008).

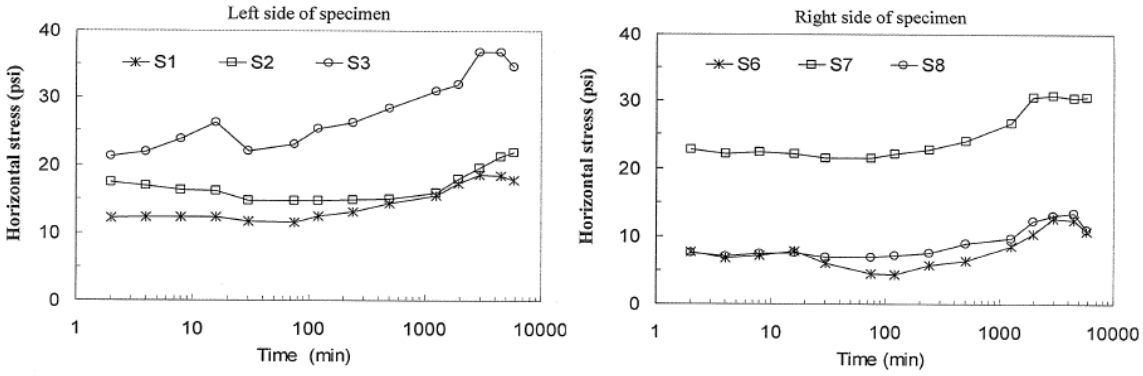

Figure 2-40. Change in horizontal stress in 2-D assembly of glass cylindersmeasured using photo-elastic methods (Jirathanathaworn, 2009).

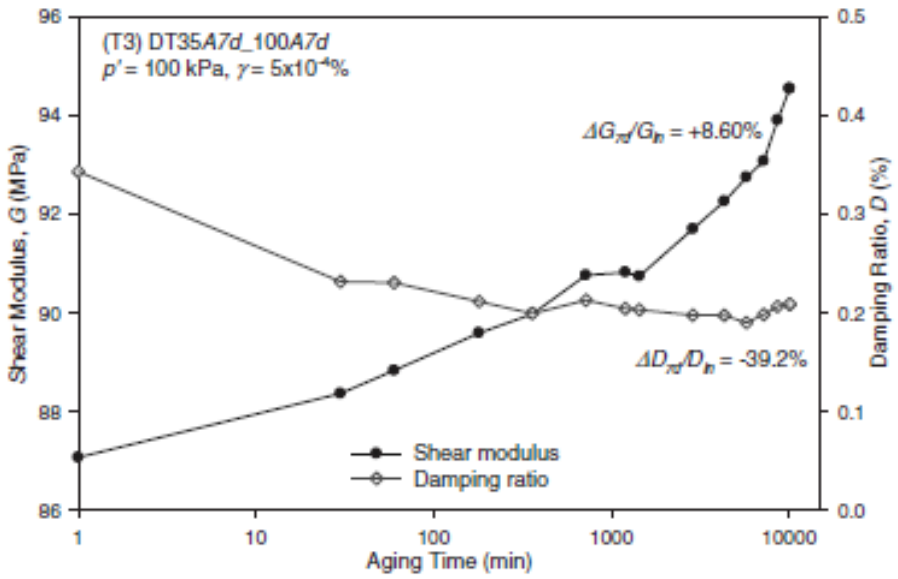

Figure 2-41. Changes in shear modulus and damping ratio in dense Toyoura sand (Wang and Tsui, 2009).

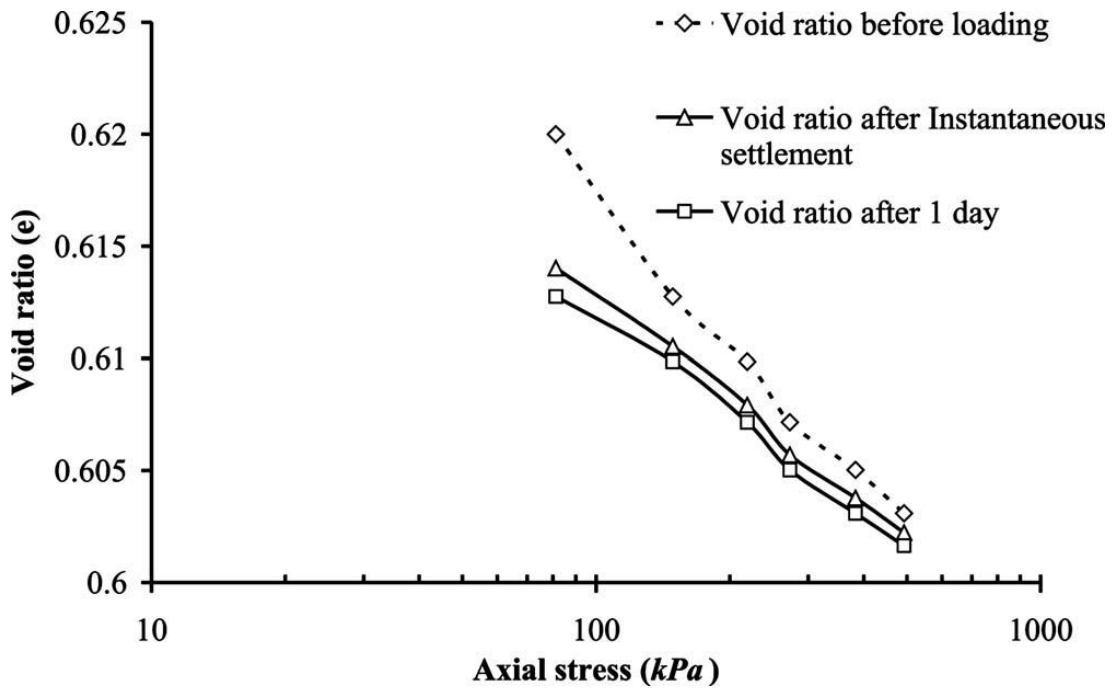

Figure 2-42. Change in void ratio during compression tests on glass beads (Ghiabi and Selvadurai, 2009).

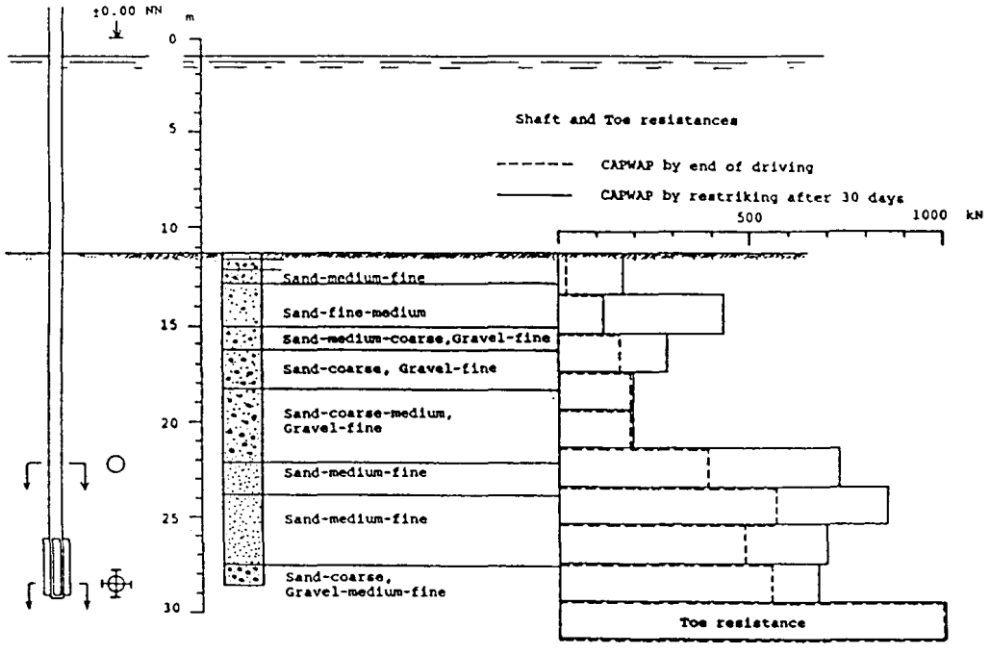

Figure 2-43. Results of shear wave analysis (CAPWAP) predicting side friction and end bearing in piles driven in Hamburg, Germany (Skov and Denver, 1988).

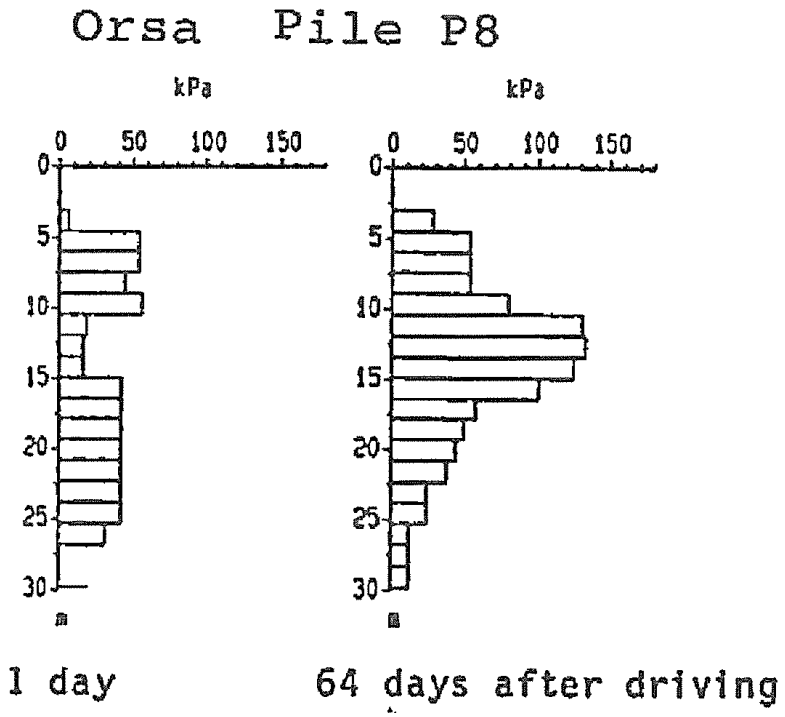

Figure 2-44. Results of shear wave analysis (CAPWAP) predicting side friction and end bearing in piles driven in Orsa, Sweden (Ghiabi and Selvadurai, 1992).

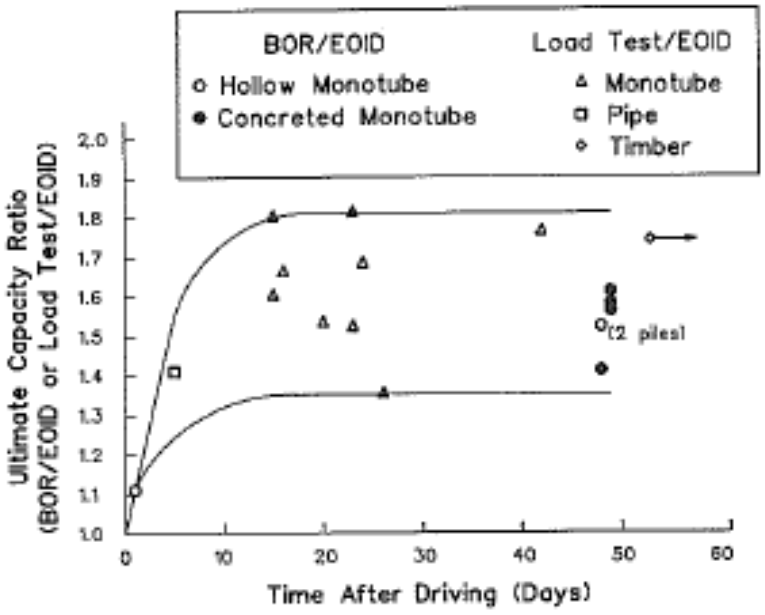

Figure 2-45. Evidence of set-up in piles driven at JFK airport, New York, New York (York et al., 1994). BOR stands for beginning of restrike and EOID stands for end of initial driving.

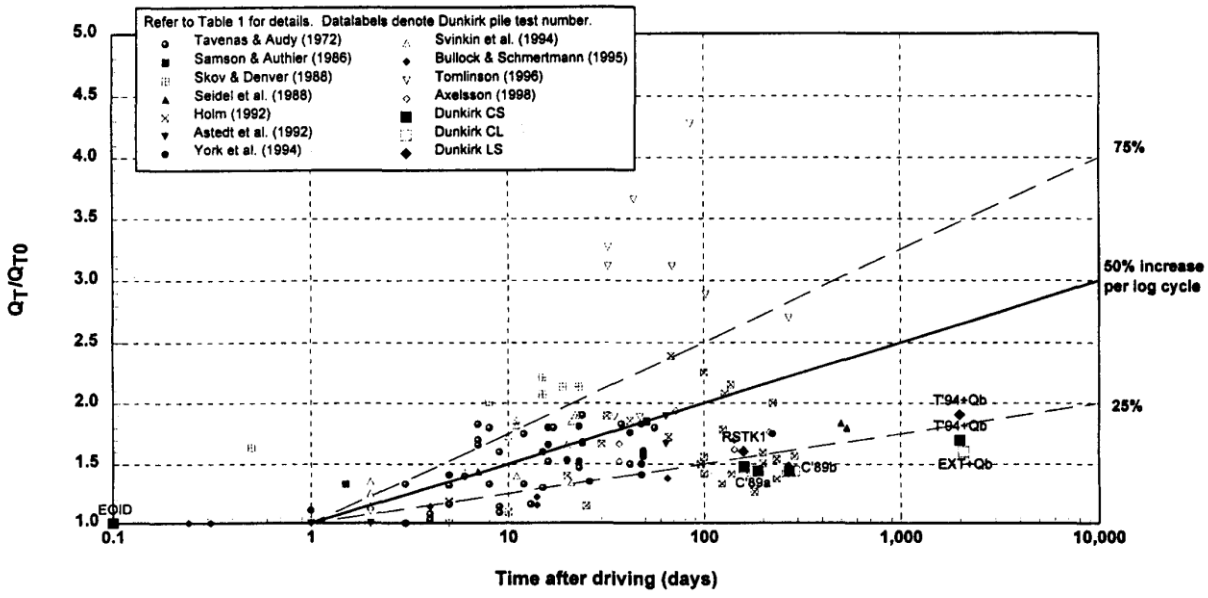

Figure 2-46. Summary of set-up evidence from many projects (Chow et al., 1998).

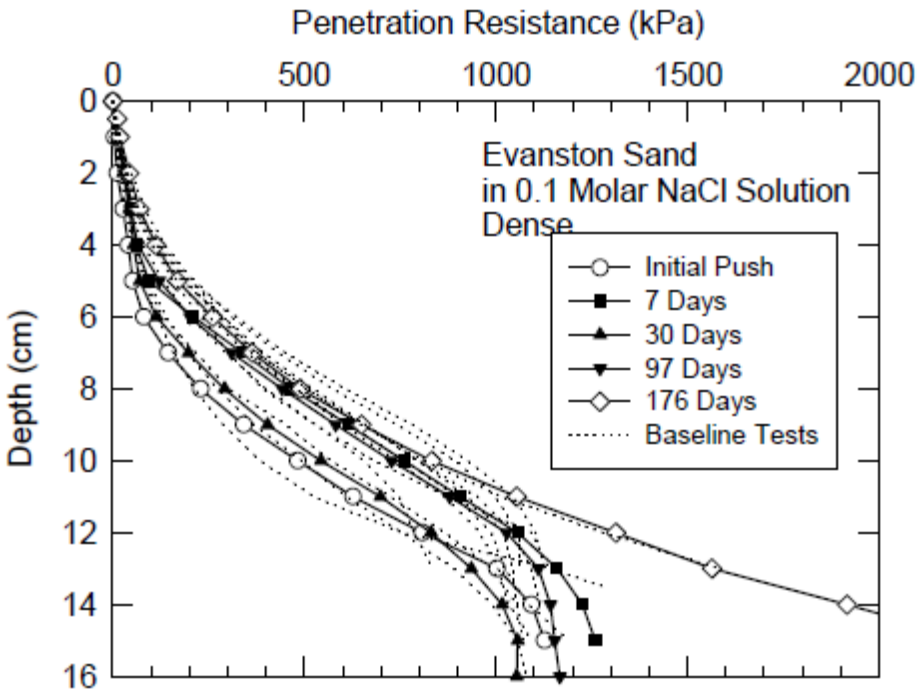

Figure 2-47. Results of laboratory cone penetration tests on a sample of Evanston sand (Baxter, 1999).

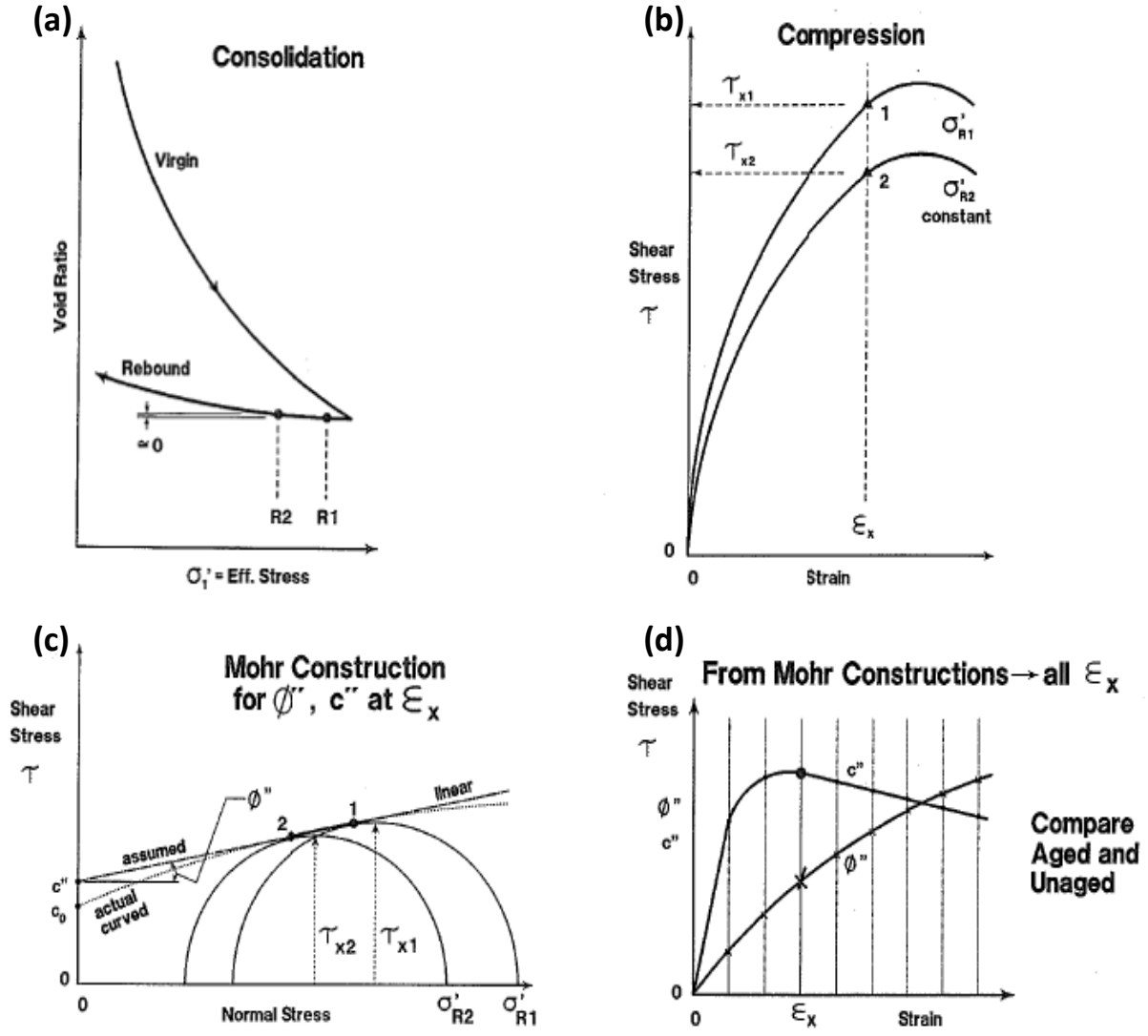

Figure 2-48. Explanation of IDS test (after Schmertmann, 1991). (a) Selection of two points on rebound curve with nearly identical structure, but different effective stresses. (b) IDS tests run on the two samples with similar structures at different effective stresses. (c) Construction of Mohr's circles based on data from step (b). (d) Plotting the results of step (c), allowing for comparison with age of samples.

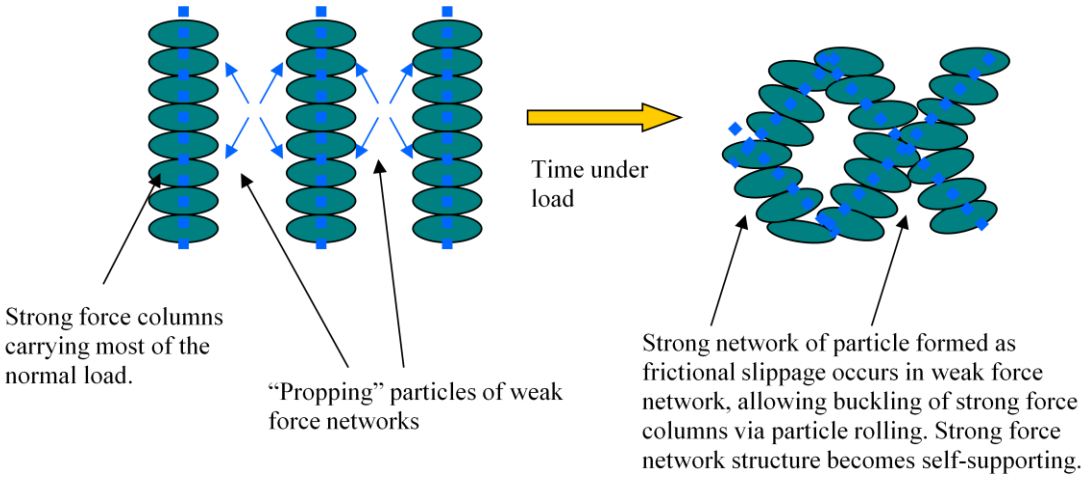

Figure 2-49. Changes in force networks with time, an explanation of mechanical aging (after Bowman, 2002).

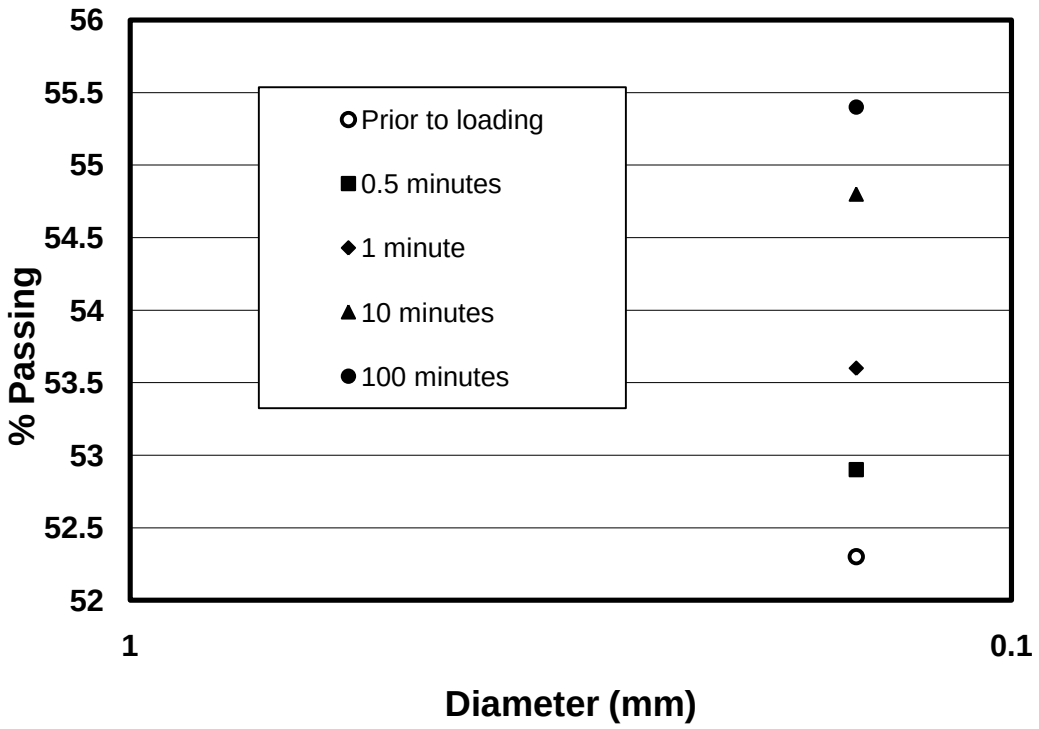

Figure 2-50. With greater time under a sustained load, Yangtze River sand becomes finer, indicating particle breakage, as shown in the % passing the #100 seive (adapted from Wang et al., 2010).

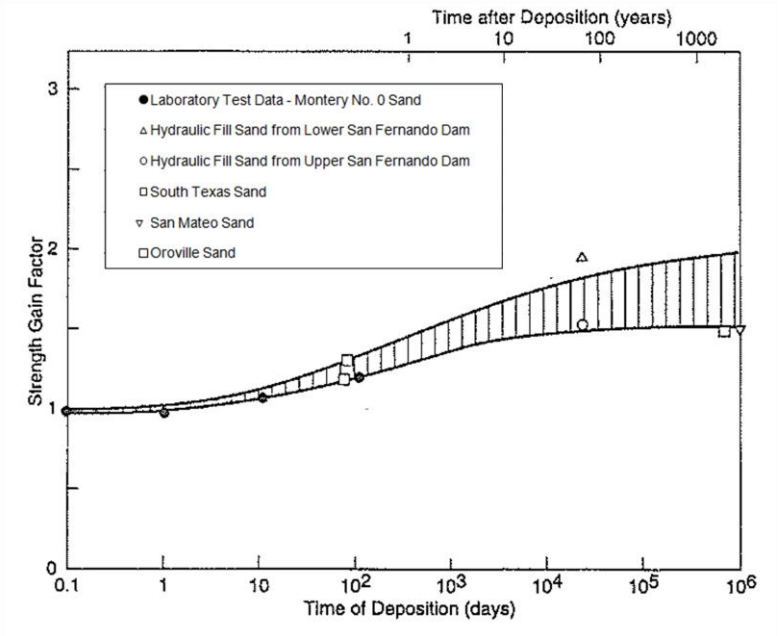

Figure 2-51. Influence of aging on liquefaction resistance (Seed, 1979).

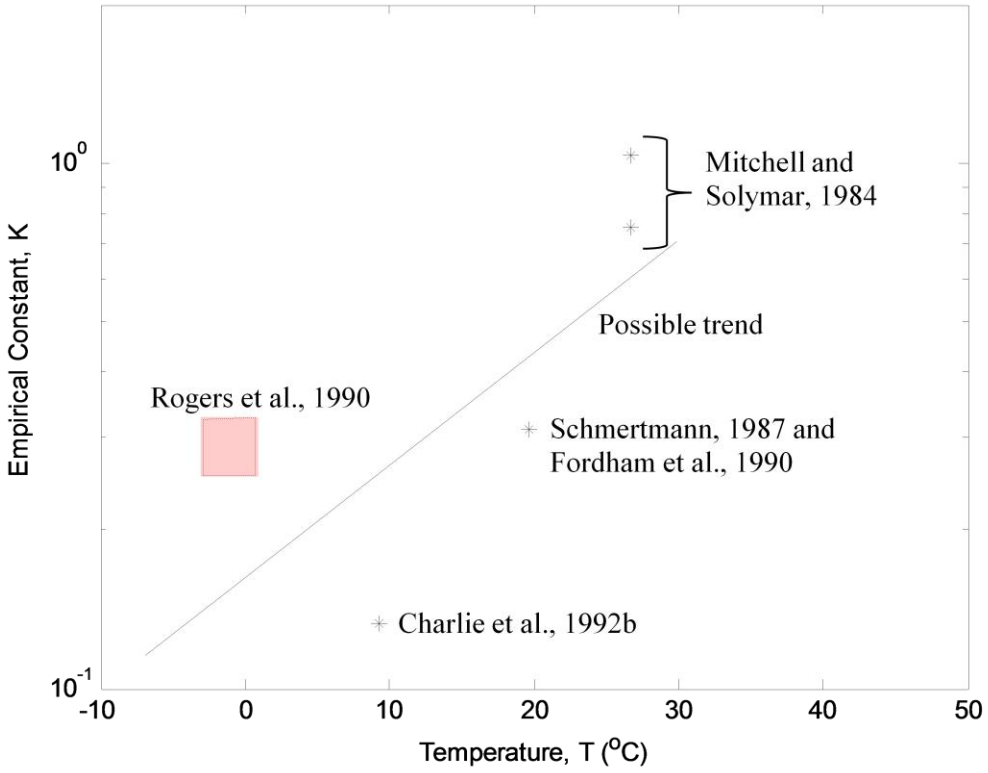

Figure 2-52. Revised normalized tip resistance vs. temperature (adapted from Jefferies and Rogers, 1993).

Chapter 3

Geostatistical Analysis of *In Situ* Geotechnical Tests

3.1 Introduction

In the previous chapter, a brief explanation of geostatistical methods was presented and examples were provided where spatial variability of standard penetration tests (SPT), cone penetration tests (CPT), soil layering, shear wave velocity (V_s), and liquefaction resistance were investigated. The purpose of this chapter is to provide a more detailed explanation of geostatistical methods. The advantages of geostatistics in accounting for spatial variability, development of a model variogram, a technique of accounting for anisotropy, and kriging methods will be presented. The methods presented in this chapter will be applied to data presented in subsequent chapters.

3.2 Advantages of Geostatistical Methods

Geostatistics is a method of interpolating and extrapolating spatially or temporally distributed data. It was developed for use in the mining industry in the 1950s, but its use has spread to other disciplines since then. Representative applications include, but are not limited to, contaminate, wildlife, precipitation, disease, temperature, and housing prices (Michalak, 2009). By recognizing that measurements closer to a point of interest better inform one about the state of that point than measurements further away, geostatistics accounts for spatial correlation.

A simple example of geostatistics' ability to account for spatial parameters is shown in Figure 3-1. Figure 3-1(a) shows that 10 snow depth measurements were made across an area. While nine of these measurements were clustered together at one end of the area, a tenth was taken far away. As shown in Figure 3-1(b), mean snow depth assuming spatial independence of these measurements is very close to the nine measurements taken close together, while the tenth measurement does not contribute significantly to the estimate of the mean. However, an estimate of the mean snow depth using geostatistical methods that assumes spatial correlation accounts for the fact that the clustered measurements do not provide as much information about the spatial

variability of snow depth across the site as the more distant measurement. As a result, the predicted mean snow depth is significantly higher and likely more accurate.

Applying geostatistical methods to the present study is critical because a soil deposit's natural variability can obscure the effects of aging. For example, Figure 2-47 shows test results that seem to demonstrate sand aging as penetration resistance increases with time since preparation of a laboratory sample. However, because all of the results after preparation fall within the bounds of penetration resistance from fresh samples, it is difficult to say with any certainty that the differences in test results at various times are due to aging effects rather than spatial variability. Therefore, results from field tests performed as part of this research project will be analyzed using geostatistical methods in order to quantify spatial variability and determine with a given amount of certainty that differences at various times following disturbance are due to aging effects rather spatial variability.

3.3 Variogram Development

The variogram is a function that describes the spatial variability of a given parameter. For demonstration purposes, creation of a variogram for a simple dataset is presented in Figure 3-2. The raw variogram forms the basis from which the theoretical variogram arises. Each data point is compared to every other point. Both the distance between the points, *h*, and raw variance, $\gamma(h)$, are calculated. The raw variance is calculated using Equation 3-1.

$$\gamma(h) = \frac{(z_i - z_{i+1})^2}{2} \quad \ldots(3\text{-}1)$$

Where z_i and z_{i+1} represent the i^{th} and $i+1^{th}$ value of the parameter of interest. A raw variogram is a plot of $\gamma(h)$ versus *h*. The dataset is shown in Figure 3-2(a), while the raw variogram is plotted in Figure 3-2(b).

The experimental variogram separates the raw variogram into bins based on the distance between points and averages all of the entries in that bin. An example is presented in Figure 3-2(c); however, larger datasets can present issues that are not apparent from this example. The selection of bin size is a difficult process. If the bin size is too small, the experimental variogram will display too much variability to fit a theoretical variogram. If the bin size is too large, the experimental variogram will not contain enough information to determine the best theoretical variogram. In this project, bin size was determined through trial and error.

Finally, a theoretical variogram is fit through the experimental variogram. There are two categories of models for theoretical variograms: stationary models and intrinsic non-stationary models. Stationary models approach a maximum value at greater separation distances, whereas intrinsic non-stationary models continue to increase with separation distance. Because data from *in situ* geotechnical testing is best described using stationary variogram models, only stationary models are discussed here. In each of the following model descriptions, *b* represents the sill, or maximum value that the model obtains at large separation distance, and *a* represents the correlation length where the models reach the sill.

A nugget model, pictured in Figure 3-3(a), can represent micro-variability or measurement error. An exponential model is pictured in Figure 3-3(b) and is the best model to describe geologic data, such as is presented in this dissertation (Chiles and Delfiner, 1999). A spherical model, pictured in Figure 3-3(c), differs from the other stationary, non-nugget models in that it reaches the sill rather than approaching the sill. A Gaussian model is pictured in Figure 3-3(d). The variogram and covariance functions for each of these models are presented in Table 3-1. A combination of the nugget model with another stationary model is another common theoretical variogram model. Due to the small number of data points used in the example shown in Figure 3-2, it is difficult to fit a theoretical variogram to the experimental variogram. However, as will be demonstrated in the following chapters, the experimental data generated in this project follows a theoretical model better than the small example data set presented here.

There are several common methods of choosing both a theoretical variogram model and the parameters for the model. In each of these methods, fitting the theoretical variogram to the points in the experimental variogram close to the origin is important. This is the case because the measured data points closest to estimation point and, therefore, with the smallest separation distance, have the greatest effect on the estimation in geostatistical analysis. The method used in this work is fitting by eye and/or physical understanding. Other methods include statistical approaches such as orthonormal residual analysis and restricted maximum likelihood. Cross-validation, where known data are removed from the set and predicted using the model, is another selection technique. In this project, the parameters *a* and *b* were chosen by eye. A sensitivity analysis showed that reasonable variations of these parameters did not significantly affect the results.

The theoretical variogram is of great importance in geostatistical analysis. Given a known estimation location and all of the existing data, one can easily determine the separation distance

between all of the points of interest. Using the theoretical variogram, one can determine the variance and covariance between the estimation location and all known data points. The covariance values make up the $\underline{\underline{\Sigma}}$ matrix. The $\underline{\underline{\Sigma}}$ matrix, expressed in Equation 3-2, is an n x n matrix, where n is the number of measured observations in the database, determined using the covariance model and the distances between each of the measured observations.

$$\underline{\underline{\Sigma}} = \begin{bmatrix} C(h_{11}) & \dots & C(h_{1n}) \\ \vdots & \ddots & \vdots \\ C(h_{n1}) & \dots & C(h_{nn}) \end{bmatrix} \quad \dots(3\text{-}2)$$

3.4 Anisotropy

Soil properties typical vary more with depth than they do with lateral distance. If this anisotropy is not considered, the geostatistical estimates will not be accurate. The method of dealing with anisotropy used in this dissertation is coordinate transform. In coordinate transform, one must determine the correlation length of the data in both the *z* direction, or depth, and the *x*-*y* direction, along the ground surface. This is accomplished using the theoretical variogram.

The first step in this process is to build a raw, then experimental, then theoretical variograms considering distance in the *z*-direction only. In this dissertation, data from one CPT was not compared to other CPT results, as differences in the *x*-*y* plane would affect the analysis. In the process of determining the theoretical variogram, the correlation length in the *z*-direction is determined. Next, a raw variogram is built using only distance in the *x*-*y* direction. For this variogram, using data points at the same depth, for example z = 0.50 m or z = 8.20 m, are used, eliminating the effects of depth in this analysis. The same theoretical model, with the same sill, fits both the *z* and *x*-*y* direction experimental variograms. The only difference is the correlation length.

The ratio of these correlation lengths become the scale factor. For example, if the *z* direction theoretical variogram reaches a sill at a separation distance of one meter and the *x*-*y* direction theoretical variogram reaches a sill at a separation distance of five meters, the scaling factor would be five. Prior to using the data in geostatistical analysis, each of the depth values would be multiplied by five to account for the anisotropy. After determining the desired estimates and uncertainty, but before presenting the data, the depth values would be returned to their true values.

3.5 Kriging

Kriging is a method of estimating an unknown value based on spatial distributed data, placing higher weights on data collected close to the estimation location. Kriging was developed by Georges Matheron in 1960s, based on work performed by D.G. Krige, for use in the mining industry in France. This section will explain three types of kriging: kriging the mean, ordinary kriging, and block kriging.

3.5.1 Kriging the Mean

Kriging the mean is a method of determining the mean value of a property in an area accounting for spatial correlation. When the correlation length between measurements is short compared to the distance between measurements, kriging the mean produces the same value for the mean as the arithmetic mean. In the case of this research, the correlation length between measurements is long enough that there is value in considering spatial variation. Therefore, kriging the mean is considered as a possible method of analyzing the data.

Equations for determining the mean and uncertainty of a data set are presented in Equations 3-3 and 3-4, respectively. The kriging mean of the data set is β and the kriging uncertainty is σ_{β}^{2}. The weighting factors, $\underline{\lambda}$, are an n x 1 vector, where n is the number of measured values. These weighting factors and the LaGrange multiplier, ν, are determined by solving Equation 3-5. In Equation 3-5, $\underline{1}$ is an n x 1 vector filled with the integer 1 and $\underline{0}$ is an n x 1 vector filled with the integer 0.

$$\beta = \underline{\lambda}^{T}\,\underline{z} \qquad \ldots(3\text{-}3)$$

$$\sigma_{\beta} = \nu \qquad \ldots(3\text{-}4)$$

$$\begin{bmatrix} \underline{\underline{\Sigma}} & \underline{1} \\ \underline{1}^{T} & 0 \end{bmatrix} \begin{bmatrix} \underline{\lambda} \\ -\nu \end{bmatrix} = \begin{bmatrix} \underline{0} \\ 1 \end{bmatrix} \qquad \ldots(3\text{-}5)$$

It is important to note that one of the equations listed in Equation 3-5's system of equations states that the sum of all $\underline{\lambda}$ terms equals one. This ensures that the estimate is unbiased. The result of this method of kriging is a mean with uncertainty across a given measurement area using a known database of measurements and a theoretical variogram. The unbiased estimate is common to all forms of kriging discussed in this dissertation.

3.5.2 Ordinary Kriging

In ordinary kriging, one develops an estimate at a point based on a known data set, assuming that there is a constant, but unknown, mean. As was the case in kriging the mean, there are three key equations in ordinary kriging. The first, expressed in Equation 3-6, provides an estimate for a variable of interest at a given point, z_0*, based on measured values at other locations, $\underline{z}$, and a set of weighting factors, $\underline{\lambda}$. The underlined terms represent vectors of dimension n x 1, where n is the number of measured observations in the database.

$$z_0^* = \underline{\lambda}^T \underline{z} \quad \ldots(3\text{-}6)$$

In order to determine the values of the $\underline{\lambda}$ vector, it is necessary to solve the system of equations listed in Equation 3-7. In this system, $\underline{\underline{\Sigma}}$ is the covariance matrix that was determined using the theoretical variogram, $\underline{1}$ is an n x 1 vector filled with 1, ν is the LaGrange multiplier, and $\underline{\sigma_0}$ is an n x 1 vector determined from the theoretical variogram using the distances between the estimation point and the n^{th} point in the database, as shown in Equation 3-8.

$$\begin{bmatrix} \underline{\underline{\Sigma}} & \underline{1} \\ \underline{1}^T & 0 \end{bmatrix} \begin{bmatrix} \underline{\lambda} \\ -\nu \end{bmatrix} = \begin{bmatrix} \underline{\sigma_0} \\ 1 \end{bmatrix} \quad \ldots(3\text{-}7)$$

$$\underline{\sigma_0} = \begin{bmatrix} C(h_{10}) \\ C(h_{20}) \\ \vdots \\ C(h_{n0}) \end{bmatrix} \quad \ldots(3\text{-}8)$$

Because the variance between points is used to determine the weighting factors, points closest to the estimation point receive the highest λ values, while points further away receive less weight. As a result, the estimation point is influenced most by the closest measurements. After determining the $\underline{\lambda}$ vector using Equation 3-7, one can use Equation 3-6 to find the value of the estimate, z_0*. Finally, Equation 3-9 should be used to determine the uncertainty of the estimate.

$$\sigma_{OK}^2 = C(0) - \underline{\lambda}^T \underline{\sigma_0} + \nu \quad \ldots(3\text{-}9)$$

The result of ordinary kriging is an estimate with uncertainty at a given estimation location using a known database of measurements and a theoretical variogram.

3.5.3 Block Kriging

One option of estimating the mean value of a given property in an area based on several measurements is kriging the mean. However, there is an assumption of infinite domain inherent in kriging the mean. Therefore, the measurements on the edges of the domain are taken to be

representative of the area outside of the measurements to a distance of the correlation length. The measurements on the edge of the area would, therefore, receive higher kriging weights and have more influence on the mean. Another option is to use ordinary kriging to estimate the parameter of interest at several locations and average the values. A disadvantage of this approach is that there is no clear method of determining the uncertainty of this estimate. A third option is to employ block kriging. When using block kriging, one does not need to average the results, the results of a block kriging analysis are the mean and uncertainty of the measured results across the domain. Additionally, when the correlation length is long compared to the domain, as is the case in this project, block kriging does not give additional weight to measurements taken at the edge of the domain. Therefore, block kriging will be used for the geostatistical analysis in this dissertation.

The equation for determining the mean of a data set using block kriging is presented in Equation 3-10. The mean of the data set is z_A^*. The weighting factors, $\underline{\lambda}$, are an *n* x 1 vector, where *n* is the number of measured values. These weighting factors and the LaGrange multiplier, ν, are determined by solving Equation 3-11. In Equation 3-11, $\underline{1}$ is an *n* x 1 vector filled with the integer 1. The definition of the *n* x 1 matrix $\underline{\sigma_A}$ is shown in Equation 3-12, while the equation used to estimate $\underline{\sigma_A}$ is presented in Equation 3-13.

$$z_A^* = \underline{\lambda}^T \underline{z} \quad \ldots(3\text{-}10)$$

$$\begin{bmatrix} \underline{\underline{\Sigma}} & \underline{1} \\ \underline{1}^T & 0 \end{bmatrix} \begin{bmatrix} \underline{\lambda} \\ -\nu \end{bmatrix} = \begin{bmatrix} \underline{\sigma_A} \\ 1 \end{bmatrix} \quad \ldots(3\text{-}11)$$

$$\sigma_{A,i} = \frac{1}{A} \int C(h_{ij})\, dx_j \quad \ldots(3\text{-}12)$$

$$\sigma_{A,i} = \frac{1}{A} \sum_{j=1}^{k} C(h_{ij})\, A_j \quad \ldots(3\text{-}13)$$

Where *A* represents the area of the domain, A_j represents the j^{th} portion of the total area, and *k* represents the number of blocks, or divisions in the domain.

The equation for determining the uncertainty of the data set is presented in Equation 3-14. The uncertainty of the data set is σ_{BK}^2. The covariance of an area with itself, *C(A)*, is defined in Equation 3-15. The estimation for *C(A)* used in this dissertation is presented in Equation 3-16.

$$\sigma_{BK}^2 = C(A) - \underline{\lambda}^T \underline{\sigma_A} + \nu \quad \ldots(3\text{-}14)$$

$$C(A) = \frac{1}{A^2} \iint C(h_{ij})\, dx_i\, dx_j \quad \ldots(3\text{-}15)$$

$$C(A) = \frac{1}{A^2} \sum_{i=1}^{k} \sum_{j=1}^{k} C(h_{ij}) A_i A_j \quad \ldots(3\text{-}16)$$

3.6 Conclusion

This chapter describes the geostatistical methods that will be applied to *in situ* geotechnical test results in order to demonstrate that differences between testing periods are due to sand aging effects and not spatial variability. Variogram development allows the difference between measurements taken over a spatially distributed area to be quantified. Additionally, a method of account for anisotropy was described. Block kriging will be used to determine the mean value of each data set in this dissertation. Block kriging represents an improvement over kriging the mean because it does not assume infinite domain and over ordinary kriging because it provides a method of quantifying uncertainty. These methods will be applied to data collected in the field in the next two chapters of this dissertation.

Table 3-1. Variogram and covariance functions.

Model	Variogram function	Covariance Function
Nugget	$\gamma(h) = \begin{cases} b, h > 0 \\ 0, h = 0 \end{cases}$	$C(h) = \begin{cases} 0, h > 0 \\ b, h = 0 \end{cases}$
Exponential	$\gamma(h) = b\left(1 - \exp\left(\frac{-h}{a}\right)\right)$	$C(h) = b * \exp\left(\frac{-h}{a}\right)$
Spherical	$\gamma(h) = \begin{cases} b\left(\frac{3}{2}\frac{h}{a} - \frac{1}{2}\frac{h^3}{a^3}\right), 0 \le h \le a \\ b, h > a \end{cases}$	$C(h) = \begin{cases} b\left(1 - \frac{3}{2}\frac{h}{a} + \frac{1}{2}\frac{h^3}{a^3}\right), 0 \le h \le a \\ 0, h > a \end{cases}$
Gaussian	$\gamma(h) = b\left(1 - exp\left(\frac{-h^2}{a^2}\right)\right)$	$C(h) = b * exp\left(\frac{-h^2}{a^2}\right)$

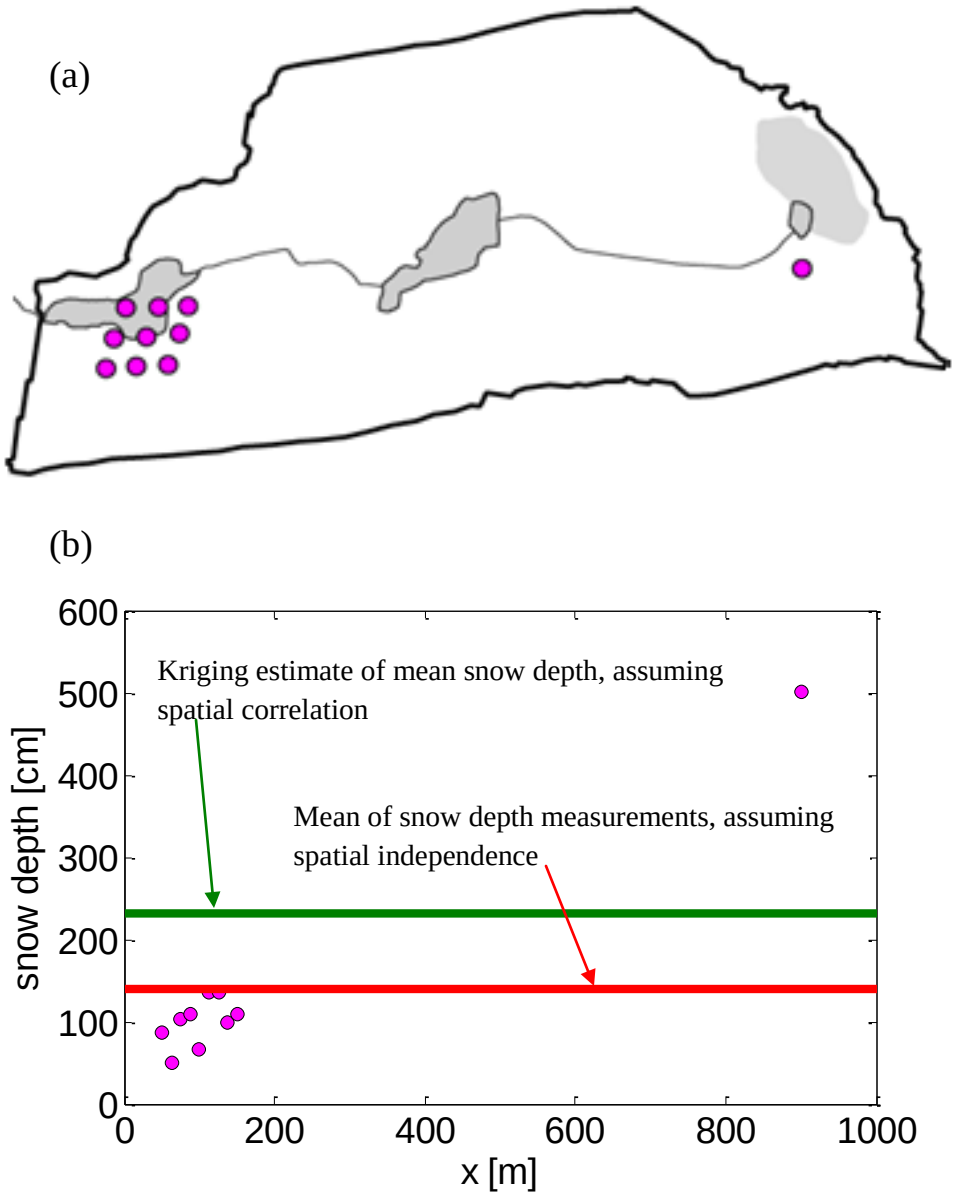

Figure 3-1. Estimate of snow depth in a valley (Michalak, 2009). (a) The sampling points are not distributed evenly throughout the area, but the majority of samples are clustered together. (b) The mean of the snow depth measurements assuming spatial independence is very similar to the clustered measurements. However, the kriging estimate of the mean snow depth, assuming spatial correlation, considers the spatial spread of the samples and places a higher weight on the value measurement taken further from the other measurements.

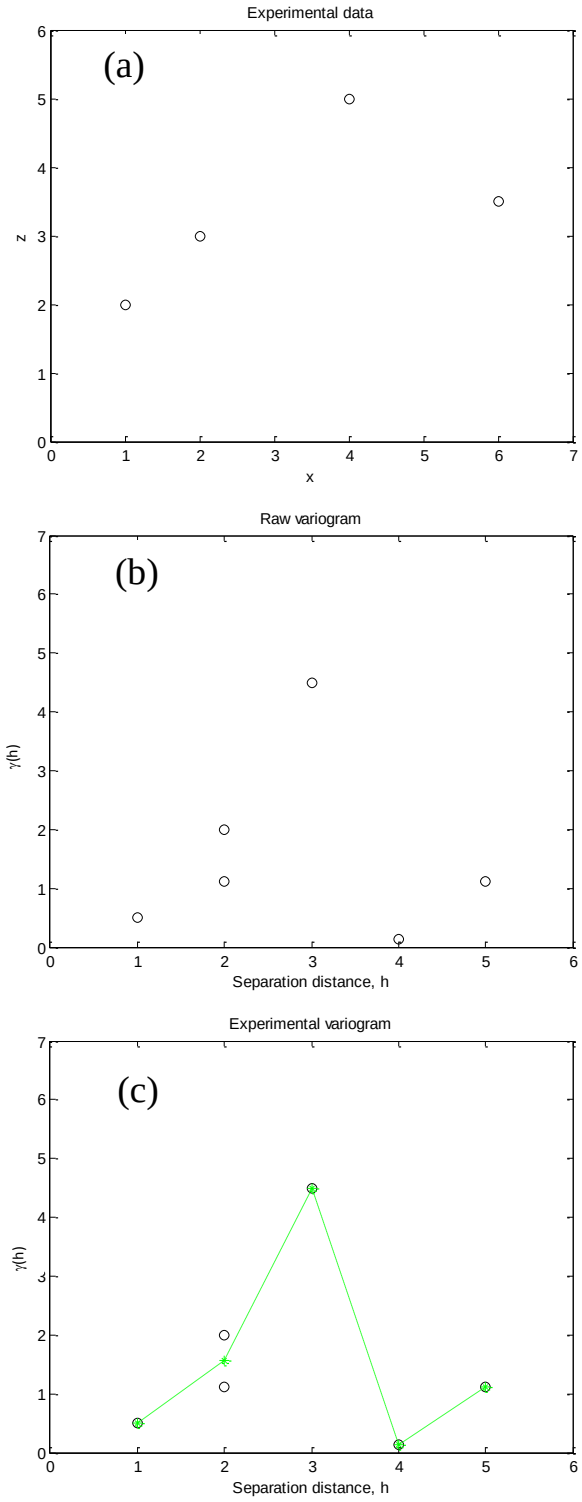

Figure 3-2. Use of experimental data, shown in (a), to generate a raw variogram, pictured in (b), and an experimental variogram, shown in (c) (adapted from Michalak, 2009).

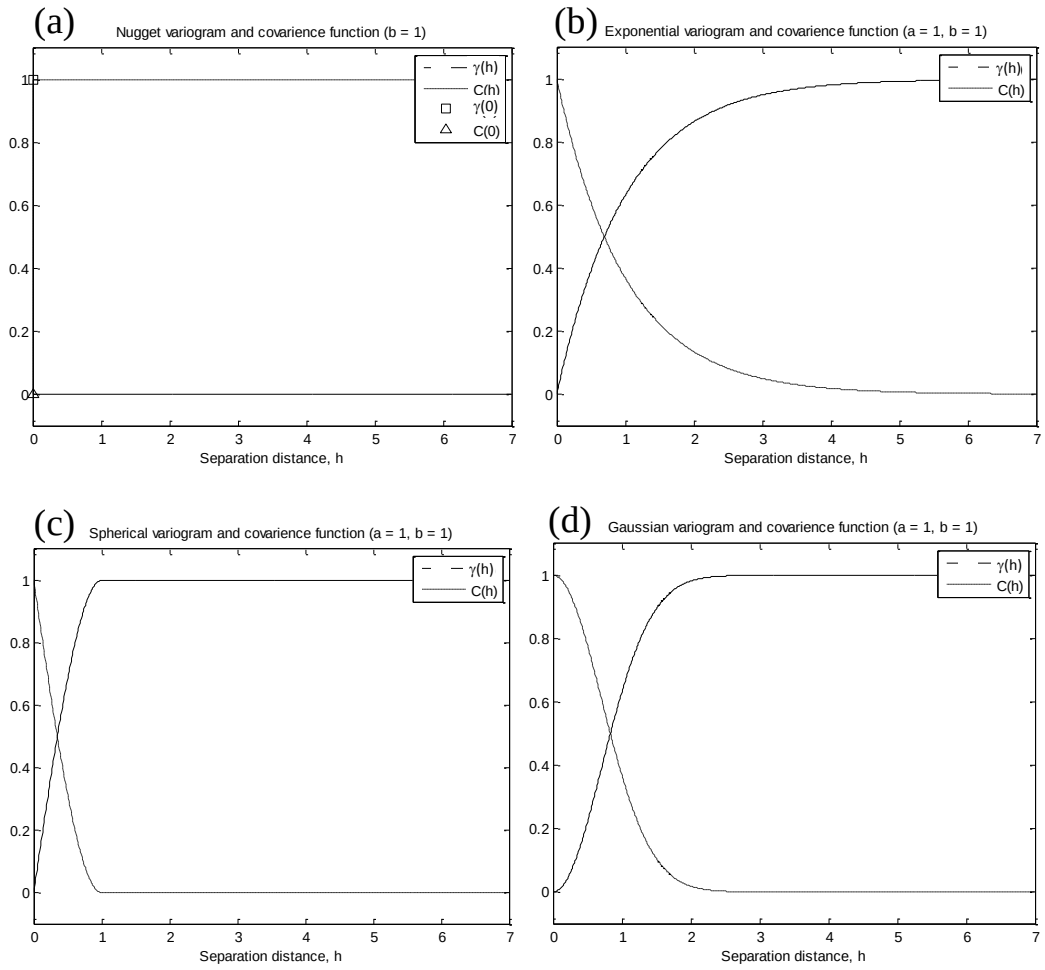

Figure 3-3. Theoretical variograms and covariance functions (adapted from Michalak, 2009): (a) nugget model, (b) exponential model, (c) spherical model, and (d) Gaussian model.

Chapter 4

Field Testing – Explosive densification

4.1 Introduction

In order to quantify aging effects, three field studies were performed. This chapter describes one of these studies, explosive densification performed at a sand and gravel quarry in Griffin, Indiana. Explosive densification was chosen because sand aging has been recorded following its use in many previous projects. Additionally, previous research has identified the amount of disturbance and aeration of pore fluid as two factors that influence sand aging effects. Explosive densification imparts a great deal of disturbance to the soil and introduces blast gas to the pore fluid. This chapter describes the site investigation, instrumentation plan, blast design and execution, post-blast testing plan, results of testing, a geostatistical analysis of the results, and a comparison of the predicted cyclic resistance ratio (CRR) based on different *in situ* tests.

4.2 Site Investigation

The following section discusses the site investigation conducted prior to field experimentation. The process of selecting a field site and an experiment location within the field site is presented as well as a description of the soil profile and pre-blast *in situ* test results.

4.2.1 Site Selection

Site investigation began in 2006 and focused on the selection of an appropriate field site to perform the field experiments. Site selection was complicated by the planned use of explosive densification, as several site owners were hesitant to allow explosive detonations on their property. Eventually a seemingly ideal site, a sand and gravel quarry owned by Mulzer Crushed Stone, Inc. and pictured in Figure 4-1, was identified in Griffin, Indiana. The presence of a sand and gravel quarry suggested that the course grained soil layers would be clean. This is important because fine grained soils reduce the effectiveness of explosive densification and vibroseis shaking.

Additionally, there was evidence of prehistoric liquefaction at the site, indicating that the sand layers were liquefiable. Paleo-liquefaction features, such as shown in Figure 4-2, were found along the banks of the borrow pit. The company that owns the quarry excavates a clay cap prior to dredging the sand and gravel at greater depths. This leaves vertical cuts in the clay along the edge of the dredged lake. Contained in these cuts are vertical dikes of sand and gravel. In a previous liquefaction event, excess pore pressure dissipated through a weak point in the clay, carrying sand and gravel from the deeper liquefied layer, and leaving such paleo-liquefaction features that are visible around the edge of the lake.

Because Mulzer Crushed Stone, Inc. was willing to donate the use of the property for our experimentation, the site contained clean, saturated sand deposits, and there was pre-historical evidence indicating liquefaction potential, this site was chosen for further investigation. *In situ* testing, including cone penetration tests (CPT), vision CPT (VisCPT), seismic CPT (SCPT), and Marchetti dilatometer tests (DMT), was conducted in the summer of 2006; however, the area that was tested was cleared for dredging operations the following spring. While this testing did not lead to the selection of an experimental site, the low CPT tip resistance (q_c) readings demonstrated that the Griffin quarry was an appropriate field site to investigate sand aging.

4.2.2 Experiment Location Selection

In 2007, 14 *in situ* tests, including VisCPT and SCPT, were conducted at the quarry. Both the 2006 and 2007 test areas are shown in Figure 4-1. Results of CPT-9 and CPT-11, tests showing low q_c, are presented in Figure 4-3. The locations of these tests are also highlighted in Figure 4-1. Explosive densification is more effective when several charges are set off using delays, shearing the soil multiple times as several shock waves pass (Ivanov, 1967; Hryciw, 1986). Therefore, it was necessary to find an area to accommodate several blast points with low q_c. The area between CPT-9 and CPT-11 was selected for the blast testing.

4.2.3 Soil Profile

Throughout the Griffin quarry, there are four principle soil layers. From the surface, they are: a clay layer, a loose sand layer, a dense sand layer, and a loose gravelly sand layer. Below the loose gravelly sand layer is a gravelly sand layer between 16 and 18 m below the surface that becomes too dense for penetration testing, rotary drilling, and dredging. These layers were identified from the cone penetration data. A drop in the friction ratio (F_r) delineates the clay and loose sand layer. Increasing q_c marks the bottom of both the loose sand layer and loose gravelly sand layer.

Decreasing q_c shows the break between the dense sand layer and the loose gravelly sand layer. These delineations were determined by the author, but are corroborated through empirical correlations relating soil type to CPT results.

The layer thicknesses vary across the site, but are fairly consistent in the blast area. As shown in Figure 4-4, the thickness of the clay, loose sand, dense sand, and loose gravelly sand layers are 1.5m, 2.5m, 6m, and 4m respectively. As shown in Figure 4-5, the soil becomes coarser with depth. It is a poorly graded sand (SP by the Unified Classification System) in the loose sand layer and a poorly graded sand with gravel (SP with >15% gravel by the Unified Classification System) in the loose gravelly sand layer.

Fraser et al. (1981 and 1997) describe the geologic history of the area. The dense sand and loose gravelly sand layers are made up of Pleistocene sand and gravel outwash. They were deposited by the Trafalgar ice sheet. The loose sand layer is an early Holocene fluvial sand. Fidler (1935) states that the area has not undergone any major geologic changes since the retreat of the Illinois ice sheets in the early Holocene period.

4.2.4 Cone Penetration Testing

The CPT is the primary *in situ* test used in this study. As shown in Figure 4-6, the cone has a 10 cm^2 cross sectional area and 60˚ apex angle. The test measures q_c, F_r, and pore pressure, u. Additionally, VisCPT and SCPT were used. A camera is fitted above the cone in the VisCPT, allowing visual inspection of soil continuously with depth. As shown in Figure 4-7, the SCPT, using an accelerometer inside the cone, measures arrival times of shear wave originating from a source at the ground surface. This test provides a V_s profile to complement the CPT data.

In order to assess the spatial variability of the blast area, several CPT were conducted before the blast.The pre-blast cone testing included five CPT, one VisCPT, and one SCPT, as shown in Figure 4-8. The pre-blast range of q_c and F_r values are shown in Figure 4-9. SCPT-15 provided the only V_s data prior to the blast. Results from this test are shown in Figure 4-10.

4.2.5 Dilatometer Testing

The DMT, developed by Marchetti (1980), is shown in Figure 4-11. The DMT blade is 9.5 cm wide, 1.5 cm thick with a 6 cm diameter, thin membrane on one side. The membrane is pressurized and the operator records the pressures required to move the membrane off the blade and to expand the membrane to a distance of 1 mm away from the blade. These pressures are

used to compute the DMT indices: I_D (material index), K_D (horizontal stress index), and E_D (dilatometer modulus). Empirical correlations relate these indices to soil type, the coefficient of lateral earth pressure at rest, the modulus of elasticity, and others. Pre-blast DMT results are presented in Figure 4-12.

4.3 Instrumentation and Data Collection

The instrumentation plan was designed to measure pore pressure, particle acceleration, and settlement. This section will also describe the instrumentation used to measure V_s using a down-hole method. Pore pressure is of interest to quantify the excess pore pressure generation and dissipation, ensuring that excess pore pressure has dissipated prior to *in situ* testing. Acceleration is an indication of disturbance. Settlement provides information about densification. Down-hole V_s measurements provide comparison for V_s measurements from SCPT. Data acquisition through wireless and cable-based systems is also described.

4.3.1 Pore Pressure

Explosive densification creates a shock wave of high magnitude and high frequency. Therefore, any pore pressure transducers used for this application must be able to survive the shock wave and still have enough precision to measure residual excess pore pressure. Rollins et al. (2005) describe blast experiments using several types of pore pressure transducers. They recommend the Sensotec P-050 piezo-resistive transducers, shown in Figure 4-13, designed specifically for measuring pore pressure in soils exposed to explosive densification. These transducers are capable of surviving an approximate 6,000 psi shock pressure wave while having a resolution of 0.1 psi. They are, therefore, responsive enough to measure the pore pressure build up and dissipation from explosive densification. Because the bandwidth of the transducers is 0-300 Hz, it is unlikely that the peak pressure from the blast shock wave can be accurately recorded; however, the instruments are capable of measuring residual pore pressure generation and dissipation, parameters of greater interest to this work.

Another issue relating to measuring pore pressure is the placement and recovery of the transducers. The instruments are housed in cone tips for ease of placement. The cone tips are made of nylon because it is easy to mill, durable, and has a unit weight close to soil. They are, therefore, less likely to sink during liquefaction. However, a disadvantage of nylon cone tips is that they are not as strong as metal cone tips and cannot withstand being pushed to the depth required in this study. Rollins et al. (2005) solved this problem by pre-drilling a slurry filled bore

hole to a depth of ~1' shallower than the desired placement depth. The cone tips then only need be pushed the additional foot beyond the bottom of the bore hole to the desired placement depth. Experience has shown that the cone tips were strong enough to withstand penetrating 1' of soil, which is also enough distance from the slurry to ensure that the measured response is not significantly influenced by the slurry filled bore hole (Rollins et al., 2005). A steel cable was attached to the nylon cone tip and run back to the surface. The transducers were recovered by by pulling the steel cable through the slurry filled bore hole.

4.3.2 Acceleration

Piezoelectric shock accelerometers can withstand the large amplitude motions generated from an explosion and were used in this experiment. Figure 4-14 shows data from Hryciw (1986) on the frequency and amplitude of blast pulses in saturated soils as a function of cube root scaled distance, defined as distance divided by the cube root of the charge weight. The frequency (*f*) of the peak acceleration was determined by calculating the inverse of four times the rise time, t_p (Equation 4-1).

$$f = \frac{1}{4 * t_p} \quad \ldots(4\text{-}1)$$

In extrapolating to scaled distances less than ~10 ft/lb$^{1/3}$ factors of safety were applied in estimating the peak accelerations and maximum frequencies to account for uncertainties in the field conditions and explosive energies. It was determined that the shock accelerometers must capture frequencies greater than 15k Hz and peak amplitudes of 500, 2,500, and 20,000 g for scaled distances of 30, 15, and 5 ft/lb$^{1/3}$, respectively. Dytran 3200 series shock accelerometers were selected.

The accelerometers were emplaced and recovered in a similar manner to the pore pressure transducers. One difference was the importance of the accelerometer orientation toward the blast. Prior to installation, the accelerometers were attached to 1-D and 3-D mounting brackets, ensuring proper location within the cone tip. These mounting brackets were secured inside the nylon cone and orientation of the accelerometers was marked on the exterior of the cone. The cone was then filled with wax to waterproof the accelerometers. During installation, care was taken to ensure that the cones were installed with the proper orientation. Because it is possible that the orientation of the cone changed during installation, when the accelerometer cones were recovered, attempts were made to avoid rotating the cone, allowing for inspection of orientation

at the surface. In every case, the accelerometer cones appeared to be correctly oriented upon recovery.

One final concern was the filtering of high frequency acceleration pulses if the diameter of the cone tip housing the accelerometers was too large. These accelerometers are sufficiently small in size, 5.8 cm when housed in the nylon cones for placement in the ground, relative to the estimated wave length of the blast (15 cm near the charge increasing to 0.5 m away from the charge) that high frequencies should not have been filtered.

The instrumentation failed to record any significant acceleration during explosive densification. A similar problem occurred during a test of the instrumentation system. A swimming pool, pictured in Figure 4-15, was filled initially with water, then sand. Blasting caps were placed at the center of the pool and both pore pressure transducers and accelerometers were placed at the same scaled distance as in the explosive densification experiment. While it was not expected that the blasting caps would generate large excess pore pressures, the pore pressure transducers recorded small, brief changes in pore pressure as expected. However, the accelerometers did not record significant acceleration. At the time, it was believed that the relationship between distance and acceleration amplitude did not scale to very small explosions, like the one produced by the blasting cap and the accelerometers were validated by other methods in the laboratory. In retrospect, verification of the Hryciw (1986) relationship should have been performed in an experiment more closely resembling field conditions. The amplitude may have been lower than predicted and lower than the trigger level on the data acquisition (DAQ) system. The frequency may have been higher than predicted, causing the cone tips containing the instruments to filter the impulse. In any case, the accelerometers did not record any data from the explosion.

4.3.3 Settlement

Settlement is used as a measure of densification and was measured in two ways. First, surface elevations were recorded using a transit. The location of the measurement points is shown in Figure 4-16. Elevations were taken from stakes driven into the ground in a regular pattern surrounding the blast holes. Because several months passed between elevation readings and the transit did not remain in place, readings from stakes installed far outside the blast area were used as benchmarks.

One early suggested theory for sand aging was that settlement continued to occur for weeks to months following disturbance; thereby, increasing q_c or V_s could be explained by increases in

density. As such, settlements were measured with time after the blast. Because it took roughly an hour to collect measurements from all the elevation points, readings were taken at five select locations for several hours following the blast, as shown in red in Figure 4-16.

The second method of monitoring settlement was by Sondex settlement tubes, shown in Figure 4-17. The Sondex settlement system uses metallic rings on a corrugated pipe that settles or heaves with the soil around it. A probe that detects the location of the rings is passed through a pipe placed inside the corrugated pipe. These measurements allow total settlement to be determined, as well as incremental settlement with depth.

4.3.4 Down-Hole Shear Wave Velocity Measurement

While the SCPT provides a method of determining V_s, its results are subject to soil variability because cone tests are not performed at the same location. In order to measure V_s in a manner unaffected by variability, a down-hole V_s measurement system was developed for this study. Accelerometers were mounted in CPT rods and emplaced near the area where SCPTs were performed. Because the down-hole system was stationary, soil variability did not affect its results.

Five Silicon Designs Model 2260-002 accelerometers were used in the down-hole system. The bandwidth of these instruments is 0-400 Hz and they accurately measure accelerations between ±2 g. After providing the accelerometers some protection from moisture using liquid electrical tape, they were inserted into five CPT rods 5 cm from the bottom of each rod. A dummy cone was manufactured and placed at the tip of the first rod. Connecting subsequent rods, the accelerometers were pushed into the ground spaced 1 m apart from a depth of 1.95 m to 5.95 m. Because the accelerometers were not waterproof, care was taken to keep water out of the down-hole system. Silicon gel was placed at each connection to prevent ground water from penetrating the down-hole system and the top of the tube was covered between measurements to prevent rain water from entering.

In order to create a shear wave, a source was placed near the down-hole tube. As shown in Figure 4-18, a railroad tie was buried to a depth where the top of the tie was nearly even with the ground surface. Several sandbags were added to the top of the tie in order to improve the coupling with the ground. A small trench was dug at one end of the railroad tie to allow room for the strike. This is a true-interval method of measuring V_s, where one shear wave's arrival at a series of instruments is measured, rather than a pseudo-interval method such as the SCPT, where the arrival time at each depth comes from a different shear wave. Another difference from the SCPT

is the lack of a trigger in the down-hole system. When the hammer strikes the pad in an SCPT, it completes a circuit and timing begins. In the down-hole method, the shear wave's arrival at the first accelerometer became the point of comparison for calculating V_s between it and the next deepest point. Therefore, V_s cannot be calculated at depths shallower than the first accelerometer using this system. For the purposes of this experiment, this is not an important limitation because response of the clay layer was not of interest.

Since there was no trigger, data from the accelerometers began being recorded prior to striking the railroad tie. Data was recorded for three seconds while the tie was struck approximately once per second. Therefore, each down-hole V_s recording contains three or four separate shear wave arrivals. The arrival of one shear wave at each of the five accelerometers is shown in Figure 4-19. Results from the down-hole tube presented in this dissertation represent the mean value of these multiple V_s measurements.

4.3.5 Data Acquisition

Two methods of data acquisition were used in this experiment. A cable-based system, an Olson Instruments, Inc. Freedom Data PC, was used for the piezoelectric accelerometers. This DAQ system uses a National Instruments 1.25 MS/s, 16 channel PCI data acquisition card. A separate DAQ system was used with the accelerometers because they output an AC voltage, which is compatible with the tethered system but not the wireless system.

Wireless sensing networks offer several advantages over traditional tethered systems. First, cables running from the sensors in the ground to DAQ can be replaced with cables only from the sensors to the surface, where the wireless capabilities handle the transmission. This reduces the chances of cable damage and data corruption. This is particularly important in the field because site improvement projects are rarely performed outside of larger construction projects. Cables running from instruments to a DAQ are often not practical and prevent engineers from obtaining otherwise useful data. Also, the wireless sensing network allows for a greater number of sensors to be used. For example, the Olson Instruments cable-based DAQ has 16 channels and the Network for Earthquake Engineering Simulation (NEES) vibroseis has a 72 channel cable-based DAQ. The wireless DAQ limits the number of sensors only in cases of high sampling rates for long duration. In such cases, data transmission must occur before the wireless sensing unit's random access memory (RAM) becomes full and begins to overwrite existing data with new data. Because high frequency, long duration events are rarely of interest in geotechnical engineering, the system has significant potential for geotechnical applications.

Geotechnical use of wireless sensing has increased in recent years. In an example of wireless sensing use in geotechnical engineering practice, Pennington et al. (2007) discuss the use of wireless sensors to monitor settlement around tunneling projects while constructing a mass transit system for Washington Dulles Airport. Wireless sensing is also popular in centrifuge testing (Wilson et al., 2007). Examples of wireless sensing use in geotechnical field research are also presented by Abdoun et al. (2007), wireless accelerometers used to monitor slope stability, by Garich and Blackburn (2007), wireless accelerometers and moisture sensors used for landslide warning, and by Nasipui et al. (2007), wireless sensors used to monitor a bioreactor landfill in an example of geo-environment wireless sensing use.

The primary means of data collection in this experiment was a wireless sensing network developed at the University of Michigan (Lynch et al., 2005; Swartz et al., 2005). The equipment used in this experiment is pictured in Figure 4-20 and is primarily built from commercial components. The network was originally developed for structural health monitoring and is capable of performing analog-to-digital conversion, data aggregation, data processing, and wireless transmission of raw and/or processed data to a receiving computer. The analog-to-digital converter (ADC) has a resolution of 16-bits, matching the capabilities of most tethered DAQ. It is controlled by the unit's 8-bit Atmel Atmegal28 microcontroller, which has 128 kB of read only memory (ROM) where different algorithms can be embedded for execution. Because the microcontroller has limited RAM, 128 kB of off-chip RAM is included in the design of the unit's computational core allowing 64,000 data points to be stored on the wireless sensor at one time. In this application, an earlier generation wireless sensor, commonly called the Stanford unit and described by Lynch et al. (2005), was connected to three pore pressure transducers and sampled data at 5 Hz. For down-hole shear wave velocity measurements, a newer generation sensor, called the Narada unit as described by Swartz et al. (2005), was connected to one accelerometer output and sampled data at 10,000 Hz.

4.4 Blast Design and Execution

The following section describes the design, preparation, and implementation of the explosive densification experiment. The experience-based explosive densification design methods considered in this work are presented along with the final design. Instrumentation installation and blast-hole preparation are also discussed. Finally, comments and observations are recorded concerning the execution of the explosive densification experiment.

4.4.1 Experimental Design

There are several explosive densification design guides; however, there is no widely accepted method. Therefore, this project considered two recent design methods in Gohl et al. (2000) and Narin van Court and Mitchell (1998). Additionally, Ivanov's (1967) recommendations about the maximum charge weight at a given depth were followed. VisCPT-15 was representative of the site's pre-blast soil conditions and was used for the blast design. Results of DMT testing can be empirically correlated to unit weight. DMT-2 was used to show that the dry unit weight was 19 kN/m^3 and the buoyant unit weight was 8.9 kN/m^3. The goal of the explosive densification was to increase the density and q_c in the upper liquefiable layer. While experience has shown that explosive densification is not effective in older deposits, explosive densification was also planned for the lower liquefiable layer. Improvement was not expected in this layer, but it was still possible that sand aging could occur after the disturbance (i.e. Charlie et al., 1992b).

The first step in the design process was to estimate the maximum charge weight at the depths of interest. Ivanov (1967) provides a relationship between the maximum weight to prevent cratering in Equation 4-2.

$$C = 0.055\, h^3 \qquad \ldots(4\text{-}2)$$

Where C is the weight of the charge in kilograms and h is the depth of the charge in meters. Because the upper liquefiable layer was relatively thin and close to the surface, it was decided to place the shallowest charge at 5 m, just below the the upper liquefiable layer in the dense sand layer. An additional benefit to placing the shallowest charge in the dense sand layer was the possibility that the blast would disturb the dense sand enough that aging could be observed in it as well. The deepest charge was planned at 12 m, which is roughly at the center of the lower liquefiable layer. Using 5 m and 12 m for the depth in Equation 4-2, the maximum charge weight should be 3.5 kg in the upper liquefiable layer and 95 kg in the lower liquefiable layer. Ivanov's (1967) relationship was developed for shallow depths, which may explain the unrealistically large estimation for 12 m depth. Narin van Court and Mitchell (1994) report that most explosive densification projects use between 2 and 10 kg with up to 30 kg being reported.

The Gohl et al. (2000) method was also used to calculate the charge weight and spacing. Their relationship, which is based on dimensional analysis, is shown in Equation 4-3.

$$E = k \left(\frac{W}{\rho}\right)^{0.33} h^{-0.5}\, R^{-1} \qquad \ldots(4\text{-}3)$$

Where E is the fraction of maximum achievable strain, k is a site specific coefficient, ρ is the mass density of the explosive in g/m^3, h is the burial depth in meters, W is the weight of the charge in grams, and R is the radius of the circle compacted by the blast in meters. In these calculations, E was set equal to 1 because the design aimed to achieve the highest possible strain. The site specific constant, k, was set equal to 120 after comparing the soil type at the Griffin site to soil types from the case histories from which this relationship was developed. The upper liquefiable layer contains clean, medium fine sand and sites with similar soil types were assigned k values of roughly 120. A typical value of ρ, 1.4x10^6 g/m, based on TNT was assigned. The burial depth is 5 m for the upper liquefiable layer and 12 m for the lower liquefiable layer. The remaining variables, W and R, are related and are the desired outcome for this analysis. Experience from similar projects (Solymar, 1984; Hryciw and Dowding, 1988; Charlie et al., 1992; Ashford et al., 2004) and recommendations from Gohl et al. (2000) show that borehole spacings of 4 to 9 m are typical. Therefore, this project designed the weight of the charges based on a spacing of ~6.1 m or 20'. The radius of the circle compacted by the blast should be at least half of that spacing, or 3 m. The result of the Gohl et al. (2000) method is a charge weight of 4.4 kg in the upper liquefiable layer and 10.5 kg in the lower liquefiable layer. Because the mass density of the explosive is based on TNT, it is important to remember that the recommend charge weight is also the weight of TNT.

The Narin van Court and Mitchell (1998) method was also used. Their recommended relationship, based on curve fitting between energy input and measured results, is presented in Equation 4-4.

$$q_{1,f} = 0.45 \left(\Sigma \left(\frac{W_i}{R_i^2} \right) \right)^{0.321} q_{1,0}^{0.5} \quad \ldots(4\text{-}4)$$

Where $q_{1,f}$ is the final normalized average tip resistance in the layer of interest in MPa, W_i is the weight of the individual charges in grams, R_i is the distance between the charge and the middle of the layer in meters, and $q_{1,0}$ is the initial normalized average tip resistance in the layer of interest in MPa, as defined in Equation 4-5. It should be noted that Narin van Court and Mitchell (1999) did not account for different types of explosives when developing their relationship because the differences were believed to be minimal. This dissertation will treat the resulting weight as grams of TNT.

$$q_{1,0} = q_{c,avg} \left(\frac{\sigma_{atm}}{\sigma'_v} \right)^{0.5} \quad \ldots(4\text{-}5)$$

Where $q_{c,avg}$ is the average measured tip resistance in the layer in MPa, σ_{atm} is atmospheric pressure, and σ'_v is vertical effective stress in the center of the layer in the same units as σ_{atm}. Using VisCPT-15 as a guide for the design and defining the upper liquefiable layer between 1.2-3.9 m, $q_{c,avg}$ = 2.85 MPa, σ'_v = 48.4 kPa, and σ_{atm} = 101.3 kPa. The same method of finding the spacing between the charges was used in the Narin van Court and Mitchell (1999) method as was used in Gohl et al.'s (2000) method; therefore, the spacing between charges was 20'. While the Narin van Court and Mitchell (1999) method recommends summing all of the charges, only the three closest charges in the triangular blast pattern were considered. If the charge spacing is 20' and the depth of the charges is 5 m, the vector distance to the center of the triangle at the middle of the upper liquefiable layer, a depth of 2.75 m, is 4.2 m. Therefore the summation term can be replaced with three times the charge weight divided by 4.2 m^2. Ivanov (1967) and Narin van Court and Mitchell (1994) both believe that the maximum achievable relative density, D_r, after explosive densification is approximately 80%. The desired $q_{1,f}$ after explosive densification was, therefore, determined by finding the tip resistance corresponding to a D_r of 80%. Using Jamilokowski et al.'s (1985) relationship between tip resistance and relative density, shown in Equation 4-6, it was determined that $q_{1,f}$ = 15.7 MPa.

$$D_r = -98 + 66\, log\left(\frac{q_c}{\sqrt{\sigma'_v}}\right) \quad \ldots(4\text{-}6)$$

Admittedly, this relationship was not ideal for the Griffin site because the relationship was developed for uncemented, unaged, quartz sands. However, considering the scatter in Narin van Court and Mitchell's (1998) relationship, pictured in Figure 4-21, it is believed that, even with the potential error introduced due to the use of this relationship, the final result of the analysis was still valid.

Finally, Equation 4-4 was used to determined that the charge weight in the upper liquefiable layer should be 4.2 kg at a spacing of 20'. Using the same procedure described above for the lower liquefiable layer, defined between 10.5 and 14.75 m with the charges at a depth of 12 m, $q_{c,avg}$ = 15 MPa, σ'_v = 152.6 kPa, R_i = 3.5 m, and $q_{1,f}$ = 15.7 MPa. The charge weight as determined using Equation 4-4 is 5.5 kg.

Using the charge weights computed from the Gohl et al. (2000) and Narin van Court and Mitchell (1999) relationships, the maximum charge weight using Ivanov's (1967) recommendation, as well as a review of the charge weights, spacings, and depths of explosive densification case histories summarized for this dissertation, it was determined that the charge weight in the upper

liquefiable layer will be 2.5 kg of TNT and 9 kg of TNT in the lower liquefiable layer. Numerous studies (i.e. Ivanov, 1967; Solymar, 1984; Hryciw, 1986; Narin van Court and Mitchell, 1994) have shown that multiple shearing from several blast delays are more effective than one blast. Therefore, it was determined to detonate only two blast holes at a time, resulting in 4 delayed blasts. The utilized blast design is summarized in Figure 4-22.

4.4.2 Instrumentation Emplacement

As discussed in Section 4.3.2, the accelerometers were chosen based on their ability to capture peak acceleration at scaled distances of 5, 15, and 30 ft/lb$^{1/3}$. Based on the sizes of the charges and the desire to simplify the installation of instrument bore holes, the installation plan shown in Figure 4-23 was implemented. Moving out from the northeast corner of the blast area, instrumentation was installed at a depth of 13' in order to measure the response to the blast in the loose sand layer. The three instrumentation points in the array were place at distances of 10', 28', and 56' from the nearest blast. The equivalent scaled distances for these points were 5.6, 15.7, and 31.5 ft/lb$^{1/3}$ from the nearest blast point. Because these instruments were installed fairly close to the surface and maintaining borehole integrity was not of major concern, both pressure transducers and accelerometers were installed in the same larger diameter (12") borehole. Moving out from the southwest corner of the blast area, instrumentation was installed at a depth of 38.5' in order to measure the effects of the blast in the loose gravelly sand layer. The three instrumentation points in the array were placed at distances of 17', 44', and 83.5' from the nearest blast. The equivalent scaled distances for these points were 6.2, 16.1, and 30.6 ft/lb$^{1/3}$ from the nearest blast point. Accelerometers and pore pressure transducers were installed in adjacent bore holes to facilitate comparison of trends.

Determining the composition of the slurry to be used with drilling proved to be a challenge. Small scale laboratory tests were conducted in a liquefaction tank prior to field installation. Boreholes with a 4" diameter were installed in Ottawa 20-30 sand in a liquefaction tank, as pictured in Figure 4-24. Several slurry mixes were tested and it was determined that 80 lb of bentonite per 100 gal of water maintained the integrity of the borehole while the sand was liquefied. However, during field installation, this mix proved insufficient. The grain size distribution in the loose gravelly sand layer is considerably different from that of Ottawa 20-30 sand and the designed slurry mix was not thick enough maintain integrity of the borehole. Through trial-and-error testing in the field, greater amounts of bentonite were added to the slurry mix without success until the slurry became too thick to pump efficiently. At that point, the decision to add revert, a

powder that produces a biodegradable drilling mud, to the mix was made based on the experience of the local driller. Using slurry composed of a mix of bentonite and revert, installation of the instrument and blasting boreholes proceeded smoothly. Because revert is biodegradable and degrades with time, the boreholes were all cased with PVC pipes in order to prevent collapse prior to the blast experiment or during blast-induced liquefaction.

The location of the Sondex tubes and survey points is shown in Figure 4-16. Installation of the Sondex settlement tubes was simpler than installation of instrumentation boreholes because the recommended mix provided by Sondex worked well at the blast site. A mix of water, bentonite, and cement held the borehole open during installation and hardened with time and held the flexible corrugated tube in place once the cement set up. The Sondex tubes were filled with water during installation to reduce the uplift pressure and keep them in the ground. However, the northeast Sondex tube did not resist the uplift pressure even when filled with water. Two sandbags were placed on top of the tube for one day. After a day, the cement had set up enough to the hold the Sondex tube in place. These tubes were installed to a depth of 50', or roughly 10' beneath the location of the deepest charge. The additional burial depth anchored the tube beneath the soil layers that could liquefy or lose strength during the blast.

Finally, the accelerometers and pore pressure transducers were installed. Cone tips were placed at the end of a string of CPT rods with instrument cables strung through the center of the rods. An adaptor was placed at the end of the string of rods, allowing the delicate instrument cables to avoid damage while the rods were pushed into the ground. As pictured in Figure 4-25, the quarry owners used their large front end loader to push the rods 1' beyond the end of the borehole. Following the blasting experiment, the instruments were recovered by pulling the steel cables attached to the nylon cone tips.

4.4.3 Explosive Densification Experiment

The Austin Powder Company was chosen to install and detonate the explosive charges. They used their cast booster products to provide a blast that would release roughly the same amount of energy as the blast designed in the manner described above. Cast boosters are a mix of TNT, military surplus RDX, and other explosives. While the precise mix of explosives used in the cast boosters is proprietary and differs for each batch based on the availability of various components, the company released a conversion factor to allow for comparison between a given weight of their product and TNT. The explosives used in this experiment had a conversion factor of 1.125 pounds of TNT per 1 pound of cast booster weight. In the loose sand layer, 5 orange cap cast

boosters were installed. This package was 2.3” in diameter, 22.5” in length, and the equivalent of 5.625lbs of TNT. In the loose gravelly sand layer, 9 white cap cast boosters were installed. This package was 3.1” in diameter, 45.9” in length, and the equivalent of 20.25lbs of TNT. The delays between blasts were 0.475 seconds.

As shown in Figure 4-26, large sections of borehole casings were ejected from the ground during the explosion. This shows that some of the energy from the blast escaped through the borehole and was not maintained in the ground. Because the local blasters used in this experiment were familiar with mine blasting and not blasting used in geotechnical site improvement, this was likely due to the method of emplacing the charges. As can be seen in Figure 4-27, concrete gravel (½ -1” length for the longest axis) was poured by the bucket load into the borehole to stem the material. A better method of maintaining the explosive energy in the ground is to use pea gravel (1/8” to 3/8” length for the longest axis), added in 1’ lifts and compacted, for stemming.

Additionally, the northeast Sondex tube can be seen to extend from the ground in Figure 4-26. During installation, this tube did not resist uplift pressure until after the cement had setup for a day. Excess pore pressures generated during the blast lowered the effective stress of the soil and confining pressure on the tube, causing the tube to rise during the blast. Anchoring the tube further beneath the location of the deepest charge or stacking sand bags on top of the tube while blasting would have helped to prevent this problem.

4.5 Post-Blast Testing

The following section discusses the post-blast testing plan and results. Data collected from the pore pressure transducers, settlement data, and results of the various *in situ* tests are presented.

4.5.1 Testing Plan

Hryciw and Dowding (1988) showed that distance from a blast point greatly affects the results of *in situ* tests. Therefore, all of the *in situ* tests were conducted 10’ from the nearest blast point. For comparison, CPTs were conducted at 25’ and 40’ from the blast points at the time of each suite of testing. Because the test depends on horizontal stress, all DMTs were conducted with the diaphragm oriented radially outward from the closest blast point. Location of Sondex settlement tubes and survey points are shown in Figure 4-16. Locations of the pore pressure transducers are shown in Figure 4-23. The locations of *in situ* tests conducted 10’ from the closest blast hole are shown in Figure 4-28. The locations of CPT conducted 25’ and 40’ from the closest blast hole are shown in Figure 4-29, with the NE and eastern-most blast point shown for orientation.

4.5.2 Pore Pressure Dissipation

Three pore pressure transducers were installed in each of the loose sand and loose gravelly sand layers. The poor pressure time histories in the loose sand layer located 10', 28', and 56' from the nearest blast point are presented in Figures 4-30, 4-31, and 4-32, respectively. These pressure transducers were installed roughly 1m below the ground water table at a depth of 4m. Subsequent cross-hole measurements conducted at the northeast vibroseis site at a depth of 4m showed that the soil was not saturated at this depth, as described in Chapter 5.5.6. The transient pore pressure response at each of these transducers can be explained by the unsaturated soil conditions at this depth. The trend with distance from the blast shows that the blast has less effect on pore pressure, both in terms of magnitude and duration of the response, with greater distance from the blast.

Results from the three pressure transducers installed at a depth of 12 m and a distance from the nearest blast point of 17', 44', and 83.5' are shown in Figures 4-33, 4-34, and 4-35, respectively. These pressure transducers were installed approximately 9 m below the ground water table. At PPT-4, the maximum excess pore pressure ratio, r_u, reached 0.4 and pore pressures remained elevated for 30 seconds. At PPT-5, the maximum excess pore pressure reached 0.3 and pore pressures remained elevated for 2 minutes. While PPT-6 functioned properly before and after the blast, as evidenced through laboratory testing, it did not record pressures consistent with the other pressure transducers. After a momentary spike to an excess pore pressure ratio of 0.9, the transducer recorded a water pressure of roughly 1 psi for roughly 90 seconds. After that time, the transducer recorded pressures consistent with hydrostatic pressure. Regardless, excess pore pressure at the blast site dissipated within 3 minutes following the blast. Therefore, any changes to tip resistance compared to pre-blast results were not due to elevated pore pressures and decreased effective stress.

4.5.3 Settlement

As described in Section 4.3.3, settlement was monitored using both surface elevation measurements and Sondex settlement tubes. As shown in Figure 4-36, transit readings conducted following the blast showed 11.7" of settlement at the center of the blast site. There was no measurable settlement 60' away from the closest blast point.

Immediately following the blast, repeated measurements were made at the locations indicated in Figure 4-16. Five readings taken between 10 minutes and 3.5 hours following the blast showed that surface settlement was nearly immediate. Three more sets of surface elevation measurements

were taken within the first week, showing no significant change from the original readings. However, measurements conducted one month after the blast showed that additional settlement had occurred between one week following the blast and one month following the blast. This additional settlement is shown in Figure 4-37 and was less than ¾". Following the transit measurements taken at one month, no additional surface settlement was observed. The maximum settlement at the blast site was 12.1". The total settlement between the blast and one month readings is shown in Figure 4-38.

The Sondex settlement tube measurements from the southwest tube were consistent with surface settlement, showing 10.6" of settlement initially, 0.75" additional settlement between one week and one month following the blast, and no additional settlement after one month. The northeast tube did not provide meaningful data because it floated following the blast, rendering comparison to pre-blast measurements useless. Settlement throughout the soil profile with time following the blast is presented in Figure 4-39. In Figure 4-39, positive slope indicates that the soil settled between the two rings, while negative slope indicates greater distance between the two rings compared to their original spacing. The depths showing dilation, shown with negative slope in Figure 4-39, correspond to the depths where the charges were placed. While these results may be due to dilation, it is possible that the corrugated pipe rebounded or stretched at these depths and the dilative readings did not correspond to loosening of the soil.

One final indication of settlement at the blast site was cracks that appeared on the ground surface in the desiccated clay. These cracks are shown in Figure 4-40 and roughly occur in a circle surrounding the blast area. The survey of these cracks occurred 1.5 hours after the blast. An important observation about the settlement at the blast site is that, for the most part, settlement occurred nearly immediately following the blast. Additional settlement of approximately 0.75" does not represent a meaningful increase in relative density.

4.5.4 Cone Penetration Testing

Pre-blast CPT testing consisted of six CPT, one VisCPT, and one SCPT. Post-blast testing was conducted immediately following the blast for one week and at one month, 2.5 months, 3.5 months, one year and two years following the blast. With the exception of the 3.5 month testing, at least five total CPT were conducted at each time: one SCPT at 10', one VisCPT at 10', one CPT at 10', one CPT at 25', and one CPT at 40' from the closest blast point. The 3.5 month testing interval occurred at the same time as the one month testing following vibroseis shaking when the majority of the testing effort was focused on the vibroseis sites. Therefore, only one

SCPT at 10', one CPT at 25', and one CPT at 40' were conducted in the blast area. Testing conducted in the week following the blast and at two years included several tests in addition to the standard suite. In the week following the blast, three CPT at 10', two VisCPT at 10', one SCPT at 10', one CPT at 25', and one CPT at 40' from the closest blast point were conducted. Two years after the blast, one CPT at 10', two VisCPT at 10', one SCPT at 10', one CPT at 25', and one VisCPT at 40' from the closest blast point were conducted. In this section, only standard CPT results will be discussed. Vision data from the VisCPT and V_s from the SCPT will be discussed in Sections 4.5.5 and 4.5.7, respectively.

The locations of SCPT, VisCPT, and CPT at 10' from the closest blast points are shown in Figures 4-41 through 43, respectively. The locations of the tests at 25' and 40' from the closest blast holes are presented in Figure 4-29. All pre- and post-blast testing locations located within 10' of the closest blast point are shown in Figure 4-28. The test names, time of the test, and miscellaneous notes are listed in Table 4-1.

Pre-blast testing consisted of 8 CPT, including one SCPT and VisCPT. Because SCPT-19 was representative of pre-blast conditions and because it was the deepest pre-blast test, SCPT-19 results are presented in Figure 4-44 along with V_s and K_D, which will be discussed in Sections 4.5.6 and 4.5.7, respectively. Throughout CPT testing at the Griffin quarry, pore water pressure measurements varied with the water table depth, but always defined the hydrostatic line. Additionally, the friction ratio was consistent with the results shown in Figure 4-3. Therefore, individual CPT results subsequently presented in this dissertation will include only tip resistance. A summary of pre-blast CPT results is shown in Figure 4-45.

CPTs were performed for one week following the blast. In the first week following the blast, CPT were conducted at 25' and 40' from the blast, as well as 6 CPT, including one SCPT and VisCPT, at 10' from the blast. As shown in Figure 4-46, time-dependent change in tip resistance was not distinguishable from variations between tests due to natural spatial variability of soil properties; therefore, all tests conducted in the first week following the blast were treated as one group. As shown in Figure 4-47, the range of q_c recorded 10' from the blast points remain generally consistent in the loose sand layer and dropped in deeper layers compared to pre-blast readings. This occurred despite approximately 1' of surface settlement. These results are typical following explosive densification (i.e. Denisov et al., 1963; Mitchell and Solymar, 1984; Hryciw and Dowding, 1988; Rogers et al., 1990; Charlie et al., 1992b; Wheeler, 1995; Ashford et al., 2004; Liao and Mayne, 2005; Narsilio, 2006; and Camp et al., 2008).

During one month, two and a half month, and one year testing, CPTs were conducted at 25' and 40' from the blast points, as well as 3 CPTs, including one SCPT and VisCPT, at 10' from the blast points. Three and a half months after the blast, CPTs were conducted at 10', 25' and 40' from the blast points. Two years after the blast, CPTs were conducted at 25' and 40' from the blast points, as well as 4 CPTs, including one SCPT and two VisCPTs, at 10' from the blast points. Results from the CPTs conducted 10' from the blast points are shown in Figure 4-48 for one month testing, Figure 4-50 for two and a half month testing, Figure 4-52 for three and a half month testing, Figure 4-53 for one year testing, and Figure 4-55 for two year testing. As pictured in Figure 4-49 for one month testing, Figure 4-51 for two and a half month testing, Figure 4-54 for one year testing, and Figure 5-56 for two year testing, the range of q_c values recorded 10' from the blast points increased in the loose and loose gravelly sand layers, but remained generally consistent with one week testing in the dense sand layer.

The mean q_c profile is shown for each testing interval in Figure 4-57. Tip resistance in the loose sand layer showed little change immediately following explosive densification. However, tests at one month and later following the blast showed a roughly 50% increase in q_c compared to pre-blast and one week values. In the dense sand layer, q_c did not show clear changes with time. In the loose gravelly sand layer, the mean q_c shows time-dependent increases. Additionally, q_c values in the dense and loose gravelly sand layers do not approach pre-blast values despite their increased density, evidenced through surface settlement and Sondex readings. It is likely that the blast destroyed the benefits of geologic aging in these Pleistocene deposits, rendering the benefits of increased density less important in comparison.

CPT results for tests conducted at 25' and 40' from the nearest blast point are presented in Figure 4-58 and 4-59, respectively. An initial inspection of these figures shows a trend of increasing q_c with time if one considers the one year tests outliers. However, a comparison of these results with the location of these tests in Figure 4-29 shows that q_c increased from north to south. Likely explanations for the results include natural variation and non-uniform effectiveness of explosive densification. It is possible that sand aging is not the cause of these variations.

In conclusion, explosive densification reduced q_c of the dense sand and loose gravelly sand layers. Time-dependent increase in penetration resistance occurred in the loose gravelly sand layer, but not in the dense sand layer. In the loose sand layer, immediately following explosive densification, there was no change in penetration resistance. However, one month following the

blast, q_c had noticeably increased from values recorded before the blast and one week following the blast.

4.5.5 Vision Cone Penetration Testing

A qualitative method of assessing vision data was employed. While conducting the VisCPT, the cone advance was stopped every 10 cm. These pauses allowed for visual observation of the soil. At some of these pauses, sand was observed to flow or boil, indicating that the sand is very loose and liquefied during the cone's advance. While lack of boiling in loose sand should not be interpreted as the soil being not susceptible to earthquake-induced liquefaction, the observation of local liquefaction by the VisCPT indicates high liquefaction susceptibility.

There were 7 VisCPT soundings, shown in Figures 4-23. As shown in Figure 4-60, prior to the blast, there were six zones of observed liquefaction with a maximum thickness of 40 cm. All of these areas were located in either the dense sand or the loose gravelly sand. The presence of zones where liquefaction during cone penetration was observed to occur in the dense sand layer can be explained through the destruction of the benefits of geologic aging. The layer was classified as dense sand based on interpretation of CPT tip resistance, which was measured while the soil was first being disturbed. The camera is located 64 cm away from the tip; therefore, observation of liquefaction occurred in disturbed soil.

Because the blast destroyed the benefits of geologic aging, as evidenced by lower q_c, V_s, and K_D, the zones of observed liquefaction increased following the blast. Similar to pre-blast data, in all of the post-blast tests, there is a small zone where liquefaction was observed beginning at roughly 7 m depth and extending 30 to 80 cm. The differences between pre- and post-blast vision results occur in the zone of observed liquefaction beginning at roughly 8.5 m. In the pre-blast vision test, there are sporadic zones of observed liquefaction extending to roughly 15 m depth. Following the blast, there was generally a continuous zone of observed liquefaction between approximately 8.5 and 15 m. Consistent with the results of other *in situ* tests in the dense sand and loose gravelly sand layers, there was not a significant difference between the results with time following the blast.

4.5.6 Dissipation Cone Penetration Testing

Following the blast, two dissipation CPTs (uCPT) were run using the methods described in Lee et al. (2008). The first of these tests, referred to as D-1 and shown as a dissipation test in Figure 4-29, was conducted 75' from the closest blast point in the hopes that it was unaffected by the blast,

but close enough to provide representative data. The second, titled D-2 and shown as a dissipation test in Figures 4-28 and 4-29, was conducted 10' from the closest blast point. As can be seen in Figure 4-61, the results from D-1 and D-2 are generally similar. The area affected by the blast, tested in D-2, shows more uniformity than the area unaffected by the blast, tested in D-1.

4.5.7 Shear Wave Velocity

Shear wave velocity was determined using SCPT data and down-hole data. Because SCPTs from each testing interval were collected at different locations, as shown in Figure 4-41, V_s from this method shows more variability than the down-hole data, which remained in place throughout the experiment. Both methods show the same trend of increasing V_s with time following the blast.

There were 7 SCPT soundings, and the resulting V_s profiles are presented in Figures 4-62. Because presenting all 7 soundings at once creates a cluttered graph that is difficult to understand, only 4 soundings are presented in each of the graphs contained in Figure 4-62. The SCPT conducted 2.5 months after the blast is common to both graphs and can be used for comparison between Figure 4-62a and 4-62b. While there is scatter in the profiles due to spatial variability of soil properties, one can see in Figure 4-62a that the pre-blast V_s is the highest of any of the soundings and the one week data is generally the lowest. This shows that V_s decreased significantly as a result of the disturbance and increased with time after the disturbance. The data presented in Figure 4-62b shows that there is no clear trend between V_s and time. While it is possible that V_s did not increase with time, it is also possible that V_s increased, but not at a rate large enough to overcome the scatter in the data due to spatial variability of soil properties. In summary, the data presented in Figure 4-62 shows that the blast caused a significant decrease in V_s. While V_s increased from soundings taken immediately following the blast to those at least one month after the blast, any possible trend with time following the one month sounding is lost within the scatter due to spatial variability of soil properties.

The down-hole V_s data with time is presented in Figure 4-63. Because the shear wave velocity collected from the down-hole measurement system was not affected by spatial variability of soil properties, the data is easier to interpret and augments the V_s data from SCPT. In Figure 4-63, the one week average data consist of 6 tests conducted between 43 and 160 hours following the blast. These tests were generally similar and small differences were attributed to the difficulty in choosing a precise arrival time in shear waves. A difference of 0.01 milliseconds in shear wave velocity arrival causes 1.3 m/sec difference in the shear wave velocity at a depth of 11 m. With few exceptions, there is a clear increase in shear wave velocity with time following the blast at

each measured depth. No data was collected after 3.5 months. Weather proofing installed after the last measurement in the fall of 2008 in order to prevent water from filling the down-hole tube. However, the weather proofing was removed by a passer-by prior to the spring of 2009 and the tube filled with water, destroying the accelerometers.

Considering both SCPT and down-hole data, it is clear that the blast decreased V_s initially. Shear wave velocity then increased between one week and one month measurements. After the first 24 hours, there was not a clear trend of increasing V_s within the first week following the blast. Additionally, it becomes difficult to see a trend in measurements taken one month and later after the blast. This data shows a similar trend as the CPT data with respect to aging.

4.5.8 Dilatometer Testing

There are 6 DMT soundings and the resulting horizontal stress index, dilatometer index, and material index profiles are presented in Figures 4-64 through 4-66, respectively. Because presenting all 6 soundings at once creates a cluttered graph that is difficult to understand, 3 to 4 soundings are presented in each of the graphs contained in Figures 4-64 through 4-66. The DMT conducted one month after the blast is common to both graphs and can be used for comparison.

The horizontal stress index, K_D, is related to the horizontal stress; therefore, changes with time were expected to be similar to those seen in q_c. The dilatometer index, E_D, is analogous to soil stiffness; therefore, changes with time were expected to be similar to those seen in V_s. As seen in Figure 4-64a for K_D and Figure 4-65a for E_D, there was an initial decrease following the blast and an increase between one week and one month. At one month, K_D and E_D exceeded pre-blast values in the upper portion of the loose sand layer and remained lower than pre-blast values in other layers. As seen in Figures 4-64b and 4-65b, any time-dependent changes can not be distinguished from the spatial variability in the results and no trends with time can be discerned. Similar to q_c in the case of K_D and similar to V_s in the case of E_D, there was an initial decrease after the blast followed by an increase. Following one month measurements, no trend with time can be established. The K_D and E_D values in the loose sand exceeded pre-blast values, but the rest of the layers did not recover to pre-blast levels.

The material index, I_D, is a function of soil type; therefore, changes with time were not expected. The data largely confirms this expectation. As seen in Figure 4-66a, pre-blast and one month data are very similar. As seen in Figure 4-66b, one month through two year data are very similar. One

week data is the only outlier. Differences between individual tests can be explained through spatial variation in soil properties.

In summary, K_D and E_D showed time-dependency, while I_D did not change with time. Both K_D and E_D initially dropped after the blast and increased between one week and one month. Measurements taken after one month do not show time-dependent behavior. In the loose sand layer, K_D and E_D are greater than pre-blast values, but other layers to not recover to pre-blast values.

4.6 Geostatistical Analysis of Aging

To begin the geostatistical analysis of the CPT data, the first step was to determine basic statistical information. Next a theoretical variogram was fit to the experimental data. Anisotropy in soil properties was accounted for using the coordinate transform method. Block kriging based on q_c from one testing period was then used to predict the mean and standard deviation of the normalized tip resistance, q_{c1N}, from a given test location and time. These values were finally compared to values from other time periods using two-tailed hypothesis testing. The result of this analysis is a percent confidence that the differences between two sets of tests at different ages are due to sand aging and not spatial variability of soil properties.

4.6.1 Basic Statistical Analysis

Initially, basic statistical information was generated. Considering the eight CPT tests performed in the blast area prior to any disturbance, there were 4,492 data points contained in a roughly 20 m x 20 m x 20 m cube. From this information a histogram, shown in Figure 4-67 was generated using q_{c1N} from all pre-blast CPT soundings. As recommended by Kulhawy and Mayne (1990) and Schnaid (2009), q_{c1N} was determined by Equation 4-7.

$$q_{c1N} = \frac{q_c/\sigma_{atm}}{\sqrt{\sigma_v'/\sigma_{atm}}} \quad \ldots(4\text{-}7)$$

Where σ_v' is vertical effective stress and σ_{atm} is atmospheric pressure.

The mean of q_{c1N} is 155.4 and the standard deviation is 89.9. An initial geostatistical analysis of this data did not produce good results. When geostatistical methods are used to form an estimate far from measured data, the results tend toward the mean. However, the mean tip resistance of the

site is not a good predictor of tip resistance in each individual layer. Therefore, analyzing each of the layers of interest individually provided more accurate results.

A histogram of q_{c1N} data is provided in Figures 4-68 for the clay layer, Figure 4-69 for the loose sand layer, Figure 4-70 for the dense sand layer, and Figure 4-71 for the loose gravelly sand layer. All of the figures mentioned in this paragraph refer to data collected prior to the blast. Figures are not presented for testing periods following the blast because the shape of the histograms shown in Figures 4-68 through 4-71 remain consistent at later testing periods. However, a summary of the mean and standard deviation of q_{c1N} for each layer at each time period is presented in Table 4-2. One important note is that the data from the three sand layers shows a generally normal distribution, matching one of the assumptions in geostatistical analysis. The clay layer does not demonstrate a normal distribution; however, the results of analysis from the clay layer are not of interest in this study.

4.6.2 Variogram Selection

As described in Section 3.3, a theoretical variogram was matched to the experimental variogram visually, using a physical understanding of soil properties. Experience has shown that exponential models best fit geologic properties (Chiles and Delfiner, 1996), so exponential models were fit visually to experimental variograms created using data from each soil layer at each testing time. A sensitivity analysis was performed on theoretical variograms from each soil layer. Varying the sill, correlation length, and nugget within reasonable bounds did not significantly vary the results of the analysis. The theoretical variograms from the clay layer at each of the six testing periods (pre-blast, one week, one month, two months, one year, and two years) are shown in Figure 4-72 and described in Table 4-3. The theoretical variograms from the loose sand, dense sand, and loose gravelly sand layers from each of the six testing times are shown in Figures 4-73 through 4-75, respectively, and described in Table 4-3.

4.6.3 Anisotropy

As described in Section 3.4, soil properties typically vary more with depth than they do with lateral distance. Raw, experimental, and theoretical variograms were constructed using only the vertical distance between points, shown in Figure 4-76, and only the horizontal distance between points, shown in Figure 4-77. An exponential model, with the same sill of 3,500 and the same nugget of 10, fits both the horizontal and vertical experimental variograms. However, in the

vertical direction, the correlation length is 1 m, while in the horizontal direction, the correlation length is 8 m.

The ratio of these correlation lengths becomes a scale factor of eight. In this dissertation, prior to using the data in block kriging analysis, each of the depth values was multiplied by eight to account for the anisotropy. After determining the desired estimates and uncertainty, but before presenting the data, the depth values were returned to their true values.

4.6.4 Block Kriging and Hypothesis Testing

A code was written in MATLAB to perform block kriging on data sets from the four soil layers at each of the six testing periods. Locations of each of the tests, the deepest data points in each of the soil layers, and variogram information was required for each analysis. While variogram information was presented in Table 4-3, the rest of the input data is presented in Table 4-4. Locations of the tests were based on the coordinate system shown in Figure 4-78. The number of blocks in each analysis was dependent on the thickness of the layer being analyzed. In plan view, the rectangular area encompassing each of the testing time's tests was split into four equal sized blocks. With depth, a new block was established every 10 cm. Therefore, the number of blocks was 40 times the thickness of the layer in meters. The mean and uncertainty of q_{c1N} data sets determined from the block kriging analysis are presented in Table 4-5.

The results from the same layer at different testing times were compared using two tailed hypothesis tests. Conceptually, the two tailed hypothesis test compares two statistical distributions and determines the confidence that they are the same. Subtracting this value from 100% gives the confidence that they are different. The p-value, or confidence that the distributions are the same, was determined using a MathCad function and values of the test statistic, *t*, and degrees of freedom, *df*. The test statistic and degrees of freedom are defined by Equations 4-8 and 4-9, respectively.

$$t = \frac{z_{A1} - z_{A2}}{\sqrt{\sigma_{BK1}^2 + \sigma_{BK2}^2}} \quad \ldots(4\text{-}8)$$

$$df = \frac{(\sigma_{BK1}^2 + \sigma_{BK2}^2)^2}{\frac{\sigma_{BK1}^2}{n_1 - 1} + \frac{\sigma_{BK2}^2}{n_2 - 1}} \quad \ldots(4\text{-}9)$$

Where z_{A1} is the block kriging mean from the first testing period in the comparison, z_{A2} is the block kriging mean from the second testing period in the comparison, n_1 is the number of data points in the first testing period's data set, n_2 is the number of data points in the second testing

period's data set, σ^2_{BK1} is the uncertainty block kriging estimate from the first testing period in the comparison, and σ^2_{BK2} is the uncertainty block kriging estimate from the second testing period in the comparison.

The results of some comparisons are of greater interest than others. For example, the clay layer was not expected to and did not change with time. However, the loose sand layer was expected to exhibit the effects of sand aging. While a qualitative assessment of the *in situ* test results confirmed this expectation, a geostatistical analysis was desired to quantify a level of certainty. Therefore, the comparisons of particular interest to this research link the one week tests to the testing periods with longer aging times. Values of the test statistic, degrees of freedom, p-value, and confidence that the testing periods are different are presented in Table 4-6, with the comparisons of interest highlighted with bold typeface. Because the tests were conducted close to each other, the only difference between the different data sets is the time since disturbance. Therefore, one can say with the percent confidence determined in this analysis that test results from different time periods are different due to aging and not due to the natural spatial variability of soil properties.

The block kriging analysis confirmed the conclusion, initially based on a visual inspection of the CPT logs, that q_{c1N} increased between the one week tests and the following testing times in the loose sand layer. The analysis showed 58%, 77%, 50%, and 63% confidence that the one week were different, due to aging, from the one month, two month, one year, and two year tests, respectively. If one considers that significant aging was complete one month after the blast and groups all tests performed one month and later after the blast in one data set, block kriging yields a 74% confidence that one week tests are different, due to aging, than the tests performed after one week.

Thirteen other comparisons produced greater than 50% confidence that the q_{c1N} data from different time periods were different. Eleven of these comparisons came from comparing pre-blast data to post-blast data in the dense sand and loose gravelly sand layers. A visual comparison of the pre-blast data to post-blast data in both the dense sand and loose gravelly sand layers shows clear differences that were also reflected in the geostatistical analysis. In the dense sand layer, confidence ranged from 59% comparing pre-blast data to 2 year data to 70% comparing pre-blast data to one week data. There was great change between pre- and post-blast data in the loose gravelly sand. The confidence ranged from 92% when comparing pre-blast data to 2 year data to 99% comparing pre-blast data to one month data. In the loose sand layer, the confidence that the

pre-blast data was different than the one week data was 60%. The two comparisons showing greater than 50% confidence in the clay layer were between pre-blast to one year and one year to two year data. These were likely due to degree of saturation changes. The one year tests were performed during a wetter than average summer, while both the pre-blast and two year tests were performed during drier than average summers.

4.7 Comparison of Cyclic Resistance Ratio from Several *In Situ* Tests

Because several different *in situ* tests were used to characterize the site and monitor aging, there is an opportunity to compare the results of different tests at the same site. In this section, methods of determining cyclic resistance ratio (CRR) from V_s, K_D, and q_c are presented. Additionally, a method that was developed to assess liquefaction resistance using the video collected during VisCPT soundings is presented. The results of CRR calculations from each type of test are compared. This analysis is enriched by data at different time periods as well as different types of tests. Finally trends with time are discussed and the results are summarized.

4.7.1 Determination of CRR

For each test type, an equivalent CRR is found for a reference earthquake magnitude of 7.5 using recently proposed liquefaction resistance prediction methods. The Andrus and Stokoe (2000) method was used to estimate CRR from V_s. For DMT data, CRR was determined using the Monaco et al. (2005) procedure. Marchetti (2010) believes that the K_D value has the potential to provide a very reliable measure of liquefaction susceptibility claiming that it exhibits a greater sensitivity to stress history and aging than does q_c. However, Marchetti also states that "an extensive database of liquefaction - non-liquefaction CRR-K_D data is (still) badly needed for better defining the location of the CRR-K_D curve."

The CPT procedures used to determine CRR are by Robertson and Wride (1998), Moss et al. (2006), and Idriss and Boulanger (2008), with a 5% probability of liquefaction used in the Moss et al. (2006) method. There are two important notes about comparing these methods. First, q_c is normalized differently by σ'_v in each method. Second, the Robertson and Wride (1998) and Idriss and Boulanger (2008) methods require calculation of K_σ, a term that accounts for the influence of effective vertical stress on CRR. While Idriss and Boulanger (2008) detail their method of finding K_σ, Robertson and Wride (1998) do not prescribe a method for determining K_σ. For the Robertson and Wride (1998) method, the Youd et al. (2001) recommendations for K_σ were used. It should be

noted that the Youd et al. (2001) K_σ procedure was also applied to the V_s and DMT-based CRR methods.

As shown in Figure 4-79, the Moss et al. (2006) method yields very similar results to the Idriss and Boulanger (2008) method in the loose sand layer (2-4 m depth) and yields similar results to the Robertson and Wride (1998) method in the loose gravelly sand layer (10-14 m depth). These trends are expected because, as shown in Figure 4-80, at low values of q_{c1N} the Moss et al. (2006) and Idriss and Boulanger (2008) curves are similar and predict lower CRR values than the Robertson and Wride (1998) curve. However, at higher q_{c1N} values, Robertson and Wride (1998) generally agrees with Moss et al. (2006) while Idriss and Boulanger (2008) predict the lowest CRR values. For the rest of the analysis in this paper, the Idriss and Boulanger (2008) method is used for obtaining q_{c1N}, K_σ and CRR. For values of q_{c1N} less than approximately 50 and CRR less than about 0.05, the Idriss and Boulanger (2008) CRR curve is between the other two curves. At higher q_{c1N}, the Idriss and Boulanger (2008) method predicts lower CRR values than the other two methods.

Finally, a qualitative method of assessing liquefaction resistance based on vision data was employed. As described in Section 4.5.4, while conducting the VisCPT, the cone advance was stopped every 10 cm. These pauses allowed for visual observation of the soil. At some of these pauses, sand was observed to flow or boil, indicating that the sand is very loose and liquefied during the cone's advance. While lack of boiling in loose sand should not be interpreted as the soil not being susceptible to earthquake-induced liquefaction, the observation of local liquefaction by the VisCPT indicates high liquefaction susceptibility.

4.7.2 Comparison of Pre-Blast CRR from Different *In Situ* Tests

The CRR calculated from CPT, V_s, and DMT data, as well as the zones over which the VisCPT observed boiling from pre-blast testing are shown in Figure 4-81. As seen in this figure, there is some agreement among the CRR values predicted by the different *in situ* tests. For example, variations in liquefaction potential reflect the site layering in all the tests. There are, however, several disagreements between the test methods in predicting CRR. The shear wave velocity predicts the least potential for liquefaction, while the DMT-based CRR shows the greatest potential. Indeed, the results appear to be vastly different.

The V_s based CRR is higher than CRR calculated by the other tests in all soil layers. This result is explained by Andrus et al.'s (2009) hypothesis that shear wave velocity provides a better

indication of the age of the deposit than do other *in situ* tests. The loose sand deposit is of early Holocene age and has developed larger increases in stiffness due to geologic aging compared to more recent Holocene soils. The case histories used to establish the Andrus and Stokoe (2000) shear wave velocity based CRR method came largely from seismically active areas in the western United States, Japan, and Taiwan. As Andrus et al. (2009) point out, in terms of liquefaction resistance, the age of a deposit is better determined from the time since the last major disturbance, rather than the time since deposition. As such, the case histories that were used to create the Andrus and Stokoe (2000) method are from young deposits compared to the loose sand layer at Griffin. The deeper soil layers are Pleistocene deposits and should have an even greater resistance to liquefaction according the V_s based method for determining CRR.

The DMT data shows lower CRR than the other *in situ* tests in the dense and gravelly sand layers. Monaco et al. (2005) propose that the DMT is more responsive to factors that influence liquefaction potential, such as stress history, age, cementation, and structure, than other *in situ* tests that also require penetration of the soil, as opposed to seismic methods. Evidence from the Griffin quarry supports this hypothesis for the loose sand layer, as shown in Figure 4-81. In the older layers, especially those containing greater amounts of gravel, the DMT-based CRR calculation method shows a different result than the CPT-based methods. While further discussion of these differences is included in the following sections, after initially inspecting the results, the author gave more credence to the CPT-based results than the DMT-based results. The CPT-based CRR curves are based on a larger set of case histories than is the DMT curve. Although the CPT case history database does not contain many gravelly sand cases, the liquefaction response of the gravelly sand layer at the site is likely to be controlled by the finer-grained soil in the layer (i.e., the sand) because the gravel is largely floating in the sand matrix with only ~15% gravel. Additionally, the VisCPT videos show mostly a sand matrix with occasional gravel. Although larger gravel pieces may cause occasional large tip resistances, in most cases this only occurs for a very short depth interval and the gravel pieces get pushed out of the way with a commensurate drop in q_c, as evidenced by the large "chatter" in q_{c1N} in this layer.

The qualitative method of assessing liquefaction potential from VisCPT observations identifies only soil layers that liquefy as a result of the cone advance and does not necessarily identify all liquefiable layers nor does it quantify the cyclic resistance of the soil. The VisCPT showed liquefaction over relatively small vertical increments that correspond to low q_{c1N}. The advantage of this method lies in its ability to distinguish low density, contractile sands from simply fine grained soil that could actually have a higher resistance to liquefaction. Additionally, the VisCPT

is not effected by short duration motions because the camera is far from the cone tip. The VisCPT augments other liquefaction assessment methods and confirms soil type, particularly in thin layers that may be misclassified by the CPT.

4.7.3 Comparison of One Week CRR from Different *In situ* Tests

Figure 4-82 compares the CRR calculated from CPT, VisCPT, V_s, and DMT conducted one week following explosive densification. These results do not show agreement between the methods of determining CRR from different *in situ* tests. However, the layering is well reflected in the changes to liquefaction potential according to each type of test. Each of these methods also showed that the site was at greater risk of liquefaction following explosive densification. This occurred despite nearly one foot of settlement, indicating that the site was denser. Many explosive densification projects have shown similar results immediately following explosive densification, for example, Mitchell and Solymar (1984) and Charlie et al. (1992). At the Griffin site, this sensitivity is more pronounced in the dense sand and loose gravelly sand layers, which are both of Pleistocene deposits that were last liquefied ~12,000 years ago. A probable explanation for this behavior is the disruption of cementation or soil skeleton developed over geologic time.

Following explosive densification, the V_s-based CRR agrees more closely with that predicted by CPT data in the loose sand layer. This result again supports Andrus et al.'s (2009) hypothesis that V_s provides a better indication of age than other *in situ* tests. The loose sand deposit is several thousand years old and developed increased strength and stiffness due to geologic aging. Following explosive densification and the disruption of any aging benefits, the CRR from V_s and CPT in the loose sand layer closely agree.

The DMT data show that the site has higher liquefaction potential than the other *in situ* tests in the dense and gravelly sand layers prior to the blast. Monaco et al. (2005) propose that the DMT is more responsive to factors that influence liquefaction potential, such as stress history, age, cementation, and structure, than other *in situ* tests. Empirical evidence has supported this hypothesis in young deposits, as shown in the pre-blast DMT results in the loose sand layer. However, in older deposits, it is unlikely that the DMT is an appropriate test for liquefaction potential. The CPT disturbs the soil and destroys the benefits of age, structure, and/or cementation during data collection, at least in part accounting these factors in q_c. Shear wave velocity measurement is non-destructive and, as previously discussed, has been shown to provide a good indication of aging benefits. However, insertion of the DMT blade occurs prior to inflation of the membrane, destroying beneficial aging prior to testing and underestimating liquefaction

resistance. Finno (1993) demonstrates that K_D, upon which Monaco et al.'s (2005) CRR calculation method is based, reflects both *in situ* horizontal stress and effects of penetration disturbance. While Finno's (1993) work computed strain fields during DMT penetration through saturated cohesive soil, similar magnitudes of strain are expected close to the DMT blade in sands. Finno (1993) computed a normal strain of 10^{-1} at a distance of 0.5 cm perpendicular from the DMT membrane. This strain is large enough to destroy the benefits of aging, as evidenced by resonant column testing performed by Thomann and Hryciw (1992a). Because the DMT essentially tests disturbed soil, the Monaco et al. (2005) method is overly conservative in geologically aged deposits.

Considering CPT, V_s, and DMT data, it appears that explosive densification did not completely destroy the effects of geologic age in the dense sand and loose gravelly sand layers, but changed the younger, loose sand layer to a nearly fresh state. In the older, deeper layers, V_s-based CRR remains higher than CPT-based CRR, while CRR from DMT data remains lower than that calculated from CPT data. However, the CRR calculated from one week CPT, DMT, and V_s data in the younger, loose sand layer are very similar. This suggests that explosive densification reset the age of the loose sand layer, but did not complete destroy the benefit of geologic age in the older deposits. Evidence from this study suggests that CPT, DMT, and V_s derived CRR agree only in fresh deposits. When DMT-based CRR is low and V_s-based CRR is high compared to CPT-based CRR, the results suggest an aged deposit at lower risk of liquefaction. These conclusions demonstrate the benefit of multiple *in situ* test methods at one site.

The qualitative method of assessing liquefaction potential from VisCPT shows the same trend in the loose gravelly sand layer following explosive densification as the other *in situ* tests. Prior to the blast, it showed that the loose gravelly sand was somewhat at risk of liquefaction, with increased risk following explosive densification. While this trend is consistent with the other *in situ* tests, the lack of liquefaction risk in the loose sand layer shows that this method of assessing liquefaction resistance does not identify all potential problem layers. The qualitative method of assessing liquefaction potential using video data from VisCPT is best used in conjunction with other liquefaction assessment methods.

4.7.4 Comparison of One Month and Later CRR from Different *In situ* Tests

The results of CRR analysis from one month, two and a half month, one year, and two year testing are shown in Figures 4-83 through 4-86, respectively. The trends discussed in the previous section concerning one week testing are present in each of these testing periods as well. As

discussed previously, the majority of sand aging occurred between the one week and one month testing periods, with tests performed one month and later following the blast falling within the same range of results.

4.7.5 Summary of Results

Using data from CPT, VisCPT, DMT, and SCPT, liquefaction resistance was determined for a sand and gravel quarry in Griffin, IN. Of three methods for determining CRR by CPT data, the Idriss and Boulanger (2008) method provided the median CRR predictions compared to the Moss et al. (2006) and Robertson and Wride (1998) methods at low q_{c1N} values and predicted the lowest CRR at higher q_{c1N} values.

The Idriss and Boulanger (2008) method was compared to predictions of CRR by the other *in situ* tests in this study. The CRR values predicted by V_s data were higher than CRR values predicted by the other tests. This is due to the higher sensitivity of V_s to geologic age compared to CPT and DMT. DMT-based CRR is overly conservative in geologically aged deposits. Insertion of the DMT blade destroys the beneficial effects of aging prior to testing the material; therefore, the DMT-based CRR does not include the beneficial effects of aging that are known to increase liquefaction resistance. Vision data from the VisCPT was consistent with the other *in situ* test results. It shows increased liquefaction potential when q_{c1N} values are very low. The VisCPT also confirms that low q_{c1N} values are due to low density, contractive sand and not due to the presence of finer grained soils. The results of this analysis demonstrate the benefits of performing multiple *in situ* tests at a site.

4.8 Conclusion

This chapter describes the explosive densification experiment that was performed at Griffin, IN. A description of the site investigation, instrumentation and data collection methods, and experimental design was presented. Additionally, the results of the experiment and subsequent *in situ* testing were presented and discussed. A geostatistical analysis of this data showed with 74% confidence that the differences in CPT results from the one week testing period were different from the testing periods that followed due to aging and not due to spatial variability. Additionally, comparing the results of widely accepted CRR calculation methods based on the *in situ* tests performed at the Griffin quarry showed that V_s-based methods are more sensitive to geologic aging and DMT-based methods are less sensitive to geologic aging compared to CPT-based methods. This is because the V_s measurements are non-destructive and do not disrupt the effects

of aging. By contrast, insertion of the DMT blade occurs prior to inflation of the membrane and collection of DMT data. Penetration of the DMT blade destroys aging benefits and does not account for them when determining CRR. Results of the explosive densification experiment will be compared to other sand aging studies in Chapter 8.

Table 4-1. Testing times and notes from the blast sites.

	Date	Time	Hours after Blast	Notes
CPT-21	07 AUG 08	1000	18	
CPT-22	07 AUG 08	1400	20	
CPT-23	07 AUG 08	1600	24	
DMT-2	08 AUG 08	0800	38	
SCPT-24	08 AUG 08	1430	46.5	
VisCPT-25	09 AUG 08	0930	65.5	
CPT-27	10 AUG 08	0800	88	
CPT-28	10 AUG 08	1100	91	
PSU-1	11 AUG 08	0930	113.5	
PSU-2	11 AUG 08	1430	118.5	
VisCPT-29	12 AUG 08	1300	141	
CPT-30	05 SEP 08	0800	712	
CPT-31	05 SEP 08	0900	713	
CPT-32	05 SEP 08	1030	714.5	
DMT-3	05 SEP 08	1430	718.5	Hole in diaphragm at 8.0 m
VisCPT-33	06 SEP 08	0800	736	
SCPT-34	06 SEP 08	0930	737.5	
CPT-40	18 OCT 08	1500	1751	
VisCPT-41	19 OCT 08	0800	1768	
SCPT-42	19 OCT 08	1000	1770	Rods caught on cams, bad data below 9.24m
CPT-43	19 OCT 08	1300	1773	
CPT-44	19 OCT 08	1400	1774	
DMT-4	20 OCT 08	1300	1797	Hole in diaphragm at 14.1 m
SCPT-56	23 NOV 08	1300	2613	
CPT-57	23 NOV 08	1430	2614.5	
CPT-58	23 NOV 08	1530	2615.5	
SCPT-60	20 JUL 09	0930	8345.5	
CPT-61	20 JUL 09	1130	8347.5	
CPT-62	20 JUL 09	1230	8348.5	

Table 4-1 (cont.). Testing times and notes from the blast sites.

	Date	Time	Hours after Blast	Notes
CPT-63	20 JUL 09	1530	8351.5	
VisCPT-64	20 JUL 09	1800	8354	
DMT-11	13 AUG 09	1200	8900	Hole in diaphragm at 11.2 m
SCPT-71	07 JUN 10	0830	16072.5	
CPT-72	07 JUN 10	1100	16075	
CPT-73	07 JUN 10	1200	16076	
VisCPT-74	07 JUN 10	1430	16078.5	
DMT-12	08JUN 10	0930	16097.5	
VisCPT-75	08 JUN 10	1400	16102	
VisCPT-76	08 JUN 10	1600	16104	

Table 4-2. Mean and standard deviation by layer and testing period.

Layer	Testing Period	Normalized Tip Resistance Mean, μ	Normalized Tip Resistance Standard Deviation, σ^2
Clay	Pre-Blast	110	4884
Clay	One Week	163	16033
Clay	One Month	267	97753
Clay	2.5 Months	223	33779
Clay	One Year	83	547
Clay	Two Years	118	5078
Loose Sand	Pre-Blast	78	1688
Loose Sand	One Week	79	1180
Loose Sand	One Month	112	728
Loose Sand	2.5 Months	106	423
Loose Sand	One Year	96	577
Loose Sand	Two Years	110	1723
Dense Sand	Pre-Blast	198	8865
Dense Sand	One Week	109	1703
Dense Sand	One Month	112	1979
Dense Sand	2.5 Months	119	1546
Dense Sand	One Year	117	1638
Dense Sand	Two Years	123	2509
Loose Gravelly Sand	Pre-Blast	130	404
Loose Gravelly Sand	One Week	75	195
Loose Gravelly Sand	One Month	77	112
Loose Gravelly Sand	2.5 Months	77	240
Loose Gravelly Sand	One Year	82	146
Loose Gravelly Sand	Two Years	82	526

Table 4-3. Exponential variogram inputs by layer and testing period.

Layer	Testing Period	Correlation Length, a (m)	Partial Sill, b	Nugget, c
Clay	Pre-Blast	2	4,000	500
Clay	One Week	2	30,000	500
Clay	One Month	1.5	100,000	500
Clay	2.5 Months	1.5	60,000	500
Clay	One Year	1.5	500	150
Clay	Two Years	2	6,000	500
Loose Sand	Pre-Blast	4	1,950	50
Loose Sand	One Week	1.5	1,000	50
Loose Sand	One Month	1.5	1,250	50
Loose Sand	2.5 Months	1.5	600	50
Loose Sand	One Year	2	950	50
Loose Sand	Two Years	1.5	1,150	50
Dense Sand	Pre-Blast	1.5	6,950	50
Dense Sand	One Week	2	1,450	50
Dense Sand	One Month	2	1,450	50
Dense Sand	2.5 Months	1.5	1,050	50
Dense Sand	One Year	2	1,450	50
Dense Sand	Two Years	1.5	1,450	50
Loose Gravelly Sand	Pre-Blast	1.5	550	50
Loose Gravelly Sand	One Week	2	165	10
Loose Gravelly Sand	One Month	2	90	10
Loose Gravelly Sand	2.5 Months	1.5	120	10
Loose Gravelly Sand	One Year	1.5	140	10
Loose Gravelly Sand	Two Years	1.5	400	10

Table 4-4. Location of CPT soundings and depth to each soil layer.

Test	Testing Time	E-W Location, x (m)	N-S Location, y (m)	Depth of Test, z (m)	Depth of Clay Layer (m)	Depth of Loose Sand Layer (m)	Depth of Dense Sand Layer (m)	Depth of Loose Gravel Sand Layer (m)
CPT-9	Pre-blast	3.4	4.2	6.9	1.5	2.8	N/A	N/A
CPT-11	Pre-blast	3.3	18.3	8.5	1.5	3.5	N/A	N/A
VisCPT-15	Pre-blast	9.9	3.9	15.4	1.5	3.2	10.6	14.7
CPT-16	Pre-blast	6.3	8.4	8.6	1.5	3.3	N/A	N/A
CPT-17	Pre-blast	9.1	13.2	6.9	1.6	3.3	N/A	N/A
CPT-18	Pre-blast	9.1	14.0	10.0	1.5	3.5	9.9	N/A
SCPT-19	Pre-blast	9.1	12.3	18.7	1.7	3.3	9.7	14.9
CPT-20	Pre-blast	15.5	8.4	15.0	1.5	3.0	10.2	13.8
CPT-21	1 week	9.1	9.6	18.1	1.7	3.5	10.1	14.2
CPT-22	1 week	1.8	6.4	17.5	1.5	2.9	9.8	14.4
CPT-23	1 week	14.1	10.2	18.2	1.8	3.0	9.2	13.7
SCPT-24	1 week	11.1	11.3	18.2	1.5	3.1	10.0	14.9
VisCPT-25	1 week	11.0	2.5	15.3	1.5	3.1	9.0	14.5
VisCPT-29	1 week	9.3	1.5	18.1	1.7	3.1	9.1	14.4
CPT-30	1 month	0.7	4.7	17.5	1.5	2.8	10.5	14.5
VisCPT-33	1 month	7.4	2.0	15.5	1.5	2.9	9.1	14.6
SCPT-34	1 month	12.2	12.7	17.8	1.8	3.3	9.9	14.5
VisCPT-41	2.5 months	11.7	3.7	15.7	1.5	3.0	9.3	14.6
SCPT-42	2.5 months	7.1	14.2	9.2	1.5	3.7	7.9	N/A
CPT-44	2.5 months	1.1	2.6	17.0	1.5	3.0	8.7	15.3
SCPT-60	1 year	10.6	10.4	17.7	1.5	2.9	10.1	14.4
CPT-61	1 year	2.3	12.1	15.7	1.5	2.9	10.2	14.3
VisCPT-64	1 year	12.1	5.0	15	1.5	3.0	9.5	14.2
SCPT-71	2 years	5.2	12.9	17.0	1.6	3.2	8.0	14.2
CPT-72	2 years	3.6	1.9	17.0	1.5	2.9	8.6	15
VisCPT-74	2 years	5.3	3.0	17.1	1.5	3	8.4	13.9
VisCPT-76	2 years	4.4	14.5	16.0	1.5	2.6	7.9	14.2

Table 4-5. Block kriging mean and standard deviation by layer and testing period.

Layer	Testing Period	Normalized Tip Resistance Mean from Block Kriging, z_A*	Normalized Tip Resistance Standard Deviation from Block Kriging, σ^2_{BK}
Clay	Pre-Blast	176	4501
Clay	One Week	173	21558
Clay	One Month	276	90259
Clay	2.5 Months	230	51376
Clay	One Year	79	374
Clay	Two Years	130	1764
Loose Sand	Pre-Blast	118	1572
Loose Sand	One Week	81	367
Loose Sand	One Month	110	931
Loose Sand	2.5 Months	110	212
Loose Sand	One Year	101	560
Loose Sand	Two Years	111	746
Dense Sand	Pre-Blast	189	6208
Dense Sand	One Week	102	821
Dense Sand	One Month	111	1187
Dense Sand	2.5 Months	117	817
Dense Sand	One Year	116	1162
Dense Sand	Two Years	119	1074
Loose Gravelly Sand	Pre-Blast	127	322
Loose Gravelly Sand	One Week	80	47
Loose Gravelly Sand	One Month	79	42
Loose Gravelly Sand	2.5 Months	78	87
Loose Gravelly Sand	One Year	83	87
Loose Gravelly Sand	Two Years	82	322

Table 4-6. Results of two-tailed hypothesis test comparisons using mean and standard deviation from block kriging analysis.

Layer	Comparison	Test Value, t	Degrees of Freedom, df	P-value, p	Confidence of Difference (%)
Clay	Pre-blast to week	0.02	13,024,011	0.98	2
	Pre-blast to month	0.32	23,510,719	0.75	25
	Pre-blast to 2.5 months	0.23	13,186,760	0.83	17
	Pre-blast to year	1.40	2,616,189	0.16	84
	Pre-blast to 2 years	0.59	2,973,870	0.56	44
	Week to month	0.31	29,822,987	0.76	24
	Week to 2.5 months	0.21	19,407,950	0.83	17
	Week to year	0.63	10,367,757	0.53	47
	Week to 2 years	0.28	10,768,594	0.78	22
	Month to 2.5 months	0.12	33,219,599	0.90	10
	Month to year	0.65	21,835,775	0.51	49
	Month to 2 years	0.48	22,267,085	0.63	37
	2.5 months to year	0.66	11,591,938	0.51	49
	2.5 months to 2 years	0.43	12,009,087	0.66	34
	Year to 2 years	1.11	613,142	0.27	73
Loose Sand	Pre-blast to week	0.83	1,222,425	0.40	60
	Pre-blast to month	0.15	935,730	0.88	12
	Pre-blast to 2.5 months	0.18	1,030,967	0.86	14
	Pre-blast to year	0.35	936,285	0.72	28
	Pre-blast to 2 years	0.14	1,092,795	0.89	11
	Week to month	**0.81**	**321,217**	**0.42**	**58**
	Week to 2.5 months	**1.21**	**204,707**	**0.23**	**77**
	Week to year	**0.67**	**252,396**	**0.50**	**50**
	Week to 2 years	**0.90**	**357,219**	**0.37**	**63**
	Week to all post-blast	**1.13**	**408,420**	**0.26**	**74**
	Month to 2.5 months	0.01	248,602	1.00	0
	Month to year	0.23	316,559	0.82	18
	Month to 2 years	0.02	396,856	0.98	2
	2.5 months to year	0.31	174,536	0.75	25
	2.5 months to 2 years	0.03	263,836	0.97	3
	Year to 2 years	0.27	325,133	0.79	21

Table 4-6 (Continued). Results of two-tailed hypothesis test comparisons using mean and standard deviation from block kriging analysis.

Layer	Comparison	Test Value, t	Degrees of Freedom, df	P-value, p	Confidence of Difference (%)
Dense Sand	Pre-blast to week	1.03	15,510,949	0.30	70
	Pre-blast to month	0.91	13,936,416	0.36	64
	Pre-blast to 2.5 months	0.86	13,106,381	0.39	61
	Pre-blast to year	0.85	14,023,655	0.39	61
	Pre-blast to 2 years	0.82	14,056,957	0.41	59
	Week to month	0.19	2,545,427	0.85	15
	Week to 2.5 months	0.37	1,873,919	0.71	29
	Week to year	0.30	2,553,616	0.76	24
	Week to 2 years	0.39	2,495,612	0.70	30
	Month to 2.5 months	0.14	1,855,867	0.89	11
	Month to year	0.10	2,428,533	0.92	8
	Month to 2 years	0.17	2,354,688	0.86	14
	2.5 months to year	0.04	1,847,724	0.97	3
	2.5 months to 2 years	0.04	1,771,515	0.97	3
	Year to 2 years	0.07	2,350,843	0.94	6
Loose Gravelly Sand	Pre-blast to week	2.45	259,453	0.01	99
	Pre-blast to month	2.53	240,332	0.01	99
	Pre-blast to 2.5 months	2.45	267,821	0.01	99
	Pre-blast to year	2.19	267,539	0.03	97
	Pre-blast to 2 years	1.76	548,794	0.08	92
	Week to month	0.13	85,548	0.89	11
	Week to 2.5 months	0.22	108,338	0.82	18
	Week to year	0.23	108,122	0.81	19
	Week to 2 years	0.12	458,865	0.90	10
	Month to 2.5 months	0.11	86,537	0.91	9
	Month to year	0.35	86,259	0.73	27
	Month to 2 years	0.19	409,178	0.85	15
	2.5 months to year	0.40	113,717	0.69	31
	2.5 months to 2 years	0.24	421,562	0.81	19
	Year to 2 years	0.02	421,529	0.99	1

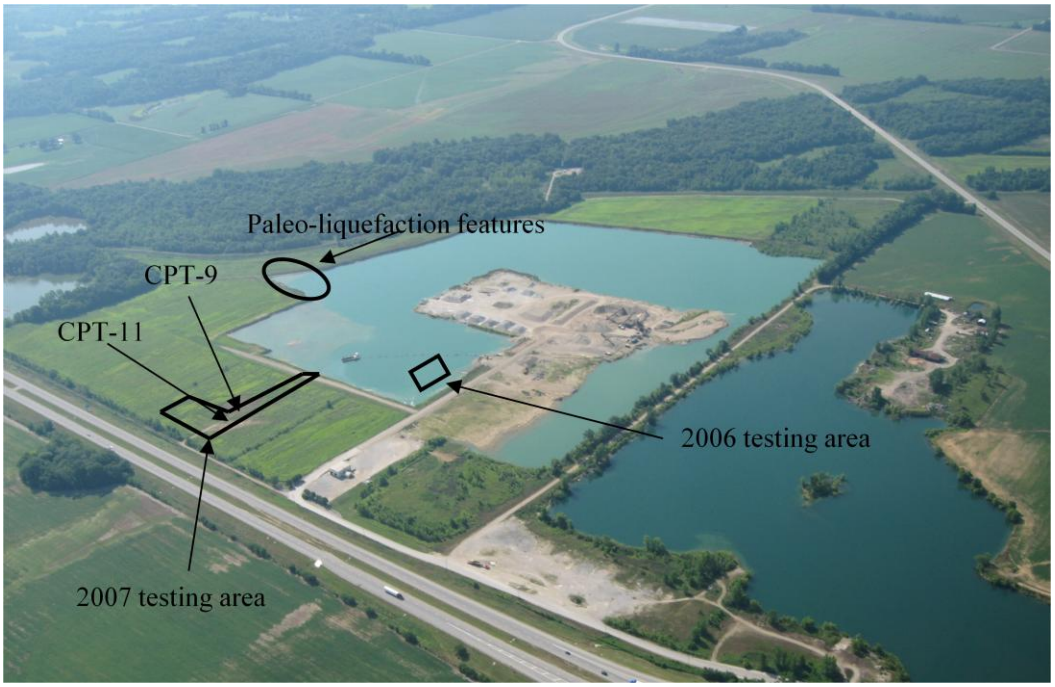

Figure 4-1. Aerial photograph of the Mulzer Crushed Stone, Inc. sand and gravel quarry in Griffin, IN (photo courtesy of Mulzer Crushed Stone, Inc.).

Figure 4-2. Paleo-liquefaction feature in a vertical cut along the side of the lake at the Griffin field site (photo courtesy of Russell Green).

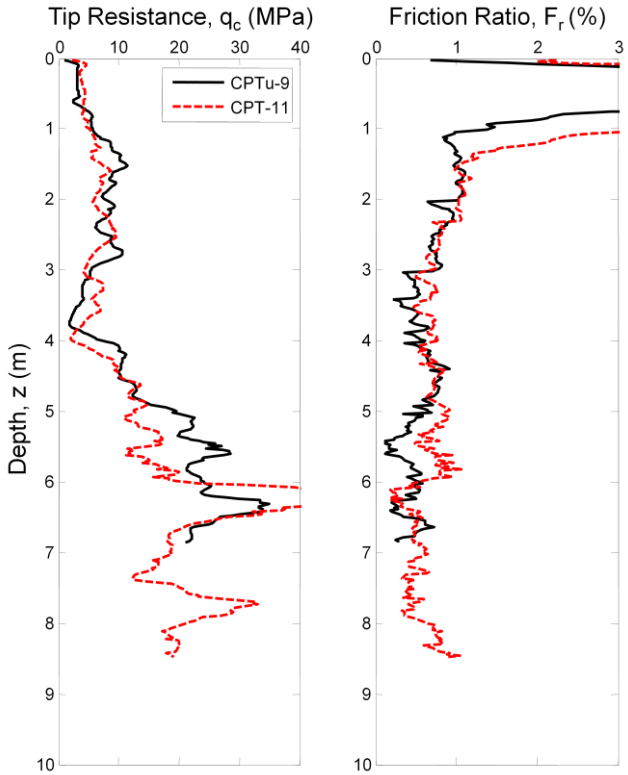

Figure 4-3. Results of CPT-9 and CPT-11. The blast area was between these CPT locations.

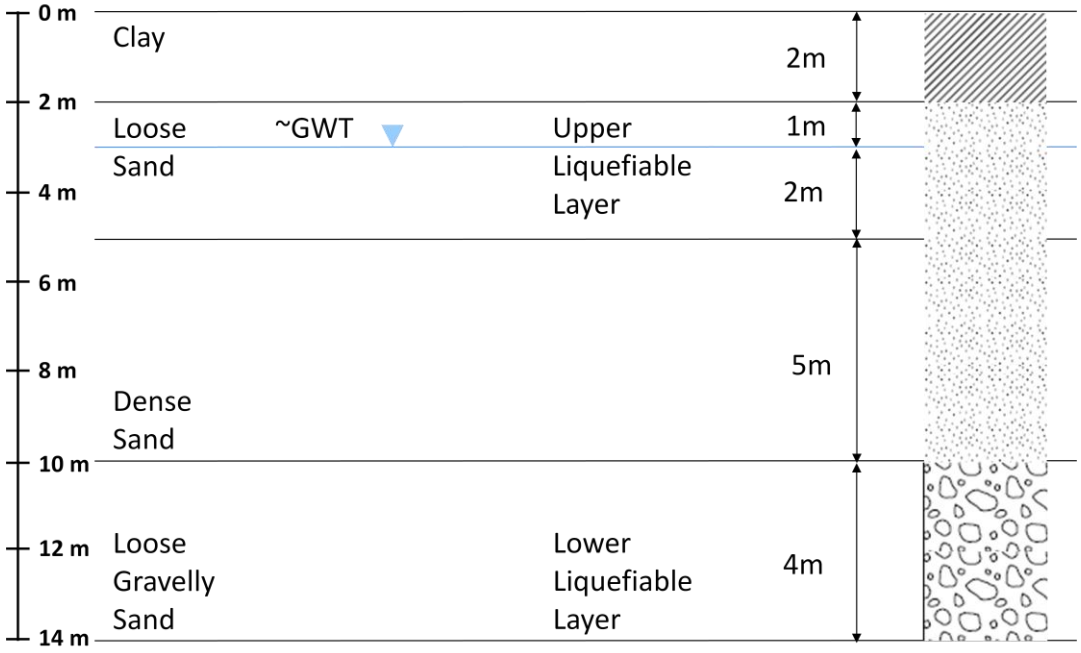

Figure 4-4. Soil layering at the blast site.

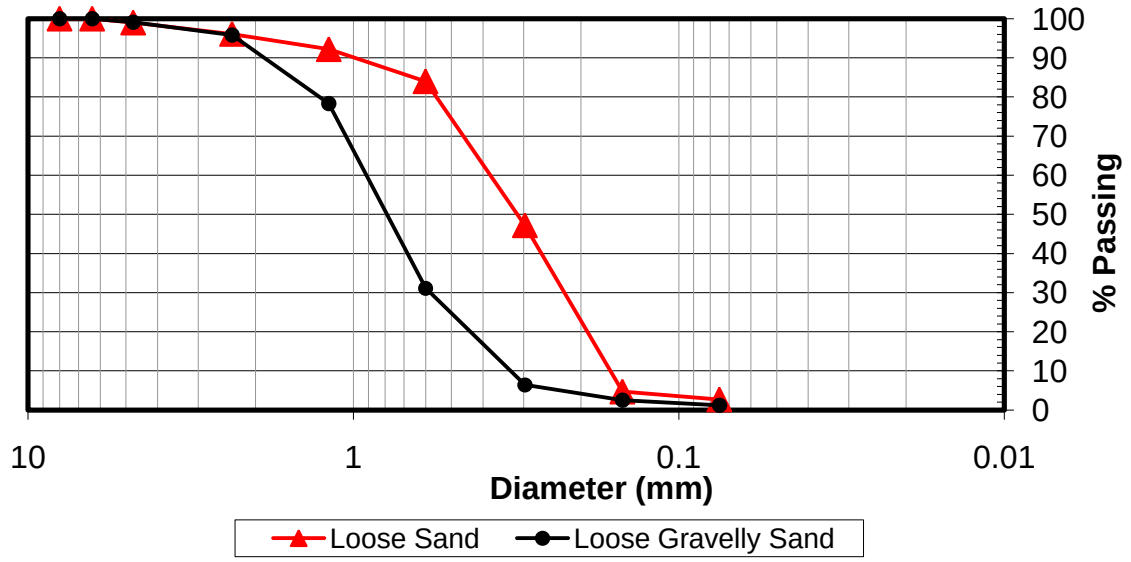

Figure 4-5. Grain size distribution curves from the loose sand and loose gravelly sand layers at Griffin, IN.

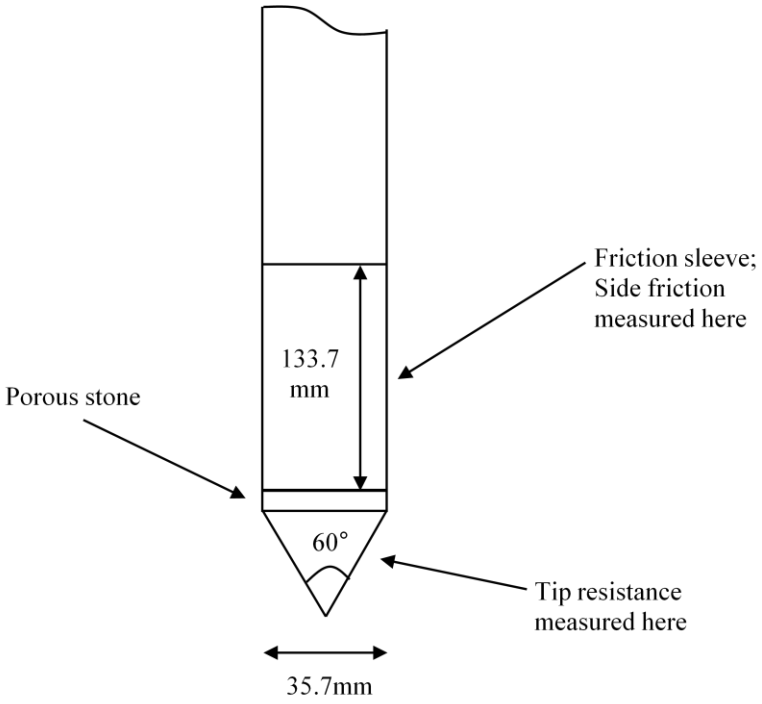

Figure 4-6. Schematic of the cone used in the cone penetration test.

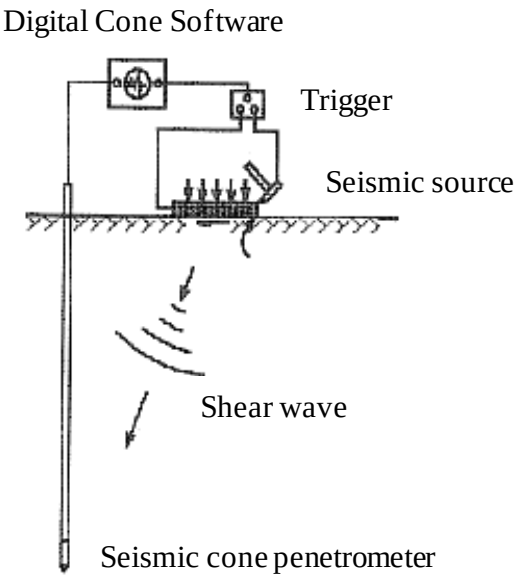

Figure 4-7. Seismic cone penetration test (adapted from Lunne et al., 1997).

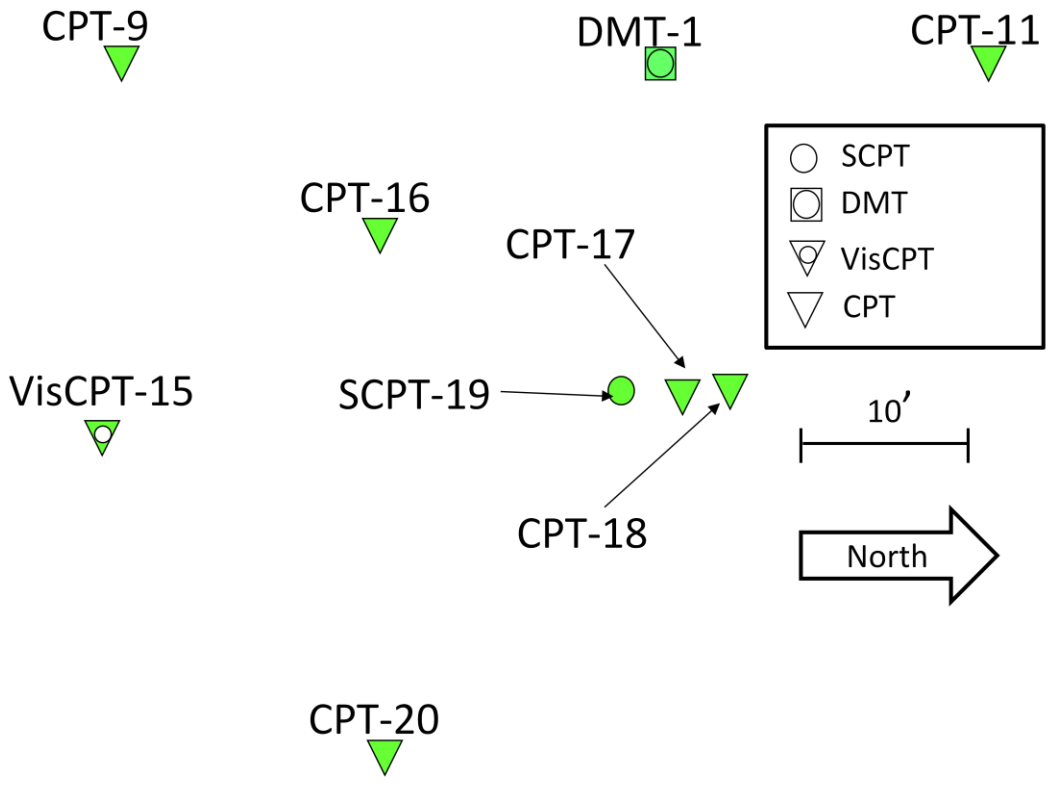

Figure 4-8. Layout of pre-blast *in situ* testing.

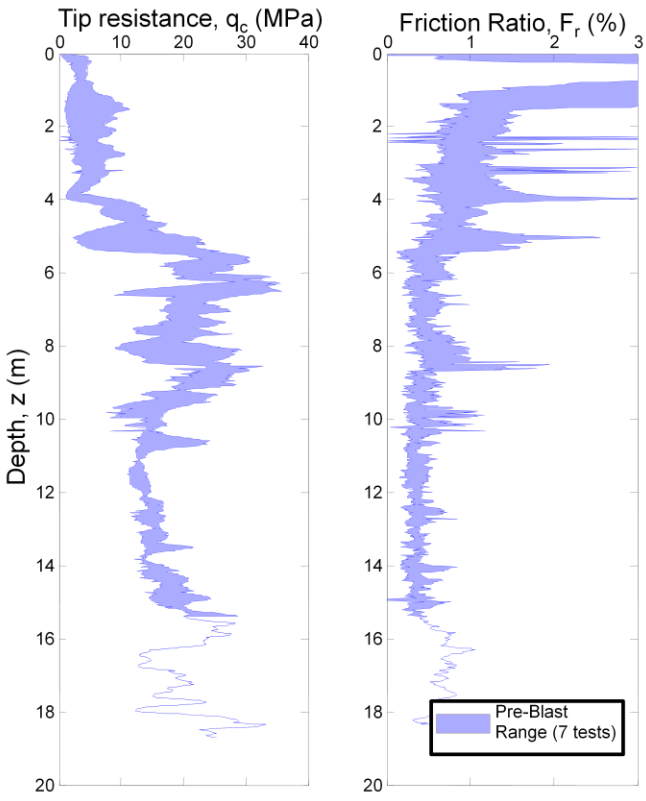

Figure 4-9. Range of pre-blast CPT results.

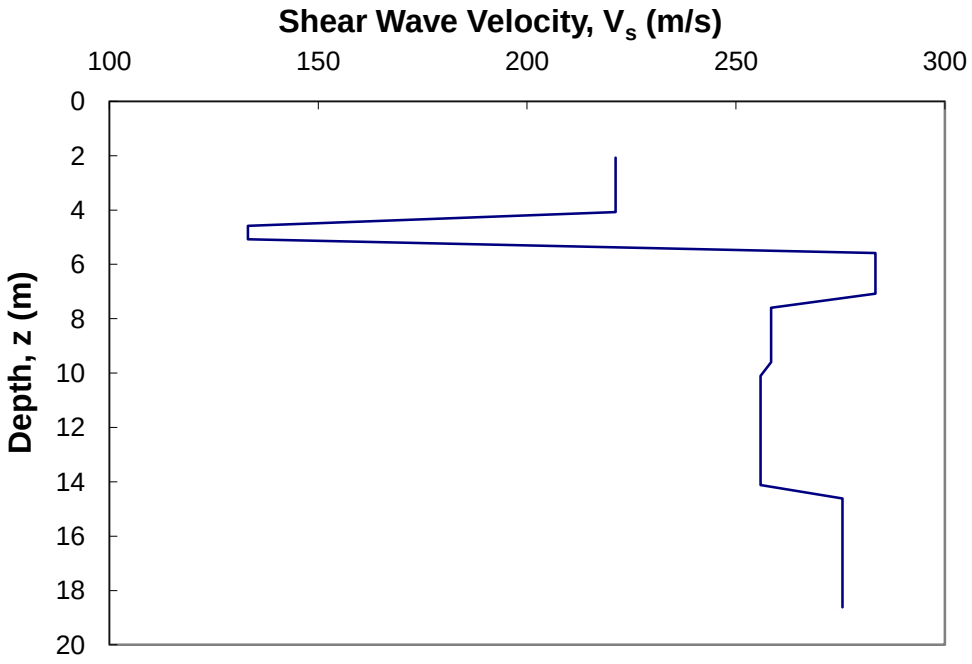

Figure 4-10. Pre-blast shear wave velocity from SCPT-19.

Figure 4-11. Dilotometer blade (photo courtesy of Roman Hryciw).

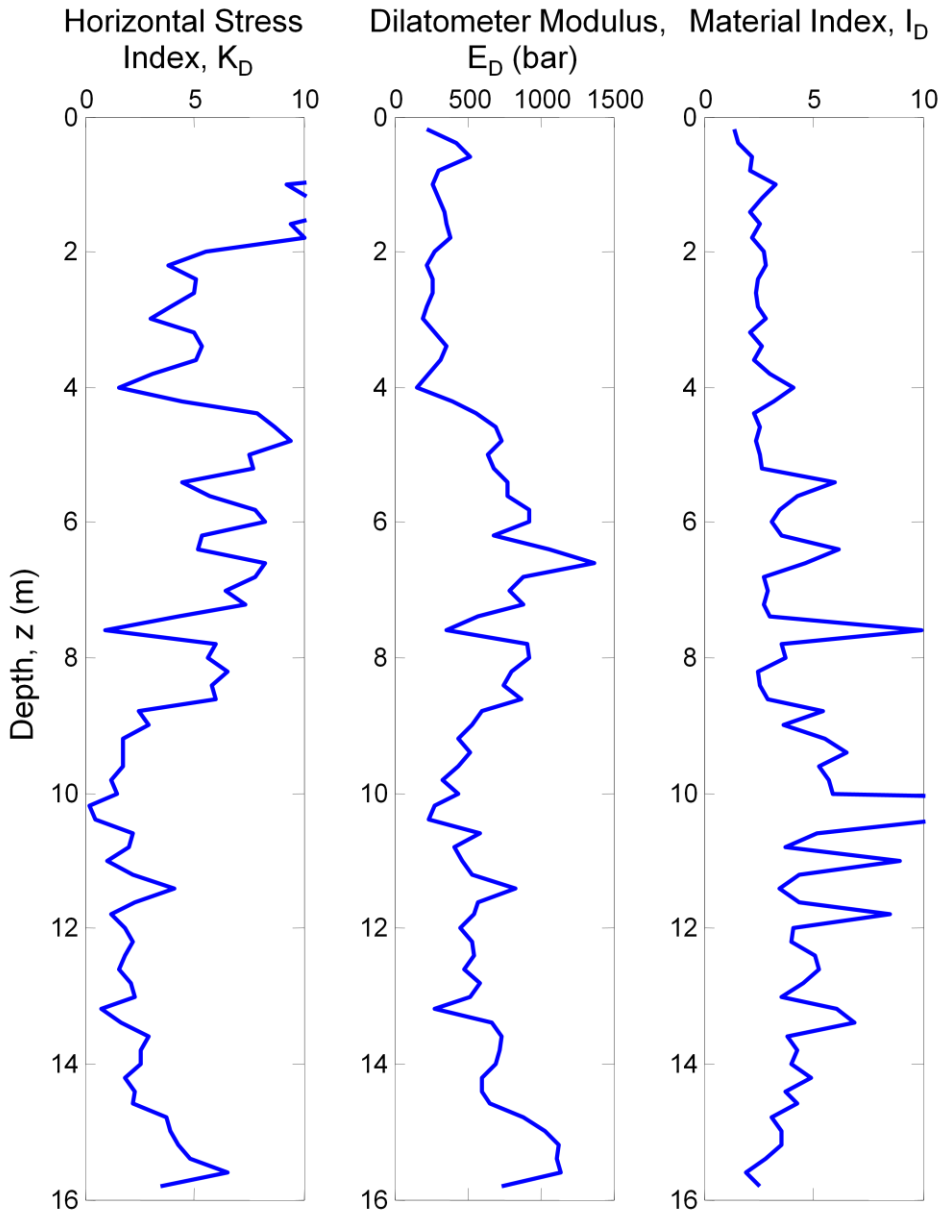

Figure 4-12. Pre-blast DMT results: (a) K_D, the horizontal stress index, (b)E_D, the dilatometer modulus, and (c) I_D, the material index.

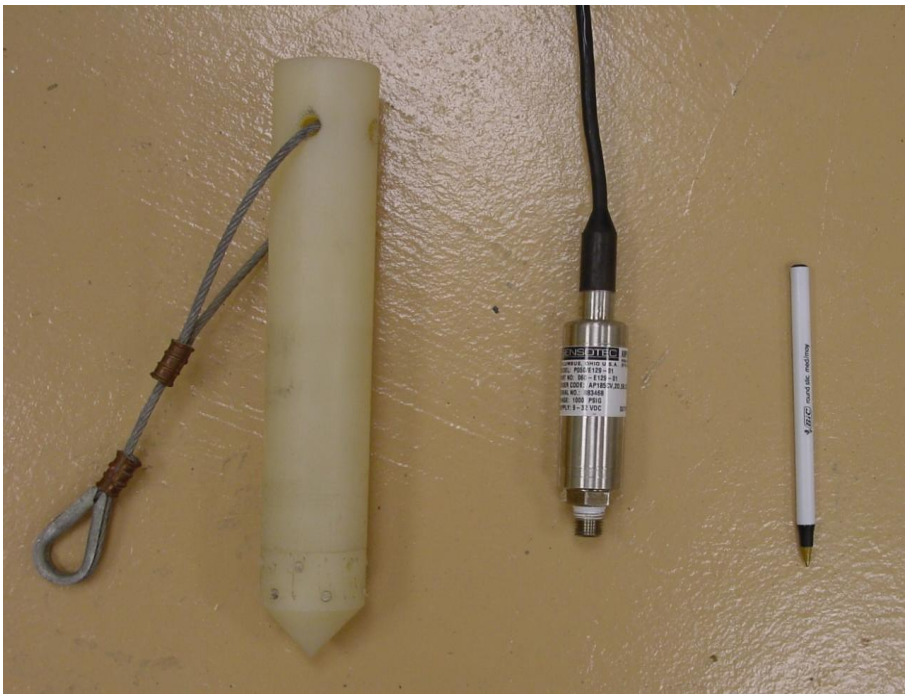

Figure 4-13. Sensotec pore pressure transducer with nylon cone.

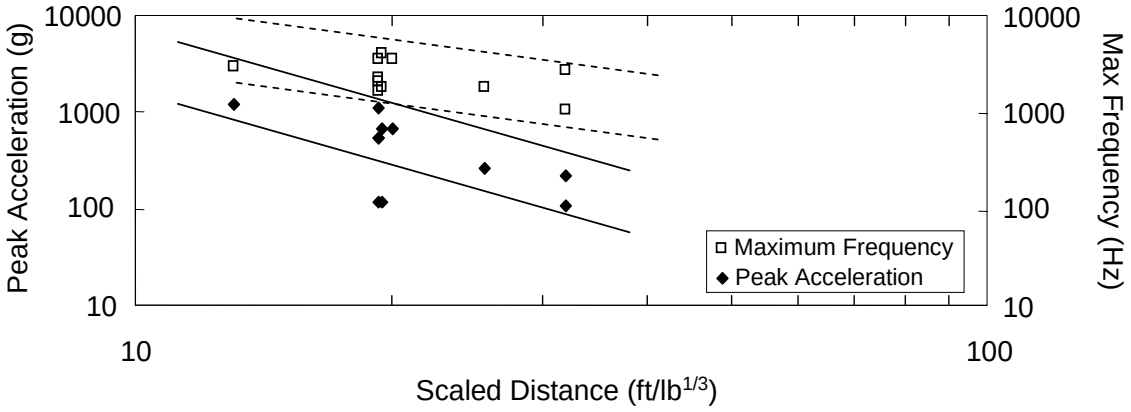

Figure 4-14. Peak acceleration and maximum frequency of blast vibrations as a function of cube root scaled distance (adapted from Hryciw, 1986).

Figure 4-15. Set up for the swimming pool instrument experiment (photo courtesy of Russell Green).

Figure 4-16. Location of survey points. Survey points shown in red were repeated measured following the blast.

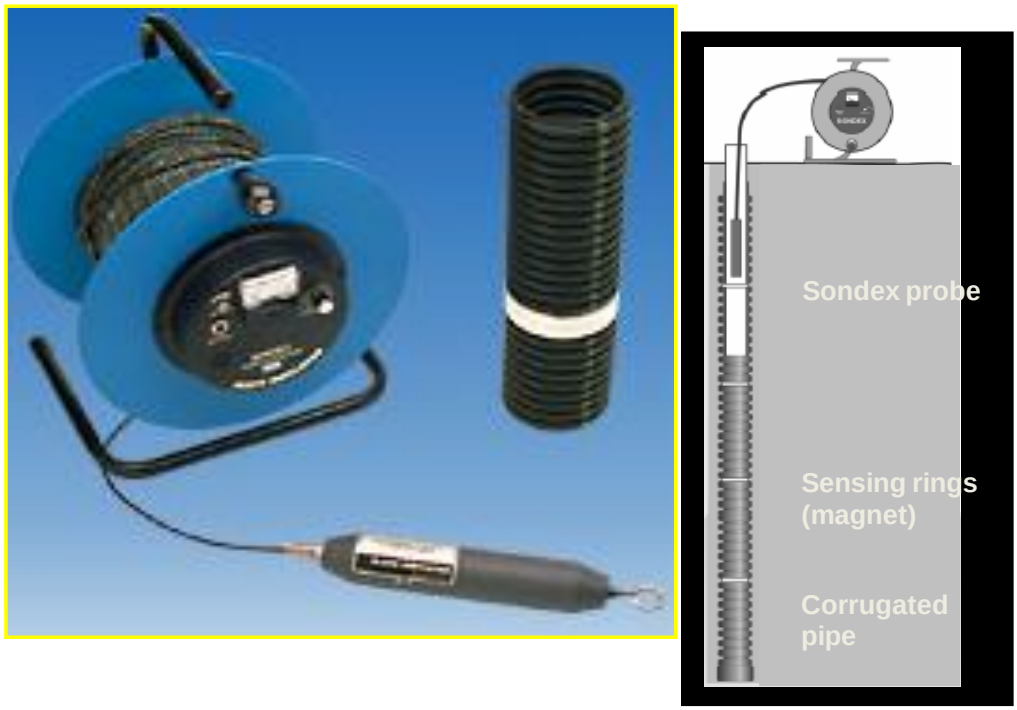

Figure 4-17. Sondex settlement tube equipment (from http://www.slopeindicator.com/instruments/ext-sondex.html).

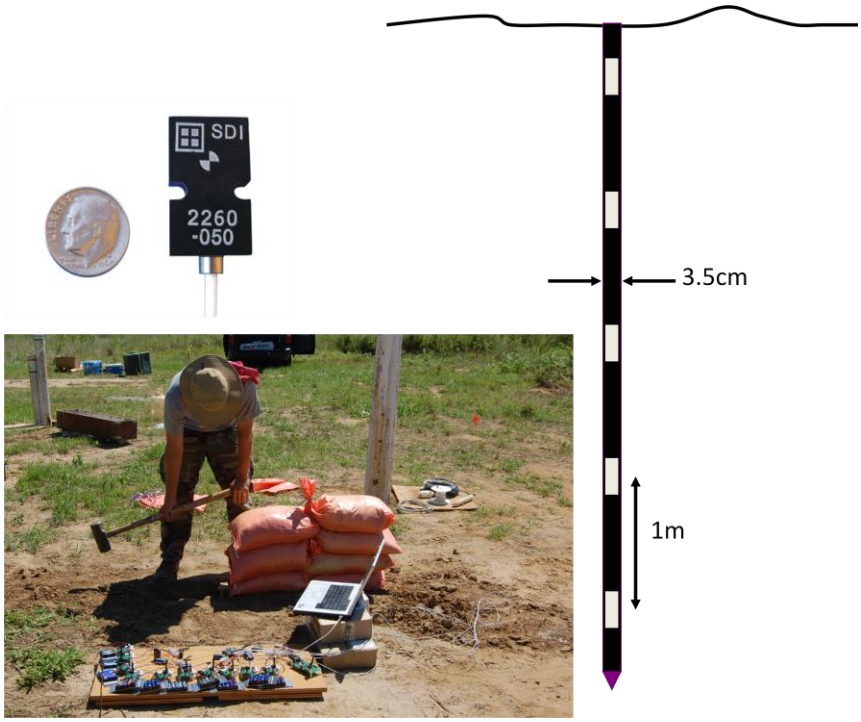

Figure 4-18. Down-hole tube set up (photo courtesy of Roman Hryciw).

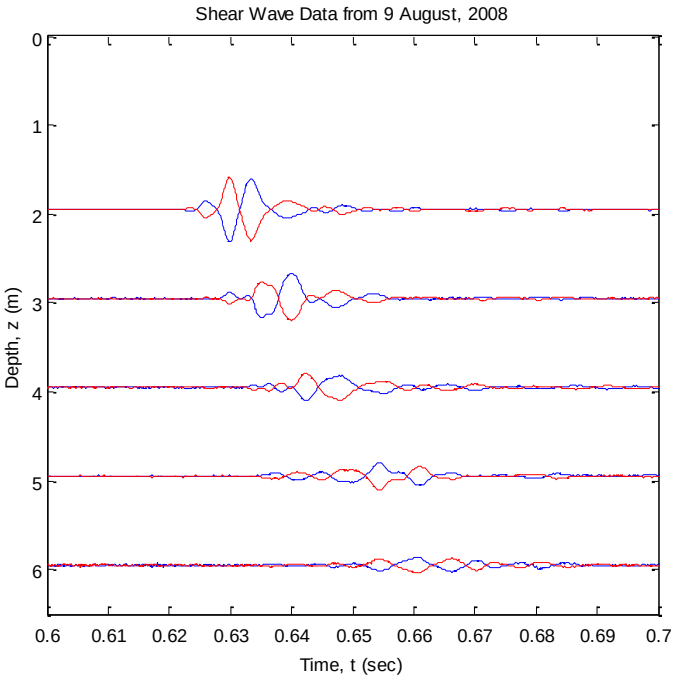

Figure 4-19. Shear wave arrival at the down-hole tube.

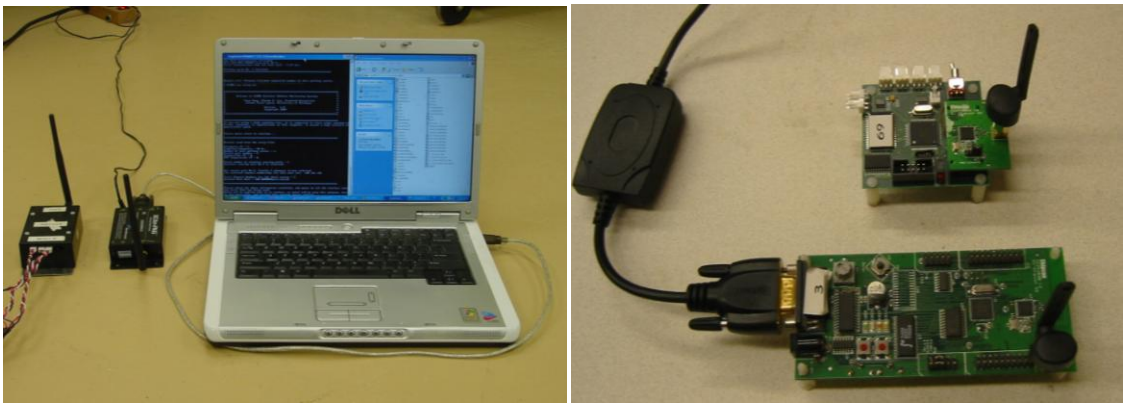

Figure 4-20. Photos of (a) the Stanford wireless units and (b) the Narada wireless units.

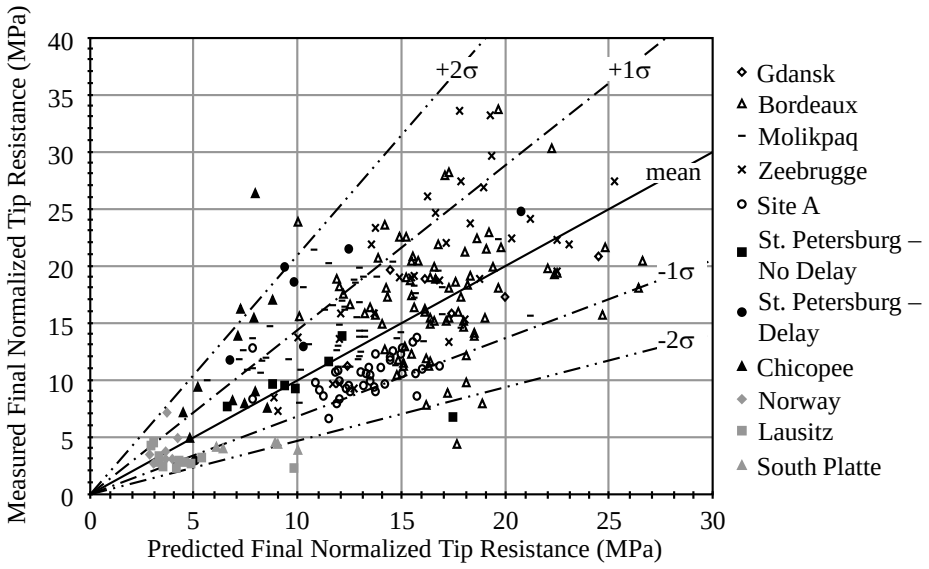

Figure 4-21. Relationship between measured and predicted final normalized tip resistance (adapted from Narin van Court and Mitchell, 1990).

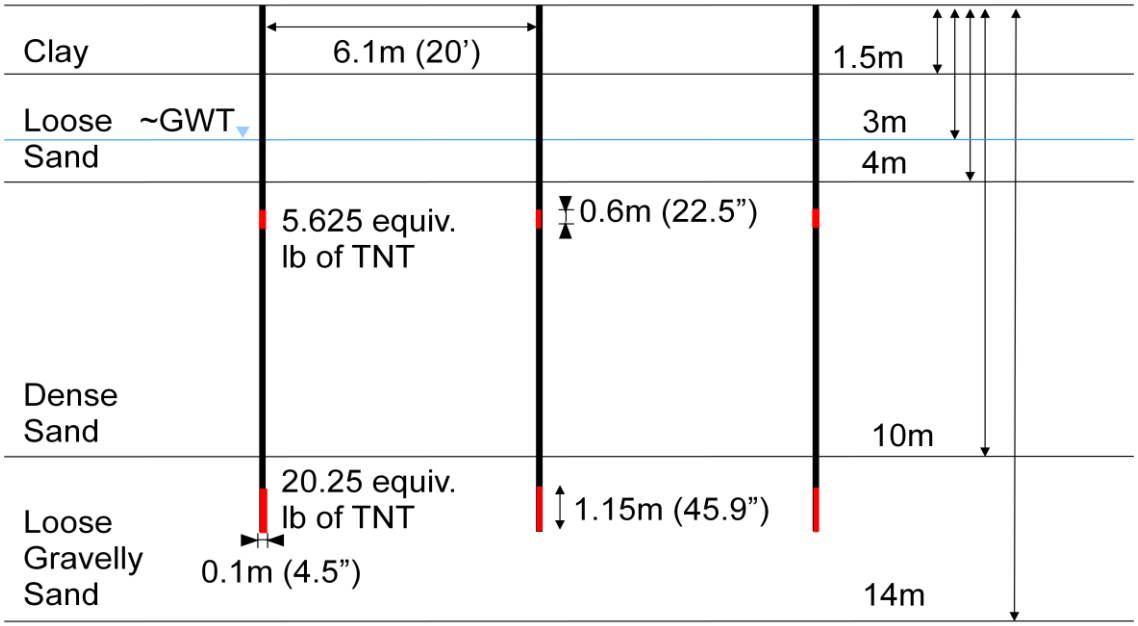

Figure 4-22. Location of charges in the soil column.

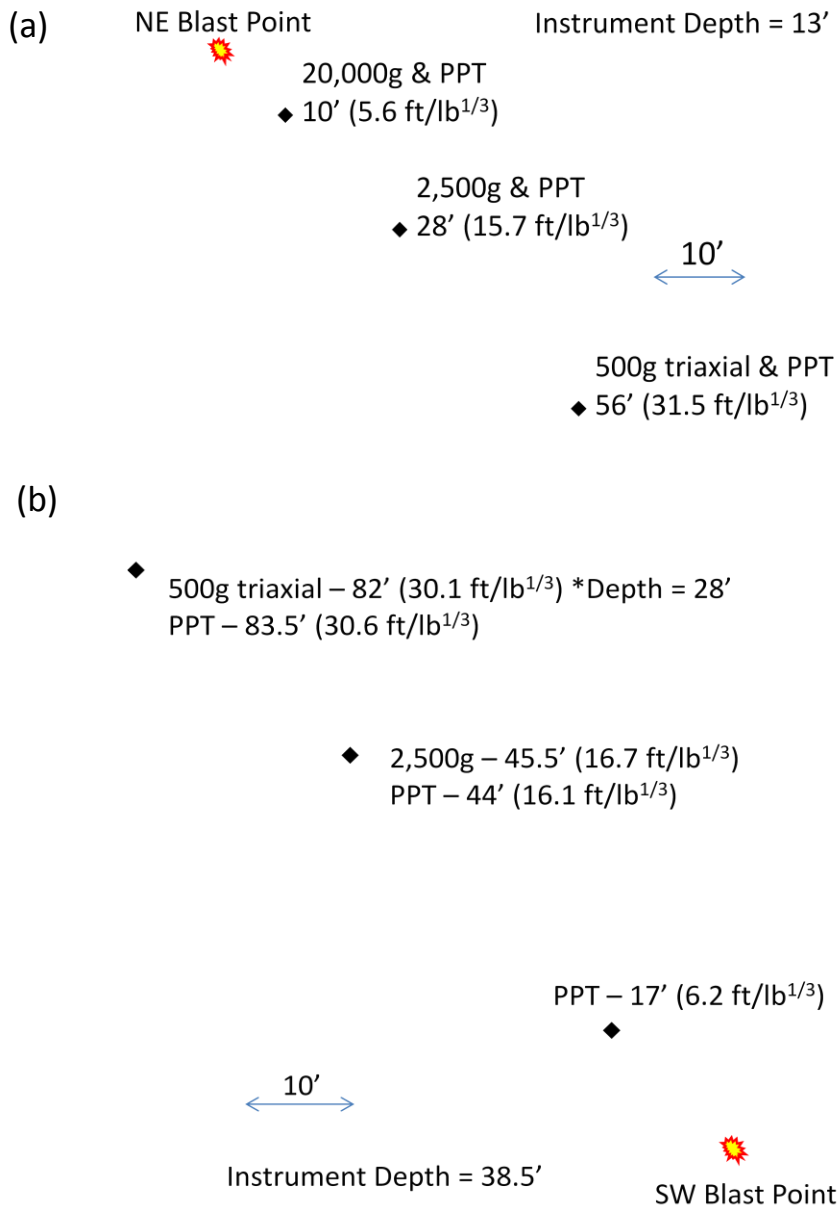

Figure 4-23. Location of instrument holes in relation to (a) the NE blast point and (b) the SW blast point.

Figure 4-24. Tests performed in a liquefaction tank were used to determine the amount of bentonite in the slurry mix. (a) Slurry maintained a 4" diameter borehole during liquefaction. (b) Poring slurry into the bore hole.

Figure 4-25. A large loader was used to push the instrumentation 1' into undisturbed soil (photo courtesy of Russell Green).

Figure 4-26. Explosive densification at Griffin, IN (photo courtesy of Roman Hryciw).

Figure 4-27. Stemming the blast hole (photo courtesy of Roman Hryciw).

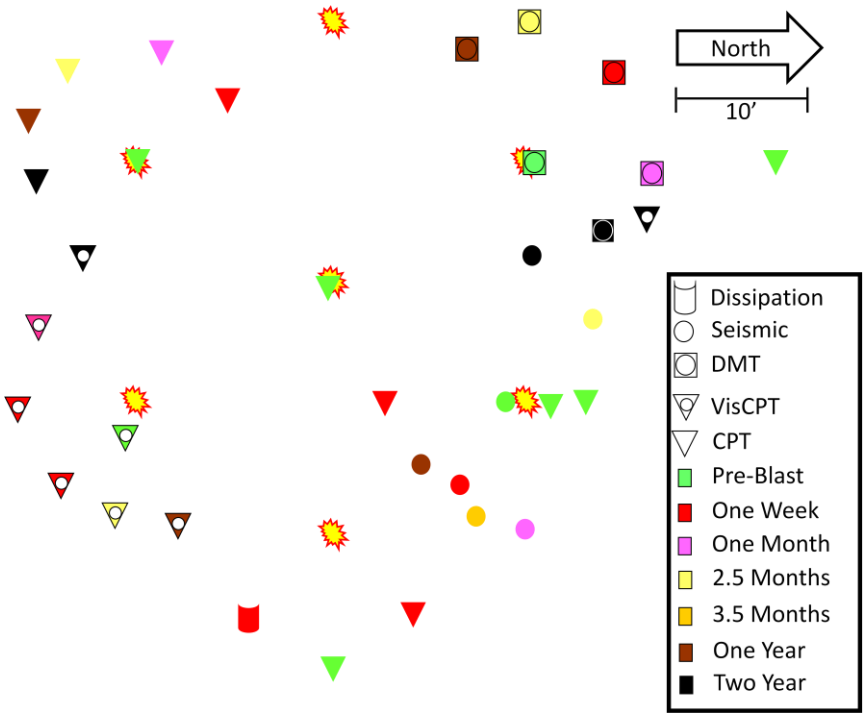

Figure 4-28. Location of *in situ* tests conducted before the blast and within 10’ of the nearest blast point.

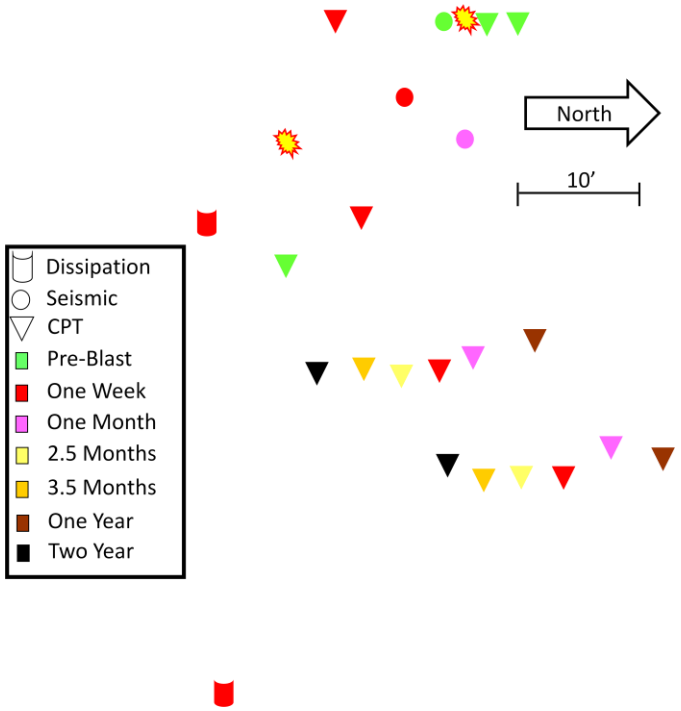

Figure 4-29. Location of *in situ* tests conducted 25’ and 40’ from the nearest blast point.

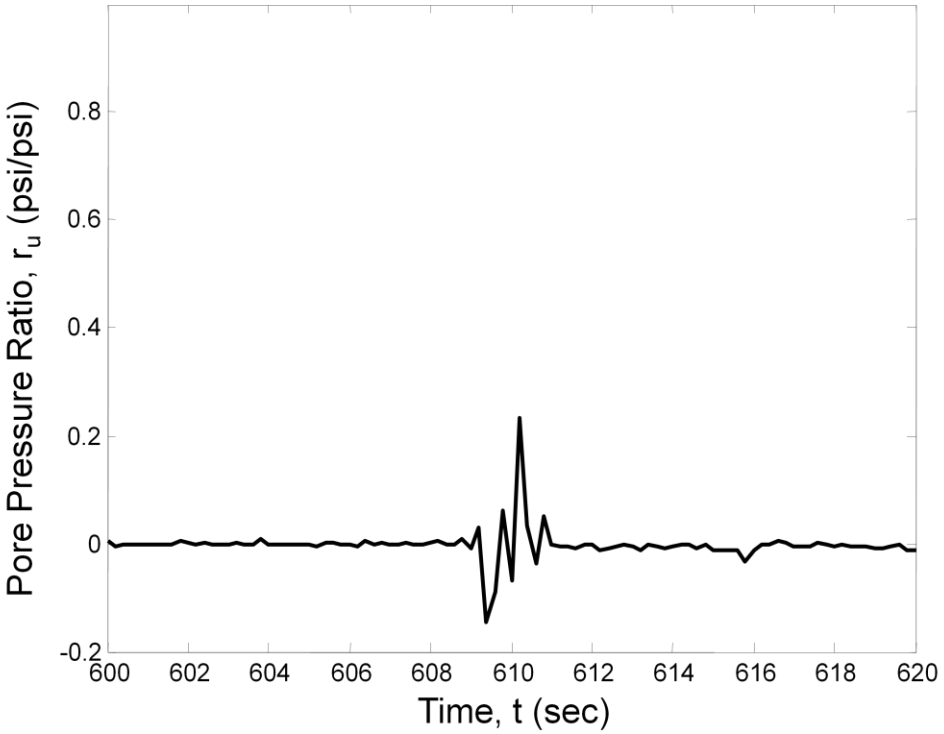

Figure 4-30. Pore pressure response from the transducer located 10' from the NE blast point in the loose sand layer.

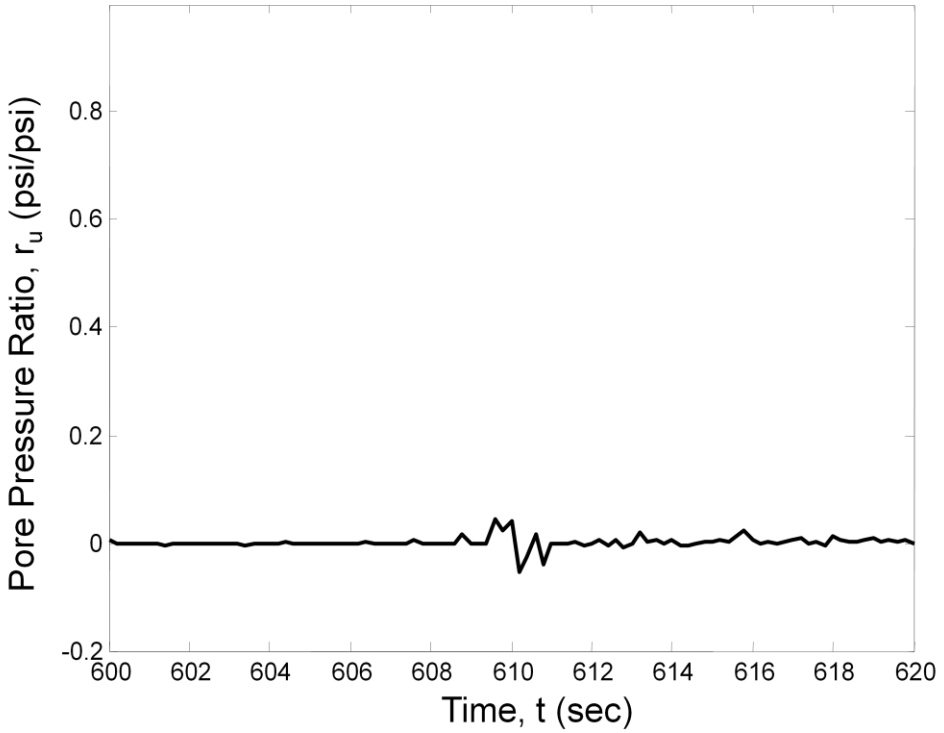

Figure 4-31. Pore pressure response from transducer located 28' from the NE blast point in the loose sand layer.

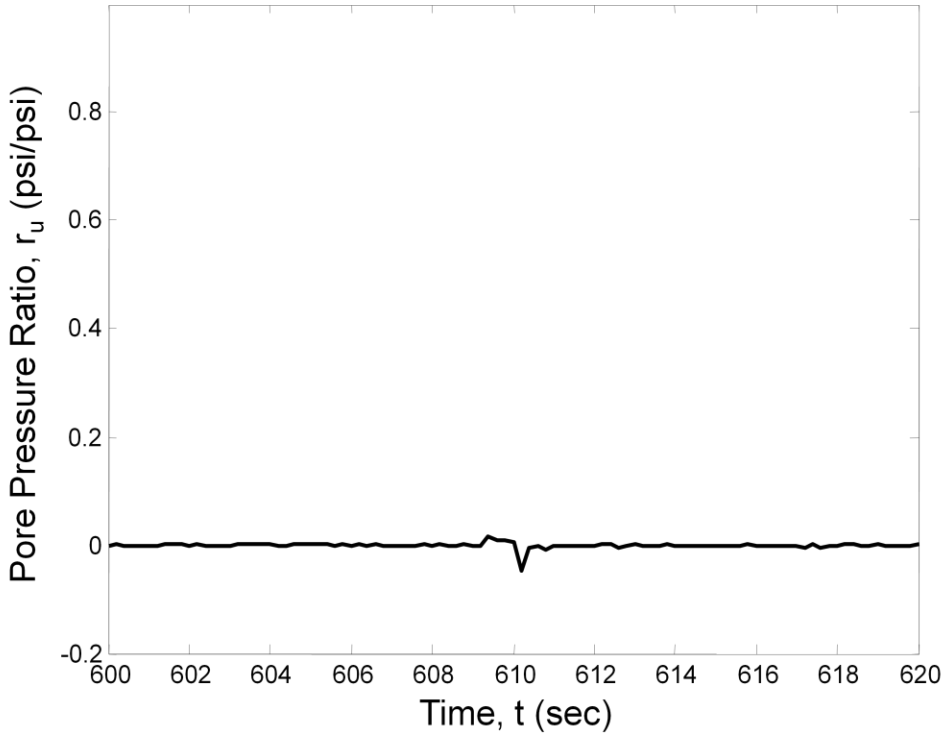

Figure 4-32. Pore pressure response from the transducer located 56' from the NE blast point in the loose sand layer.

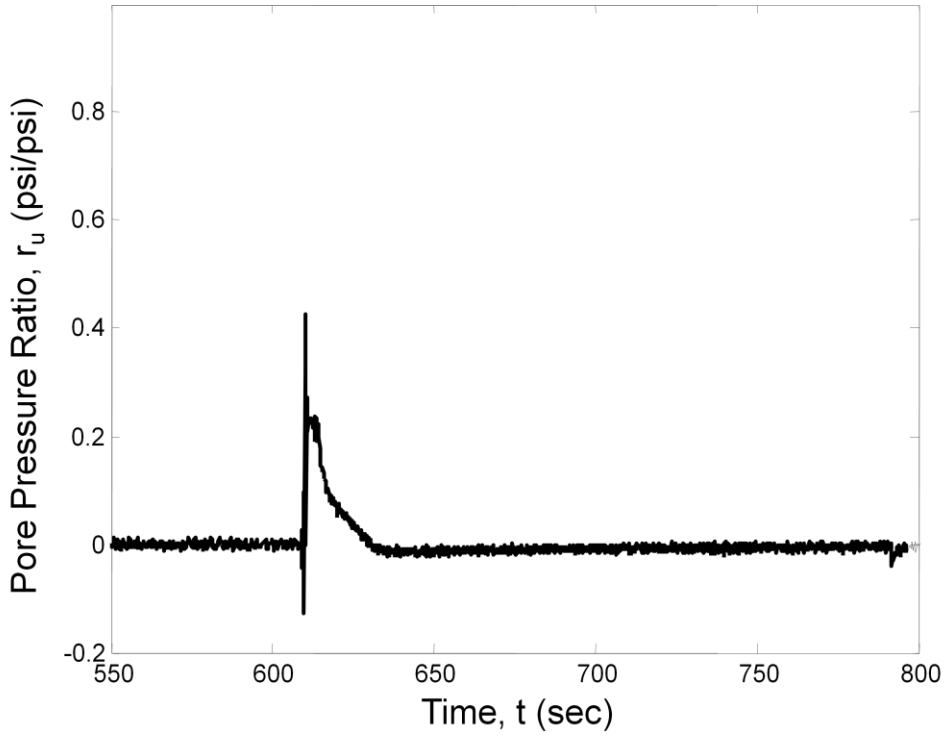

Figure 4-33. Pore pressure response from transducer located 17' from the SW blast point in the loose gravelly sand layer.

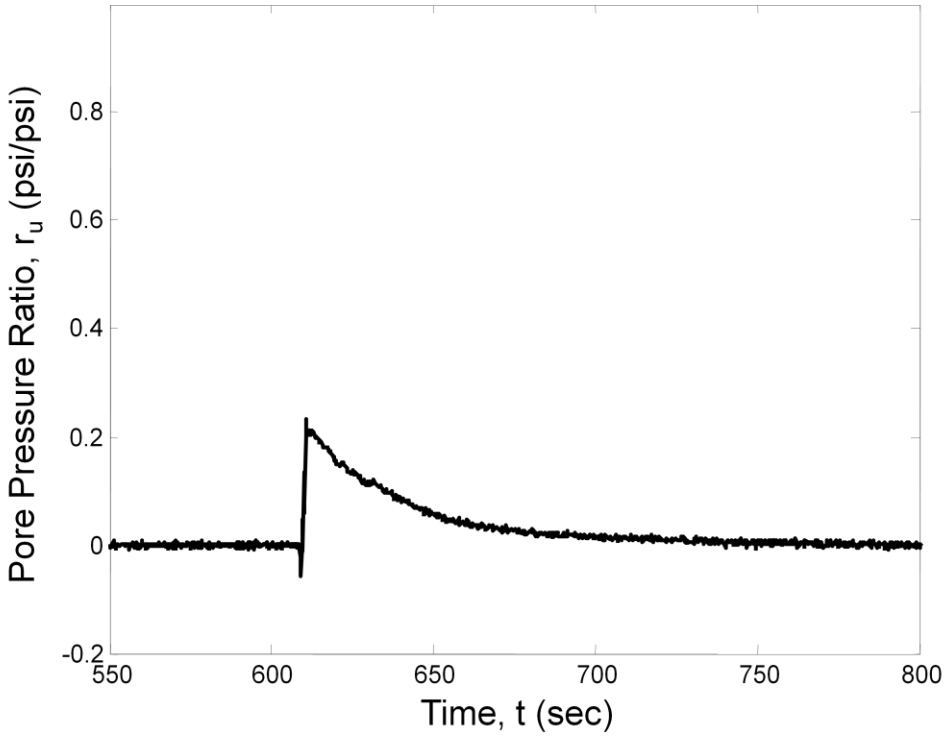

Figure 4-34. Pore pressure response from the transducer located 44' from the NE blast point in the loose gravelly sand layer.

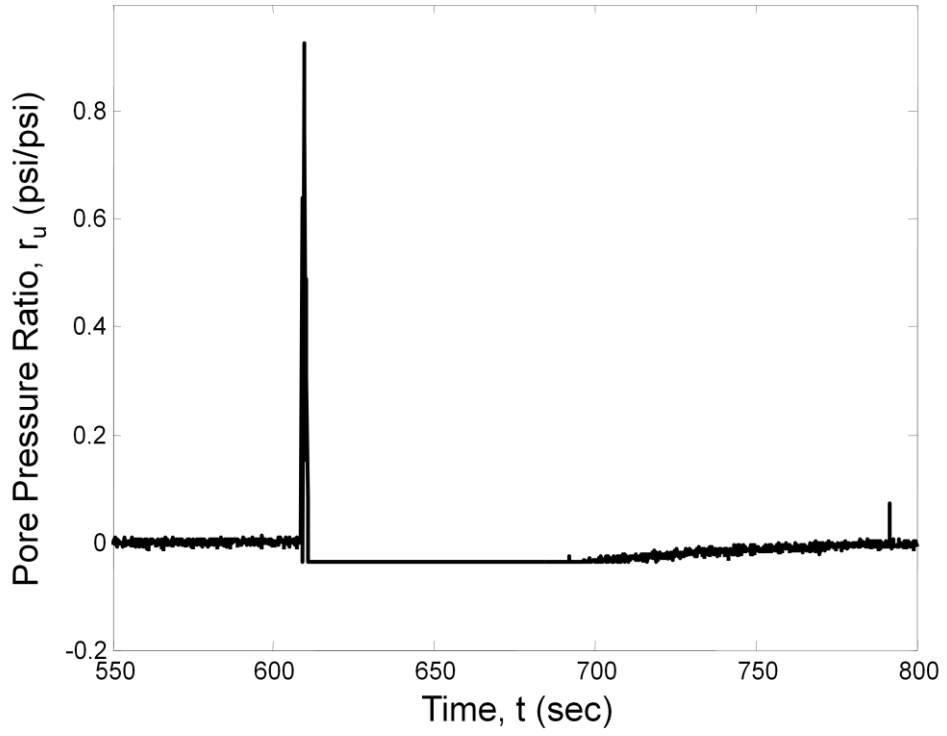

Figure 4-35. Pore pressure response from transducer located 83.5' from the SW blast point in the loose gravelly sand layer.

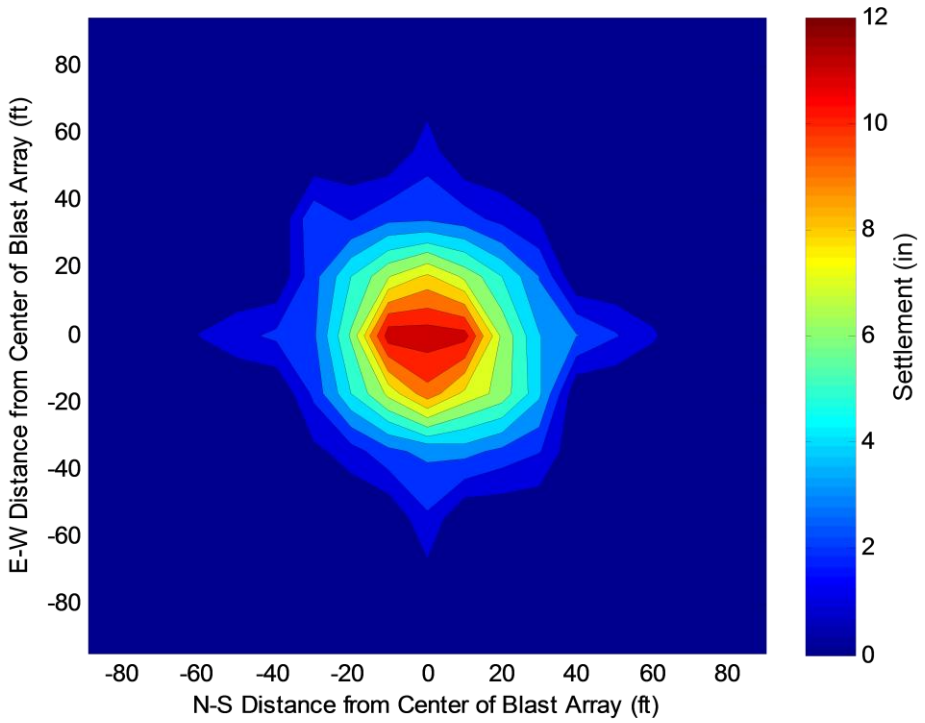

Figure 4-36. Settlement following the blast.

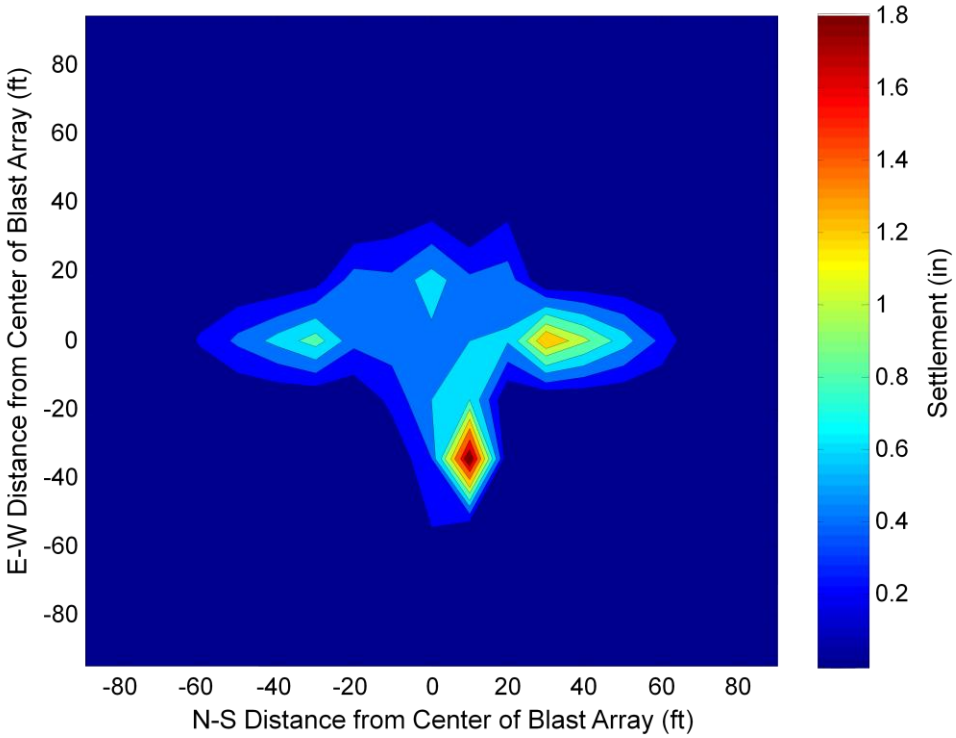

Figure 4-37. Settlement occurring between one week and one month following the blast.

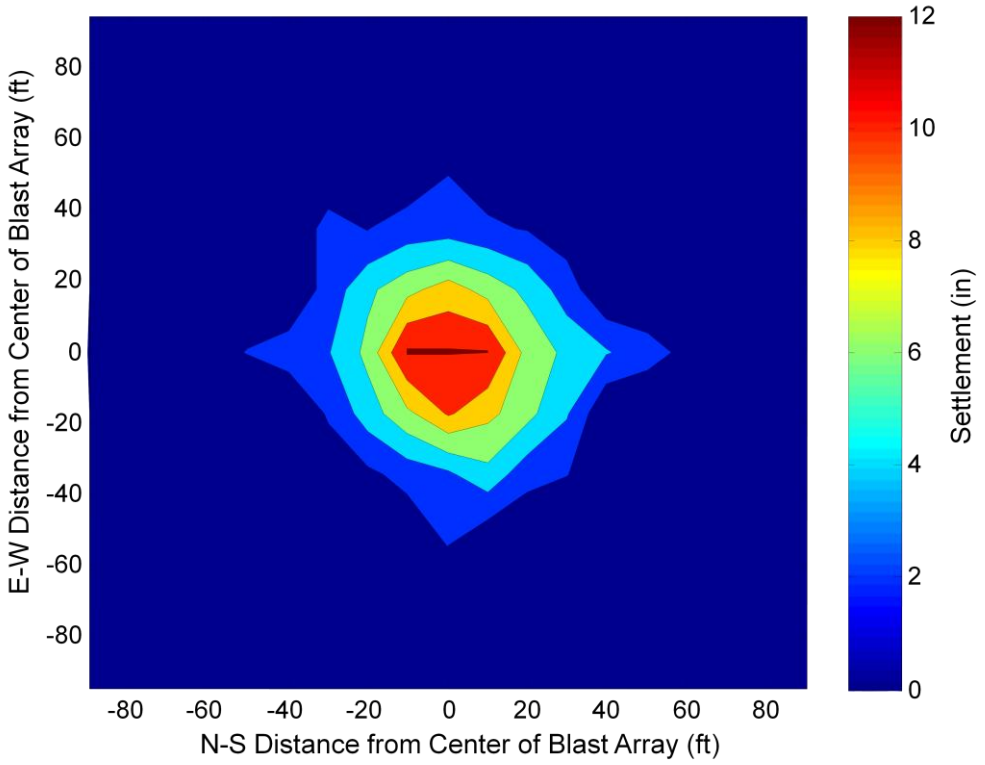

Figure 4-38. Total settlement following the blast.

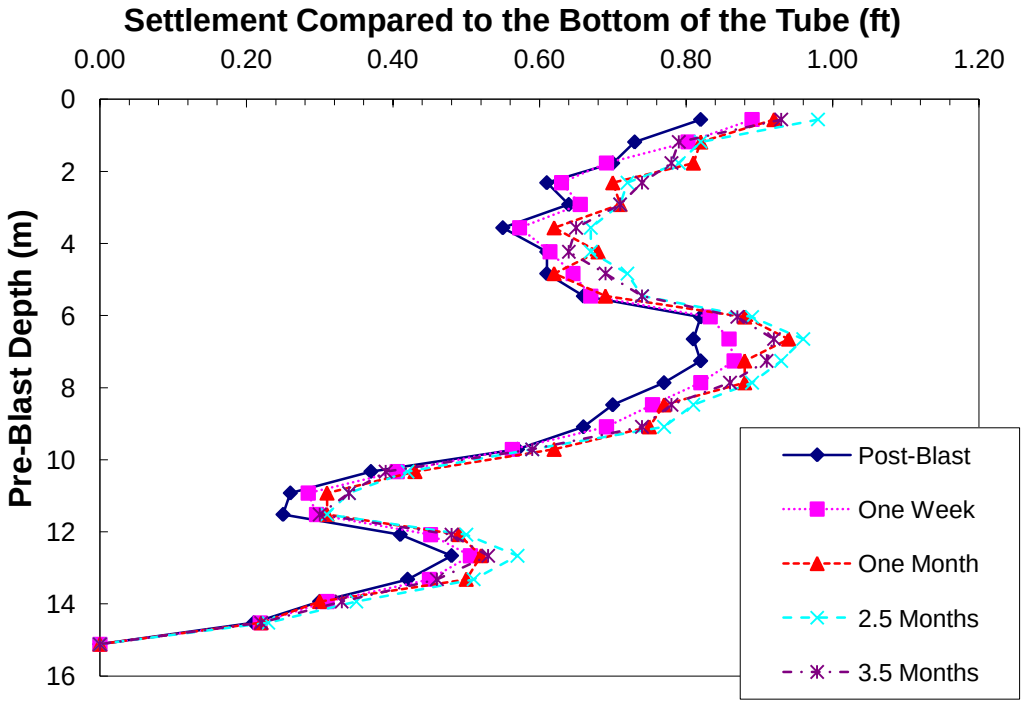

Figure 4-39. Settlement with depth recorded in the Sondex settlement tubes.

Figure 4-40. Surface cracks observed following explosive densification.

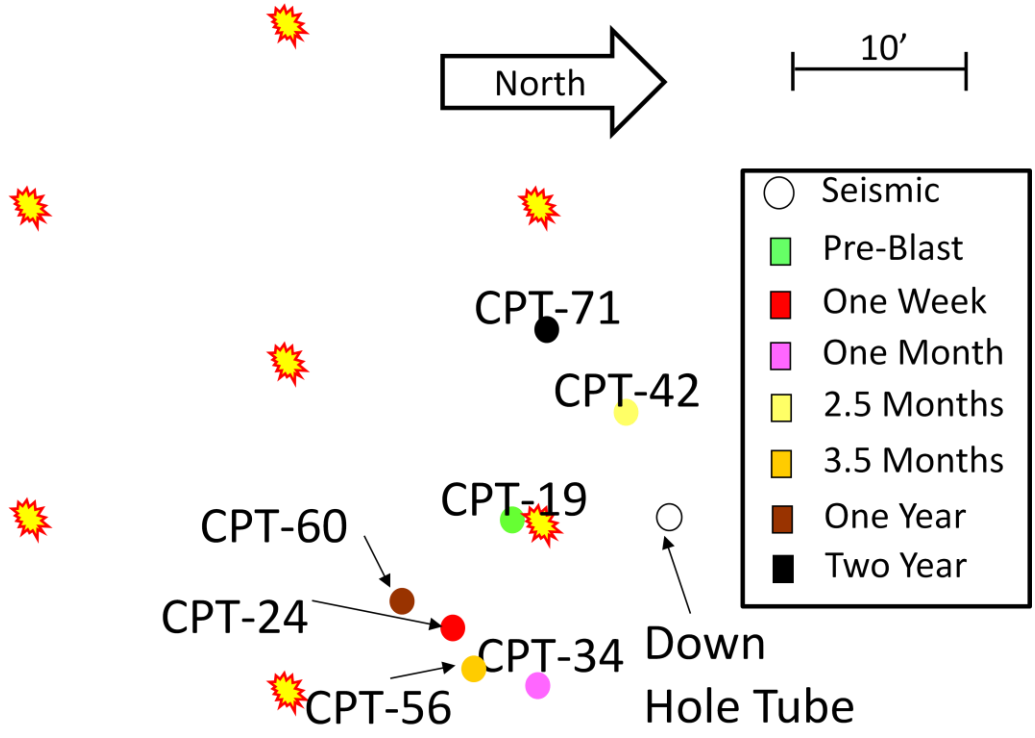

Figure 4-41. Location of SCPTs.

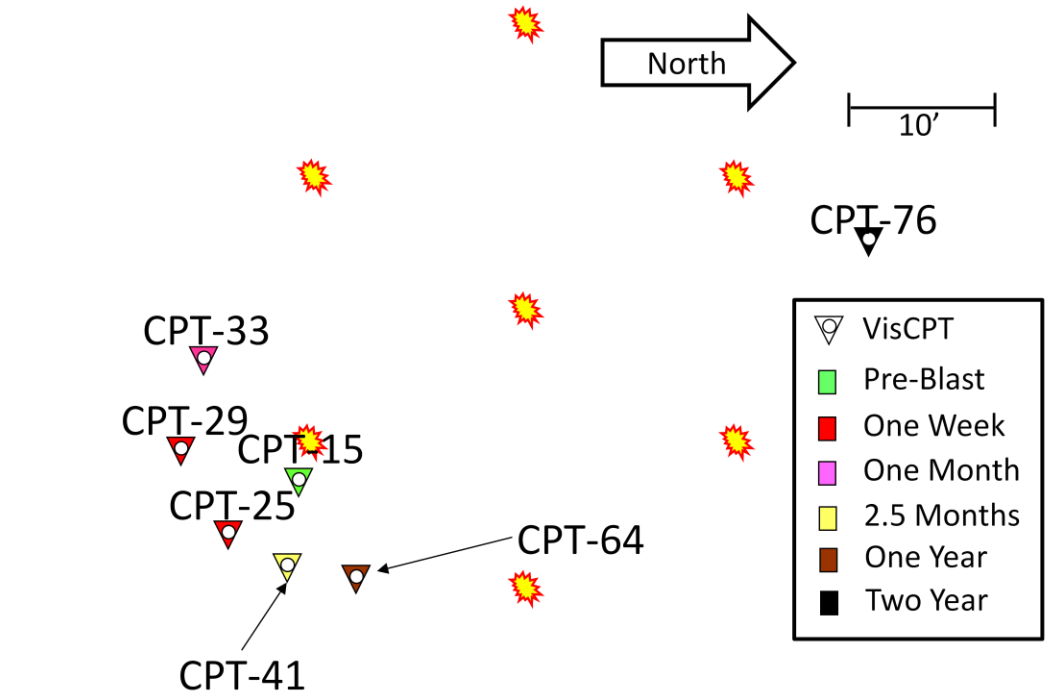

Figure 4-42. Location of VisCPTs.

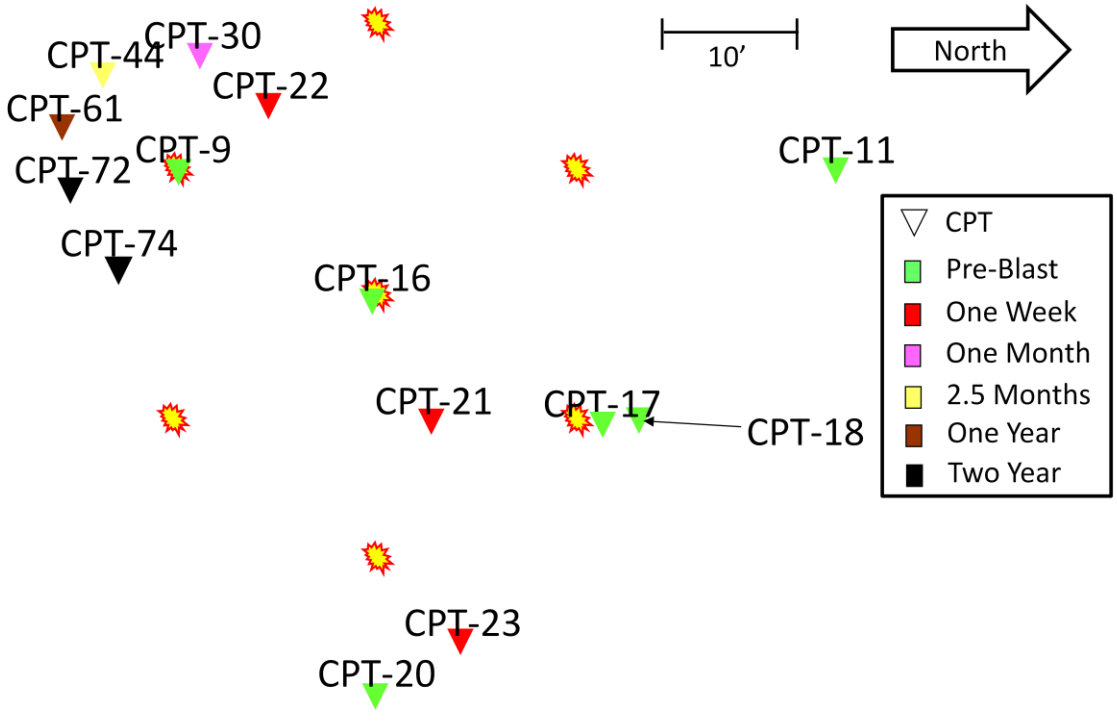

Figure 4-43. Location of CPTs.

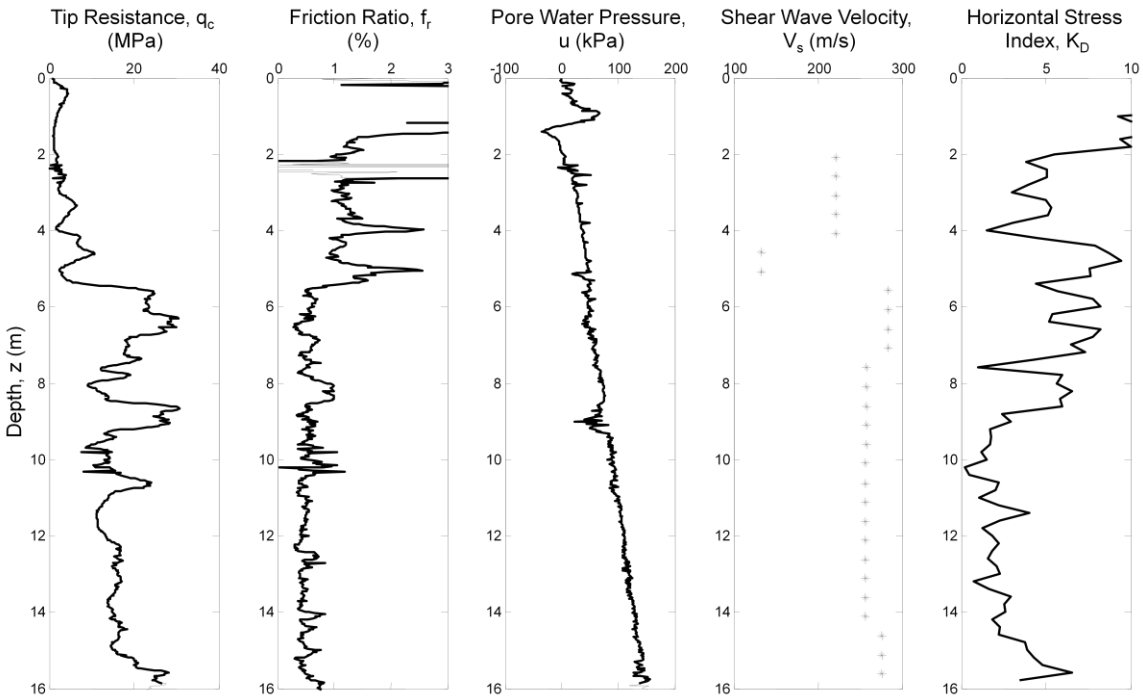

Figure 4-44. CPT and shear wave velocity results from SCPT-19 compared to DMT-1.

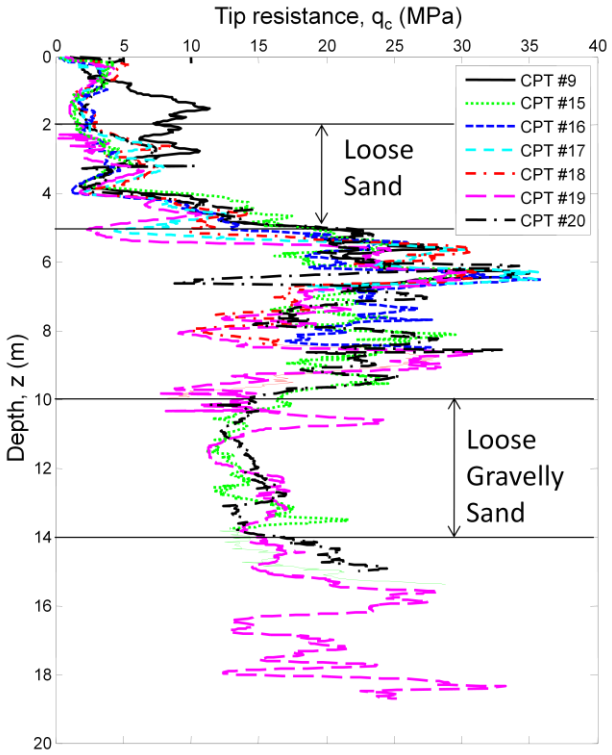

Figure 4-45. Results of pre-blast CPTs at 10’ from the nearest blast point.

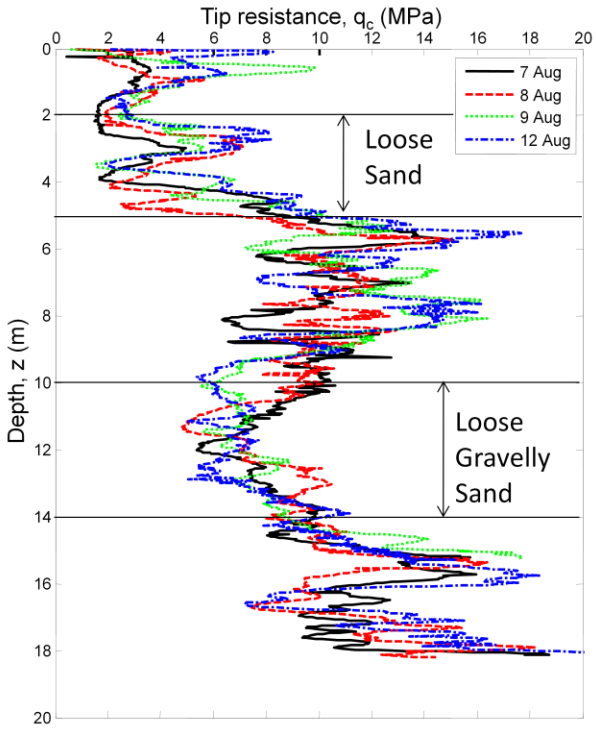

Figure 4-46. CPTs conducted within one week of the blast 10' from the nearest blast point plotted by date conducted.

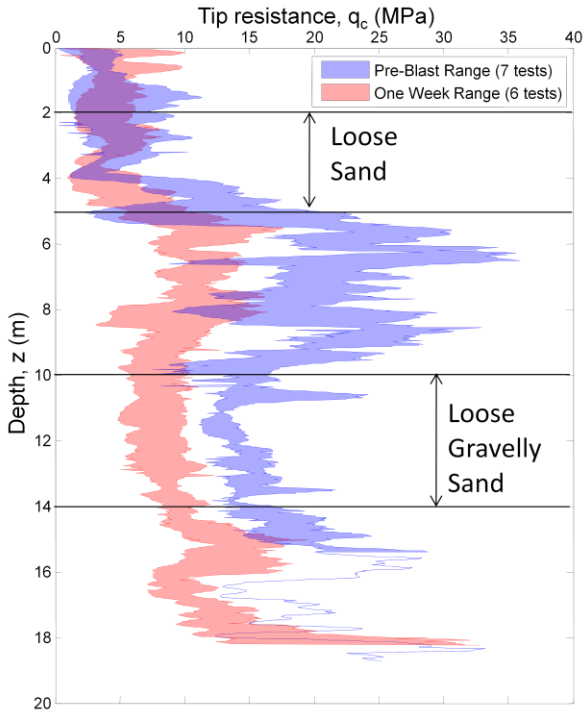

Figure 4-47. Pre-blast CPT range at 10' from the nearest blast point compared to one week CPT range at 10' from the nearest blast point.

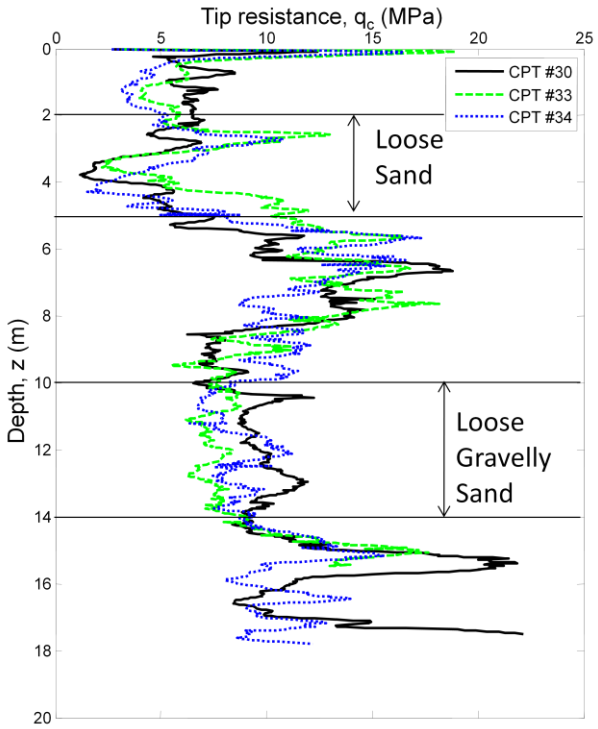

Figure 4-48. CPTs conducted one month following explosive densification 10' from the nearest blast point.

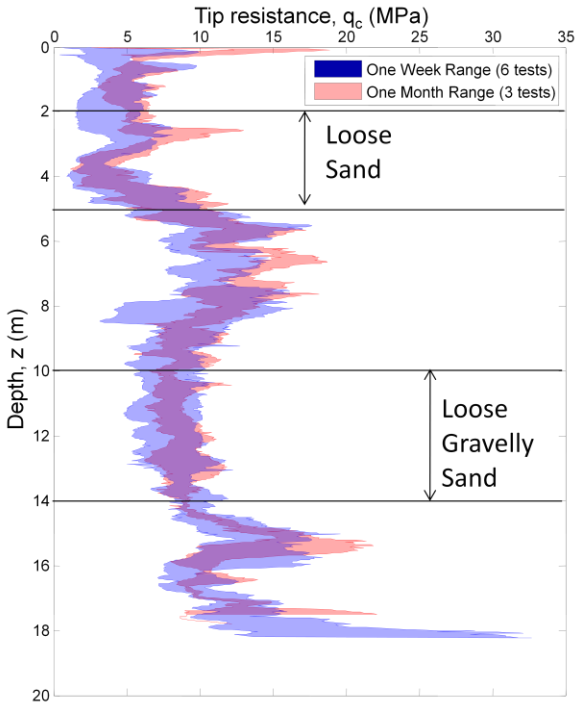

Figure 4-49. One week CPT range at 10' from the nearest blast point compared to one month CPT range at 10' from the nearest blast point.

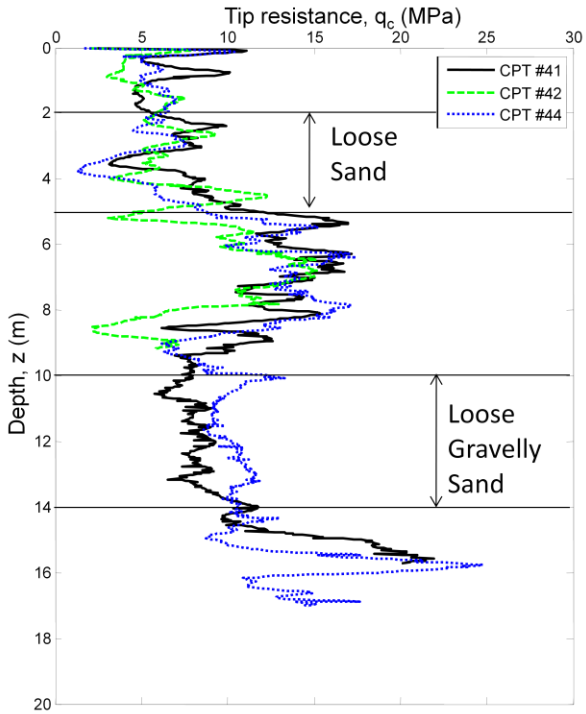

Figure 4-50. CPTs conducted two and a half months following explosive densification 10' from the nearest blast point.

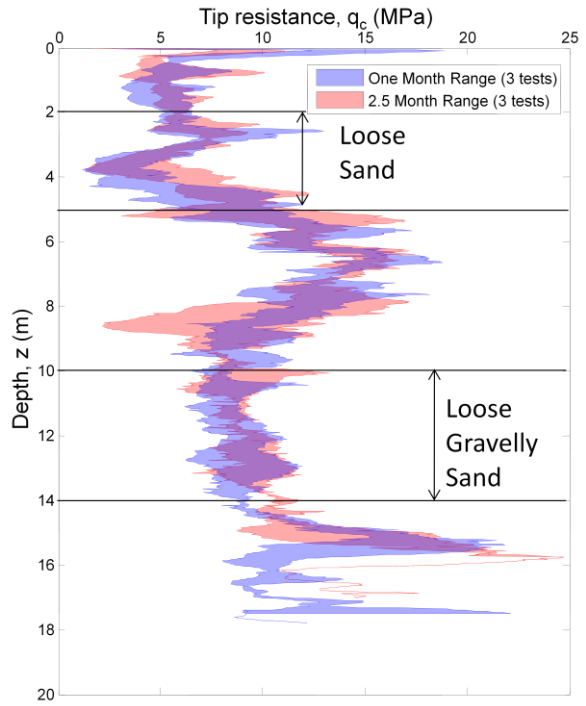

Figure 4-51. One month CPT range at 10' from the nearest blast point compared to two and a half month CPT range at 10' from the nearest blast point.

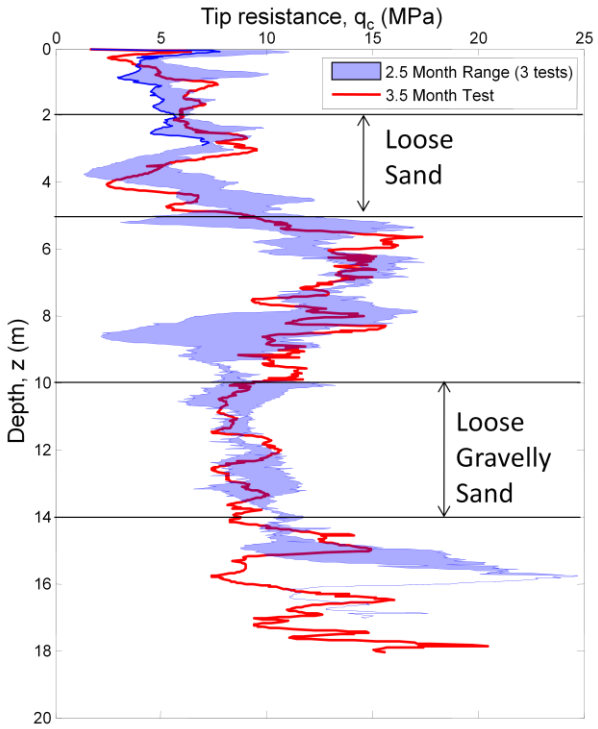

Figure 4-52. Two and a half month CPT range at 10’ from the nearest blast point compared to the three and a half month CPT 10’ from the nearest blast point.

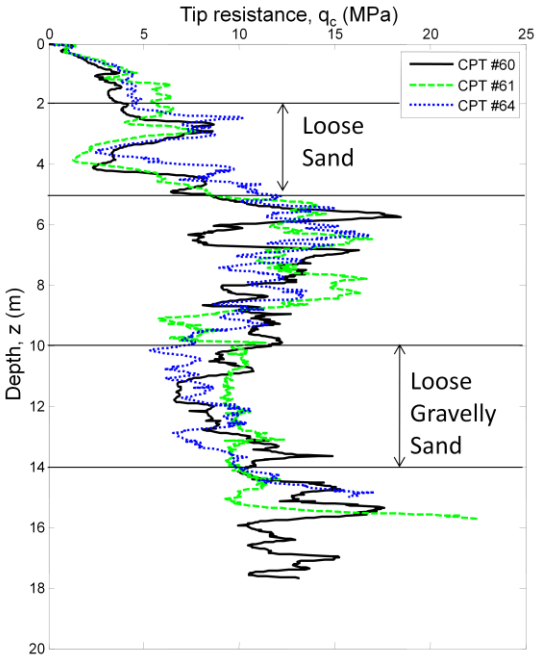

Figure 4-53. CPTs conducted one year following explosive densification 10’ from the nearest blast point.

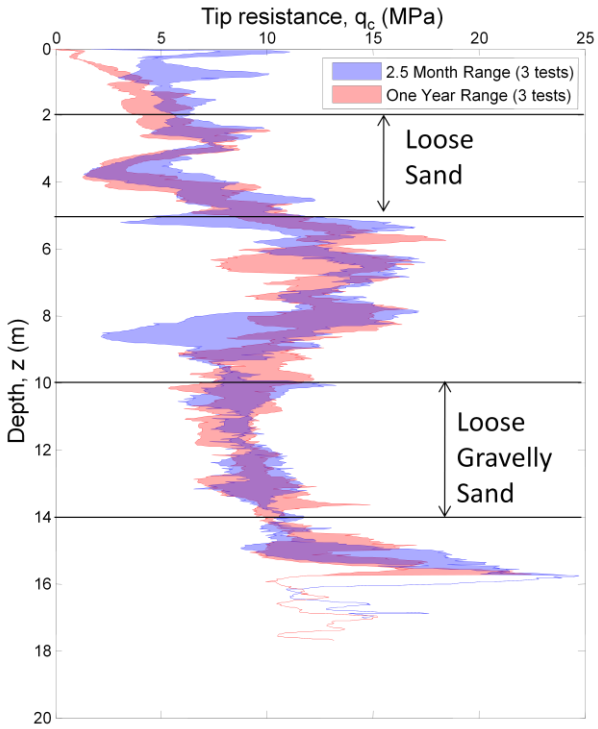

Figure 4-54. Two and a half month CPT range at 10' from the nearest blast point compared to one year CPT range at 10' from the nearest blast point.

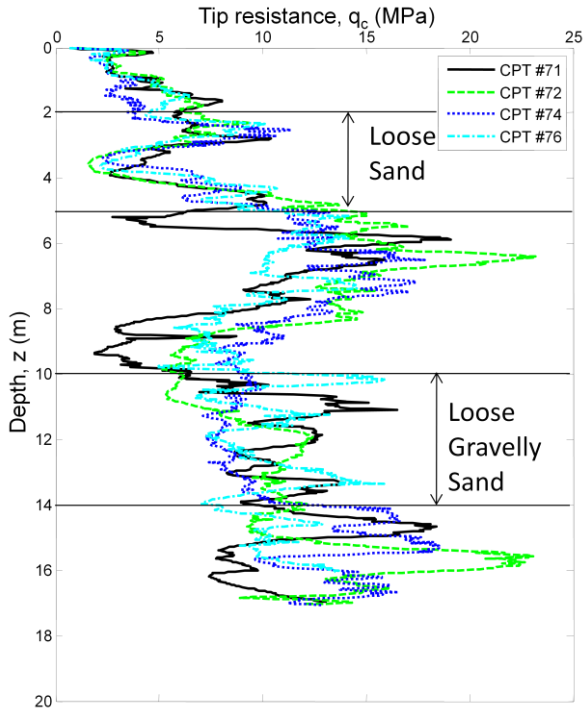

Figure 4-55. CPTs conducted two years following explosive densification 10' from the nearest blast point.

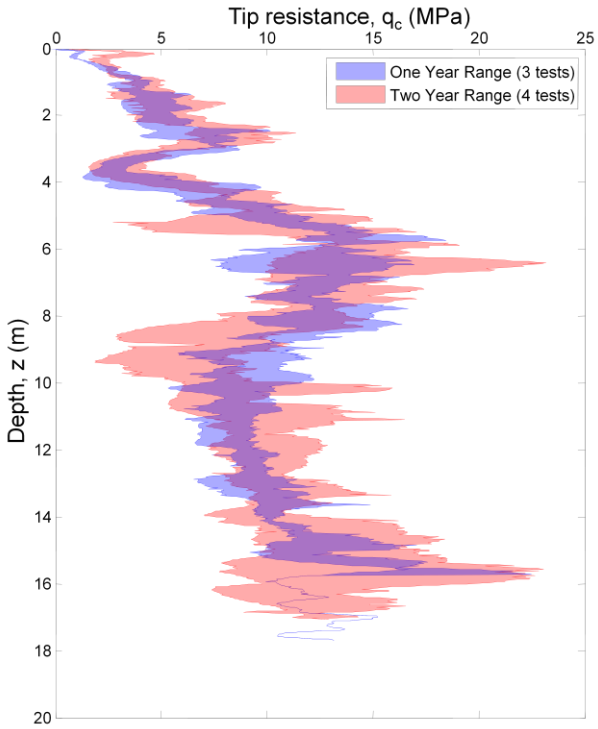

Figure 4-56. One year CPT range compared at 10' from the nearest blast point to two year CPT range at 10' from the nearest blast point.

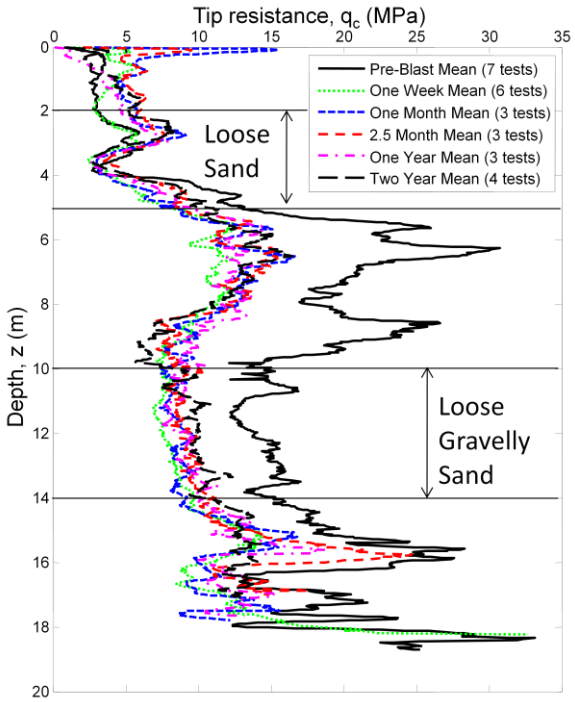

Figure 4-57. Mean CPT results from soundings conducted 10' from the nearest blast point for each testing period.

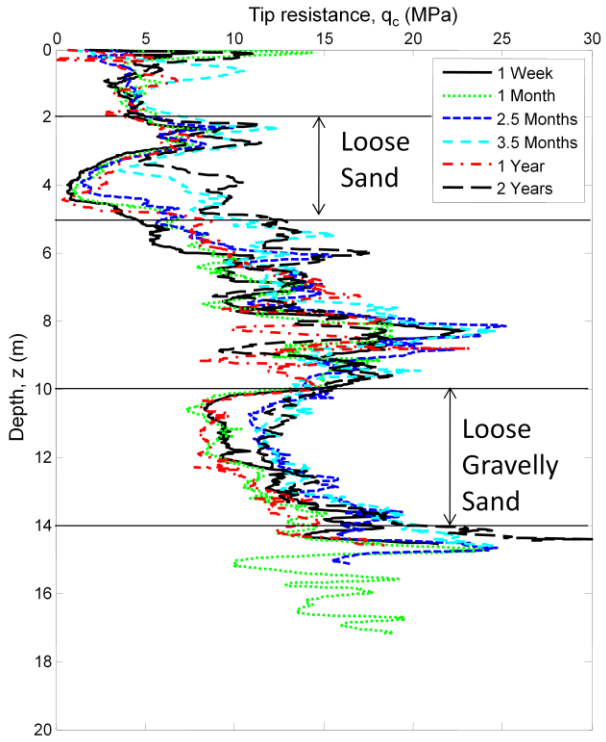

Figure 4-58. Results of CPTs conducted 25' from closest blast point with time.

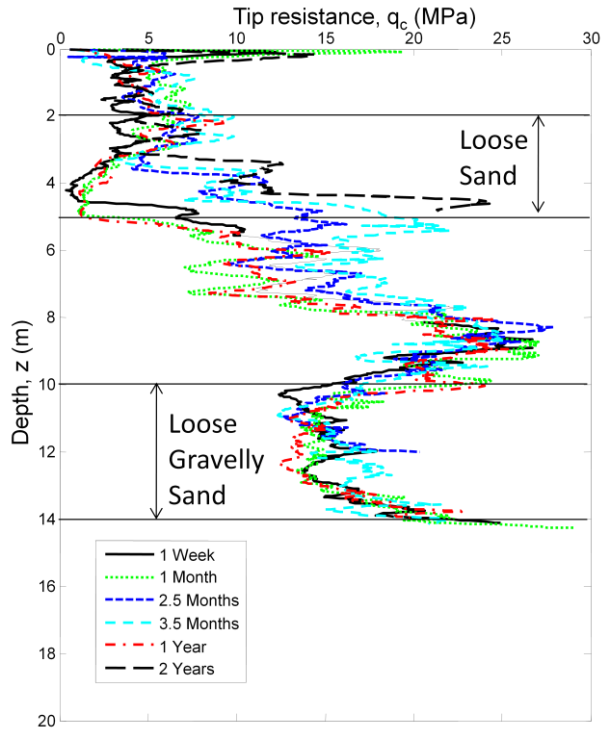

Figure 4-59. Results of CPTs conducted 40' from closest blast point with time.

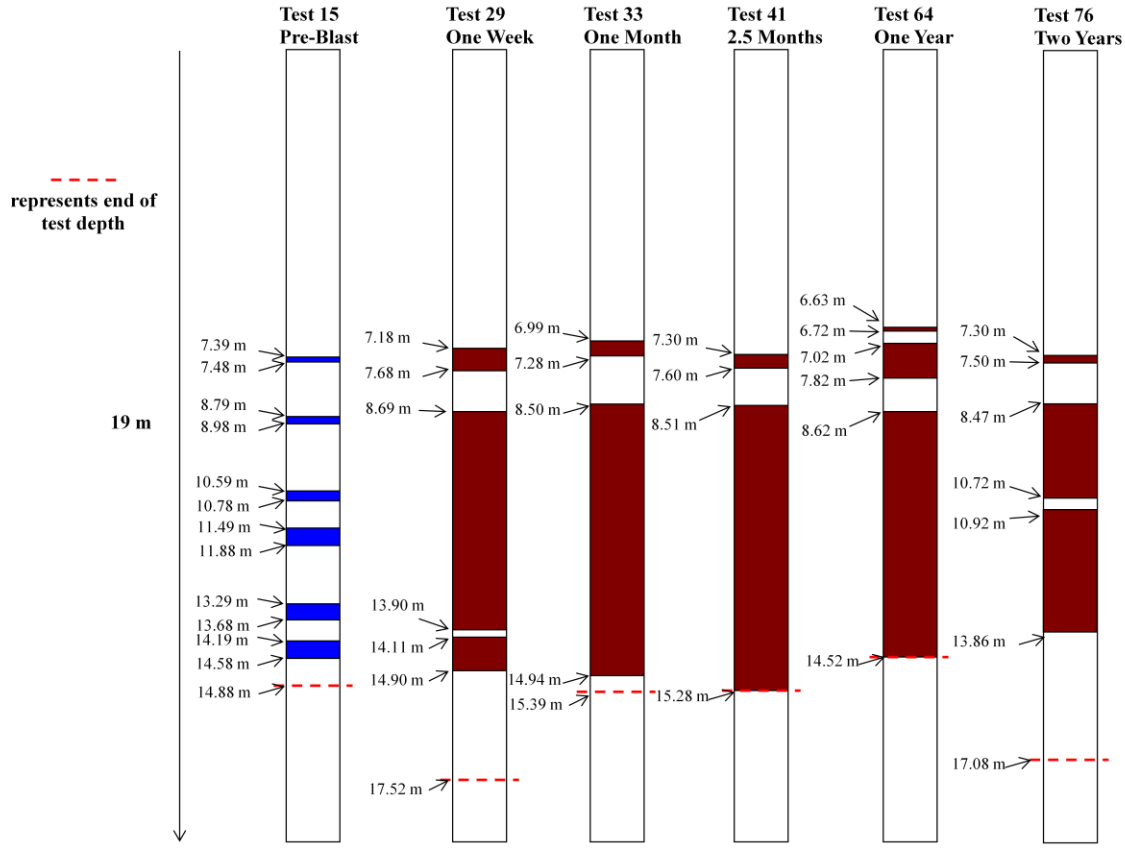

Figure 4-60. Results of VisCPT testing showing the areas with visual evidence of liquefaction (adapted from Jung, 2010).

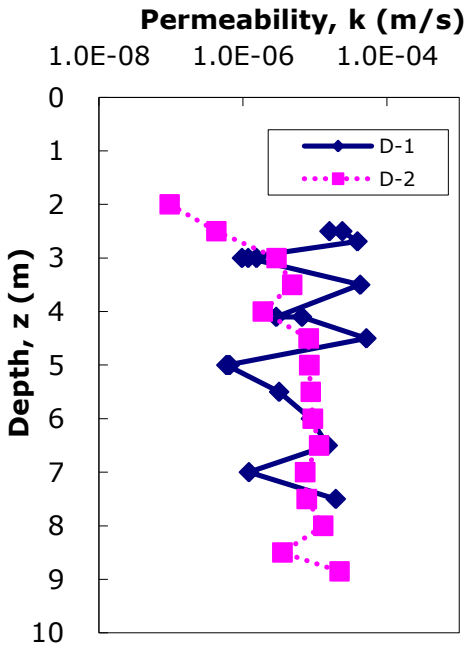

Figure 4-61. Permeability results from dissipation testing.

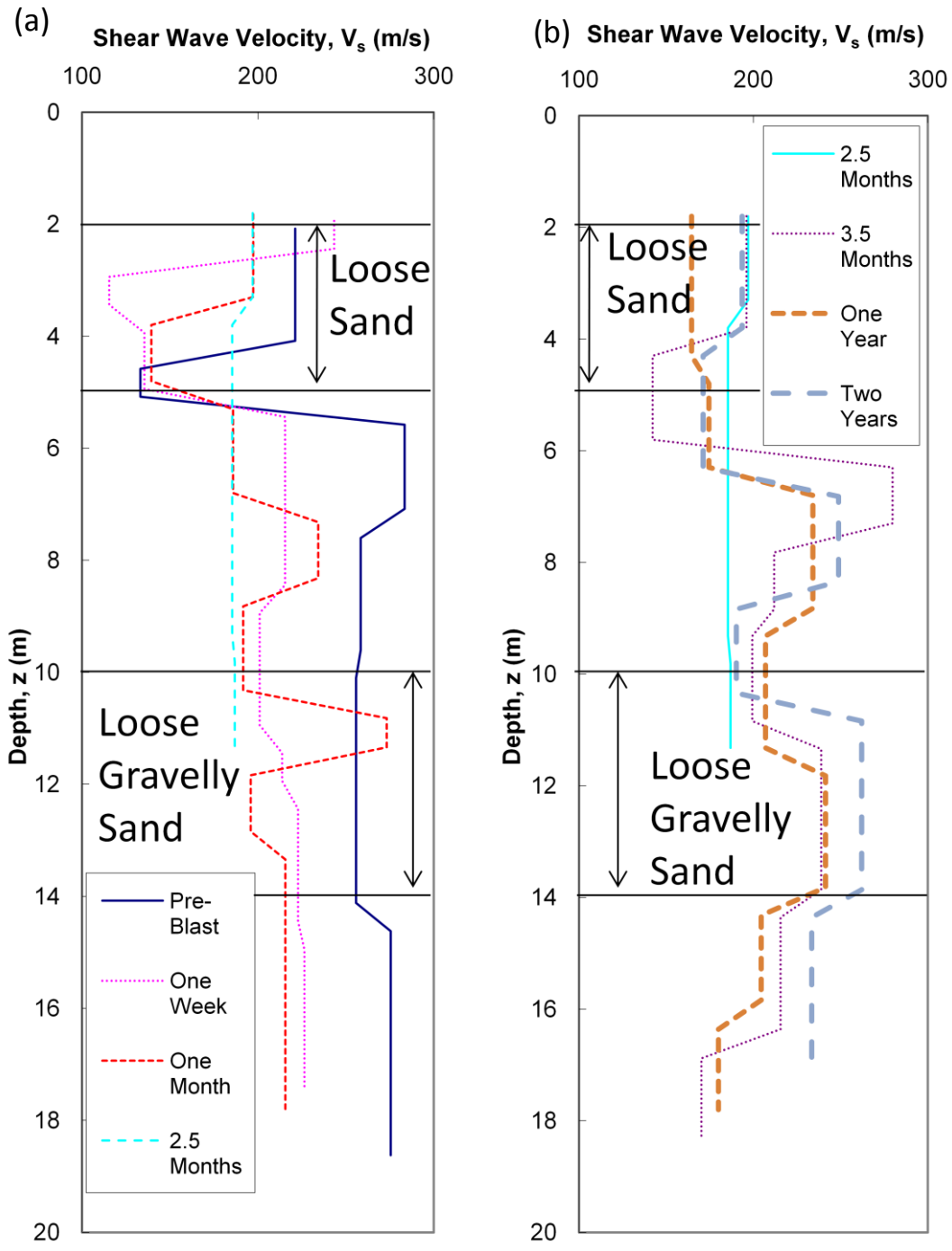

Figure 4-62. (a) Shear wave velocity 2.5 months following the blast and before. (b) Shear wave velocity 2.5 months following the blast and later.

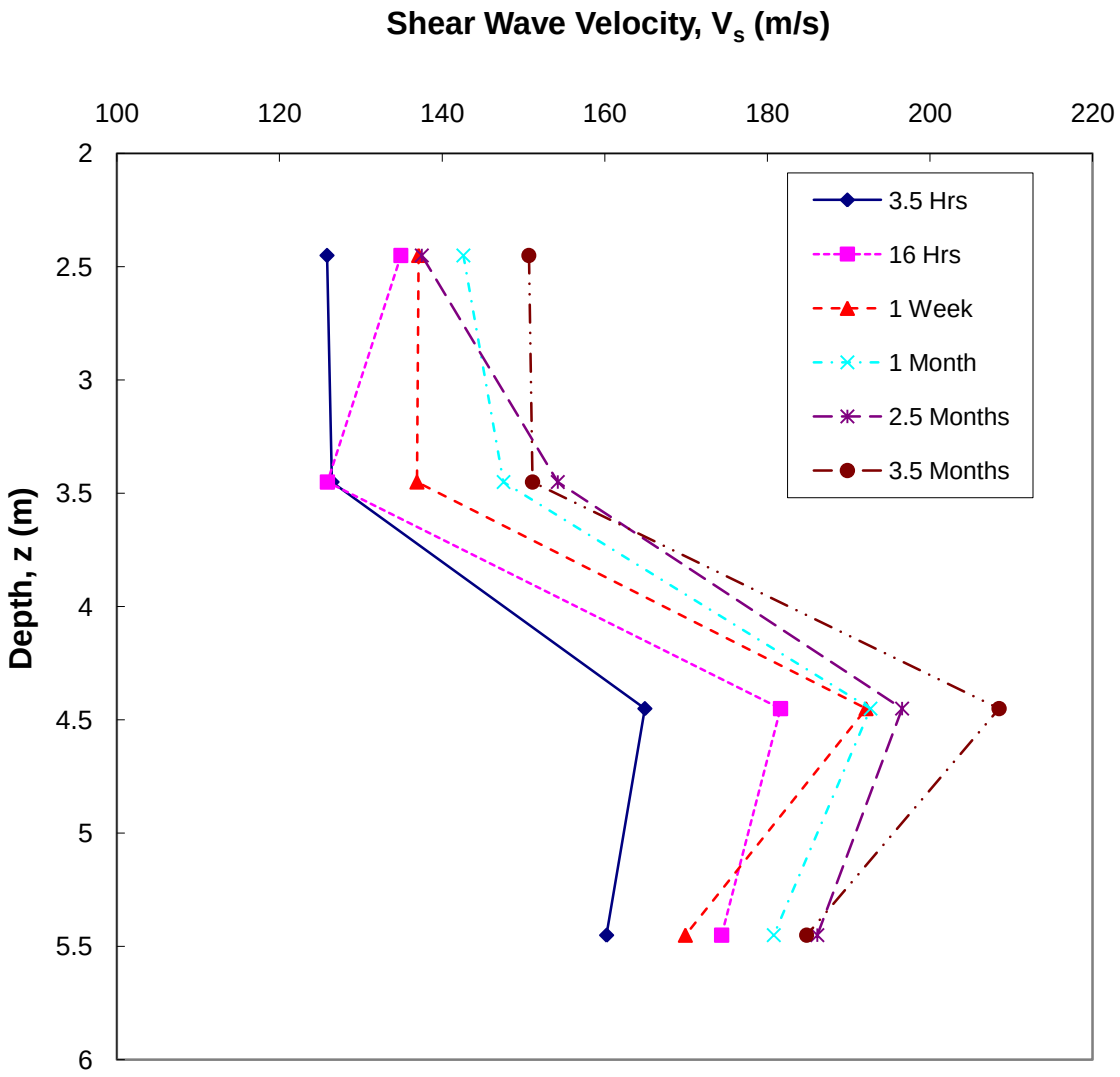

Figure 4-63. Down-hole shear wave velocity with time following the blast.

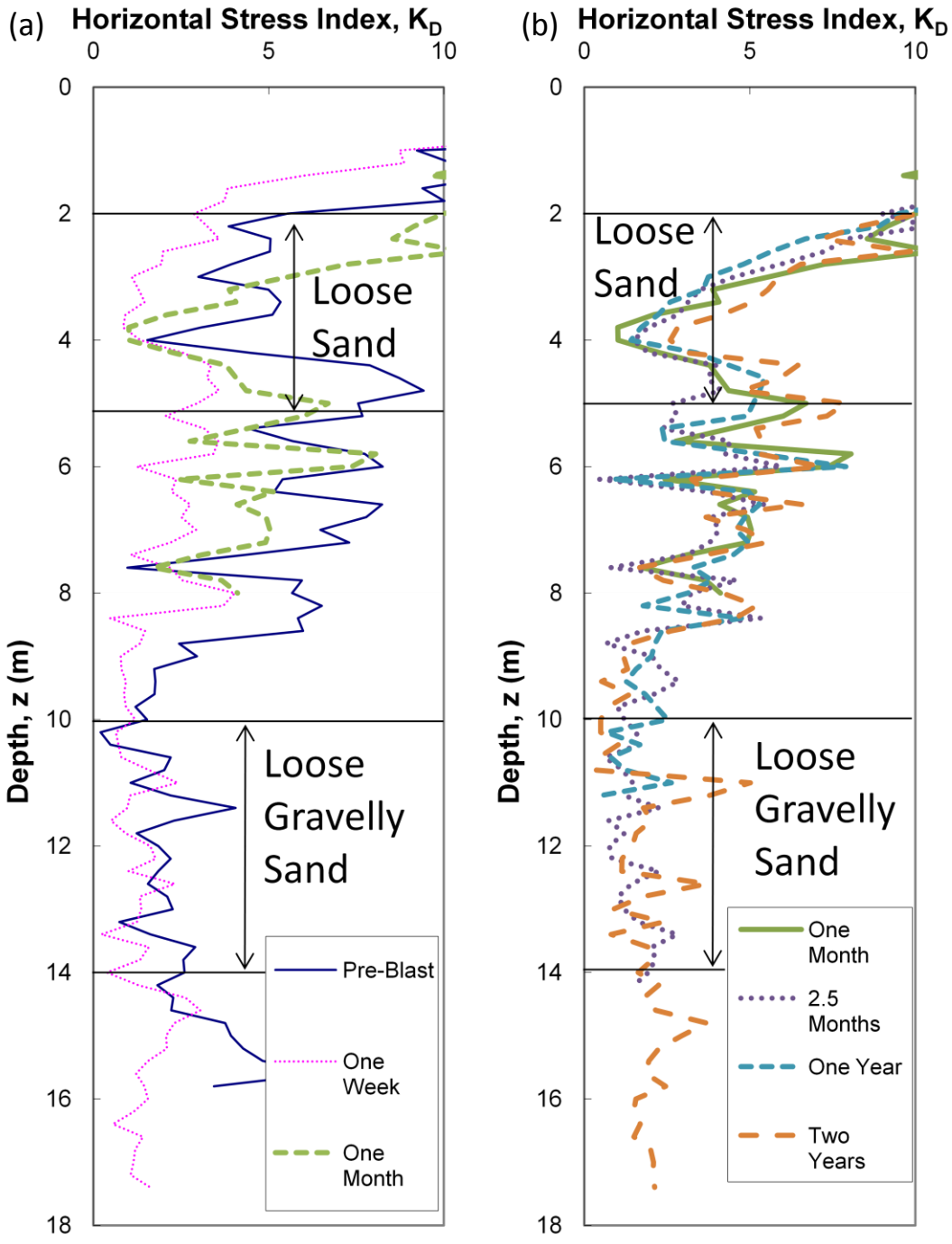

Figure 4-64. (a) DMT horizontal stress index one month following the blast and before. (b) DMT horizontal stress index one month following the blast and later

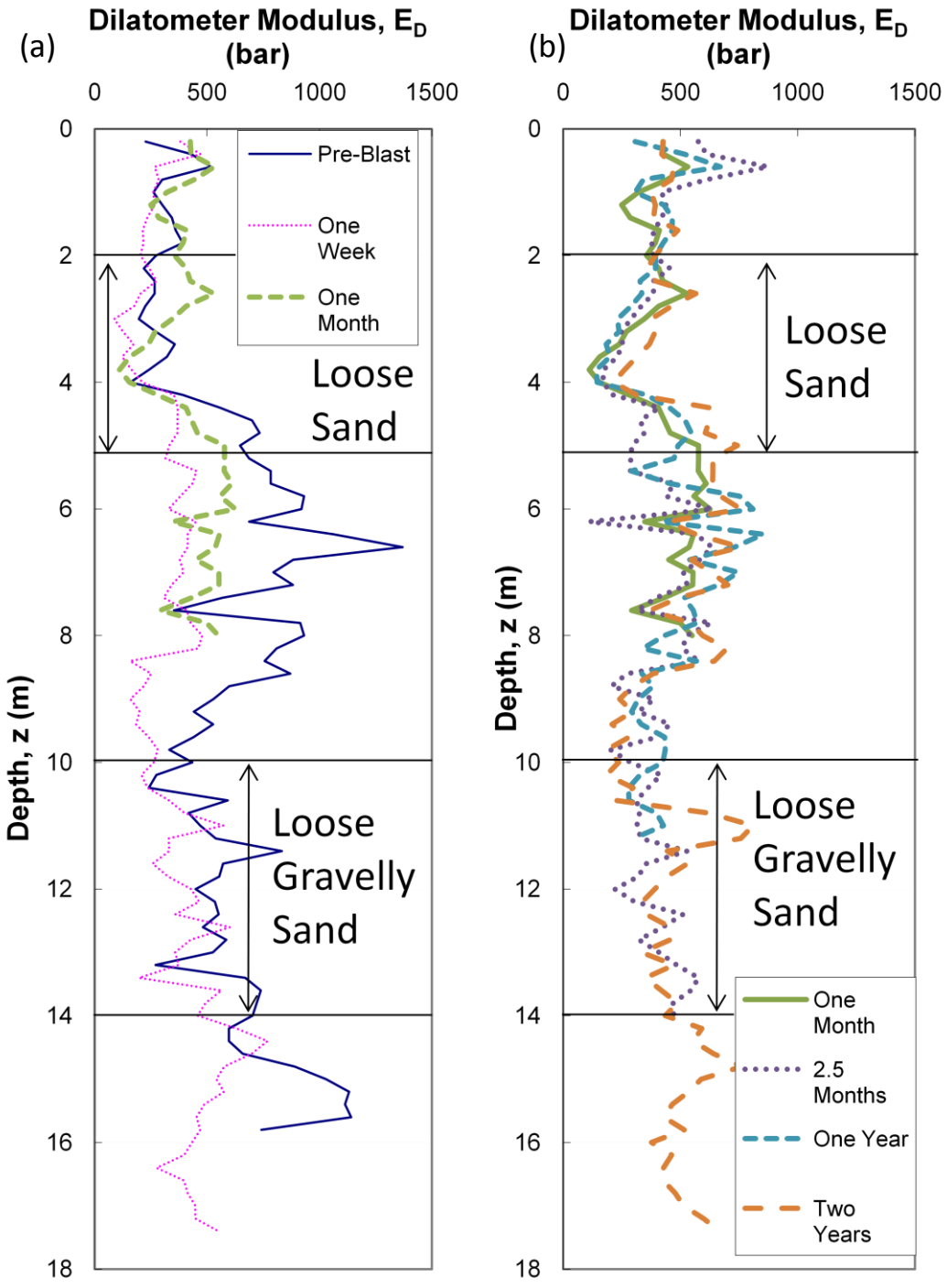

Figure 4-65. (a) Dilatometer modulus one month following the blast and before. (b) Dilatometer modulus one month following the blast and later.

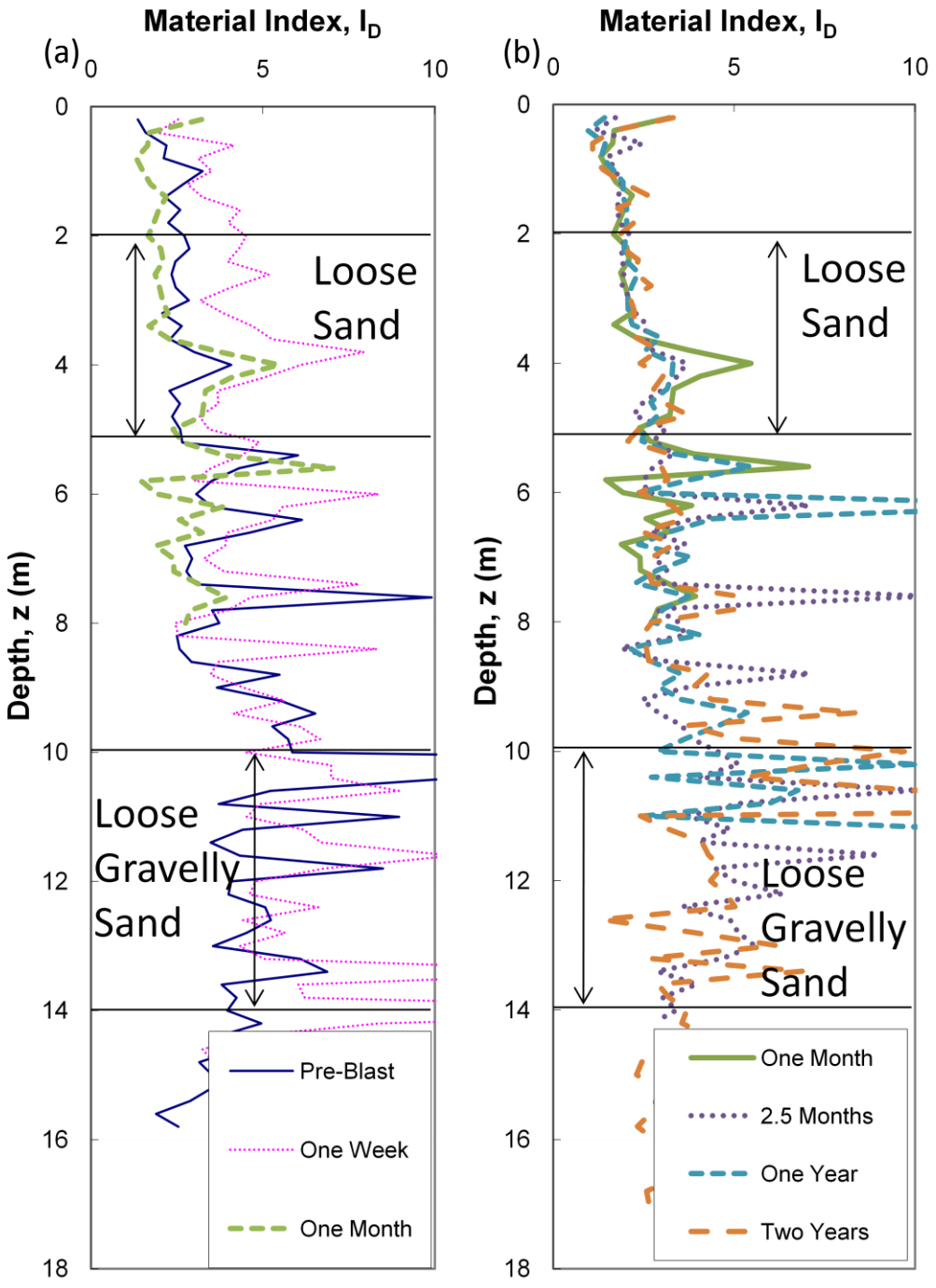

Figure 4-66. (a) Dilatometer material index one month following the blast and before. (b) Dilatometer material index one month following the blast and later.

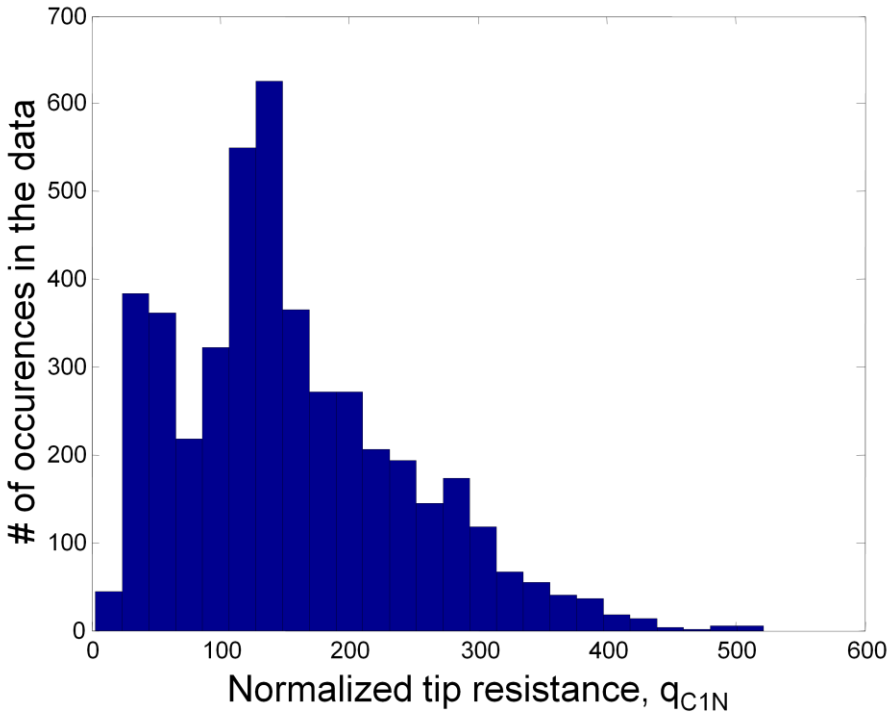

Figure 4-67. Histogram of CPT normalized tip resistance from every layer before explosive densification.

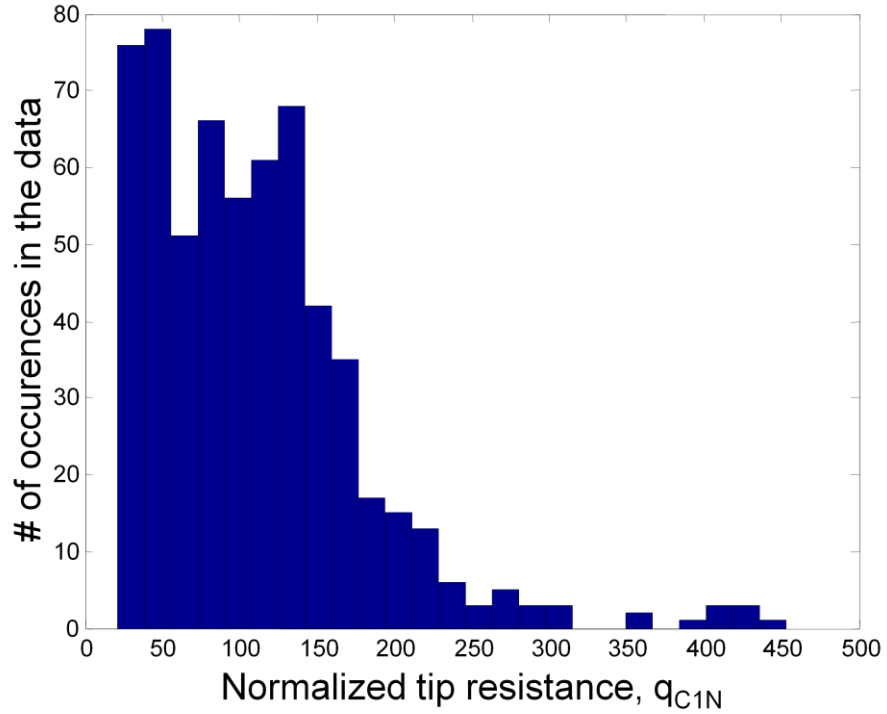

Figure 4-68. Histogram of CPT normalized tip resistance from the clay layer before explosive densification.

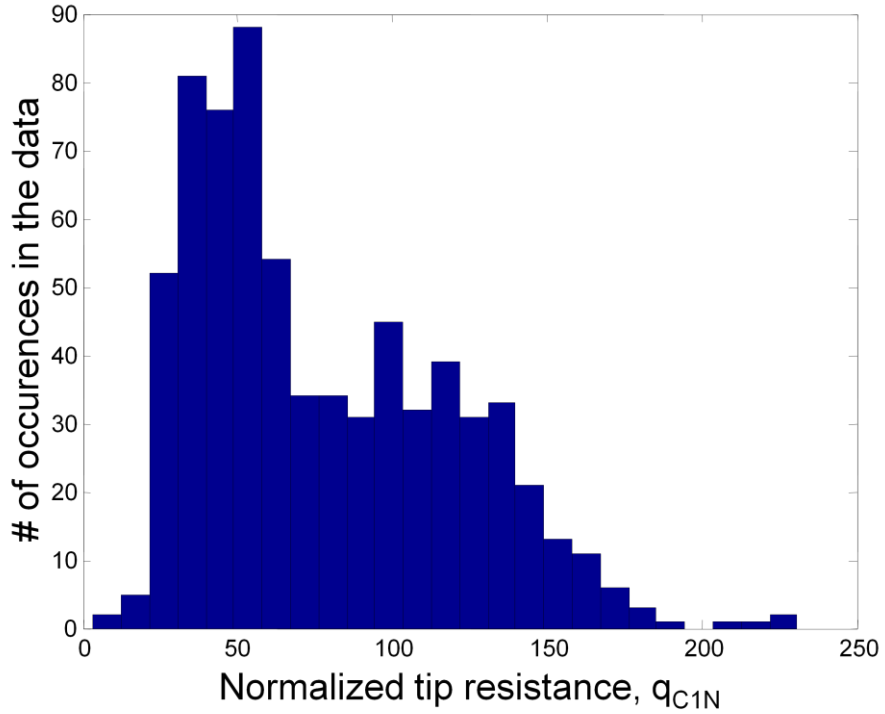

Figure 4-69. Histogram of CPT normalized tip resistance from the loose sand layer before explosive densification.

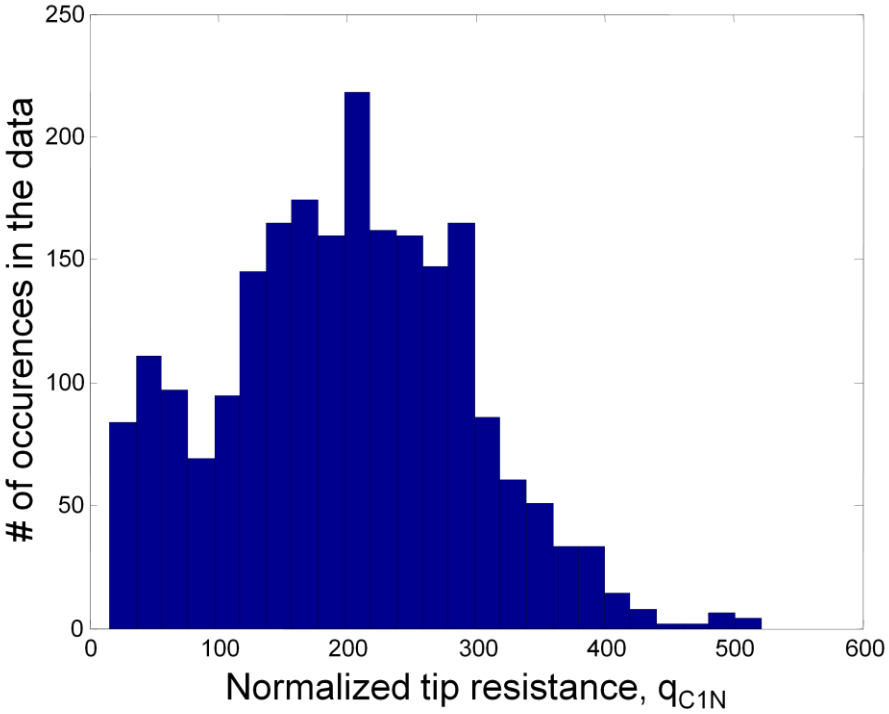

Figure 4-70. Histogram of CPT normalized tip resistance from the dense sand layer before explosive densification.

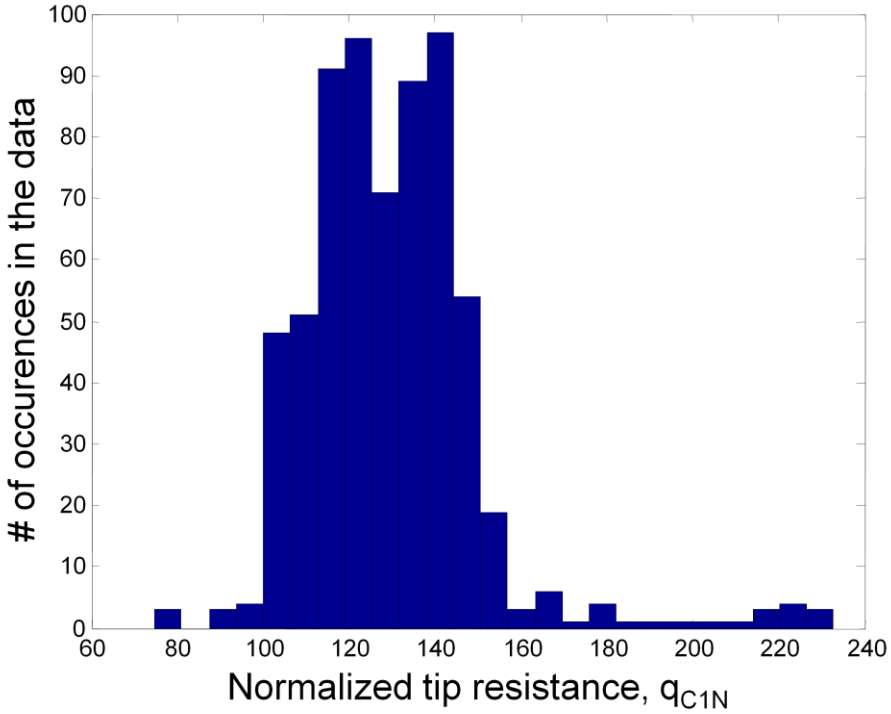

Figure 4-71. Histogram of CPT normalized tip resistance from the loose gravelly sand layer before explosive densification.

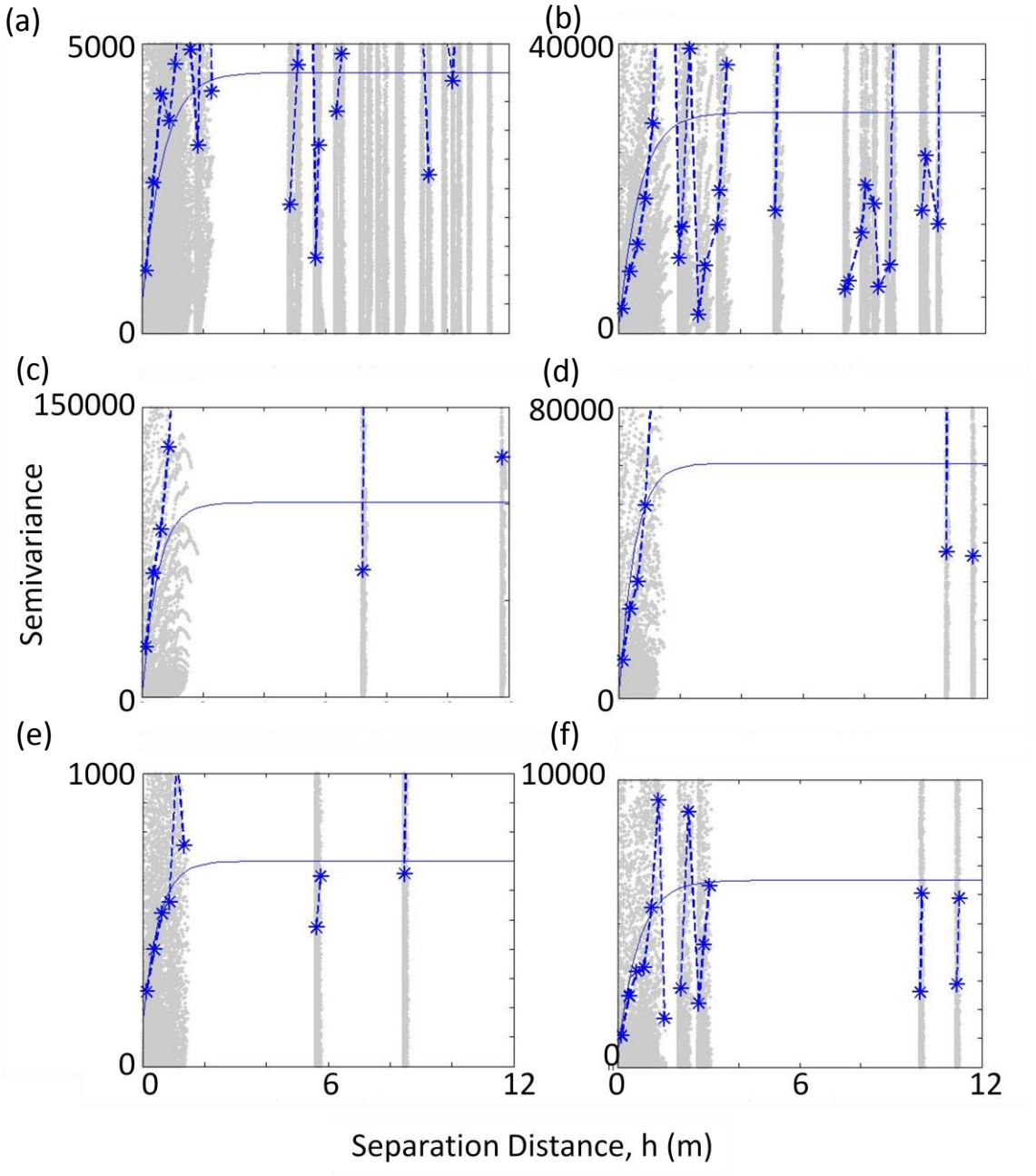

Figure 4-72. Raw, experimental, and theoretical variograms in the clay layer from (a) pre-blast testing, (b) one week testing, (c) one month testing, (d) two and a half month testing, (e) one year testing, and (f) two year testing.

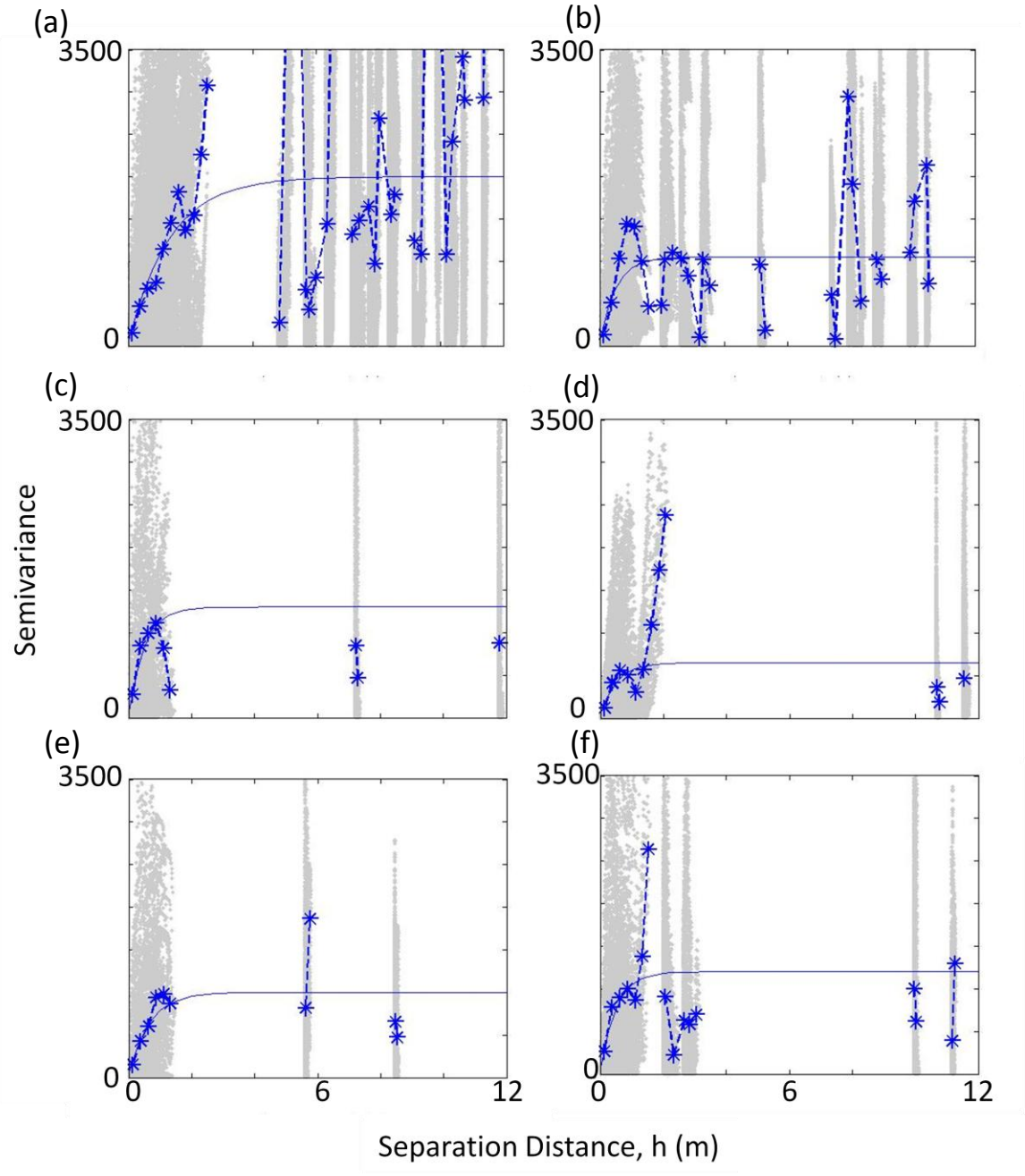

Figure 4-73. Raw, experimental, and theoretical variograms in the loose sand layer from (a) pre-blast testing, (b) one week testing, (c) one month testing, (d) two and a half month testing, (e) one year testing, and (f) two year testing.

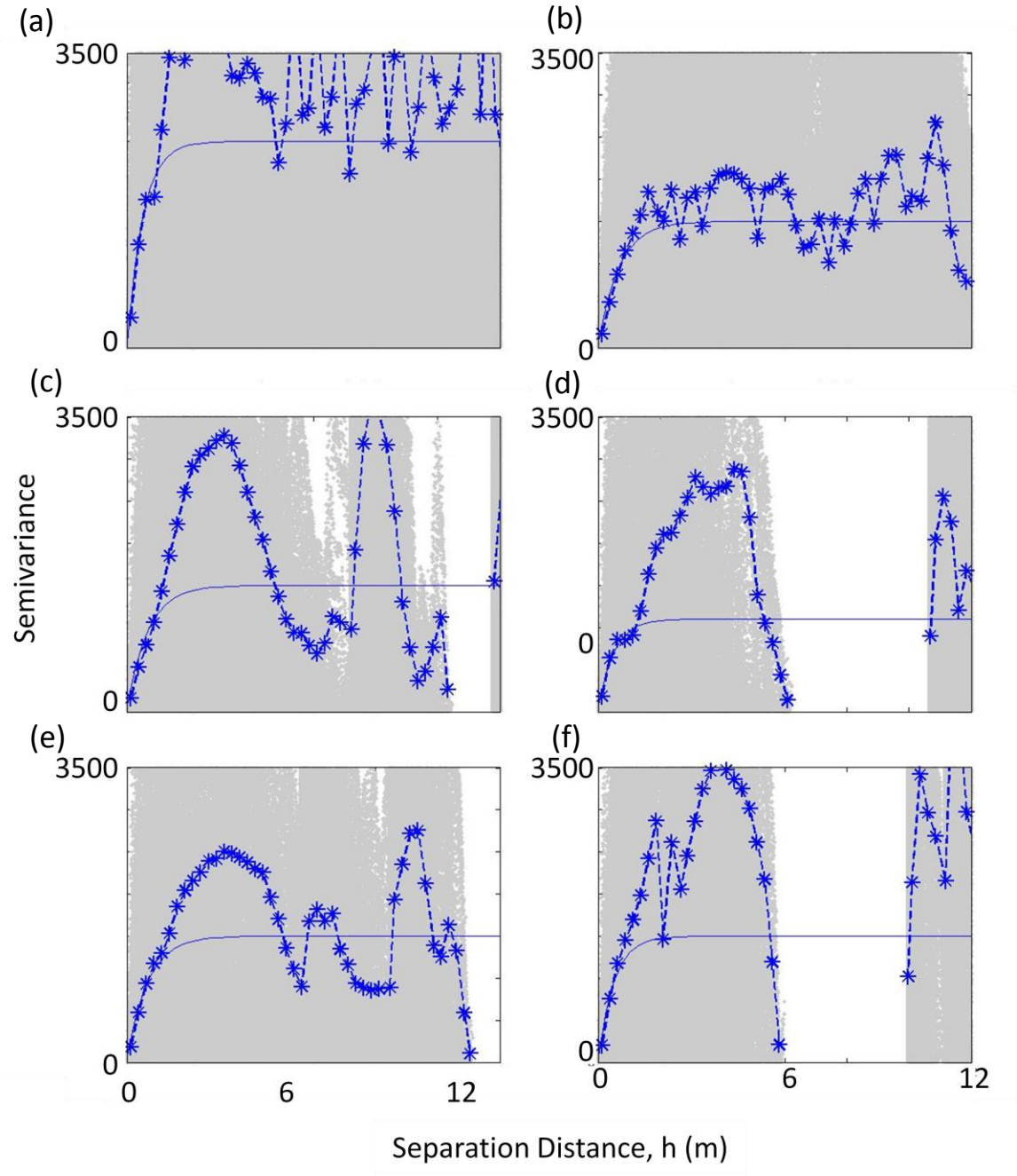

Figure 4-74. Raw, experimental, and theoretical variograms in the dense sand layer from (a) pre-blast testing, (b) one week testing, (c) one month testing, (d) two and a half month testing, (e) one year testing, and (f) two year testing.

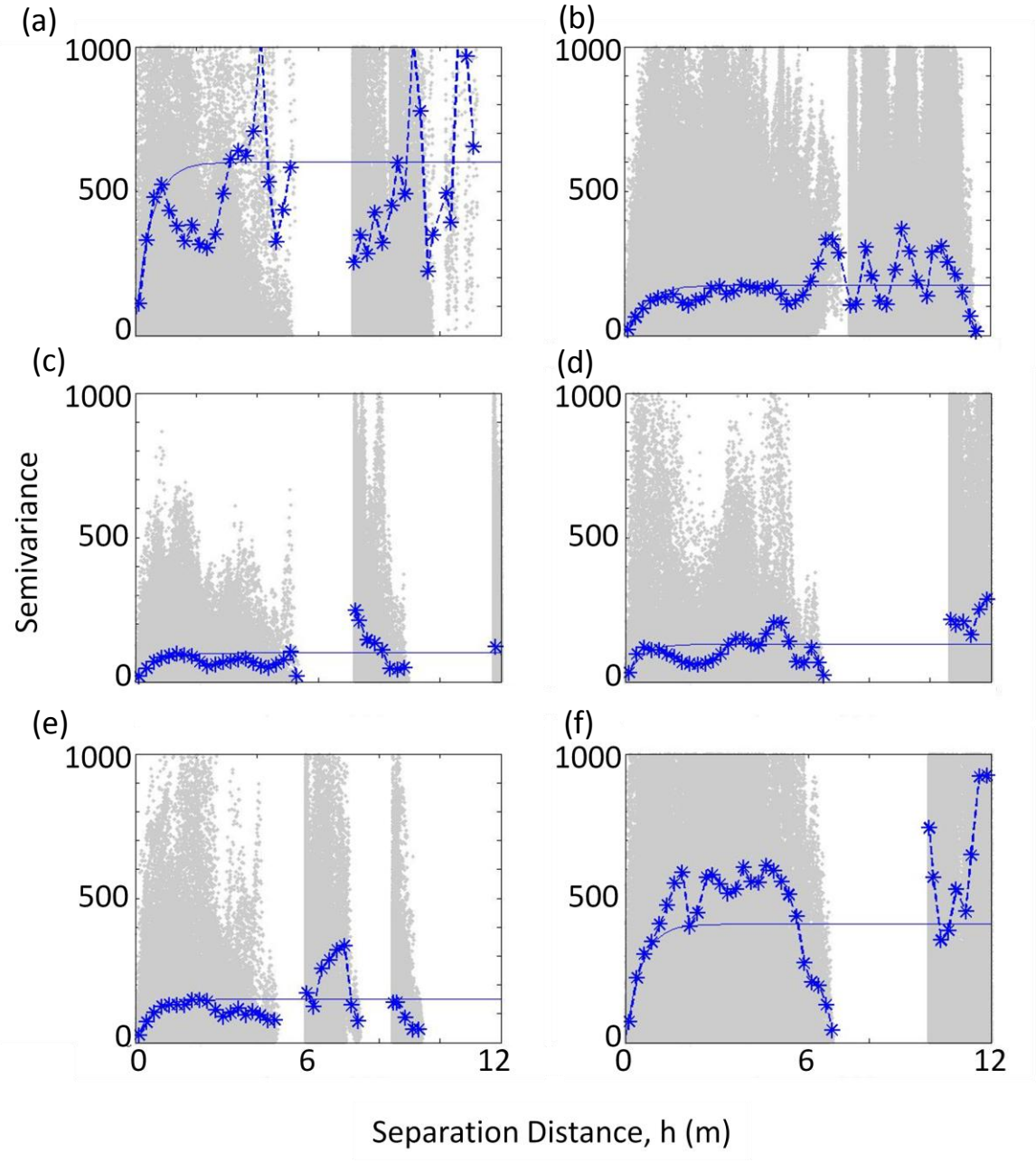

Figure 4-75. Raw, experimental, and theoretical variograms in the loose gravelly sand layer from (a) pre-blast testing, (b) one week testing, (c) one month testing, (d) two and a half month testing, (e) one year testing, and (f) two year testing.

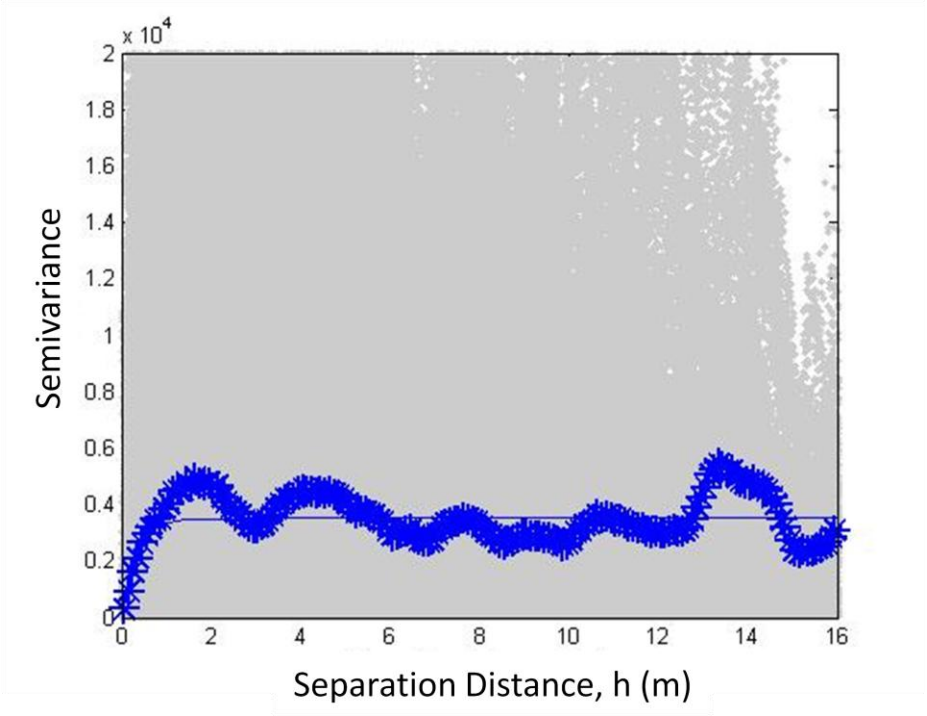

Figure 4-76. Histogram of CPT normalized tip resistance considering only distance between points with depth.

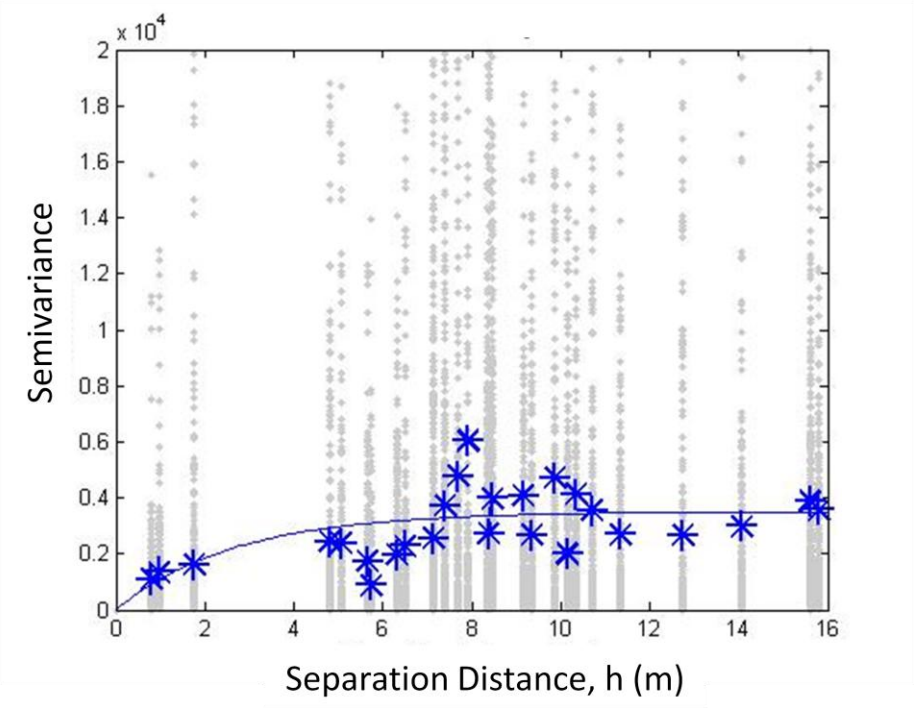

Figure 4-77. Histogram of CPT normalized tip resistance considering only distance in plan view.

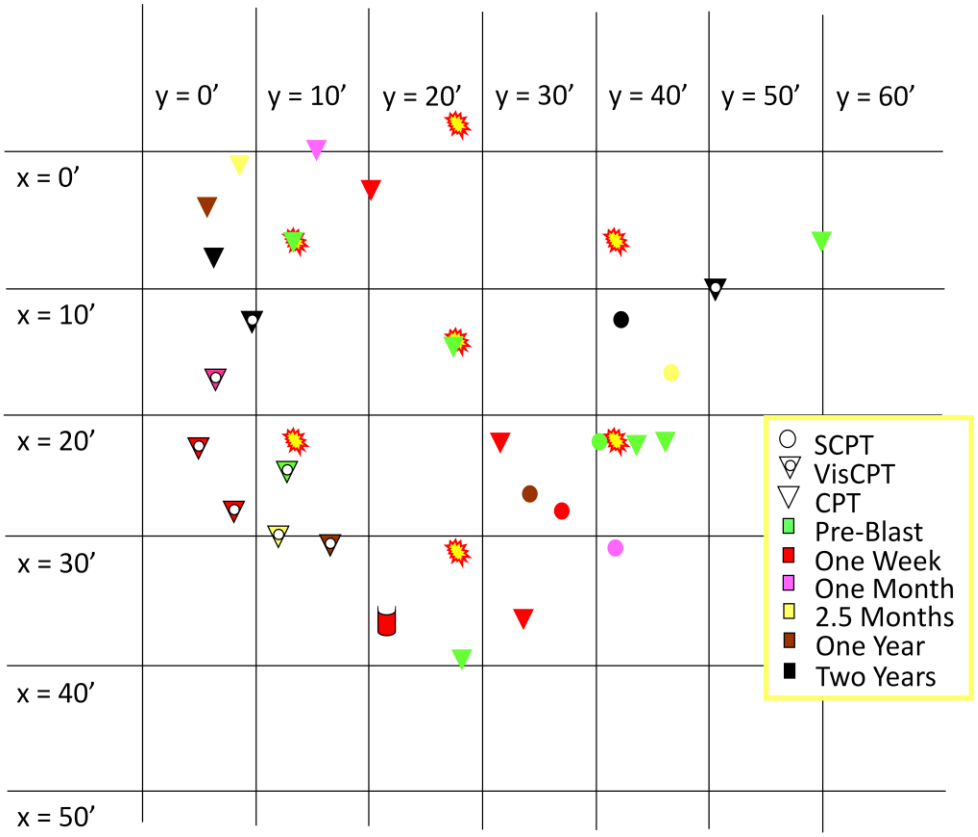

Figure 4-78. Location of CPTs with E-W and N-S distance grid shown.

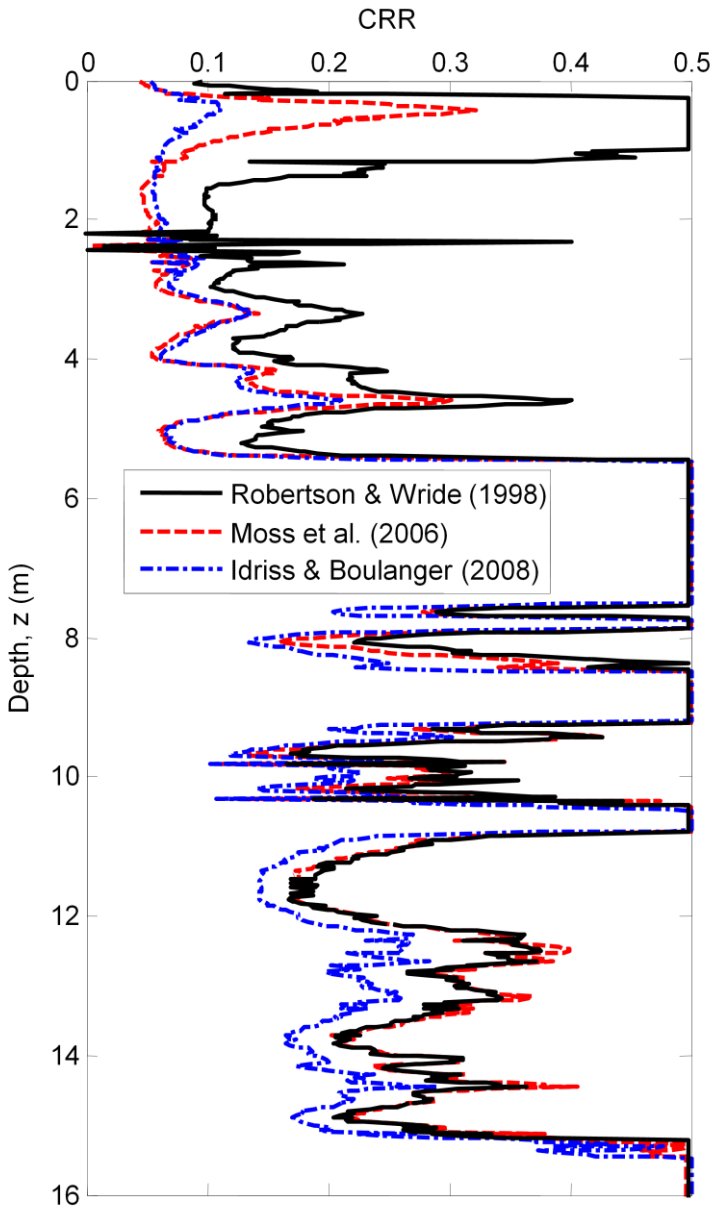

Figure 4-79. Comparison of CRR predictions from SCPT-19 data using three different CPT-CRR calculation methods.

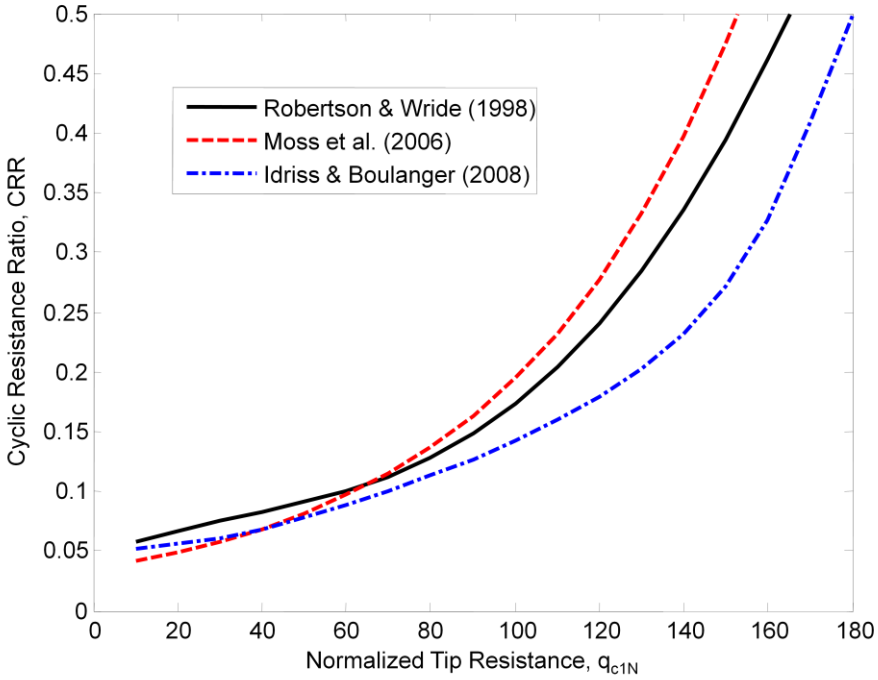

Figure 4-80. Comparison of CRR prediction from CPT results using the Robertson and Wride (1998), Moss et al. (2006) and Idriss and Boulanger (2008) methods.

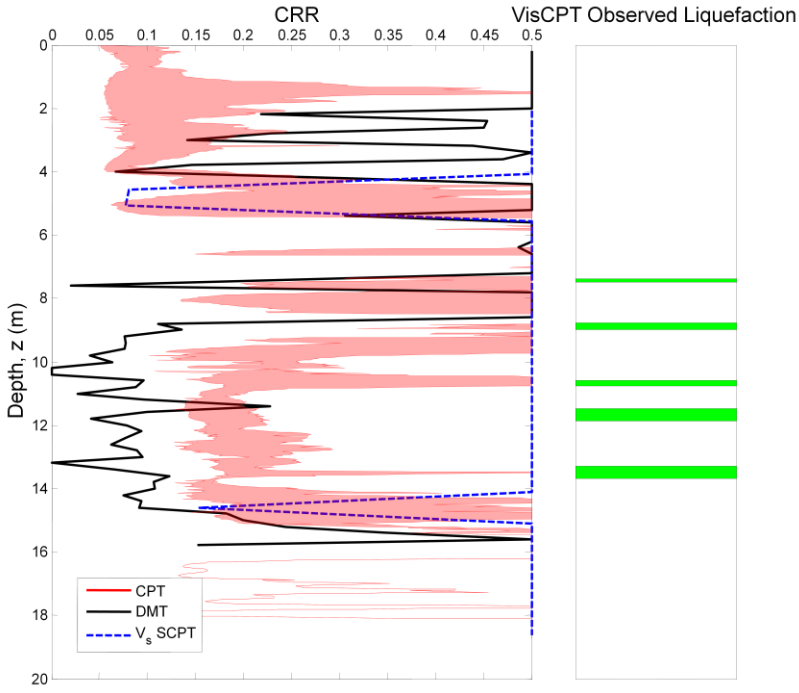

Figure 4-81. Comparison of CRR predictions from CPT, DMT, and shear wave velocity prior to the blast.

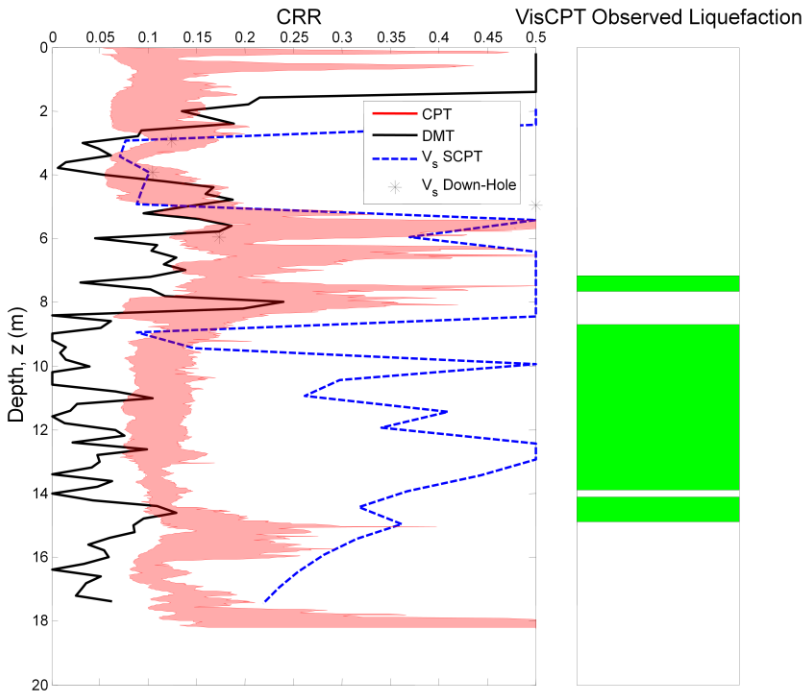

Figure 4-82. Comparison of CRR predictions from CPT, DMT, and shear wave velocity from one week tests.

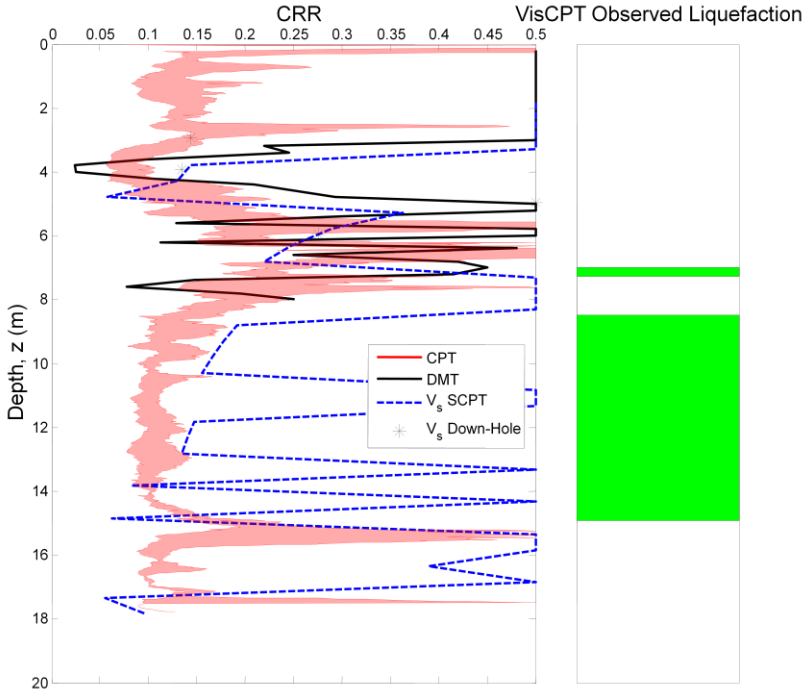

Figure 4-83. Comparison of CRR predictions from CPT, DMT, and shear wave velocity from one month testing.

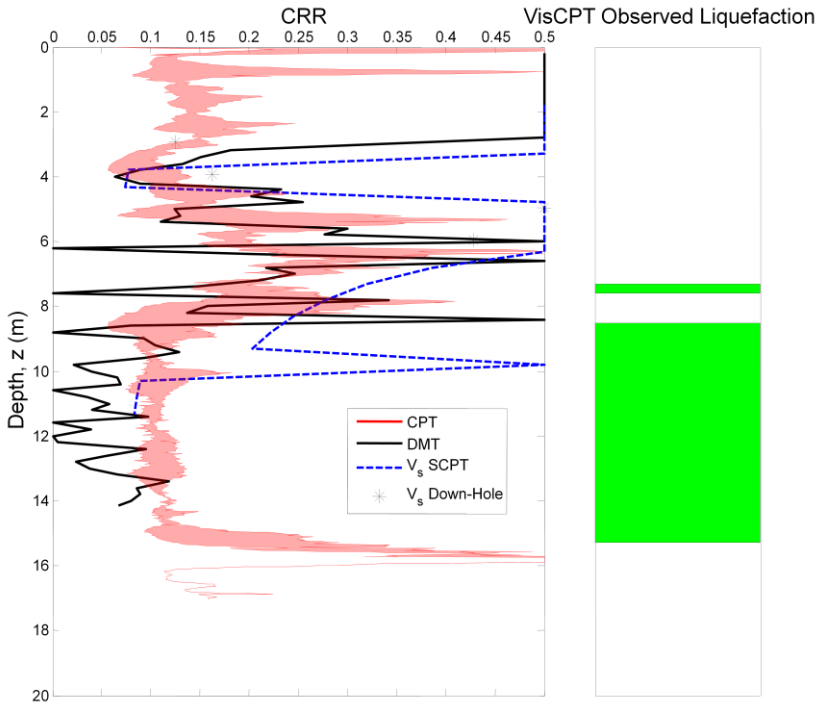

Figure 4-84. Comparison of CRR predictions from CPT, DMT, and shear wave velocity from two and a half month tests.

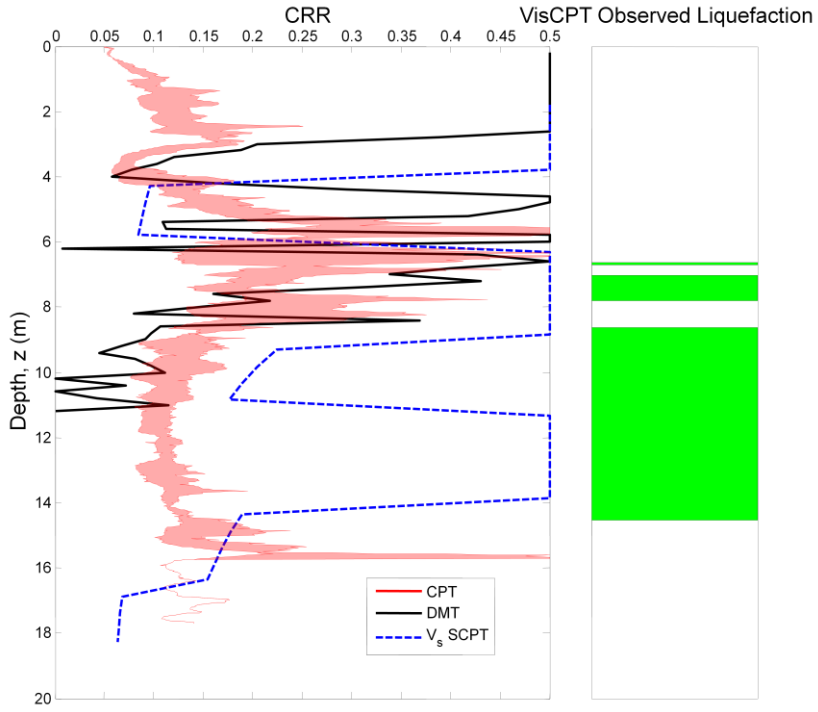

Figure 4-85. Comparison of CRR predictions from CPT, DMT, and shear wave velocity from one year testing.

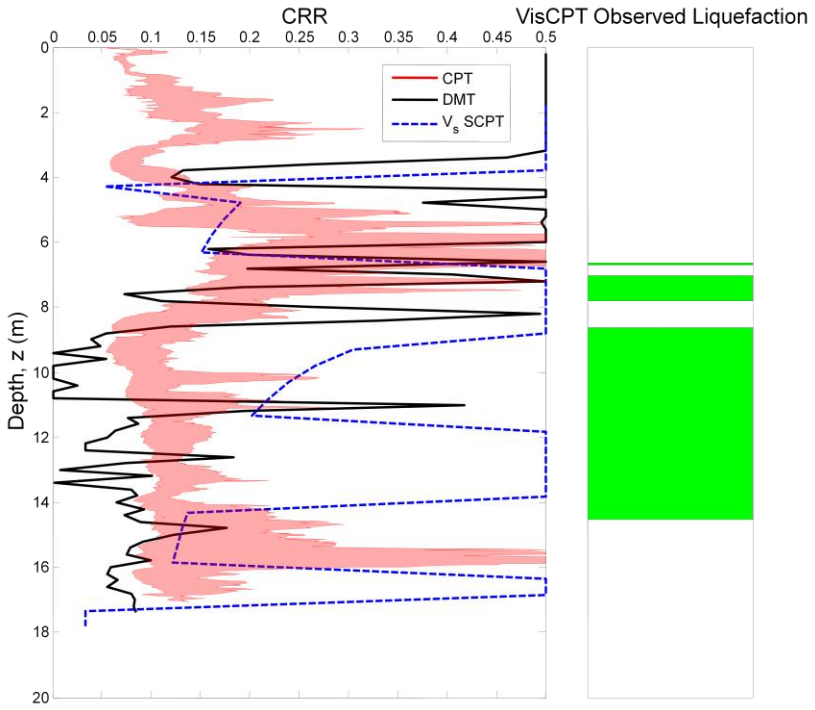

Figure 4-86. Comparison of CRR predictions from CPT, DMT, and shear wave velocity from two year tests.

Chapter 5

Field Testing – Vibroseis

5.1 Introduction

In order to quantify aging effects, this study included three field experiments and compared the results from each. This chapter describes one of those experiments, vibroseis shaking performed at the sand and gravel quarry in Griffin, Indiana. Vibroseis shaking was chosen because previous research has identified that the amount of disturbance and aeration of pore fluid are two important factors that influence sand aging effects. Vibroseis shaking imparts less energy disturbing the soil than explosive densification and impact piers and does not aerate the pore fluid. The vibroseis used in this experiment was a triaxial shaker, nicknamed T-Rex, from the University of Texas' Network for Earthquake Engineering Simulation (NEES) equipment. This chapter will describe the site investigation, instrumentation plan, shake design and execution, post-shake testing plan, and results of testing.

5.2 Site Investigation

In 2007, 14 *in situ* tests, including cone penetration tests (CPT), vision CPT (VisCPT), and seismic CPT (SCPT), were conducted in the quarry. Both the 2006 and 2007 test areas are shown in Figure 5-1. Results of VisCPT-13 and VisCPT-14, tests showing low CPT tip resistance (q_c), are presented in Figure 5-2. The locations of these tests are also highlighted in Figure 5-1. The areas around VisCPT-13 and VisCPT-14 were selected for the southwest (SW) and northeast (NE) vibroseis sites, respectively, because these tests showed the lowest tip resistances in the loose sand layer of the 2006-07 tests, excluding the tests affected by explosive densification. General site investigation, a description of the soil profile, and a description of *in situ* tests are presented in Chapter 4.2.

5.3 Instrumentation and Data Collection

The instrumentation plan for this project was designed to measure pore pressure and particle acceleration. Additionally, this section will describe the instrumentation used to measure shear wave velocity using the down-hole and cross-hole methods. Pore pressure is of interest to quantify the excess pore pressure generation and dissipation, ensuring that excess pore pressure has dissipated prior to *in situ* testing. Acceleration provides a measure of disturbance. Down-hole and cross-hole shear wave velocity measurements provide comparison for shear wave velocity measurements from SCPT. Cross-hole primary wave velocity measurements provide an indication of saturation. Data acquisition through wireless and cable-based systems will also be described. Surface settlement was not recorded at the vibroseis sites because of the difficulty in determining settlement caused by the weight of the truck and settlement caused by near-surface soil compaction. The instrumentation used to in cross-hole testing, pore pressure measurement and acceleration measurement, as well as the data acquisition (DAQ) systems associated with these instruments, were provided by the University of Texas as part of their NEES equipment.

5.3.1 Pore Pressure

The selection and calibration of pore pressure transducers is describe in detail by Cox (2006). Two separate pore pressure transducers were used in this experiment. The first was a miniature transducer placed in the same cone as an accelerometer, forming what Cox (2006) describes as a liquefaction sensor. The Entran model EPX-V02-25P pressure transducer has a 25 psi range. Cox (2006) found that the miniature pressure transducer had a tendency to drift, especially in the first hours after powering up. Additionally, the voltage corresponding to zero pressure was different after shutting the sensor down and powering it up again. The combination of these problems led to the conclusion that the miniature pressure transducers were suitable to monitor dynamic pressure changes, but not for determining static pressure. Therefore, a larger, more stable pressure transducer is included in the instrumentation array in order to provide a measure of static water pressure and a reliable comparison for the miniature pressure transducers' results. The Druck model PDCR 35/D with a 10 psi range was used in this experiment. Experiments showed that the Druck pressure transducers were accurate in both static and dynamic applications. These pressure transducers are pictured in their acrylic cones in Figure 5-3.

Another issue related to measuring pore pressure is the placement and recovery of the transducers. The instruments are housed in cone tips for ease of placement. The cone tips were made of nylon. Similar to the instrumentation installed at the explosive densification site, these

instrument cases were not strong enough to withstand being pushed to the desired depth. Therefore, a pilot cone of larger diameter than the instrument cones, picture in Figure 5-4, was pushed to a depth of 2.5 m, just above the ground water table. The instruments were then dropped into the hole in the clay cap and pushed through the disturbed sand to their desired depth. A wire rope was attached to the nylon cone tip and run back to the surface. Pulling this cable allowed for recovery of the transducers after vibroseis shaking.

5.3.2 Acceleration

As described by Cox (2006), micro-electrical mechanical systems (MEMS) accelerometers were chosen for this application. The MEMS accelerometers respond to gravity, allowing them to be used to determine the orientation of the cones in the soil. Additionally, a small size accelerometer was desired in order to place it in the same cone as the miniature pore pressure transducer. Using these criteria, Silicon Designs model 2430-002 accelerometers were selected by Cox (2006). These accelerometers have a frequency range of 0-300 Hz, and are capable of measuring accelerations between ±2 g. The accelerometers used in this experiment are pictured installed in the cone in Figure 5-3a. Because the accelerometers were located in the same cone as the miniature pore pressure transducers, they were emplaced and recovered in a similar manner to the pore pressure transducers. Similar to the explosive densification experiment, the orientation of the accelerometers was important. Orientation was monitored prior to installation to align the sensor in the desired direction.

5.3.3 Down-Hole Shear Wave Velocity Measurement

While the SCPT provides a method of determining shear wave velocity (V_s), its results are subject to soil variability because cone tests are not performed at the same location. In order to measure V_s in a manner unaffected by variability, a down-hole V_s measurement system was developed for this experiment. Accelerometers were mounted in CPT rods and emplaced in the area where SCPT were performed. Because the down-hole system did not move, soil variability would not affect its results. The down-hole system shares its design with the system described in Section 4.3.4 and is shown in Figure 5-5.

5.3.4 Cross-Hole Primary and Shear Wave Velocity Measurement

Both primary and shear wave velocity were measured using the cross-hole technique. Two accelerometers were installed at the same depth. A cone was then pushed to the same depth in line with the accelerometers. Striking the source rod, as shown in Figure 5-6, created a

horizontally propagating primary and shear wave. By determining the arrival time of these waves at both of the accelerometers, one can calculate the primary and shear wave velocity between the accelerometers. Because the primary wave travels through water in saturated soil and through the soil skeleton in dry soil, measuring primary wave velocity gives an indication of the degree of saturation between the accelerometers. The cross-hole method of determining V_s provided another point of comparison for V_s determined from the down-hole method and from the SCPT.

5.3.5 Data Acquisition

Two data acquisition systems were used in this experiment. The wireless DAQ system used when collecting data for the down-hole system was described in Section 4.3.5. This down-hole system at the NE vibroseis site utilized the Narada units described in that section.

Cox (2006) describes the NEES DAQ system, pictured in Figure 5-7, in detail. A connector box was used to link the instruments to the DAQ system and the power source. This 72-channel DAQ system uses VXI hardware and Data Physics software. For the experiments described below, up to 20 channels were utilized. The first three channels measured the input signal to the T-Rex shaking pad, the output signal from the shaking pad, and the output from an accelerometer installed on the shaking pad. Four cones were installed containing miniature pore pressure transducers and a triaxial accelerometer. Each of these cones required four channels to record the output from the pressure transducer and each direction of the accelerometers. The final channel recorded the output from the stable, larger pore pressure transducer. Some of applications in this experiment did not use all of the instrumentation. In those cases, less than 20 channels of data were recorded.

5.4 Vibroseis Shaking Design and Execution

The following section describes the design, preparation, and implementation of the vibroseis shaking experiment. The design of the vibroseis shaking experiment is presented. Instrumentation installation is also discussed. Finally, comments and observations concerning the execution of the vibroseis shaking experiment are presented.

5.4.1 Experimental Design

The vibroseis shaking was designed to meet the project's goal of studying post-disturbance changes to soil through *in situ* tests with time. All CPT and dilatometer tests (DMT) were conducted at least 3' apart in order to ensure that test results were not influenced by disturbed

soil. The shake pad on the T-Rex vibroseis is roughly 7.5' square, so several adjacent shake points were required to accommodate post-shake testing. Six shake points placed in a 2x3 pattern provided an area of roughly 15' x 22.5', adequate for post-shake testing.

The frequency of shaking was set at 10 Hz with a maximum amplitude. Under ideal conditions, T-Rex is capable of imparting 134 kN of force when shaking in the horizontal direction. The frequency of shaking was chosen to be close to the natural frequency of the soil, roughly 14 Hz as determined from loose sand layer's average shear wave velocity. The shaking duration was 10 minutes rather than the 1 minute interval that was used in previous vibroseis experiments described by Cox (2006). The purpose of this experiment was to disturb the loose sand layer in order to begin the sand aging process. Because disturbance is dependent on both amplitude and number of cycles, it was determined that a longer duration tests would better suit the purpose of the experiment. Additionally, the clay cap at the Griffin quarry is 1.5 to 2 m thick. This is thicker than the cap at the Wildlife Site in California, studied by Cox (2006). Additional shaking would increase the energy imparted to the loose sand layer.

Two separate experiment sites were used because the large area available in the quarry allowed for greater testing. Depending on how sand aging manifested itself, the 15' x 22.5' testing area at each shake site may not have been sufficient for all of the desired post-shake testing. Having two sites increased the chances of success. The NE site includes an area that was not shaken due to installed instrumentation. Cone rods were protruding from the ground in this area. The NE site was chosen for additional instrumentation because it had lower pre-shake tip resistance, as shown in Figure 5-2.

5.4.2 Instrumentation Emplacement

Instruments at the NE shake site were placed according to the plan recommended by Cox (2006) based on his vibroseis experiments at the Wildlife Site. As shown in Figure 5-8, two cones containing both accelerometers and miniature pore pressure transducers were installed 0.6 m apart at a depth of 3.2 m. Two more cones with the same instrumentation were installed to a depth of 3.8 m. Each of the cones was pushed along the same line as the shallower cones, but each was placed 0.3 m further from the center line of the array. Finally, the stable pore pressure transducer was installed in the center of the array, at a depth of 3.5 m. Two rods were placed on the eastern end of the instrument array. The rod closest to the array was pushed to a depth of 3.2 m, while the furthest rod was pushed to a depth of 3.8 m. Additionally, the down-hole system was installed in the same manner as was described in Section 4.3.4.

This instrumentation was left in place following the shaking in order to conduct cross-hole and down-hole testing with time following the shaking. Therefore, it was not available for use at the SW shake site. As shown in Figure 5-9, the SW shake site instrumentation consisted only of one stable pore pressure transducer.

In order to install the instrumentation cones, a larger pilot cone was first pushed into the ground. The pilot cone was pushed to only 2.8 m, at least 0.4 m above its final destination. This opened a hole in the clay cap and loosened the sand layer without disturbing the soil at the final depth of the instrument. The instrument cones were placed at the end of a string of rods and pushed into the ground. After reaching the desired depth, the rods were retracted 7.6 cm so that the instrument cone was no longer attached to the rods. At the completion of testing, a steel cable attached to the cone was pulled while the rods were retracted from the ground.

5.4.3 Vibroseis Shaking Experiment

The order of the shake points is shown in Figure 5-10. The instrument array pictured in Figure 5-8 and down-hole system recorded acceleration and pore pressure response during the shaking at each NE shake point. The pressure transducer recorded pore pressure response during the shaking at the SW site. Post-shake CPT soundings began 17 hours after the final shake at the NE site and 5 hours after the final shake at the SW site.

One note of interest is that the shaking occurred after several days of rain. The initial shaking occurred on wet, muddy ground so it is unlikely that the maximum force was imparted in this experiment due to poor coupling between the T-Rex shake pad and the wet clay. At shake points 2 and 3, dry sand was added to the surface of the ground so the shake pad had better coupling with the ground. After drying for several hours, the surface of the ground became more firm and the sand was not required at other shake points.

5.5 Post-Shake Testing

The following section discusses the post-shake testing plan and results. Data collected from the pore pressure transducers, accelerometers, and results of the various *in situ* tests are presented.

5.5.1 Testing Plan

While vibroseis shaking disturbs soil outside the footprint of the shaking pad, all *in situ* tests were conducted within the shaking footprint. Within the roughly 15’ x 22.5’ shaking footprint, each

cell was disturbed by the shaking directly above it and the adjacent shaking cells. The locations of *in situ* tests conducted at both the NE and SW shake sites are shown in Figure 5-11.

5.5.2 Pore Pressure Dissipation

At the NE shake site, four miniature pore pressure transducers and one stable pore pressure transducers were installed in the loose sand layer. At the SW shake site, one stable pore pressure transducer was installed in the loose sand layer. Pore pressure response was recorded for the duration of shaking at each of the shake points. The results from the stable and miniature transducers at the NE shake site are presented in Figure 5-12 and 5-13, respectively. At both shake sites the instruments' response to shaking directly above the transducers is shown. Similar trends with lower peak pore pressure were recorded when shaking at adjacent shake points. The peak excess pore pressure ratio reached an average value of 0.25 and dissipated to zero within 1.5 minutes after shaking. All five pressure transducers recorded a spike in pore pressure between 920 and 930 seconds. There was no external excitation at this time. This response must have been due to an electrical surge. After 930 seconds, the pore pressure recordings return to where they were prior to the spike. Another point of interest regarding the response of pressure transducers is that the northern most miniature pressure transducer, installed at a depth of 3.8 m, did not accurately record dynamic response. During the shaking, the transducer recorded negative pore pressure. Following the shaking, the transducer returned to recording hydro-static pore pressure. The transducers at the shallowest depth, 3.2 m, recorded a maximum excess pore pressure ratio of approximately 0.2 with dissipation complete within 4 minutes after the end of shaking. The functioning transducer at the deepest depth, 3.8 m, recorded a maximum excess pore pressure ratio of approximately 0.1 with dissipation also completed within 4 minutes after cessation of shaking.

Results from the stable pore pressure transducer at the SW shake site are shown in Figure 5-14. The peak excess pore pressure ratio reached an average value of only 0.08 and dissipated to zero within 1 minute after the end of shaking. The NE shake site was more heavily instrumented because the site investigation showed lower q_c values. Higher density in the loose sand layer at the SW site explains both the increased q_c readings and the generation of less excess pore pressure during vibroseis shaking.

5.5.3 Acceleration

Acceleration was recorded by four triaxial accelerometers in the loose sand layer at the NE shake site for the duration of shaking at each shake point. Similar to the pore pressure transducers, only data from the second shake point, as labeled in Figure 5-10, is presented in Figure 5-15. Recorded acceleration from other shake points is less significant because the shaking occur farther from the transducer. Only during the shaking at the second shake point did the accelerometers at depths of 3.2 and 3.8 m record any signal.

As shown in Figure 5-15, the shallow instruments recorded horizontal vibrations in both directions reaching ~0.15 g. Vertical acceleration fluctuated between 0.2 and -0.1 g. At the deep instruments, horizontal vibrations reached ~0.1 g, while vertical acceleration reached ~0.12 g. Additionally, the down-hole system recorded accelerations at four depths during portions of shaking at each shake point, as shown in Figure 5-16. Each of the three shallowest accelerometers showed 0.08 g of acceleration, while the deepest accelerometer did not record significant acceleration.

5.5.4 Cone Penetration Testing

Pre-shake CPT testing at the NE shake site consisted of two CPTs, one VisCPT, and one SCPT. Pre-shake CPT testing at the SW shake site consisted of one CPT, one VisCPT, and one SCPT. Post-shake testing was conducted immediately following disturbance for one week, at one month, and nine months following the shaking. Three CPTs were conducted at each testing time, including one SCPT and one VisCPT. In this section, only the standard CPT results will be discussed. Vision data from the VisCPT and V_s from the SCPT will be discussed in Sections 5.5.5 and 5.5.7, respectively.

The locations of SCPTs, VisCPTs, and CPTs at the NE shake site are shown in Figures 5-17 through 19, respectively. The location of SCPTs, VisCPTs, and CPTs at the SW shake site are shown in Figures 5-20 through 22, respectively. The test name, time, and miscellaneous notes are presented in Table 5-1. Throughout CPT testing at the Griffin quarry, the friction ratio (F_r) remained consistent. Pore water pressure results varied with the water table depth, but always generally followed the hydrostatic line. Therefore, CPT results presented subsequently in this dissertation will include only q_c information. A summary of pre-shake CPT results at both shake sites is shown in Figure 5-23.

CPTs were performed following the shake. Tests at both the NE and SW shake sites were completed within 48 hours after completion of shaking, but are referred to as "one week" tests in this dissertation to maintain consistency with terminology used in the explosive densification experiment. Results from the CPTs conducted at both shake sites are shown in Figure 5-24. As shown in Figure 5-25, the range of q_c values at both shake sites remain generally consistent with the results from pre-shake testing throughout the soil profile.

One month after the blast, 3 CPTs, including one SCPT and VisCPT, were conducted at each shake site. Results from both shake points are shown in Figure 5-26. As pictured in Figure 5-27, the range of tip resistance values at the NE shake sites remained generally consistent with one week testing throughout the soil profile. At the SW shake site, the one week range appears lowers than the one month range due to one test, CPT-47, recording unusually low q_c during one week testing. The difference in this test is likely due to spatial variability.

Nine months after the blast, 3 CPTs, including one SCPT and VisCPT, were conducted at each shake site. Results from both shake points are shown in Figure 5-28. As pictured in Figure 5-29, the range of tip resistance values at the NE shake sites remained generally consistent with one month testing throughout the soil profile. At the SW shake site, the nine month range appears lowers than the one month range due to one test, CPT-68, recording unusually low q_c during one week testing. The difference in this test is likely due to spatial variability.

The mean tip resistance profile is shown for each testing interval in Figure 5-30 for both shake sites. Tip resistance throughout the soil profile remained generally consistent with time following the shake. It is likely that the shake did not significantly disturb the sand layers.

5.5.5 Vision Cone Penetration Testing

Visual evidence of liquefaction was not as prominent at the vibroseis sites as it was at the explosive densification site. This result was expected because initial CPT results showed lower q_c at the explosive densification site compared to the vibroseis sites. VisCPT results showed several small layers that liquefied as a result of cone penetration. At the NE shake site, VisCPT-45, conducted one week after shaking, showed liquefaction between 6.22 m and 6.32 m, while VisCPT-65, conducted nine months after shaking, showed liquefaction between 4.69 m and 4.79 m. At the SW shake site, VisCPT-13, conducted prior to shaking, showed liquefaction between 4.2 m and 4.3 m, while VisCPT-46, conducted one week after shaking, showed liquefaction

between 6.88 m and 7.09 m. These small layers that show visual evidence of liquefaction do not reflect a pattern across either of the shake sites.

5.5.6 Primary Wave Velocity

Primary wave velocity was determined by picking arrival times of the waves shown in Figure 5-31. The primary wave velocity was 365 m/sec. Because primary waves travel through water at roughly 1,450 m/sec, it is clear that the loose sand was not saturated. This result also likely explains the transient pore pressure response to explosive densification described in Chapter 4.5.2 as the loose sand layer was possibly not completely saturated at the blast location as well.

5.5.7 Shear Wave Velocity

At the NE shake site, V_s was calculated using SCPT data, cross-hole data, down-hole data, and spectral analysis of surface waves (SASW) data. Because SCPTs from each testing time were collected at different locations, as pictured in Figure 5-17, V_s from this method shows more variability than the cross-hole and down-hole data, which remained in place throughout the experiment. These methods both show the same trend of generally consistent V_s with time following shaking. At the SW shake site, V_s was calculated using SCPT data, at locations shown in Figure 5-20.

SASW testing was conducted prior to shaking at the NE shake site (Menq, 2009). The pre-shake V_s profile from all four V_s determination methods is shown in Figure 5-32. Shear wave velocity determined from SASW is generally lower than V_s determined from the other methods. There is good agreement between V_s from SCPT, down hole and cross hole testing.

There are 4 SCPT soundings at the NE shake site and 3 soundings at the SW shake site. The resulting V_s profiles are presented in Figures 5-33 and 34, respectively. While there is scatter in the profiles due to spatial variability of soil properties, there is no clear trend with time.

The down-hole V_s data with time is presented in Figure 5-35. Because the V_s collected from the down-hole measurement system was not affected by spatial variability of soil properties, the data is easier to interpret and augments the V_s data from SCPT. The tests conducted after shaking were generally similar and small differences were attributed to the difficulty in choosing a precise arrival times of the shear waves. A difference of 0.01 milliseconds in shear wave arrival time causes 1.3 m/sec difference in V_s at a depth of 11 m. There is a slight increase in shear wave velocity following shaking, but no time depended increase following the shaking. When installing

the down-hole system, the CPT rods containing the accelerometers were pushed until the top of the rod was level with the ground surface. Between one week and one month testing, rain flooded the down-hole tube and destroyed the accelerometers.

The cross-hole V_s data with time is presented in Figure 5-36. The shear wave velocity collected from the cross-hole measurement system was also not affected by spatial variability of soil properties. The tests conducted after shaking were generally similar and small differences were attributed to the difficulty in choosing a precise arrival time in shear waves. A difference of 0.01 milliseconds causes 1 m/sec difference. There is a slight increase in V_s following shaking, but no time depended increase following the shaking. The instruments used in cross-hole testing did not remain in the ground after the 65 hour measurement, as they were part of the mobile NEES system that left the site following shaking.

Considering SCPT, cross-hole data, and down-hole data, it is clear that the shaking did not significantly affect V_s. Down-hole and cross-hole data show small changes after the shaking, but SCPT results do not show changes with time after shaking.

5.5.8 Dilatometer Testing

There are 3 DMT soundings at each shake site. For the NE shake site, the resulting horizontal stress index, K_D, dilatometer index, E_D, and material index, I_D, profiles are presented in Figures 5-37 through 5-39, respectively. For the SW shake site, the resulting K_D, E_D, and I_D profiles are presented in Figures 5-40 through 5-42, respectively.

The horizontal stress index is related to the horizontal stress; therefore, a lack of change with time, similar to those seen in the CPT tip resistance, was expected. As seen in Figure 5-37 and 5-40, any time-dependent changes in K_D values do not exceed the variability in the results and no trends with time can be discerned.

The dilatometer index was also not expected to change with time, similar to the trend seen for V_s. As seen in Figure 5-38 and 5-41, any time-dependent changes in E_D values do not exceed the variability in the results and no trends with time can be discerned.

The material index is a function of soil type; therefore, changes with time were not expected. The data largely confirms this expectation. As seen in Figure 5-39 and 5-42, pre-shake, one week, and one month data are very similar. Differences between individual tests can be explained through spatial variation in soil properties.

5.6 Geostatistical Analysis of Aging

To begin the geostatistical analysis of the CPT data, the first step was to determine basic statistical information. The next step was to fit a theoretical variogram to the experimental data. Anisotropy in soil properties was accounted for using the coordinate transform method. Block kriging based on CPT data from one testing period was then used to predict the mean and standard deviation of the normalized tip resistance from a given test location and time. Finally, these values were compared to values from other time periods using two-tailed hypothesis testing. The result of this analysis is a percent confidence that the differences between two sets of tests at different ages are due to sand aging and not spatial variability of soil properties.

5.6.1 Basic Statistical Analysis

Initially, basic statistical information was generated. Considering the four CPT tests performed in the NW vibroseis area prior to any disturbance, there were 1,800 data points contained in a roughly 5m x 7m x 15m rectangular prism. From this information a histogram, shown in Figure 5-43 was generated using the normalized tip resistance, q_{c1N}, from all pre-shake CPT soundings. Normalized tip resistance was determined using Equation 4-7.

The mean of the q_{c1N} is 203.6 and the standard deviation is 97.8. An initial geostatistical analysis of this data did not produce good results. When geostatistical methods are used to form an estimate far from measured data, the results tend toward the mean. However, the mean q_{c1N} of the site is not a good predictor of q_{c1N} in each individual layer. Therefore, analyzing each of the layers of interest individually provides more accurate results.

A histogram of the q_{c1N} data is provided in Figures 5-44 for the clay layer, Figure 5-45 for the upper liquefiable layer, Figure 5-46 for the dense sand layer, and Figure 5-47 for the lower liquefiable layer. Figures 5-44 through 5-46 refer to data collected prior to the shake. Figure 5-47 uses data from 9 months following the shake because that test period contained three CPTs that penetrated into the loose gravelly sand layer. In other time periods, only one or two CPTs were conducted to that depth. Due to the small number of data points from these testing periods, the histograms were not as informative as the one presented in Figure 5-47. Histograms are not presented for other time periods in the upper three layers because the trends shown in Figures 5-44 through 5-46 remain constant at following time periods. A summary of the mean and standard deviation of q_{c1N} for each layer at each time period is presented in Table 5-2. One important note is that the data from the three sand layers shows a generally normal distribution, matching one of the assumptions in geostatistical analysis.

5.6.2 Variogram Selection

As described in Section 3.3, a theoretical variogram was matched to the experimental variogram by eye, using a physical understanding of soil properties. Experience has shown that exponential models best fit soil properties (Chiles and Delfiner, 1996), so exponential models were fit by eye to experimental variograms created using data from each soil layer at each testing period. A sensitivity analysis was performed on theoretical variograms from each soil layer. Varying the sill, correlation length, and nugget within reasonable bounds did not significantly vary the results of the analysis. The theoretical variograms from the clay layer at each of the four testing periods (pre-shake, one week, one month, and nine months) are pictured in Figure 5-48, for the northeast testing site, and Figure 5-49 for the southwest test site. This data is presented in Table 5-3. The theoretical variograms from the loose sand, dense sand, and loose gravelly sand layers from each of the four testing periods are pictured in Figures 5-50, 5-52, and 5-54 for the northeast test site, and Figures 5-51, 5-53, and 5-55 for the southwest test site, respectively, This data is presented in Table 5-3.

5.6.3 Anisotropy

As described in Section 3.4, soil properties typical vary more with depth than they do with lateral distance. Raw, experimental, and theoretical variograms were constructed using only vertical distance between points, shown in Figure 5-56, and only horizontal distance between points, shown in Figure 5-57. An exponential model, with the same sill of 8,500 and the same nugget of 10, fits both the horizontal and vertical experimental variograms. The only difference is the correlation length. In the vertical direction, the correlation length is 1 m. In the horizontal direction, the correlation length is 8 m.

The ratio of these correlation lengths becomes a scale factor of eight. In this dissertation, prior to using the data in block kriging analysis, each of the depth values was multiplied by eight to account for the anisotropy. After determining the desired estimates and uncertainty, but before presenting the data, the depth values would be returned to their true values. While only data from the northeast shake site was described here, a similar analysis using data from the southwest shake site produced the same scale factor.

5.6.4 Block Kriging and Hypothesis Testing

A code was written in MATLAB to perform block kriging on data sets from the four soil layers at each of the four testing periods. Locations of each of the tests, the deepest data points in each of

the soil layers, and variogram information was required for each analysis. While variogram information was presented in Table 5-3, the rest of the input data is presented in Table 5-4. Locations of the tests were based on an arbitrary coordinate system, shown in Figure 5-58. Because distance between the tests were important, but absolute location was not important, the location of the zero axis was not of concern. The number of blocks in each analysis was dependent on the thickness of the layer being analyzed. In plain view, the rectangular area encompassing each of the testing period's tests was split into four equal sized blocks. With depth, a new block was established every 10 cm. Therefore, the number of blocks was 40 times the thickness of the layer in meters. The mean and uncertainty of the normalized tip resistance data sets determined from the block kriging analysis is presented in Table 5-5.

The results from the same layer at different testing periods were compared using two tailed hypothesis tests. Conceptually, the two tailed hypothesis test compares two statistical distributions and determines the confidence that they are the same. Subtracting this value from 100% gives the confidence that they are different. The p-value, or confidence that the distributions are the same, was determined using a MathCad function and values of the test statistic, *t*, and degrees of freedom, *df*. The test statistic and degrees of freedom are defined in Equations 4-7 and 4-8, respectively.

While a visual assessment of the *in situ* test results showed no change with time, a geostatistical analysis was desired to quantify a level of certainty. Values of the test statistic, degrees of freedom, p-value, and confidence that the testing periods are different are presented in Table 5-6. Because the tests were conducted close to each other, the only difference between the different data sets is age since disturbance. Therefore, one can say with the percent confidence determined in this analysis that test results from different time periods are different due to aging and not the natural spatial variability of soil properties.

The block kriging analysis confirmed the conclusion, initially based on a visual inspection of the CPT logs, that tip resistance did not change with time at the vibroseis sites. The analysis showed that only four comparisons were different, due to aging, two each at both the northeast and southwest shake sites. In all cases, these comparisons were between pre-shake data and later time periods in the loose gravelly sand layer. The pre-shake data is sparse in the loose gravelly sand layer, containing only 4 points at the northeast shake site and 58 points at the southwest site. Due to the small sample size, it is difficult to draw significant conclusions based on these

comparisons. Therefore, the geostatistical analysis confirmed that sand aging did not manifest itself at the vibroseis sites.

5.7 Conclusion

This chapter describes the vibroseis shaking experiment that was performed at Griffin, IN. A description of the site investigation, instrumentation and data collection methods, and experimental design was presented. Additionally, the results of the experiment and subsequent *in situ* testing were presented and discussed. A geostatistical analysis of this data showed with >80% confidence that the differences in CPT results between testing periods in the loose sand layer were due to spatial variability. Results of the vibroseis shaking experiment will be compared to other sand aging studies in Chapter 8.

Table 5-1. Testing times and notes from the vibroseis shake sites.

Northeast Layer	Date of Test	Time of Test	Hours after Last Shake	Notes
VisCPT-45	25 OCT 08	1100	17	
SCPT-48	26 OCT 08	0800	38	
SCPT-49	26 OCT 08	1000	40	
DMT-8	27 OCT 08	0800	62	
DMT-9	21 NOV 08	1100	665	
SCPT-51	22 NOV 08	1200	690	
CPT-53	22 NOV 08	1700	695	
VisCPT-54	23 NOV 08	0900	711	
VisCPT-65	21 JUL 09	0800	6446	
SCPT-69	21 JUL 09	1700	6455	
CPT-70	21 JUL 09	1830	6456.5	

Southwest Layer	Date of Test	Time of Test	Hours after Last Shake	Notes
VisCPT-46	25 OCT 08	1430	5	
SCPT-47	25 OCT 08	1600	6.5	
CPT-50	26 OCT 08	1200	26.5	
DMT-7	26 OCT 08	1630	31	
DMT-10	21 NOV 08	1530	669.5	
SCPT-52	22 NOV 08	1500	693	
VisCPT-55	23 NOV 08	1030	712.5	
CPT-59	23 NOV 08	1700	718.75	
VisCPT-66	21 JUL 09	1130	6482	
SCPT-67	21 JUL 09	1330	6484	
CPT-68	21 JUL 09	1530	6486	

Table 5-2. Mean and standard deviation by layer and testing period.

Northeast Layer	Testing Period	Normalized Tip Resistance Mean, μ	Normalized Tip Resistance Standard Deviation, σ^2
Clay	Pre-Blast	108	6,910
Clay	One Week	149	1,768
Clay	One Month	90	2,492
Clay	Nine Months	58	444
Loose Sand	Pre-Blast	125	2,003
Loose Sand	One Week	113	2,326
Loose Sand	One Month	117	1,426
Loose Sand	Nine Months	113	1,126
Dense Sand	Pre-Blast	264	4,091
Dense Sand	One Week	246	4,017
Dense Sand	One Month	254	3,676
Dense Sand	Nine Months	225	3,582
Loose Gravelly Sand	Pre-Blast	144	44
Loose Gravelly Sand	One Week	172	512
Loose Gravelly Sand	One Month	186	745
Loose Gravelly Sand	Nine Months	180	1,865

Southwest Layer	Testing Period	Normalized Tip Resistance Mean, μ	Normalized Tip Resistance Standard Deviation, σ^2
Clay	Pre-Blast	122	18,563
Clay	One Week	114	7,799
Clay	One Month	91	6,439
Clay	Nine Months	46	482
Loose Sand	Pre-Blast	109	2,368
Loose Sand	One Week	108	1,532
Loose Sand	One Month	99	1,465
Loose Sand	Nine Months	92	1,092
Dense Sand	Pre-Blast	266	3,192
Dense Sand	One Week	241	5,680
Dense Sand	One Month	251	4,265
Dense Sand	Nine Months	235	3,084
Loose Gravelly Sand	Pre-Blast	195	843
Loose Gravelly Sand	One Week	127	1,183
Loose Gravelly Sand	One Month	142	2,933
Loose Gravelly Sand	Nine Months	124	2,508

Table 5-3. Exponential variogram inputs by layer and testing period.

Northeast Layer	Testing Period	Correlation Length, a (m)	Partial Sill, b	Nugget, c
Clay	Pre-Blast	3	20,000	500
Clay	One Week	4	60,000	500
Clay	One Month	3	5,500	50
Clay	Nine Months	3	1,500	50
Loose Sand	Pre-Blast	2	5,000	250
Loose Sand	One Week	2	5,000	250
Loose Sand	One Month	3	4,000	250
Loose Sand	Nine Months	3	3,000	100
Dense Sand	Pre-Blast	2	6,950	50
Dense Sand	One Week	1.5	5,950	50
Dense Sand	One Month	1.5	5,950	50
Dense Sand	Nine Months	1.5	4,950	50
Loose Gravelly Sand	Pre-Blast	1.5	1,090	10
Loose Gravelly Sand	One Week	1.5	900	10
Loose Gravelly Sand	One Month	1.5	1,190	10
Loose Gravelly Sand	Nine Months	1.5	2,290	10

Southwest Layer	Testing Period	Correlation Length, a (m)	Partial Sill, b	Nugget, c
Clay	Pre-Blast	3	50,000	500
Clay	One Week	3	25,000	500
Clay	One Month	3	18,000	500
Clay	Nine Months	3	800	200
Loose Sand	Pre-Blast	1.5	6,750	250
Loose Sand	One Week	1.5	3,250	250
Loose Sand	One Month	1.5	3,500	250
Loose Sand	Nine Months	1.5	2,750	250
Dense Sand	Pre-Blast	1.5	4,950	50
Dense Sand	One Week	1.5	4,950	50
Dense Sand	One Month	1.5	5,450	50
Dense Sand	Nine Months	1.5	3,450	50
Loose Gravelly Sand	Pre-Blast	2	3,500	10
Loose Gravelly Sand	One Week	2	2,800	10
Loose Gravelly Sand	One Month	1.5	4,200	10
Loose Gravelly Sand	Nine Months	1.5	3,200	10

Table 5-4. Location of CPT soundings and depth to each soil layer.

Northeast Test	Testing Period	E-W Location, x (m)	N-S Location, y (m)	Depth of Test, z (m)	Depth of Clay Layer (m)	Depth of Loose Sand Layer (m)	Depth of Dense Sand Layer (m)	Depth of Loose Gravel Sand Layer (m)
CPT-14	Pre-shake	3.6	4.8	6.1	1.8	3.5	N/A	N/A
CPT-35	Pre-shake	1.3	4.6	5.3	2.1	3.8	N/A	N/A
CPT-36	Pre-shake	3.9	2.5	11.8	2.0	3.7	11.8	N/A
CPT-37	Pre-shake	5.3	5.0	12.7	1.7	3.6	12.7	N/A
CPT-45	1 week	2.5	7.5	8.8	2.0	3.5	N/A	N/A
CPT-48	1 week	4.8	5.3	9.8	1.7	3.8	N/A	N/A
CPT-49	1 week	4.9	2.3	15.2	1.8	3.2	12.4	N/A
CPT-51	1 month	4.6	3.1	14.9	1.8	3.6	12.4	N/A
CPT-53	1 month	2.6	6.7	15.8	2.1	3.6	12.1	N/A
CPT-54	1 month	4.7	6.4	12.3	1.7	3.9	N/A	N/A
CPT-65	9 months	3.2	7.6	17.6	2.1	3.6	12.5	N/A
CPT-69	9 months	4.6	1.5	17.6	1.9	3.9	12.2	N/A
CPT-70	9 months	4.0	3.4	16.9	1.9	3.7	11.7	N/A

Southwest Test	Testing Period	E-W Location, x (m)	N-S Location, y (m)	Depth of Test, z (m)	Depth of Clay Layer (m)	Depth of Loose Sand Layer (m)	Depth of Dense Sand Layer (m)	Depth of Loose Gravel Sand Layer (m)
CPT-13	Pre-shake	3.3	4.1	6.3	2.2	4.3	N/A	N/A
CPT-38	Pre-shake	2.8	2.1	13.3	2.4	4.0	12.3	N/A
CPT-39	Pre-shake	5.0	2.3	11.1	2.1	3.9	N/A	N/A
CPT-46	1 week	3.3	6.7	8.5	2.1	4.2	N/A	N/A
CPT-47	1 week	3.2	2.7	9.7	2.3	4.0	N/A	N/A
CPT-50	1 week	4.9	3.1	15.4	2.2	3.9	12.8	N/A
CPT-52	1 month	3.8	3.0	15.7	2.2	4.2	13.9	N/A
CPT-55	1 month	3.1	5.9	9.3	2.2	3.2	N/A	N/A
CPT-59	1 month	5.7	2.9	15.5	2.3	3.7	13.9	N/A
CPT-66	9 months	2.5	7.0	17.6	2.2	4.1	13.9	N/A
CPT-67	9 months	3.9	1.5	15.7	2.1	3.9	13.8	N/A
CPT-68	9 months	3.7	2.4	15.7	2.3	4.2	11.5	N/A

Table 5-5. Block kriging mean and standard deviation by layer and testing period.

Northeast Layer	Testing Period	Normalized Tip Resistance Mean from Block Kriging, z_A*	Normalized Tip Resistance Standard Deviation from Block Kriging, σ^2_{BK}
Clay	Pre-Blast	157	13,096
Clay	One Week	118	44,247
Clay	One Month	126	4,411
Clay	Nine Months	77	968
Loose Sand	Pre-Blast	122	2,732
Loose Sand	One Week	106	3,546
Loose Sand	One Month	112	2,367
Loose Sand	Nine Months	109	2,020
Dense Sand	Pre-Blast	252	6,639
Dense Sand	One Week	241	5,697
Dense Sand	One Month	247	5,610
Dense Sand	Nine Months	221	4,633
Loose Gravelly Sand	Pre-Blast	146	821
Loose Gravelly Sand	One Week	170	828
Loose Gravelly Sand	One Month	186	1,121
Loose Gravelly Sand	Nine Months	185	2,190

Southwest Layer	Testing Period	Normalized Tip Resistance Mean from Block Kriging, z_A*	Normalized Tip Resistance Standard Deviation from Block Kriging, σ^2_{BK}
Clay	Pre-Blast	112	39,227
Clay	One Week	119	20,877
Clay	One Month	117	14,360
Clay	Nine Months	65	478
Loose Sand	Pre-Blast	101	5,178
Loose Sand	One Week	107	1,821
Loose Sand	One Month	94	2,368
Loose Sand	Nine Months	97	1,169
Dense Sand	Pre-Blast	258	4,712
Dense Sand	One Week	237	4,738
Dense Sand	One Month	245	5,170
Dense Sand	Nine Months	229	3,164
Loose Gravelly Sand	Pre-Blast	198	2,420
Loose Gravelly Sand	One Week	137	2,167
Loose Gravelly Sand	One Month	157	3,799
Loose Gravelly Sand	Nine Months	135	3,059

Table 5-6. Results of two-tailed hypothesis test comparisons using mean and standard deviation from block kriging analysis.

Northeast Layer	Comparison	Test Value, t	Degrees of Freedom, df	P-value, p	Confidence of Difference (%)
Clay	Pre-shake to week	0.16	16,717,807	0.87	13
	Pre-shake to month	0.23	6,172,195	0.81	18
	Pre-shake to 9 months	0.67	5,304,791	0.51	49
	Week to month	0.04	13,277,532	0.97	3
	Week to 9 months	0.19	12,319,662	0.85	15
	Month to 9 months	0.67	1,529,810	0.51	49
Loose Sand	Pre-shake to week	0.21	1,795,715	0.83	17
	Pre-shake to month	0.15	1,557,948	0.88	12
	Pre-shake to 9 months	0.19	1,430,572	0.85	15
	Week to month	0.07	1,542,715	0.94	6
	Week to 9 months	0.04	1,423,730	0.96	4
	Month to 9 months	0.04	1,166,455	0.97	3
Dense Sand	Pre-shake to week	0.10	12,899,134	0.92	8
	Pre-shake to month	0.04	14,157,742	0.97	3
	Pre-shake to 9 months	0.29	12,820,209	0.77	23
	Week to month	0.06	12,863,867	0.95	5
	Week to 9 months	0.20	11,533,972	0.84	16
	Month to 9 months	0.26	13,030,244	0.79	21
Loose Gravelly Sand	Pre-shake to week	0.60	9,724	0.55	45
	Pre-shake to month	0.91	13,065	0.36	64
	Pre-shake to 9 months	0.71	32,789	0.48	52
	Week to month	0.36	389,741	0.72	28
	Week to 9 months	0.27	1,020,452	0.79	21
	Month to 9 months	0.02	1,711,092	0.98	2

Table 5-6 (Continued). Results of two-tailed hypothesis test comparisons using mean and standard deviation from block kriging analysis.

Southwest Layer	Comparison	Test Value, t	Degrees of Freedom, df	P-value, p	Confidence of Difference (%)
Clay	Pre-shake to week	0.03	20,337,972	0.98	2
	Pre-shake to month	0.02	18,241,602	0.98	2
	Pre-shake to 9 months	0.24	13,589,812	0.81	19
	Week to month	0.01	11,720,252	0.99	1
	Week to 9 months	0.37	7,067,578	0.71	29
	Month to 9 months	0.43	4,967,766	0.67	33
Loose Sand	Pre-shake to week	0.07	1,893,376	0.94	6
	Pre-shake to month	0.08	1,901,802	0.93	7
	Pre-shake to 9 months	0.05	1,724,849	0.96	4
	Week to month	0.20	1,005,228	0.84	16
	Week to 9 months	0.18	822,378	0.85	15
	Month to 9 months	0.05	837,360	0.96	4
Dense Sand	Pre-shake to week	0.21	8,764,149	0.83	17
	Pre-shake to month	0.13	10,366,070	0.89	11
	Pre-shake to 9 months	0.33	7,975,141	0.74	26
	Week to month	0.08	11,214,444	0.94	6
	Week to 9 months	0.10	8,780,449	0.92	8
	Month to 9 months	0.18	10,950,985	0.86	14
Loose Gravelly Sand	Pre-shake to week	0.91	289,550	0.36	64
	Pre-shake to month	0.52	565,678	0.60	40
	Pre-shake to 9 months	0.86	568,613	0.39	61
	Week to month	0.27	742,367	0.79	21
	Week to 9 months	0.03	843,861	0.98	2
	Month to 9 months	0.27	1,674,405	0.78	22

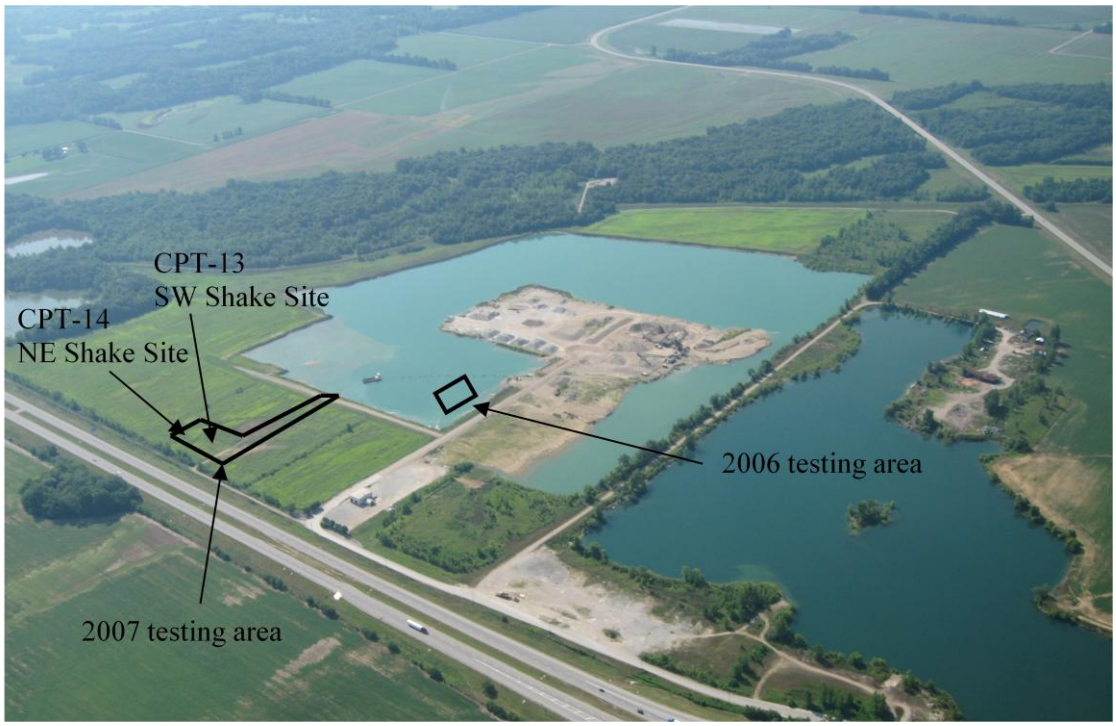

Figure 5-1. Griffin, IN field site showing locations of CPT-13 and CPT-14 (photo courtesy of Mulzer Crushed Stone, Inc.).

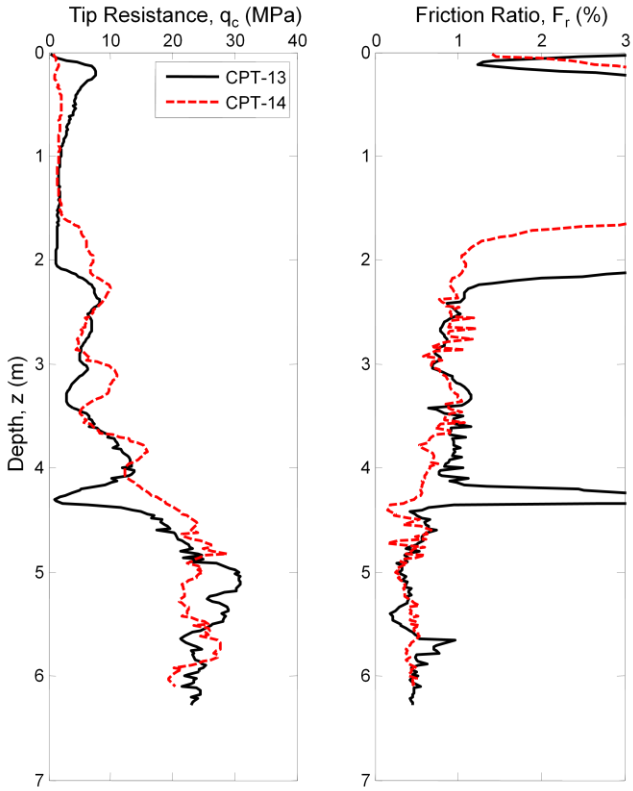

Figure 5-2. Results from CPT-13 (SW shake site) and CPT-14 (NE shake site).

Figure 5-3. (a) Stable PPT and (b) unstable pore pressure transducers and accelerometers in the same cone (photos courtesy of Russell Green).

Figure 5-4. Pilot cone pushed ahead of instrumentation.

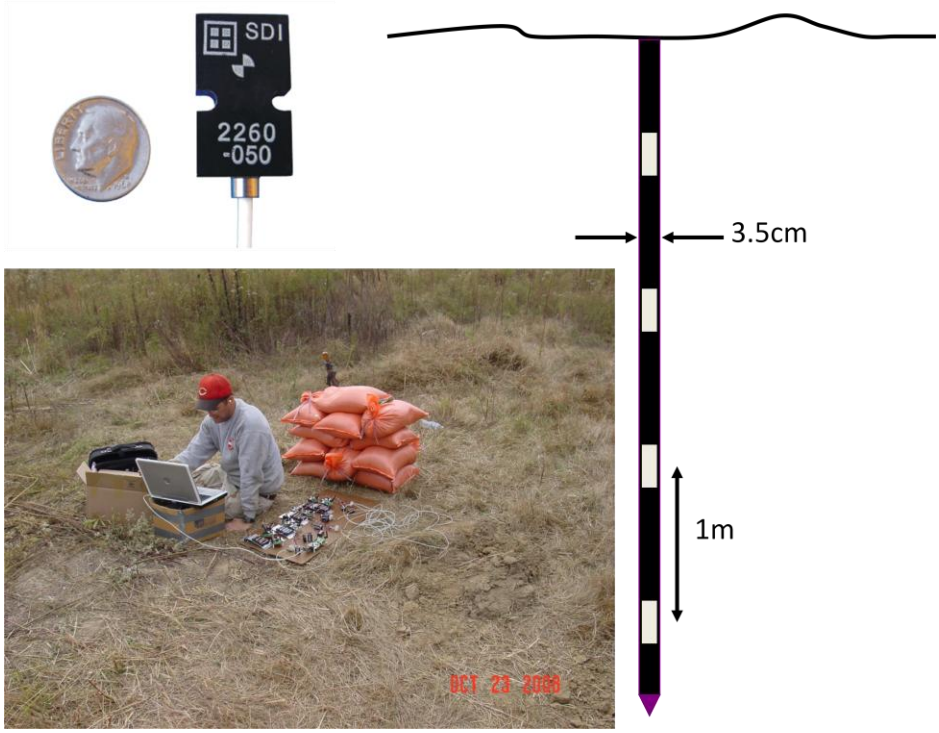

Figure 5-5. Down-hole tube set-up (upper right photo from Silicon Designs, lower left photo courtesy of Russell Green).

Figure 5-6. Cross-hole source rod.

Figure 5-7. University of Texas data acquisition.

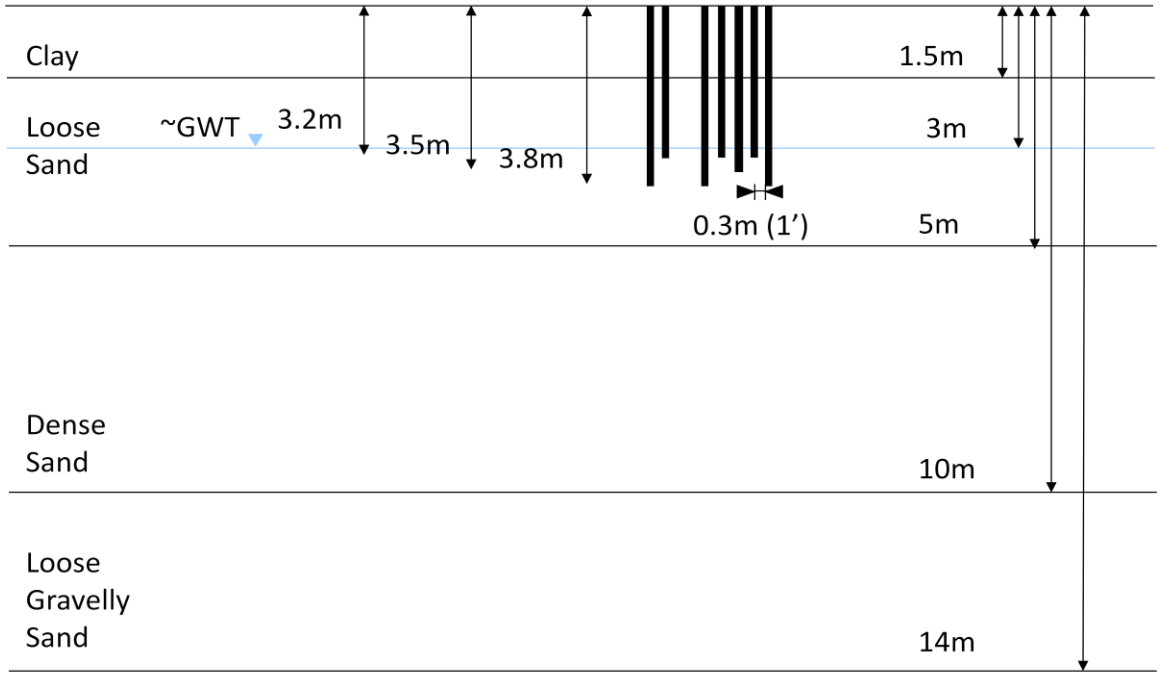

Figure 5-8. Instrumentation layout at the NE shake site.

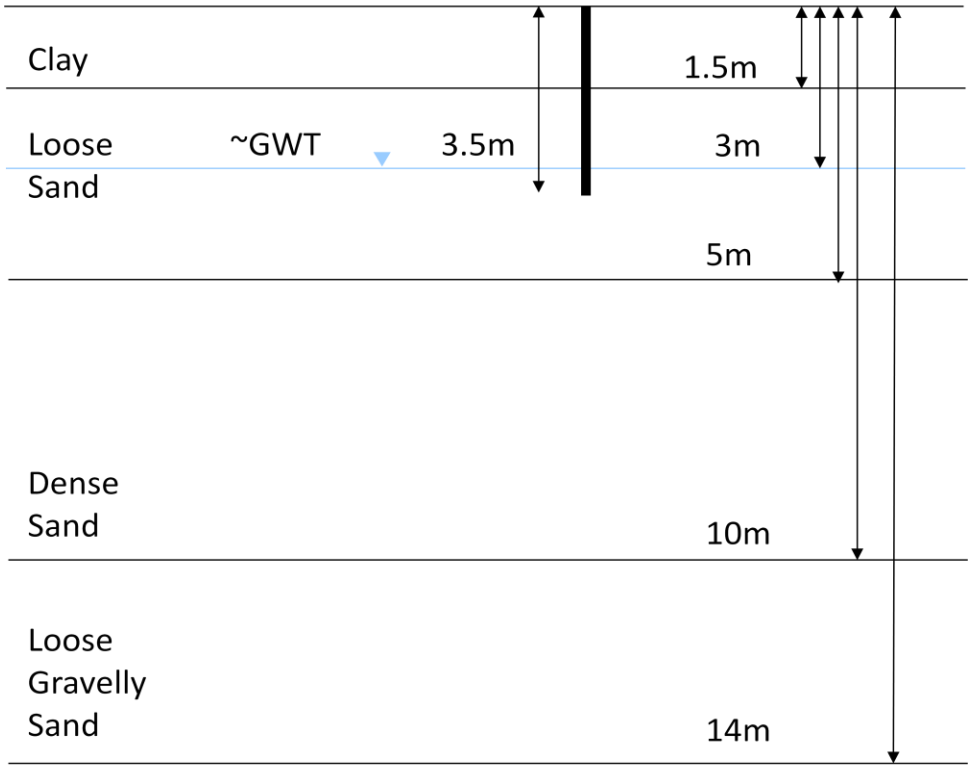

Figure 5-9. Instrumentation layout at the SW shake site.

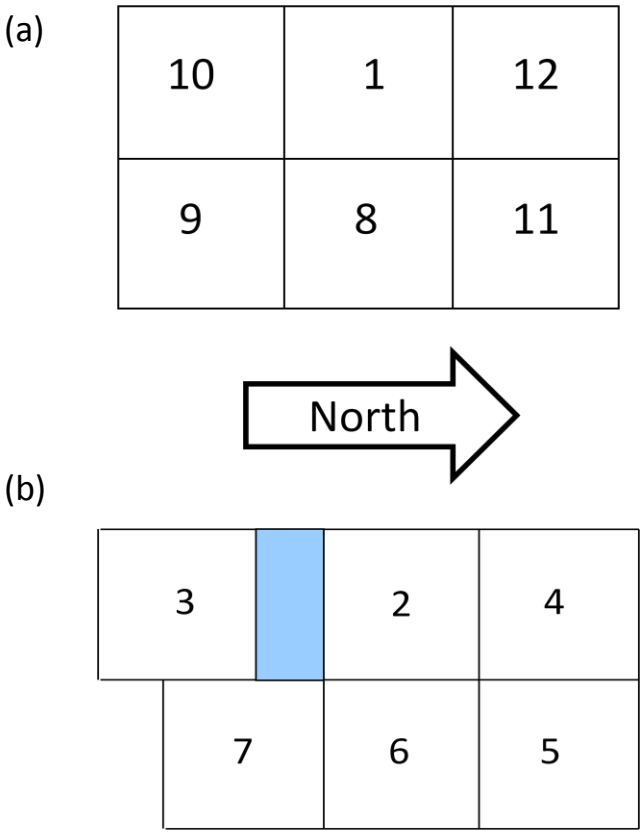

Figure 5-10. Order of shake points at the (a) SW shake site and (b) NE shake site. The shaded area shows the location of instrumentation. Each shake point is 7.5’ square.

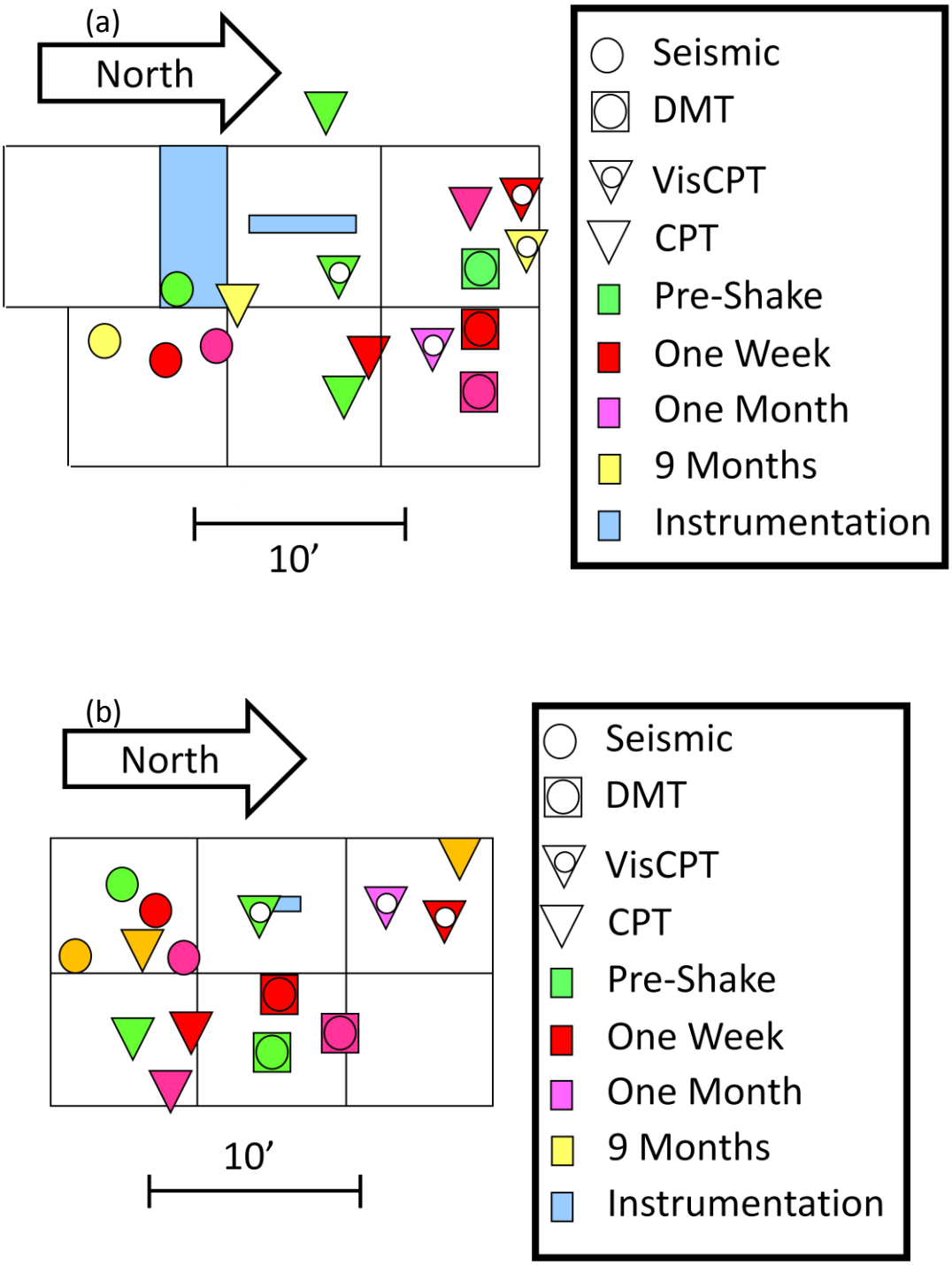

Figure 5-11. Testing layout at the (a) NE shake site and (b) SW shake site.

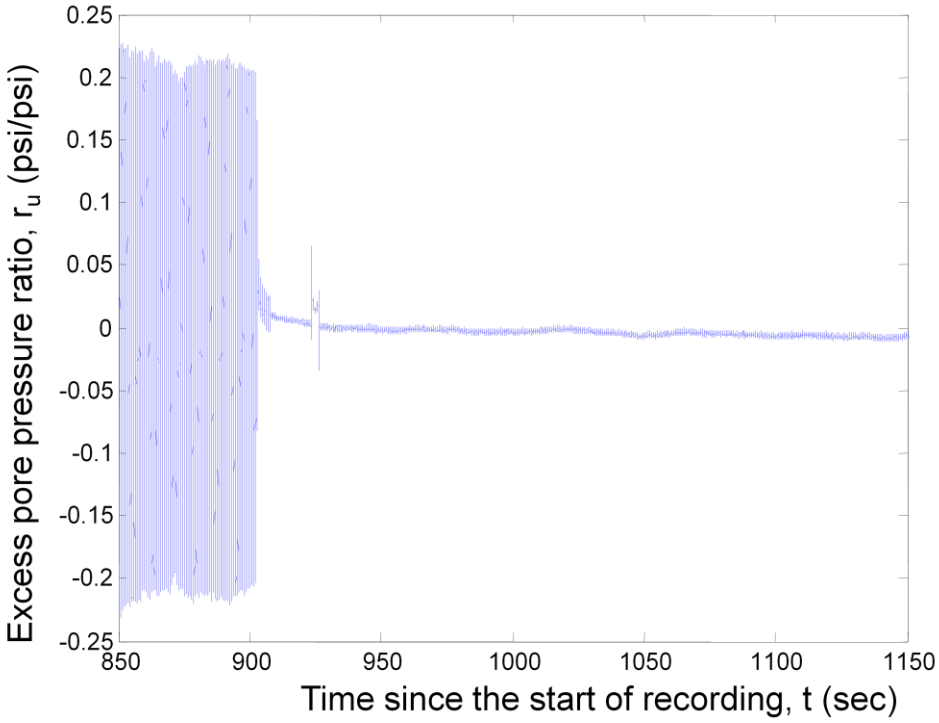

Figure 5-12. Response of the stable PPT to shaking at the NE shake site.

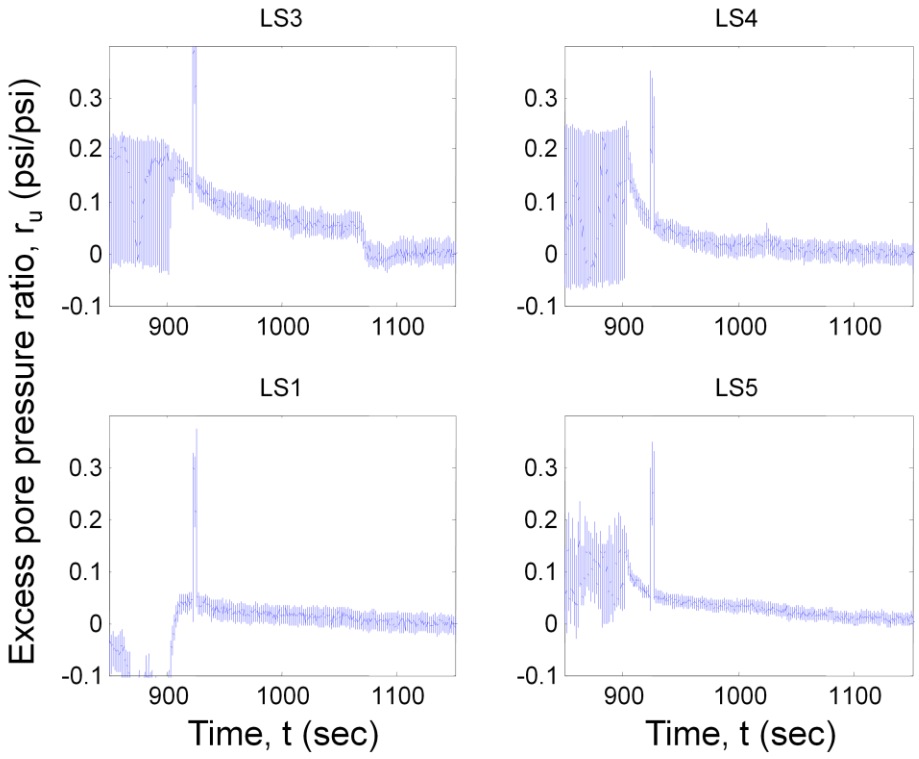

Figure 5-13. Response of miniture PPTs at the NE shake site.

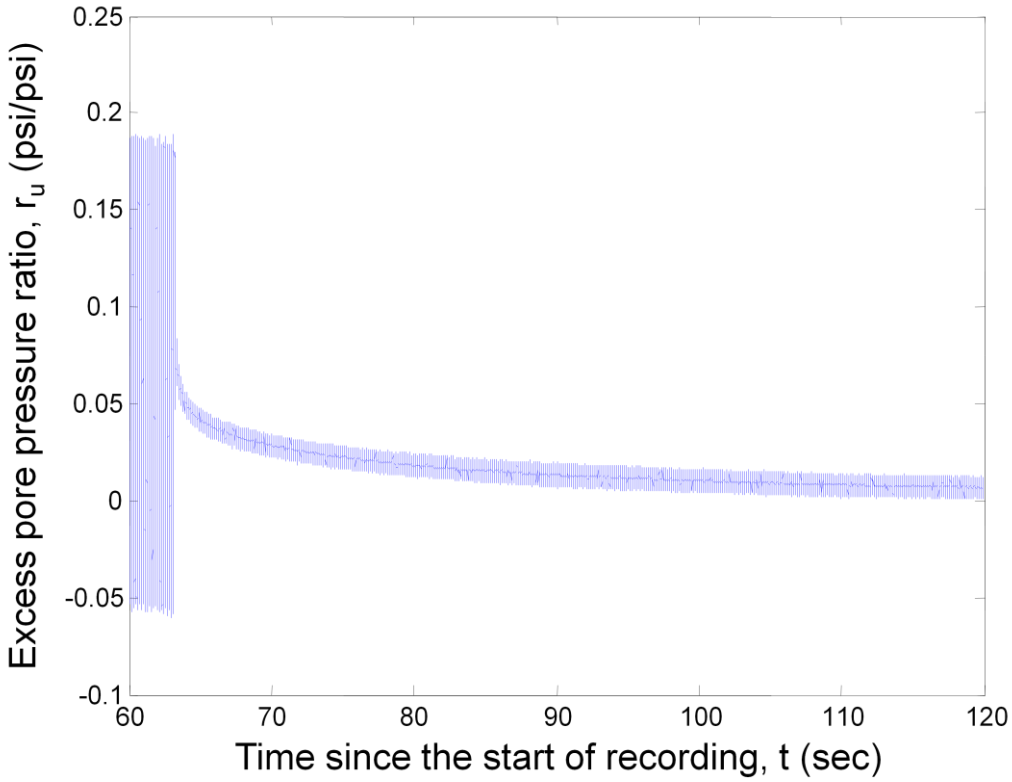

Figure 5-14. Response of the stable PPT to shaking at the SW shake site.

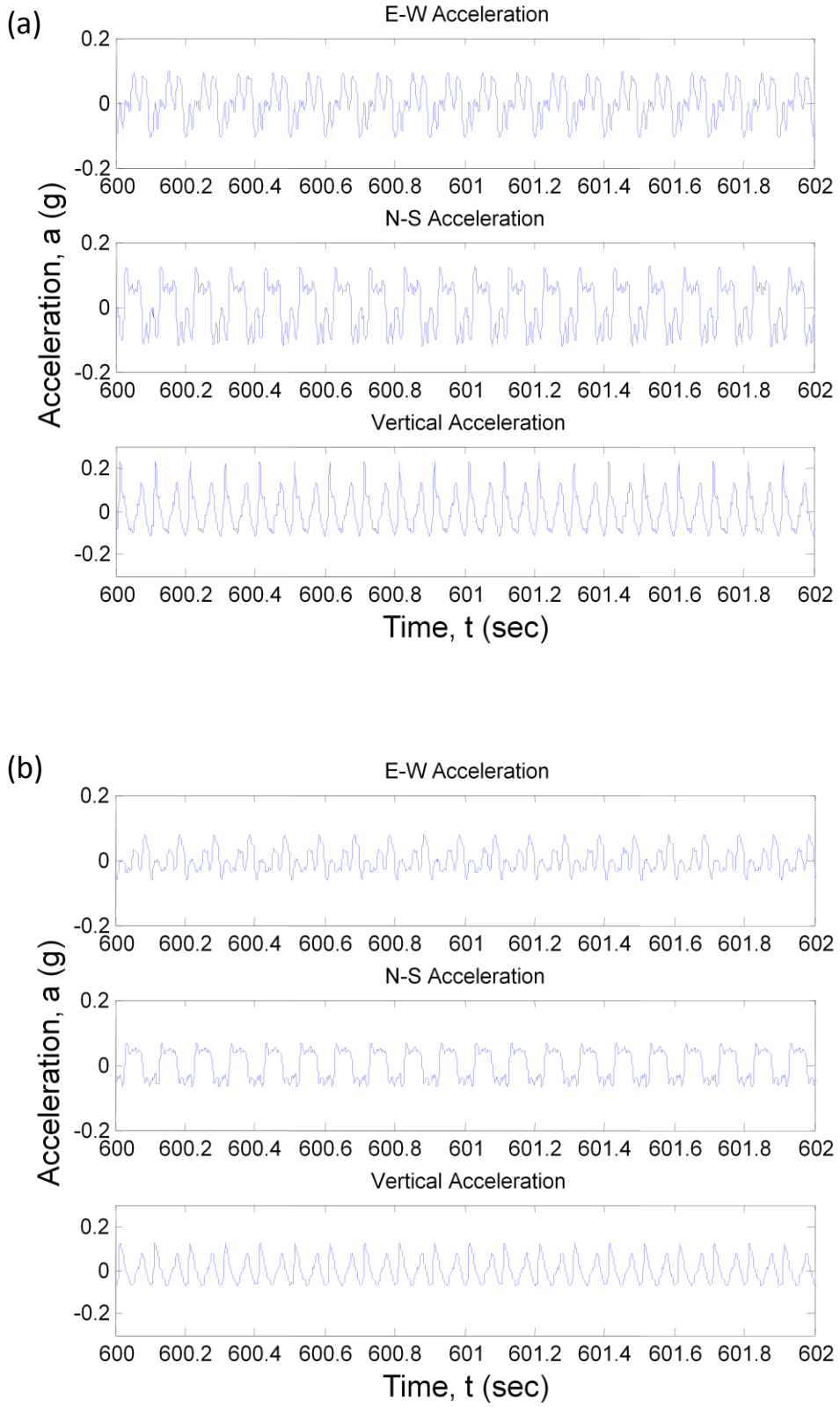

Figure 5-15. Response of the (a) shallow and (b) deep accelerometers to shaking at the NE shake site.

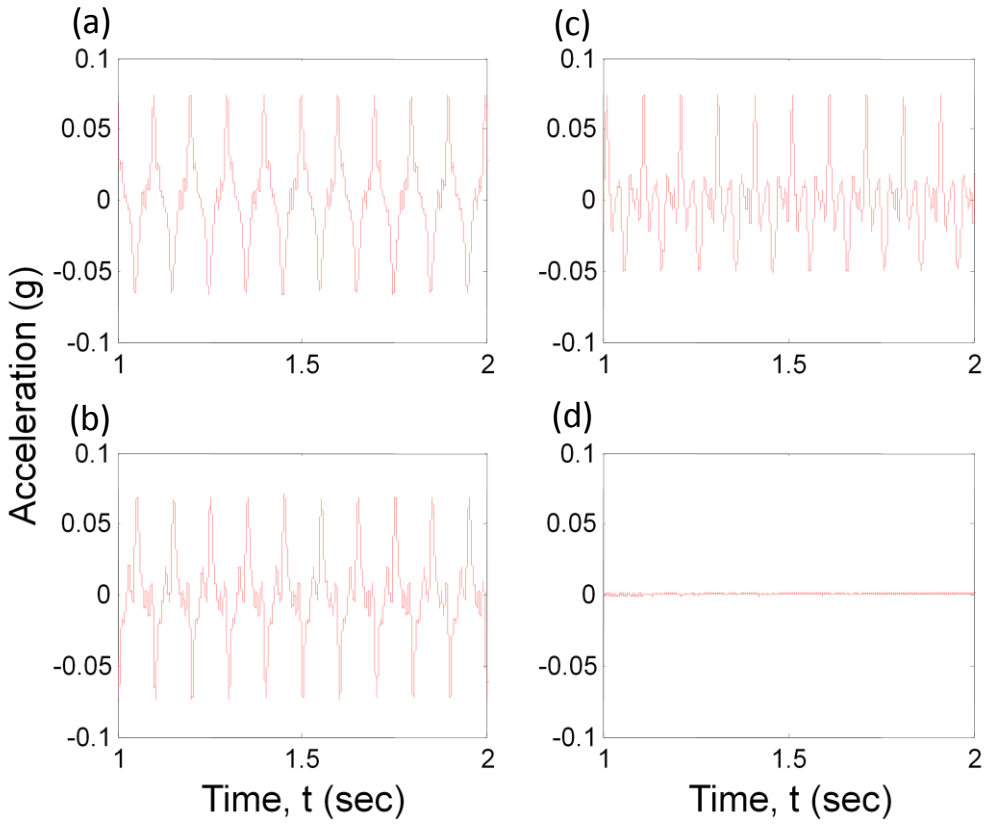

Figure 5-16. Response of the down-hole tube accelerometers to shaking at the NE shake site at (a) 2 m, (b) 3 m, (c) 4 m, and (d) 5 m.

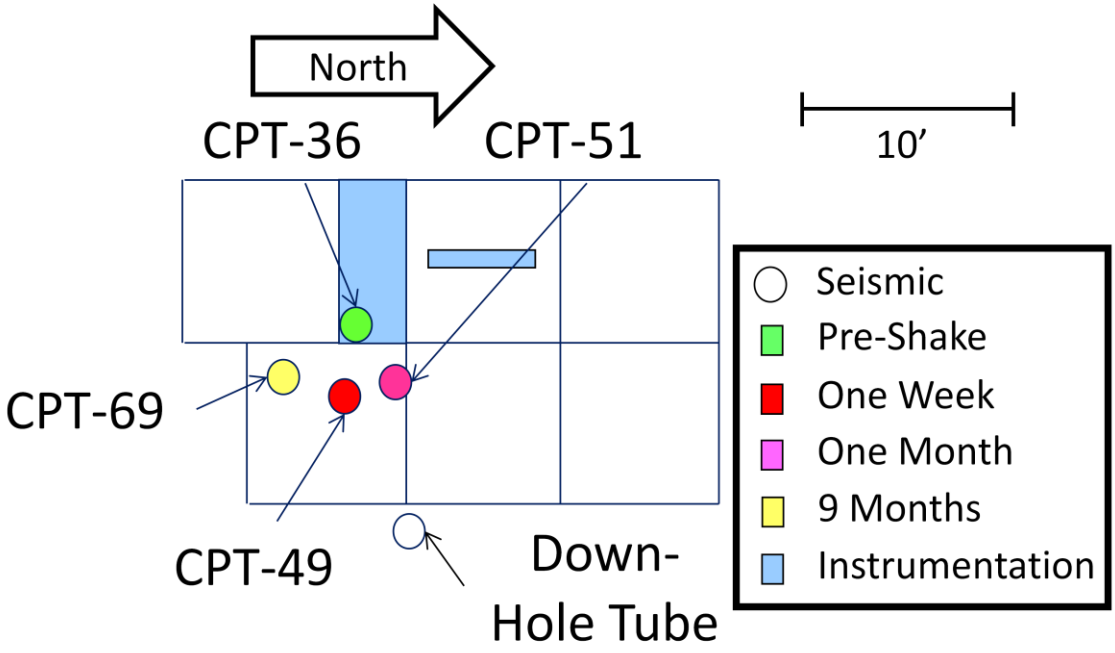

Figure 5-17. Location of SCPTs at the NE shake site.

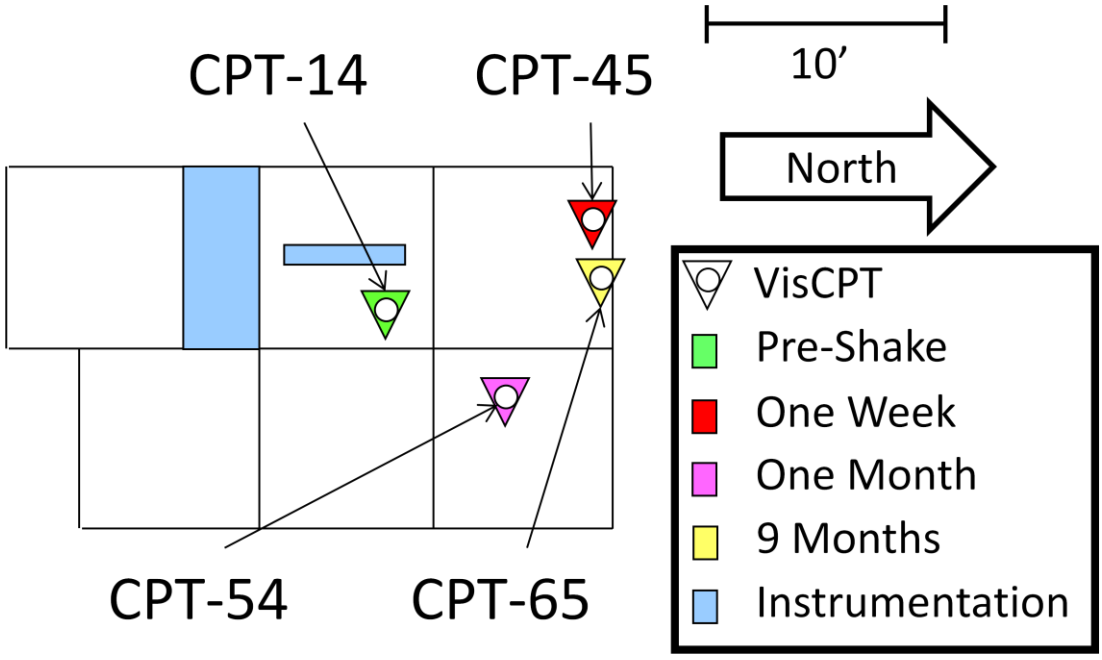

Figure 5-18. Location of VisCPTs at the NE shake site.

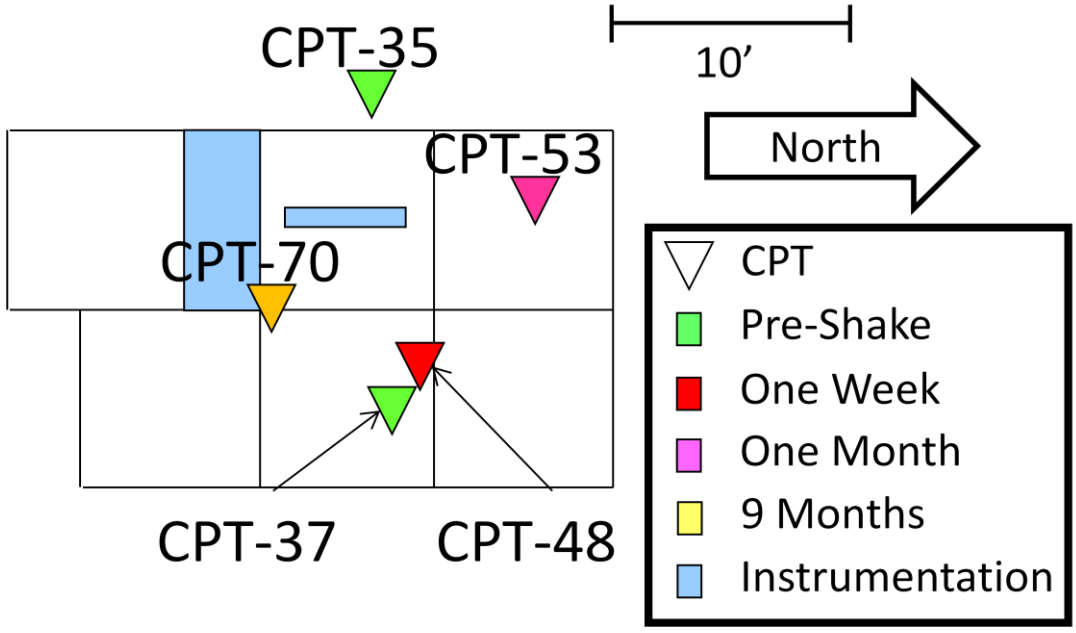

Figure 5-19. Location of CPTs at the NE shake site.

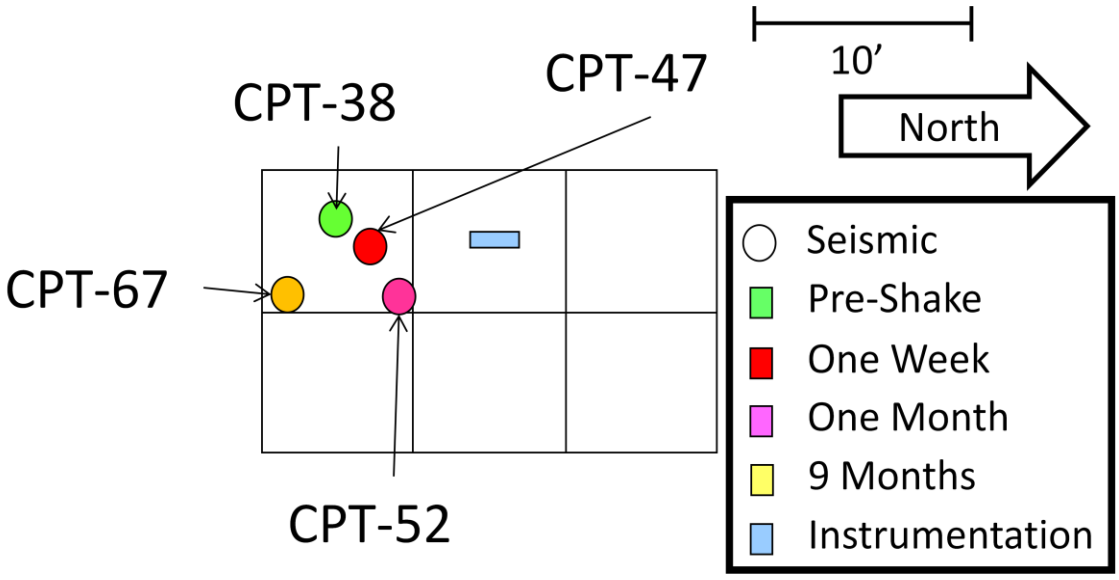

Figure 5-20. Location of SCPTs at the SW shake site.

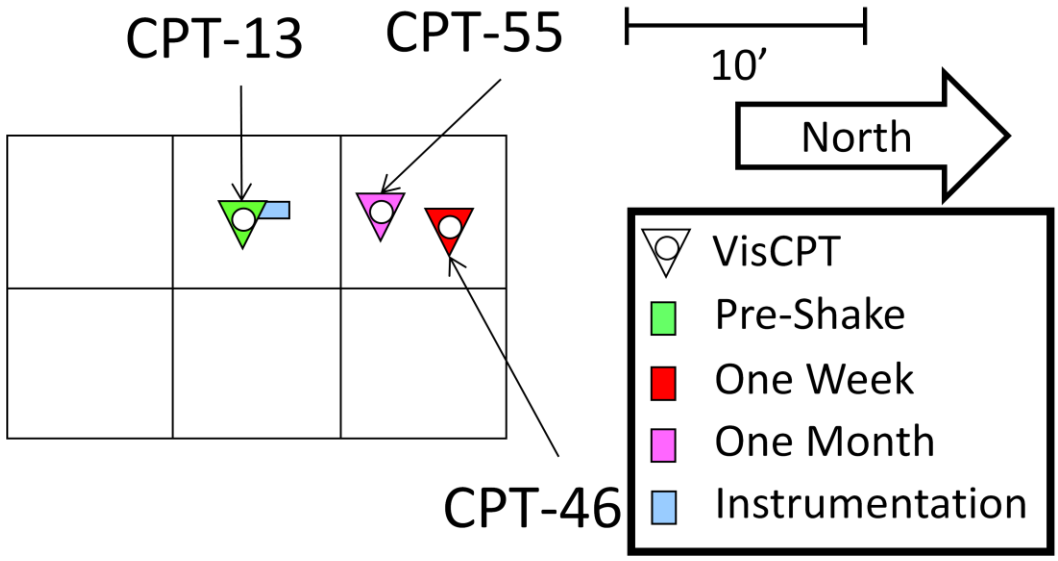

Figure 5-21. Location of VisCPTs at the SW shake site.

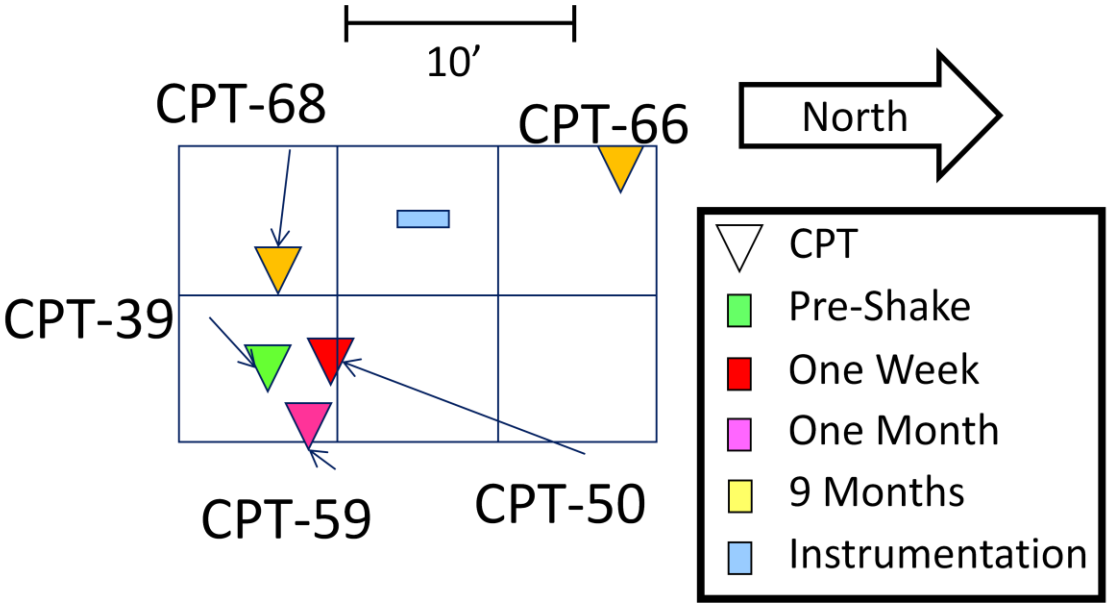

5-22. Location of CPTs at the SW shake site.

(a)

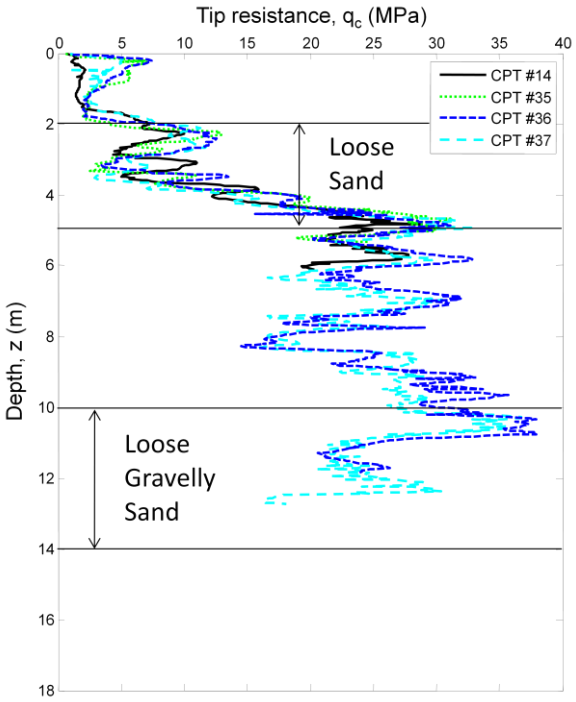

(b)

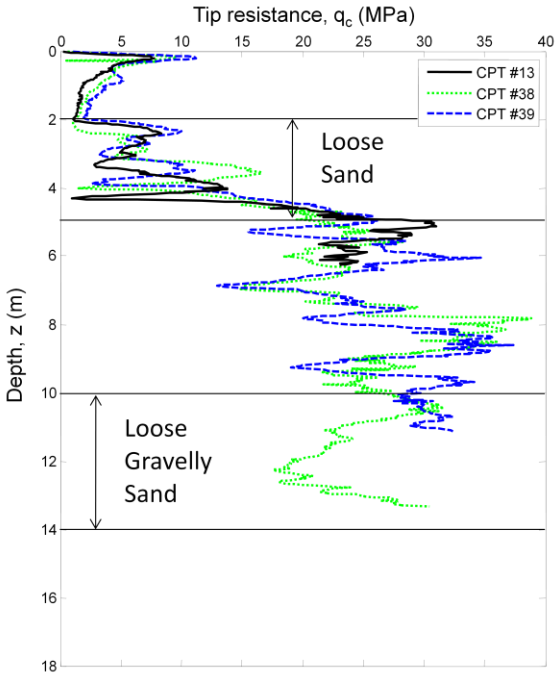

Figure 5-23. Results of pre-shake testing at (a) the NE shake site and (b) the SW shake site.

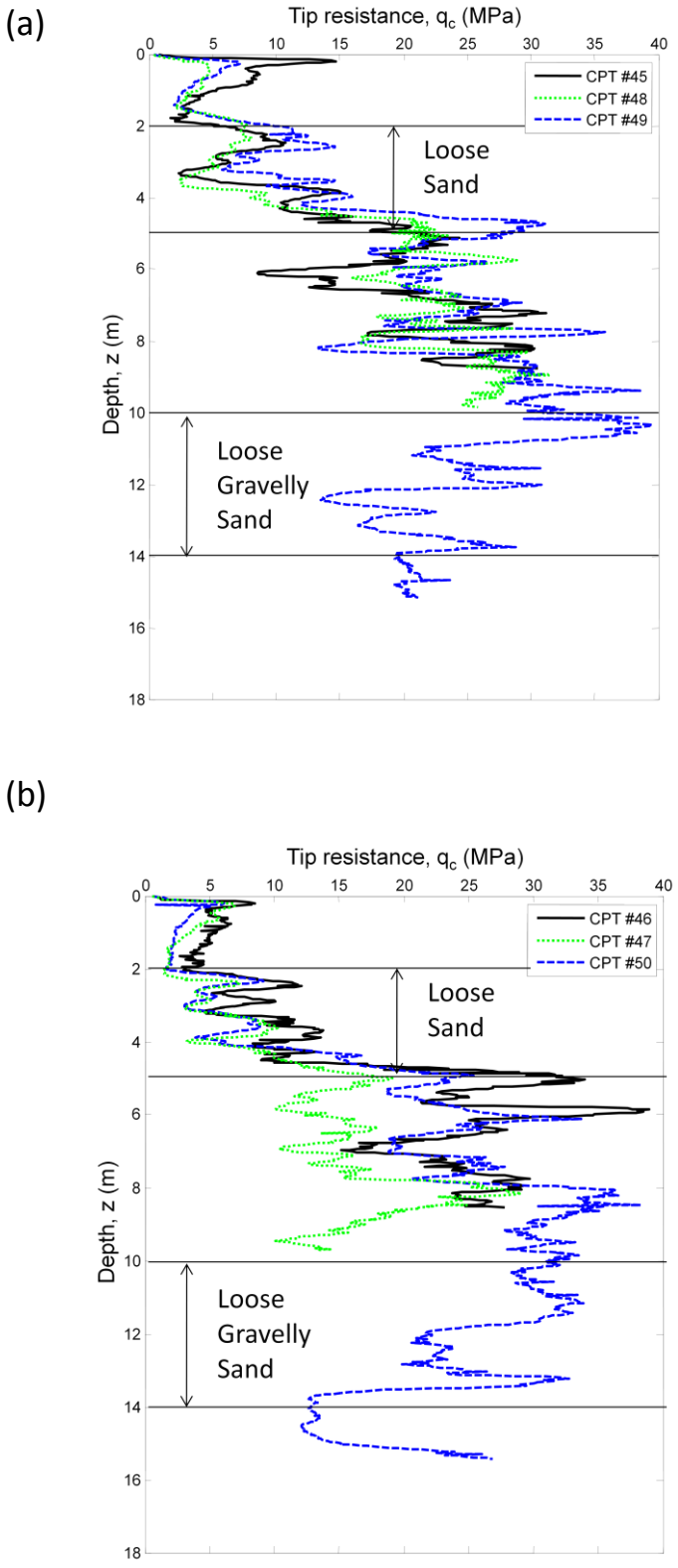

Figure 5-24. Results of one week testing at (a) the NE shake site and (b) the SW shake site.

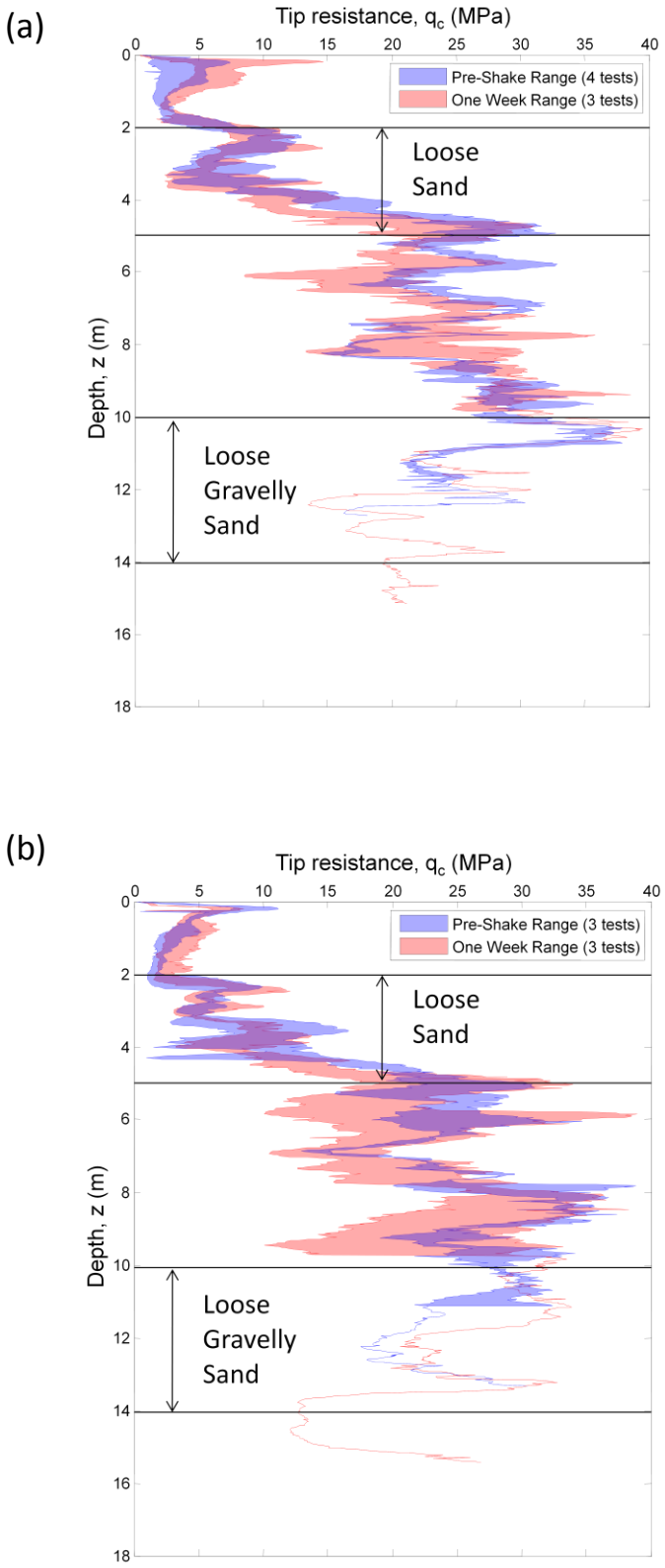

Figure 5-25. Range of pre-shake testing compared to range of one week testing at (a) the NE shake site and (b) the SW shake site.

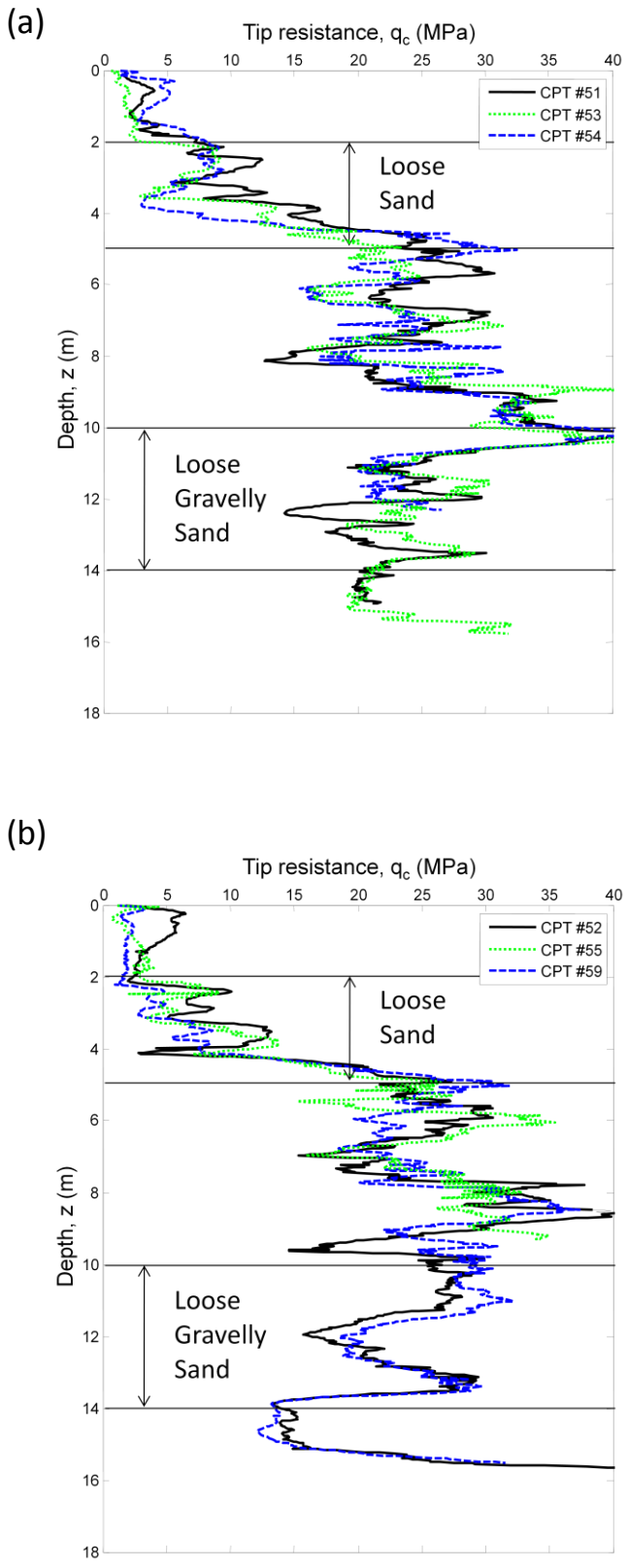

Figure 5-26. Results of one month testing at (a) the NE shake site and (b) the SW shake site.

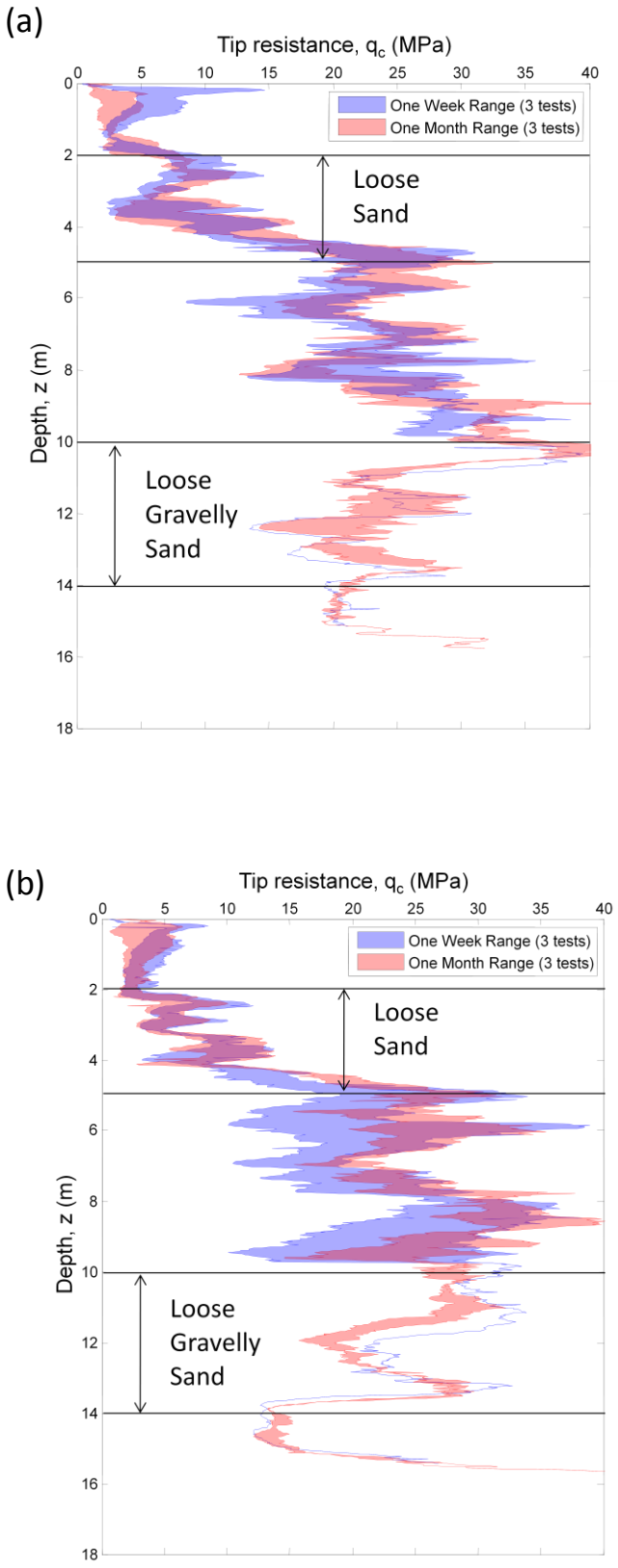

Figure 5-27. Range of one week testing compared to range of one month testing at (a) the NE shake site and (b) the SW shake site.

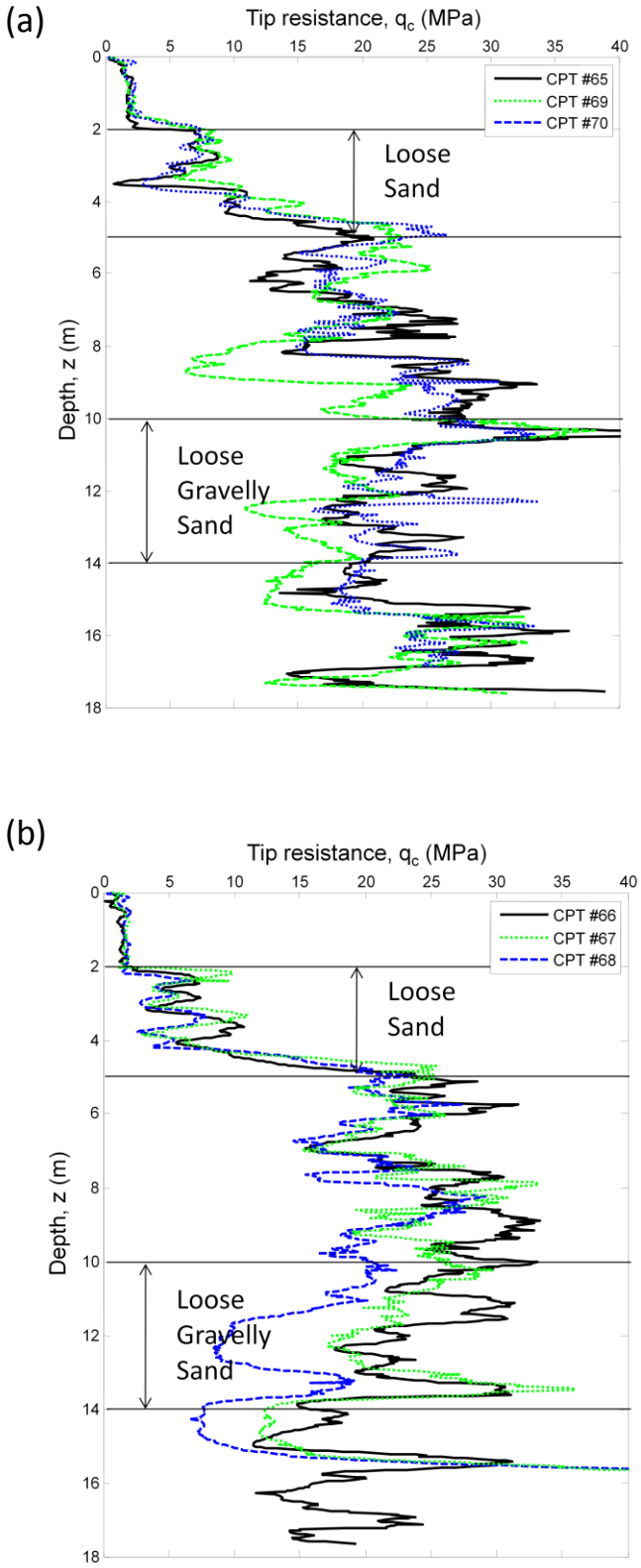

Figure 5-28. Results of nine month testing at (a) the NE shake site and (b) the SW shake site.

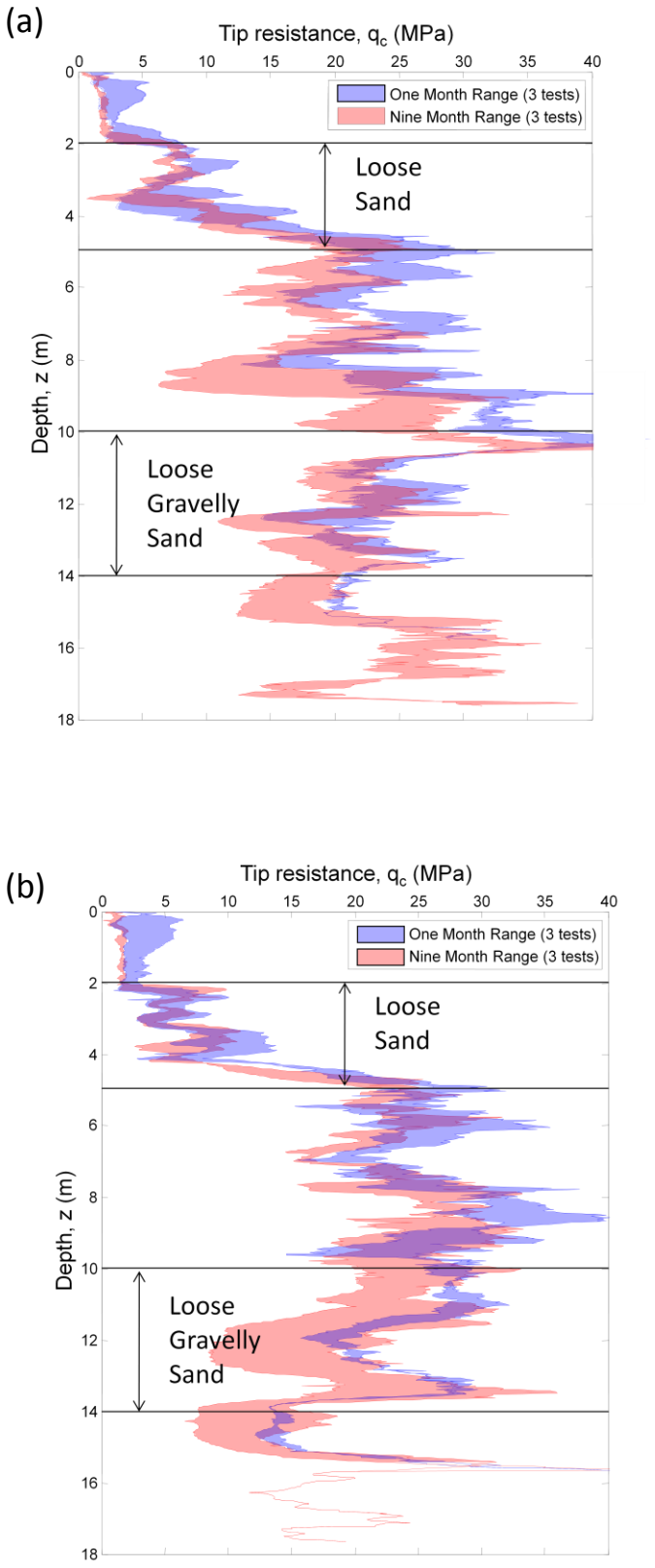

Figure 5-29. Range of one month testing compared to range of nine month testing at (a) the NE shake site and (b) the SW shake site.

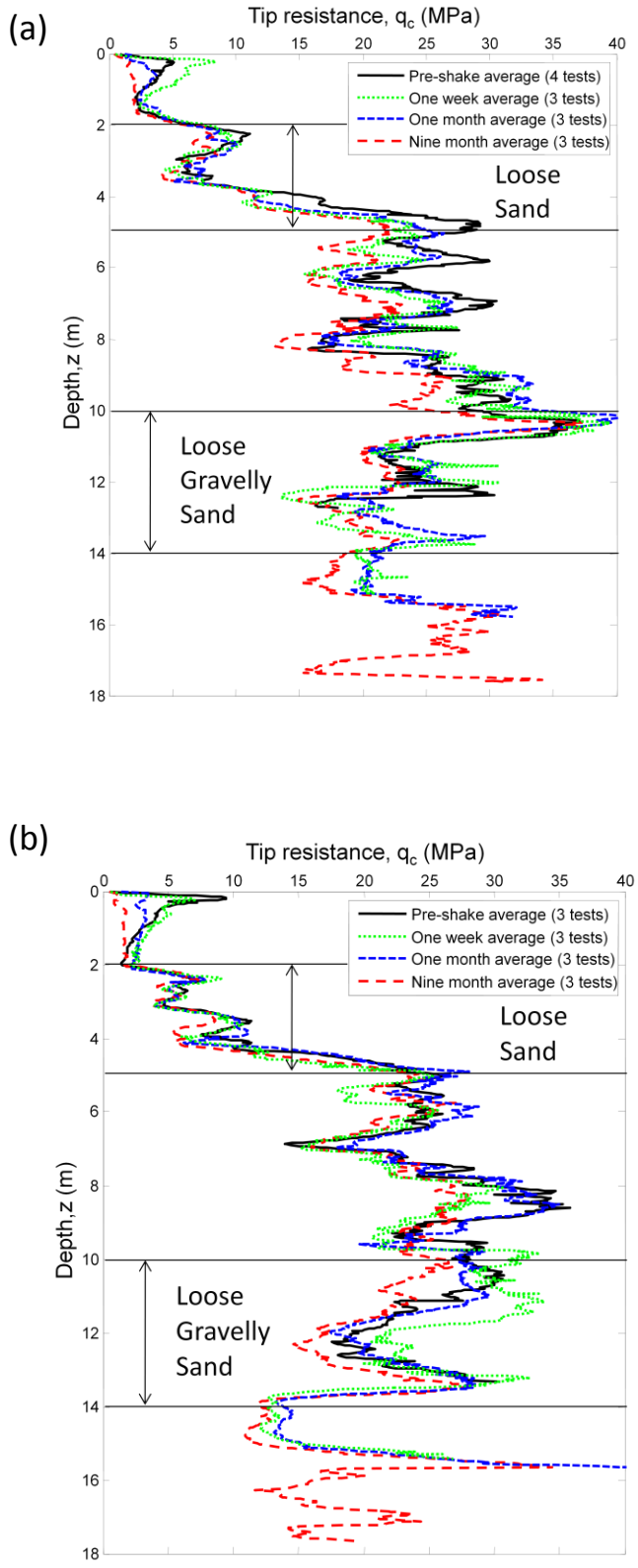

Figure 5-30. Mean tip resistance from each of the testing intervals at (a) the NE shake site and (b) the SW shake site.

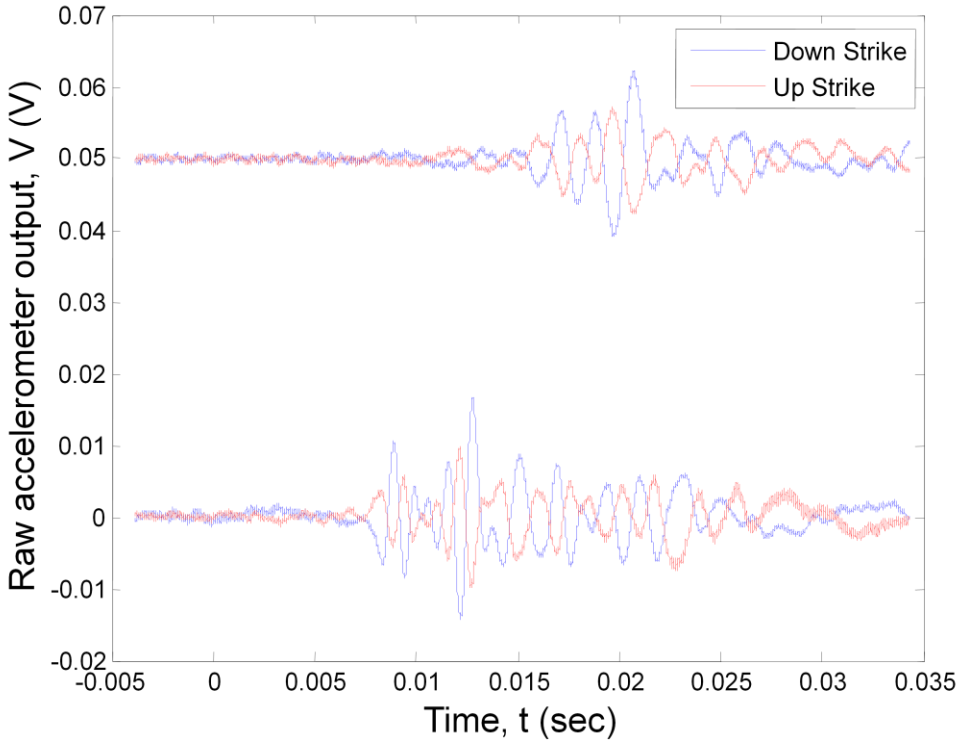

Figure 5-31. P-wave arrival from the cross-hole system.

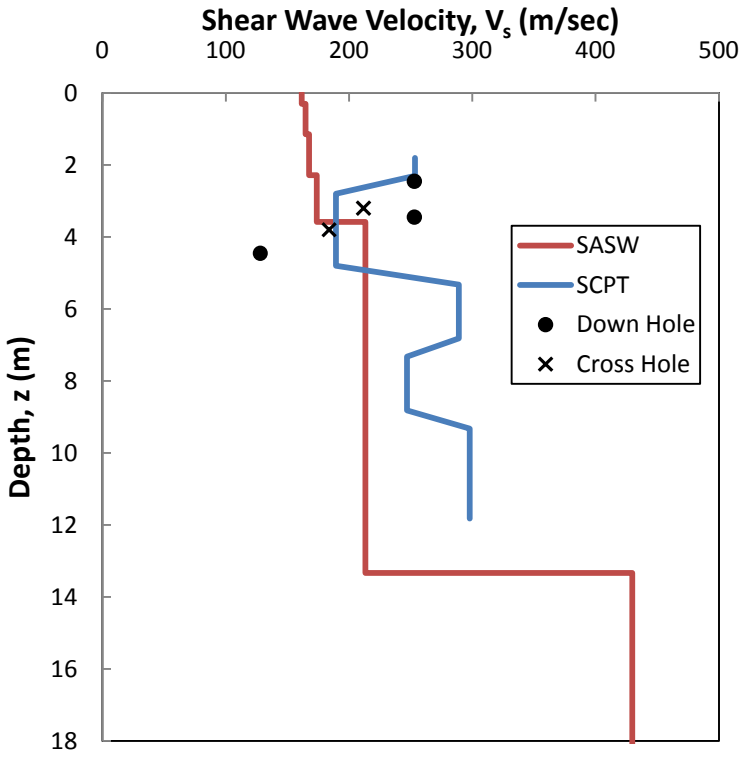

Figure 5-32. Pre-shake V_s from SASW, SCPT, down hole testing and cross hole testing.

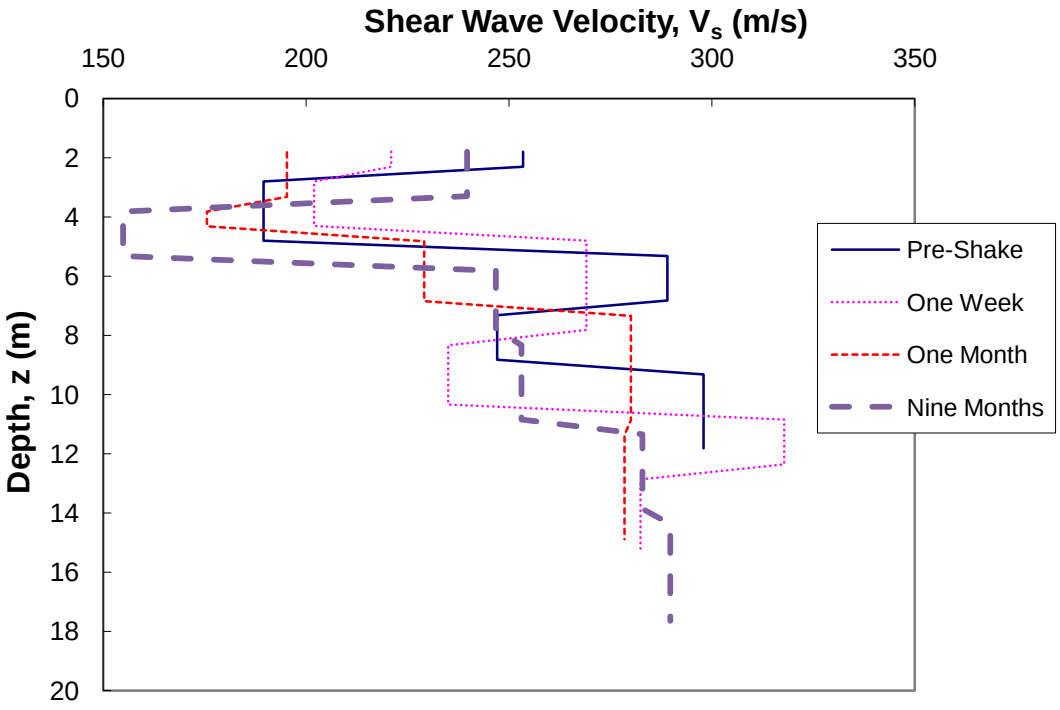

Figure 5-33. Shear wave velocity from SCPTs at the NE shake site.

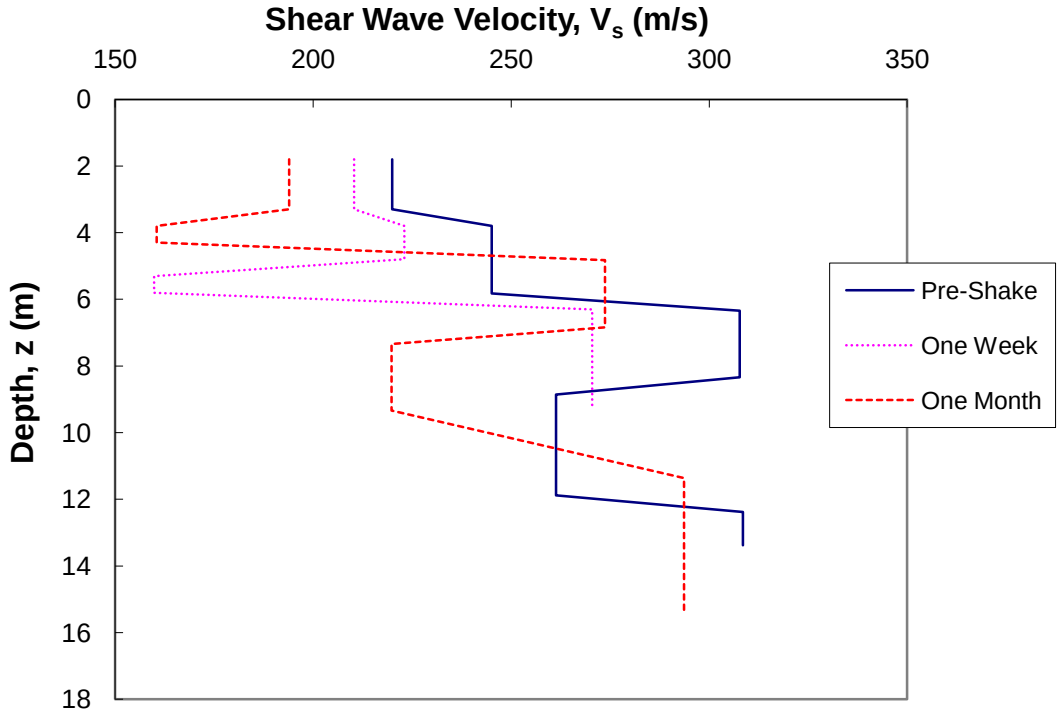

Figure 5-34. Shear wave velocity from SCPTs at the SW shake site.

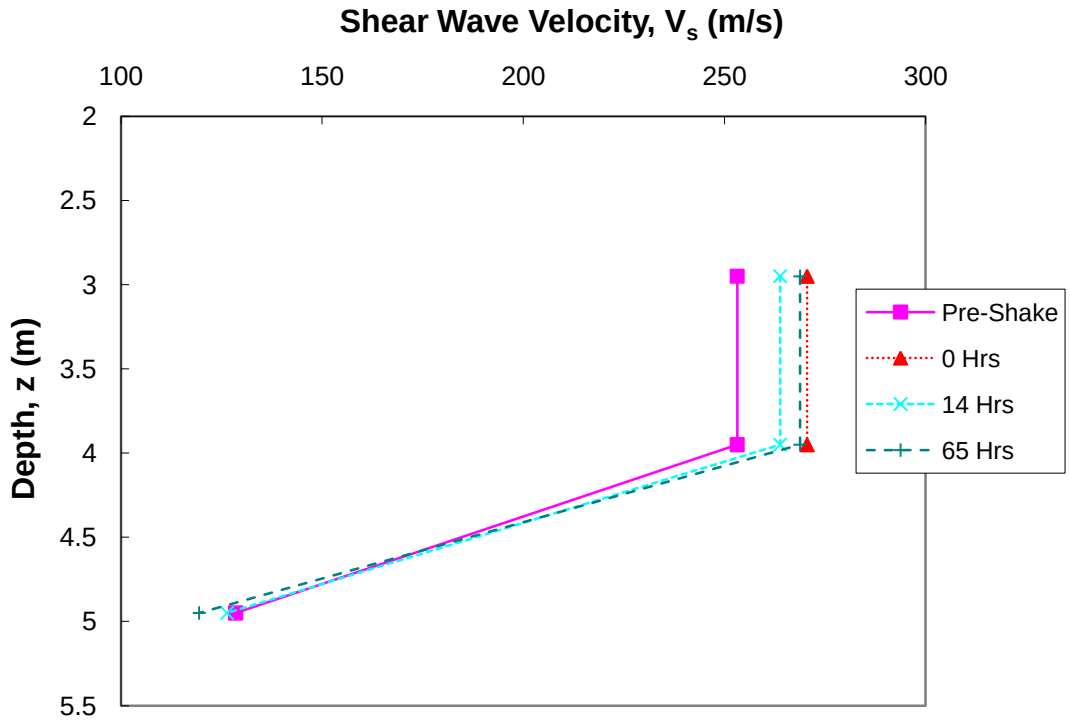

Figure 5-35. Shear wave velocity from the down-hole tube at the NE shake site.

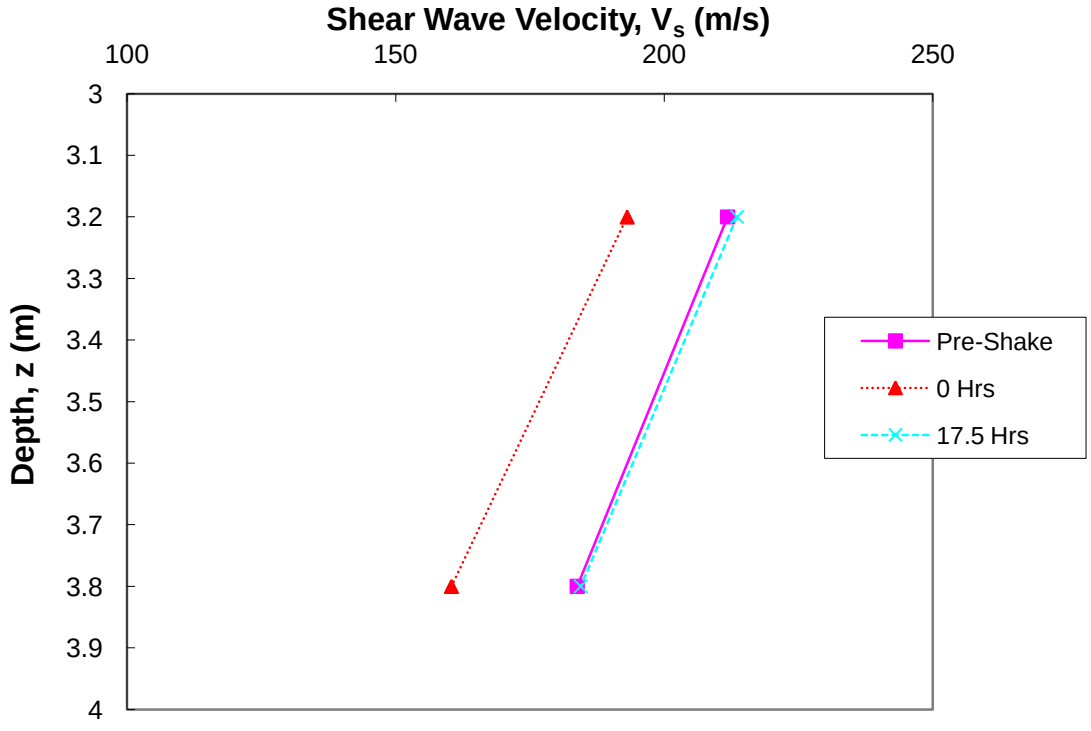

Figure 5-36. Shear wave velocity from cross-hole system at the NE shake site.

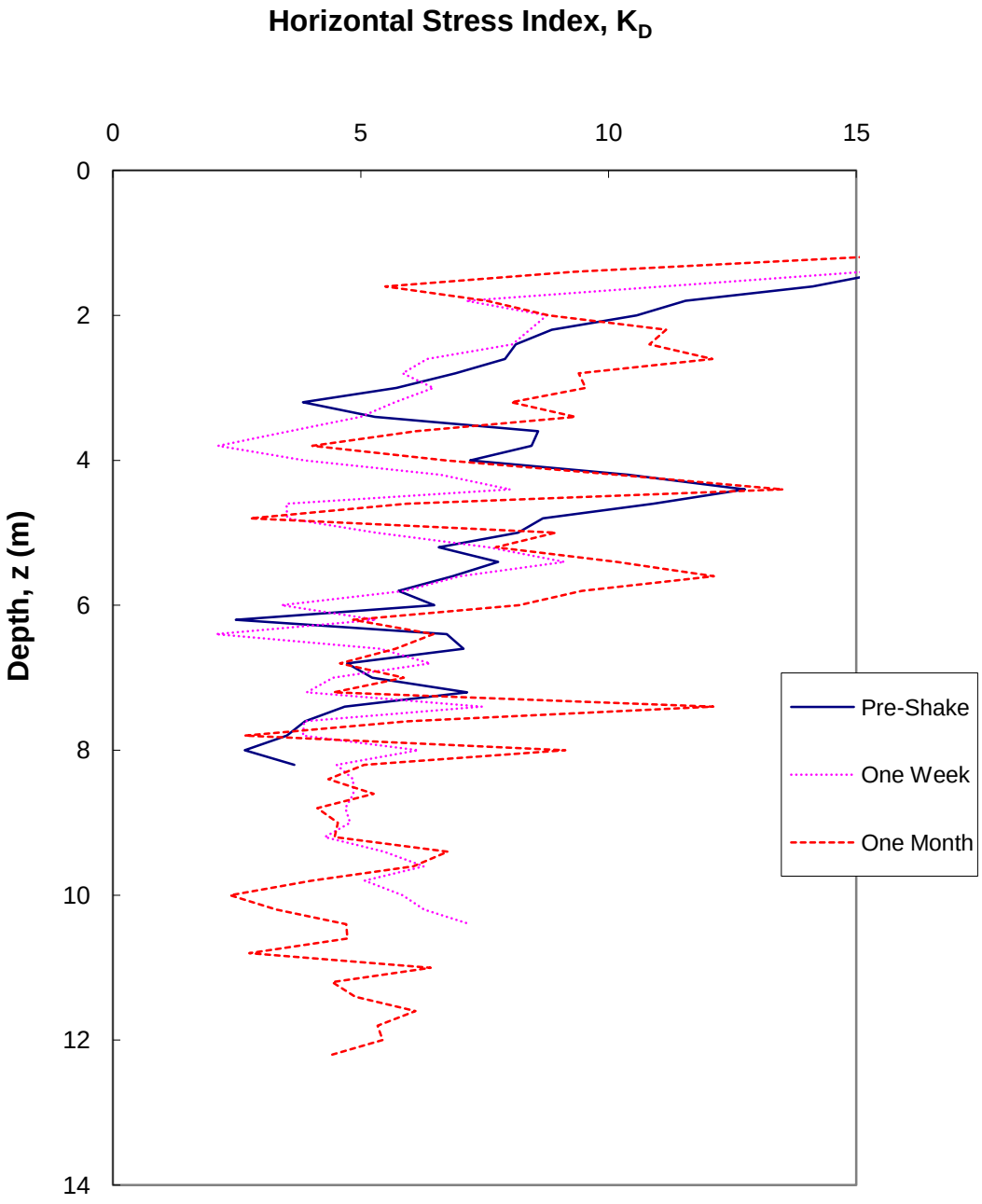

5-37. Horizontal stress index from testing at the NE shake site.

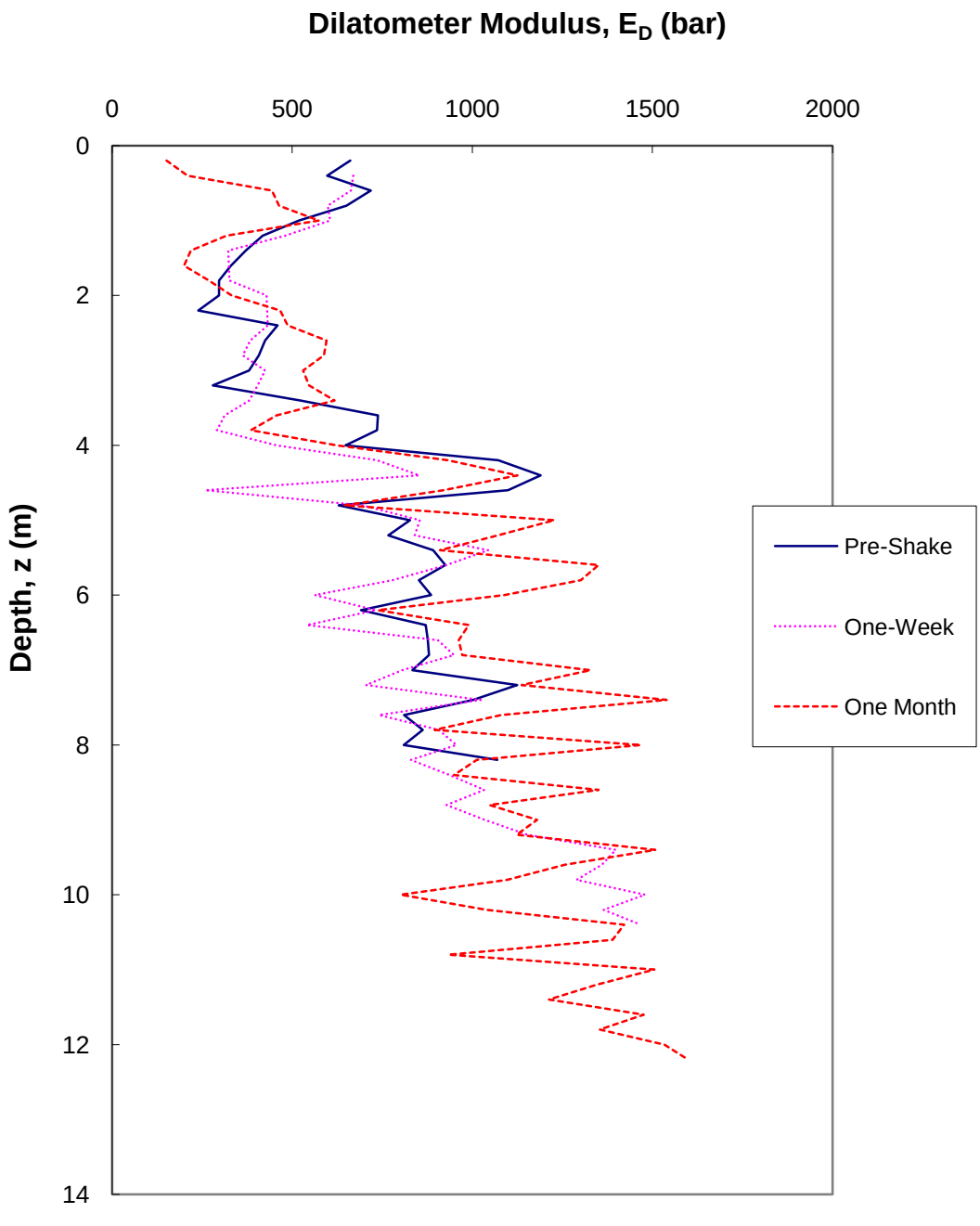

Figure 5-38. Dilatometer modulus from testing at the NE shake site.

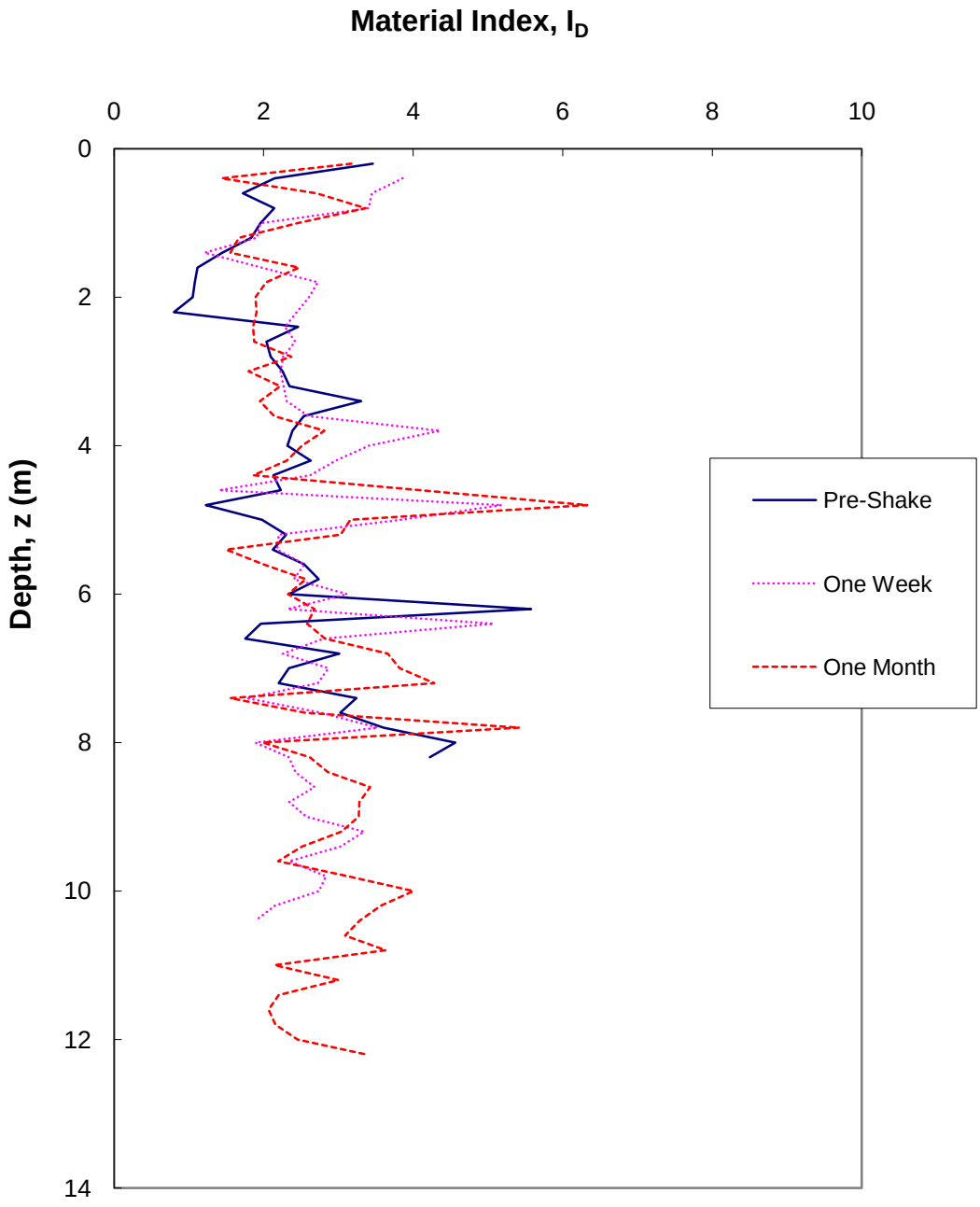

Figure 5-39. Material index from testing at the NE shake site.

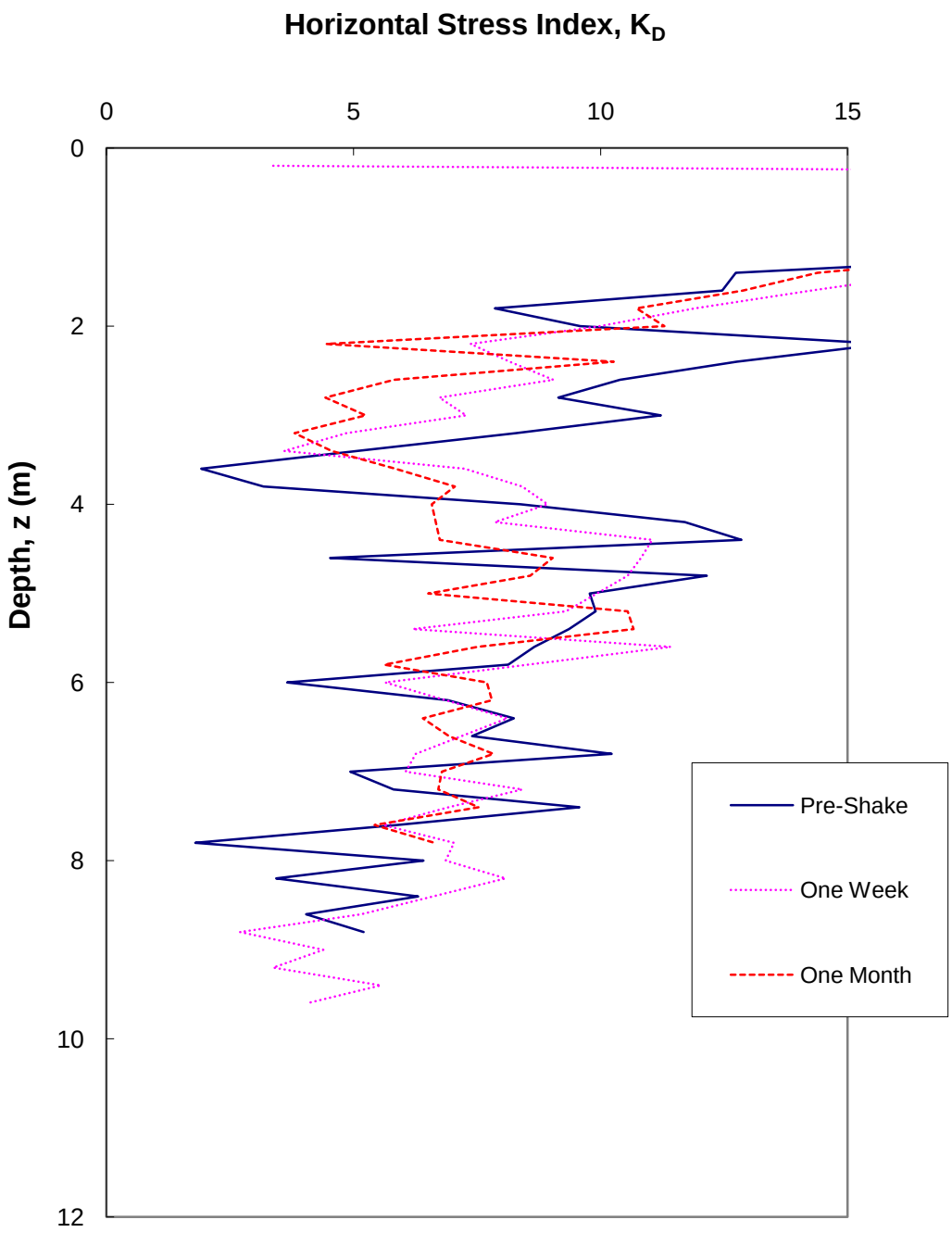

Figure 5-40. Horizontal stress index from testing at the SW shake site.

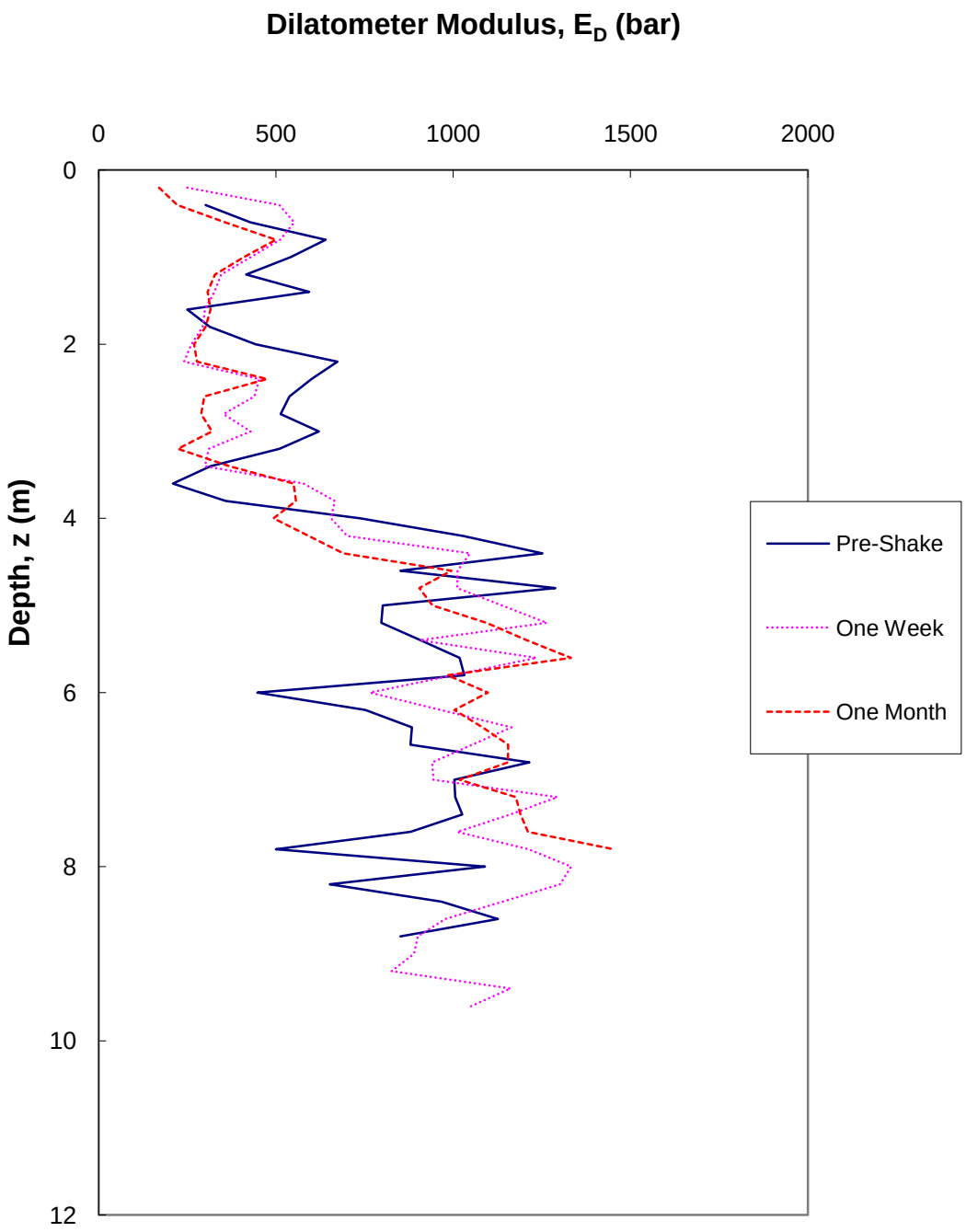

Figure 5-41. Dilatometer modulus from testing at the SW shake site.

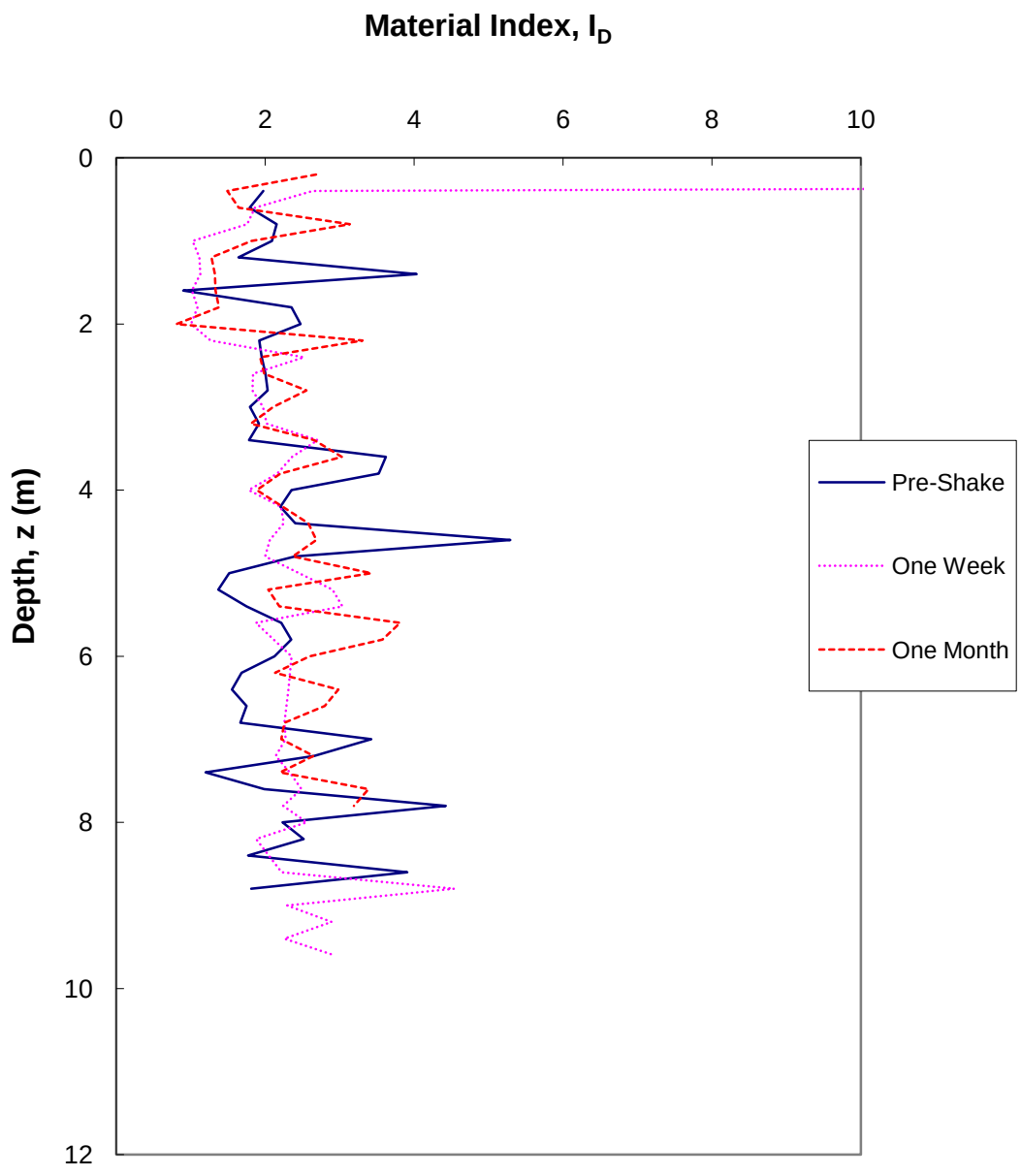

Figure 5-42. Material index from testing at the SW shake site.

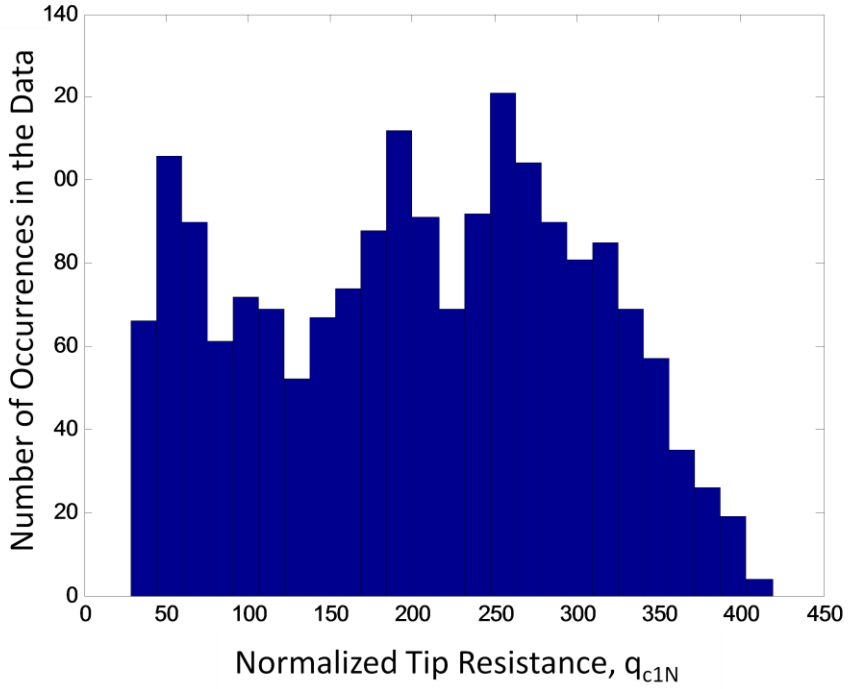

Figure 5-43. Histogram of all CPT normalized tip resistance from the NE shake site.

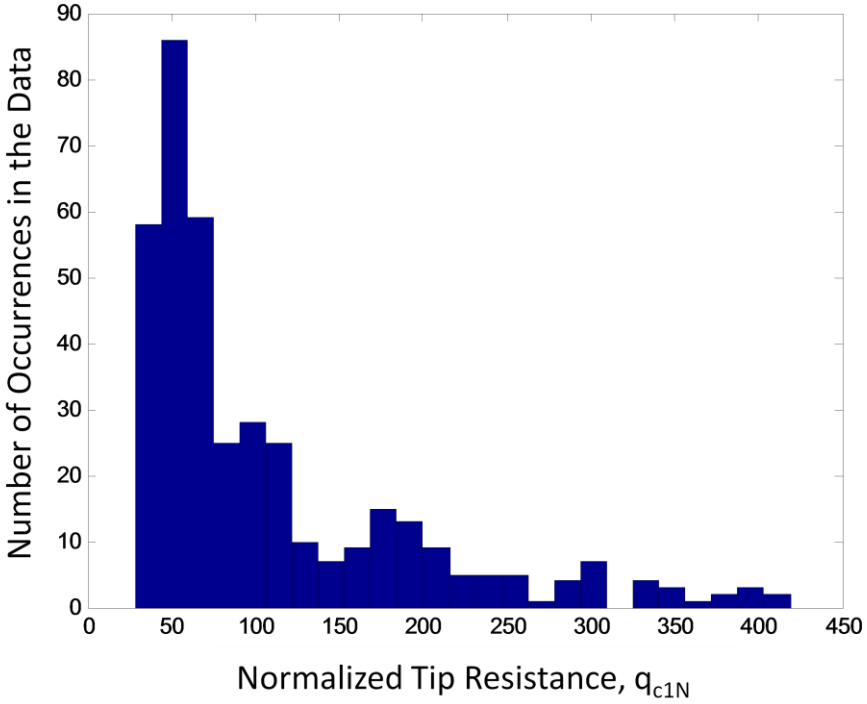

Figure 5-44. Histogram of CPT normalized tip resistance from the clay layer at the NE shake site.

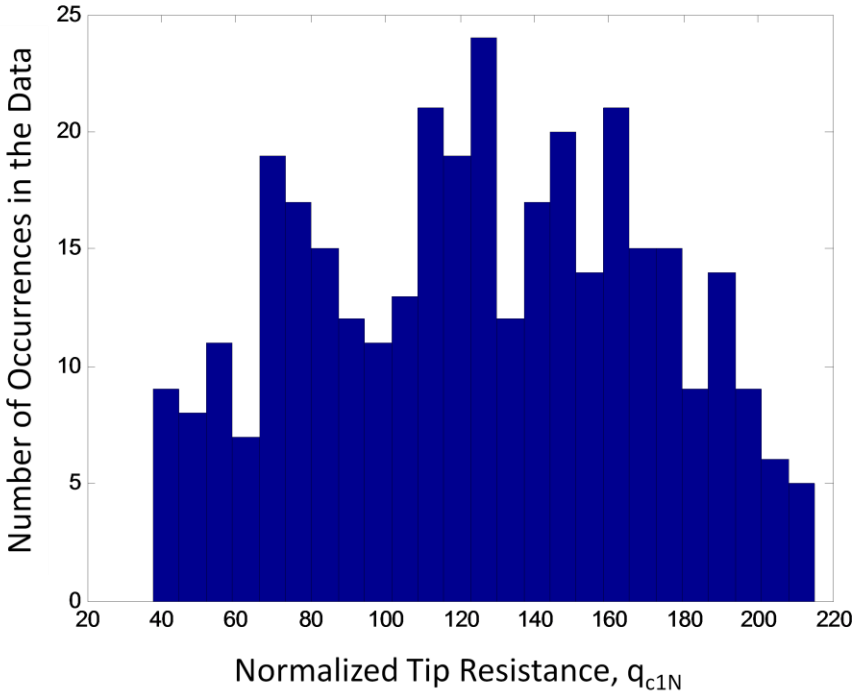

Figure 5-45. Histogram of CPT normalized tip resistance from the loose sand layer at the NE shake site.

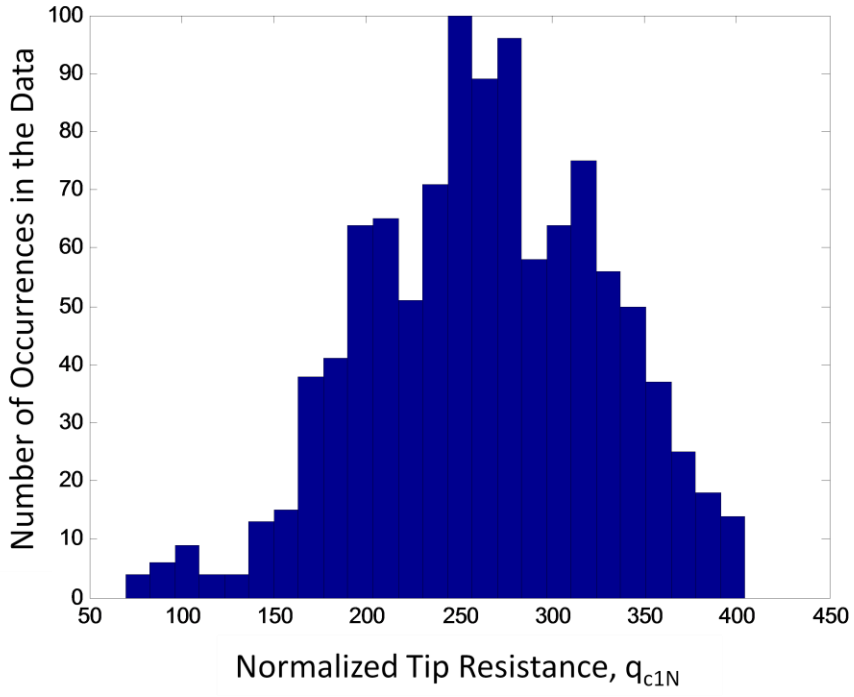

Figure 5-46. Histogram of CPT normalized tip resistance from the dense sand layer at the NE shake site.

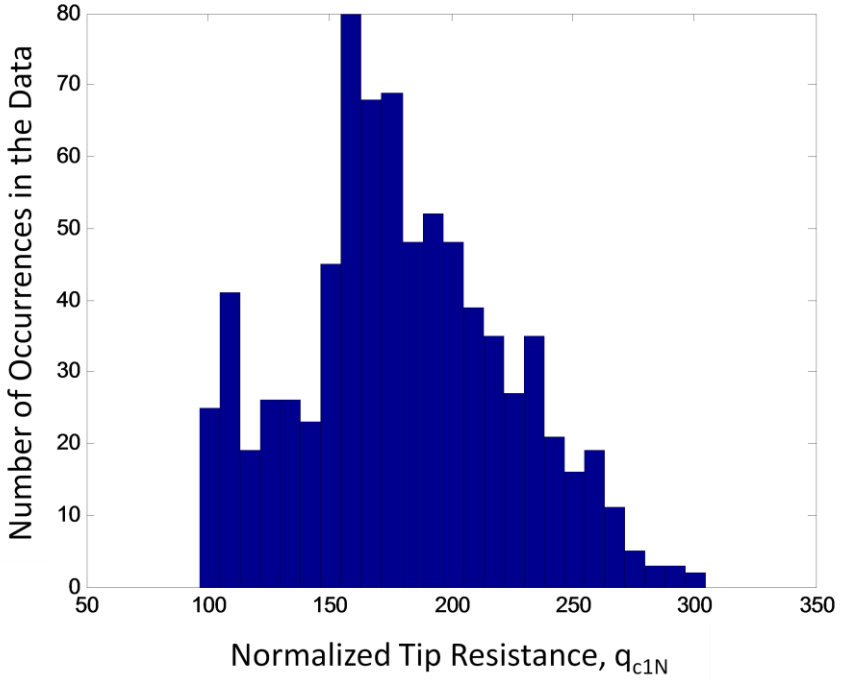

Figure 5-47. Histogram of CPT normalized tip resistance from the loose gravelly sand layer at the NE shake site.

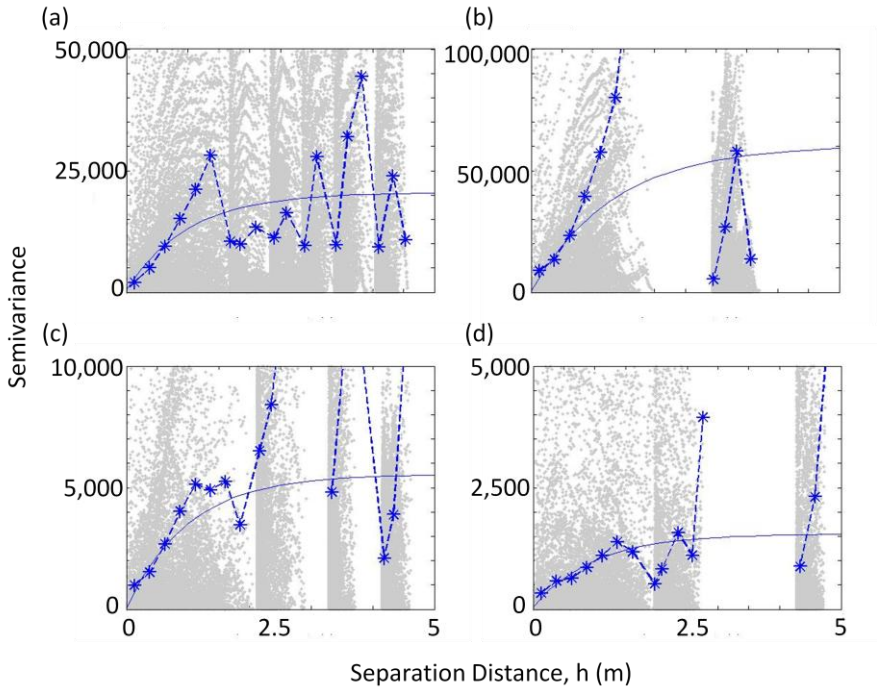

Figure 5-48. Variograms from the clay layer at the NE shake site from the (a) pre-shake, (b) one week, (c) one month, and (d) nine month testing periods.

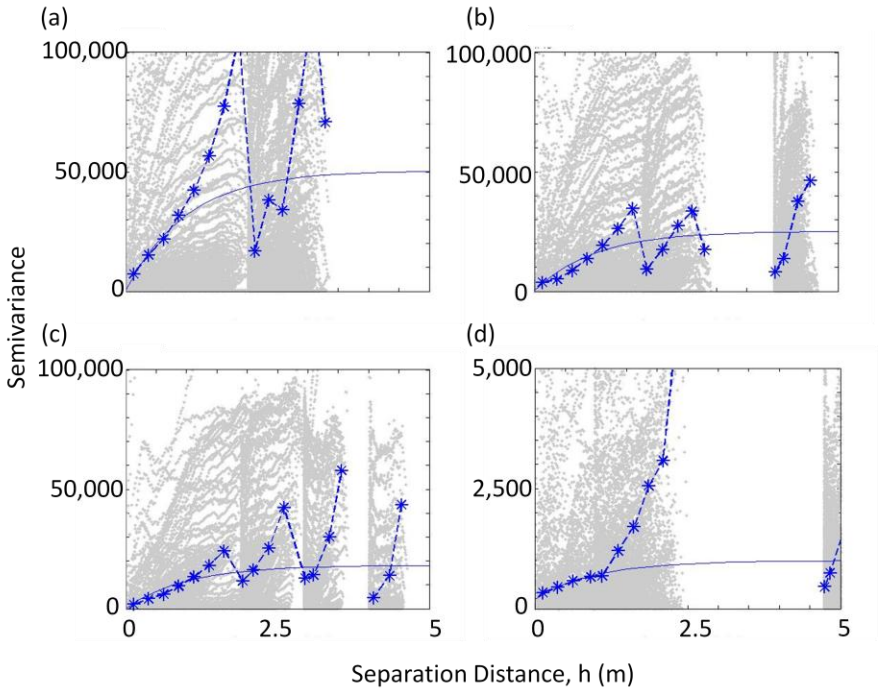

Figure 5-49. Variograms from the clay layer at the SW shake site from the (a) pre-shake, (b) one week, (c) one month, and (d) nine month testing periods.

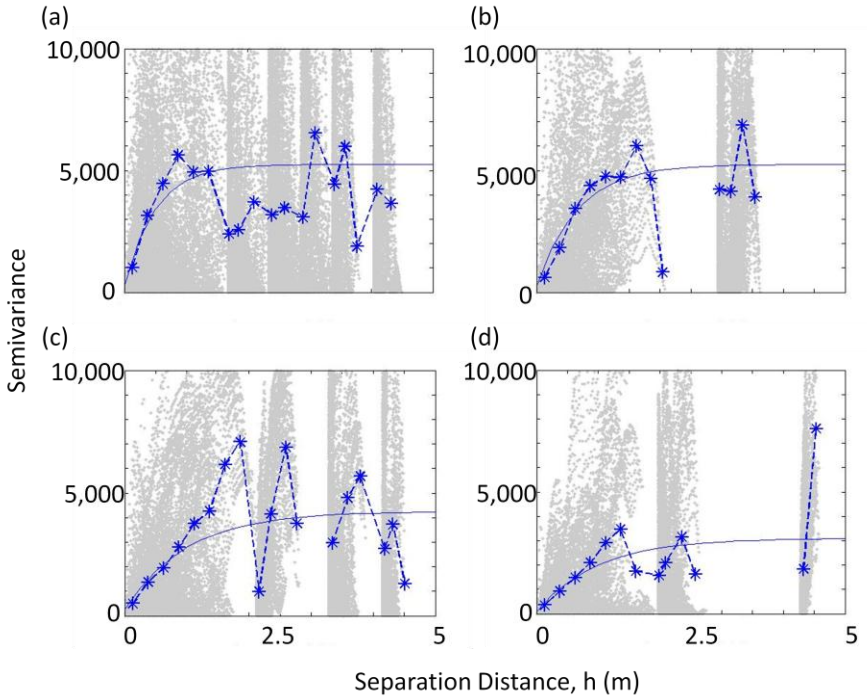

Figure 5-50. Variograms from the loose sand layer at the NE shake site from the (a) pre-shake, (b) one week, (c) one month, and (d) nine month testing periods.

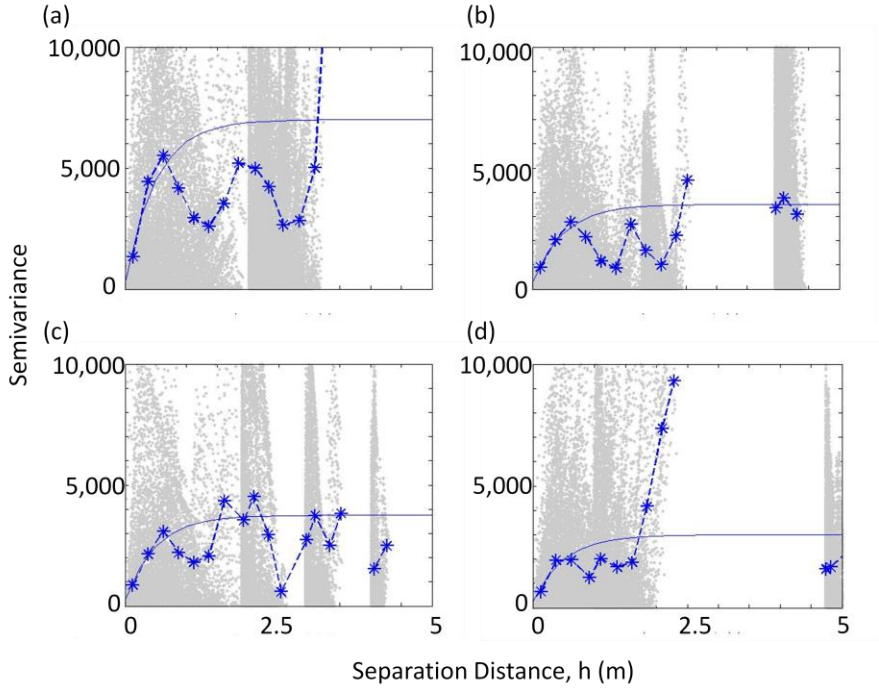

Figure 5-51. Variograms from the loose sand layer at the SW shake site from the (a) pre-shake, (b) one week, (c) one month, and (d) nine month testing periods.

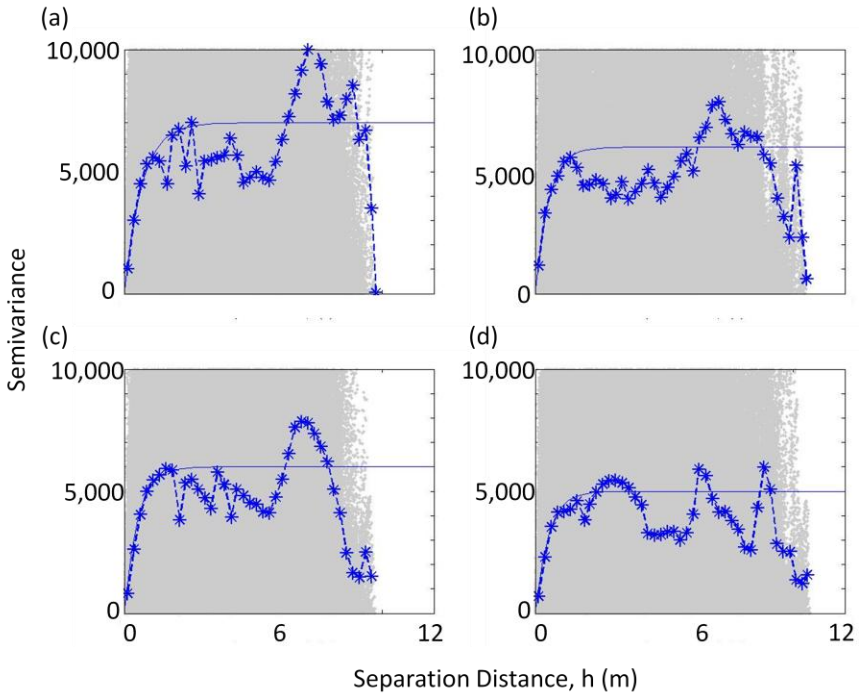

Figure 5-52. Variograms from the dense sand layer at the NE shake site from the (a) pre-shake, (b) one week, (c) one month, and (d) nine month testing periods.

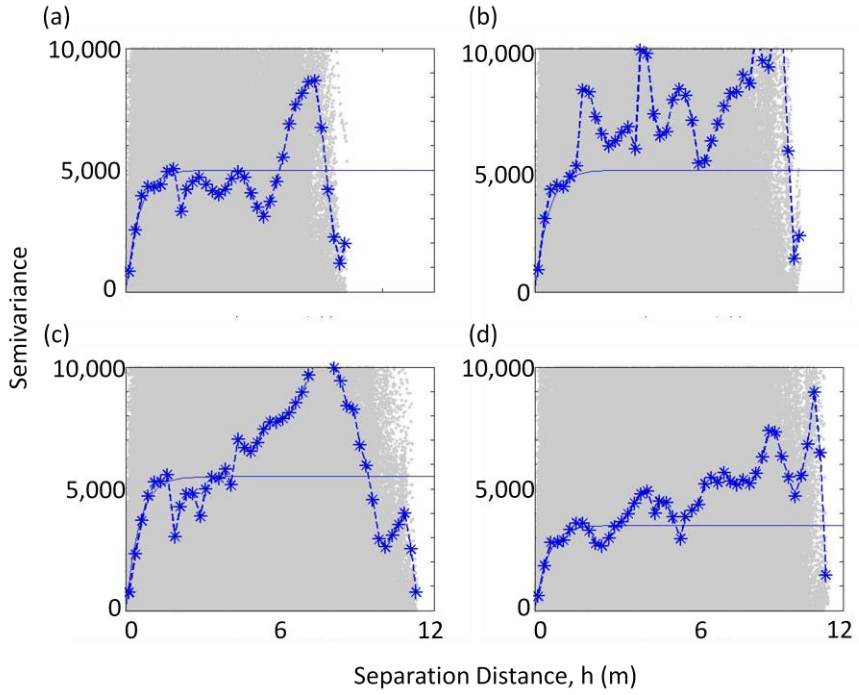

Figure 5-53. Variograms from the dense sand layer at the SW shake site from the (a) pre-shake, (b) one week, (c) one month, and (d) nine month testing periods.

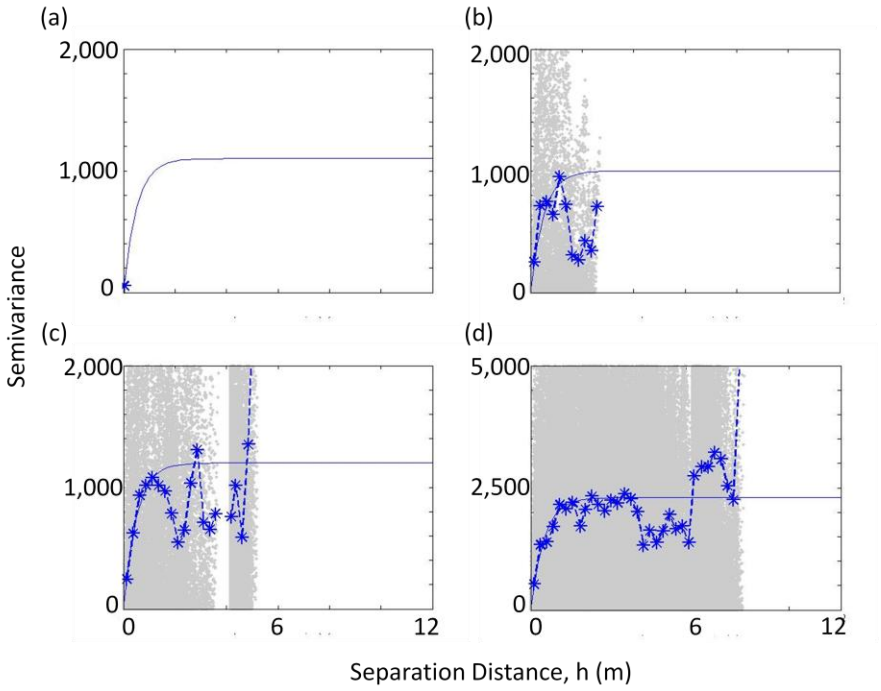

Figure 5-54. Variograms from the loose gravelly sand layer at the NE shake site from the (a) pre-shake, (b) one week, (c) one month, and (d) nine month testing periods.

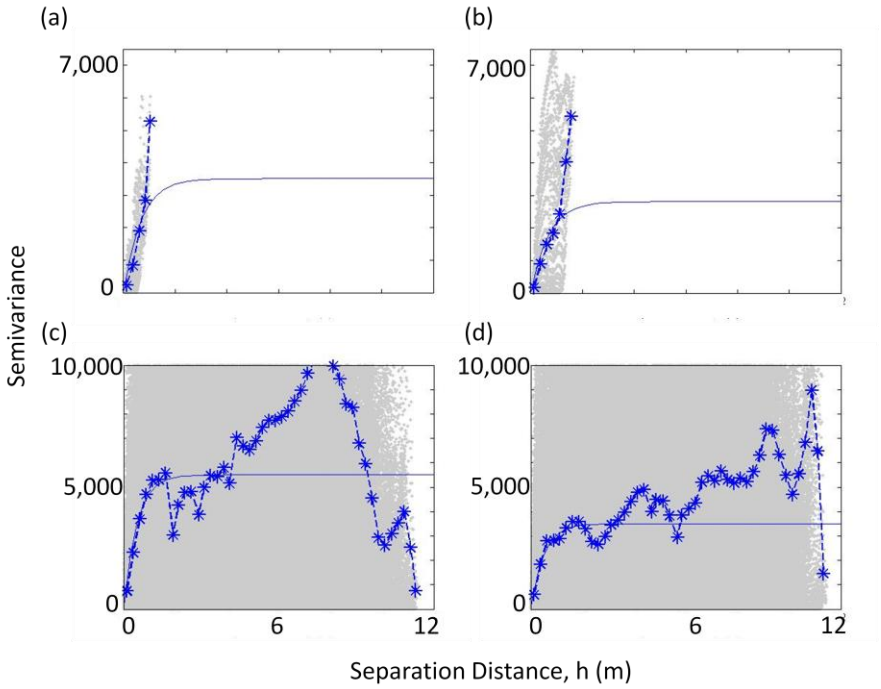

Figure 5-55. Variograms from the loose gravelly sand layer at the SW shake site from the (a) pre-shake, (b) one week, (c) one month, and (d) nine month testing periods.

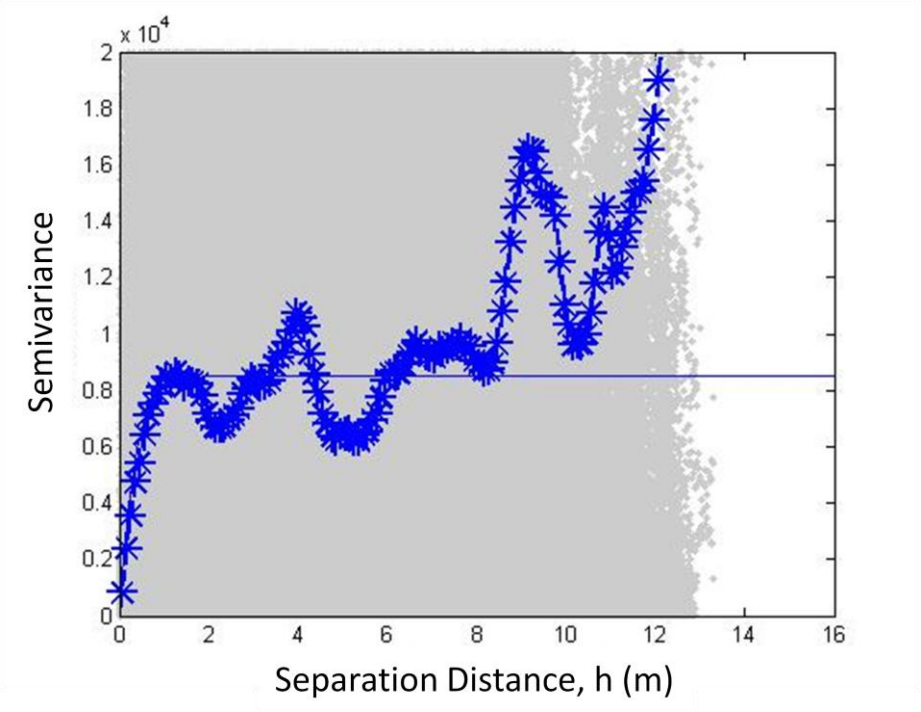

Figure 5-56. Variograms considering only vertical distance using data from pre-shake normalized tip resistance at the NE shake site.

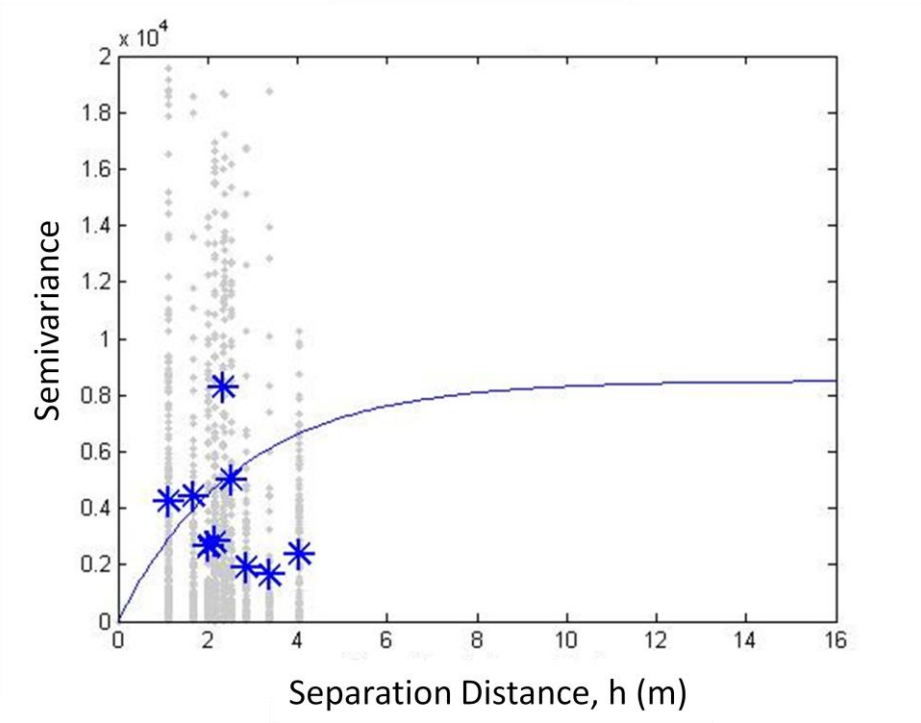

Figure 5-57. Variograms considering only horizontal distance using data from pre-shake normalized tip resistance at the NE shake site.

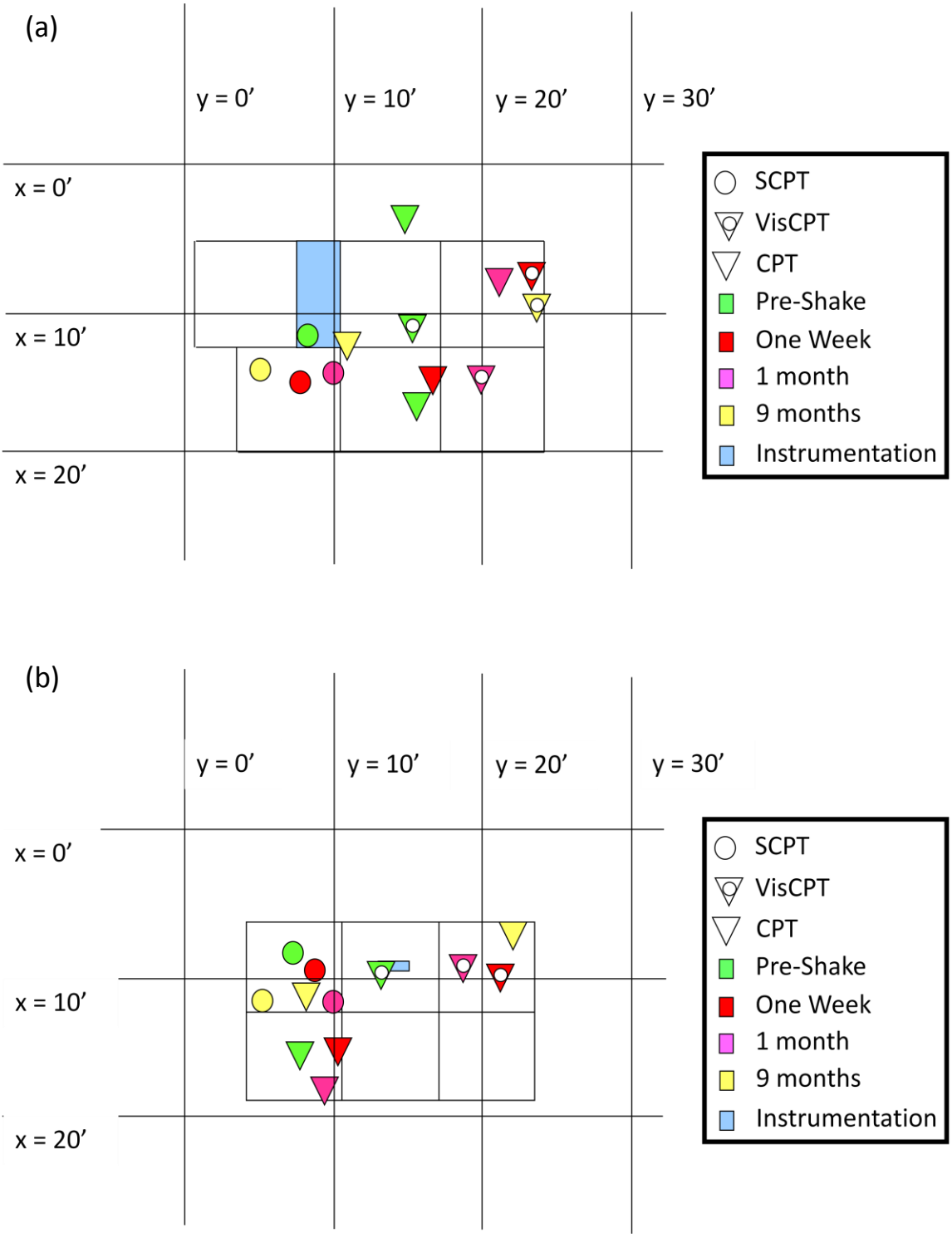

Figure 5-58. Location of CPTs relative to the grid used to determine distance between tests at (a) the NE shake site and (b) the SW shake site.

Chapter 6

Field Testing – Impact Piers

6.1 Introduction

In order to quantify aging effects, this research performed three field experiments and compared the results. This chapter describes one of those experiments, impact piers installation at the site of a soybean processing plant under construction in New Madrid, Missouri. Impact piers were chosen because previous research has identified the amount of disturbance and aeration of pore fluid as two factors that influence sand aging effects. Impact piers impart more disturbance to the soil than vibroseis shaking, but less disturbance than explosive densification. Additionally, it introduces aeration to the pore fluid. This chapter will describe the site investigation, the pier installation plan, post-installation testing plan, results of testing, and a comparison of the predicted cyclic resistance ratio (CRR) based on different *in situ* tests.

6.2 Site Investigation

The following section discusses the site investigation conducted prior to impact pier installation. The process of selecting a field site and the experiment location within that field site will be presented as well as a description of the soil profile.

6.2.1 Site Selection

Site investigation occurred in July, 2010. The Geopier Foundation Company, LLC offered to participate in the sand aging study if the company was installing impact piers in liquefiable sand at a location close enough to University of Michigan to allow for travel to the site. Pioneer Hi-Bred was constructing a soybean production plant and warehouse near New Madrid, Missouri. The site is pictured in Figure 6-1. The 1811-1812 New Madrid earthquakes and aftershocks produced well documented cases of liquefaction in the area, indicating that the sand layers at the site were liquefiable.

Because Geopier Foundation Company was willing to arrange for study, Pioneer Hi-Bred was willing to donate the use of the property. The site contained clean, saturated sand deposits, and there was historical evidence indicating liquefaction potential. Therefore, this site was chosen for further investigation. *In situ* tests, including cone penetration tests (CPT), vision CPT (VisCPT), seismic CPT (SCPT), and dilatometer tests (DMT), were conducted in the summer of 2010.

6.2.2 Experiment Location Selection

The testing site selection was driven by the construction schedule. Installation of the piers was proceeding from the north side of the building's footprint to the south side. *In situ* testing conducted as part of the construction project's site investigation showed little variability throughout the site. Following significant rains, the surface near the southeast corner of the building's footprint remained dry enough to allow the CPT rig to maneuver. It was also out of the way of on-going construction activities. Therefore, the testing was performed near the southwest corner of the building's footprint.

6.2.3 Soil Profile

Throughout the site, there are four principle soil layers of consequence to this study. From the surface, they are: a stiff sandy silt layer, a clean sand layer, a silty sand layer, and a sand layer. These layers were selected through interpretation of CPT, DMT, and VisCPT data. A drop in the friction ratio (F_r) shows the delineation between the stiff sandy silt and clean sand layer, as well as between the silty sand and sand layer. An increase in F_r shows the change from the clean sand layer and the silty sand layer. These distinctions were determined through the author's anaylsis, but are corroborated through empirical correlations relating soil type to CPT results. As shown in Figure 6-2, the thickness of the stiff sandy silt, clean sand, and silty sand are 2 m, 1 m, and 3 m respectively. While the sand layer is loose and required improvement to a depth of 12 m, it continues until it becomes too dense for penetration testing around 20 m. As shown in Figure 6-3, samples from sand layer are SP by the Unified Classification System.

Blum et al. (2000) describe the geologic history of the area. The soil layers are Pleistocene sand and silt fluvial deposits. They were deposited by the Mississippi River during the Wisconsin ice age. However, the 1811-1812 earthquakes caused a major disturbance in this area, effectively resetting its geologic age of the area (Andrus et al., 2009). For the purposes of this study, the geologic age of the New Madrid area is considered to be 200 years.

6.3 Impact Pier Installation

GeoPiers are installed using a hollow mandrel was inserted in a pre-augered hole to the depth of installation, as pictured in Figure 6-4. At this site, the piers extended from the surface to 12 m depth. Once the hollow mandrel reachs the desired depth, a basket is placed on top of the mandrel. The hollow mandrel and bucket are then filled with gravel. A lift is installed by withdrawing the mandrel ~1.5'. A group of hanging chains at the bottom of the mandrel, shown in Figure 6-5, allowed gravel to fall while the mandrel is withdrawn but creates a barrier when downward pressure is applied to the mandrel. Each lift is hammered down to ~1' thickness using the chain system. The resulting pier displaces the *in situ* soil outward from the pier, increasing its density and horizontal stress. Additionally, the gravel pier was thought to have a higher hydraulic conductivity than the *in situ* soil. Rollins et al. (2008) demonstrated that similarly installed gravel piers did not prevent liquefaction in an experiment using explosive densification. However, they hypothesized that the rapid build-up of excess pore pressure in explosive densification led to liquefaction. In cases where excess pore pressure builds more slowly, as it would in earthquakes, they believe that gravel drains, such as the ones installed in New Madrid, would be an effective liquefaction mitigation tool. It is also possible that during installation, the soil surrounding the piers liquefies and infiltrates the piers. In that case, the piers would have the same permeability as the surrounding soil.

Impact pier installation proceeded smoothly at the New Madrid site. Two important notes resulted from installation. First, the piers were relatively simple to install when the piers were placed adjacent to an unimproved area. However, auguring the mandrel to the desired depth and compacting each lift to the desired density was difficult in improved areas. This implies that the horizontal stresses in the soil had increased as a result of installing adjacent piers. Additionally, the installation of impact piers created vibrations that affected *in situ* testing. Because pier installation occurred only several hundred meters from the *in situ* test site, CPT and DMT testing were unaffected by pier installation. However, vibrations from installation were significant enough to make shear wave velocity, V_s, measurements impossible during installation.

6.4 *In Situ* Testing

The following section discusses the testing plan as well as pre- and post-installation results. Results of the various *in situ* tests are presented.

6.4.1 Testing Plan

Installation of impact piers was performed in an equilateral triangle pattern, as shown in Figure 6-6. *In situ* tests were performed near the center of the equilateral triangles. The majority of testing was performed on the interior of the triangles, where the test results were influenced by all three installed piers. Two exceptions, CPT-5 and CPT-201, were conducted at an exterior triangle, where the soil was not improved on the western side of the test. However, results of these tests are similar to the results of other tests conducted at the same testing interval.

6.4.2 Cone Penetration Testing

Pre-installation CPT testing consisted of two CPTs and two VisCPTs. One of the CPTs was intended to be an SCPT. However, installation of piers during testing rendered the seismic data useless because of excessive background vibration. Post-installation testing was conducted in the afternoon following installation and one month following installation. The one day testing interval included one SCPT, conducted during a shift change when no pier installation was occurring, and one CPT. Testing conducted one month following installation included four CPTs conducted by a contractor hired by GeoPier Foundation Company. In this section, only standard CPT results will be discussed. Vision data from the VisCPT and V_s from the SCPT will be discussed in Sections 6.4.3 and 6.4.4, respectively. The test name, time, and miscellaneous notes are presented in Table 6-1.

Pre-installation testing consisted of 4 CPTs, including two VisCPTs. Because the results of CPT-4 were representative of pre-installation testing and it was the deepest pre-installation test, CPT-4 results are presented in Figure 6-7. Throughout CPT testing at the New Madrid construction site, pore water pressure results varied with the water table depth, but always generally followed the hydrostatic line. Additionally, F_r was consistent with time throughout testing. Therefore, individual CPT results presented subsequently in this dissertation will include only tip resistance, q_c, information. A summary of pre-installation CPT results is shown in Figure 6-8.

A summary of one day CPT results is shown in Figure 6-9. As pictured in Figure 6-10, the range of q_c values recorded following installation remain generally consistent in the stiff sandy silt and silty sand layers when compared to pre-installation results. Tip resistance increased following installation in the clean sand layer, as well as in the sand layer to the depth of installation. Below the depth of installation, there was no discernable change in q_c.

One month after the blast, CPTs were conducted by a contractor hired by Geopier Foundation Company. Results from the four CPTs are shown in Figure 6-11. As pictured in Figure 6-12, the range of q_c values increased in the silty sand layer and in the sand layer to the depth of installation. Tip resistance values remained generally consistent with one week testing in the shallow layers, as well as below the depth of installation.

The mean q_c profile is shown for each testing interval in Figure 6-13. Tip resistance in the stiff sandy silt layer showed little change with time following impact pier installation. In the clean sand layer, q_c increased due to impact pier installation but remained constant with time following installation. In the silty sand layer, q_c was not clearly affected by impact pier installation, but did increase with time following installation. Finally, q_c values in the sand layer increased significantly due to impact pier installation and with time following installation up to the depth of installation. Below the depth of impact pier installation in the sand layer, there is little change to q_c.

In conclusion, impact pier installation increased q_c of the clean sand and sand layers. Time-dependent increase in penetration resistance was recorded in the sand layer. In the silty sand layer, immediately following impact pier installation, there was no change in q_c, but the layer did show an increase with time. One month following installation, q_c in the sand layer had increased roughly 33% from values recorded immediately following installation.

6.4.3 Vision Cone Penetration Testing

A qualitative method of assessing vision data was employed. While conducting the VisCPT, the cone advance was stopped every 10 cm. These pauses allowed for visual observation of the soil. Sand can be observed to flow or boil, indicating that the sand is very loose and liquefied during the cone's advance. While lack of boiling in loose sand should not be interpreted as resistance to earthquake-induced liquefaction, the observation of local liquefaction by the VisCPT indicates high liquefaction susceptibility.

There were 2 VisCPT soundings at the New Madrid construction site. The vision data was valuable in assessing the layering at the site; however, there was no observation of penetration induced liquefaction prior to installation. Following installation, the camera was pushed into the ground as part of the CPT assembly, but the vision data was not recorded due to a DVD recorder failure. Observation of this data during the test showed no changes to pre-installation trends.

6.4.4 Shear Wave Velocity

The V_s profile from SCPT-4, the only SCPT conducted at the site, is presented in Figure 6-14. Because seismic data prior to installation was not useful due to the high vibrations of adjacent pier installation, pre- and post-installation comparison of V_s is impossible. Additionally, *in situ* tests conducted one month following installation did not include SCPT, so V_s changes with time were not determined. The V_s profile confirms the site layering and is used to compare liquefaction potential determined from different *in situ* tests later in this chapter.

6.4.5 Dilatometer Testing

There were 3 DMT soundings and the resulting horizontal stress index, K_D, dilatometer modulus, E_D, and material index, I_D, profiles are presented in Figures 6-15 through 6-17, respectively. The pre-installation DMT was conducted prior to impact pier installation, while post-installation DMT-1 and -2 were conducted the morning after following installation. No DMTs were conducted one month following installation. It should be noted that a pilot cone was pushed through the stiff sandy silt layer prior to beginning the DMT. The blade is larger than the CPT and could not be pushed through the stiff sandy silt. Insertion of the pilot cone allowed the DMT blade to penetrate through the stiff sandy silt and to deeper layers, but prevented the collection of data in the stiff sandy silt. Because the stiff sandy silt layer was not of interest to this project and the insertion of the pilot cone allowed testing of the sand layers, the pilot cone was used with all post-installation DMTs.

The horizontal stress index is related to the horizontal stress; therefore, changes with time were expected to be similar to those seen in the CPT tip resistance. As seen in Figure 6-15, K_D values remained fairly consistent in the clean sand and silty sand layers. In the sand layer, K_D increased significantly at depths affected by impact pier installation. Below installation depth, pre- and post-installation values are very similar.

The dilatometer modulus, as seen in Figure 6-16, remained fairly consistent in the clean sand and silty sand layers. In the sand layer, E_D increased significantly at depths affected by impact pier installation. Below installation depth, pre- and post-installation values are very similar.

The material index is a function of soil type; therefore, changes with time were not expected. However, as seen in Figure 6-17, there was significant change in I_D comparing pre- and post-installation testing. The material index related to the ratio of E_D to K_D. Because K_D increased

more than E_D as a result of impact pier installation, pre- and post-installation testing showed different I_D values in the sand layer.

In summary, the K_D and E_D increased in the sand layer to the depth of installation, while I_D decreased in the sand layer. In the case of K_D and E_D, the increase due to impact pier installation was over 200%. This increase demonstrates that impact pier installation significantly increases horizontal pressure and soil stiffness.

6.5 Comparison of Cyclic Resistance Ratio from Several *In Situ* Tests

Because several different *in situ* tests were used to characterize the site and monitor aging, there was an opportunity to compare the results of different tests at the same site. In this section, methods of determining cyclic resistance ratio (CRR) from V_s, K_D, and q_c are presented. The results of CRR calculations from each type of test were compared. This analysis was enriched by data at different time periods as well as different types of tests. Finally, trends with time were discussed and the results are summarized.

6.5.1 Determination of CRR

The methods of determining CRR from the results of each *in situ* test are discussed in Chapter 4.7.1. Because the VisCPT did not show any penetration induced liquefaction, the qualitative method of assessing liquefaction potential using vision data is not used at this site. Otherwise, the results presented below were determined in a similar manner as presented in Chapter 4.7.

6.5.2 Comparison of CRR from Different *In situ* Tests

The CRR calculated from CPT and DMT data is shown in Figure 6-18. As seen in this figure, there is good agreement among the CRR values predicted by CPT and DMT. For example, variations in liquefaction potential reflect the site layering in all the tests. Additionally, the predicted CRR from DMT and CPT are generally very close to one another.

The CRR calculated from CPT, DMT, and V_s determined from SCPT conducted after installation is shown in Figure 6-19. The DMT and CPT based CRR predictions show good agree. The V_s based CRR prediction agrees with the penetration based CRR predictions in all except the sand layer. In the sand layer, the V_s predicts lower CRR than the other *in situ* tests. These tests were all conducted in the afternoon after pier installation in the morning. Shear wave velocity has been shown to increase in the hours and days after disturbance (Afifi and Woods, 1971; Anderson and Stokoe, 1978). It is possible that V_s would have increased with time after the installation and

would have shown better agreement with the penetration based tests' CRR predictions had the SCPT been conducted in the following days. Only CPTs were conducted one month after impact pier installation. Therefore, the CRR prediction could not be compared to other *in situ* tests; however, the CRR calculated using one month CPT results are shown in Figure 6-20. The previously mentioned increase in q_c in the sand layer between one day and one month testing is reflected in the increase in CRR between the same sets of tests.

6.5.3 Summary of Results

Using data from CPT, DMT, and SCPT, liquefaction resistance was determined at a construction site in New Madrid, MO. The CRR values predicted by CPT and DMT showed good agreement. This is due to the young geologic age of the site. Each of the CRR prediction methods was developed using data from early Holocene sites. Because the major earthquakes in the region in 1811 and 1812 reset the geologic age of the soil, CPT and DMT show similar predicted values of CRR. The V_s based CRR prediction was low in the sand layer, possibly because V_s had not yet recovered from impact pier installation.

6.6 Conclusion

This chapter describes the impact pier experiment that was performed at New Madrid, MO. A description of the site investigation and experimental design was presented. Additionally, the results of the experiment and subsequent *in situ* testing were presented and discussed. Comparing the results of widely accepted CRR calculation methods based on the *in situ* tests performed at the New Madrid construction site showed good agreement. This is because the site is geologically young due to the major disturbance of the major 1811 and 1812 earthquakes in the region. The CRR prediction methods were developed using data mainly from late Holocene sites. This site matches those conditions and the different *in situ* tests show good agreement. Results of the impact pier experiment will be compared to other sand aging studies in Chapter 8.

Table 6-1. Testing times and notes from the impact pier installation site.

	Date of Test	Time of Test	Hours after Last Shake	Notes
CPT-5	15 JUL 10	1630	1	
CPT-6	15 JUL 10	1800	2.5	
DMT-2	16 JUL 10	0900	17.5	
DMT-3	16 JUL 10	1130	20	
CPT-200	17 AUG 10	0730	784	Performed by contractor
CPT-201	17 AUG 10	0830	785	Performed by contractor
CPT-202	17 AUG 10	0930	786	Performed by contractor
CPT-203	17 AUG 10	1030	787	Performed by contractor

Figure 6-1. Construction site at New Madrid, MO with flags showing impact pier installation points (photo courtesy of Russell Green).

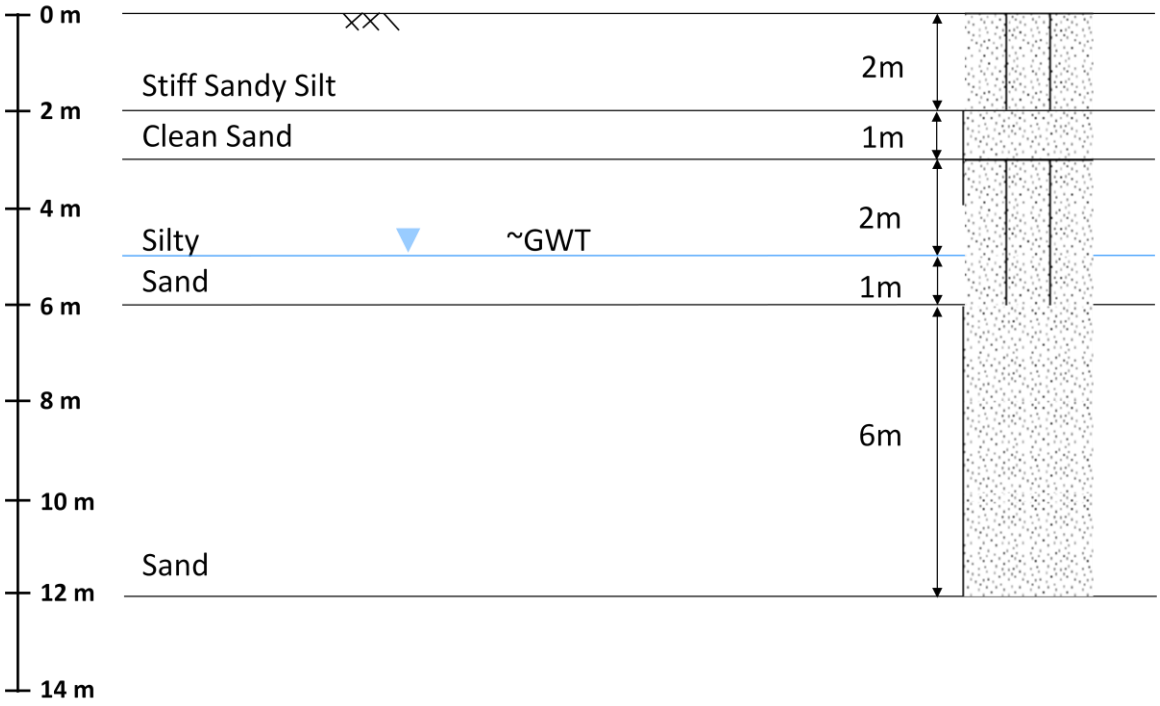

Figure 6-2. Typically soil profile at the New Madrid, MO testing site.

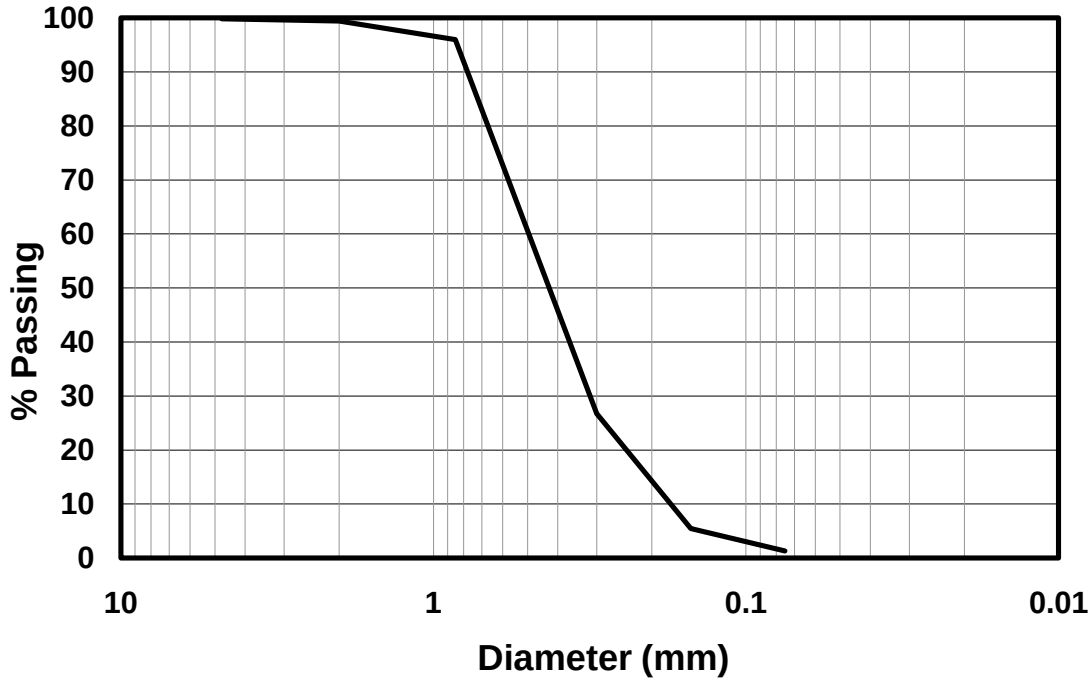

Figure 6-3. Grain size distribution curve for the sand layer at New Madrid, MO.

Figure 6-4. Installing an impact pier at the New Madrid, MO testing site.

Figure 6-5. Chains at the bottom of augers used to install impact pier (photo courtesy of Roman Hryciw).

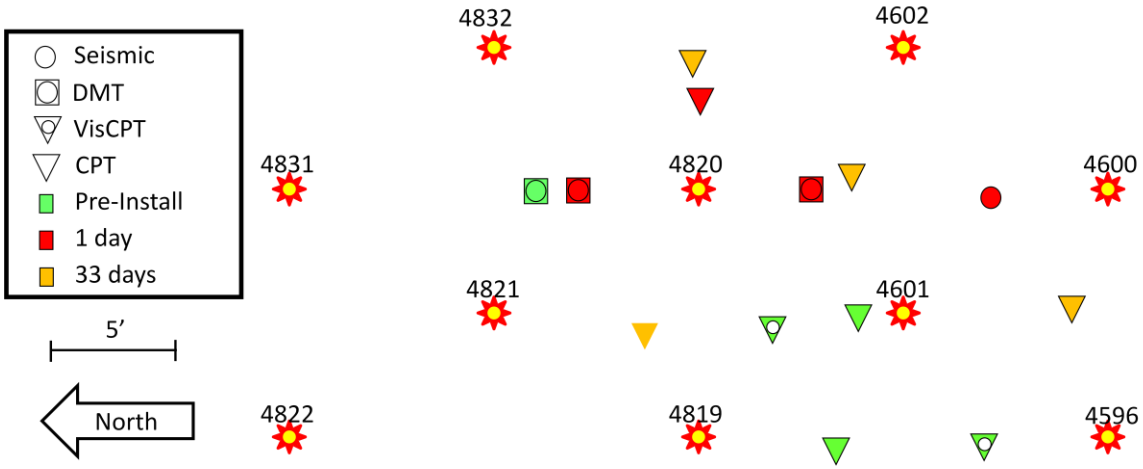

Figure 6-6. Testing locations at New Madrid, MO.

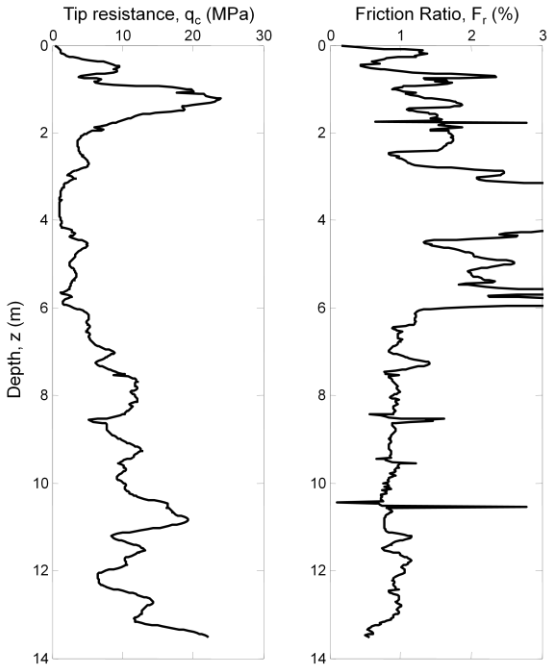

Figure 6-7. Results from CPT-4, typical of pre-installation testing.

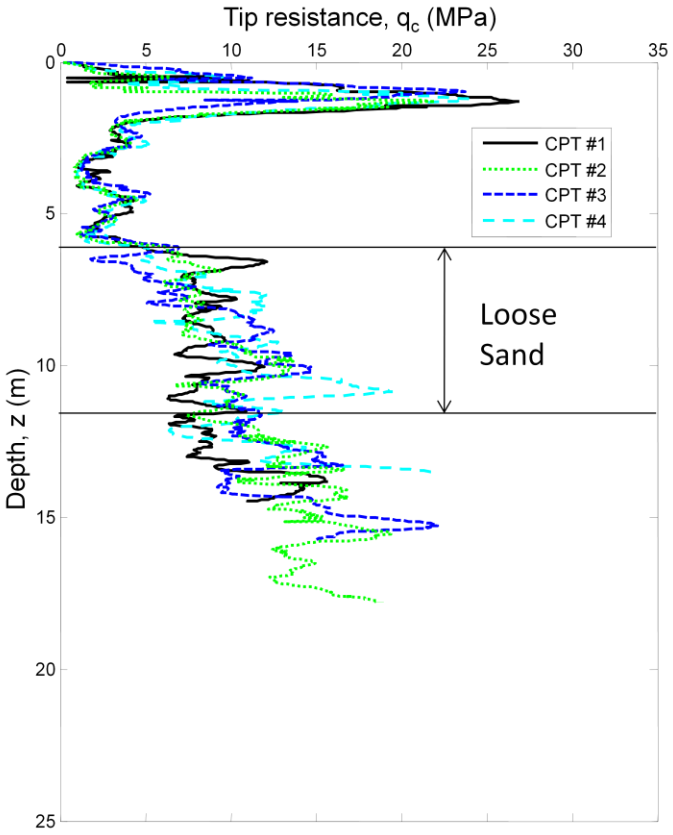

Figure 6-8. Results of pre-installation CPTs.

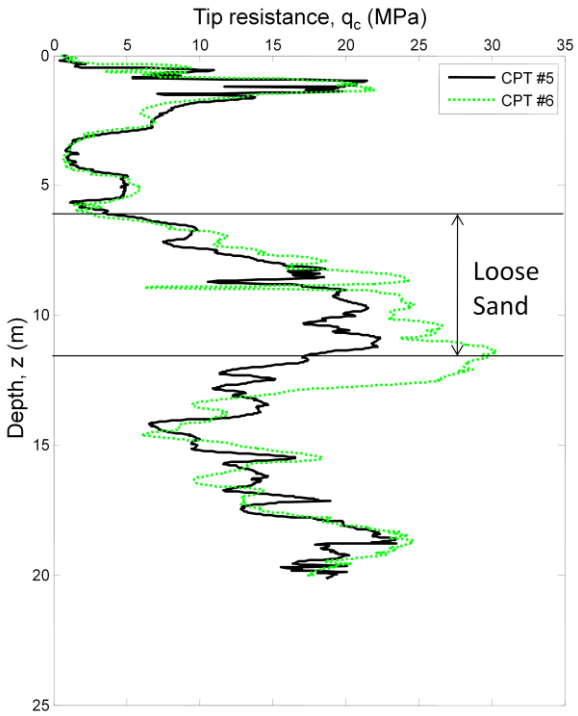

Figure 6-9. Results of CPTs conducted one day after installation.

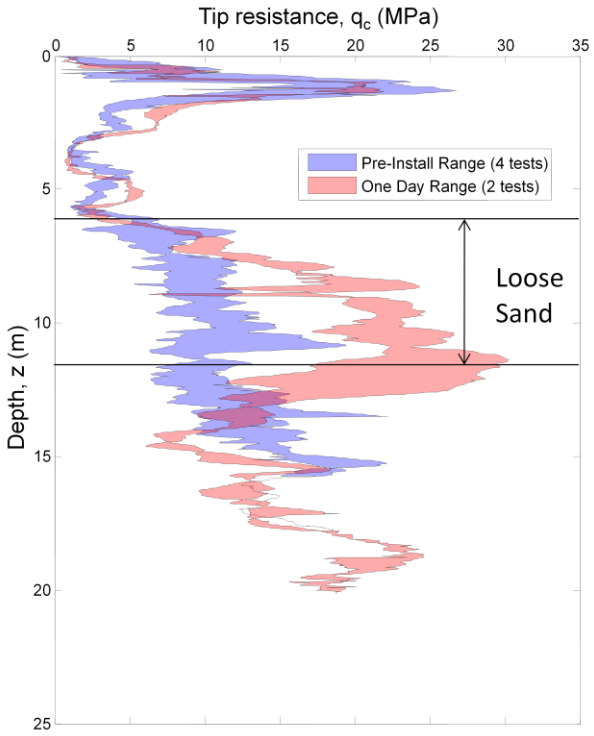

Figure 6-10. Range of pre-installation CPTs compared to the range of CPTs conducted one day after installation.

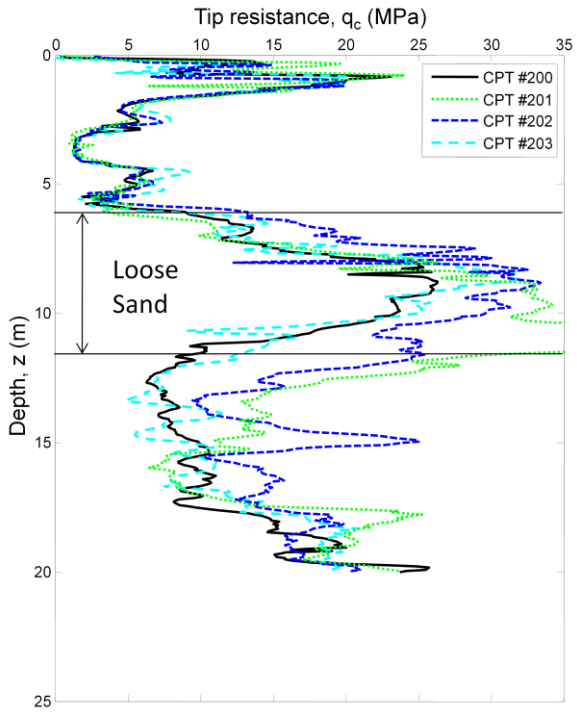

Figure 6-11. Results of CPTs conducted one month after installation.

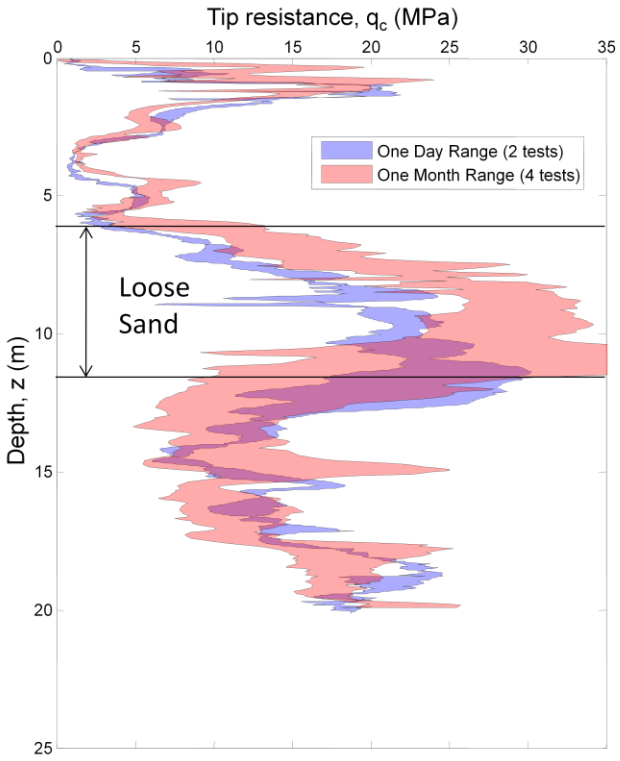

Figure 6-12. Range of CPTs conducted one day after installation compared to the range of CPTs conducted one month after installation.

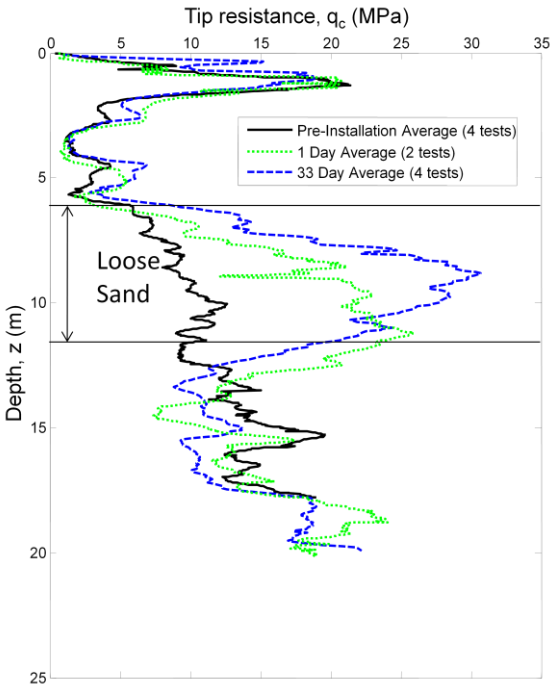

Figure 6-13. Mean CPT results from each testing interval.

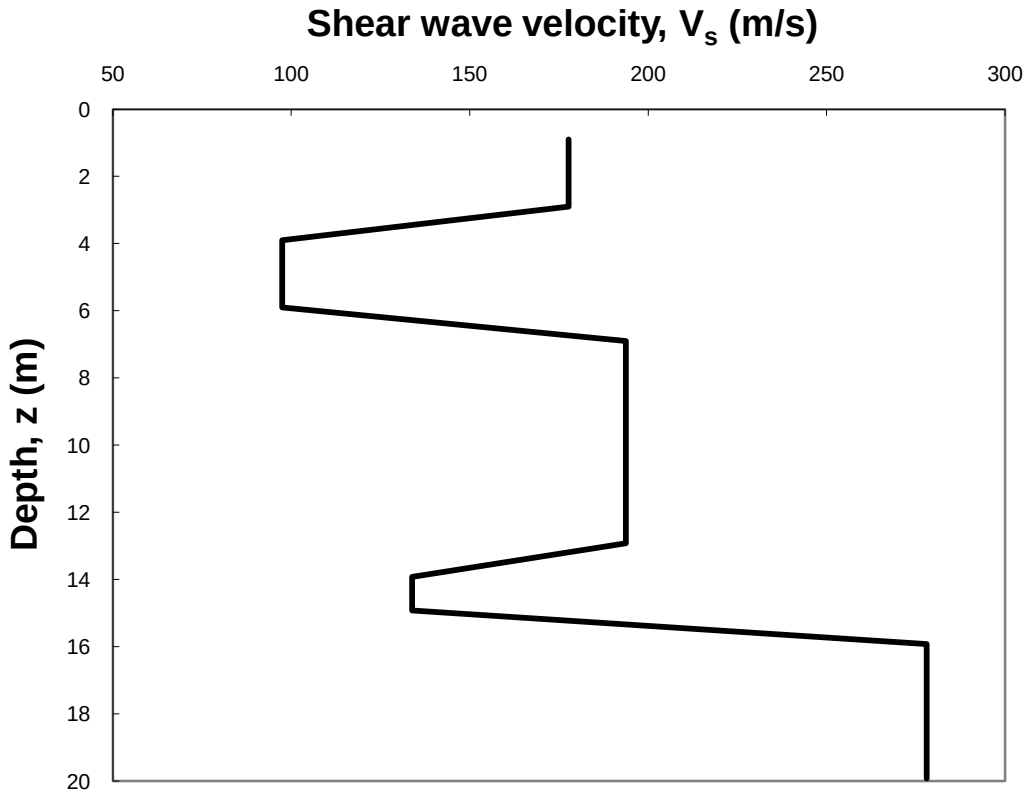

Figure 6-14. Shear wave velocity from SCPT conducted one day following installation.

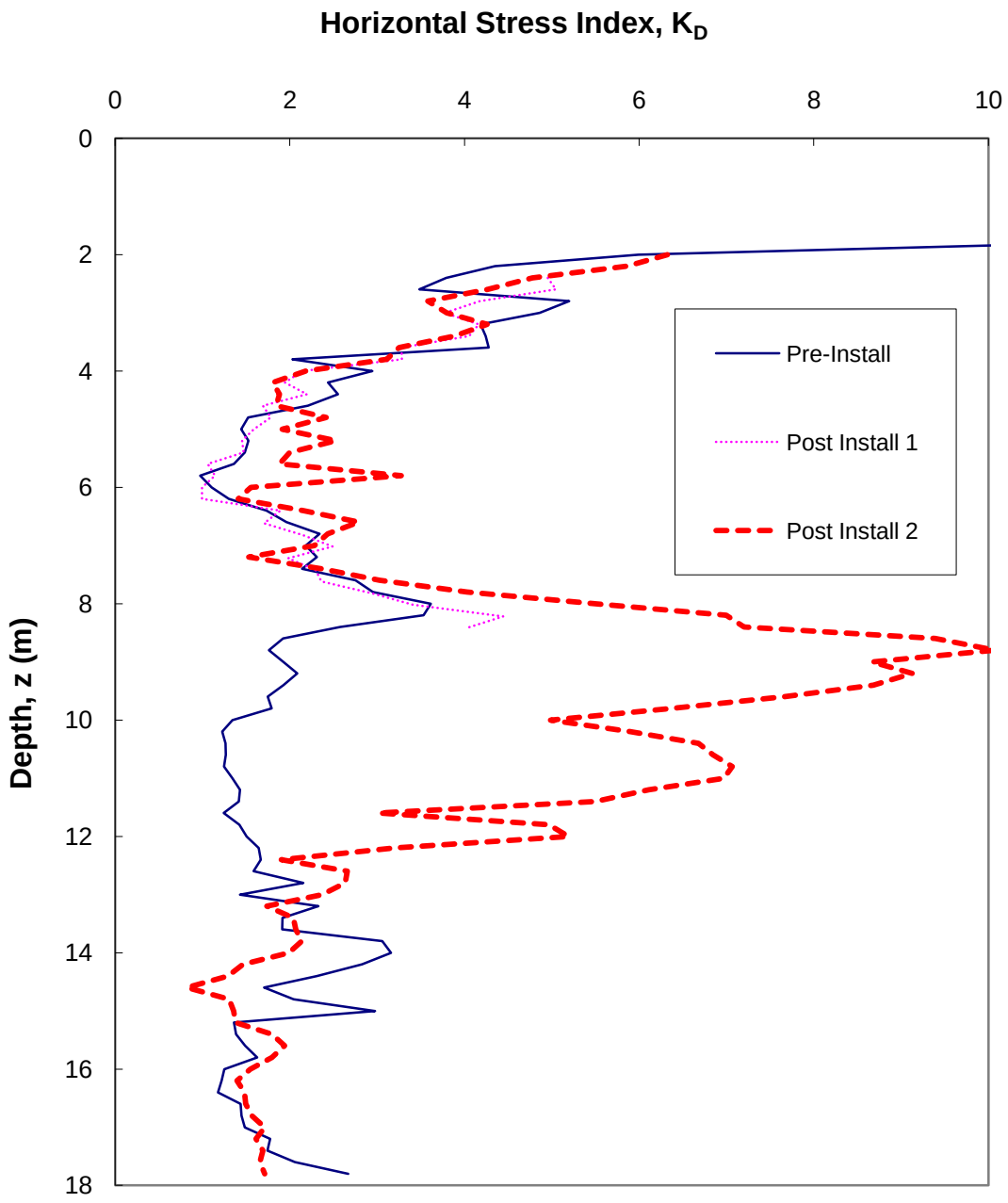

Figure 6-15. DMT horizontal stress index from tests conducted before installation and one day after installation.

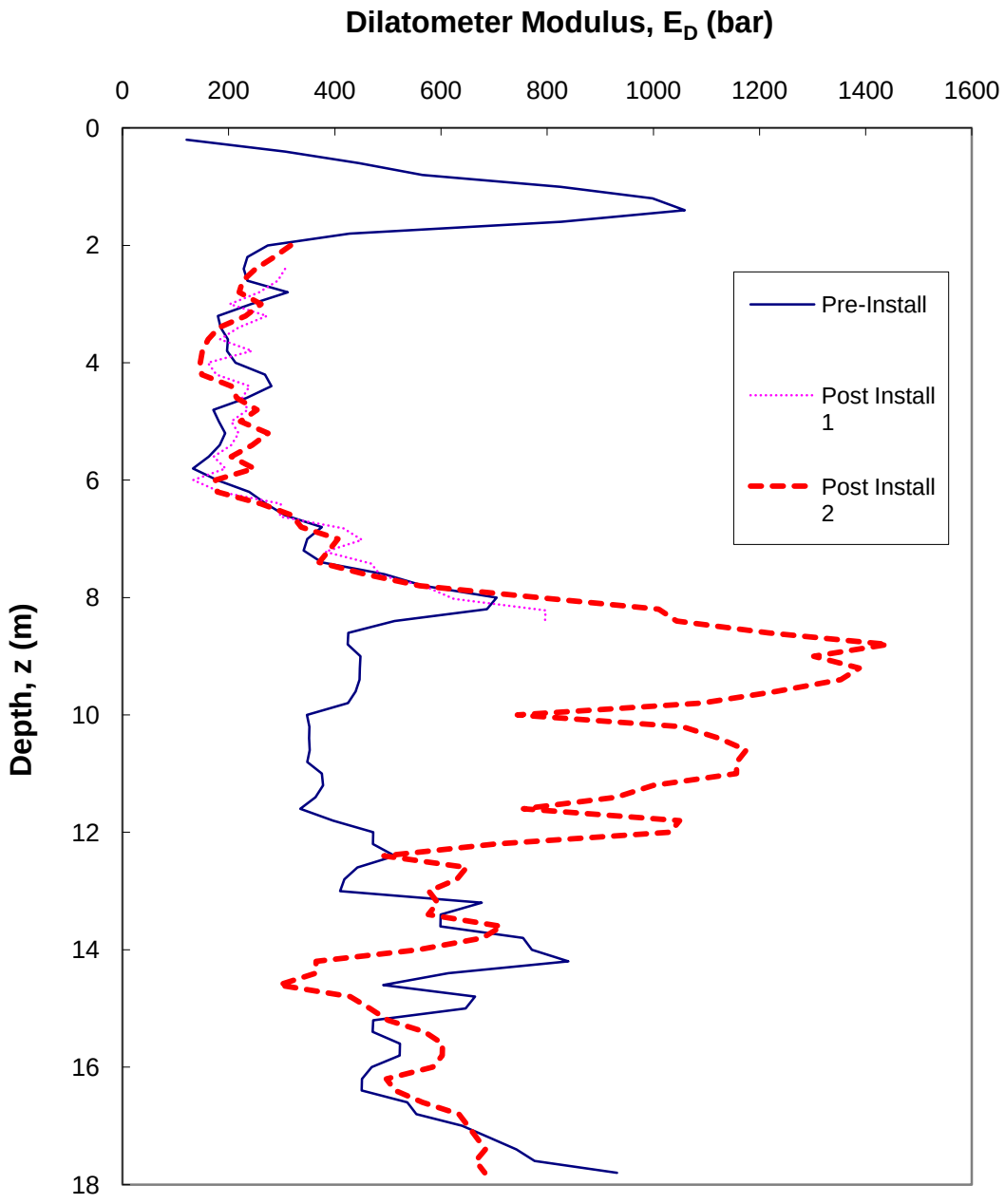

Figure 6-16. Dilatometer modulus from tests conducted before installation and one day after installation.

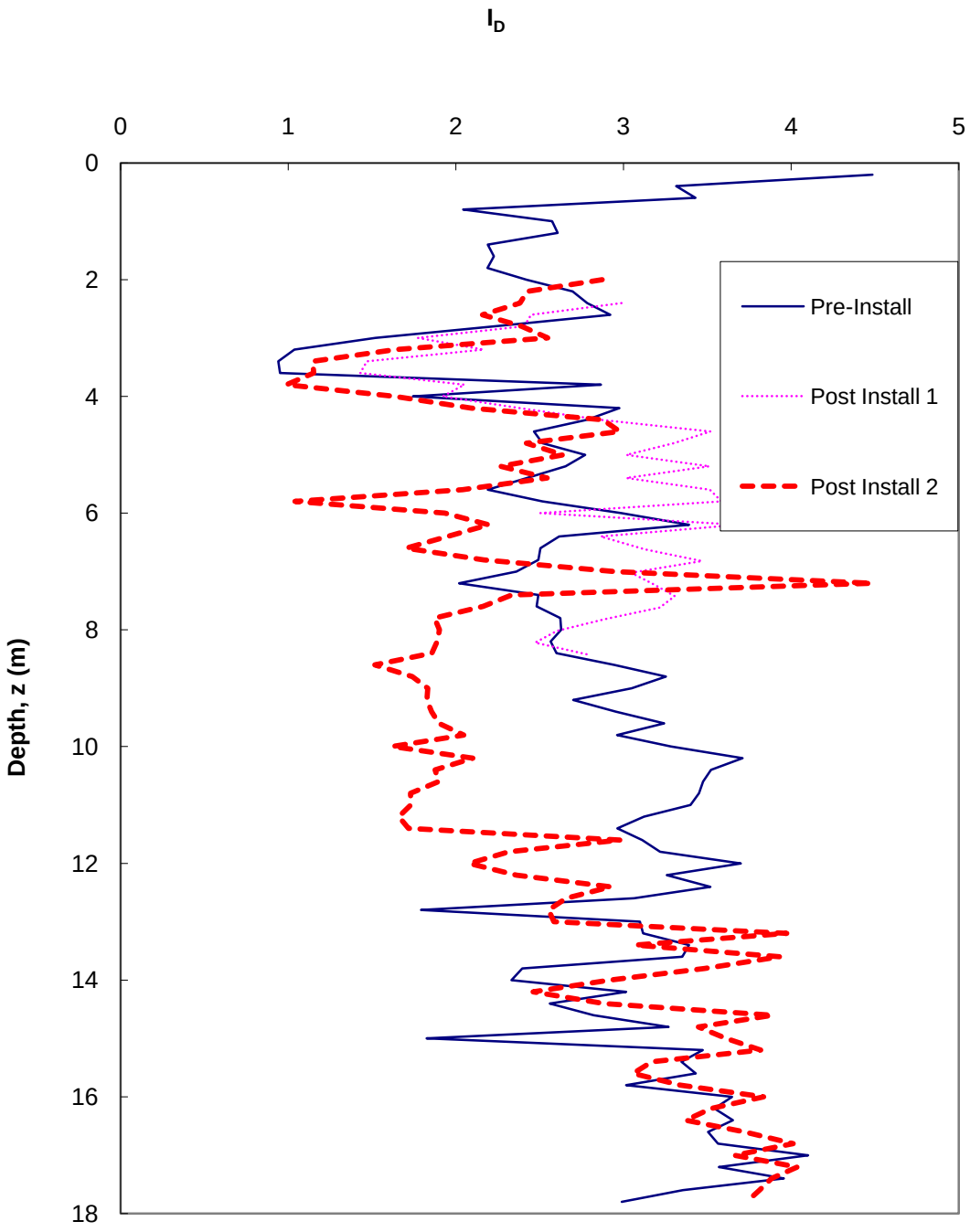

Figure 6-17. DMT material index from tests conducted before installation and one day after installation.

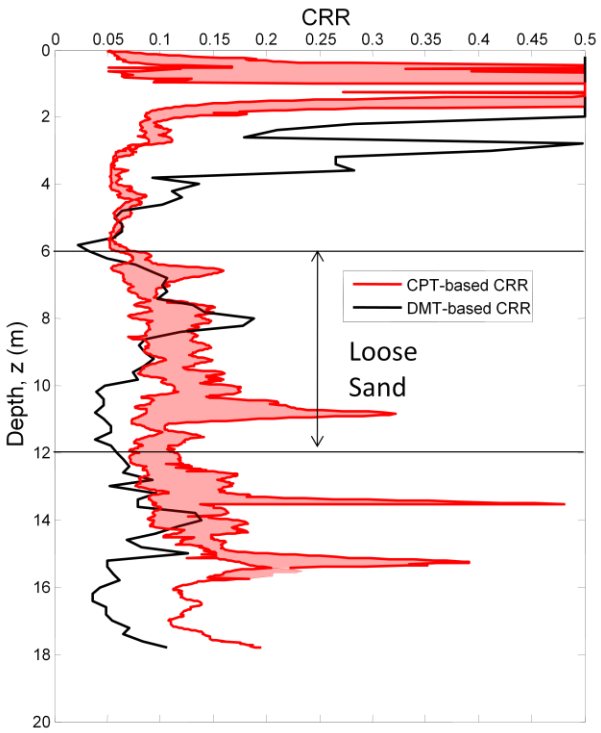

Figure 6-18. CRR predictions from CPTs and DMT conducted prior to installation.

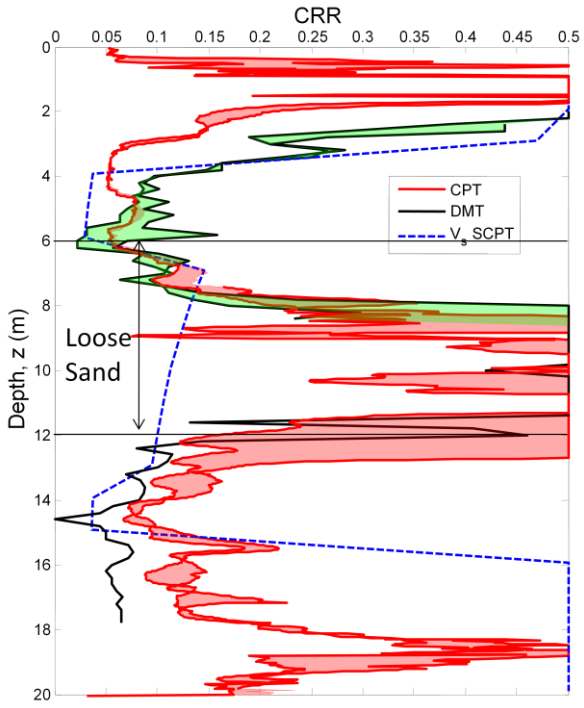

Figure 6-19. CRR predictions from CPT, DMT, and shear wave velocity conducted one day after installation.

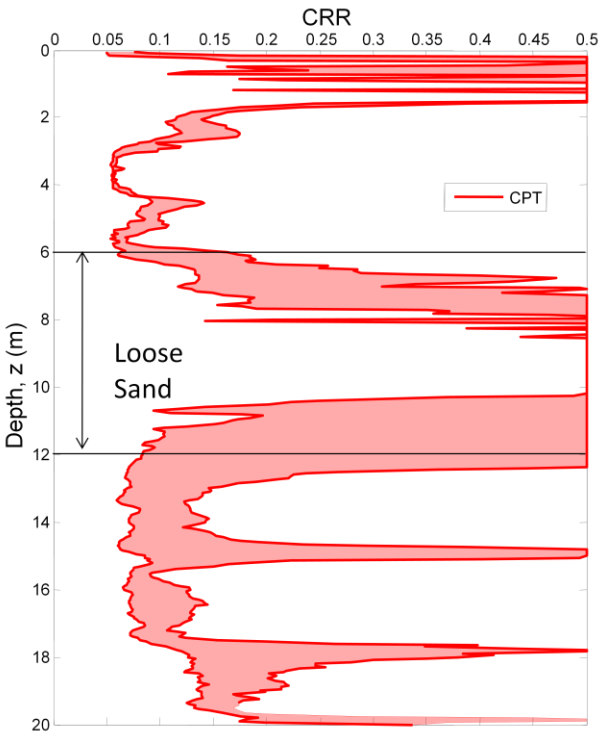

Figure 6-20. CRR predictions from CPTs conducted one month after installation.

Chapter 7

Laboratory Testing

7.1 Introduction

In order to quantify aging effects, laboratory experiments were performed on soil taken from a sand and gravel quarry in Griffin, Indiana and a construction site in New Madrid, MO. Soil characterization was necessary to compare the sand from Griffin, IN and New Madrid, MO to deposits where sand aging was reported in previous studies. Cyclic triaxial tests were performed on the Griffin sand to quantify aging in the laboratory. Comparing aging effects recorded using the same soil in both the laboratory and the field is unique to this study. This chapter will describe the soil characterization for both the field sites and for cyclic triaxial testing.

7.2 Griffin, IN Field Test Site Soil Characterization

To develop a sand aging predictive method, common soil properties from all soil deposits reported to have undergone sand aging should be compared. Therefore, the soil characterization program was designed to obtain all of the data presented in Tables 2-1 and 2-2. Soil samples were collected from Griffin, IN at two locations shown in Figure 7-1. Mulzer Crushed Stone, Inc., the company which owns the sand and gravel quarry, removed the clay cap to prepare a new area for dredging and soil samples were taken from the surface of the exposed loose sand layer.

Three grain size distribution curves are presented in Figure 7-2. Two curves were obtained by sieving the soil sampled from the loose sand layer. Mulzer Crushed Stone, Inc. determined the third curve by sieving samples obtained from a roto-sonic drilling investigation. The roto-sonic drill occurred close to the blasting and vibroseis sites, shown in Figure 7-1. Because the three grain size distribution curves show similar results, the soil sample collected in 2007 was used to determine the coefficient of uniformity, coefficient of gradation, and the effective diameter at 10% and 50% finer by weight. This soil sample was chosen because it contained the greatest amount of soil and used in other laboratory tests described below.

The minimum and maximum dry density was determined according to ASTM D 4254-00(2006) and ASTM D 4253-00(2006). Converting these values to minimum and maximum void ratio was possible after determining the specific gravity according to ASTM D 854-06. The results of the Griffin soil characterization are presented in Tables 7-1 and 7-2.

7.3 New Madrid, MO Field Test Site Soil Characterization

Soil samples were collected from New Madrid, MO from the auger while an impact pier was being prepared for installation. As a result, the exact depth of the sample is unknown. The auger depth at the time of sampling was greater than 8 m, placing the soil samples in the sand layer. It is possible that the samples contain some soil from shallower layers as the auger passed through those layers on its way to the surface. While the sampling method is imperfect, it was the best available method and provides a reasonably representative sample.

The grain size distribution curve is presented in Figure 7-3. The minimum and maximum dry density was determined according to ASTM D 4254-00(2006) and ASTM D 4253-00(2006). Converting these values to minimum and maximum void ratio was possible after determining the specific gravity according to ASTM D 854-06. The results of the New Madrid soil characterization are presented in Tables 7-1 and 7-2.

7.4 Cyclic Triaxial Testing

The following section describes the cyclic triaxial test, experimental design, and results. The literature contains many studies, summarized in Chapter 2.2.2, where sand aging was observed in the lab. The aging results from this project's cyclic triaxial testing can be compared to other laboratory aging results and, because the tests were conducted using sand from the Griffin, IN field site, to aging results from the explosive densification and vibroseis field experiments.

7.4.1 Test Description

The cyclic triaxial test is used to evaluate a soil sample's liquefaction potential. Reconstituted soil samples were used in this project and were consolidated to an effective confining stress similar to that which was experienced in the field. The sample was then subjected to a cyclic axial load. Failure can be defined when excess pore pressure reaches a givespecified value or when axial strain reaches a specified value. Results of cyclic triaxial testing are the number of cycles to cause failure for a given cyclic stress ratio (CSR), where CSR is defined as the ratio of the shear stress on the plane of interest, equal to one half the deviator stress, to the effective confining stress.

Because the number of cycles to failure is influenced by more than simply CSR, it is important to hold other factor constant through the testing program. Efforts to achieve this goal during this project are described below.

The cyclic traxial testing system designed by Clarence Chan was used in this project and is pictured in Figure 7-4. The test was controlled using GeoRobot Triaxial Testing System Version 5.2 software. Five channels of data were recorded during each sample's consolidation and cyclic loading phases: axial load, axial displacement, cell pressure, effective pressure, and volume change. Axial load was measured using a load cell. Axial displacement was measured by an LVDT. Cell pressure, effective pressure, equal to cell pressure minus the back pressure, and volume change were all measured with pressure transducers.

7.4.2 Experimental Design

Several factors influence the liquefaction resistance of a soil. The efforts taken in this project to hold those factors constant are described in this section. Sand from the loose sand layer at Griffin, IN was reconstituted into a cylindrical sample with a nominal diameter of 2.78" and a nominal height of 6.16". The actual diameter and height of each test specimen was recorded and ranged from 2.75" to 2.79" for the diameter and 6.14" to 6.21" for the height. The estimated relative density of the Griffin loose sand layer was roughly 50%, determined from empirical relationships correlating cone penetration test (CPT) tip resistance to relative density. Therefore, all samples in this project's cyclic triaxial testing program were prepared to be at a nominal 50% relative density. The actual relative density of each sample, determined from the known weight of soil and known volume, ranged between 47% and 56%, as listed in Table 7-3.

Moist tamping, a method proposed by Ladd (1978), was used for sample preparation. Moist tamping produces a consistent void ratio throughout samples and avoids the segregation problems common with pluviation preparation methods. While moist tamping does not replicate natural deposition, maintaining a consistent preparation method throughout testing ensured that all results were equally affected by the preparation method. Comparison of test results from samples of different ages is possible regardless of the preparation method.

Several studies have shown the importance of saturation in liquefaction resistance. Ladd (1978) and Polito (1999) recommend that Skempton's (1954) pore pressure parameter B be greater than 0.94 in order to prevent increased liquefaction resistance due to decreased saturation. In this

project, the minimum acceptable B value was set at 0.96. The B value of the samples in this project ranged from 0.96 to 0.98, as listed in Table 7-3.

During loading, valves were closed to ensure that the sample was undrained, closer replicating field conditions during an earthquake. The loading cycles were applied as sine waves in compression initially at a rate of one cycle per second. Finally, a consistent definition of failure was defined as 5% double amplitude axial strain. The GeoRobot software ended a test when 5% axial strain was reached. At that point, the cell and back pressures were recorded, allowing determination of the excess pore pressure ratio at failure. Excess pore pressure ratio at failure was typically between 0.9 and 0.95, with maximum and minimum values of 0.98 and 0.85, respectively, as listed in Table 7-3.

The purpose of cyclic triaxial testing in this study was to determine the change in liquefaction resistance with time. Therefore, specimens were prepared and allowed to age for varying lengths of time. Tests were conducted using CSR values of 0.150, 0.175, 0.200, and 0.225 immediately following consolidation, as well as three days, seven days (one week), and twenty eight days (one month) following consolidation. Three tests were performed at each CSR for the samples tested immediately following consolidation. Two tests were performed at each CSR for the samples tested three days after consolidation. Multiple tests were conducted at these aging periods in order to determine the variability of the results. Only one test was performed at each CSR for samples tested one week and one month following consolidation in order to complete the testing program in a reasonable time. Initial tests on samples immediately after consolidation showed that a CSR of 0.125 did not fail in 100 cycles, the maximum number of cycles allowed by the GeoRobot software at a loading rate of 1 Hz.

7.4.3 Results

The results of cyclic triaxial testing are shown in Figure 7-5 and summarized in Table 7-3. Three samples each were tested at CSRs of 0.225, 0.2, and 0.175 immediately after consolidation. Two samples each were tested at a CSR of 0.15 immediately after consolidation. One sample tested at a CSR of 0.1 and two of the three samples tested at a CSR of 0.125 did not fail within 100 cycles. At all other values of CSR, the samples failed between 7 and 37 cycles. While there is some variability in the number of cycles to failure at each CSR, a consistent trend of greater cycles to reach failure at lower CSRs was observed. Samples tested at lower CSR values showed greater variability in the number of cycles required to reach failure.

For cyclic triaxial tests conducted three days after the end of consolidation, two tests each were conducted at CSRs of 0.225, 0.2, 0.175, and 0.15. One sample tested at a CSR of 0.125 did not fail within 100 cycles. The samples aged three days prior to testing showed less variability in the number of cycles to failure than the tests conducted immediately after consolidation. Tests at the three day aging period showed the same trend of increasing number of cycles to failure with decreasing CSR as the fresh testing period. Additionally, the three day samples required a larger number of cycles to fail than fresh specimens.

Seven more cyclic triaxial tests were conducted at aging periods longer than three days. After aging for one week following consolidation, tests were conducted at CSRs of 0.225, 0.2, 0.175, and 0.15. The one week sample tested at a CSR of 0.15 did not fail within 100 cycles. One week specimens took more samples to reach failure than specimens aged for three days.

Only one sample was tested after aging for two weeks. At a CSR of 0.225, the two week sample failed at 18 cycles, showing an increased liquefaction resistance compared to samples with less aging time.

Two samples were tested at CSRs of 0.225 and 0.175 following a 28 day aging period. The results of cyclic triaxial testing focusing on tests conducted at a CSR of 0.225 and 0.175 are shown in Figure 7-6. The 28 day sample tested at a CSR of 0.225 failed after 19 cycles compared to 18 cycles after two weeks of aging, 15 cycles after one week of aging, an average of 12.5 cycles after three days of aging, and an average 9.3 cycles for tests conducted immediately after consolidation. The 28 day sample tested at a CSR of 0.175 failed after 34 cycles. While tests conducted at lower CSR values showed more variability, the 28 day value of 34 cycles to failure is comparable to the one week value of 35 cycles to failure, but shows a clear increase compared to the average three day and average fresh values of 20 and 24.3 cycles to failure, respectively.

7.5 Conclusion

This chapter describes the soil characterization performed on soil specimens taken from the Griffin, IN and New Madrid, MO field experiment sites, as well as cyclic triaxial experiments that were performed on reconstituted samples of Griffin sand. A description of the soil characterization efforts and cyclic triaxial testing was presented. Soil characterization of the Griffin, IN and New Madrid, MO sites allowed the sand aging effects from this project's field experiments to be compared to sand aging effects reported in previous studies. Additionally, the results of the cyclic triaxial tests were presented and discussed. Cyclic triaxial testing showed that

liquefaction resistance increased with time following consolidation across the range of tested CSR values.

Table 7-1. Summary of soil properties for the Griffin, IN and New Madrid, MO studies.

Sand, Section #	C_u	C_c	D_{10} (mm)	D_{50} (mm)	USCS Classification	$\gamma_{d,max}$ (pcf)	$\gamma_{d,min}$ (pcf)	e_{min}	e_{max}	Reference
Griffin, IN Loose Sand Layer	2.05	0.78	0.19	0.27	SP	120	97	0.38	0.72	
	4.09	0.56	0.65	1.25	SP					
New Madrid, MO	3.13	1.20	0.16	0.42	SP					

Table 7-2. Summary of chemical properties and depositional details for the Griffin, IN and New Madrid, MO studies.

Sand	% Quartz	% Feldspar	Other minerals	Description	Age	Depositional Process	Reference
Griffin, IN Loose Sand Layer	Mostly				Early Holocene	Fluvial	
Griffin, IN Loose Gravelly San d Layer	Mostly				12,000 since liquefaction event	Glacial	
New Madrid, MO	Mostly				200 since liquefaction event	Glacial	

Table 7-3. Results of cyclic triaxial testing on reconstituted samples from the loose sand layer in Griffin, IN.

Aging Period	CSR	Relative Density, D_r (%)	Skempton's B-Value	Excess pore pressure ratio, r_u	Number of Cycles to Failure
Fresh	0.225	49	0.98	0.91	14
	0.225	48	0.97	0.85	7
	0.225	49	0.98	0.91	7
	0.200	56	0.98	0.89	7
	0.200	49	0.96	0.91	7
	0.200	50	0.97	0.95	13
	0.175	48	0.97	0.91	28
	0.175	49	0.97	0.90	27
	0.175	47	0.97	0.86	18
	0.150	49	0.98	0.92	28
	0.150	50	0.96	0.95	37
	0.125	52	0.98	0.92	39
	0.125	47	0.96	0.82	Did not fail
	0.125	51	0.98	0.75	Did not fail
	0.100	50	0.98	0.78	Did not fail
3 day	0.225	49	0.96	0.97	13
	0.225	47	0.96	0.90	12
	0.200	50	0.97	0.95	16
	0.200	53	0.98	0.97	21
	0.175	48	0.96	0.98	20
	0.175	49	0.98	0.85	20
	0.150	47	0.98	0.93	22
	0.150	48	0.97	0.88	17
	0.125	51	0.96	0.60	Did not fail
1 week	0.225	48	0.96	0.88	15
	0.200	49	0.98	0.95	16
	0.175	49	0.98	0.94	35
	0.150	48	0.97	0.93	Did not fail
2 weeks	0.225	49	0.96	0.93	18
1 month	0.225	49	0.96	0.93	19
	0.175	48	0.96	0.89	34

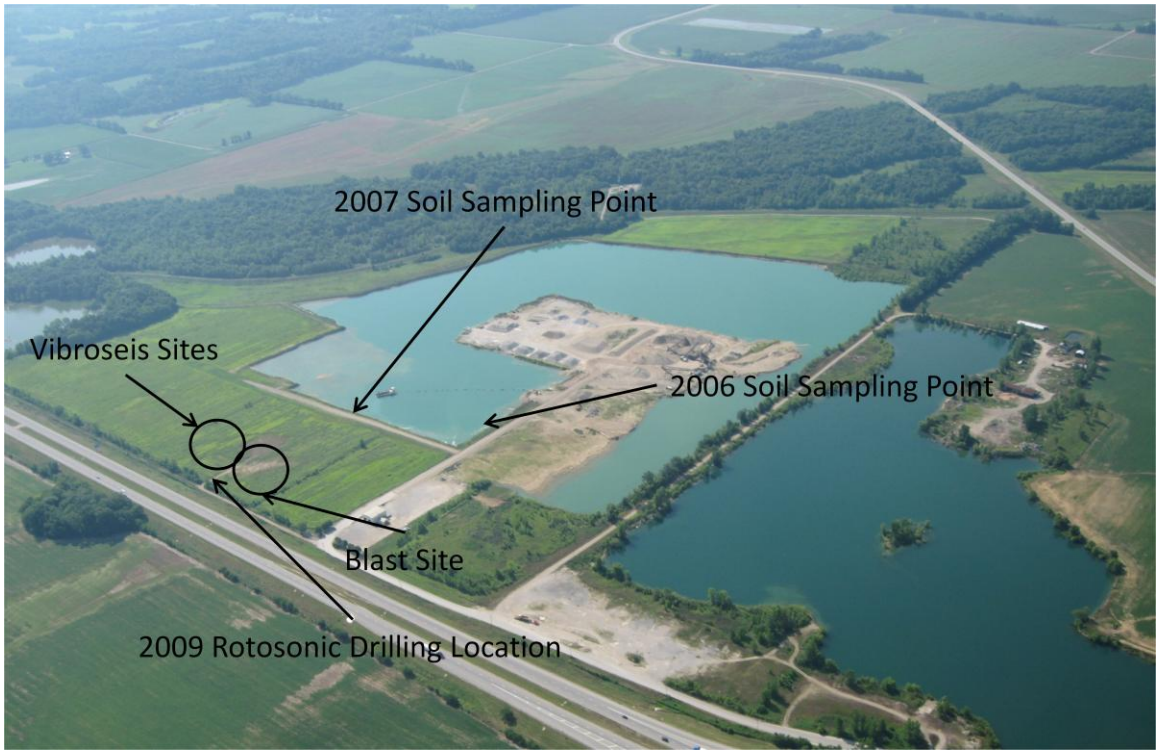

Figure 7-1. Aerial photograph of the Griffin, IN field site with sample locations highlighted (photo courtesy of Mulzer Crushed Stone, Inc.).

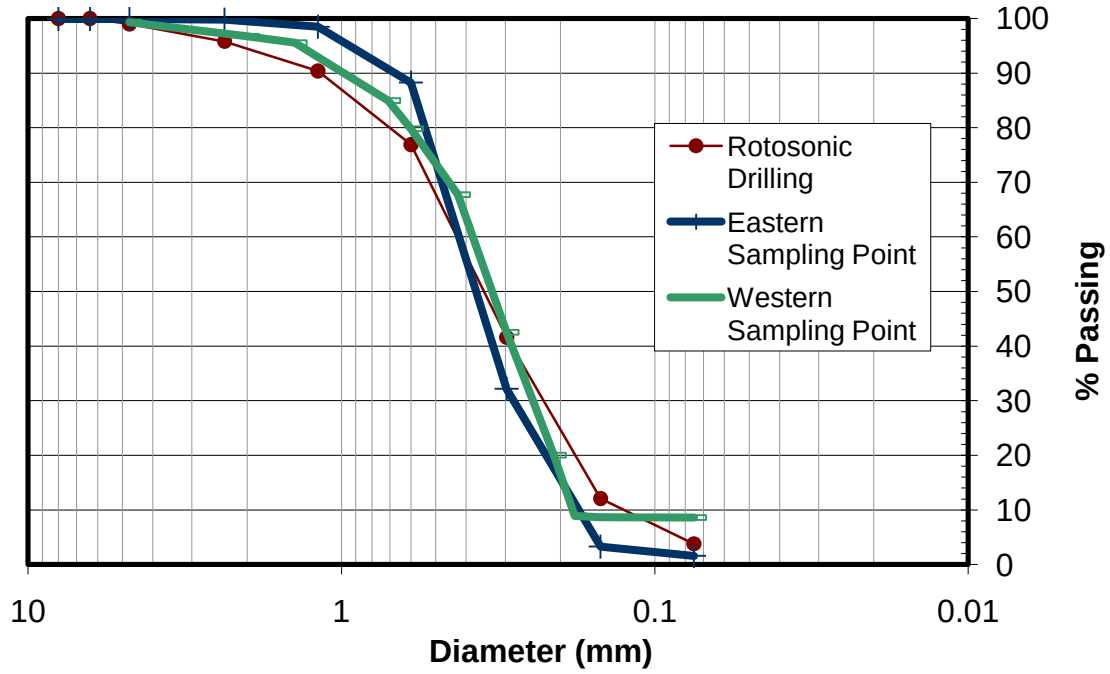

Figure 7-2. Grain size distribution curves from the three Grffin, IN sampling points in the loose sand layer.

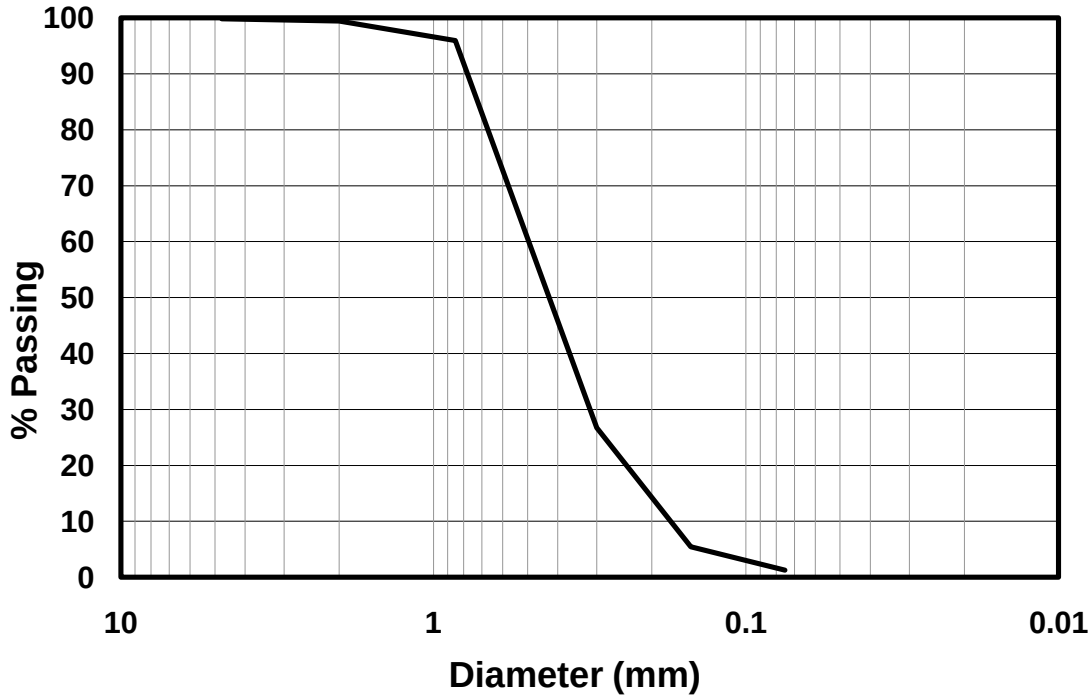

Figure 7-3. Grain size distribution curve for the New Madrid, MO loose sand layer.

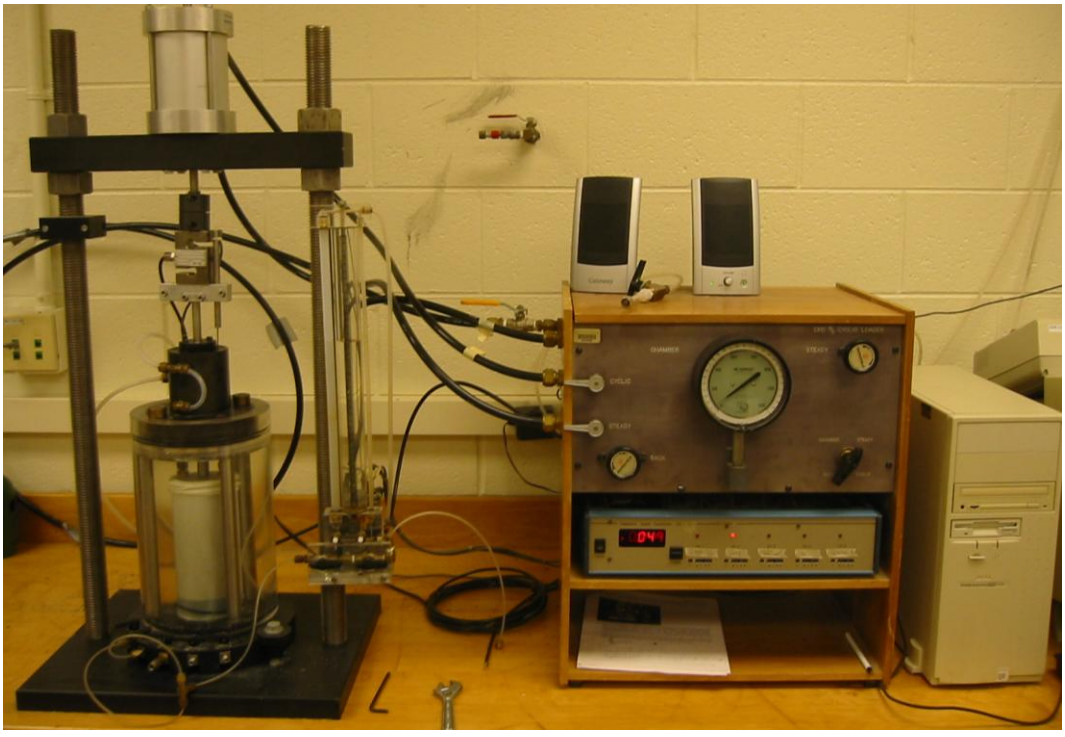

Figure 7-4. CKC cyclic triaxial device.

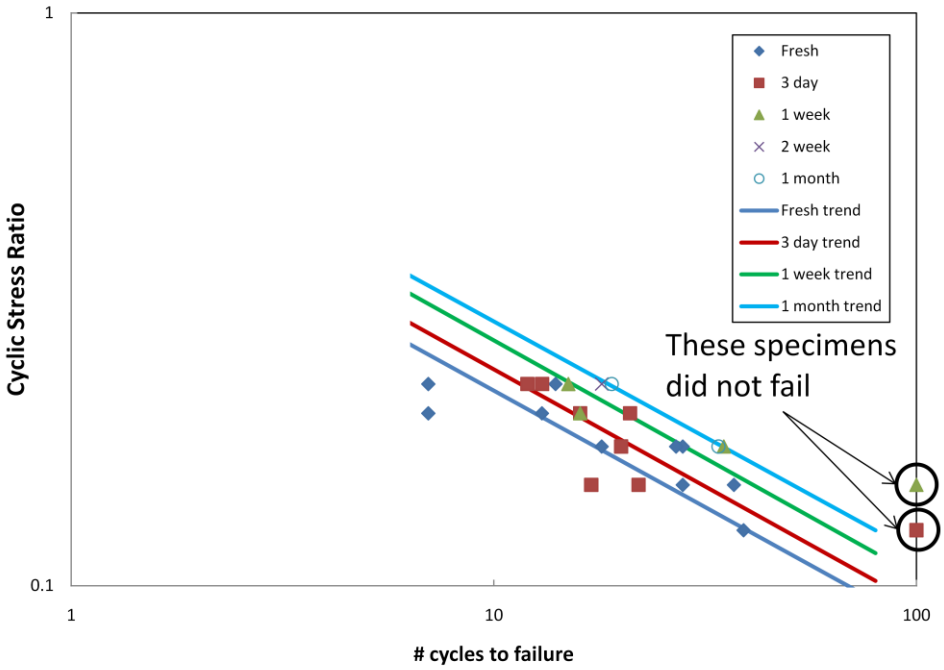

Figure 7-5. Results of cyclic triaxial testing at various aging periods with trend lines showing increased liquefaction resistance with time.

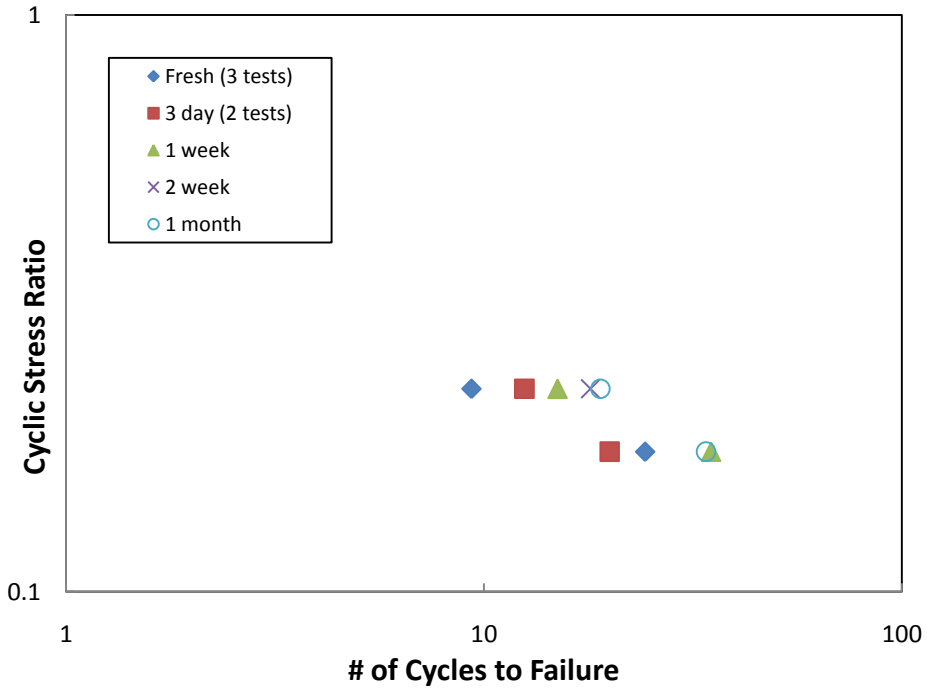

Figure 7-6. Mean value of number of cycles to failure at CSRs of 0.225 and 0.175 showing increased liquefaction resistance with time.

Chapter 8

Predictive Sand Aging Method

8.1 Introduction

Three field experiments were performed and results were compared to previous studies. Previous research on sand aging identified factors that influence the magnitude of sand aging. Focusing on those factors, this chapter describes the development of a method of predicting sand aging effects. This chapter will also describe the preparation of data for use in the analysis, factors influencing sand aging, and the predictive sand aging method.

8.2 Preparation of Experimental Data and Data Reported in Previous Studies

The three field experiments described in Chapters 4 through 6 of this dissertation, in addition to 22 documented studies of sand aging manifested in the field through penetration resistance, were considered. Determining a representative cone penetration test (CPT) normalized tip resistance (q_{c1N}) before and after sand aging was necessary prior to developing a method of predicting sand aging. Normalized tip resistance was computed by Equation 4-7. In cases where unit weight, effective stress, or q_{c1N} were not reported, 16 kN/m^3 and 9.2 kN/m^3 were assumed for dry unit weight and buoyant unit weight, respectively, in order to estimate *in situ* effective stress. The ratio of aged tip resistance ($q_c(t)$) to fresh or post-disturbance tip resistance ($q_{c,fresh}$) was determined. Using q_c or q_{c1N} will result in the same ratio.

Table 8-1 lists the project title, project identification number used to identify data points in figures, depth of the center of the layer of interest, depth to the ground water table, effective vertical stress (σ'_v), days between disturbance and initial CPT soundings, $q_{c,fresh}$, q_{c1N}, days between disturbance and aged CPT soundings, and $q_{c,aged}$. Hanford (1988) reported standard penetration test (SPT) blow count (N) rather than q_{c1N}. His data was converted to q_{c1N} using Kulhawy and Mayne's (1990) correlation between SPT-N_{60} and q_c and the reported mean grain size of 0.15 mm.

8.3 Sand Aging Influence Factors

Previous research has identified precipitation of silica cement (Mitchell and Solymar, 1984), dissipation of bubbles in the pore fluid (Dowding and Hryciw, 1986), amount of disturbance (Dumas and Beaton, 1988; Thomann and Hryciw, 1990), temperature (Charlie et al., 1992b), the number of granular contacts leading to increasing interlocking (Schmertmann, 1987; Mesri et al., 1990; York et al., 1994; Bowman and Soga, 2003), angularity (Joshi et al., 1995; Mejia et al., 1988), relative density (Mejia et al., 1988; Bowman, 2002), depositional age (Schmertmann, 1987), and effective vertical stress (Mejia et al., 1988; Wang and Tsui, 2009) as factors that influence aging.

Of the 25 sources of field sand aging data reported above, 10 do not report the chemical composition of the sand. Fourteen sources report that the sands were primarily quartz sands, with only one case history reporting calcium sand. While the one calcium case falls within the center of the quartz data, as shown in Figure 8-1, it is impossible to draw conclusions, particularly since there is only one data point. Therefore, no trends related to chemistry can be concluded from this data.

The composition of the pore fluid also influences the potential for chemical aging. In a dry soil, cementation of sand grains is much less likely than in saturated soil. Additionally, Joshi et al. (1995) showed that aging effects were greater when the soil was saturated with salt water. As shown in Figure 8-2, there is a trend of increasing aging effects in the following order: dry soil, soil saturated with fresh water, and soil saturated with salt water.

The amount of disturbance was first theorized to affect sand aging following deep dynamic compaction in which aging was more pronounced closer to the surface, where disturbance was greater (Dumas and Beaton, 1988). As shown in Figure 8-3, data from the disturbance methods causing more disturbance, including explosive densification, placement of hydraulic fill, deep dynamic compaction (DDC) at shallow depths, vibro-compaction, and impact piers, show greater manifestation of sand aging than the lower strain disturbance methods, including earthquakes, DDC at greater depths, and vibroseis shaking. The data shows that disturbance method influences aging effects.

Dissipation of bubbles from blast gas or source of aeration has been shown to affect aging (Dowding and Hryciw, 1986; LeClerc, 2008). Explosive densification, vibro-compaction, placement of hydraulic fill, and impact pier installation were considered to aerate the pore fluid.

Vibroseis shaking, earthquake shaking, and DDC do not aerate the pore fluid. As shown in Figure 8-4, aerating the pore fluid appears to lead to greater aging effects. However, aeration of the pore fluid is inherently tied to the soil disturbance method. DDC is the only high disturbance method included in the data where no aeration of the pore fluid occurred. Therefore, less aging was expected from the group of projects that did not aerate the pore fluid compared to the projects that, in addition to causing greater disturbance, introduced aeration into the pore fluid. It is not clear from the data that dissipation of bubbles influences aging behavior.

Charlie et al. (1992b) proposed that higher temperature led to greater aging effects because higher temperatures lead to more dissolution and precipitation of cementing agents. As mentioned by Jefferies and Rogers (1993), mean air temperature is less relevant to sand aging than the temperature in the soil. While temperatures at shallow depths vary more than at greater depths, the mean temperature is applicable for all depths. For locations outside the continental United States, the mean air temperature was used. As shown in Figure 8-5, there is no clear trend of increased aging with increased temperature.

The proposed mechanical mechanism of sand aging is heavily influenced by the number of granular contacts per unit volume. Fine, well-graded sands have more contact points per unit volume than coarse, poorly graded sands. As shown in Figure 8-6, finer sands show greater manifestation of sand aging. The trend is not as clear in well-graded sands, as shown in Figure 8-7. While a best-fit straight line through the data in Figure 8-7 shows increasing aging effects with increasing coefficient of uniformity, the slope of the line is influenced by the two data points from the explosive densification project to improve the well-graded sand at the Cooper River Bridge in Charleston, SC. If one does not consider that project, a trend of decreased aging effects with greater coefficient of uniformity emerges. Bowman (2002) and Jirathanathaworn (2009) show that intergranular forces are not transmitted through each contact point. In well-graded soils, many contacts do not transmit a significant force, rendering them less important in the manifestation of sand aging. Therefore, the coefficient of uniformity does not appear to affect sand aging because, in well-graded sand, a higher percentage of contacts do not transmit forces. Mean grain size is a better indicator of the number of contacts influencing load distribution and, therefore, sand aging.

Grain shape influences the number of contacts in a soil assembly. Angular soils have more contact points and are more compressible than rounded soils with similar grain size and uniformity. Therefore, one would expect greater aging effects in angular soils. However, as

shown in Figure 8-8, there is little evidence in the data that this distinction affects aging. This may be due to the relatively small database as only five research projects report the angularity of the soil (Mitchell and Solymar, 1984; Thomann and Hryciw, 1992a; Howie et al., 2001; Baxter and Mitchell, 2004; and Camp et al., 2008).

Relative density, D_r, also influences the number of contacts in a soil assembly and has been proposed as a factor influencing aging behavior (Mejia et al., 1988; Bowman, 2002). *In situ* test results are often correlated to D_r. Due to the uncertainty in D_r and in the most appropriate correlation for the projects referenced in this study, $q_{c1N,fresh}$ was used as a proxy for D_r. As shown in Figure 8-9, there is somewhat of a trend of increased aging effects with lower $q_{c1N,fresh}$ and, therefore, lower D_r.

Depositional age was also suggested as a factor influencing aging behavior (Schmertmann, 1987). If one considers pre-disturbance q_c as the basis for comparison, there are several projects that show a lack of aging in Pleistocene deposits (e.g. Thomann and Hryciw, 1992a; Charlie et al., 1992b; Camp et al., 2008). However, when using tests conducted immediately following disturbance as the basis for comparison, $q_{c,fresh}$ does increase with time. Because $q_{c,fresh}$ was used for comparison in this dissertation, depositional age was not considered when developing the sand aging predictive method.

Finally, vertical effective stress, σ'_v, has been proposed to influence aging behavior (Mejia et al., 1988; Wang and Tsui, 2009). As shown in Figure 8-10, the data supports this hypothesis. Deposits with lower σ'_v tend to show greater aging effects than deposits with larger σ'_v. The only project which recorded sand aging where σ'_v was greater than 200 kPa was the explosive densification project at the Jebba Dam. Data from this project does not follow the trend of decreased aging effects with increasing σ'_v. Because data from higher σ'_v conditions is scarce, additional studies should be conducted prior to drawing conclusions.

In summary, the data does not show a clear trend between aging effects and the soil's chemical composition, temperature, coefficient of uniformity, grain shape, or depositional age. Disturbance method, pore fluid composition, mean grain size, $q_{c1N,fresh}$, and σ'_v showed an influence on aging behavior.

8.4 Predictive Sand Aging Method

Initially, statistical methods such as multiple linear regression and indicator kriging were considered for development of an equation predicting sand aging effects on cone penetration tip

resistance. However, the database was judged to be too small to accurately capture the importance of each of the factors influencing sand aging and the interaction between these factors. Therefore, it was necessary to determine which factors would be included in a predictive relationship for aging as a function of time since disturbance.

The method of disturbing the sand (i.e. energy input or magnitude of shear straining) significantly influences aging behavior. The seven disturbance methods that have been observed to yield sand aging can be placed in two categories: vibratory methods and compactive methods. Vibratory methods include explosive densification, placement of hydraulic fill, earthquakes, and vibroseis shaking. Compactive methods include vibro-compaction, deep dynamic compaction, and impact piers. The fundamental difference is the induced horizontal stress state by implementation of the method. After vibratory disturbances, the soil is close to normally consolidated conditions, while compactive methods significantly increase the horizontal stress, effectively creating an overconsolidated state. In terms of *in situ* tests, this distinction is important because of the major role that horizontal stress has on penetration resistance. Therefore, the data was grouped by disturbance method prior to further analysis.

As described in Chapter 8.3, σ'_v, $q_{c1N,fresh}$ and D_{50} appear to influence aging. The influence of σ'_v, $q_{c1N,fresh}$ and D_{50} on the relationship between aging and time since disturbance is shown in Figures 8-11 through 8-13, respectively. As each of these values increases, aging effects decrease, as previously shown in Figures 8-6, 8-9, and 8-10. However, when plotted as a function of time since disturbance, the trend of increased rate of aging with decreased σ'_v, $q_{c1N,fresh}$, or D_{50} value is clearest for σ'_v. Therefore, the predictive sand aging method was based on time since disturbance, the method of disturbance, and σ'_v.

Projects which disturbed the sand using a vibratory method were separated into two groups: projects where $\sigma'_v < 100$ kPa and projects where σ'_v was between 100 and 200 kPa. Only one project, explosive densification at the Jebba Dam, was conducted at very high effective stress, 304 kPa. The depth of improvement was significant in this project, necessitating numerous large explosives. The amount of blast gas introduced into the pore fluid per unit volume of soil was larger in this project than any other described in this study. The higher volume of introduced gas may have led to increased rate of aging recorded following the Jebba blast. Therefore, effective stress of higher than 200 kPa was not considered. A trend line was fit through each group of data using the general form shown in Equation 8-1.

$$\frac{q_c(t)}{q_{c,fresh}} = 1 + \alpha \log(t) \quad \ldots(8\text{-}1)$$

Where t is time in days, $q_c(t)$ is the tip resistance at time t, $q_{c,fresh}$ is the initial post-disturbance tip resistance, and α is the rate of aging in units of 1 / log (days). Additional weight was given to data collected as part of this study to minimize the impact of possible errors in misinterpreting data reported in previous studies. As shown in Figures 8-14 and 8-15, $\alpha = 0.19$ when $\sigma'_v < 100$ kPa and $\alpha = 0.10$ when $100 < \sigma'_v < 200$ kPa. Both trend lines are shown together in Figure 8-16.

An exponential relationship between α and σ'_v was assumed. An exponential relationship fits the data well because it predicts a low rate of aging at high σ'_v and a maximum increase in $q_c(t) / q_{c,fresh}$ of 0.25 per log cycle of days. Because the trends shown in Figures 8-14 and 8-15 fit the data collected as part of this study's explosive densification project, the values of σ'_v in each of these cases, 45 kPa for the Griffin loose sand layer and 131 kPa for the Griffin loose gravelly sand layer, were used as the representative values of σ'_v. The resulting relationship between α and σ'_v is shown in Equation 8-2.

$$\alpha = 0.25e^{-0.75\sigma'_v/\sigma_{atm}} \quad \ldots(8\text{-}2)$$

Where σ_{atm} is atmospheric pressure. Applying this predictive relationship to the sand aging data from the Griffin explosive compaction project yields an R^2 value of 0.96. Because this model demonstrates an excellent fit with the Griffin explosive densification data, these equations are best applied when σ'_v is between the average σ'_v values in the Griffin loose sand and loose gravelly sand layers, 45 and 131 kPa, respectively.

As shown in Figure 8-17, it is expected that this relationship will be modified as more data is collected. Smaller D_{50}, lower $q_{c1N,fresh}$, and the introduction of greater volumes of gas to the pore fluid should increase the rate of aging. Similarly, larger D_{50} and higher $q_{c1N,fresh}$ should decrease the rate of aging. It is hoped that additional data documenting the manifestation of sand aging will clarify the relationship between σ'_v, D_{50}, $q_{c1N,fresh}$, and the rate of sand aging, allowing for the refinement of this model.

As shown in Figure 8-18, a trend line was also fit to the data from compactive disturbance methods using Equation 8-1 with $\alpha = 0.16$. The compactive disturbance method data was not separated by σ'_v because there was less variation in σ'_v than in vibratory projects, the scatter in the ratio of $q_c(t)$ to $q_{c,fresh}$ was smaller than in the vibratory projects, and, most importantly, the unknown horizontal stress, σ'_h, had a significant effect on this data. Results of dilatometer tests (DMT) following installation of impact piers at New Madrid showed a K_0 value of 1.1 using

Schmertmann's (1983) method of correlating friction angle and DMT horizontal stress index, K_D, to K_0. However, post-disturbance DMT data is not available for projects using other compactive methods. It is therefore difficult to determine σ'_h at each site and study its impact on sand aging. One value of α, 0.16, is recommended for predicting the rate of sand aging following compactive disturbance methods due to the uncertain impact of σ'_h. Applying this predictive relationship to the sand aging data from compactive disturbance methods yields an R^2 value of 0.85.

Equation 8-3, which combines Equations 8-1 and 8-2, is recommended to predict aging effects following vibratory disturbance methods, while Equation 8-4 is recommended for use following compactive disturbance methods.

$$\frac{q_c(t)}{q_{c,fresh}} = 1 + 0.25e^{-0.75^{\sigma'_v}/_{\sigma_{atm}}} \log(t) \quad \ldots(8\text{-}3)$$

$$\frac{q_c(t)}{q_{c,fresh}} = 1 + 0.16 \log(t) \quad \ldots(8\text{-}4)$$

It is important to note that these relationships describe short term sand aging. Over 90% of the data used to develop these relationships was collected within one year of disturbance. To predict long term sand aging, it is recommended that one of the methods described in Chapter 9 be used.

In summary, sand aging effects can be predicted using Equations 8-3 and 8-4. Collecting additional data will improve this relationship for several reasons. Post-disturbance DMTs clarify the horizontal stress following compactive disturbance, allowing for the investigation of the effect of horizontal or mean effective stress on aging behavior. Additional data would also help discern the impact of $q_{c1N,fresh}$ and D_{50} on sand aging behavior. A database containing case histories with varying combinations of σ'_v, σ'_h, $q_{c1N,fresh}$, and D_{50} would allow investigation of the interaction these factors and their influence on aging effects. With enough data, Equations 8-3 and 8-4 could be updated to also include factors accounting for the effects of σ'_h, $q_{c1N,fresh}$ and D_{50}.

8.5 Conclusion

This chapter describes the development of a sand aging prediction methodology. A description of the data taken from both the work performed as part of this dissertation and other experimental studies was presented. Additionally, various factors proposed to influence sand aging effects were discussed and compared to trends in the data. Finally, the method of determining the sand aging prediction method was presented. The sand aging prediction method developed from previous

case histories involving sand aging and work described in Chapters 4 through 6 of this dissertation was given by in Equations 8-3 and 8-4.

Table 8-1. Depth and tip resistance data used to create the sand aging predictive model.

Study	Project ID Number	Depth to Center of Layer of Interest (m)	Depth to Ground Water Table (m)	Vertical Effective Stress (kPa)	Fresh Tip Resistance (MPa)	Fresh Normalized Tip Resistance	Time After Disturbance (Days)	Aged Tip Resistacne (MPa)
Griffin loose sand bast	1	3.5	3	45	4.4	66	30	5.6
							75	6.5
							350	5.7
							671	6.3
Griffin loose gravelly sand blast	2	12	3	280	8	48	30	8.6
							75	9.3
							350	9.1
							671	9.8

Table 8-1 (Continued). Depth and tip resistance data used to create the sand aging predictive model.

Study	Project ID Number	Depth to Center of Layer of Interest (m)	Depth to Ground Water Table (m)	Vertical Effective Stress (kPa)	Fresh Tip Resistance (MPa)	Fresh Normalized Tip Resistance	Time After Disturbance (Days)	Aged Tip Resistacne (MPa)
Griffin vibroseis shaking	3	3.5	3	45	10.2	10.8	30	5.6
							270	9.4
New Madrid impact pier installation	4	9	5	132	22	192	33	27
Jebba hydraulic fill placement	5	5	0	46	2.7	40	60	4.2
Jebba vibro-compaction	6	20	0	184	20	147	15	26
							24	28
Jebba explosive densification	7	33	0	304	10	60	21	14
							36	16
							124	18

Table 8-1 (Continued). Depth and tip resistance data used to create the sand aging predictive model.

Study	Project ID Number	Depth to Center of Layer of Interest (m)	Depth to Ground Water Table (m)	Vertical Effective Stress (kPa)	Fresh Tip Resistance (MPa)	Fresh Normalized Tip Resistance	Time After Disturbance (Days)	Aged Tip Resistacne (MPa)
Jacksonville deep dynamic compaction	8	5	2	66	10	99	10	13.5
							15	14.1
							20	14.5
							30	15.3
							40	15.7
							50	16
							60	16.2
		15	2	158	20	159	45	20
Harriet's Bluff blasting	9	4	0.6	43	5	77	30	5
Beaufort Sea hydraulic fill placement	10	8	0	71	5	59	154	5

Table 8-1 (Continued). Depth and tip resistance data used to create the sand aging predictive model.

Study	Project ID Number	Depth to Center of Layer of Interest (m)	Depth to Ground Water Table (m)	Vertical Effective Stress (kPa)	Fresh Tip Resistance (MPa)	Fresh Normalized Tip Resistance	Time After Disturbance (Days)	Aged Tip Resistacne (MPa)
Beaufort Sea explosive densification	11	5	0	45	8	120	17	16
		10	0	89	11	117	17	18
		15	0	134	15	130	17	28
Port Noire Harbor deep dynamic compaction	12	4	2	56	12	161	8	16
		11	2	118	6	55	8	6
Ft McMurray blast 1	13	5	0	46	9.6	142	45	12.7
Douglas Lake explosive densification	14	6.5	0	70	6.5	78	3	7
							42	8
							217	8
					9.5	114	42	13
							217	13

Table 8-1 (Continued). Depth and tip resistance data used to create the sand aging predictive model.

Study	Project ID Number	Depth to Center of Layer of Interest (m)	Depth to Ground Water Table (m)	Vertical Effective Stress (kPa)	Fresh Tip Resistance (MPa)	Fresh Normalized Tip Resistance	Time After Disturbance (Days)	Aged Tip Resistacne (MPa)
Ft McMurray blast 2	15	Not reported	Not reported	188	5.5	40	10	6
							30	6.5
							110	8
					7.5	55	20	10
							100	11
South Platte River explosive densification	16	4	1.5	52	2.6	37	21	2.7
							126	3
Sainte Marguerite Dam explosive densification	17	5.5	1	60	5	64	12	9
							35	11
		10	1	102	14	139	12	14.5
							35	15.5

Table 8-1 (Continued). Depth and tip resistance data used to create the sand aging predictive model.

Study	Project ID Number	Depth to Center of Layer of Interest (m)	Depth to Ground Water Table (m)	Vertical Effective Stress (kPa)	Fresh Tip Resistance (MPa)	Fresh Normalized Tip Resistance	Time After Disturbance (Days)	Aged Tip Resistacne (MPa)
Hong Kong vibro-compaction	18	8	3	102	10	100	42	13.5
Treasure Island explosive densification	19	3.5	.5	36	4	66	42	10
Cooper River Bridge explosive densification	20	5	1	55	2	27	30	4
							2555	5
Fraser River vibro-compaction	21	7	0.5	69	19.5	234	365	23.5
Mississippi Embayment blast	22	10	7	161	22.9	180	229	21.1
Marked Tree blast	23	10	7	161	19.8	156	229	19.8
Charleston explosive densification	24	10	2	112	2	20	484	3
							1034	4

Table 8-1 (Continued). Depth and tip resistance data used to create the sand aging predictive model.

Study	Project ID Number	Depth to Center of Layer of Interest (m)	Depth to Ground Water Table (m)	Vertical Effective Stress (kPa)	Fresh Tip Resistance (MPa)	Fresh Normalized Tip Resistance	Time After Disturbance (Days)	Aged Tip Resistacne (MPa)
Superstition Hills earthquake	25	4.5	2	61	7	90	135	7
Massey Tunnel explosive densification	26	12	2.5	135	9	78	12	9.5
							27	12
							56	12

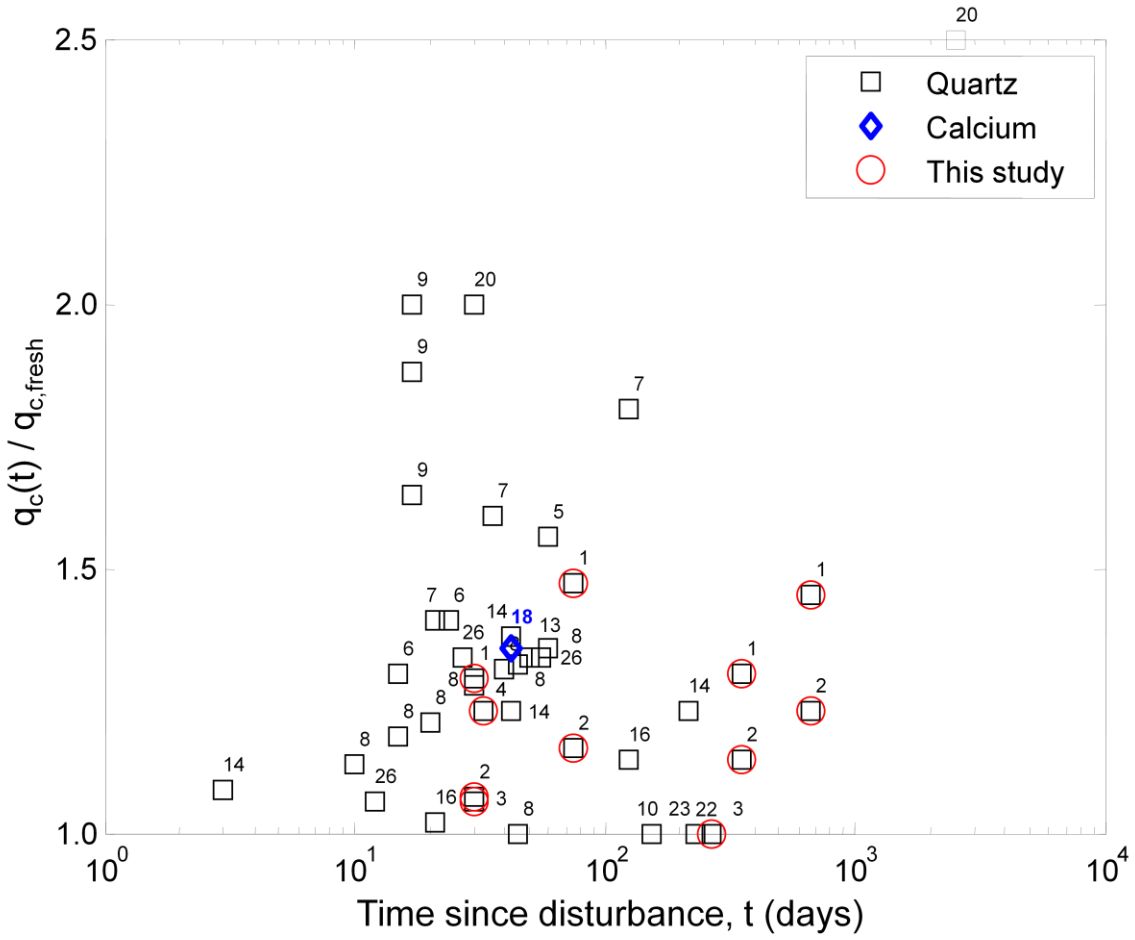

Figure 8-1. Trend of aging data considering the sand's chemical composition. The project identification number is shown next to each data point.

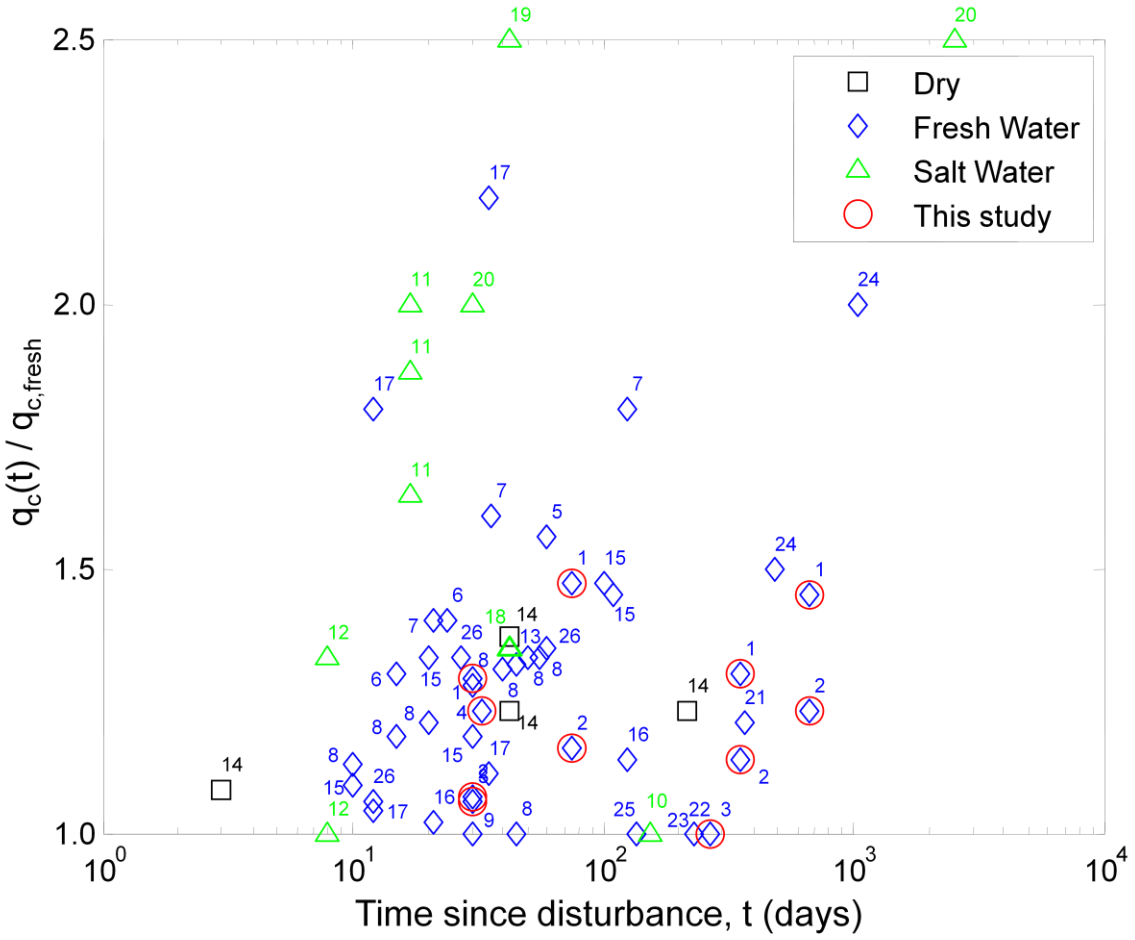

Figure 8-2. Trend of aging data considering pore fluid composition. The project identification number is shown next to each data point.

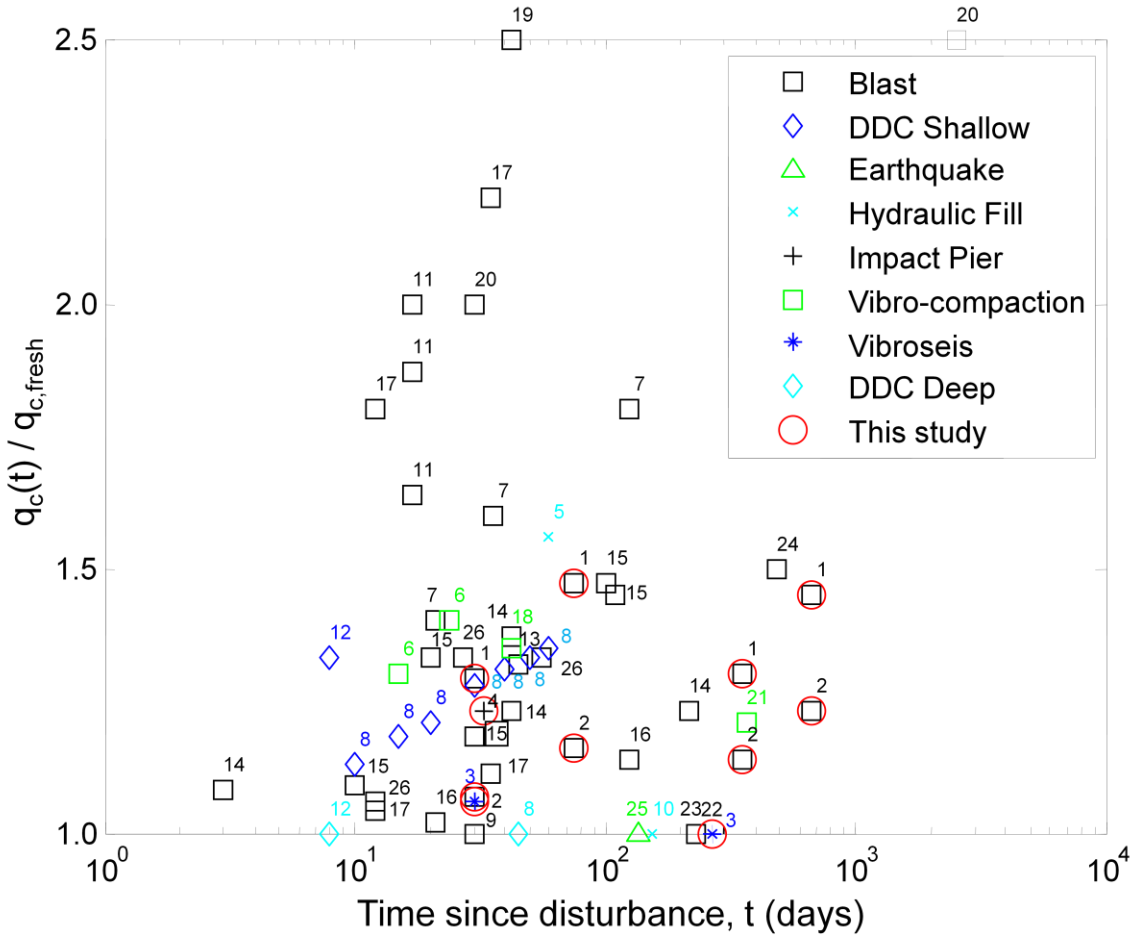

Figure 8-3. Trend of aging data considering the disturbance method. The project identification number is shown next to each data point.

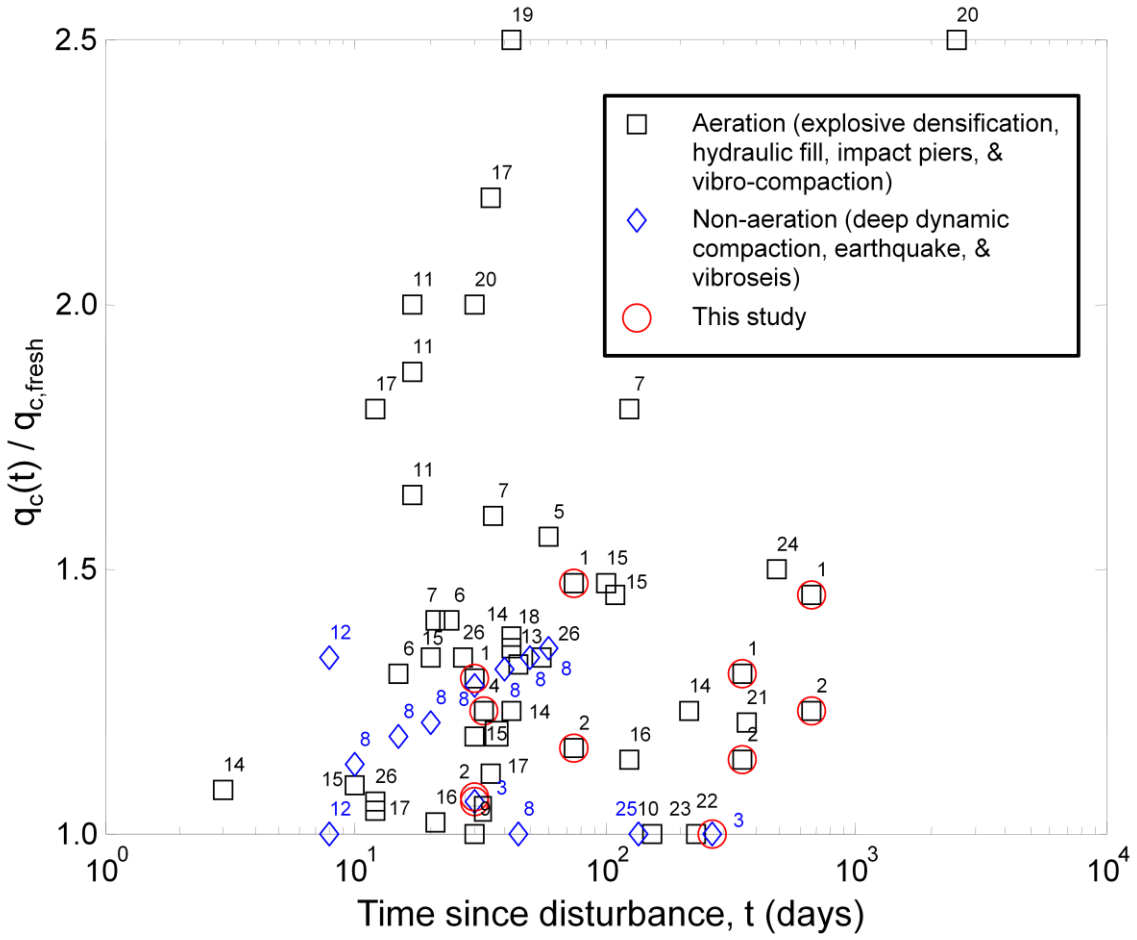

Figure 8-4. Trend of aging data considering aeration of the pore fluid. The project identification number is shown next to each data point.

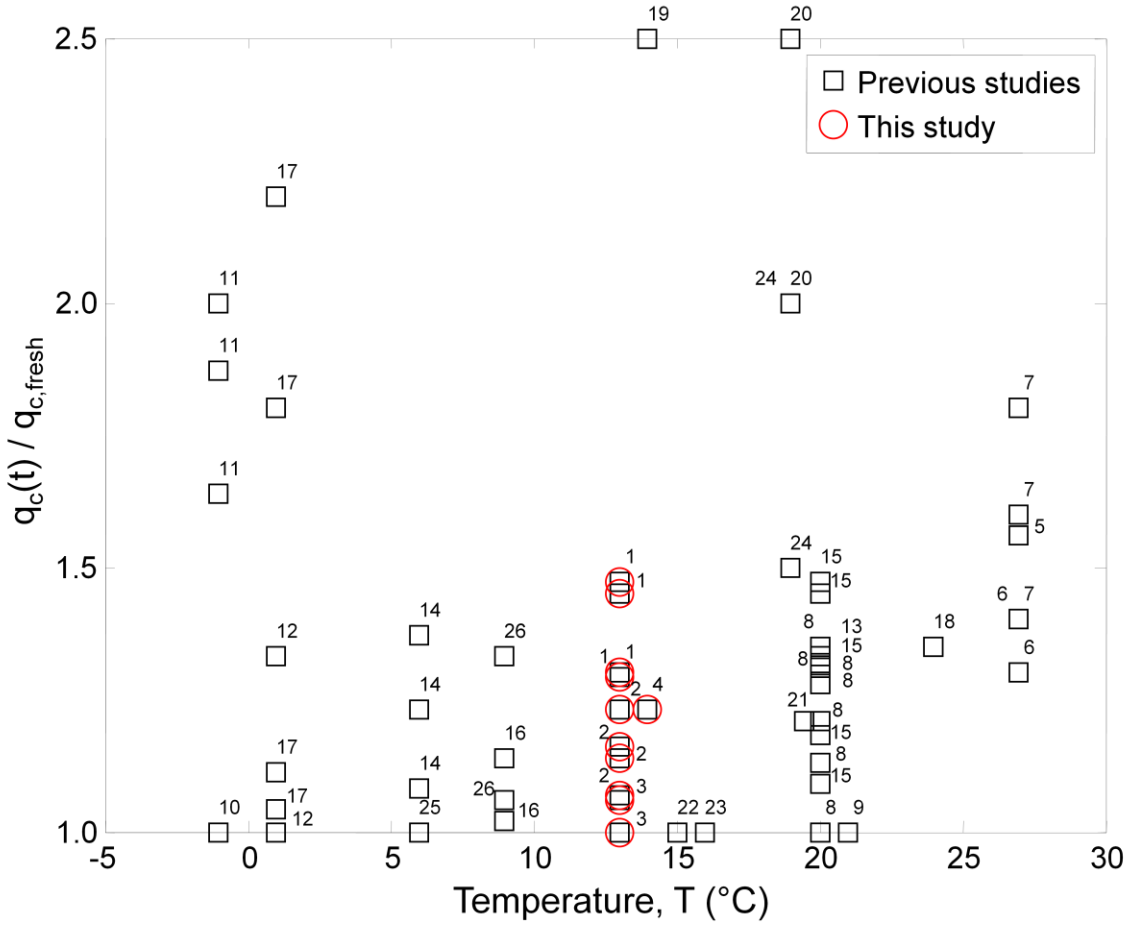

Figure 8-5. Trend of aging data considering temperature. The project identification number is shown next to each data point.

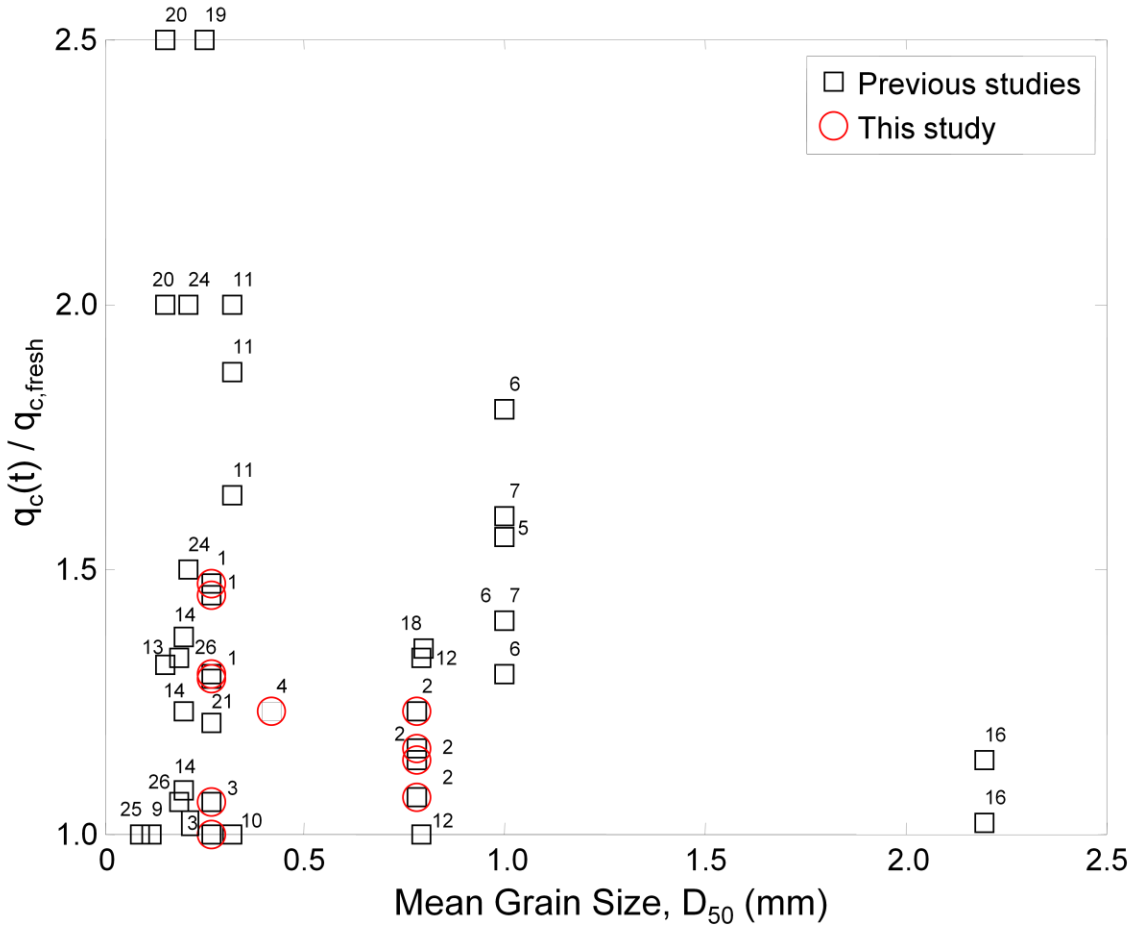

Figure 8-6. Trend of aging data considering mean grain size. The project identification number is shown next to each data point.

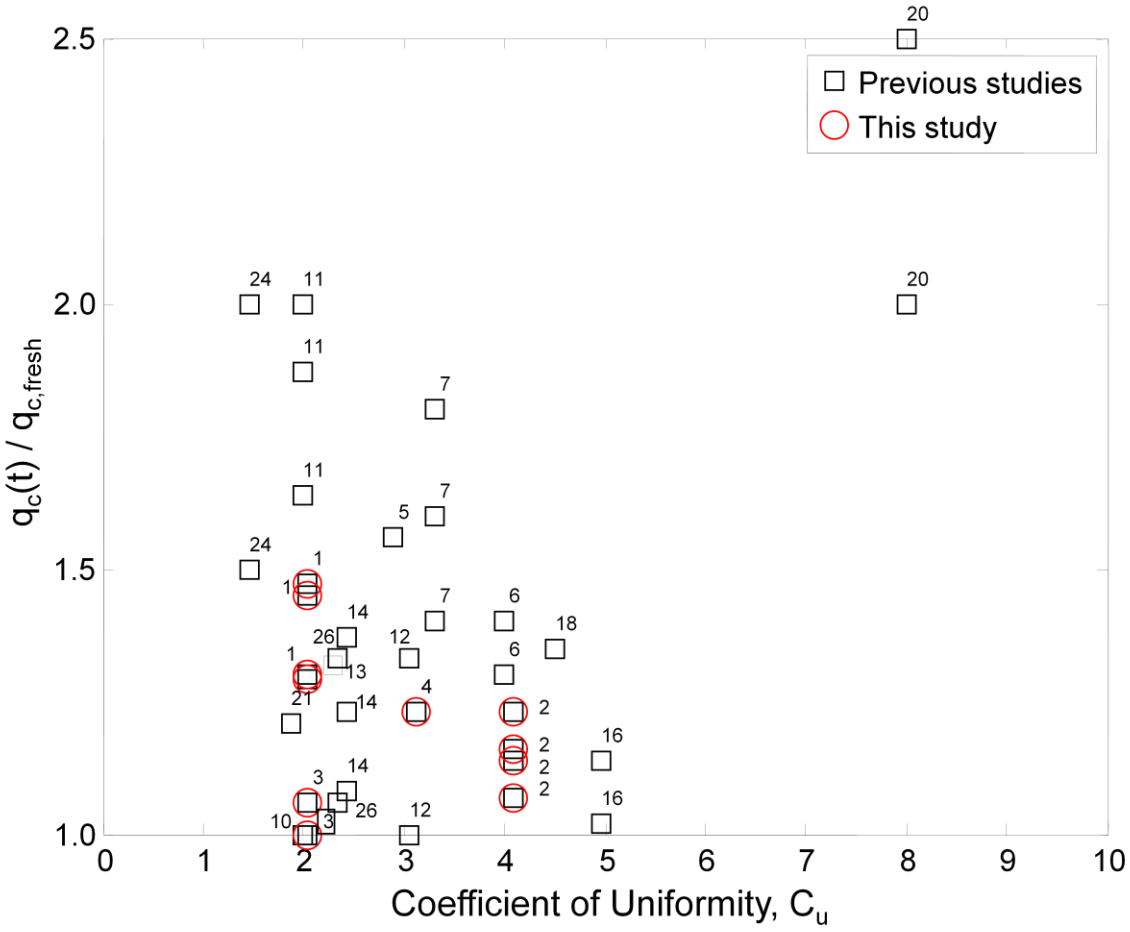

Figure 8-7. Trend of aging data considering the uniformity of the sand deposit. The project identification number is shown next to each data point.

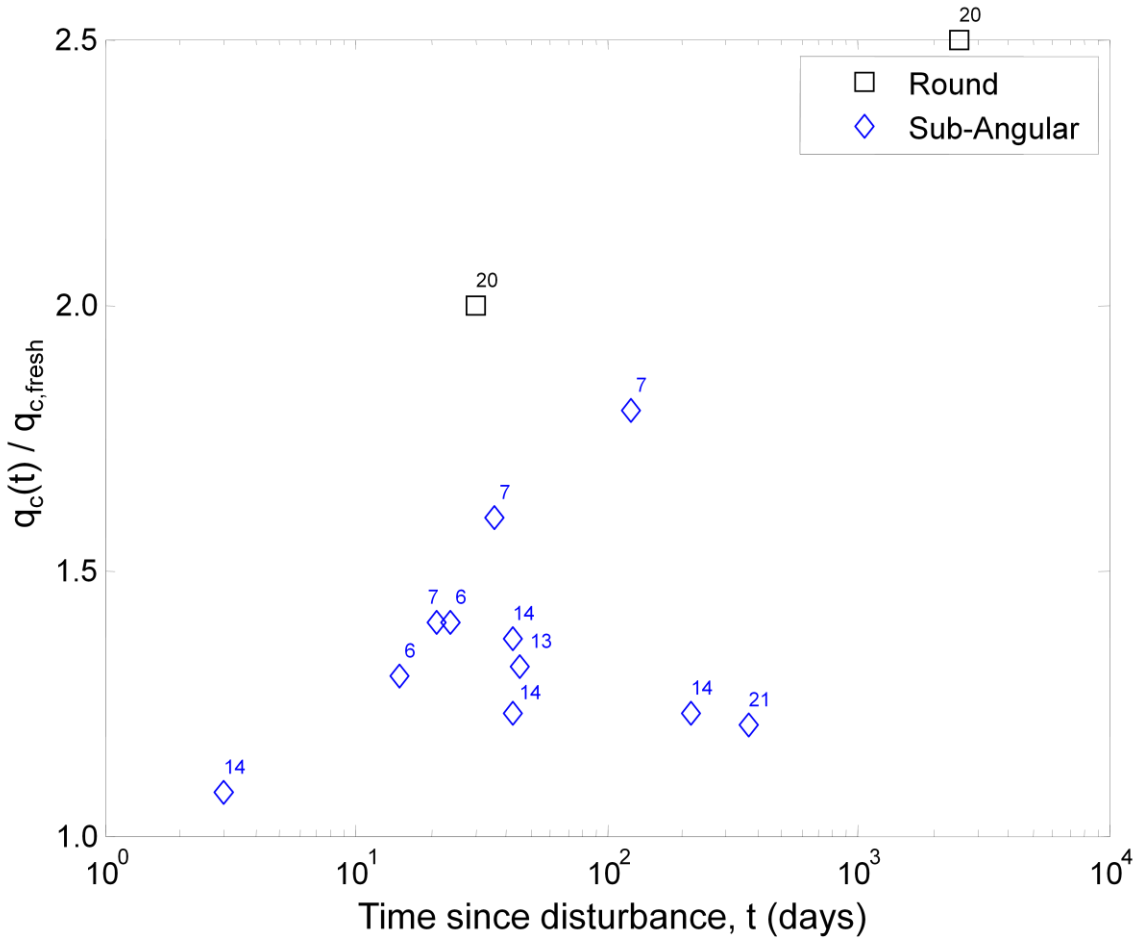

Figure 8-8. Trend of aging data considering grain shape. The project identification number is shown next to each data point.

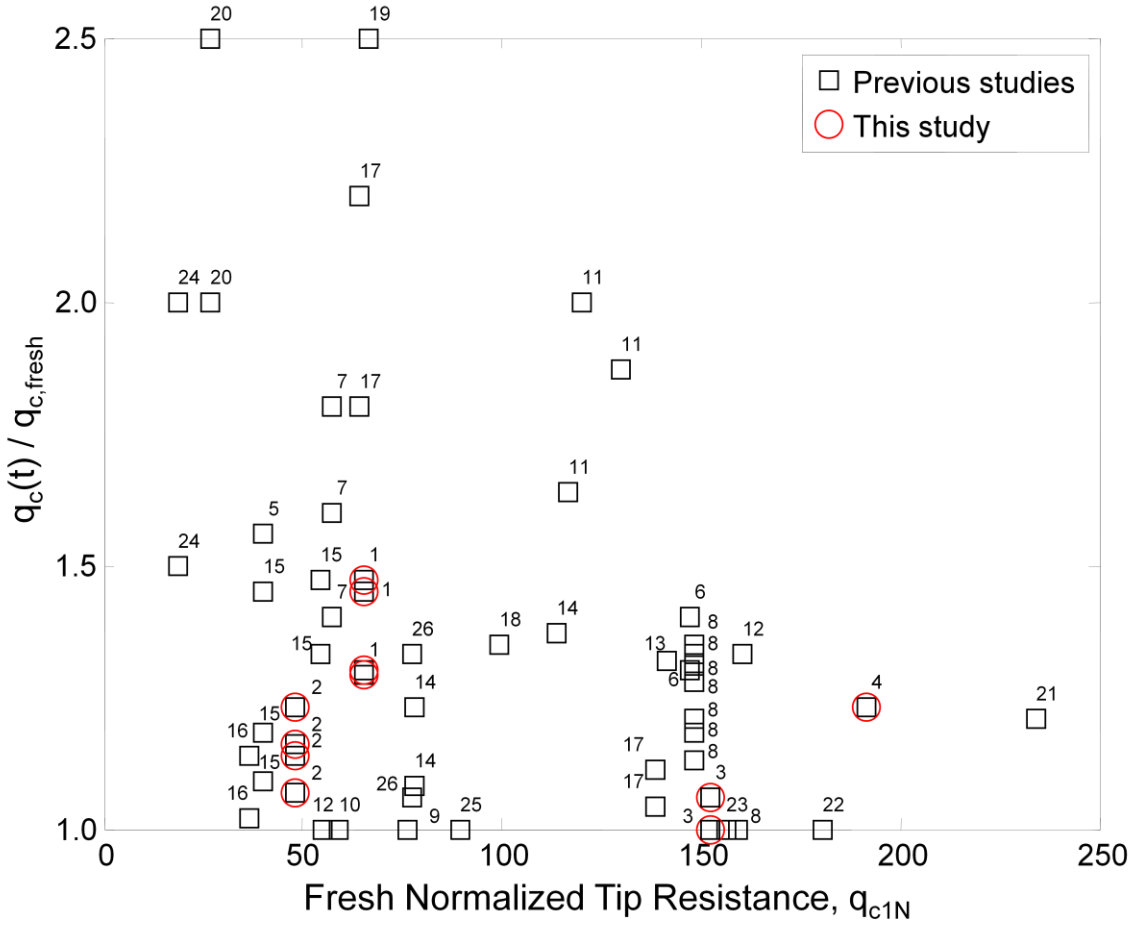

Figure 8-9. Trend of aging data considering fresh mean normalized tip resistance. The project identification number is shown next to each data point.

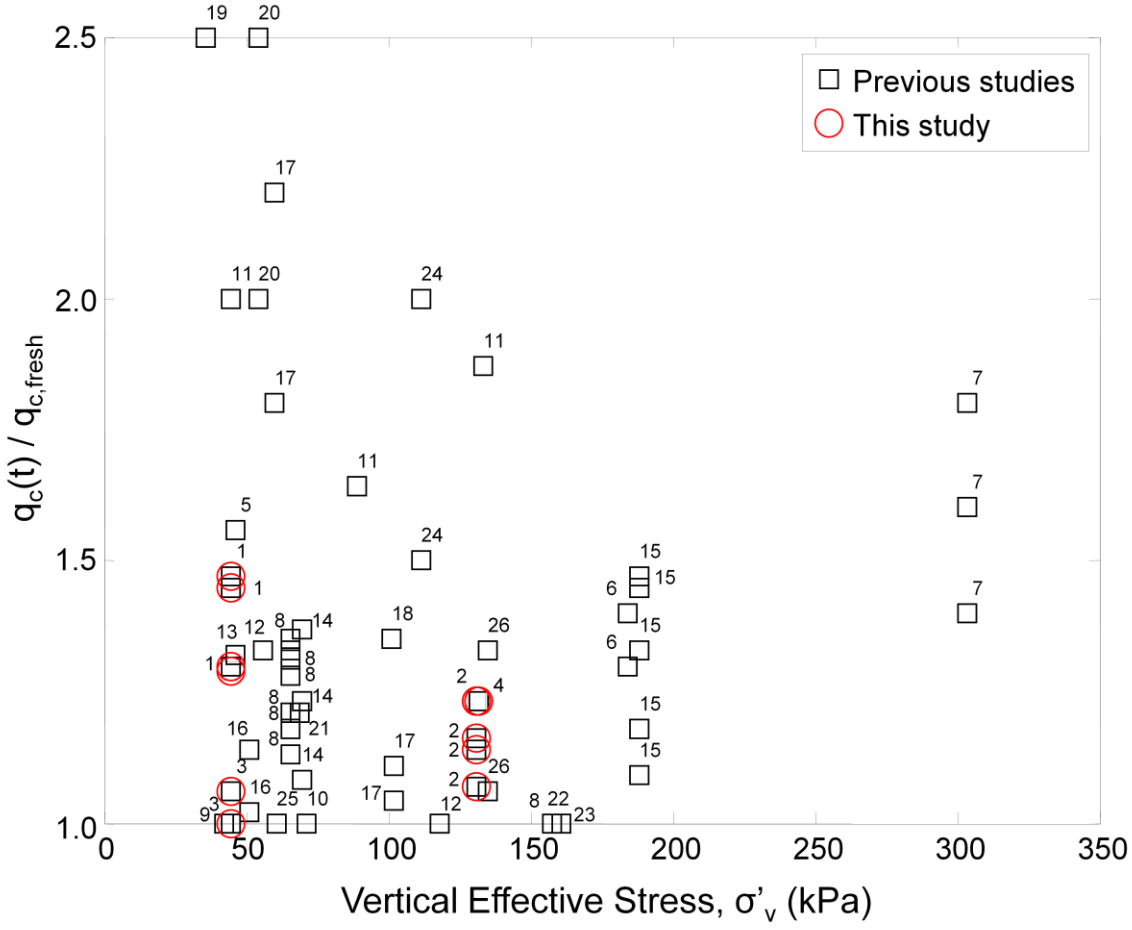

Figure 8-10. Trend of aging data considering vertical effective stress. The project identification number is shown next to each data point.

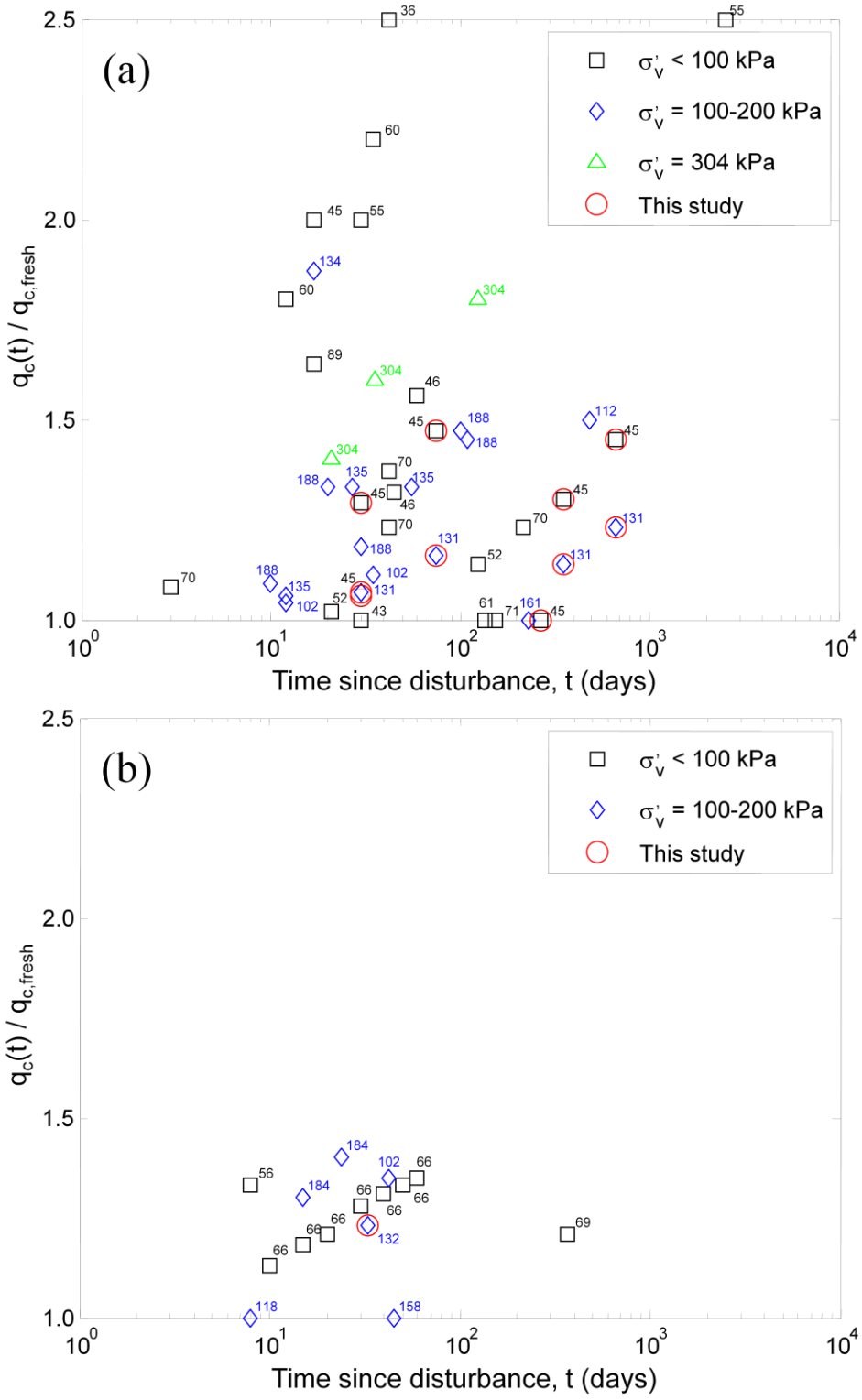

Figure 8-11. Effect of vertical effective stress on the relationship between aging effects and time since disturbance considering (a) vibratory disturbance methods and (b) compactive disturbance methods. The vertical effective stress in units of kPa is shown next to each data point.

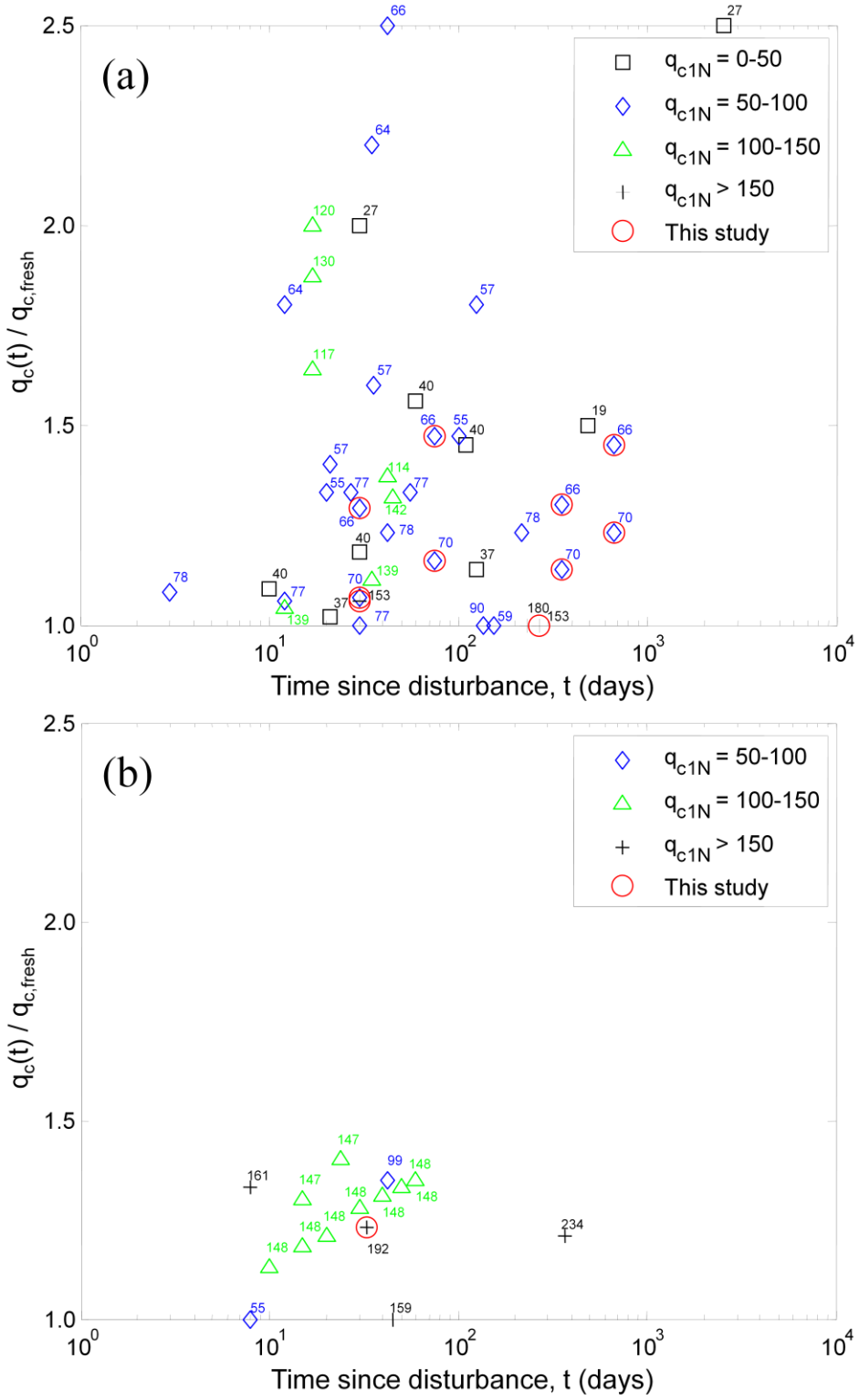

Figure 8-12. Effect of initial normalized tip resistance, $q_{c1N,fresh}$, on the relationship between aging effects and time since disturbance considering (a) vibratory disturbance methods and (b) compactive disturbance methods. The value of $q_{c1N,fresh}$ is shown next to each data point.

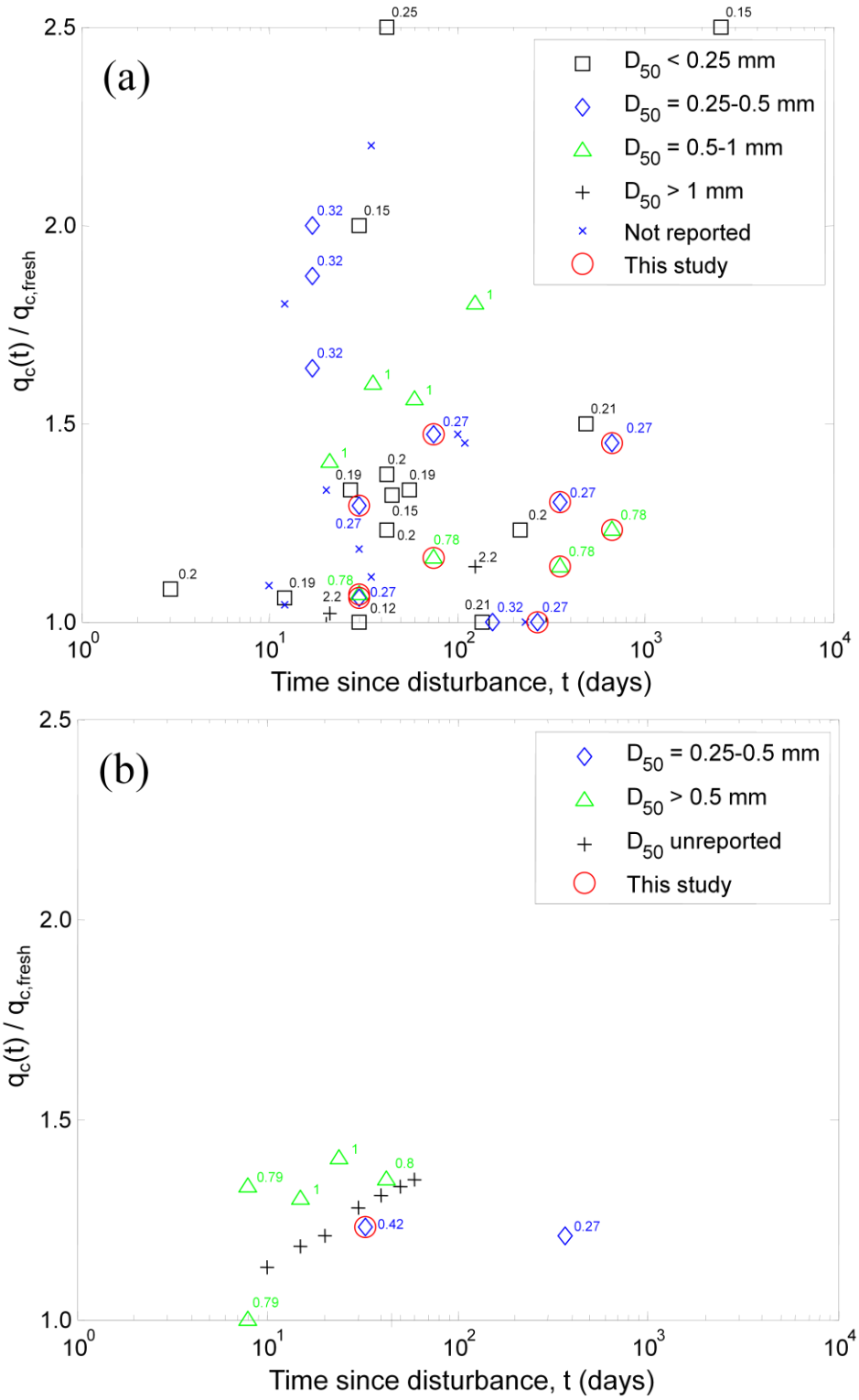

Figure 8-13. Effect of mean grain size on the relationship between aging effects and time since disturbance considering (a) vibratory disturbance methods and (b) compactive disturbance methods. The mean grain size in units of mm is shown next to each data point.

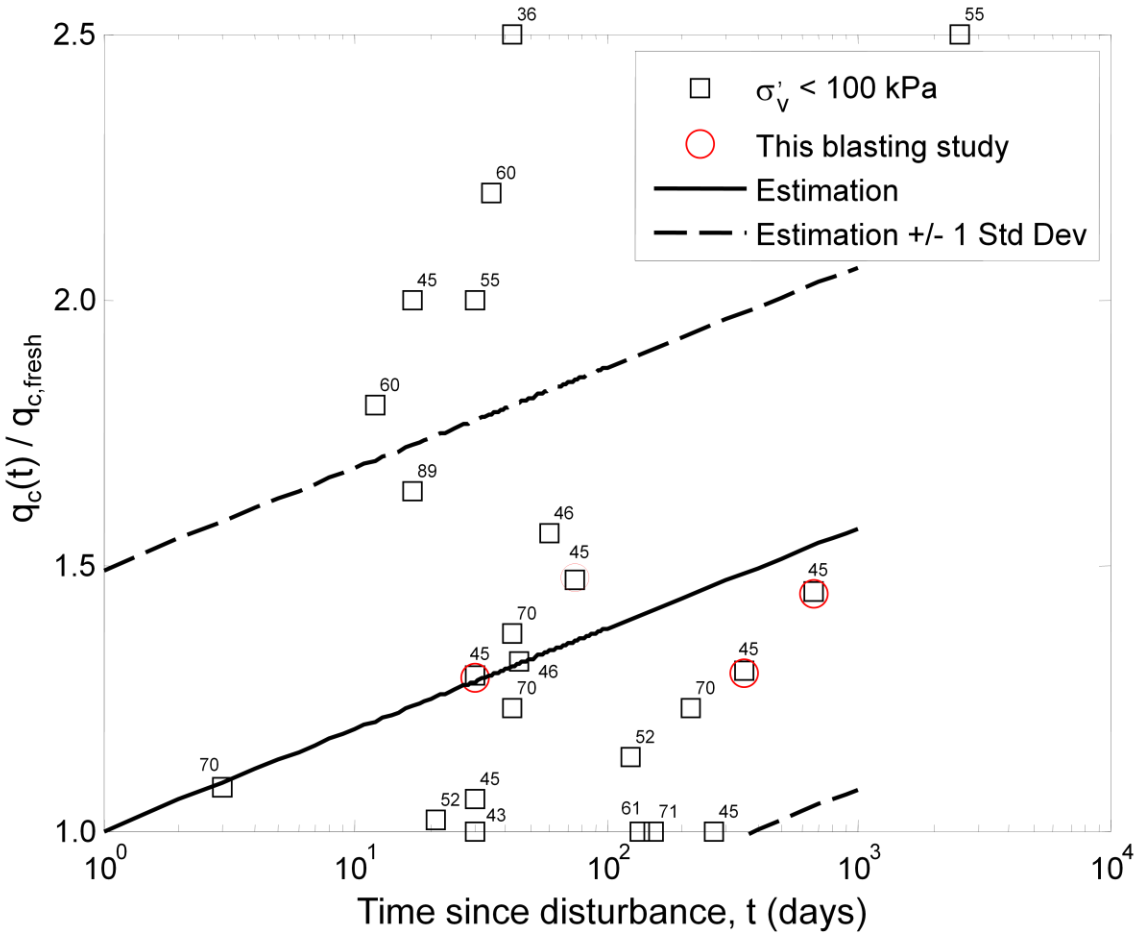

Figure 8-14. Trend line through vibratory disturbance method data with vertical effective stress less than 100 kPa.

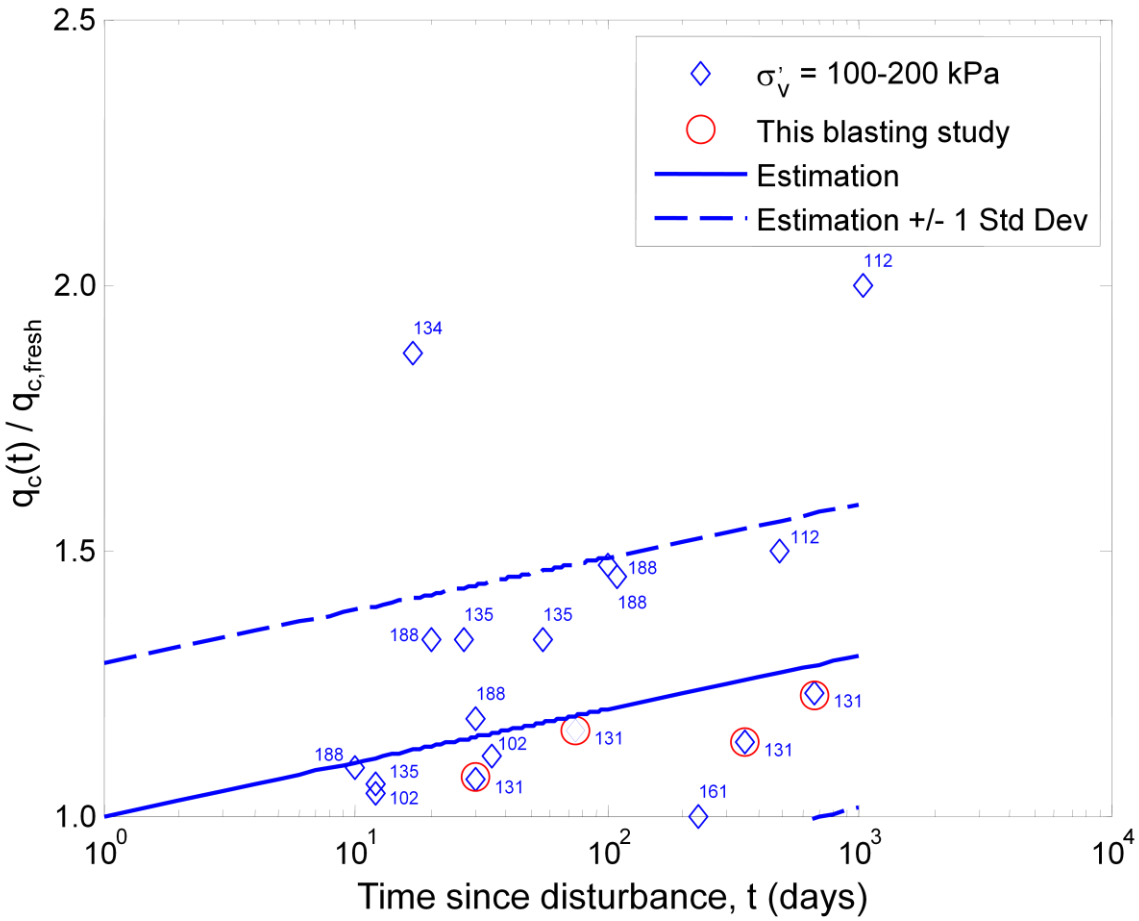

Figure 8-15. Trend line through vibratory disturbance method data with vertical effective stress between 100 and 200 kPa.

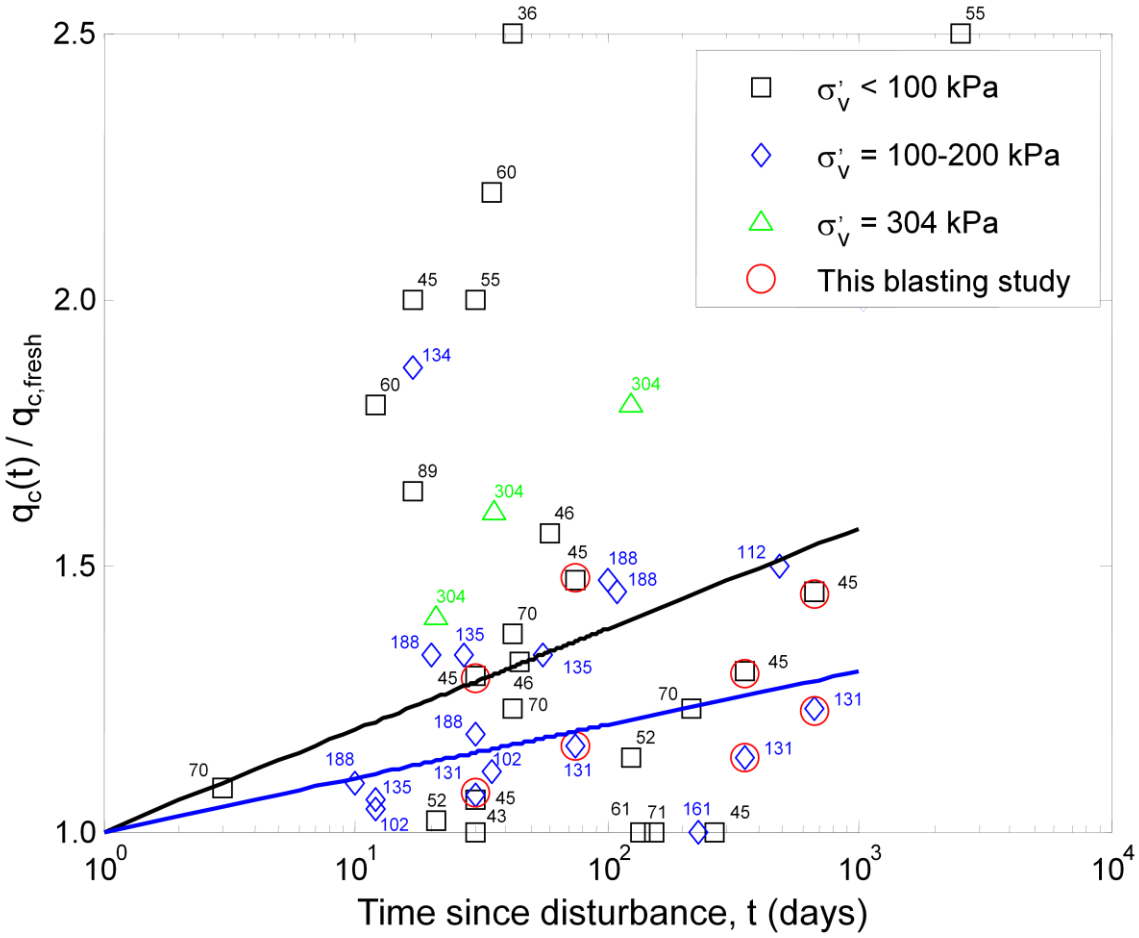

Figure 8-16. Trend lines through vibratory disturbance method data based on vertical effective stress.

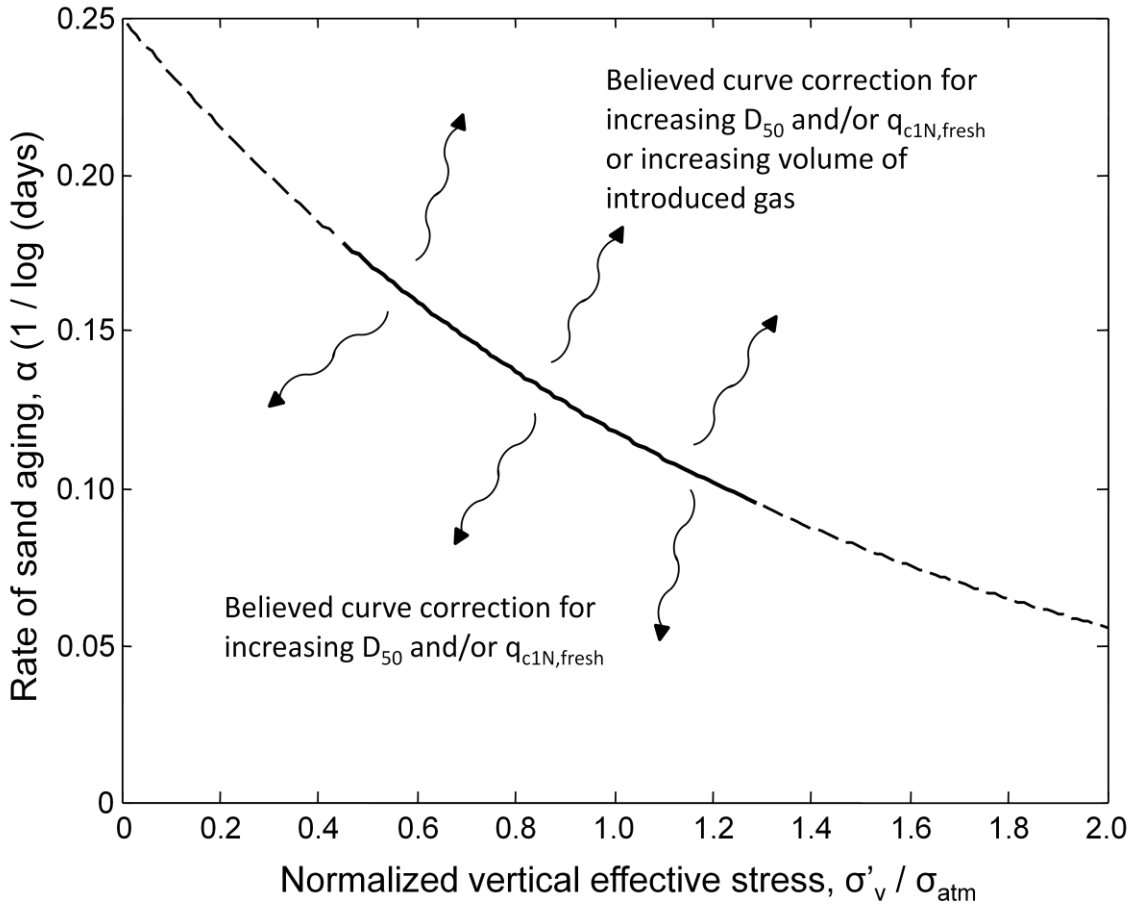

Figure 8-17. Relationship between the rate of sand aging and vertical effective stress with possible future adjustments for mean grain size, fresh normalized tip resistance, and introduced gas.

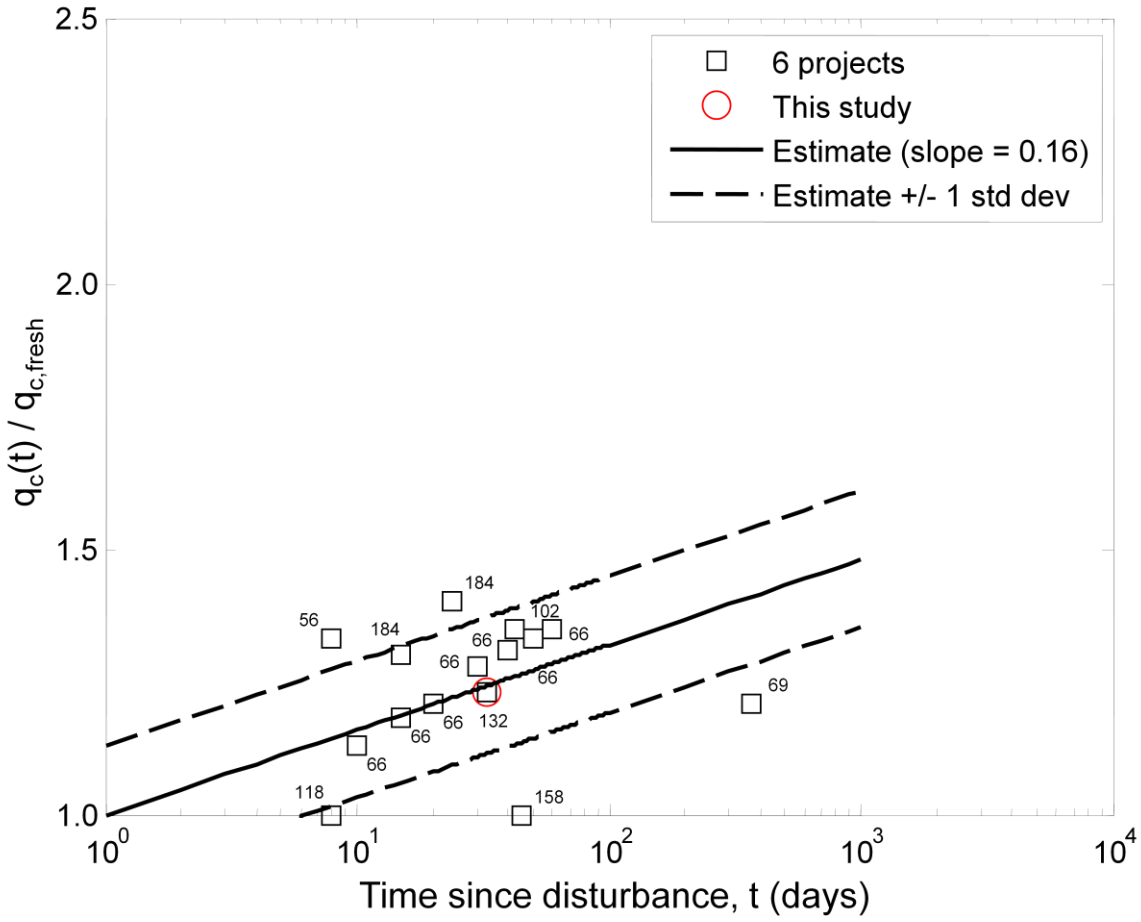

Figure 8-18. Trend line through compactive disturbance method data.

Chapter 9

Liquefaction Resistance of Geologically Aged Deposits

9.1 Introduction

The majority of the case histories used to determine the liquefaction resistance of *in situ* deposits came from site investigations in Holocene aged, from the last ice age ~12,000 years ago to the present, deposits following earthquakes (Youd et al., 2001). However, many investigators (Ohsaki, 1969; Casagrande, 1976; Youd and Perkins, 1978; Seed, 1979) have noted increased liquefaction resistance in Pleistocene aged, between 2,500,000 and 12,000 years ago, deposits. The increased liquefaction resistance accumulated over tens or hundreds of thousand years is significantly greater than the increase in liquefaction resistance seen over weeks and months, as has been discussed throughout this dissertation. There is clearly a difference between short term aging and long term aging. Several methods of accounting for geologically aged sands have been developed and are summarized in this chapter. Because very large disturbances can negate even geologic aging (Andrus et al., 2009), data from the explosive densification experiment in Griffin, IN, where both Holocene and Pleistocene deposits are present, was used to determine the aged and newly deposited *in situ* test results. In this chapter, experimental data is compared to previously proposed methods for determining aged deposits' liquefaction resistance.

9.2 Overview of Proposed Methods of Determining Liquefaction Resistance of Aged Deposits

An early method of accounting for geologic aging in liquefaction resistance was presented by Seed (1979), accounting for strength gain with time for deposits aged nearly 3,000 years. Skempton (1986) and Kulhawy and Mayne (1990) performed a similar analysis for geologically aged soils. Arango et al. (2000) extended the trend developed by Seed (1979) for deposits older than 3,000 years and added data from other projects. The resulting chart summarizing the work on increased liquefaction resistance due to geologic aging conducted prior to 2000 is presented in Figure 9-1. The strength gain factor is the increase in liquefaction resistance.

Leon et al. (2006) developed a method of accounting for geologic aging in liquefaction hazard assessment, summarized in Figure 9-2. They propose that *in situ* test results be reduced to a freshly deposited value using one of the aging relationships described above or the method proposed by Mesri et al. (1990). In their analysis, the Kulhawy and Mayne (1990) relationship was used. The freshly deposited value of *in situ* test results is then converted to a freshly deposited cyclic resistance ratio (CRR) using established relationships, such as those recommended by Youd et al. (2001). Next, the freshly deposited CRR is adjusted for aging using the Arango et al. (2000) method to determine the aged CRR. Finally, the aged CRR and original *in situ* test results are plotted. The results of the Leon et al. (2006) study show that aged deposits have significantly higher liquefaction resistance than fresh deposits with the same values of *in situ* test results. This method was not evaluated using results from this project's field experiments. Leon et al. (2006) provide a method of applying the strength gain predicted by other researchers, so a comparison of field results to the original relationships is more appropriate.

Monaco and Marchetti (2007) present results of seismic dilatometer tests (SDMT). They show that shear wave velocity and dilatometer (DMT) results yield very different predictions of CRR and provide several explanations for the differences. First, they suggest that the larger strain induced during DMT testing compared to shear wave velocity measurements more closely relates to earthquake induced strain. Similarly, they suggest that DMT results correlate better to relative density and the state parameter than shear wave velocity. However, the results of DMT, CPT, and shear wave velocity testing conducted in Griffin, IN, presented in Chapter 4, and in New Madrid, MO, presented in Chapter 6, show that DMT results predict low CRR values compared to CPT results. The work presented in this dissertation shows that the DMT destroys the benefits of geologic aging prior to the determination of K_D. As a result, DMT results are not as sensitive to geologic aging as CPT results.

Moss et al. (2008) present preliminary results of a study designed to assess liquefaction potential of aged deposits. While the initial results provide more evidence of increased liquefaction resistance in older deposits, a method of assessing the increase was not included in the initial presentation of the results.

Andrus et al. (2009) suggest comparing measured shear wave velocity to shear wave velocity estimated from empirical correlations between penetration resistance and measured shear wave velocity as a method of accounting for aging when assessing liquefaction potential. As shown in Figure 9-3, older deposits show a higher measured shear wave velocity than younger deposits

with similar tip resistance. Andrus et al. (2009) propose that the ratio between measured and estimated shear wave velocity is an accurate indicator of deposit age. Additionally, this ratio is easier to determine and apply to the simplified liquefaction procedure than uncertain estimates of deposit age. Andrus et al. (2009) recommend Equation 9-1 for relating the measured to estimated shear wave velocity ratio (MEVR) to age of deposit, t, in years.

$$MEVR = 0.0820 \log_{10}(t) + 0.935 \quad \ldots(9\text{-}1)$$

9.3 Presentation of Experimental Data

Cone penetration tests (CPT), seismic CPT (SCPT), and DMT were conducted in the area affected by the Griffin, IN explosive densification experiment. Data from the loose gravelly sand layer is of particular interest. While the loose gravelly sand layer is a Pleistocene deposit, the Skelton earthquake occurred 12,000 years ago (Munson and Munson, 1996). The resulting paleo-liquefaction features, shown in Figure 4-2, are evidence that the earthquake reset the geotechnical age of the deposit. Tests conducted prior to blasting provide information about the aged soil deposit. However, explosive densification destroyed the benefits of geologic aging in the loose gravelly sand layer, as shown by a drop in penetration resistance and shear wave velocity despite significant surface settlement. *In situ* results from tests conducted immediately following the blast provide a reasonable estimate of the freshly deposited state in the same layer. Using post-blast *in situ* results to represent the freshly deposited state and pre-blast *in situ* results as the aged state allows for comparison between the methods of accounting for geologic aging that were summarized in Section 9.2.

A comparison of pre- and post-blast CPT, DMT, and shear wave velocity data is presented in Figures 9-4 through 9-6, respectively. The figures show the *in situ* test results with depth between 10 and 14 m, highlighting the loose gravelly sand layer where explosive charges were placed. For both CPT tip resistance and shear wave velocity, the post-blast results, representing the freshly deposited state, are lower than the pre-blast, or aged, results. This shows the benefits of geologic aging. However, the DMT data does not differ significantly before and after the blast in the loose gravelly sand layer. This project show that the DMT is not as sensitive to geologic aging as CPT results.

9.4 Comparison of Proposed Methods Based on Experimental Data

To compare the data collected at the Griffin, IN blast site to the relationships summarized in Arango et al. (2000), strength gain factors were calculated. Comparing the mean of pre-blast, or geologically aged, data to the mean of post-blast, or fresh, data yields a strength gain factor. CPT data was converted to cyclic resistance ratio (CRR) using Idriss and Boulanger (2008) and the ratio of aged CRR to fresh CRR, the strength gain factor, was 1.9. The strength gain factor from this project is plotted on the Arango et al. (2000) plot in Figure 9-7. The results from this work plot below the Arango et al. (2000) proposed relationship. This project shows greater effect of aging than was predicted by Kulhawy and Mayne (1990). The relationship proposed by Arango et al. (2000) extends from the upper portion of the range proposed by Seed (1979), while data from this study agrees well with an extension of the median of Seed's (1979) relationship.

Andrus et al. (2009) predict a MEVR of 1.24 for a 12,000 year old deposit, with a range of 1.07 to 1.41 within one standard deviation. In the pre-blast, loose gravelly sand layer, the average tip resistance is 15 MPa and the friction ratio is 0.5%. Unit weight values determined from empirical correlations with DMT testing provided an average total stress in the loose gravelly sand layer of 192 kPa and an average effective stress of 128 kPa. The average shear wave in the pre-blast, loose gravelly sand layer is 256 m/sec. The average shear wave in the post-blast, loose gravelly sand layer is 205 m/sec. Using these values in the procedure prescribed by Andrus et al. (2009), pre-blast SCPT results yield a MEVR of 1.26, remarkably close to the predicted value.

Additionally, replacing the estimated shear wave velocity from pre-blast CPT results, 194 m/sec, with the post-blast, or freshly deposited, shear wave velocity corrected for effective stress and clean sands, 201 m/sec, results in a ratio of 1.22. This comparison is of interest because the estimated shear wave velocity from CPT tip resistance gives an indication of fresh shear wave velocity. If one assumes that the blast reset the loose gravelly sand layer to a freshly deposited state, post-blast shear wave velocity could replace the estimated shear wave velocity from pre-blast CPT results. Both the MEVR and ratio of pre- to post-blast shear wave velocity are similar to the Andrus et al. (2009) predicted MEVR.

9.5 Conclusion

This chapter describes the comparison of field data from the Griffin, IN explosive densification experiment to proposed relationships predicting strength gain due to geologic aging. A description of the existing relationships was presented. Assuming that the blast reset the geologic

age of the loose gravelly sand layer to a freshly deposited condition, data from before and immediately after the blast provided an opportunity to compare fresh and geologically aged results at the same deposit and compare the results to existing relationships. This comparison shows more geologic aging that Kulhawy and Mayne (1990) predict, but less than Arango et al. (2000) predict. The strength gain due to aging at Griffin, IN falls at the center of the range reported by Seed (1979) if his log-time model for strength gain was extended. The MEVR method developed by Andrus et al. (2009) shows excellent agreement with the data from the Pleistocene aged deposit in Griffin, IN.

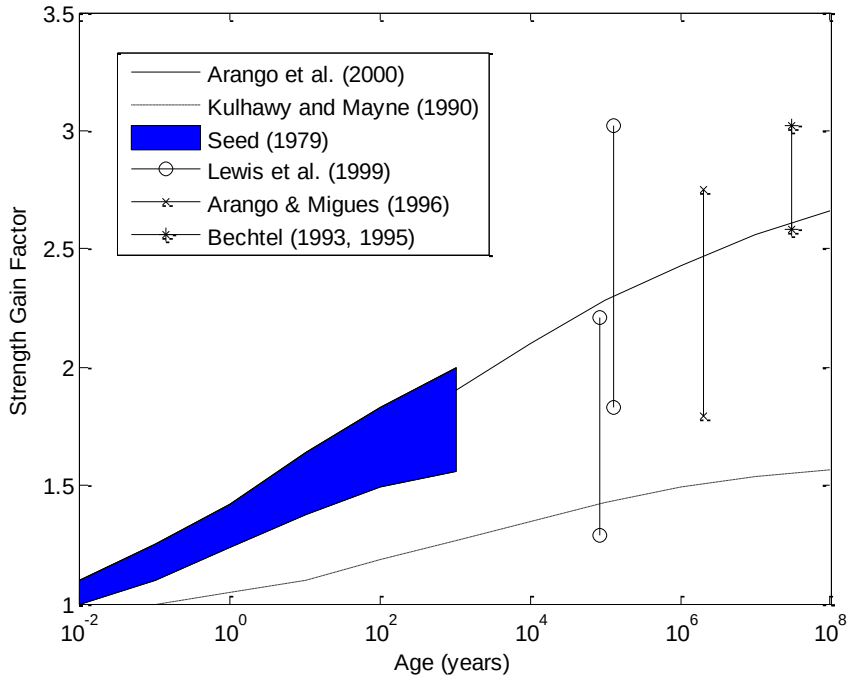

Figure 9-1. Field cyclic strength of aged sand deposits (adapted from Arango et al., 2000).

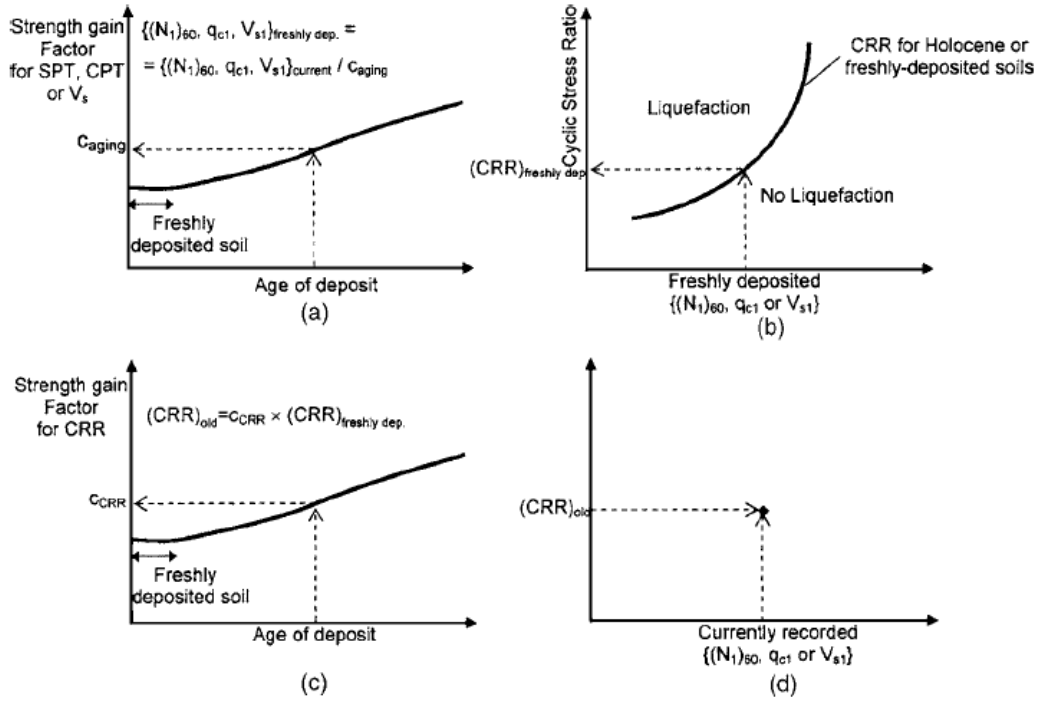

Figure 9-2. Leon et al.'s (2006) proposed method for accounting for soil age: (a) correct *in situ* test results for age, (b) determine CRR of fresh material, (c) determine CRR of aged material, and (d) plot *in situ* test results vs. aged CRR (Leon et al., 2006).

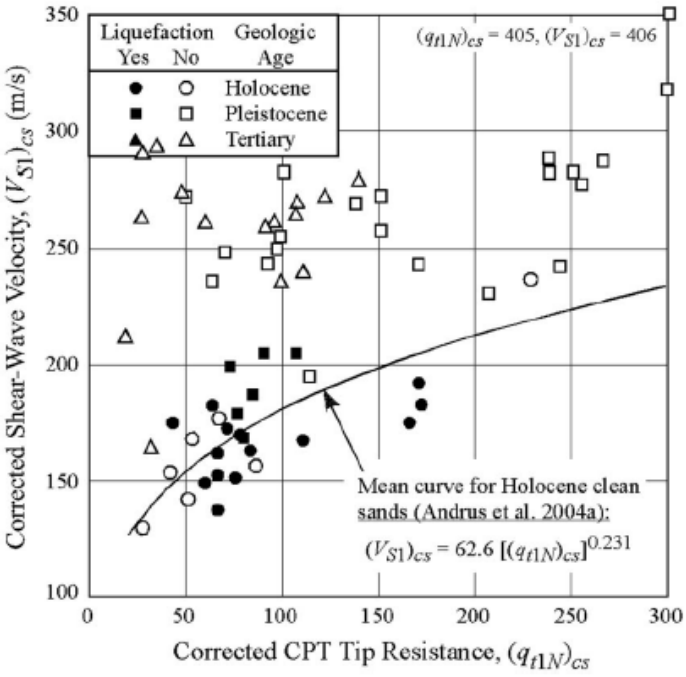

Figure 9-3. Relationship between corrected tip resistance and corrected shear wave velocity as a function of deposit age (Andrus et al., 2009).

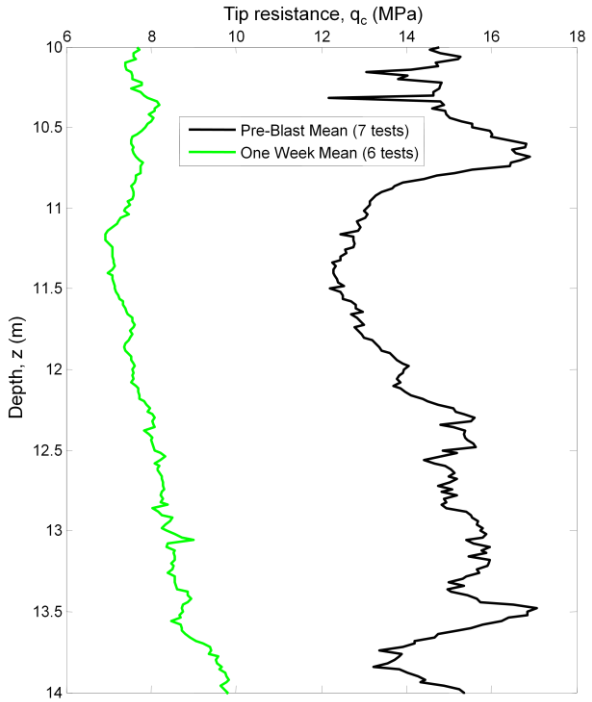

Figure 9-4. CPT tip resistance before and immediately following the blast in the loose gravelly sand deposit.

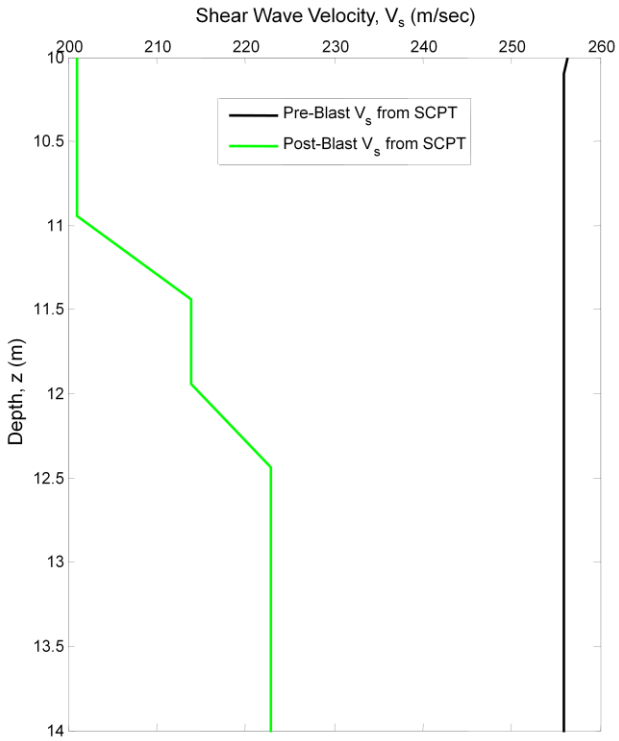

Figure 9-5. Shear wave velocity before and immediately following the blast in the loose gravelly sand deposit.

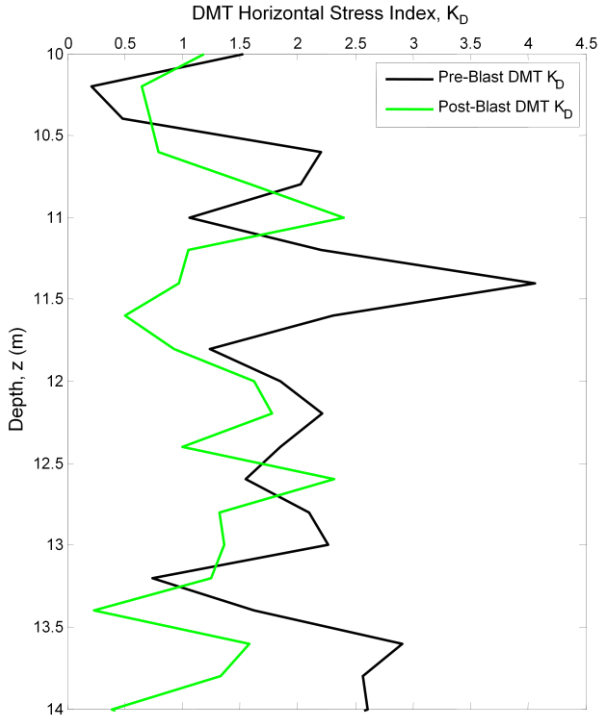

Figure 9-6. DMT horizontal stress index before and immediately following the blast in the loose gravelly sand deposit.

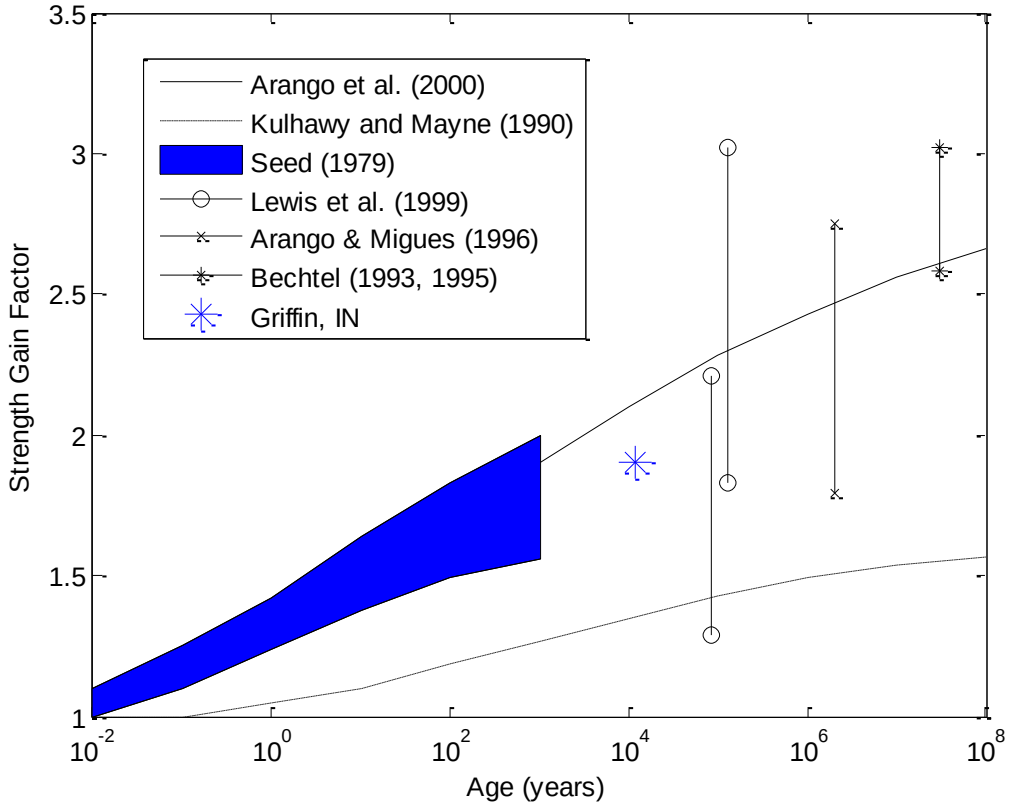

Figure 9-7. Field cyclic strength of aged sand deposits including this project's data (adapted from Arango et al., 2000).

Chapter 10

Summary and Conclusions

10.1 Overview of Research

Numerous studies have shown that recently disturbed granular materials show time-dependent increases in strength and stiffness, as measured by *in situ* or laboratory tests, a phenomenon commonly called sand aging. The majority of the research on sand aging has focused on identifying the mechanisms causing the behavior. Two primary mechanisms have been proposed: a chemical mechanism and a mechanical mechanism. Under a chemical mechanism, cementation between grains leads to the observed increases in strength and stiffness. Grain re-orientation, particle slippage, and asperity shearing or crushing are some of the explanations for sand aging under a mechanical mechanism. While research on the mechanisms behind sand aging has increased the understanding of the behavior, less work has focused on predicting sand aging effects. Because sand aging has been recorded following placement of fill, explosive densification, deep dynamic compaction (DDC), and vibro-compaction, the phenomenon is of practical importance because low initial penetration resistance can be incorrectly interpreted as indicating poor ground improvement. The objective of this project was to develop a method of predicting sand aging effects.

To accomplish this goal, three field experiments and a laboratory experiment program were conducted. Explosive densification and vibroseis shaking were performed at a sand and gravel quarry in Griffin, IN. Impact piers were installed at a construction site in New Madrid, MO. Cone penetration test (CPT) tip resistance (q_c), shear wave velocity (V_s), and dilatometer test (DMT) horizontal stress index (K_D) increased with time following explosive densification and impact pier installation. However, aging effects were not recorded following vibroseis shaking. Conducting two soil improvement methods at the same site is unique to this project and demonstrates the importance of the amount of disturbance on the magnitude of aging effects. Additionally, cyclic triaxial tests were performed on soil taken from the Griffin quarry. The number of cycles to failure at a given cyclic stress ratio (CSR) increased with time following

consolidation in cyclic triaxial testing. The laboratory testing program also included soil characterization for both the Griffin and New Madrid sites. Soil characterization is important because previous research has identified factors that influence aging. Characterizing the soil from this work allowed for comparison to other projects where sand aging was observed.

Through a review of previous projects that recorded sand aging effects, a database was developed that included the ratio of aged CPT tip resistance to CPT tip resistance immediately after disturbance, as well as soil properties typically found as part of a geotechnical investigation. The database was large, thereby allowing the investigation of some properties influence on aging. For example, if a mechanical mechanism dominates sand aging behavior, deposits with more contacts, i.e. deposits with smaller mean grain sizes, would show greater aging effects. This trend was confirmed. However, the database was not large enough to fully identify the importance of the many different factors and their interactions, i.e. chemical composition of the soil. Therefore, a method of predicting sand aging effects, shown in Figures 8-9 and 8-10, was based on the initial normalized penetration resistance (q_{c1N}) following disturbance and the time since disturbance.

10.2 Summary of Major Findings

- Sand aging was observed following explosive densification at Griffin, IN. There were clear increases in q_c, V_s and K_D with time a the loose sand layer. There were smaller increases in the loose gravelly sand layer. As determined using block kriging, there was a 74% confidence that the differences between q_{c1N} measured one week following the blast were different due to aging and not due to spatial variability.
- Aging effects were not observed after vibroseis shaking at Griffin, IN. Because vibroseis shaking disturbs the soil less than explosive densification, it was expected that the magnitude of sand aging would be smaller in this experiment. This result is significant because it demonstrates the importance of disturbance energy on aging. This project represents the first time that sand aging was quantified after disturbing the same soil layer by two different methods.
- Sand aging was observed following impact pier installation at New Madrid, MO. Impact pier installation initially increased q_c of the deposit, unlike explosive densification and vibroseis shaking. Despite higher initial q_c, the New Madrid loose sand layer still showed a time dependent increase in tip resistance.
- At both the Griffin and New Madrid sites, CPTs, DMTs, and V_s measurements were conducted. A comparison of commonly accepted methods of relating these *in situ* test results

to cyclic resistance ratio (CRR) showed that in late Holocene deposits, the different *in situ* tests predicted similar values of CRR. However, geologic aging caused the shear wave velocity based CRR prediction to become higher than by the other methods. Additionally, in geologically aged deposits, the DMT based CRR predictions were lower than CPT based predictions. These differences can be explained through the amount of disturbance each test imparts. During shear wave velocity measurements, the soil is not disturbed. The CPT disturbs the soil while determining tip resistance values. The DMT blade is inserted to a given depth, disturbing the soil prior to testing. Therefore, comparatively high shear wave velocity based CRR are an indication of geologic age. Additionally, the DMT based CRR methods under predict the liquefaction resistance of aged deposits. A qualitative method of assessing liquefaction susceptibility using the vision CPT (VisCPT) was also presented and confirmed the higher risk of liquefaction that was predicted in the CPT, DMT, and shear wave velocity based methods.

- Sand aging effects were observed in cyclic triaxial testing. The number of cycles to failure increased at a given cyclic stress ratio (CSR) with time following consolidation of the laboratory sample. Tests were conducted immediately following consolidation, as well as 3 days, 7 days, 14 days, and 28 days after consolidation.
- A method of predicting sand aging effects was developed and presented in Equations 8-3 and 8-4. Increasing vertical effective stress in a deposit was shown to decrease aging effects with time. Disturbance method also played a significant role. The disturbance methods were divided into two categories: vibratory methods, including explosive densification, placement of hydraulic fill, earthquakes, and vibroseis shaking, and compaction methods, including impact piers, vibro-compaction, and deep dynamic compaction. The vibratory methods did not initially increase the horizontal stress, while compaction methods did. A method of predicting sand aging effects was developed. Equation 8-3 is recommended for vibratory disturbance methods and Equation 8-4 is recommended for compacctive disturbance methods.
- Previous research has shown that, in terms of geotechnical behavior, a major disturbance resets a deposit's age (Andrus et al, 2009). Assuming that the Griffin, IN explosive densification experiment reset the geologic age of the geologically aged, loose gravelly sand layer, *in situ* test results from before and after the blast are representative of aged and freshly deposited conditions, respectively. Comparing these results with relationships for strength gain in geologically aged material, the data from this project is similar to, but predicts slightly less strength gain, than by the Arango et al. (2000) prediction. Additionally, the Griffin data

shows excellent agreement with the measured to estimated velocity ratio (MEVR), proposed by Andrus et al. (2009).

10.3 Recommendations for Future Work

A small database of sand aging case histories has hampered attempts to develop a model for predicting sand aging effects. The conclusion of this project was that the sand aging database is still too small to accurately quantify the dominant factors and their interactions with each other through statistical methods. Publishing case histories of soil improvement projects where sand aging is observed would be of great benefit. Ideally, these case histories would contain information about the grain size distribution, chemical composition, disturbance method, and pore fluid in order to compare the aging effects among different studies and sites.

While the majority of research supports a mechanical mechanism as the controlling factor behind sand aging, a definitive conclusion has not been reached. As summarized in Chapter 2.3.2, Schmertmann (1991) used IDS triaxial tests on clay to support a mechanical mechanism in aging behavior. These tests have not been performed in sands and such tests would increase understanding of the mechanisms behind the sand aging phenomenon.

References

Abdoun, T., Abe, A., Bennett, V., Danisch, L., Sato, M., Tokimatsu, K., and Ubilla, J., 2007. "Wireless Real Time Monitoring of Soil and Soil-Structure Systems." *Embankments, Dams, and Slopes, GSP 161*, (F. Silva-Tulla and P.G. Nicholson, eds.), DOI 10.1061/40905(224)5.

Acar, Y.B., 1987. "Discussion of 'Time-Dependent Strength Gain in Freshly Deposited or Densified Sand,' by J.K. Mitchell and Z.V. Solymar." *Journal of Geotechnical Engineering*, 113(2), 171-173.

Afifi, S.S., 1970. "Effects of Stress-History of the Shear Modulus of Soils." Ph.D. dissertation, University of Michigan, Ann Arbor, MI.

Afifi, S.S. and Richart, F.E. Jr., 1973. "Stress-History Effects on Shear Modulus of Soils." *Soils and Foundations*, 13(1), 77-95.

Afifi, S.S. and Woods, R.D., 1971. "Long-Term Pressure Effects on Shear Modulus of Soils." *Journal of the Soil Mechanics and Foundations Division*, 97(SM10), 1445-1460.

Anderson, D.G. and Stokoe K.H. II, 1978. "Shear Modulus, A Time-Dependent Soil Property." *Dynamic Geotechnical Testing*, ASTM STP 654, 66-90.

Andrus, R.D., Hayati, H., and Mohanan, N.P., 2009. "Correcting Liquefaction Resistance of Aged Sands Using Measured to Estimated Velocity Ratio." *Journal of Geotechnical and Geoenvironmental Engineering*, 135(6), 735-744.

Andrus, R.D. and Stokoe, K.H., 2000. "Liquefaction Resistance of Soils from Shear Wave Velocity." *Journal of Geotechnical and Geoenvironmental Engineering*, 126(11), 1015-1025.

Arango, I., Lewis, M.R., and Kramer, C., 2000. "Updated Liquefaction Potential Analysis Eliminates Foundation Retrofitting of Two Critical Structures." *Soil Dynamics and Earthquake Engineering*, 20, 17-25.

Ashford, S.S., Rollins, K.M., and Lane, J.D., 2004. "Blast-Induced Liquefaction for Full-Scale Foundation Testing." *Journal of Geotechnical and Geoenvironmental Engineering*, 130(8), 798-806.

Astedt, B., Wiener, L., and Holm, G., 1992. "Increase in Bearing Capacity with Time for Friction Piles in Silt and Sand." *Proceedings of the Nordic Geotechnical Meeting*, Aalborg, Denmark, 411-416.

Bachus, R.C., Hebeler, T.E., Santamarina, J.C., Othman, M.A., and Narsilio, G.A., 2008. "Use of

Field Instrumentation and Monitoring to Assess Ground Modification by Blast Densification." *Proceedings of the 15th Annual Great Lakes Geotechnical/Geoenvironmental Conference (GLGGC)*, Indianapolis, IN, 3-36.

Baker, J.W., Bayraktarli, Y.Y., and Faber, M.H., 2006. "Accounting for Soil Spatial Variability When Assessing Liquefaction Risk." *Proceedings of the International Forum on Engineering Decision Making*, Lake Louise, Canada.

Baker, J.W. and Faber, M.H., 2008. "Liquefaction Risk Assessment Using Geostatistics to Account for Soil Spatial Variability." *Journal of Geotechnical and Geoenvironmental Engineering*, 134(1), 14-23.

Baldi, G., Bellotti, R., Ghionna, V., Jamiolkowski, M., and Pasqualini, E., 1986. "Intrepretation of CPT and CPTUs, 2nd Part: Drained Penetration on Sands." *4th International Geotechnical Seminar*, Nenying Tech Institute, Singapore, Field Instrumentation and In-Situ Measurement, 143-162.

Baxter, C.D.P., 1999. "An Experimental Study on the Aging of Sands." Ph.D. dissertation, Virginia Tech, Blacksburg, VA.

Baxter, C.D.P. and Mitchell, J.K., 2004. "Experimental Study on the Aging of Sands." J*ournal of Geotechnical and Geoenvironmental Engineering*, 130(10), 1051-1062.

Blum, M.D., Guccione, M.J., Wysocki, D.A., Robnett, P.C., and Rutledge, E.M., 2000. "Late Pleistocene Evolution of the Lower Mississippi River Valley, Southern Missouri to Arkansas." *GSA Bulletin*, 112(2), 221-235.

Bowman, E., 2002. "The Aging and Creep of Dense Granular Materials." Ph.D dissertation, University of Cambridge, Cambridge, England.

Bowman, E. and Soga, K., 2003. "Creep, Aging and Microstructural Change in Dense Granular Materials." *Soils and Foundations*, 43(4), 107-117.

Bowman, E. and Soga, K., 2005. "Mechanisms of Set Up of Displacement Piles in Sand: Laboratory Creep Tests." *Canadian Geotechnical Journal*, 42, 1391-1407.

Brown, D. and Camp W.M., 2002. "Lateral Load Testing Program for the Cooper River Bridge, Charleston." *Proceedings of the International Deep Foundations Congress 2002, GSP 116*, Orlando, Florida, 95-109.

Camp, W.M. III, 2011. Personal communication, 18 February, 2011.

Camp, W.M. III, 2004. "Site Caharaaterization and Subsurface Conditions for the Cooper River Bridge." *Proceedings of Geo-Trans – Geotechnica Eningeering for Transportation Projects, GSP 126*, 347-360.

Camp, W.M. III, Mayne, P.W., and Rollins, K.M., 2008. "Cone Penetration Testing Before, During, and After Blast-Induced Liquefaction." *Geotechnical Earthquake Engineering and Soil Dynamics, GSP 181*, (D. Zeng, M.T. Manzari, and D.R. Hiltunen, eds.), DOI 10.1061/40975(318)104.

Casagrande, A., 1976. "Liquefaction and Cyclic Deformation of Sands – A Critical Review." *Harvard Soil Mechanics Series, No. 88*, Harvard University, Cambridge, MA.

Charlie, W.A., Jacobs, P.J., and Doehring, D.O., 1992a. "Blasting-Induced Liquefaction of an Alluvial Sand Deposit." *Geotechnical Testing Journal*, 15(1), 14-23.

Charlie, W.A., Rwebyogo, M.F.J., and Doehring, D.O., 1992b. "Time-Dependent Cone Penetration Resistance Due to Blasting." *Journal of Geotechnical Engineering*, 118(8), 1200-1215.

Chiles, J.P. and Delfiner, P., 1999. *Geostatistics: Modelinng Spatial Uncertainty*, Wiley, New York.

Chow, F.C., Jardine, R.J., Brucy, F., and Nauroy, J.F., 1998. "Effects of Time on Capacity of Pipe Piles in Dense Marine Sand." *Journal of Geotechnical and Geoenvironmental Engineering*, 124(3), 254-264.

Covil, C.S., Luk, M.C.W., and Pickles, A.R., 1997. "Case History: Ground Treatment of the Sandfill at the New Airport at Chek Lap Kok, Hong Kong." *Ground Improvement Geosystems*, T. Telford, ed., London, 149-156.

Cox, B.R., 2006. "Development of a Direct Test Method for Dynamically Assessing the Liquefaction Resistance of Soils In Situ." Ph.D. dissertation, University of Texas, Austin, Texas.

Daramola, O., 1980. "Effect of Consolidation Age on Stiffness of Sand." *Geotechnique*, 30(2), 213-216.

Debats, J.-M. and Sims, M., 1997. "Vibroflotation in Reclamations in Hong Kong." *Ground Improvement*, 1997(1), 127-145.

Denisov, N.Y., Dudlers, I.V., Duranti, E.A., and Khazanov, M.I., 1963. "Studies of changes of Strength and Compressibility of Hydraulically Filled Sands in Time." *Proceedings of European Conference on Soil Mechanics and Foundation Engineering*, Volume 1, Wiesbaden Germany, 221-225.

Denisov, N.Y. and Reltov, B.F., 1961. "The Influence of Certain Processes on the Strength of Soils." *Proceedings of the 5th International Conference on Soil Mechanics and Foundation Engineering*, Volume 1, 75-78.

Dowding, C.H. and Hryciw, R.D., 1986. "A Laboratory Study of Blast Densification of Saturated Sand." *Journal of Geotechnical Engineering*, 112(2), 187-199.

Dumas, J.C. and Beaton, N.F., 1988. "Discussion of 'Practical Problems from Surprising Soil Behavior,' by J.K. Mitchell." *Journal of Geotechnical Engineering*, 114 (3), 367-368.

Fidlar, M.M., 1935. "Features of the Valley Floor of the Wabash River Near Vincennes, Indiana." *Proceedings of the Indiana Academy of Science*, 45, 175-182.

Finno, R.J., 1993. "Analytical Interpretation of Dilatometer Penetration Through Saturated Cohesive Soils." *Geotechnique*, 43(2), 241-254.

Fordham C.J., McRoberts, E.C., Purcell, B.C., and McLaughlin, P.D., 1991. "Practical and Theoretical Problems Associated with Blast Densification of Loose Sands." *Proceedings of the 44th Canadian Geotechnical Conference*, Canadian Geotechnical Society, Volume 2, 92.1-92.8.

Fraser, G.S., Bleuer, N.K., Fishbaugh, D.A., 1981. "Sedimentology of Terrace Deposits at Bend Area of Wabash River." *AAPG Bulletin*, 65(5), 927.

Fraser, G.S., Thompson, T.A., Olyphant, G.A., Furer, L., and Bennett, S.W., 1997. "Geomorphic Response to Tectonically-Induced Ground Deformation in the Wabast Valley." *Seismological Research Letters*, 68(4), 662-674.

Garich, E.A. and Blackburn, J.T. (2007). "Automated, Wireless Instrumentation for Monitoring of Potential Landslide Hazards." *Proc. 1st American Landslide Conf.*, Vail, CO.

Ghiabi, H. and Selvadurai, A.P.S., 2009. "Time-Dependent Mechanical Behavior of a Granular Medium Used in Laboratory Investigations." *International Journal of Geomechanics*, 9(1), 1-8.

Gohl, W.B., Jefferies, M.G., Howie, J.A., and Diggle, D., 2000. "Explosive densification: Design, Implimentation, and Effectiveness." *Geotechnique*, 50(6), 657-665.

Hammah, R.E. and Curran, J.H., 2006. "Geostatistics in Geotechnical Engineering: Fad or Empowering?" *Proceedings of GeoCongress 2006*, (D.J. DeGroot, J.T. DeJong, J.D. Frost, and L.G. Baise, eds.), Atlanta, Georgia, DOI 10.1061/40803(187)102.

Handford, G. T., 1988, "Densification of an Existing Dam with Explosives," *Proceedings of Hydraulic Fill Structures Specialty Conference*, Fort Collins, Colorado, 750–762.

Hardin, B.O and Richart, F.E., Jr., 1963. "Elastic Wave Velocities in Granular Soils." *Journal of the Soil Mechanics and Foundations Division*, 89(SM1), 33-65.

Hayati, H., Andrus, R.D., Gassman, S.L., Hasek, M., Camp, W.M., and Talwani, P., 2008. "Characterizing the Liquefaction Resistance of Aged Soils." *Proceedings of Geotechnical Earthquake Engineering and Soil Dynamics (GEESD) IV*, Sacramento, CA.

Holzer, T.L. and Youd, T.L. (2007). "Liquefaction, Ground Oscillation, and Soil Deformation at the Wildlife Array, California." *Bulletin of the Seismological Society of America*, 97(3), 961-976.

Howie, J.A. and Amini, A., 2004. "Effect of Aging on Shear Wave Velocity by Seismic Cone." *Proceedings ISC-2 on Geotechnical and Geophysical Site Characterization*, Viana de Fonseca & Mayne, eds., Milpress, Rotterdam, 943-950.

Howie, J.A., Asalemi, A.A., Shozen, T., and Vaid, Y.P., 2001a. "Effects of Time on *In situ* Test Results After Ground Improvement – New Insights from Laboratory and Field Data." *2001: An Earth Odyssey*, Canadian Geotechnical Society, 467-474.

Howie, J.A., Shozen, T., and Vaid, Y.P., 2001b. "Effect of Aging on Stiffness of Loose Fraser River Sand." *Advanced Laboratory Stress-Strain Testing of Geomaterials*, Shibuya &

Kuwano, eds., Tatsuoka, Balkema, 235-241.

Howie, J.A., Shozen, T., and Vaid, Y.P., 2002. "Effect of Aging on Stiffness of Very Loose Sand." *Canadian Geotechnical Journal*, 39(1), 149-156.

Hryciw, R.D., 1986. "A Study of the Physical and Chemical Aspects of Blast Densification of Sand." Ph.D dissertation, Northwestern University, Evanston, Illinois.

Hryciw, R.D. and Dowding, C.H., 1988. "CPT and DMT in Evaluation of Blast-Densification of Sand." *Penetration Testing 1988, ISOPT-1*, J. DeRuiter, ed., 521-526.

Hryciw, R.D. and Thomann, T.G., 1993. "Stress-History-Based Model for G^e of Cohesionless Soils." *Journal of Geotechnical Engineering*, 119(7), 1073-1093.

Idriss, I.M. and Boulanger, R.W. (2008). *Soil Liquefaction During Earthquakes*, Monograph MNO-12, Earthquake Engineering Research Institute, Oakland, CA, 261pp.

Ivanov, P.L., 1967. "Compaction of Noncohesive Soils by Explosions." Translated from Russian, Indian National Scientific Documentation Center. Published for the U.S. Department of the Interior, Bureau of Reclamation and the National Science Foundation, Washington, D.C.

Jamiolkowski, M., Ladd, C.C., Germaine, J.T., and Lancellotta, R., 1985. "New Developments in Field and Laboratory Testing of Soils." *Proceedings of the 11th International Conference on Soil Mechanics and Foundation Engineering*, Volume 1, San Francisco, 57-153.

Jamiolkowski, M. and Manassero, M., 1995. "The Role of *In situ* Testing in Geotechnical Engineering – Thoughts about the Future." *Proceedings, International Conference in Advances in Site Investigation Practice*, Thomas Telford, 929-951.

Jardine, R.J., and Standing, J.R., 1999. *Pile Load Testing Preformed for HSE Cyclic Loading Study at Dunkirk*, Technical Report Health Safety Executive, 213pp.

Jefferies, M.G. and Rogers, B.T., 1993. "Discussion of 'Time-Dependent Cone Penetration Resistance Due to Blasting,' by W.A. Charlie, M.F.J. Rwebyogo, and D.O. Doehring." *Journal of Geotechnical Engineering*, 119(12), 2008-2012.

Jefferies, M.G., Rogers, B.T., Stewart, H.R., Shinde, S., James, D. and Williams-Fitzpatrick, S., 1988. "Island Construction in the Canadian Beaufort Sea." *Hydraulic Fill Structures, Geotechnical Special Publication 21*, D.J.A. Van Zyl and S.G. Vicks, eds., 816-883.

Jirathanathaworn, T., 2009. "Development of Photoelastic Methods Towards Study of Mechanical Aging of 2-Dimensional Granular Assemblies." Ph.D. dissertation, University of Michigan, Ann Arbor, Michigan.

Jirathanathaworn, T., Hryciw, R.D., and Green, R.A., 2010. "Photoelastic Sensors for Measurement of K_0." *GeoFlorida 2010: Advances in Analysis, Modeling & Design, Geotechnical Special Publication 199*, D. Fratta, A.J. Puppala, and B. Muhunthan, eds., 1275-1283.

Joshi, R.C., Achari, G., Kaniraj, S.R., and Wijiweera, H., 1995. "Effect of Aging on the

Penetration Resistance of Sands." *Canadian Geotechnical Journal*, 32(5), 767-782.

Jung, Y., 2010. Personal communication, 13 September, 2010.

Kaniraj, S.R., Wijeweera, H., Joshi, R.C., and Shinde, S.B., 1991. "Aging of Sands." *Proceedings of the 44th Canadian Geotechnical Conference*, Canadian Geotechnical Society, Volume 1, 4-1 – 4-7.

Kramer, C. and Arango, I., 1998. "Aging Effects on the Liquefaction Resistance of Sand Deposits: A Review and Update." *Proceedings of the 11th European Conference on Earthquake Engineering*, P. Bish, P. Labé, and A. Pecker, eds., Paris, France, Abstract 184.

Kulhawy, F.H. and Mayne, P.W., 1990. "Manual on Estimating Soil Properties for Foundation Design." *Final Report, 1493-6, EL-6800*, Electric Power Research Company, Palo Alto, CA.

Ladd, R.S., 1978. "Preparing Test Specimens Using Undercompaction." *Geotechnical Testing Journal*, 1(1), 16-23.

Lade, P.V. and Karimpour, H., 2010. "Static Fatigue Produces Time Effects in Granular Materials." *GeoFlorida 2010: Advances in Analysis, Modeling & Design, Geotechnical Special Publication 199*, D. Fratta, A.J. Puppala, and B. Muhunthan, eds., 530-539.

Lade, P.V. and Liu, C.T., 1998. "Experimental Study of Drained Creep Behavior of Sand." *Journal of Engineering Mechanics*, 124(8), 912-920.

Lade, P.V., Liggio, Jr., C.D., and Nam, J., 2009. "Strain Rate, Creep, and Stress Drop-Creep Experiments on Crushed Coral Sand." *Journal of Geotechnical and Geoenvironmental Engineering*, 135(7), 941-953.

Leclerc, M.A., 2008. "Evaluation of Gas Dissipation as a Mechanism for Aging of Sands." Master's Thesis, University of Rhode Island, Kingston, Rhode Island.

Lee, D.S., Elsworth, D., and Hryciw, R., 2008. "Hydraulic Conductivity Measurement from On-the-Fly uCPT Sounding and from VisCPT." *Journal of Geotechnical and Geoenvironmental Engineering*, 134(12), 1720-1729.

Leon, E., Gassman, S.L., and Talwani, P., 2006. "Accounting for Soil Aging When Assessing Liquefaction Potential." *Journal of Geotechnical and Geoenvironmental Engineering*, 132(3), 363-377.

Lewis, M.R., Arango, I., Kimball, J.K., and Ross, T.E., 1999. "Liquefaction Resistance of Old Sand Deposits." *Proceedings of the XI Pan-American Conference on Soil Mechanics and Geotechnical Engineering*, Foz do Iguassu, Brazil, 821-829.

Lewis, M.R., McHood, M.D., and Arango, I., 2004. "Liquefaction Evaluations at the Savannah River Site: A Case History." *Proceedings of the 5th International Conference on Case Histories in Geotechnical Engineering*, New York, NY, Paper No. 3.21.

Liao, T. and Mayne, P.W., 2004. "Cone Penetrometer Measurements During Mississippi

Embayment Seismic Excitation Experiment." *Earthquake Engineering and Soil Dynamics, Geotechnical Special Publication 133*, Paper No. 32.

Losert, W., Geminard, J.-C., Nasuno, S., and Gollbu, J.P., 2000. "Mechanisms for Slow Strengthening in Granular Materials." *Physical Review E*, 61(4), 4060-4068.

Lunne, T., Robertson, P.K., and Powell, J.J.M., 1997. *Cone Penetration Testing in Geotechnical Practice*, Blackie Academic & Professional, London.

Lynch, J.P., Wang, Y., Yi, J., Yun, C.B., Lu, K.C., and Loh, C.H., 2005. "Validation Case Studies of Wireless Monitoring Systems in Civil Structures." Proceedings of the 2nd International Conference on Structural Health Monitoring of Intelligent Infrastructure (SHMII-2), Shenzhen, China, 597-604.

Marchetti, S. (1985). "On the Field Determination of K_0 in Sand." *Proceedings of the 11th International Conference on Soil Mechanics and Foundation Engineering*, San Francisco, CA.

Marchetti, S. (2010). "Sensitivity of CPT and DMT to Stress History and Aging in Sands for Liquefaction Assessment." *Proceedings of the CPT 2010 International Symposium*, Huntington Beach, CA.

Mayne, P.W., 1995. "CPT Determination of Overconsolidation Ratio and Lateral Stresses in Clean Quartz Sands." *Proceeding of International Symposium on Cone Penetration Testing (CPT '95)*, Vol. 2, Swedish Geotechnical Sociedty, Report 3:95, Linkoping, Sweden, 215-220.

Mejia, C., Vaid, Y.P., and Negussey, D., 1988. "Time Dependent Behavior of Sand." *Proceeding of 1st International Conference on Rheology and Soil Mechanics*, Coventry, UK, 312-326.

Mesri, G., Feng, T.W., and Benak, J.M., 1990. "Postdensification Penetration Resistance of Clean Sands." *Journal of Geotechnical Engineering*, 116(7), 1095-1115.

Michalak, A.M., 2009. "CEE570: Introduction to Geostatistics Course Notes." Department of Civil and Environmental Engineering, University of Michigan, Ann Arbor, Michigan.

Miller, H.J., 1994. "Development of Instrumentation to Study the Effects of Aging on the Small Strain Behavior of Sands." Ph.D. dissertation, University of New Hampshire, Durham, New Hampshire.

Mitchell, J.K., 1986a. "Practical Problems from Surprising Soil Behavior." *Journal of Geotechnical Engineering*, 112(3), 259-289.

Mitchell, J.K., 1986b. "Ground Improvement Evaluation by *In situ* Tests." *Proceedings of In Situ '86, Geotechnical Special Publication 6*, 221-236.

Mitchell, J.K., 2004. "Seventeenth Nabor Carrillo Lecture: Time – The Fourth Dimension of Soil Behavior in Geotechnical Engineering." *XXII National Meeting of Soil Mechanics*, Guadalajara, Mexico, 73pp.

Mitchell, J.K., 2008. "Aging of Sand – A Continuing Enigma?" *Proceedings of the 6th International Conference on Case Histories in Geotechnical Engineering*, Arlington, VA.

Mitchell, J., Baxter, C., and Soga, K., 1997. "Time Effects on the Stress-Deformation Behavior of Soils." *Professor Sakuro Murayama Memorial Symposium*, Kyoto University.

Mitchell, J.K. and Santamarina, J.C., 2005. "Biological Considerations in Geotechnical Engineering." *Journal of Geotechnical and Geoenvironmental Engineering*, 131(10) 1222-1233.

Mitchell, J.K. and Soga, K, 2005. *Fundamentals of Soil Behavior*, 3rd Edition, Wiley, New York.

Mitchell, J.K. and Solymar, Z.V., 1984. "Time-Dependent Strength Gain in Freshly Deposited or Densified Sand." *Journal of Geotechnical Engineering*, 110(11), 1559-1576.

Monaco, P., Marchetti, S., Totani, G., and Calabrese, M., 2005. "Sand Liquefiability Assessment by Flat Dilatometer Test (DMT)." *Proceedings of XVI International Conference on Soil Mechanics and Geotechnical Engineering (ICSMGE)*, Osaka, Japan, 4, 2693-2697.

Monaco, P. and Schmertmann, J.H., 2007. "Discussion of 'Accounting for Soil Aging when Assessing Liquefaction Potential' by Evangelia Leon, Sarah L. Gassman, and Pradeep Talwani." *Journal of Geotechnical and Geoenvironmental Engineering*, 133(9), 1177-1179.

Monahan, P.A., Luternauer, J.L., Barrie, J.V., and Clauge, J.J., 2000. "Variation of CPT Tip Resistance with Age and Its Application to Liquefaction Susceptibility Mapping in the Fraser River Delta, BC, Canada." *Proceedings of 6th International Conference of Seismic Zonation*, Palm Springs, Claifornia, 637-642.

Moss, R.E.S., Seed, R.B., Kayen, R.E., Stewart, J.P., Der Kiureghian, A., and Cetin, K.O. (2006). "CPT-Based Probabilistic and Deterministic Assessment of In Situ Seismic Soil Liquefaction Potential." *Journal of Geotechnical and Geoenvironmental Engineering*, 132(8), 1032-1051.

Moss, R.E.S., Thornhill, D.M., Nelson, A.I., and Levulett, D.A., 2008. "Influence of Aging on Liquefaction Potential: Preliminary Results." *Proceedings of Geotechnical Earthquake Engineering and Soil Dynamics (GEESD) IV*, Sacramento, CA.

Munson, P.J. and Munson, C.A., 1996. Paleoliquefaction Evidence for Recent Strong Earthquakes since 20,000 yr BP in the Wabash Valley of Indiana: Final Report, Submitted to the US Geologic Survey. March, 1996, 137p.

Narin van Court, W.A. and Mitchell, J.K., 1994. "Explosive densification: Densification of Loose, Saturated, Cohesionless Soils by Blasting." *Geotechnical Engineering Report No. UCB/GT/94-03*, University of California, Berkeley, California.

Narin van Court, W.A. and Mitchell, J.K., 1998. "Investigation of Predictive Methodologies for Explosive densification." *Geotechnical Earthquake Engineering and Soil Dynamics III, Geotechnical Special Publication No. 75*, Volume 1, P. Dakoulas, M. Yegian, and B. Holtz, eds., 639-653.

Narsilio, G.A., 2006. "Spatial Variability and Terminal Density: Implications in Soil Behavior." Ph.D dissertation, Georgia Institue of Technology, Atlanta, Georgia.

Narsilio, G.A., Santamarina, J.C., Hebeler, T., and Bachus, R., 2009. "Blast Densification: Multi-Instrumented Case History." *Journal of Geotechnical and Geoenvironmental Engineering*, 135(6), 723-734.

Nasipuri, A., Subramanian, K.R., Ogunro, V., Daniels, J.L., and Hilger, H.A., 2006. "Development of a Wireless Sensor Network for Monitoring a Bioreactor Landfill." *Proceedings of GeoCongress 2006*, (D.J. DeGroot, J.T. DeJong, J.D. Frost, and L.G. Baise, eds.), Atlanta, Georgia, DOI 10.1061/40803(187)10.

Ng, N., Berner, P., and Covil, C., 1996. "The Aging Effects of Sands." *Ground Engineering, Geotechnical Aspects of Hong Kong's New Airport*, December, 21.

Ohsaki, Y., 1969. "The Effects of Local Soil Conditions Upon Earthquake Damage." *Proceedings of the Specialty Session 2, Seventh International Conference on Soil Mechanics and Foundation Engineering*, Mexico City, Mexico.

Parsons R.L. and Frost, J.D., 2002. "Evaluating Site Investigation Quality using GIS and Geostatistics." *Journal of Geotechnical and Geoenvironmental Engineering*, 128(6), 451-461.

Pennington, S., Gouvin, P., and Swanson, P., 2007. "Instrumentation During APM Construction at Dulles International Airport." *Proceedings of Field Measurements in Geomechanics 2007*, Boston, MA, DOI 10.1061/40940(307)12.

Phoon, K.K., Quek, S.T., and An, P., 2003. "Identification of Statistically Homogeneous Soil Layers Using Modified Bartlett Statistics." *Journal of Geotechnical and Geoenvironmental Engineering*, 129(7), 649-659.

Phoon, K.K., Quek, S.T., and An, P., 2004. "Geostatistical Analysis of Cone Penetration Test (CPT) Sounding Using the Modified Bartlett Test." *Canadian Geotechnical Journal*, 41, 356-365.

Polito, C.P., 1999. "The Effects of Non-Plastic and Plastic Fines on the Liquefaction of Sandy Soils." Ph.D. dissertation, Virginia Tech, Blacksburg, VA.

Rogers, B.T., Graham, C.A., and Jefferies, M.G., 1990. "Compaction of Hydraulic Fill Sand in Molikpaq Core," *Prediction and Performance in Geotechnique, 43rd Canadian Geotechnical Conference*, Quebec, Canada, 567-575.

Rollins, K.M., and Anderson, J.K.S., 2008. "Cone Penetration Resistance Variation with Time after Blast Liquefaction Testing." *Geotechnical Earthquake Engineering and Soil Dynamics, GSP 181*, (D. Zeng, M.T. Manzari, and D.R. Hiltunen, eds.), DOI 10.1061/40975(318)103.

Rollins, K.M., Ashford, S.A., Land, J.D., and Hryciw, R.D., 2000. "Controlled Blasting to Simulate Liquefaction for Full-Scale Lateral Load Testing." *Proceedings, 12th World Conference on Earthquake Engineering*, New Zealand Society for Earthquake

Engineering, Auckland, New Zealand, Paper 1949.

Rollins, K.M., Lane, J.D., Dibb, E., Ashford, S.A., and Mullins, A.G., 2005. "Pore Pressure Measurement in Blast-Induced Liquefaction Experiments." *Transportation Research Record: Journal of the Transportation Research Board*, Number 1936, Transportation Research Board of the National Academies, Washington, DC, 210-220.

Schmertmann, J.H., 1983. "Revised Procedure for Calculating K0 and OCR from DMT's with ID > 1.2 and Which Incorporates the Penetration Measurement to Permit Calculating the Plane Strain Friction Angle." *DMT Digest No. 1*, GPE, Inc., Gainsville, FL.

Schmertmann, J.H., 1987. "Discussion of 'Time-Dependent Strength Gain in Freshly Deposited or Densified Sand,' by J.K. Mitchell and Z.V. Solymar." *Journal of Geotechnical Engineering*, 113(2), 173-175.

Schmertmann, J.H., 1991. "The Mechanical Aging of Soils." *Journal of Geotechnical Engineering*, 117(9), 1288-1330.

Schmertmann, J.H., Baker, W., Gupta, R., and Kessler, K., 1986. "CPT/DMT QC of Ground Modification at a Power Plant." *Use of In situ Tests in Geotechnical Engineering*, ASTM STP No. 6, 985-1001.

Schnaid, F., 2009. *In Situ Testing in Geomechanics*, 1st Edition, Taylor and Francis, New York.

Seed, H.B., 1979. "Soil Liquefaction and Cyclic Mobility Evaluation for Level Ground During Earthquakes." *Journal of the Geotechnical Engineering Division*, 105(GT2), 201-255.

Skempton, A.W., 1954. "The Pore Pressure Coefficients A and B." *Geotechnique*, IV, 143-147.

Skempton, A.W., 1986. "Standard Penetration Test Procedures and the Effects of Sands of Overburden Pressure, Relative Density, Particle Size, Aging, and Overconsolidation." *Geotechnique*, 36(3), 425-447.

Skov, R. and Denver, H., 1988. "Time-Dependence of Bearing Capacity of Piles." *Proceedings of the 3rd International Conference on Applied Stress Wave Theory to Piles*, 879-888.

Soga, K., 2005. "Time Effects Observed in Granular Materials," *The COE Workshop on Evaluation of Mechanical Behavior of Granular Materials*, Hokkaido University, Sapporo, Japan, February 15, 2005, Lecture 3.

Solymar, Z.V., 1984. "Compaction of Alluvial Sands by Deep Blasting," *Canadian Geotechnical Journal*, 21, 305-321.

Solymar, Z.V., Iloabachie, B.C., Gupta, R.C., and Williams, L.R., 1984. "Earth Foundation Treatment at Jebba Dam Site." *Journal of Geotechnical Engineering*, 110(10), 1415-1430.

Stewart, H.R. and Hodge, W.E., 1988. "Molikpaq Core Densification by Explosives at Amauligak F-24." *Proceedings of the 20th Offshore Technical Conference*, Houston, TX, 23-34.

Swartz R.A., Jun D., Lynch J.P., Wang Y., Shi D., Flynn M., 2005. "Design of a wireless sensor for scalable distributed in-network computation in a structural health monitoring system." *Proceeding of the International Workshop on Structural Health Monitoring*, Stanford, California.

Thomann, T.G., 1990. "Stiffness and Strength Changes in Cohesionless Soils Due to Stress Hisotry and Dynamic Disturbance." Ph.D. dissertation, University of Michigan, Ann Arbor, Michigan.

Thomann, T.G. and Hryciw, R.D., 1992a. "Stiffness and Strength Changes in Cohesionless Soils Due to Disturbance." *Canadian Geotechnical Journal*, 29, 853-861.

Thomann, T.G. and Hryciw, R.D., 1992b. "Discussion of 'Postdensification Penetration Resistance of Clean Sands,' by G. Mesri, T.W. Feng, and J.M. Benak." *Journal of Geotechnical Engineering*, 118(4), 508-511.

Thompson, E.M., Baise, L.G., and Kayen, R.E., 2006. "Spatial Correlation of Shear-Wave Velocity within San Francisco Bay Sediments" *Proceedings of GeoCongress 2006*, (D.J. DeGroot, J.T. DeJong, J.D. Frost, and L.G. Baise, eds.), Atlanta, Georgia, DOI 10.1061/40803(187)134.

Wang, F., Miao, L., and Weihua, L.V., 2010. "Experimental Study on the Creep Behavior of the Yangtze River Sand." *GeoFlorida 2010: Advances in Analysis, Modeling & Design, Geotechnical Special Publication 199*, D. Fratta, A.J. Puppala, and B. Muhunthan, eds., 777-782.

Wang, Y.H. and Tsui K.Y., 2008. "Density Effects on the Aing Behavior of Sands and the Anisotropy of Aging-Induced Stiffness Increases." *Proceedings of Geotechnical Earthquake Engineering and Soil Dynamics (GEESD) IV*, Sacramento, CA.

Wang, Y.H. and Tsui K.Y., 2009. "Experimental Characterization of Dynamic Property Changes in Aged Sands." *Journal of Geotechnical and Geoenvironmental Engineering*, 135(2), 259-270.

Wang, Y.H, Xu, D., and Tsui, K.Y., 2008. "Discrete Element Modeling of Contact Creep and Aging in Sand." *Journal of Geotechnical and Geoenvironmental Engineering*, 134(9), 1407-1411.

Wheeler, P., 1995. "Explosive Issue." *Ground Engineering*, July/August, 25.

Wilson, D., Kutter, B., Ilankathara, M., and Robiadart, C., 2007. "The UC Davis High-Speed Wireless Data Acquisition System." *Proceedings of Field Measurements in Geomechanics 2007*, Boston, MA, DOI 10.1061/40940(307)89.

York, D.L., Brusey, W.G., Clemente, F.M., and Law, S.K., 1994. "Setup and Relaxation in Glacial Sand." *Journal of Geotechnical Engineering*, 120(9), 1498-1513.

Youd, T.L., Idriss, I.M., Andrus, R.D., Arango, I., Castro, G., Christian, J.T., Dobry, R., Liam Finn, W.D., Harder, L.F., Hynes, M.E., Ishihara, K., Koester, J.P., Liao, S.S.C., Marcuson, W.F., Martin, G.R., Mitchell, J.K., Moriwaki, Y., Power, M.S., Robertson, P.K., Seed, R.B., and Stokoe, K.H., 2001. "Liquefaction Resistance of Soils: Summary

Report from the 1996 NCEER and 1998 NCEER/NSF on Evaluation of Liquefaction Resistance of Soils." *Journal of Geotechnical and Geoenvironmental Engineering*, 127(10), 817-833.

Youd, T.L. and Perkins, D.M., 1978. "Mapping Liquefaction-Induced Ground Failure Potential." *Journal of the Geotechnical Engineering Division*, 104(4), 433-446.

Yun, T.S. and Santamarina, J.C., 2005. "Decementation, Softening, and Collapse: Changes in Small-Sgtrain Shear Stiffness in k_0-Loading." *Journal of Geotechnical and Geoenvironmental Engineering*, 131(3), 350-358.